Abdul Shakoor
Kerry Cato   *Editors*

# IAEG/AEG Annual Meeting Proceedings, San Francisco, California, 2018—

# Volume 1

## Slope Stability: Case Histories, Landslide Mapping, Emerging Technologies

IAEG/AEG Annual Meeting Proceedings,
San Francisco, California, 2018—Volume 1

Abdul Shakoor • Kerry Cato
Editors

# IAEG/AEG Annual Meeting Proceedings, San Francisco, California, 2018—Volume 1

Slope Stability: Case Histories, Landslide Mapping, Emerging Technologies

Springer

*Editors*
Abdul Shakoor
Department of Geology
Kent State University
Kent, OH, USA

Kerry Cato
Department of Geological Sciences
California State University
San Bernardino, CA, USA

Cover illustration: Golden Gate Bridge at night. Frederic Prochasson © 123rf.com

# Preface

The XIII IAEG Congress and 61st AEG Annual Meeting, San Francisco, USA, chose *Engineering Geology for a Sustainable World* as the theme for 2018. Based on the topical symposia and technical sessions, the proceedings are organized into six volumes and sub-categories as follows:

Volume 1: Slope Stability: Case Histories, Landslide Mapping, Emerging Technologies
Volume 2: Geotechnical and Environmental Site Characterization
Volume 3: Mining, Aggregates, Karst
Volume 4: Dams, Tunnels, Groundwater Resources, Climate Change
Volume 5: Geologic Hazards: Earthquakes, Land Subsidence, Coastal Hazards, and
             Emergency Response
Volume 6: Advances in Engineering Geology: Education, Soil and Rock Properties, Modeling

Participants of this joint meeting had the option to submit either a full paper or only an abstract. The editors would like to thank the authors for their valuable contributions. One hundred eighty-six full papers were submitted for review, and 153 papers successfully completed the process. Each paper submitted for the proceedings was peer-reviewed by two reviewers. Authors revised their papers in accordance with reviewers' comments. The reviewers, from across the globe, included professional experts as well as authors of other papers. The editors greatly appreciate the help provided by reviewers. A list of reviewers follows.

The editors are also very grateful to Karen Smith and Paisley Cato for their assistance throughout the review process.

Kent, OH, USA                                                                        Abdul Shakoor
San Bernardino, CA, USA                                                                  Kerry Cato
2018

# Organization

**General Meeting Chairs**

Sarah Kalika, Cornerstone Earth Group
Gary Luce, Resource Concepts, Inc.
Coralie Wilhite, United States Army Corps of Engineers

**Field Course Chairs**

Chase White, California Geological Survey
Drew Kennedy, Sage Engineers

**IAEG Planning Committee Heads**

Scott Burns, Portland State University
Jeffrey R. Keaton, Wood

**Proceedings Editors**

Abdul Shakoor, Kent State University
Kerry Cato, Cato Geoscience, Inc./California State University, San Bernardino

**Editorial Assistants**

Karen Smith, Kent State University
Paisley Cato, Cato Geoscience, Inc.

**Short Course Chairs**

E. Morley Beckman, Kleinfelder
Byron Anderson, Kleinfelder
Chrissey Villeneuve, Shannon & Wilson, Inc.

**Technical Program Committee**

Abdul Shakoor, Kent State University
Kerry Cato, Cato Geoscience, Inc./California State University, San Bernardino
William Godwin, Consulting Geologist
Sarah Kalika, Cornerstone Earth Group

**Symposium Chairs**

Robert E. Tepel, Retired Professional Geologist and Certified Engineering Geologist
Brian H. Greene, United States Army Corps of Engineers
Donald Bruce, Geosystems, L.P.
Holly Nichols, California Department of Water Resources
Keith Turner, Colorado School of Mines
Fred Baynes, Consulting Engineering Geologist
Kevin McCoy, Colorado Geological Survey

Hilary Whitney, Environmental Resources Management
Michelle Sneed, United States Geological Survey
Thomas Oommen, Michigan Technological University
Julien Waeber, AECOM
Ed Medley, Consulting Geological Engineer
Mark Bailey, Asbestos TEM Labs
Atiye Tugrul, Istanbul University, Avcilar Campus, Turkey
Lindsay Swain, Dudek
Ike Isaacson, Brierley Associates
Mike Piepenburg, Aldea Services, LLC
Bruce Hilton, Kleinfelder
Anne Rosinski, California Geological Survey
Steve Parry, Parry Engineering Geological Services
Jan Novotny, Ceska Geologicka Sluzba, Czech Republic
Xiaolei Liu, Shandong Provincial Key Laboratory of Marine Environment and Geological
Engineering (Ocean University of China), China

**Field Course Leaders and Contributors**

William Godwin, Consulting Geologist
William McCormick, Kleinfelder
Bradley Erskine, Kleinfelder
Marina Mascorro, Langan
Frank Rollo, Rollo & Ridley
John Egan, Sage Engineers
Ken Johnson, WSP
John Wallace, Cotton, Shires and Associates, Inc.
Ryan Seelbach, Geosyntec
Tom Barry, California Department of Conservation, Division of Oil, Gas and Geothermal
Resources
John Wakabayashi, Fresno State University
Greg Stock, Yosemite National Park
Janet Sowers, Fugro
Jim Lienkaemper, United States Geological Survey
Keith Kelson, United States Army Corps of Engineers
Carol Prentice, United States Geological Survey
Gordon Seitz, California Department of Conservation
Chris Madugo, Pacific Gas & Electric Company
Mike Jewett, Miller Pacific Engineers
Ray Sullivan, San Francisco State University
George Ford, Geosyntec
Wayne Akiyama, APTIM
Ryan Coe, Terracon
Kate Zeiger, AECOM
John Murphy, California State Water Resources Control Board
Jennifer Gomez, Syar Industries
Mike George, BGC Engineering
Nick Sitar, University of California, Berkeley
Peter Holland, California Geological Survey
Chris Hundemer, C2earth
Jake Hudson, Holdrege & Kull/NV5
Shane Cummings, Holdrege & Kull/NV5
Chris Hitchcock, InfraTerra
Roxanne Renedo, BSK Associates
Tim Dawson, California Department of Conservation

Margaret Doolittle, Kleinfelder
Kevin Clahan, Lettis Consultants
Donald Wells, AMEC/Foster Wheeler
Jennifer Dean, California State Water Resources Control Board
Felix Desperrier, Lettis Consultants
Karen Grove, San Francisco State University

**Guest Tour Chairs**

Alice Tepel
Linda Upp

**Publicity Committee**

Nathan Saraceno, DiGioia Gray & Associates
Courtney Johnson, Sage Engineers
Maggie Parks, ENGEO

**Sponsorship Chair**

Courtney Johnson, Sage Engineers

**Technical Session Editing**

Bill Yu, Case Western Reserve University

**Guidebook App**

Clayton Johnson, Golder Associates
Nathan Saraceno, DiGioia Gray & Associates

**Fed IGS**

Jean-Louis Briaud, Texas A&M University

**K-12 Teacher Workshop**

Cynthia Pridmore, California Geological Survey

**Special Event**

E. Morley Beckman, Kleinfelder

**AEG Meeting Manager**

Heather Clark, Association of Environmental & Engineering Geologists

**AEG Headquarters**

AMR Management

# List of Reviewers

David Abbott, USA
Biljana Abolmasov, Serbia
Okechukwu Aghamelu, Nigeria
M. Farooq Ahmed, Pakistan
Paolo Allasia, Italy
Priyanthi Amarasinghe, USA
Sofia Anagnostopoulou, Greece
Pedro Andrade, Portugal
Luis Bacellar, Brazil
Marco Baldo, Italy
Elizabeth Beckman, USA
Zbigniew Bednarczyk, Poland
Eduardo Bergillos Navarro, Spain
David Bieber, USA
Candan BíLen, Turkey
Andrée Blais-Stevens, Canada
Peter Bobrowsky, Canada
Nana Bolashvili, Georgia
James Borchers, USA
Anika Braun, Germany
Stephanie Briggs, USA
Luke Brouwers, United Arab Emirates
Brian Bruckno, USA
Matthias Brugger, Germany
Fintan Buggy, Ireland
Domenico Calcaterra, Italy
Michael Carpenter, USA
Kerry Cato, USA
Andrea Cevasco, Italy
Hannah Chapella, USA
Xiaoli Chen, China
Sibonakaliso Chiliza, South Africa
Jeff Coe, USA
Mike Collins, USA
Brian Conway, USA
Jasper Cook, UK
Isabela Coutinho, Brazil
John Cripps, UK
Balázs Czinder, Hungary
Ranjan Kumar Dahal, Nepal
Jerome De Graff, USA
Rachael Delaney, USA
Artem Demenev, Russia

Diego Di Martire, Italy
Matthys Dippenaar, South Africa
Angelo Doglioni, Italy
Anastasia Dorozhko, Russia
Peter Ellecosta, Germany
Selman Er, Turkey
Olga Eremina, Russia
Georg Erharter, Austria
Moises Failache, Brazil
Andrew Farrant, UK
Zhen Feng, China
Clark Fenton, New Zealand
Maria Ferentinou, South Africa
Kenneth Fergason, USA
Isabel Fernandes, Portugal
Paz Fernandez, Spain
Mohammad Feruj Alam, Bangladesh
Phil Flentje, Australia
Yannis Fourniadis, UK
Edwin Friend, USA
Irina Galitskaya, Russia
George Gaprindashvili, Georgia
George Gardner, USA
Jesus Garrido Manrique, Spain
Eldon Gath, USA
Ben Gilson, UK
Daniele Giordan, Italy
William Godwin, USA
Robert Goldsmith, Australia
Dick Gray, USA
Brian Greene, USA
James Hamel, USA
Hans-Balder-Havenith, Belgium
Greg Hempen, USA
Egerton Hingston, South Africa
Peter Hudec, Canada
Matthew Huebner, USA
Maria Ingunza, Brazil
Upali De Silva Jayawardena, Sri Lanka
Filipe Jeremias, Portugal
Brendon Jones, South Africa
Frank Jordan, USA
Kumud Raj Kafle, Nepal
Sarah Kalika, USA
Efstratios Karantanellis, Greece
Ekaterina Karfidova, Russia
Hamza Karrad, Algeria
Heiko Käsling, Germany
Brian Katz, USA
Katerina Kavoura, Greece
Andrey Kazeev, Russia
Jeffrey Keaton, USA
Klaus-Peterkeilig, Germany
Alexey Kindler, Russia
Matheus Klein Flach, Brazil

Aliki Kokkala, Greece
Goh Thian Lai, Malaysia
Hana Lee, Austria
Nkopane Lefu, South Africa
Leticia Lescano, Argentina
Cheng Li, China
Wenping Li, China
Qian Liu, Austria
José Lollo, Brazil
Silvina Marfil, Argentina
Vassilis Marinos, Greece
Milos Marjanovic, Serbia
Kristofer Marsch, Germany
Pedro Martins, New Zealand
Flora Menezes, Germany
Amira Merchichi, Algeria
Olga Meshcheriakova, Russia
Stuart Millis, Hong Kong
Omar Mimouni, Algeria
Oleg Mironov, Russia
Matthew Morris, USA
Tim Mote, Australia
Elena Mraz, Germany
Marcos Musso, Uruguay
Masashi Nakaya, Japan
Arpita Nandi, USA
Marivaldo Dos Nascimento, Brazil
Monique Neves, Brazil
Holly Nichols, USA
Vanessa Noveletto, Brazil
Takehiro Ohta, Japan
Kazuhiro Onuma, Japan
Thomas Oommen, USA
Rolando Orense, New Zealand
Ibrahim Oyediran, Nigeria
George Papathanasiou, Greece
Steve Parry, UK
Darren Paul, Australia
Osni Jose Pejon, Brazil
Giacomo Pepe, Italy
Regina Pläsken, Germany
Lindsay Poluga, USA
Joaquim Pombo, Portugal
Martin Potten, Germany
Constantin Prins, Germany
Mário Quinta-Ferreira, Portugal
Rute Ramos, Portugal
Emanuele Raso, Italy
Liana Rocha, Brazil
Valéria Rodrigues, Brazil
Michael Rucker, USA
Nicholas Sabatakakis, Greece
Rosanna Saindon, USA
Mahin Salimi, Iran
Ligia Sampaio, Brazil

Paul Santi, USA
Regiane Sbroglia, Brazil
David Scarpato, USA
Malcolm Schaeffer, USA
William Schulz, USA
Jorge Sfragulla, Argentina
Sachin Shah, USA
Abdul Shakoor, USA
Timothy Shevlin, USA
Anna Shidlovskaya, Russia
Roy Shlemon, USA
Zachary Simpson, South Africa
Alessandra Siqueira, Brazil
Young-Suk Song, South Korea
Georg Stockinger, Germany
Alexander Strom, Russia
Wanghua Sui, China
Valentina Svalova, Russia
Debora Targa, Brazil
Ashley Tizzano, USA
Ákos Török, Hungary
Emil Tsereteli, Georgia
Ryosuke Tsuruta, Japan
Atiye Tugrul, Turkey
Alan Keith Turner, USA
Anatilii Tushev, Ukraine
Resat Ulusay, Turkey
Isabella Magalhães Valadares, Brazil
Lazaro Valezuquette, Brazil
J. Louis Van Rooy, South Africa
Ioannis Vazaios, Canada
Marlene Villeneuve, New Zealand
Nicholas Vlachopoulos, Canada
Yasuhiko Wakizaka, Japan
Chester (Skip) Watts, USA
Luke Weidner, USA
Baoping Wen, China
Charles Wilk, USA
Stephen Wilkinson, UK
John Williams, USA
Louis Wong, Hong Kong
Martin Woodard, USA
Richard Wooten, USA
Yang Yang, China
Katherine Yates, New Zealand
Julia Yeakley, USA
Murat Yilmaz, Turkey
Zelin Zhang, China

# Contents

# Rock Mass Characterization of Mount Rushmore National Memorial, Keystone, South Dakota

S. Lindsay Poluga and Abdul Shakoor

## Abstract

The purpose of this study was to characterize the rock mass at the Mount Rushmore National Memorial (MORU) site that exhibits the sculptures of four American presidents (Washington, Jefferson, Roosevelt, and Lincoln) carved in granite rock. In addition to granite, quartz-mica schist and minor outcrops of pegmatite are present within the memorial site. We used both the Rock Mass Rating System (RMR) and Rock Quality System (Q-system) to characterize the rock mass. For collecting the data required for rock mass characterization, we divided the MORU site into four regions. Field investigations for each region included detailed mapping of the discontinuities (orientation, spacing, continuity, aperture, nature of infilling material, presence/absence of water), estimating Rock Quality Designation, and collecting rock samples for laboratory testing. Additionally, we evaluated the degree of rock weathering for each region. In the laboratory, we determined unconfined compressive strength and second-cycle slake durability index values for the granite and schist samples. Both the RMR and Q-systems indicate the granite, schist, and pegmatite classify as fair to good rock. The granite and schist are moderately to highly weathered whereas the pegmatite is moderately to completely weathered. The second-cycle slake durability test results indicate a slight potential for undercutting of granite by schist. Considering the importance of the sculptures, we recommended that differential weathering between schist and granite rock from which the sculptures are carved be monitored on a long-term basis by periodically measuring the depth of undercutting using a tape measure and by maintaining a photographic record.

S. L. Poluga (✉)
The Ruhlin Company, 6931 Ridge Rd., P.O. Box 190
Sharon Center, OH 44274, USA
e-mail: lpoluga@ruhlin.com

A. Shakoor
Department of Geology, Kent State University, Kent, OH 44242, USA
e-mail: ashakoor@kent.edu

## 1 Introduction

The objective of this study was to characterize the rock mass at the Mount Rushmore National Memorial (MORU) site in Keystone, South Dakota, using both the Rock Mass Rating (RMR) system proposed by Bieniawski (1989) and the Rock Mass Quality system (Q-system) developed by Barton et al. (1974). The results were used to evaluate the stability of MORU. The focus of this article is rock mass characterization.

MORU exhibits the sculptures of four well-known presidents, George Washington, Thomas Jefferson, Theodore Roosevelt, and Abraham Lincoln (Fig. 1). Representing the first 150 years of American history, MORU attracts approximately two million visitors annually from all around the world (Graham 2008; Jones 2011; National Park Service 2014). Work on the sculptures, led by Gutzon Borglum, began on August 10, 1927 and finished on October 31, 1941 (Graham 2008; Jones 2011). The sculptures are 18 m high and have an elevation of 1745 m (Graham 2008).

MORU is located in the Black Hills of South Dakota (Fig. 2). The Black Hills, a 200 km × 105 km dome structure elongated in a north–south direction, forms the core of a prominent uplift associated with the Laramide Orogeny (Graham 2008). The Precambrian core of the Black Hills dome is surrounded by concentric rings of Paleozoic and Mesozoic sedimentary rock (Graham 2008). The core is composed mainly of metasedimentary, metavolcanic, and intrusive rocks (Dahl et al. 1993). About 1.7 billion years ago, the Harney Peak Granite, in which the sculptures are carved, intruded the country rock (National Park Service 2005).
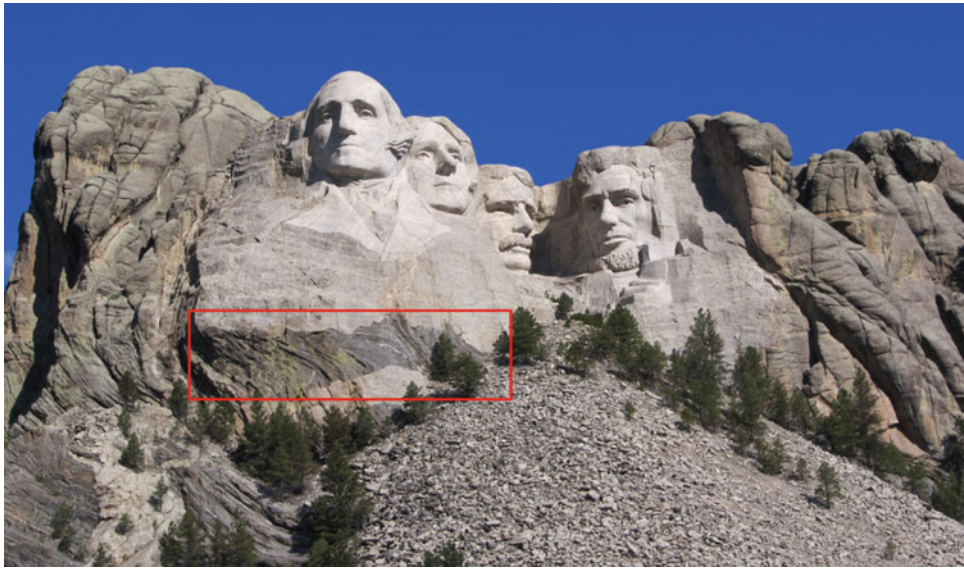
**Fig. 1** Presidential sculptures of Mount Rushmore National Memorial (view to the northwest). The box shows a schist band present within the bust area of Washington's sculpture



**Fig. 2** The location of MORU in the Black Hills of South Dakota (Google Earth Pro 2018)

Very coarse-grained pegmatite sills and dikes are present within the main body of granite (Graham 2008; RESPEC Inc 1989). The other rocks within the memorial are mostly schists with some quartzite present as well (Powell et al. 1865). The schists are older than the granite, but are younger than 2.5 billion years (RESPEC Inc 1989). Figure 1 shows a dark, horizontal band of schist above Washington's waist.

The granite within MORU is highly variable in composition, but is mainly composed of potassium feldspar, albite, and quartz with smaller amounts of perthite and muscovite (Graham 2008; Powellet al. 1865). The average grain size of the minerals in the granite is about 3 mm except perthite which can be several centimeters or longer (Graham et al. 2008; Powell et al. 1865). The primary minerals in the pegmatite are quartz, albite, microcline, and muscovite mica (Graham 2008).

The schist rock at MORU is also highly variable, but is primarily composed of quartz, biotite, and muscovite (Graham 2008). The typical grain size ranges from 0.3 to 1.0 mm and the rock cleaves easily (Graham 2008; Powell et al. 1865). Figure 3 shows pictorial views of the Harney Peak Granite, the pegmatite, and the schist outcrops.

## 2 Field and Laboratory Investigations

### 2.1 Field Investigations

We conducted field investigations to map discontinuities, estimate Rock Quality Designation (RQD), and collect samples for laboratory testing. To accomplish this, we divided the MORU area into four "regions", each with multiple locations where we collected discontinuity data (Fig. 4). The area was divided into regions to identify any variations in the rock present around the MORU site.

Regions were divided based collection locations. Region 1 was located along or near Highway 244, Region 2 was near the MORU Administrative Headquarters, Region 3 was nearest to the sculptures, and Region 4 was located behind the MORU sculptures.

During the mapping process, the parameters for both the RMR system (Bieniawski et al. 1989) and the Q-system (Barton et al. 1974) were measured. Table 1 shows the input parameters, rating calculation procedure, and categorization of the rock mass based on calculated ratings.

We used the window mapping method (Priest 1993; Wyllie 2004) to collect data regarding the following aspects of discontinuities: orientation, continuity, spacing, surface irregularities, nature of the infilling material, and the presence of water. A total of 695 discontinuity measurements were made, 386 for granite, 279 for schist, and 30 for pegmatite. A Brunton compass was used to measure discontinuity orientations. The continuity of the discontinuities was based on visual inspection. Spacing was determined by stretching a tape measure across the face of the slope and recording the distances between all discontinuities intersecting the tape. The average spacing was calculated from these recordings. Surface irregularities were documented as Joint Roughness Coefficient (JRC) using the chart by Barton (1982), found in (Singh and Goel 1999). The JRC values range from 0 to 20 and are determined by assessing the amplitude of the asperities and the length of the joint profile (Singh and Goel 1999). The asperities and length of the joint profile were based on visual inspection. Since a correlation between JRC values and the RMR roughness categories is not available, in this study we classified any JRC value ranging from 0 to 1 as slickensided, JRC values of 1–2 as smooth, JRC values of 2–12 as slightly rough, JRC values of 12–18 as rough, and JRC values of 18–20 as very rough. Infilling material type (if present) was documented by visual inspection as well.
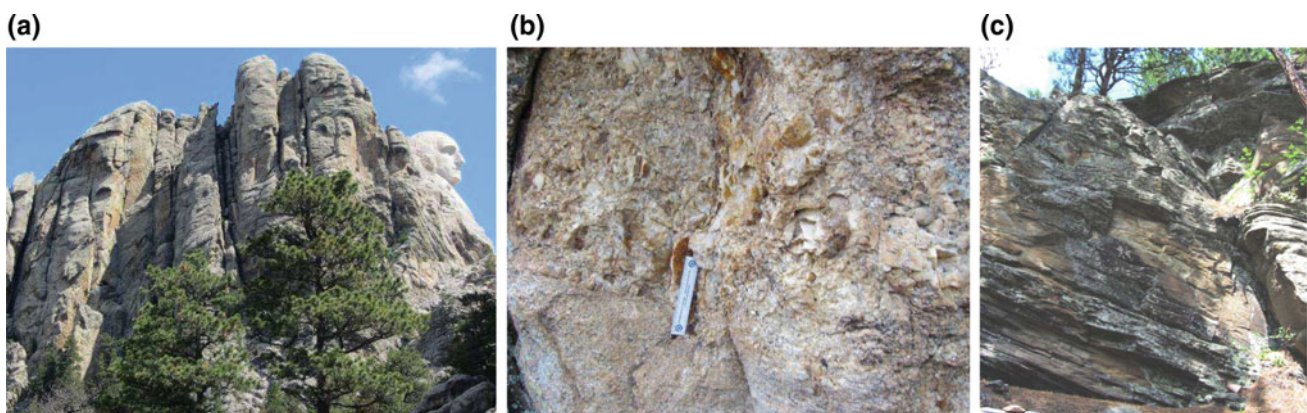


Fig. 3 (a) Harney Peak Granite at MORU (b) a pegmatitic area within the Harney Peak Granite, and (c) a schist outcrop at MORU

**Fig. 4** Locations of the selected sites for discontinuity mapping at MORU. Each location (L) number represents the general area within each region where data were collected. The location numbers were only used for recording purposes. The red star indicates the closest location to the sculptures a granite sample was collected. The polygon indicates the general area of the sculptures. Map created using the ArcGIS® software by (Esri 2014). Point locations were imported from Google Earth (2013). *Note* 1 foot = 0.3048 m
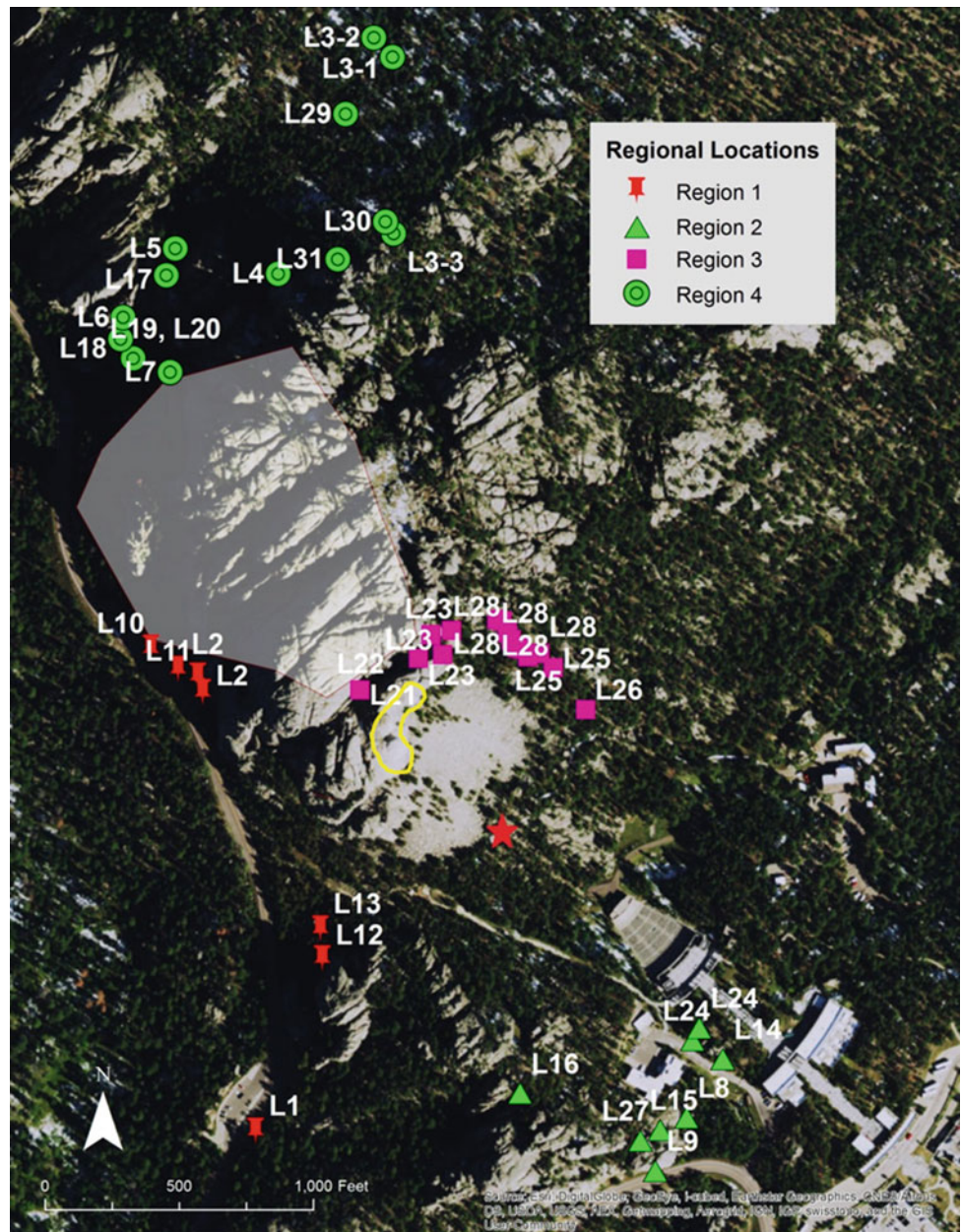


**Table 1** Input parameters for the RMR and Q-systems and rating calculation procedures

|  | RMR system | Q-system |
|---|---|---|
| Input parameters | UCS of intact rock; RQD; spacing of discontinuities; condition of discontinuities; groundwater conditions; orientation of discontinuities | Joint water reduction factor ($J_w$); RQD; joint set number ($J_n$); joint roughness number ($J_r$); joint alteration number ($J_a$); stress reduction factor (SRF) |
| Calculation | Sum of input parameters | $Q = (RQD/J_n)*(J_r/J_a)*(J_w/SRF)$ |

Water presence within the discontinuity was recorded as completely dry, damp, wet, dripping, or flowing (following the RMR system parameters for groundwater). The degree of weathering of discontinuity surfaces was evaluated using the classification chart by Dearman (1976) that divides the degree of weathering into six classes: I (fresh), II (slightly weathered), III (moderately weathered), IV (highly weathered), V (completely weathered), and VI (residual soil).

Both RMR and Q-systems use RQD as an input parameter. Since core data were not available, we used Palstrom's

method (1982) to estimate RQD. This method determines RQD by counting the number of joints within 1 m$^3$ of the rock outcrop. The following equation was used to calculate RQD: RQD = 115 − 3.3 Jv, where Jv = total number of joints per cubic meter (RQD = 100 for Jv < 4.5). Palstrom and Broch (2006) report that for Jv = 4 to 44 the equation, RQD = 110 − 2.5 Jv, gives a better correlation and thus was used when applicable.

In the field, we collected two schist and four granite rock block samples for laboratory testing. The schist samples were collected at L12 and L1 on Fig. 4. The granite samples were collected at L11, L12, and at the location of the red star on Fig. 4.

## 2.2 Laboratory Investigations

We performed laboratory tests to determine UCS and second-cycle slake durability index (Id$_2$). UCS is an input parameter for the RMR system. Both the standard method (ASTM D7012-13) (American Society for Testing and Materials (ASTM) 2013) and the point load test method (ASTM D5731-08) (American Society for Testing and Materials (ASTM) 2008) were used to determine UCS. The slake durability test was conducted following ASTM method D4644-08 (American Society for Testing and Materials (ASTM) 2008). This test is used to evaluate the durability of weak rocks after two cycles of wetting and drying. A band of schist is present within the bust area of the Washington sculpture (Fig. 1). The slake durability test was used to evaluate the potential for differential weathering between the granite and schist rock types.

## 3 Results of Field and Laboratory Investigations

Table 2 provides the highest frequency (from histograms) of each parameter used for the calculations in the rock mass classification systems. The table shows that the discontinuities in the granite and schist in Region 3, the area closest to the sculptures (Fig. 4), are on average more continuous than in other regions. The table also shows that the average discontinuity spacing in the granite in Region 2 is largest, while in the schist it is largest in Region 3. Furthermore, the average JRC is highest for the discontinuities in both the granite and schist in Region 4. Generally, the discontinuities in granite and schist did not have any infilling material and were dry. The granite and schist are moderately to highly weathered, whereas the pegmatite is moderately to completely weathered.

The laboratory test results indicate the granite and schist rocks have average UCS values of 33.4 and 58.0 MPa,

respectively, whereas their Id$_2$ values are 96 and 78.5%, respectively (Poluga 2017). The Id$_2$ indicate a slight potential for undercutting of granite by schist. Considering the importance of the sculptures, we recommended that differential weathering between schist and granite rock from which the sculptures are carved be monitored on a long-term basis by periodically measuring the depth of undercutting using a tape measure and by maintaining a photographic record.

## 4 Rock Mass Characterization

### 4.1 Rock Mass Characterization Using the Rock Mass Rating (RMR) System

We used the RMR system, developed by Bieniawski (1989), to classify the MORU rock in each region. The ratings for each parameter were assigned based on the data summarized in Table 2 and the UCS values determined in the laboratory. The presence of water was negligible in the field; therefore, the rock was rated as dry. If there was a range in the data, an average value was used to assign the rating value. The RQD and spacing value for the pegmatite rock in Region 1 were assigned based on values from Region 2 because they were not measured for this rock in Region 1 (this was also done for Q-value determination using the Q-system). Table 3 presents the final RMR scores for all four regions. Individual RMR parameter ratings can be found in (Poluga 2017). All of the rocks studied in each of the four regions at MORU were classified as good rock. This explains the longevity of this important memorial since its construction and suggests its continued stability in the future, with proper maintenance and monitoring. The engineering properties such as the cohesion of the rock mass and the angle of internal friction of the rock mass can be estimated using the RMR classification. For a rock classified as "good", the estimated rock mass cohesion ranges from 0.3 to 0.4 MPa, and the rock mass angle of internal friction ranges from 35° to 40° (Bieniawski et al. 1989).

### 4.2 Rock Mass Characterization Using the Rock Mass Quality System (Q-System)

We also used the Q-System, developed by Barton et al. (1974), to classify the MORU rock. The parameters for the system were estimated using the data in Table 2, the principal joint sets determined in the study (J$_n$ parameter rating ranged from 4 to 15), and visual estimates made in the field. If there was a parameter value that had a range, the average value was used to assign a rating value. Table 4 summarizes the Q-system ratings and results. Individual Q-system

**Table 2** Highest frequency data obtained from histograms of various discontinuity data

| MORU region | Rock type | Degree of weathering | RQD (%) | Continuity (m) | Spacing | JRC | Infill | Average aperture (mm) |
|---|---|---|---|---|---|---|---|---|
| 1 | Granite | Moderate–high | 90–100 | 3–10 | 0.6–2 m | 2–12 | None | >5 |
| 1 | Schist | High–complete | 25–50; 90–100 | <1 | 200–600 mm | 2–12 | None | 0 |
| 1 | Pegmatite | High–complete | NA | 1–3 | NA | 12–18 | None | 0 |
| 2 | Granite | Moderate | 90–100 | 3–10 | 0.6–2 m | 2–12 | None | >5 |
| 2 | Schist | High | 50–75 | <1 | 0.6–2 m | 1–2 | None | 0 |
| 2 | Pegmatite | High | 75–90 | <1; 1–3; 3–10 | 0.6–2 m | 2–12 | None | 0 to >5 |
| 3 | Granite | Moderate | 90–100 | 3–10 | 0.6–2 m | 1–2; 2–12[a] | None | >5 |
| 3 | Schist | Moderate | 50–75; 75–90 | 1–3 | 0.6–2 m | 1–2 | None | 0 |
| 4 | Granite | Moderate | 90–100 | 3–10 | 0.6–2 m | 18–20 | None | >5 |
| 4 | Schist | Moderate | 75–90 | 1–3 | 200–600 mm | 2–12 | None | >5 |

*Note* [a]indicates the 2–12 category was included for region 3 because even though it was not the highest frequency for the data, its frequency was very close to that of the 1–2 category

**Table 3** Rock mass rating (RMR) scores and description for each rock type in the regions studied at MORU

|  | Region 1 | Region 2 | Region 3 | Region 4 |
|---|---|---|---|---|
| Granite | 70 (good rock) | 71 (good rock) | 70 (good rock) | 74 (good rock) |
| Schist | 66 (good rock) | 70 (good rock) | 72 (good rock) | 65 (good rock) |
| Pegmatite | 76 (good rock) | 72 (good rock) | NA | NA |

*NA* indicates pegmatite data were not collected in these regions

**Table 4** Rock mass quality (Q) system parameter values (Q-value) and classifications

|  | Region 1 | Region 2 | Region 3 | Region 4 |
|---|---|---|---|---|
| Granite | 28 (good rock) | 7 (fair rock) | 7 (fair rock) | 14 (good rock) |
| Schist | 5 (fair rock) | 4 (fair rock) | 7 (fair rock) | 10 (good rock) |
| Pegmatite | 24 (good rock) | 6 (fair rock) | NA | NA |

*NA* indicates pegmatite data were not collected in these regions

parameter ratings can be found in (Poluga 2017). The results indicate that the granite and pegmatite in Region 1 classify as good rock, the granite and schist in Region 4 also classify as good rock, but the rock studied in the other regions at MORU all classify as fair rock. The difference between the two classifications are for the granite rock in Regions 2–3, schist rock in Regions 1–3, and pegmatite in Region 2. The differences may be due to the fact that the SRF value in the Q-system calculations were based on the "low stress, near surface" value as there is not a value for surface excavations because the Q-system was developed for tunneling.

## 5 Conclusions

The main conclusions of this study are: (1) the granite, schist, and pegmatite rock masses studied in the four regions at MORU classify as good rock according to the RMR system and fair to good rock according to the Q-system, and (2) the second cycle slake durability test results indicate a slight potential for undercutting of granite by schist. Due to the importance of the sculptures, it is recommended that differential weathering between schist and granite rock from

which the sculptures are carved be monitored on a long-term basis by periodically measuring the depth of undercutting using a tape measure and by maintaining a photographic record.

# References

American Society for Testing and Materials (ASTM): Standard Test Method for Determination of the Point Load Strength Index of Rock and Application to Rock Strength Classification D5731-08, ASTM International, West Conshohocken, PA (2008). https://doi.org/10.1520/d5731-08, www.astm.org

American Society for Testing and Materials (ASTM): Standard Test Method for Slake Durability of Shales and Similar Weak Rocks D4644-08, ASTM International, West Conshohocken, PA (2008). https://doi.org/10.1520/d4644-08, www.astm.org

American Society for Testing and Materials (ASTM): Standard Test Method for Compressive Strength and Elastic Moduli of Intact Rock Core Specimens Under Varying States of Stress and Temperatures D7012-13, ASTM International, West Conshohocken, PA (2013). https://doi.org/10.1520/d7012, www.astm.org

Barton, N.R.: Shear strength investigations for surface mining. In: Chapter 7, 3rd International Conference on Surface Mining. Vancouver, SME, pp. 171–196 (1982)

Barton, N.R., Lien, R., Lunde, J.: Engineering classification of rock masses for the design of tunnel support. Rock Mech. Rock Eng. 6, 189–239 (1974)

Bieniawski, Z.T.: Engineering Rock Mass Classifications. Wiley, New York, 251 p (1989)

Dahl, P.S., Wehn, D.C., Feldmann, S.G.: The systematics of trace-element partitioning between coexisting muscovite and biotite in metamorphic rocks from the Black Hills, South Dakota, USA. Geochimica et Cosmochimica Acta 57(11), 2487–2505 (1993). https://doi.org/10.1016/0016-7037(93)90412-P

Dearman, W.R.: Weathering classification in the characterisation of rock: a revision. Bull. Int. Assoc. Eng. Geol. 13, 123–127 (1976)

Esri: ArcGIS® desktop release 10.2.2: Computer Software. Available at www.esri.com (2014)

Google Earth Pro: Version 7.1.2.2041. Available at www.google.com/earth/ (2013)

Google Earth Pro: Version 7.3.3.4507. Available at www.google.com/earth/ (2018)

Graham, J.: Mount Rushmore National Memorial Geologic Resource Evaluation Report: natural Resource Report NPS/NRPC/GRD/NRR—2008/038. National Park Service, Denver, Colorado. NPS D-95, June 2008, 36 p

Jones, J.: A symbol of democracy: the Mount Rushmore National Memorial. Civ. Eng. 81(2), 48–51 (2011)

National Park Service.: Geology fieldnotes. Mount Rushmore National Memorial South Dakota (2005). http://www.nature.nps.gov/geology/parks/moru/

National Park Service.: Park statistics. Mount Rushmore National Memorial, South Dakota (2014). http://www.nps.gov/moru/parkmgmt/statistics.htm

Palstrom, A.: The volumetric joint count—a useful and simple measure of the degree of rock jointing. In: Proceedings: fourth International Congress of the International Association of Engineering Geology, Delhi, pp. 221–228 (1982)

Palstrom, A., Broch, E.: Use and misuse of rock mass classification systems with particular reference to the Q-system: tunnels and underground. Space Technol. 21, 575–593 (2006)

Poluga, S.L.: Rock mass characterization and stability evaluation of Mount Rushmore National Memorial, Keystone, South Dakota: Unpublished Master Thesis, p. 352. Kent State University, Kent, OH (2017)

Powell, J.E., Norton, J.J., Adolphson, D.G.: Water Resources and Geology of Mount Rushmore National Memorial, South Dakota: U. S. Geological Survey Water-Supply Paper 1865, 57 p (1973)

Priest, S.D.: Discontinuity Analysis for Rock Engineering. Chapman and Hall, London, 473 p (1993)

RESPEC Inc.: Structural Analysis of Mount Rushmore, Mount Rushmore National Memorial, Keystone, South Dakota: Report RSI/P-358, Prepared by RESPEC Inc., Rapid City, South Dakota, pp. 1–24 (1989)

Singh, B., Goel, R.K.: Rock Mass Classification: a Practical Approach in Civil Engineering. Elsevier, Oxford, 267 p (1999)

Wyllie, D.C., Mah, C.W.: Rock Slope Engineering: Civil and Mining. Spon, London, 431 p (2004)

# Variation in Residual Strength of the Large-Scale Landslides' Slip Zones in the Three Gorges Reservoir of China

Baoping Wen and Boxun Ji

## Abstract

Since water impoundment of the Three Gorges reservoir, more than 200 large-scale existing landslides have reactivated in the reservoir area. It has been extensively recognized that seepage and uplift water pressure following rise and drawdown of the reservoir water played important roles in reactivation of these landslides, while variation of residual strength of landslides' slip zones which were immersed by the reservoir water and its contribution to these landslides' reactivation has been paid little attention. To explore this, residual strength of five large-scale landslides' slip zones in the reservoir area, which were composed of clayey soils with significant amount of gravel, was experimentally investigated after being soaked for different periods. It was found that a significant reduction in residual strength of the landslides' slip zones occurred after being soaked for around 30 days, and very minor reduction occurred after being soaked for a longer period. This indicates that reduction in residual strength of their slip zones may contribute to the landslides' reactivation which occurred during early time of the reservoir's operation. Particle size analysis and water chemical analysis of the slip zones' materials after being soaked suggest that residual strength reduction of the landslides' slip zones may be mainly attributed to slaking of coarse particles, followed by hydration of clay minerals, dissolution of calcite and hydrolysis of feldspar due to soaking.

B. Wen (✉)
School of Water Resources and Environment, China University of Geosciences (Beijing), Beijing, 100083, China
e-mail: wenbp@cugb.edu.cn

B. Ji
Beijing Satcom IOT Technology Development Co., Ltd., Beijing, 100192, China

## 1 Introduction

Residual strength of slip zones of existing landslides is one of the most important parameters to evaluate their reactivation potential and is crucial for understanding their reactivation mechanisms. The materials making up slip zones of existing landslides essentially behave like soils and their residual strength is commonly determined by laboratory reversal direct shear and ring shear, or in situ direct shear tests. It has been extensively studied that residual strength of soils is controlled by both their particle size distribution and shearing rate under saturated and consolidated drained conditions. Previous studies unanimously demonstrated that residual strength of fine grained soils deceases with increasing clay content and the decreasing magnitude varies significantly with soil types and their dominant clay minerals (e.g., Skempton 1985; Wen et al. 2007). Based on a survey of 170 landslides in the Three Gorges reservoir of China, Wen et al. (2007) found that residual strength of these landslides' slip zones are largely dependent on gravel and fines (clays + silts) contents. Relationship between soils' residual strength and shearing rate varies greatly with range and magnitude of shearing rate (e.g., Tika et al. 1996; Kimura et al. 2014). What if soils are soaked for a certain period in addition to saturation, is there any variation in their residual strength? Scarce attention has been paid to this issue. However, this is particularly the case for the existing landslides in a reservoir area where they are immersed more or less by the reservoir water.

The Three Gorge reservoir of China is one of the largest reservoirs in the world, where water level of the Yangtze River raised from 70 up to 175 m. The Three Gorges area has been one of the densest and most frequent landsliding terrains in China due to its adverse landform and geological setting (Li 2002). More than 2490 old landslides have been identified along mainstream of the Yangtze River in the area, among which more than 250 are large-scale with volume greater than 1,000,000 m$^3$ (Li 2002). Thus landslide hazard

has been one of the major concerns to both Chinese government and public. Since water impoundment of the reservoir, more than 200 large-scale old landslides, including those along the mainstream and its attributes, have been reactivated (Huang et al. 2016). It has been extensively recognized by Chinese professionals that seepage and uplift water pressure following rise and drawdown of the reservoir respectively played important roles in reactivation of these landslides (Huang et al. 2016), while variation in residual strength of their slip zones as well as its contribution to the landslides' reactivation has been paid little attention. To explore this, residual strength variation of the slip zones of five large-scale landsides in the Three Gorges area was experimentally investigated after being soaked for different periods.

## 2  Landslides and Their Slip Zones

Five large-scale landslides involved in this study are Tanping (TP), Huangtupo No. 2 (HTP), Lianhuatuo No. 1 (LHT), Xietan (XT) and Qianjingping (QJP) landslides respectively near Badong and Zigui counties of Hubei province. Former four landslides are on the banks of the Yangtze River's mainstream, and the last one is on the bank of the Qinggan River, a tribute of the Yangze River. Volumes of these landslides range from 6,000,000 to 21,000,000 m³. The landslides of TP, HTP and XT were soil slides, which were composed of colluvium and residual soils derived from mudstone, siltstone and marls of Middle Triassic, and sandstone and siltstone of upper Triassic, respectively. The landslides of LHT and QJP were rock slides, which consisted of highly fractured sandstone and mudstone of the middle and lower Jurassic, respectively (Fig. 1).

Slip zones of these landslides were exposed successfully in exploratory adits (Fig. 1). This provided a rare opportunity to collect samples for laboratory study. Due to complex origin of these landslides, occurrence and materials of their slip zones are quite different, nature of each landslide's slip zone is highly inhomogeneous. Basic characteristics of these landslides' slip zones are summarized in Table 1.

## 3  Samples and Testing Method

### 3.1  Samples

Particle size analysis using combined wet sieving and hydrometer method confirmed that particle compositions of the five landslides' slip zones varied in a large range with clay fraction of 11–40%, silt fraction of 12–39%, sand fraction of 15–32% and gravel fraction of 10–35%. Dry densities in average of these landslides' slip zones measured using a few small size undisturbed samples were between 18 and 18.5 kN/m³ (Table 2). Since residual strength of soils is independent of their initial structure (Bishop et al. 1971), the disturbed samples taken from these slip zones were used in this study. After being air-dried and thoroughly mixed, samples from each landslide's slip zone were divided into four groups with different particle compositions. Due to space limited, this paper only presents results of one group samples of each slip zone, which had relatively the least clay and the most gravel content. These samples were numbered following their landslides' name hereafter. Particle size distribution of these samples is shown in Table 2, which were determined following CNS GB/T50123-1999 (SAC et al. 1999). Bulk and clay mineralogy of the samples measured using X-ray diffractometer are given in Table 3. The Yangtze River water near sampling sites was slightly alkaline with very low salinity (Wen et al. 2014). Deionized water was thus used to soak the samples in this study to substitute the river water.



**Fig. 1** Slip zones of the Lianhuatuo (**a**) and Xietan (**b**) landslides
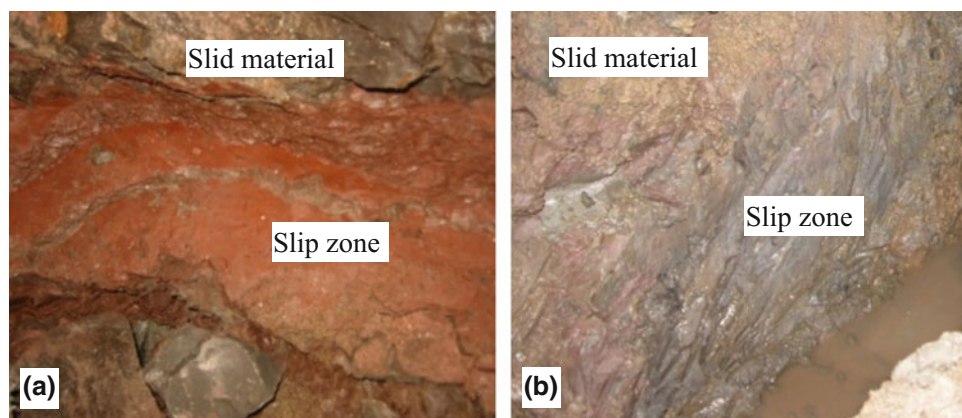
**Fig. 2** Represent curves of shear stress versus shear displacement of the samples tested under different normal stresses: **a** sample HTP; **b** sample LHT
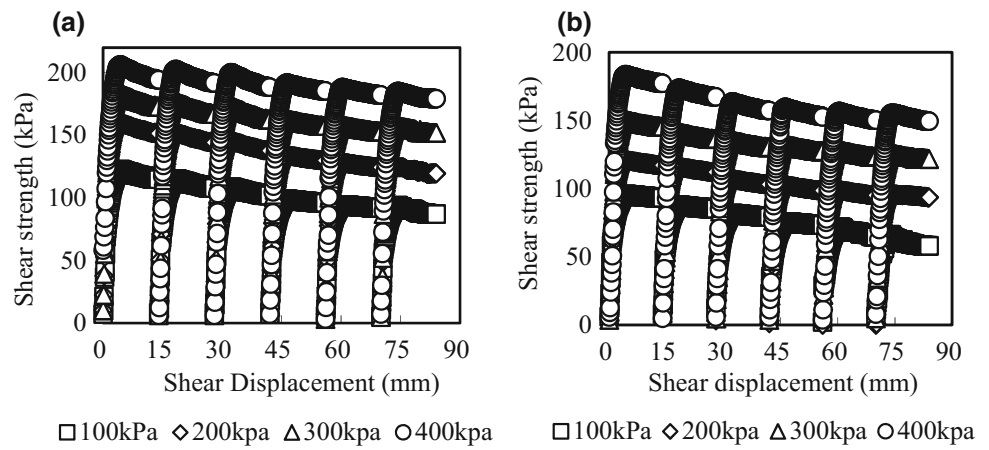


**Table 1** Basic characteristics of the landslides' slip zones in this study

| Landslide | Occurrence | Material |
|---|---|---|
| TP | Along the contact between residual soil and bedrock | Very wet and loose purplish red clayey soil with various amount of fine particles and gravels of mudstone and siltstone fragments. 0.5–2 m thick |
| HTP | Along the contact between residual soil and bedrock | Very wet and loose brownish yellow clayey soil with various amount of fine particles and gravels of marl fragments. 0.3–0.5 m thick |
| XT | Along the contact between highly and moderately weathered rock | Very wet and loose grey clayey soil with various amount of fine particles and gravels of sandstone and siltstone fragments. 0.8–1.0 m thick |
| LHT | Along a bedding weak zone | Very wet and loose red clayey soil with various amount of fine particles and gravels of mudstone and siltstone fragments. 0.5–2 m thick |
| QJP | Along a bedding weak zone | Very wet and loose dark grey clayey soil with various amount of fine particles and gravels of shale and siltstone fragments. 0.1–0.3 m thick |

**Table 2** Basic properties of the samples used in this study

| Sample | Dry density (kN/m$^3$) | Particle size fraction (mm, %) | | | |
|---|---|---|---|---|---|
| | | Clay (>0.005) | Silt (0.005–0.075) | Sand (0.075–2) | Gravel (>2) |
| TP | 18.0 | 13 | 37 | 17 | 33 |
| HTP | 18.2 | 13 | 35 | 20 | 32 |
| XT | 18.3 | 17 | 33 | 20 | 30 |
| LHT | 18.5 | 11 | 39 | 20 | 30 |
| QJP | 18.0 | 20 | 29 | 20 | 31 |

**Table 3** Mineralogical compositions of the samples

| Sample | Bulk sample (%) | | | | | Clay portion (%) | | | | |
|---|---|---|---|---|---|---|---|---|---|---|
| | Quartz | Feldspar | Calcite | Hematite | Clay in total | I/S | I | K | C | K/C |
| TP | 37 | 2 | 2 | / | 58 | 27 | 63 | / | 10 | / |
| HTP | 27 | 1 | 22 | / | 50 | 11 | 73 | / | 16 | / |
| XT | 41 | 2 | 2 | / | 54 | 13 | 58 | / | 29 | / |
| LHT | 44 | 13 | 5 | 2 | 36 | 66 | 15 | 3 | 6 | 10 |
| QJP | 34 | 1 | 4 | / | 61 | 29 | 43 | 28 | / | / |

*Note* *I/S*—Interlayered illite/smectite; *I*—Illite; *K*—Kaolinite; *C*—Chlorite; *K/C*—Interlayered kaolinite/chlorite

## 3.2 Testing Method and Sample Preparation

Due to equipment availability, ShearTrac II, a fully automated reversal direct shear test apparatus (by Geocomp Corporation, USA) was employed to measure the residual strength of the samples. This apparatus is capable of applying a horizontal displacement up to 15 mm and has a square shear box with side length of 15 cm and height of 10 cm, which is suitable for the soils with significant amount of coarse particles. Specimens were sheared back and forth until a steady minimum strength was reached. Although residual strength of clayey soils determined using reversal direct shear test may not be as accurate as that using ring shear test, variation trend of residual strength using the two tests are same (Dewoolkar and Huzjak 2005).

To investigate residual strength variation of the samples with different soaking periods, six groups of specimens were prepared for each sample, each of which included four specimens. For all samples, particles larger than 10 mm were removed considering size of the shear box used in the study. Before being remolded, each sample was wetted with deionized water and stored in an airtight container for at least 24 h. Subsequently the remolded samples were produced by pressing the wet soil to a prescribed unit weight using a customized pressure molder. To eliminate density effect on residual strength of the samples, all the remolded samples had the same unit dry weight of 18 kN/m$^3$. For each sample, the specimens were trimmed from their remolded samples to fit the size of the shear boxes using sample cutters. The specimens confined by cutters and fixed with a customized saturator were saturated using vacuum saturation method following CNS GB/T50123-1999 (SAC et al. 1999). The saturated specimens of each group of the samples were then submerged in containers for 1, 5, 10, 20, 30 and 60 days respectively. Four specimens of each group were fully consolidated under normal stress of 100, 200, 300 and 400 kPa respectively before being sheared. A displacement rate of 0.02 mm/min was adopted in accordance with an estimate following ASTM D3080-98 (American Society for Testing Materials 2000) based on consolidation data to avoid building up of pore water pressure within specimen during shearing. Normal stress applied on each specimen during shearing was consistent with that during consolidation.

## 4 Results

Results of residual shear tests of all samples under different levels of normal stresses displayed very similar characteristics. Representative results of the tested samples are given in Fig. 2. The results show that all samples reached their residual state after six cycles of shearing.

## 4.1 Variation in Residual Strength of the Samples with Soaking Time

Test results disclosed that residual strength of the five samples under each normal stress decreased markedly with soaking time (Fig. 3). Notably for the five samples their residual strength reduction occurred largely when soaking time was less than 30 days, and mostly in a period of 20 days. After being soaked for another 30 days, i.e., 60 days, except sample XT, other samples' residual strength displayed little further reduction. Residual strength of sample XT showed minor reduction after being soaked for another 15 days, i.e., 75 days. This indicates that reduction in residual strength of the landslides' slip zones did occur when they were submerged by the reservoir water and give an implication that their residual strength reduction may be significant after the reservoir impoundment kept for less than 30 days.

## 4.2 Variation in Residual Friction Angle of the Samples with Soaking Time

It has been widely recognized that soil's residual fiction angle is the only significant component of its residual strength because its residual cohesion would be near zero or very little once the residual state has been reached (Skempton 1985; Dewoolkar and Huzjak 2005). The same was found in this study too. Only results of residual friction angles of the five samples are therefore shown in Fig. 4. Similar to their residual strength, residual friction angles of the five samples also displayed pronounced reduction with soaking time (Fig. 4). Reduction trend and magnitude of the samples' residual friction angles with soaking time was equal to their residual strength, showing that significant reduction of their friction angles also occurred when soaking time was less than 30 days, and mostly in a period shorter than 20 days (Fig. 4). Among the five samples, after being soaking for 30 days, residual friction angles of samples TP, QJP and XT reduced 4.3° to 4.4°, and those of samples HTP and LHT reduced around 2°. After being soaked for another 30 days, sample XT's residual friction angle reduced further about 0.5°, and those of other samples reduced less than 0.15° (Fig. 4).

## 5 Discussion

Particle size analysis revealed that these samples had more particles finer than silt and less particles coarser after being soaked for 60 days than those before soaked (Fig. 5). Such phenomenon suggests that slaking of particles coarser than silts occurred when the samples were soaked. Slaking of coarse particles then contributed to residual strength

**Fig. 3** Variation in residual strength of the samples with soaking time
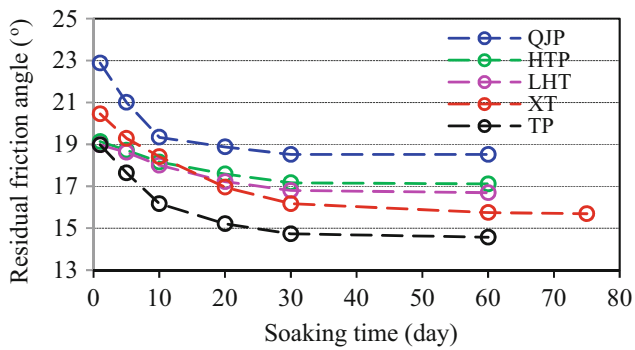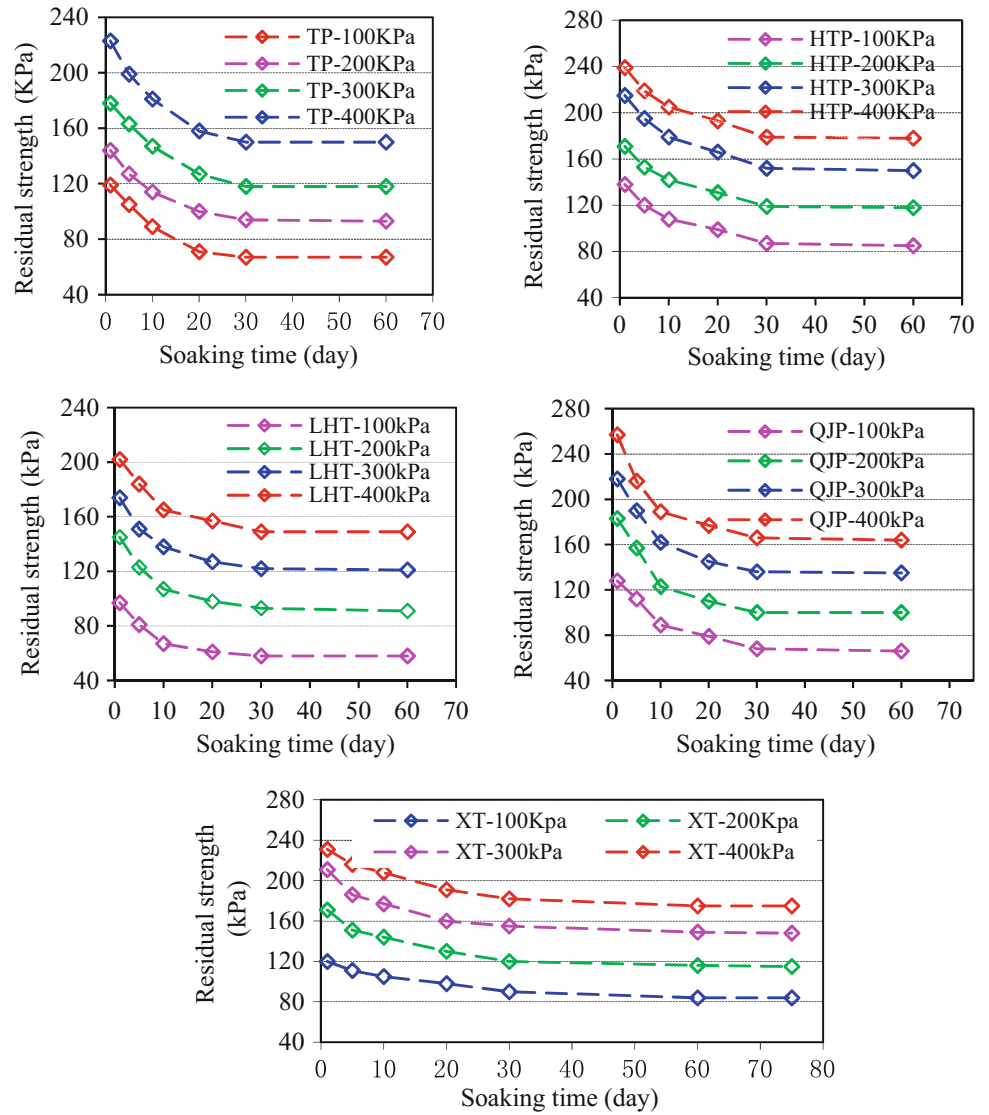


**Fig. 4** Variation of residual friction angle of the samples with soaking time



reduction of the samples after being soaked. It is believed that particles coarser than silt in these samples may be mainly rock fragments which has not fully discomposed yet. The rock fragments may be those cemented by clay, thus being readily slaked after being soaked for a short period. It is noted that after being soaked change of particle size distribution of samples TP, XT and QJP was greater than that of samples HTP and LHT (Fig. 5). This could explain why reduction in residual strength and friction angles of samples TP, XT and QJP was greater than those of samples HTP and LHT.

On other hand, hydration of clay minerals, most likely interlayered illite/smectite and illite, may also occur during

**Fig. 5** Particle size distribution of the samples after and before being soaked
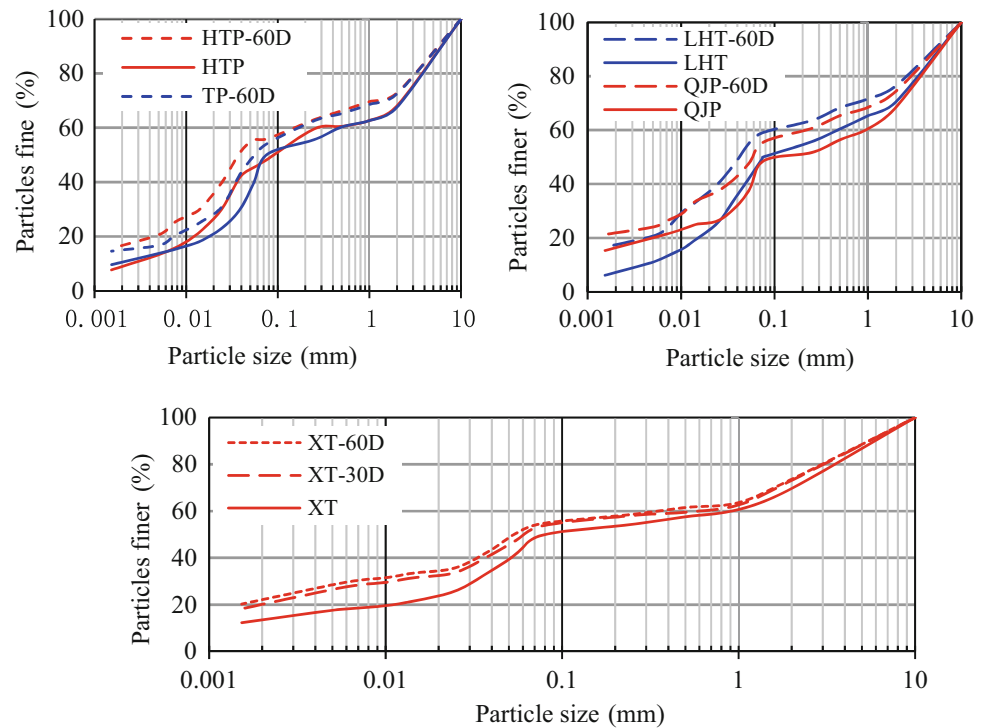


soaking of the samples because these clay minerals readily swell when they encounter water. Referring to mineral composition of these samples (Table 2), it is believed that such effect may be more prevalent within samples TP, XT and QJP than within samples HTP and LHT, as former of which had more clays.

Water chemical analysis of the soaked samples disclosed that there were various ions with low concentration, including $K^+$, $Na^+$, $Ca^{2+}$, $Mg^{2+}$, $HCO_3^-$, $Cl^-$ and $SO_4^{2-}$ and their concentration increased with soaking time. Since deionized water was used for soaking the samples, occurrence of these ions indicates that some chemical reactions also occurred. Consistently for the five samples $Ca^{2+}$ and $HCO_3^-$ were the most abundant among the cations and anions respectively followed by $Mg^{2+}$, $Na^+$, and $K^+$; $Cl^-$ and $SO_4^{2-}$. Recording the constituent minerals of the samples (Table 2), it is deduced that two kinds of chemical interactions between the samples and water may occur: dissolution of some calcites ($Ca^{2+}$ and $HCO_3^-$); hydrolysis of some feldspars (cations of $Na^+$, $K^+$, $Ca^{2+}$ and $Mg^{2+}$), including albite and anorthite. Although calcite is generally recognized to be insoluble, it is known that dissolution of calcite may occur in an open system with circulation of chemical nutrients, like carbon oxide, oxygen and nitrogen. Such system could also accelerate hydrolysis of feldspar. Dissolution of calcite and hydrolysis of feldspar may accelerate slaking of particles coarser than silts within the samples. Variation trend of the ions' concentration in the soaked water suggests that dissolution of calcites and hydrolysis of feldspar with soaking time. Nevertheless their contribution to slaking of coarse particles and in turn to reduction in residual strength of the samples may be very minor.

As a result of combination of the effects discussed above, significant reduction in residual strength of the samples occurred after being soaked, and same for residual strength reduction of the landslides' slip zones after impoundment of the reservoir (Fig. 6).

**Fig. 6** Ion concentration in the soaked water of the samples
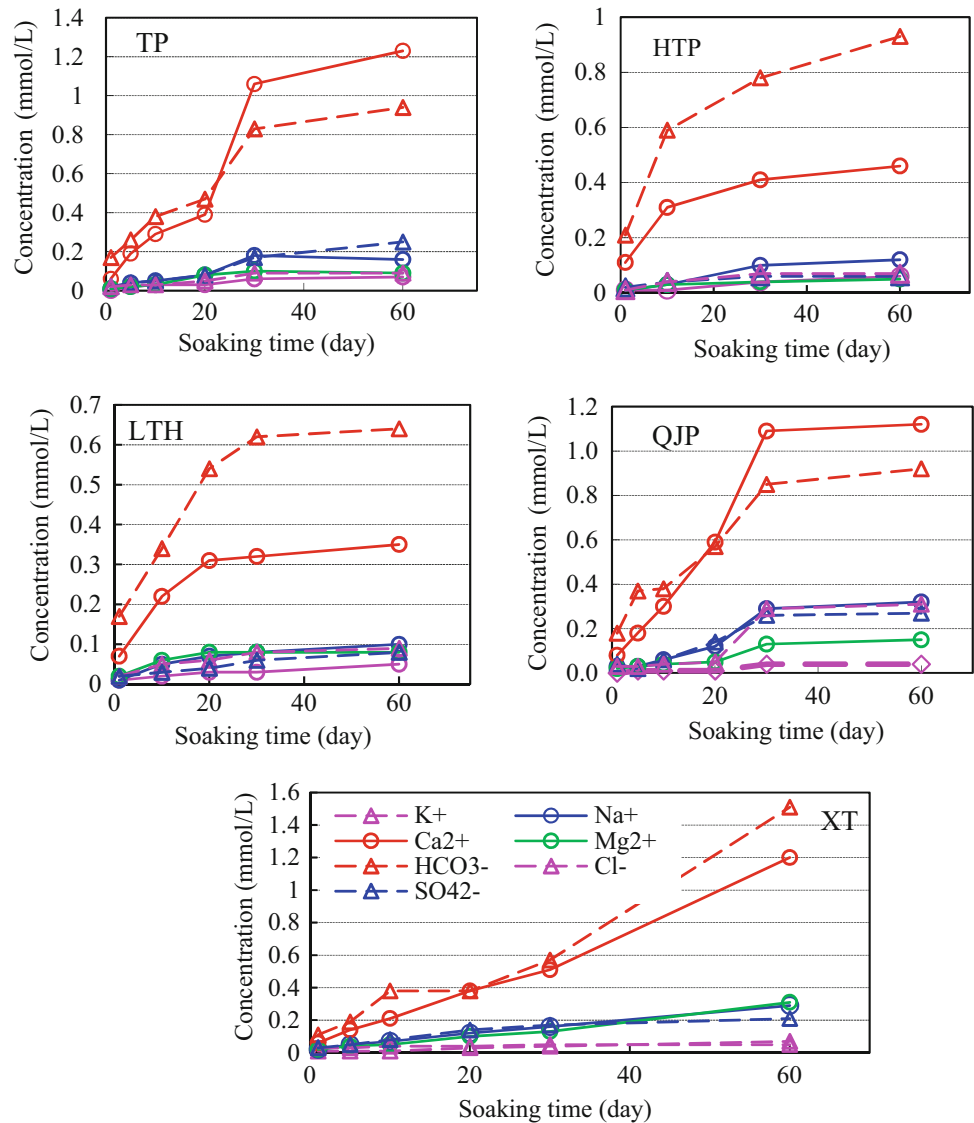


## 6 Conclusions

This experimental investigation clarified that soaking significantly reduces residual strength of the existing large-scale landslides' slip zones in the Three Gorges reservoir area. This supports the assumption that residual strength reduction may have contribution to landslides' reactivation in the reservoir. Following specific conclusions can be drawn from this study:

(1) Residual strength of samples from the five landslides' slip zones significantly reduced after being soaked for 30 days, whilst further reduction was very minor after being soaking for a longer period.

(2) Reduction in residual strength of the samples due to soaking may be associated with slaking of particles coarser than silt, hydration of clay minerals, dissolution of calcite and hydrolysis of feldspar, of which slaking may be predominant, others may be minor.

(3) Results of this study also clarifies that residual strength of clayey soils does vary with soaking time in addition to varying with soil type and shearing rate.

(4) Variation in residual strength of the samples from the five landslides' slip zones after being soaked implies that reactivation of the landslides after the Three Gorges reservoir impoundment for a short period, probably shorter than two months, may be also related to reduction in residual strength of their slip zones in addition to rise and drawdown of the reservoir water level.

# References

American Society for Testing Materials.: Annual Book of ASTM Standards, vol. 04.08: Soil and Rock (I). Standard No. D 3080–98 "Standard Test Method for Direct Shear Test of Soils Under Consolidated Drained Conditions", West Conshohocken, PA, pp. 324–329 (2000)

Bishop, A.W., Green, G.E., Garga, V.K., Andresen, A.: A new ring shear apparatus and its application to the measurement of residual strength. Geotechnique **21**(4), 273–328 (1971)

Dewoolkar, M.M., Huzjak, R.J.: Drained residual shear strength of some claystones from front range, Colorado. J. Geotech. Geoenviron. Eng. **131**(12), 1543–1551 (2005)

Huang, B., Yin, Y., Du, C.: Risk management study on impulse waves generated by Hongyanzi landslide in three gorges reservoir of China on June 24, 2015. Landslides **13**, 603–616 (2016)

Kimura, S., Nakamura, S., Vithana, S.B., Sakai, K.: Shearing rate effect on residual strength of landslide soils in the slow rate range. Landslides **11**, 969–979 (2014)

Li, L.R.: Geological hazards and prevention in the three gorges dam area. Land Resour. **4**, 4–7 (2002). (In Chinese)

Skempton, A.W.: Residual strength of clays in landslides, folded strata and the laboratory. Géotechnique **35**(1), 3–18 (1985)

Standardization Administration of China (SAC): Ministry of Construction, Ministry of Water Resources. China National Standards (CNS) GB/T50123-1999: Standard for soil test method. China Planning Press, Beijing (1999) (In Chinese)

Tika, T.E., Vaughan, P.R., Lemos, L.J.L.: Fats shearing of pre-existing shear zones in soils. Geotechnique **46**(2), 197–233 (1996)

Wen, B.P., Aydin, A., Duzgoren-Aydin, N.S., Li, Y.R., Chen, H.Y.: Residual strength of slip zones of large landslides in the three gorges area, China. Eng. Geol. **93**, 82–98 (2007)

Wen, B.P., Li, H., Ke, K.H.: Effect of soaking on shear strength of weathered argillaceous rocks susceptible to landsliding in the Three Gorges area of China. In: Sassa, K., Canuti, P., Yin Y. (eds.) Landslide Science for a Safer Geoenvironment, pp. 135–140. Springer, Cham (2014)

# Failure Mechanisms of the Lotus Pond Landslide: A Reactivated Landslide from Large-Scale Cataclinal Slope Failure in the Three Gorges Reservoir Area of China

Zhen Feng, Nan Zhang, Hui Yan, and Zhenwei Dai

## Abstract

The Lotus Pond landslide developed in a large-scale cataclinal slope on the right bank of Yangtze River. It has been reactivated by impounding of the Three Gorges Reservoir. Based on geological survey and experimental tests, deformation characteristics and failure mechanism have been ascertained. The Lotus Pond landslide is a successive landslide formed by three periods of sliding at different elevations; the three slides have similar shapes in the longitudinal profile. The toes of the later slides thrust and overlie the heads of the early slides on circular rupture surfaces. However, the successive slides exhibit different failure mechanisms, namely, buckling, planar slide, and "toe-break" mechanisms.

## Keywords

Successive landslide • Buckling failure • Planar slide • Toe-break mechanism

Z. Feng (✉)
Key Laboratory of Neotectonics and Geological Hazards, Ministry of Land and Resources of PRC, Beijing, China
e-mail: fengzhencgs@126.com

Z. Feng
Institute of Geomechanics, Chinese Academy of Geological Sciences, Beijing, China

N. Zhang
China Institute for Geo-Environment Monitoring, Geological Survey, Beijing, China

H. Yan
Geological Survey Team 107, Chongqing Bureau of Geology and Minerals Exploration, Chongqing, China

Z. Dai
Wuhan Center of China Geological Survey, Wuhan, China

## 1 Introduction

The water level of Yangtze River rose from approximately 90 to 145–175 m under the influence of the impounding of the three Gorges reservoir. More than 3000 landslides have been triggered by the impounding of water and fluctuation of the water level, including the Lotus Pond landslide (Yin et al. 2016). The Lotus Pond landslide is located on the south bank of Yangtze River in An'ping, Chongqing. The site is approximately 177 km away from the Three Gorges Dam. It was earlier a relocation site for An'ping town. According to the previous survey reports, the Lotus Pond landslide occurred thousands of years ago. In recent years, however, signs of reactivation of the landslide were observed. For example, a large number of cracks appeared in the ground, causing cracks in the walls of houses and other damage (Dai et al. 2015). This paper introduces the geological conditions and characteristics of the Lotus Pond landslide, and then reveals the failure mechanism that involves multiple periods and modes of slides.

## 2 Geological Background

The rock bedding in the Lotus Pond landslide dips to the north–east. The slope angle reaches up to 38° at the upper part and decreases to 12° at the lower part, where the main area of An'ping town and the constructions are located. The Lotus pond landslide originates from the south–eastern limb of the Guling Syncline, and the landslide is surrounded by folded mountains.

The outcrops around landslide area mainly include the overlying gravel soil of Quaternary Holocene eluvium, depleted landslide accumulations, and the underlying early Jurassic and late Triassic sandstone. The depleted landslide accumulations are composed of partially disturbed sandstone rock mass and basically preserve bedding planes and joints. The bedrock consists of sandstone layers of intermediate to

high thickness and intercalated carbonaceous mudstone layers. The rock mass dips in the direction 320°–350° with dip angles of 20°–28°. Two conjugate sets of joints have developed in the rock mass. The attitude of one joint is 120°–150°∠55°–75° with a spacing of 1.1–2.0 m and that of the other joint is 40°–70°∠60°–85° with a spacing of 1.2–3.3 m.

Pore water is poorly stored within the superficial eluvium and the sliding mass. It is recharged mainly by the infiltration of natural precipitation, and it is discharged as springs and steams at the turning points of the terrace. The underground water table is deep within the depleted mass. In the upper area, the water table is located around the slide plane and is maintained relatively stable despite rainfall and reservoir water fluctuation. On the other hand, at the foot of the slides, the underground water table varies with the reservoir water level.

## 3 Geological Characteristics

The volume of the Lotus Pond landslide is about 90 million m$^3$. The head of the Lotus Pond landslide is approximately 580 m wide, and its toe is approximately 1.1 km wide and is submerged in the Yangtze River (Fig. 1). The elevations of the landslide top at the head and landslide tip at the toe are 705 and 95 m, respectively. The total longitudinal slope length of the displaced mass is approximately 1800 m.

In the longitudinal profile, the ground surface appears as a broken line that can be divided into three sections according to the topography (Fig. 2). Geological surveys revealed that the three sections correspond to three periods of sliding events.

The lower and middle slides have a common slip plane and the upper slide occurs on a deeper weak plane. The slides present a spoon shape in profile that rock mass bedding and rupture surfaces are approximately parallel to the bedrock at the head, and then become sub-horizontal and even reverse to the slope surface at the foot.

The elevation of the head of the lower slide is 300–370 m. The depleted mass is very blocky, but the bedding planes and joints are still preserved. The thickness of the lower slide increases downslope from 50 to 120 m. The elevation of the middle slide ranges from 300 to 530 m. The geological structure and geometric form are similar to the lower slide. The foot is thrust and overlies on the head of the lower slide. The depth of the displaced mass varies from 30 m at the head to 60 m at the foot. Observation of drills and adits revealed that the slip plane is 0.3–0.5 m thick and is constituted of black carbonaceous claystone, generally angular clasts, and rock fragments. It contains approximately 60–80% silt and clay particles. Hence, the slip plane exhibits strong plasticity. Sand clasts and rock fragments were strongly sheared to a size of 0.5–6 cm and arranged directionally. The presence of slickensides and the steeped appearance indicate a landslide direction of 330°–345°, which is in agreement with bedrock bedding direction.

The elevation of the upper slide is 400–705 m. The surface of rupture gradually turns into a circular arc at the foot, and it dips into the slope at an angle of 5°–15° in the toe area. The depth of the depleted mass is approximately 15–30 m. The slip plane is 0.2 m thick on an average, and it is composed of 38–73% silt and clay and also exhibits high plasticity.

The western boundary of the Lotus pond landslide is formed by a north–east-striking ridge (Fig. 1). This ridge obstructs landslide movement in the dip direction. Field investigations revealed that the strata at the ridge is twisted slightly and dips to the north and north–east, while beyond the ridge, the dip direction of the strata is maintained between 330° and 345°. This variation is attributed to the thrust originating from the Lotus Pond landslide. Planar rotation occurred after the initial planar dip slide. Its case is similar to that of the Lianziya perilous rock mass (Yin 1995). The depleted mass slid north–west in the apparent dip direction owing to the obstruction in the west.

## 4 Failure Mechanism and Evolution

The Lotus Pond Landslide was formed by a sequence of three sliding events. ESR dating tests validated that the slip planes of the lower slide, middle slide, and upper slide formed approximately 120–130, 48–68, and 47–51 ka ago, respectively. The three slides clearly involve planar sliding. However, note that the bedrock beneath the rupture surface of the middle slide and upper slide have been barely disturbed, while that at the toe area of the lower slide rock mass is characterized by drag folding strata. It can be inferred that the lower slide underwent buckling failure.

Buckling develops in dip slope of relatively thin-layered strata with no sub-horizontal or gently inclined planes daylighting at the toe. The friction angle of the weak planes should be less than the dip angle so that the overlying rock mass can slip downslope, causing bending deformation. Most assessment methods for buckling failure in dip slope are based on the limit equilibrium technique in combination with Euler's buckling theory (Cavers 1981; Zhang et al. 1994). Using deflection formulas derived from the Euler–Bernoulli beam equation (Roark et al. 2002), a simplified solution can be obtained to calculate the length of the passive segment as follows (Garzon 2016):

**Fig. 1** Geological map of the
Lotus Pond landslide
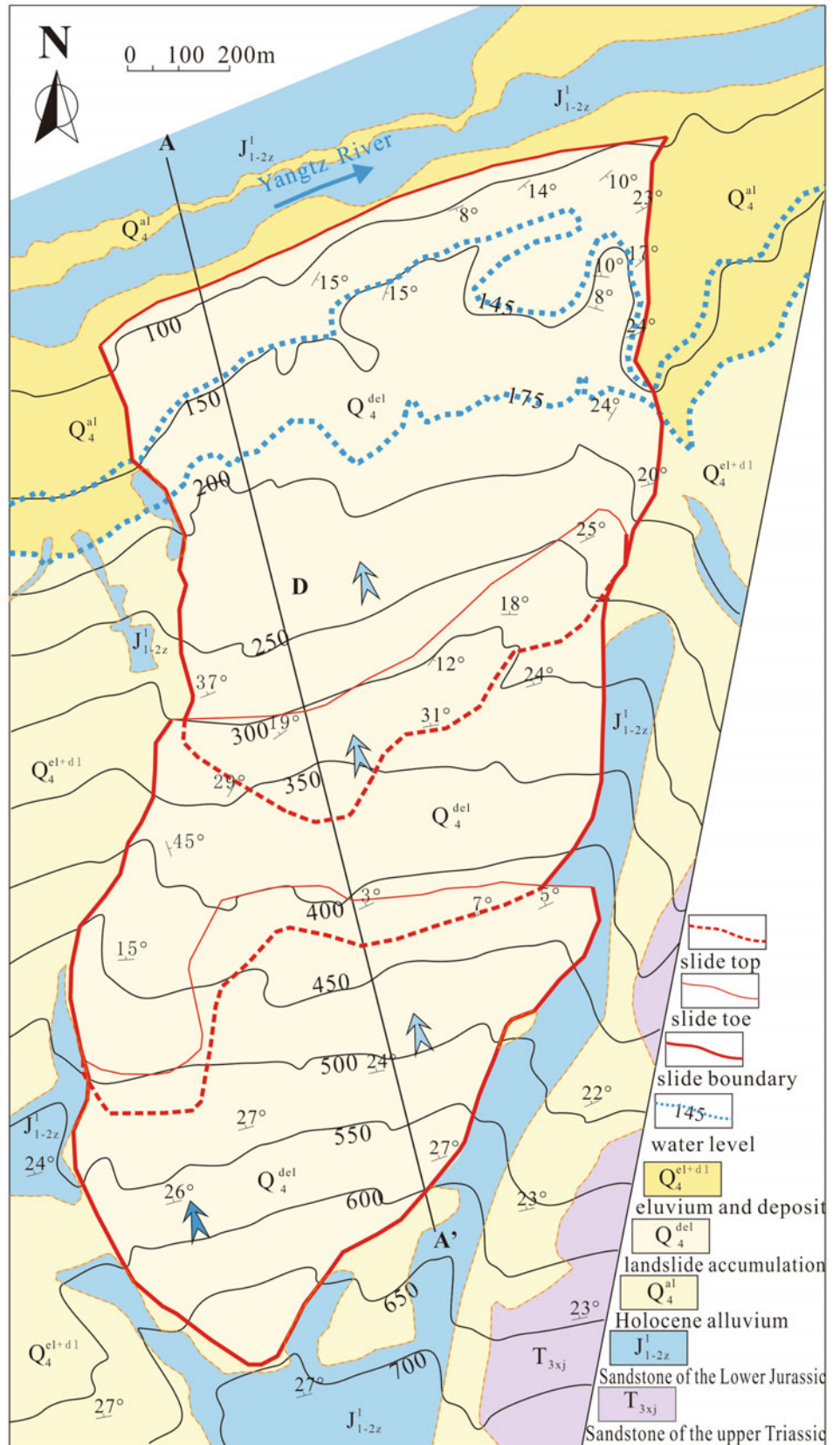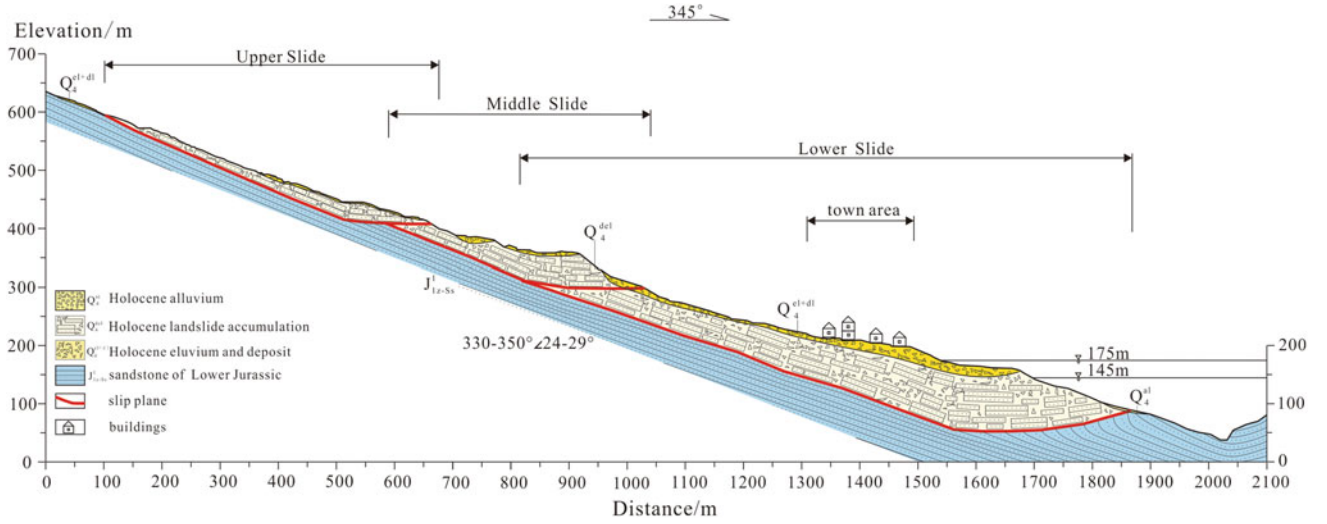
**Fig. 2** Longitudinal profile of the Lotus pond landslide along A − A′

$$l = \sqrt{C_1^2 + 2C_1 L_s} - C_1 \tag{1}$$

$$C_1 = 2.4(\gamma d \sin \alpha - c - \gamma d \cos \alpha \tan \varphi)/\gamma \cos \alpha \tag{2}$$

For slope under buckling failure, the potential; unit weight, $\gamma$; slab thickness, $d$; friction angle of slip plane, $\varphi$; cohesion of the failure surface, $c$; slope angle, $\alpha$; and total slope length, $L_s$, could be obtained to calculate the length of the passive segment $l$ (Sergio 2016). In fact, the depleted range is usually less than the total slope length. Therefore, assessing the slope stability using total slope length is irrational.

For most landslides, determining the total slope length is difficult because of the lack of a significant boundary between the drive segment and passive segment after a large-scale displacement. In addition, the lower part of the passive segment underlies the landslide foot. For simplicity, the length of the surface of rupture, $l_r$, can be considered as the sum of the upper half of the passive segment, $l/2$, and the drive segment. Equation (1) is thus rewritten as Eq. (2).

$$l = \left( \sqrt{C_1^2 + 8C_1 L_r} - C_1 \right)/2 \tag{3}$$

Table 1 summarizes the dimensions and properties of the lower slide. Values of the physical and mechanical properties, such as the unit weight were obtained via experimental

tests. The slab thickness was determined by using drills located at the foot of the landslide. The lengths of the passive segment and drive segment were calculated as 262 and 966 m, respectively. The ratio of slab thickness to total slope length was 0.073.

The depleted range of the lower slide is shorter than the original slope which is approximately 1600 m. A steep scarp was formed after the lower slide occurred around 120–130 ka ago, and it provided a free face for initiating the middle slide. The middle slide occurred approximately 48–68 ka ago, and it proceeded via planar slide on the same slip plane as that of the lower slide. A simple sliding block model can be used for the stability analysis of the planar slide. The factor of safety (FOS) is described as the ratio of resistance to the drive force (Eq. 4). The FOS of planar slide for the lower slide is 0.63, which ensured sufficient drive force leading to the bending and buckling deformation of the passive segment.

$$K = (\gamma d \cos \alpha \cdot \tan \varphi + c)/\gamma d \sin \alpha \tag{4}$$

The middle slide was displaced by more than 200 m so that the foot thrusts and overlies the head of the early slide. The underlying bedrocks were exposed in the upper area of the slope. In contrast to the lower slide, the upper slide underwent a toe-break mechanism instead of buckling failure. The slip plane was buried approximately 30 m deep and

**Table 1** Calculation parameters for the passive segment of the lower slide

| Unite weight $\gamma$ (kN/m³) | Friction angle of slip plane $\varphi$ (°) | Cohesion of the failure surface $c$ | Slope angle, $\alpha$ (°) | Slab thickness $d$ (m) | Length of the surface rupture $l_r$ (m) | Length of the passive segment $l$ (m) |
|---|---|---|---|---|---|---|
| 27 | 37 | 22.4 | 15.2 | 90 | 1100 | 269 |

no joints are daylighted at the toe. The slide underwent cross-layer shear failure right behind the top of the Middle Slide. The stability mainly depends on the strength of the rock mass. The stability number can be used to assess slope stability (Hungr and Evans 2004).

$$N = (\gamma d \sin \alpha - \gamma d \cos \alpha \tan \varphi - c)/\sigma_c \qquad (5)$$

where $\sigma_c$ is the uniaxial compressive strength (UCS) of the rock mass. Three parameters, namely, the UCS of the intact rock, disturbance factor, and geological strength index are needed to derive the UCS using the Hoek–Brown failure criterion (Hoek et al. 2002).

## 5 Conclusion

The Lotus Pond landslide is a reactivated mega rockslide. It originated from a large-scale dip slope with gently inclined rock mass with joints. The displaced materials are mainly composed of fractured sandstone, which maintains partially disturbed structure. The Lotus Pond landslide is controlled by two layers of carbonaceous claystone that evolved into slip planes. In plan view, the apparent dip slide in the northeastern direction is involved because of the obstruction of the ridge in the west.

The Lotus Pond landslide is also known as a successive landslide that was formed during three periods of slides at different elevations. Though the depleted mass of three slides basically preserve the original structures and have similar shapes in the longitudinal profile, the three slides exhibit different failure modes and mechanism. The main

body of the lower slide underwent planar sliding movements, and bending and buckling occurred at the toe. Only planar slide occurred in the case of the middle slide when the weak layer was exposed after the early slide. A toe-break mechanism in combination with planar sliding occurred in the upper slide.

## References

Cavers, D.S.: Simple methods to analyze buckling of rock slopes. Rock Mech. **14**(2), 87–104 (1981)

Dai, Z.W., Yin, Y.P., Wei, Y.J., et al.: Characteristics, origin and formation mechanism of the Outang landslide in the three gorges reservoir area. Hydrogol. Eng. Geol. **42**(6), 145–153 (2015)

Hungr, O., Evans, G.S.: The occurrence and classification of massive rock slope failure. Felsbau **22**(2), 1–11 (2004)

Garzon, S.E.R.: Analytical solution for assessing continuum buckling in sedimentary rock slopes based on the tangent-modulus theory. Int. J. Rock Mech. Min. Sci. **90**, 53–61 (2016)

Hoek, E., Carranza-Torres, C., Corkum, B.: Hoek-Brown failure criterion-2002 edition. In: Proceedings of the North American Rock Mechanics Symposium and Tunneling Association of Canada Conference, pp. 267–273. Toronto, 7–10 July 2002

Roark, R.J., Young, W.C., Budynas, R.G.: Roark's Formulas for Stress and Strain. McGraw-Hill, NewYork (2002)

Yin, Y.P.: Engineering geology design supporting system and reinforcement design for Lianziya Perilous rock mass. Geology Press, Beijing (1995)

Yin, Y.P., Huang, B.L., Wang, W.P., et al.: Reservoir-induced landslides and risk control in three gorges project on Yangtze River, China. J. Rock Mech. Geotech. Eng. **8**(5), 577–595 (2016)

Zhang, Z.Y., Wang, S.T., Wang, L.S.: Analytical Principle of Engineering Geology. Geology Press, Beijing (1994)

# An Example of Landslide Scar Remediation by Soil Bioengineering from Hong Kong

Stuart Millis and Robbin Sotir

## Abstract

The topographic and climatic conditions of Hong Kong result in frequent landslides within the natural hillsides surrounding much of the urbanized and developed area. When failures do occur and in view of the high-risk levels associated with retrogression/reactivation of landslide scars, urgent repair works comprising of debris clearance and minor trimming back and shotcreting of landslide scars are frequently undertaken. Although effective in terms of reducing further landslide risk in the short term, these approaches have resulted in many unsightly concrete 'scars' within otherwise naturally vegetated slopes. To counter these impacts and enhance slope stability in a more sustainable and aesthetic manner, soil bioengineering techniques have recently been implemented within natural terrain catchments on Lantau Island that were subject to intense landsliding and subsequent emergency works in 2008. This paper discusses the design and implementation of some of the techniques implemented for landslide scar.

## Keywords

Landslides • Remediation • Soil bioengineering Hong Kong

## 1 Introduction

The topographic and climatic condition in Hong Kong mean that landslides within natural hillsides are a common phenomenon, with on average about 300 natural terrain landslides occurring each year. The limited availability of land for development means that many of these landslides occur near existing developments and infrastructure, thus presenting hazards not only in terms of the initial landslide occurrence but also the threat of further retrogression of the landslide scar. Because of this, the Government of the Hong Kong Special Administrative Region (HKSAR) frequently implements emergency landslide repair works to ensure public safety through the trimming back of landslide scars as well as the provision of temporary shotcrete surface covers to prevent further erosion and reactivation of the scar. Although effective from a safety management point of view, such actions often result in unsightly and intrusive scars within natural areas.

## 2 The Site

A severe rainstorm in June 2008 resulted in the occurrence of about 1600 natural terrain landslides in Hong Kong, predominantly within the western part of Lantau Island. This included 27 shallow, relatively small volume (<100 $m^3$) debris slides and debris flows within the catchment overlooking the Fat Hwa Yuen Monastery at Upper Keung Shan (Fig. 1). Although no debris directly affected the monastery, the risk of further landslide activity mean that extensive urgent repair works mainly comprising debris clearance and application of 4500 $m^2$ approx. of shotcrete cover was undertaken. This resulted in a notable visual scar within the catchment (Fig. 2).

In view of the rural setting of the site, the catchment at Upper Keung Shan was selected for a pilot study on the implementation of soil bioengineering measures to rehabilitate shotcrete covered landslide scars. In view of the limited track record this approach has in Hong Kong, conventional hazard mitigation using flexible debris resisting barriers at the toe of the catchment was also implemented.

S. Millis (✉)
Ove Arup & Partners Hong Kong Ltd., Hong Kong, China
e-mail: stuart.millis@arup.com

R. Sotir
Robbin B. Sotir & Associates, Inc., Georgia, USA
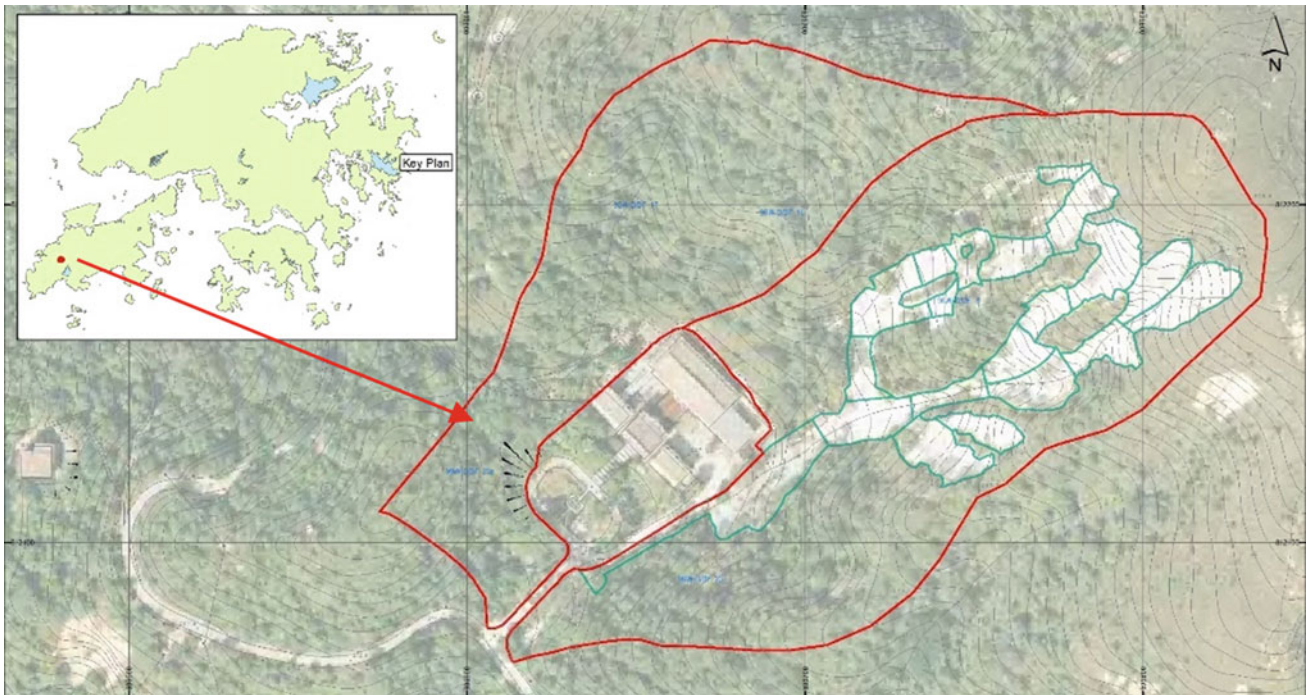
**Fig. 1** Site location



**Fig. 2** Site condition following the implementation of urgent repair works

## 3 Soil Bioengineering

Soil bioengineering can be defined as "the combined application of engineering practices and ecological principles to design and construct systems composed of living plant material, frequently in association with inert materials such as rock, wood, geo-synthetics and geo-composites and other manufactured products, to repair past damage and/or control soil erosion and shallow slope movements" (Gray and Sotir 1996). Soil bioengineering methods can broadly be divided into two categories, namely 'living' and 'combined living and non-living' approaches. The living approach comprises the installation of woody species whilst the combined living

and non-living approach includes the use of inert structural components in combination with the living woody plant parts.

Often misunderstood as a surface vegetation treatment alone, the soil bioengineering approach involves far more than just applying a green vegetative cover to degraded slopes and, through the embedment of cuttings and rooted plants in the ground can be used to augment solutions to many engineering issues (GEO 2006). Such works not only result in the direct strengthening and stability enhancement of the shallow soil profile through the insertion of wooded material, but also utilise plants to provide both surface and sub-surface drainage enhancement as well as surface erosion control.

## 4 Design Objectives

The overall objective of the soil bioengineering measures provided at the Upper Keung Shan site was to rehabilitate a shotcrete landslide scar using a self-sustaining, natural, and aesthetically unobtrusive method that also enhances the shallow stability and safety of the hillslope. The design of the soil bioengineering measures was undertaken with several key objectives in mind, namely:

- To revegetate the hillside to a seemingly natural condition;
- To enhance the shallow soil stability condition within the catchment;
- To provide enhanced run-off control and surface erosion protection; and
- To facilitate the on-site re-use of the excavated shotcrete material as far as practicable.

### 4.1 Selection of Soil Bioengineering Measures

A detailed summary of the soil bioengineering measures suited to the enhancement of slope stability and landslide scar remediation is provided in Gray and Sotir (1996) and GEO (2006). In addition to documenting the type of measures that can be considered for slope stability enhancement, these documents also include matrices highlighting the different slope characteristics (e.g. gradient, soil depth etc.) under which the soil bioengineering measures are considered most effective (Table 1). This matrix provides a valuable framework for the rapid and semi-quantitative development of soil bioengineering strategies for a site. Indeed, the types of soil bioengineering measure considered most suitable for landslide scar remediation at the Upper Keung Shan site were assessed based on this matrix (Tables 1) together with

a site-specific quantification guideline for the various condition/intensity factors (Table 2 refers).

The assessment and strategy development for the Site was undertaken through sub-division and zoning based on the topographic, hydrologic and geomorphologic characteristics of areas within the hillside (Fig. 3). The condition/intensity of each factor within the matrix was then assessed zone-by-zone to identify the most suitable soil bioengineering approach within it.

This revealed that the following measures would prove most effective at the site: (i) live fascines; (ii) hedgelayer; (iii) brushlayer; (iv) woven coir bender fences; (v) live crib walls; (vi) live triple central pole drains; and (vii) vegetated rock drains with live siltation control. The exact layout of the works was determined on-site during detailed site inspections to ensure that due consideration to local conditions and factors such as subsoil geology, drainage condition/concentration and slope aspect/exposure was made. The final layout of the works at Upper Keung Shan is presented in Fig. 4, with schematic details and photographic examples of the measures implemented provided in Fig. 5.

### 4.2 Species Selection

The second key element of the soil bioengineering design was the selection of suitable and appropriate plant species for the various measures included in the design. This was undertaken following the completion of an ecological survey to identify and document the habitat characteristics of the site and surrounding areas in terms of the naturalness and diversity of existing plant species, the presence of any rare or protected species, the recreatability of the of habitat, as well as the overall habitat value. The survey revealed the hillside to primarily comprise open secondary forest with a canopy cover of about 30%. This included medium sized native tress ranging from 3 to 6 m in height and a rich understorey of herbs, ferns and climbers. Aside from grass species, up to 82 vascular species were found within the hillside, including three protected species (i.e. *Arundina graminifolia, Enkianthus quinqueflorus* and *Nepenthes mirabilis*).

Although controlled harvesting of plant material was the preferred approach to the procurement of the stock needed to facilitate the soil bioengineering works, this was precluded by regulators due to a lack of information demonstrating the impacts such harvesting would have on the surrounding ecology. As such it was necessary to construct the soil bioengineering works using nursery grown plants. This imposed a limitation on the variety of plant species available for use by the works, especially given the quantities of material required for such a large hillside. Once again, a matrix chart was developed to define which of the native plant species identified within the hillside were potentially

**Table 1** Soil bioengineering suitability assessment matrix

| Factor | Condition /Intensity | Potentially Suitable Soil Bioengineering Measures | | | | | | | | |
|---|---|---|---|---|---|---|---|---|---|---|
| | | Live Stake | Live Fascine | Pole Drain | Bender Fences | Live Gully Repair | Brush-layer | Hedge-layer | Branch-packing | Live Crib Walls |
| Slope Gradient | Steep | | • | • | | • | | | • | • |
| | Moderate | • | • | • | • | • | • | • | • | • |
| | Gentle | • | • | • | • | n/a | n/a | n/a | n/a | • |
| Slope Height | High | • | • | • | | • | • | • | | |
| | Low | • | • | • | • | | • | • | • | • |
| Soil Depth | Deep | • | • | • | | • | • | • | • | n/a |
| | Moderate | • | • | • | • | • | • | • | • | n/a |
| | Shallow | | • | • | • | • | | | | |
| Soil Permeability | High | | | | | | • | | • | n/a |
| | Moderate | • | • | • | • | • | • | • | • | n/a |
| | Low | • | • | • | • | • | • | • | • | n/a |
| Soil Erodability | High | | • | • | | • | • | | • | n/a |
| | Moderate | | • | • | • | • | • | • | • | n/a |
| | Low | • | • | • | • | • | • | • | • | n/a |
| Soil Strength | Moderate | • | • | • | • | • | • | • | n/a | n/a |
| | Low | n/a | | | • | | • | • | n/a | n/a |
| Moisture | Sub-surface | • | • | • | | • | • | • | • | • |
| | Surface | | • | • | • | • | • | • | | |
| Erosion | - | | • | • | • | • | • | • | • | |
| Mass Movement | Shallow | • | • | • | • | | • | • | • | • |
| | Moderate | | | | | | • | | • | • |

| | |
|---|---|
| • | Potentially suitable soil bioengineering measure for that site condition/intensity |
| (grey) | Unsuitable soil bioengineering measure for that site condition/intensity |
| (green) | Soil Bioengineering Measures suitable for implementation within the Site |

**Table 2** Quantification of key factors/intensity for assessment matrix

| Key factor | Condition/intensity | Classification scheme |
|---|---|---|
| Slope gradient | Steep | Average gradient >40° |
| | Moderate | Average gradient between 15° and 40° |
| | Gentle | Average gradient <15° |
| Slope height | High | >20 m elevation difference within zone |
| | Low | <20 m elevation difference within zone |
| Soil depth | Deep | >5 m soil thickness |
| | Moderate | Between 1 and 5 m soil thickness |
| | Shallow | <1 m soil thickness |
| Soil permeability | High | Permeability $>1 \times 10^{-4}$ m/s |
| | Moderate | Permeability between $1 \times 10^{-4}$ and $1 \times 10^{-6}$ m/s |
| | Low | Permeability $<1 \times 10^{-6}$ m/s |
| Soil erodability | High | Existing erosion rills and/or gullies are present |
| | | Within drainage line or on steep channel bank (>40°) |
| | Moderate | Within 10 m distance of drainage line |
| | | Moderately steep channel bank setting (20°–40°) |
| | Low | Ridge or spur line setting |
| Soil strength | Moderate | Soil is 'medium dense'/'dense' or 'firm'/'stiff' |
| | Low | Soil is 'very loose'/'loose' or 'soft' |
| Moisture | Sub-surface | Soil is damp/seepages present |
| | Surface | Within 10 m of drainage line |
| Erosion | – | Present/not present |
| Mass movement | Shallow | Failures typically <1.5 m in depth |
| | Moderate | Failures between 1.5 and 3 m in depth |
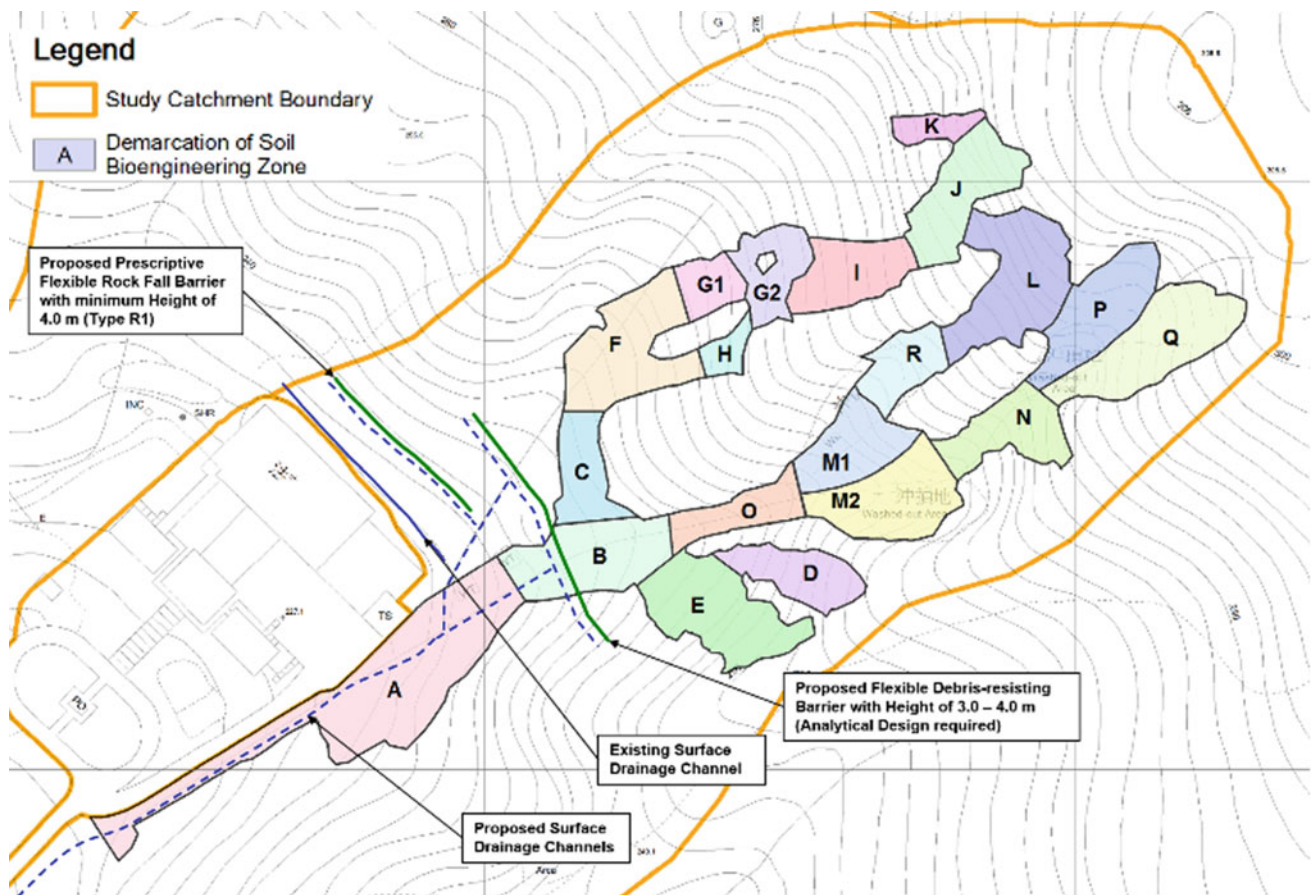
**Fig. 3** Site zoning plan

suited for use as part of the various soil bioengineering measures elected for the site. This matrix facilitated the selection of commercially available plant stock for each soil bioengineering measure such that they could subsequently be specified in the contract specifications.

### 4.3 Construction and Establishment Works

The construction of the soil bioengineering measures was undertaken between June 2016 and September 2017 as part of a larger contract for the construction of natural terrain hazard mitigation works throughout the West Lantau region. The initial works comprised the stripping of the existing shotcrete cover, which was also broken up into gravel and cobble-sized fragments to be re-used through integration within some of the soil bioengineering measures

(e.g. vegetated rock drains, pole drains, live crib walls and live siltation control). This negated the need to remove and dispose of about 250 m³ of construction and demolition material. The shotcrete stripping was undertaken top-down within the catchment, with the soil bioengineering measures following on within those newly exposed areas. The condition of the site following the substantial completion of the works in December 2017 is shown in Fig. 6. This will further develop a more 'green' outlook over time as the soil bioengineering measures further take hold and because of the natural colonisation of vegetation that such measures promote. To further enhance this and ensure the continued performance of the measures throughout the immediate post-construction period, especially throughout the dry winter season experienced in Hong Kong, a solar powered automatic irrigation system has also been provided at the site (Fig. 7).
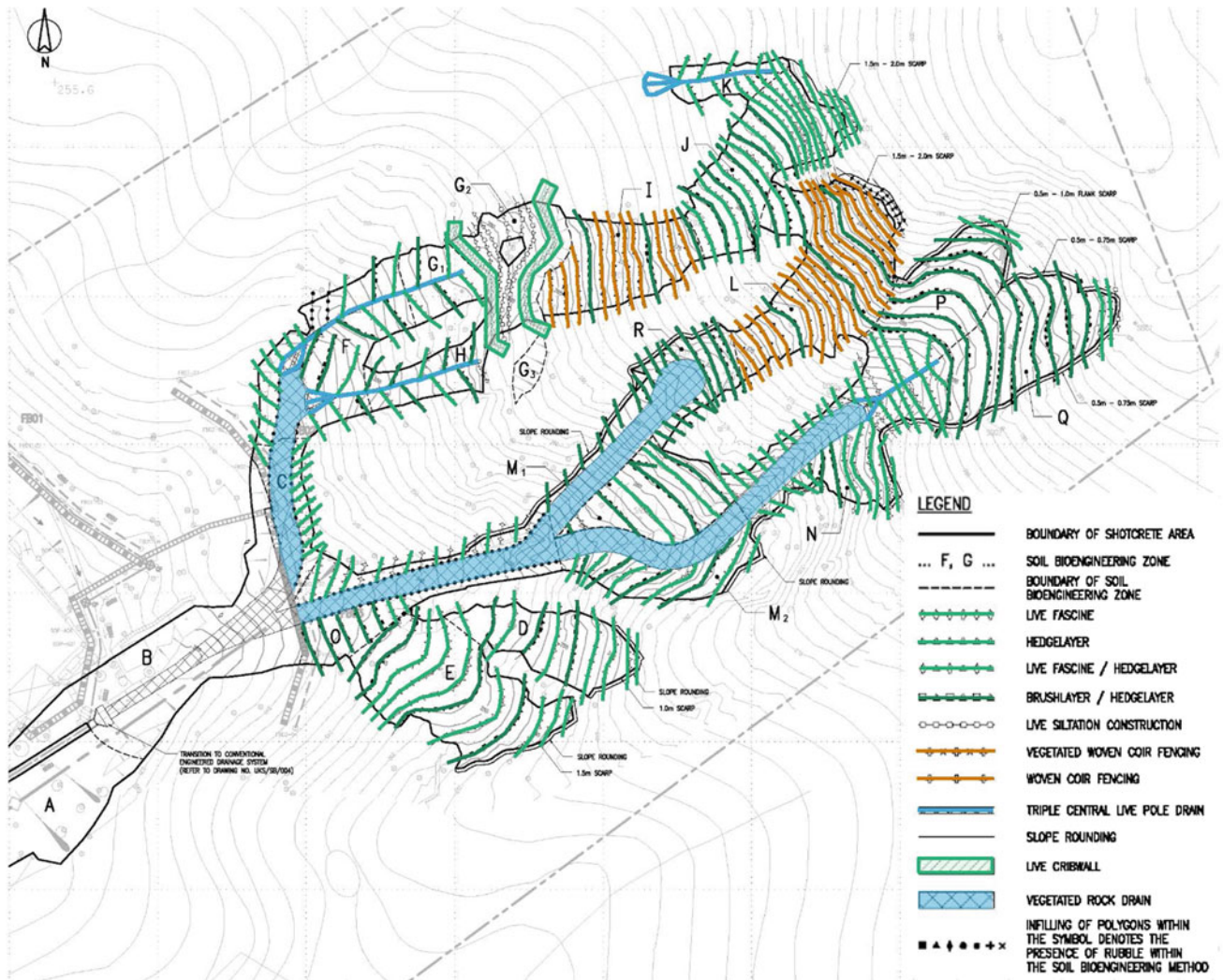
**Fig. 4** Soil bioengineering measures layout

## 5 Performance Evaluation

At the time of writing, the construction of the soil bioengineering works had only been completed a matter of months. As such the overall performance of the measures together with the species survival rate remains to be seen. However, initial observation of field performance during these first few months have been promising (Fig. 8), with erosion control measures appearing to limit run-off rates and erosion during significant rainstorms and the irrigation measures implemented ensuring reasonable survival of plant stock during Hong Kong's dry season.

**Fig. 5** Examples of soil
bioengineering measures
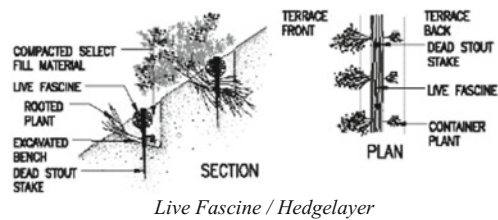


*Live Fascine / Hedgelayer*
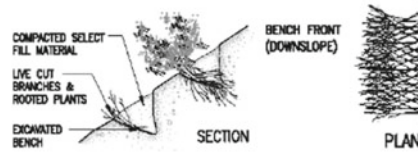


*Brushlayer / Hedgelayer*
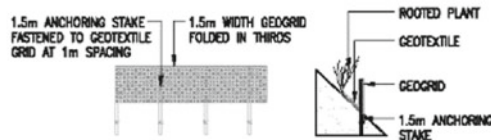


*Woven Coir Fence*
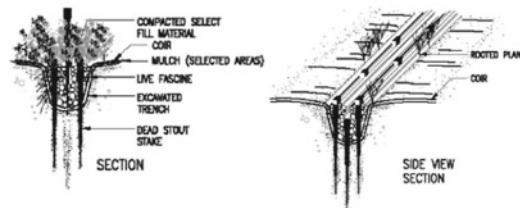


*Vegetated Triple Central Pole Drain*
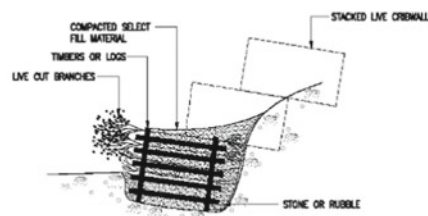


*Vegetated Crib Wall*
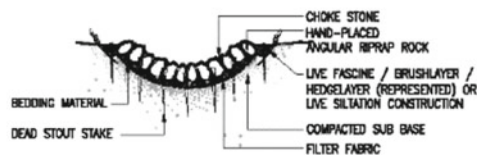


*Vegetated Rock Drain*

**Fig. 6** Pre- and post-construction site conditions
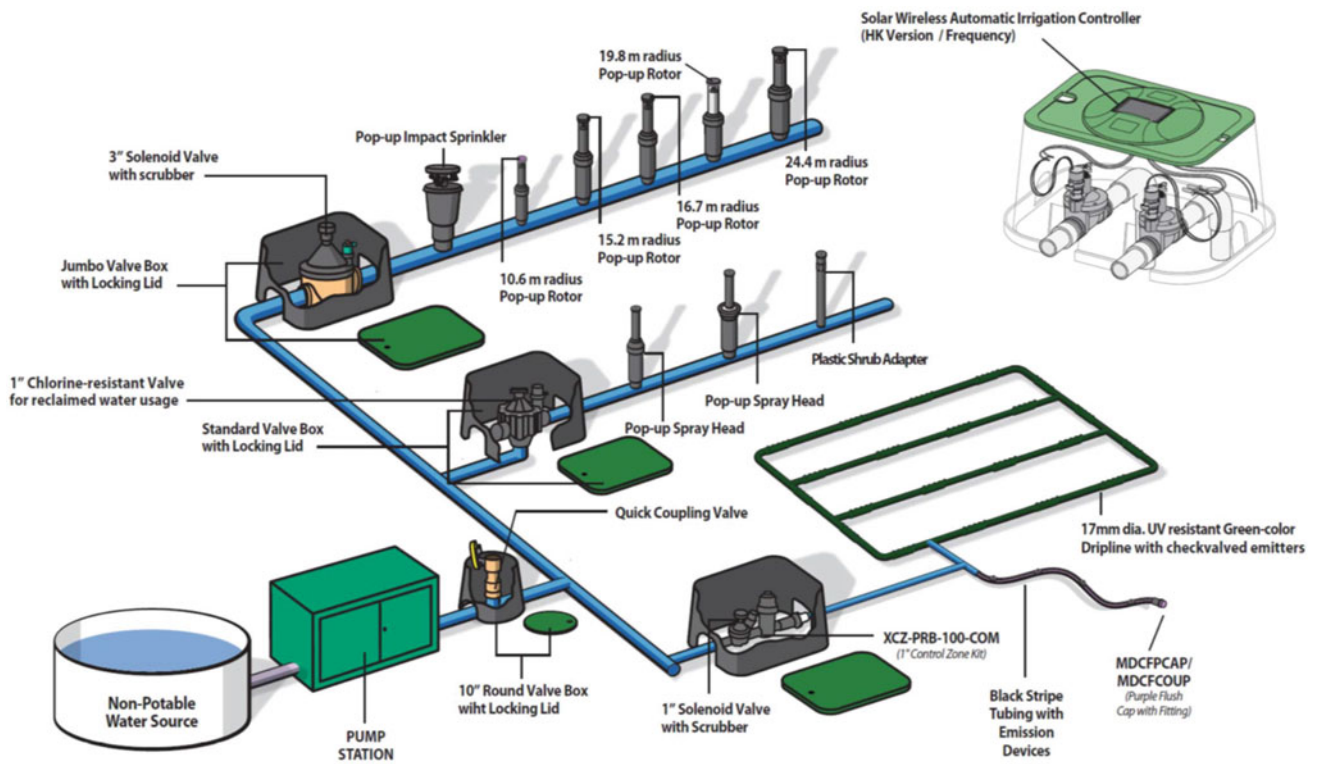


**Fig. 7** Schematic for solar powered irrigation system

**Fig. 8** Examples of soil bioengineering measure establishment

## 6   Conclusions

Landslides are a frequent and largely unavoidable occurrence within Hong Kong's natural hillsides. Historically, shotcrete cover has been used as the main measure to prevent further erosion and retrogression of potentially hazardous landslide scars. Whilst this approach may still be necessary to reduce risks at some sites, the work undertaken at Upper Keung Shan demonstrates that soil bioengineering could provide an alternative approach that provides a more sustainable and eco-friendly long-term solution to the management and control of landslide scar stability.

The soil bioengineering approach appears to offer notable benefits not only in terms of landslide scar remediation, but also in terms of the pro-active and ecological management of erosion control and shallow hillslope stability within hillside catchments prone to landslide occurrence. With such apparent benefits, a more widespread application is anticipated for slope works in Hong Kong in the future.

## References

Geotechnical Engineering Office (GEO, 2006) GEO Report No. 227: Guidelines for Soil Bioengineering Applications on Natural Terrain Landslide Scars. Geotechnical Engineering Office, The Government of the HKSAR (2006)

Gray, D.H., Sotir, R.B.: Biotechnical and Soil Bioengineering Slope Stabilization—A Practical Guide for Erosion Control. Wiley (1996)

# Reinforced Slope Stability Analysis— Application to a Highway in Algeria

Hamza Karrad

### Abstract

Slope design of highway construction projects in Algeria has always been a difficult engineering problem. The study site has a complex geological setting with notable regional seismic events, faults and slope instability. The designed slope is situated over a marl bedrock, Maastrichtian (late Cretaceous) to Paleocene in age, which comprises a monotonous series of marls, locally covered by the recent topsoil layer, fill deposits and the quaternary cover comprising clay-matrix conglomerates which include sandstone gravels and blocks and interbedded layers of resistant travertines. This study describes the stability analysis of a highway slope before and after the reinforcement by a pile wall and prestressed anchor cables using finite element program in two-dimensional problems, i.e. computation of the factors of safety (FOS) and location of the critical slide surface and simulated the various stages of execution of work and the situations for the structural design.

### Keywords

Slope • Safety factor • Reinforcement • Highway • Finite element

## 1 Introduction

The East–West motorway (known also as the A1 highway) is a highway project in Algeria. With a length of 1216 km, the East–West motorway links twenty (20) Algerian cities from Annaba (eastern Algeria) to Tlemcen (west). The East-West Highway is part of the large regional project called the "Autoroute TransMaghrébine" (Maghrebian highway), with a total length of 7000 km and whose construction is ensured by the countries of the Arab Maghreb Union.

The North of Algeria is characterized by widespread landslides. The Geological aspect of northern Algeria can be divided into three structural zones: The Tellian Atlas, the high plateaus and the Saharian Atlas. The Highway passes mainly on the Tellian atlas and the high plateaus. The location of the slope relative to the highway is presented in Fig. 1.

The Algerian active tectonics is located in the northern part of the country, mainly in the Tell. In this region—the boundary between African and Eurasian plates—the tectonic deformation is the expression of the current convergence of these two plates and results in the gradual closure of the Neogene basins and the continued construction of the mountain chain. This regional geodynamic context has engendered a set of tectonic structures with high seismic activities, as indicated by the frequent earthquakes recorded in the Algerian territory in the recent past. The geological aspect of northern Algeria is shown in Fig. 2.

This paper presents the stability analysis of the designed slope before and after the reinforcement with pile wall and prestressed anchor cable using computer programs PLAXIS (Brinkgreve 2002). For the design of the anchored pile wall were used models of finite elements that simulated the various stages of execution of work and the situations for the structural design (Askri 1995).

## 2 Geological Setting

Algeria's tectonic structure is subdivided into two major structural units which are separated by the South Atlas fault:

- Northern Algeria, mainly affected by Alpine tectonics.
- The Saharan Platform, a relatively stable area where tectonic activity is low.

H. Karrad (✉)
University of Batna, Batna, Algeria
e-mail: karrad-hamza@hotmail.fr

**Fig. 1** Slope location on the east–west highway (Algeria)
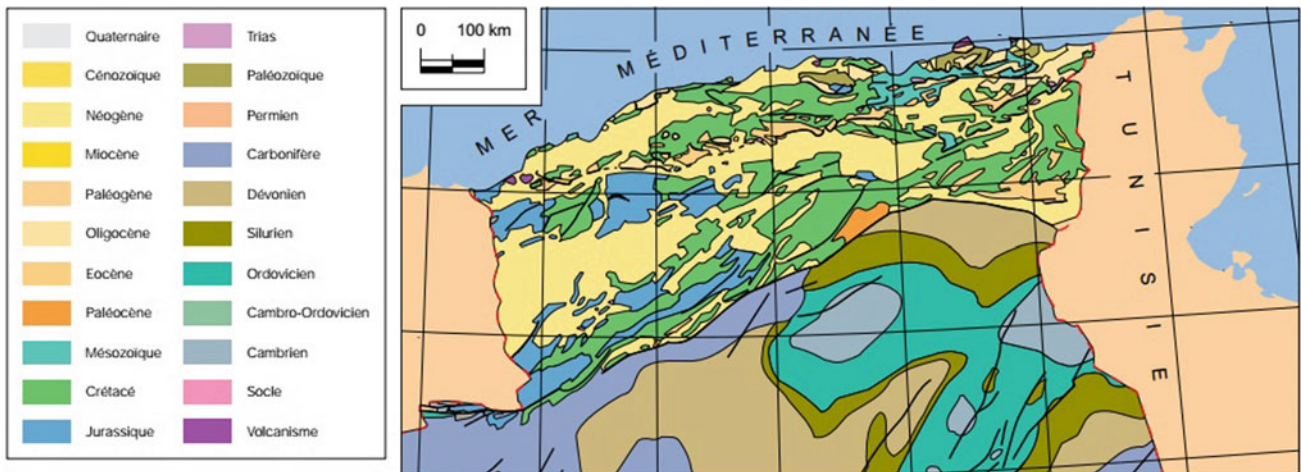


**Fig. 2** The geological aspect of northern Algeria

The region on which the project is constructed is located in the Northern part of Algeria and exactly in the Tellian Atlas (Tell) domain and into the Alpine tectonic unity which is separated from the relatively stable Saharan Platform by the South Atlas fault shown in Fig. 3.

Northern Algeria is delineated by the following features, separated by tectonic structures (overthrusts and nappes) and differentiated by structural background and geomorphologic evolution:

- The Saharan Atlas, a mountain range of Alpine origin to the south.
- Large plains in the center such as the Oran Meseta to the west and Ain Regada highs to the east.
- The Tellian Atlas (Tell), a complex area comprising a succession of nappes set in place during the Lower Miocene to the north.
- Late Neogene basins such as the Chelif Basin or the Hodna.

The Saharan platform is comprised of a Precambrian basement covered by transgressive Phanerozoic sediments. Different tectonic elements delimit sedimentary basins in which the lithostratigraphy is more or less complete. Since the highway is constructed in an active landslide area, a pile wall was constructed to stabilize the ground. The geological and geotechnical conditions of the pile walls were accessed via the interpretation of the results of the carried according survey. Additionally, laboratory tests were also performed on the samples collected in the boreholes.

The topsoil and fill deposits are predominantly composed of clay and sands with lower percentages of the gravel and silt fractions. The characteristic unit weight of these deposits is 19.5 kN/m³. The following classification and physical characteristics for the quaternary cover: grain size analysis—predominance of the gravel, cobble and sand sizes, plasticity–non-plastic, unit weight: 21.0 kN/m$^{-3}$.

The marl bedrock has a particle size distribution with the predominance of the silt and clay fractions, a plasticity index

**Fig. 3** The geological units of Algeria

within the 20–40% interval at the shallow layers (upper 2 m) and 15–28% below 2 m depth, an activity index is in most cases below 0.75, thus having an inactive clay fraction with no swell potential, a characteristic unit weight of 20.5–21.5 and 23 kN/m$^3$ for the shallow layers (0–10 m depth) and deep layers, respectively.

According to the available geological geotechnical data, the pile wall intercepts the following geotechnical layers shown in Figs. 4 and 5:

- The topsoil layer and the fill deposits presenting poor geotechnical characteristics, usually in a loose to medium density state.

- The ancient quaternary cover, which is in a medium density state at the lower elevation areas, very dense at higher elevation areas and with a rock behavior varying from "very weak" to "weak" at the interbedded layers of resistant travertines.
- The marl residual soil, which state varies from a "very soft" to "stiff" consistency.
- The completely weathered marl bedrock of very stiff to hard consistency.
- The moderately weathered and highly fractured marl bedrock with an "extremely weak" to "very weak" rock.

**Fig. 4** Geological section of the slope
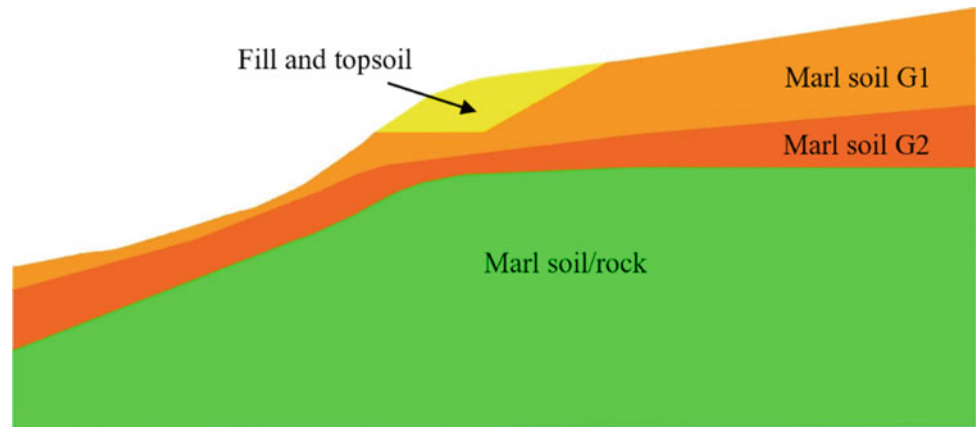


**Fig. 5** Geometry model
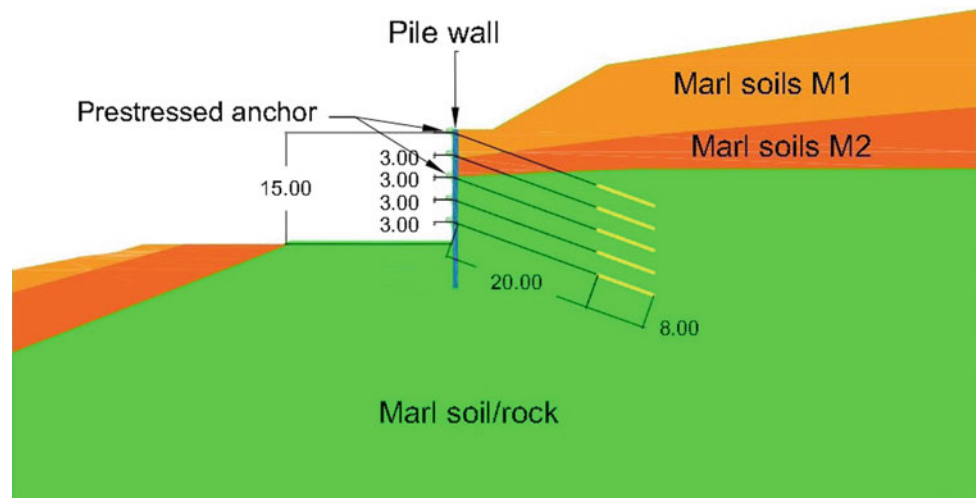


**Table 1** The adopted geotechnical parameters

| Materials | $\gamma$ (kN/m$^3$) | $c'$ (kPa) | $\varphi'$ (°) | $\nu$ (-) | E (MPa) |
|---|---|---|---|---|---|
| Fill and topsoil | 21 | 0 | 36 | 0.3 | 30 |
| Marl soils G1 | 20.5 | 5 | 28 | 0.3 | 15 |
| Marl soils G2 | 20.5 | 15 | 28 | 0.3 | 40 |
| Marl soil/rock | 21 | 40 | 28 | 0.28 | 90 |

The analysis and interpretation of the geotechnical data, and with the aid of proven, valuable in practice correlations, it was possible to establish the following main geotechnical parameters that are sown in Table 1 with:

γ   Specific weight [kN/m$^3$].
c′   Effective cohesion [kPa].
φ   Angle of effective friction [°].
ν   Poisson's ratio [-].
E   Young's modulus [MPa].

## 3 Modelling

The pile wall is designed using the finite element software (Plaxis) for soil analyses. The finite element type is a plane strain 15-node triangular element. The soil is modeled in accordance with the parameters defined in Table 1. The constitutive model for all geo-materials is The Hardening-Soil model. Material properties used for input appear in Table 2. The mesh density is increased in the zone through

**Table 2** Geotechnical parameters used in numerical model

| Material | $\gamma$ (kN/m$^3$) | $c'$ (kPa) | $\phi'$ (°) | $\nu$ (-) | $E_{50}^{ref}$ (MPa) | $E_{oed}^{ref}$ (MPa) | $E_{ur}^{ref}$ (MPa) |
|---|---|---|---|---|---|---|---|
| Fill and topsoil | 21 | 0 | 36 | 0.3 | 30 | 30 | 90 |
| Marl soils M1 | 20.5 | 5 | 28 | 0.3 | 15 | 15 | 75 |
| Marl soils M2 | 20.5 | 15 | 28 | 0.3 | 40 | 40 | 200 |
| Marl soil/rock | 21 | 40 | 28 | 0.28 | 90 | 90 | 450 |
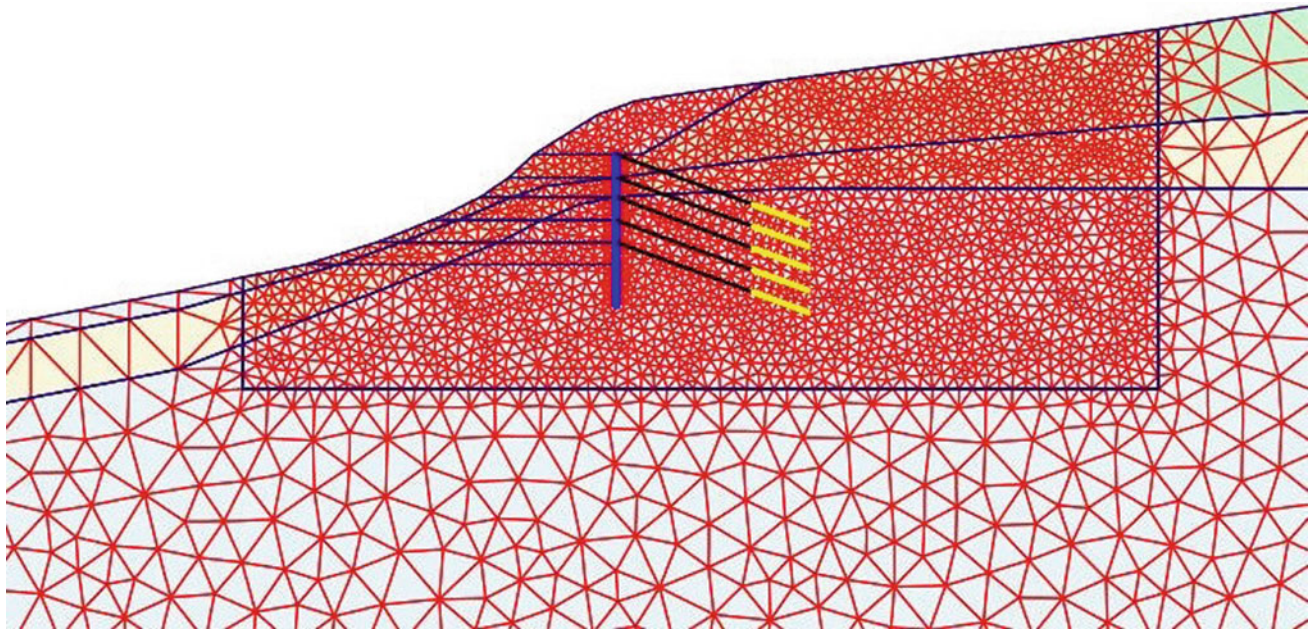


**Fig. 6** Finite element mesh of PLAXIS 2-D model, initial conditions

which the critical slope failure plane is expected to pass. The finite element mesh is illustrated in Fig. 6. The drained static stability analysis is naturally carried out as an effective stress analysis, with effective strength properties and all materials set to Drained. The pile wall is defined as an elastic beam with a maximum yielding moment. The anchors are modeled as elastic elements in the static load case where the maximum anchor force is determined. The phreatic surface at some 5 m below ground (Hamza and Djaafar 2017).

The slope reinforced by a wall of concrete piles, with height above the platform is 15.0 m. If the height exceeds 6 m, the wall will be anchored. The depth of the foundation piles in conjunction with the length and strength of anchors are designed to meet the global equilibrium standards with small deformations. In the construction process we considered progressive excavation limited to a maxim height of 3.0 m. The foundation is indirect with a 0.80 m diameter piles. The anchor has a bond length with 8 m and an unbounded length of 20 m. The structural security checks were performed accordingly to the European Codes (Eurocode 7) (Comité Européen de Normalization (CEN) 1997).

Security checks were carried out to ensure the overall stability of equilibrium of the piles and anchors, as well as to obtain the state of deformation.

The computations were made during different phases of construction. The first phase is the creation of the work platforms and the digging and filling of the piles. Next, the piles are trimmed. The next phase is the construction of the beams and the prestressing of the first level anchors. The next level anchor cannot be excavated until the preceding level anchor is prestressed. The works progress like mentioned until the lower beam is completed.

The material factors for effective strength properties are $\gamma_{\tan(\varphi')} = \gamma_c = 1.25$ according to Table A.4 of the Eurocode (Comité Européen de Normalization (CEN) 1997), while the material factor for undrained shear strength is $\gamma_{cu} = 1.4$. Because Plaxis 2D scales effective and undrained material factors with the same factor, it is necessary to scale artificially the undrained strength with the factor 1.25/1.4 = 0.893 before the phi-c reduction is used. This will have the effect that a reduction factor of 1.25 will correspond to a material factor of 1.25 on $\tan(\varphi')$ and 1.40 on cu. The phi-c reduction

**Table 3** Construction phases and phi/c reduction analyses to determine material safety factors

| Phases | Material safety factors anchors 600 kN | Material safety factors anchors 350 kN |
|---|---|---|
| Critical failure surface for the slope | 1.05 | 1.05 |
| First excavation | 1.23 | 1.23 |
| Installation of pile walls | 1.21 | 1.21 |
| Second excavation and installing the first anchor | 1.28 | 1.24 |
| Third excavation and installing the second anchor | 1.29 | 1.30 |
| Next excavation stage and installing the next anchor | 1.32 | 1.31 |
| Next excavation stage and installing the next anchor | 1.29 | 1.33 |
| Last excavation stage and installing the next anchor | 1.34 | 1.20 |
| Installing the lowest anchor | 1.40 | 1.24 |

factor corresponding to failure found in Plaxis is called Msf and has to comply with Msf $\geq$ 1.25, as (cu modified) characteristic values have been used as input.

The parameters on Table 2 are:

$E_{50}^{ref}$    Secant stiffness in standard drained triaxial test.
$E_{oed}^{ref}$    Tangent stiffness for primary oedometer loading.
$E_{ur}^{ref}$    Unloading/realoading stiffness.

The Plaxis calculations are done in the following stages, from in situ geometry to final geometry:

- Defining first excavation stage (work platforms are made for the execution of the concrete piles)
- Defining model geometry (soil layers, ground parameters, structure parameters)
- Defining first excavation stage Defining water table
- Defining second excavation stage and installing the first anchor

- Defining third excavation stage and installing the second anchor
- Defining the next excavation stage and installing the next anchor
- Defining the last excavation stage and installing the lowest anchor.

Security checks were carried out to ensure the overall stability of equilibrium of the wall and anchors, as well as to obtain the state of safety factor. The calculations for all steps are summarized in Table 3 and Figs. 7, 8, 9, 10, 11, 12, 13 and 14, where calculated safety factors Msf from phi-c reduction can be found. The results of the friction circle analysis are now presented. Two stages have been analyzed (during and at the end of construction), this has resulted in values of MSf larger than the required value of 1.25 of the Eurocode requirements (Comité Européen de Normalization (CEN) 1997) as shown in Fig. 15. The Reinforced Slope

**Fig. 7** Critical failure surface for the slope
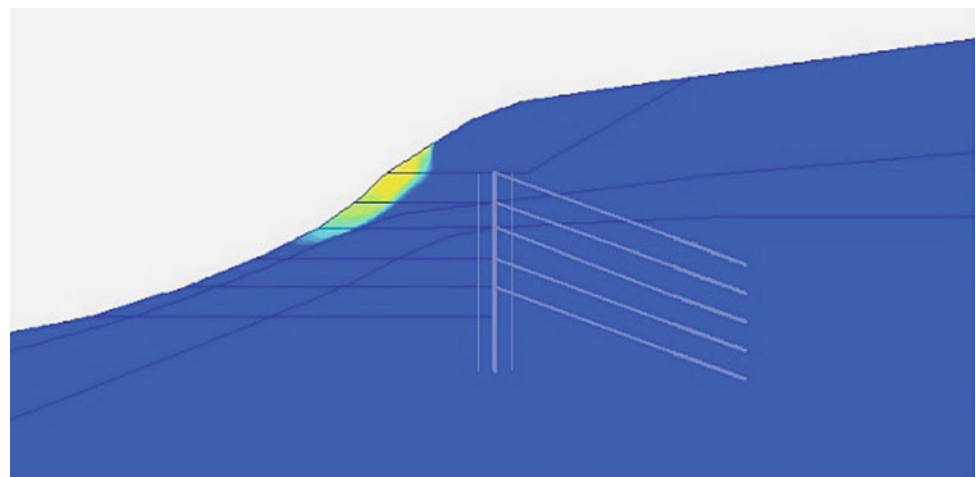
**Fig. 8** Critical failure surface for the first excavation
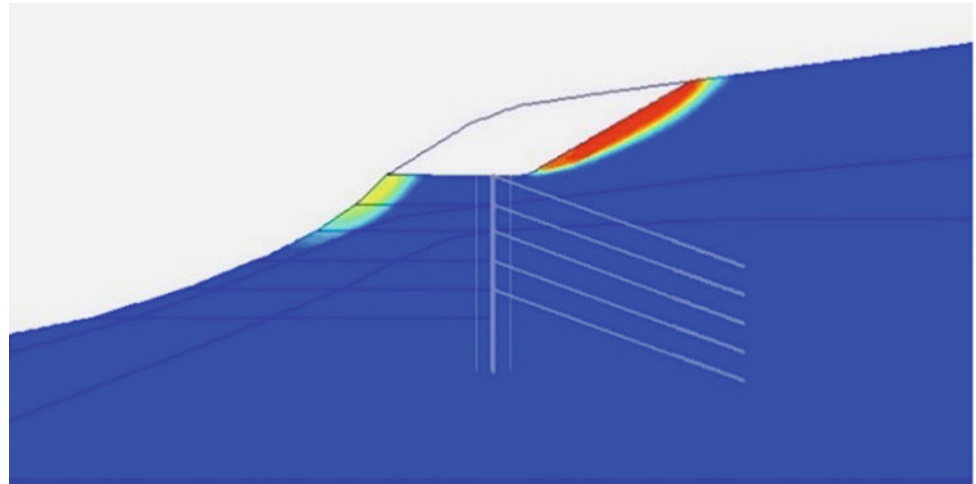


**Fig. 9** Critical failure surface after the installation of pile walls
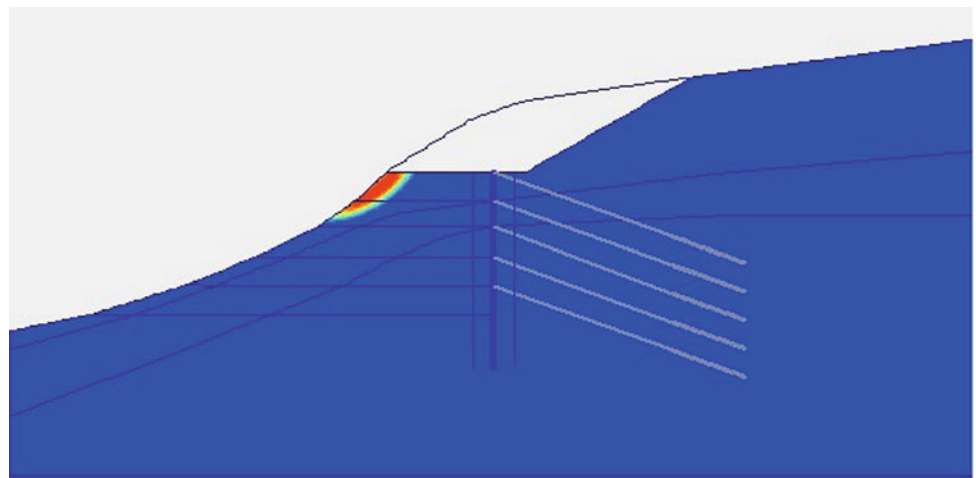


**Fig. 10** Critical failure surface for second
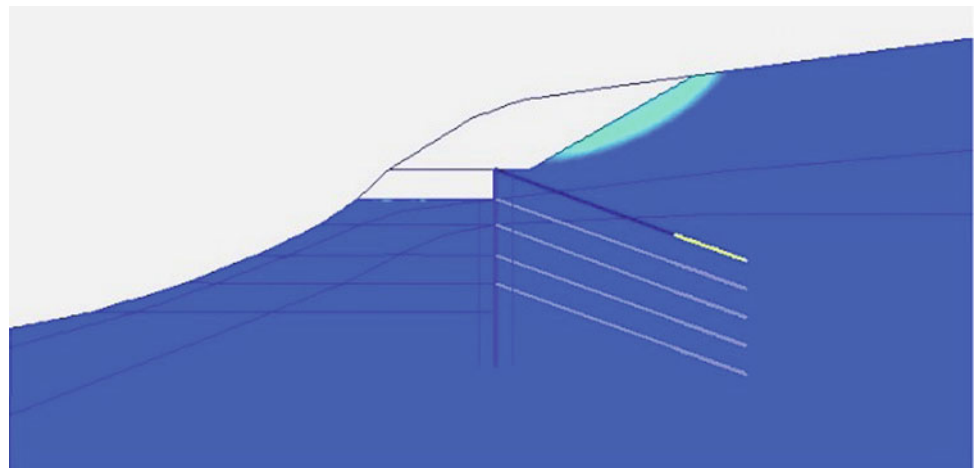
**Fig. 11** Critical failure surface for the next excavation stage and installing the next anchor
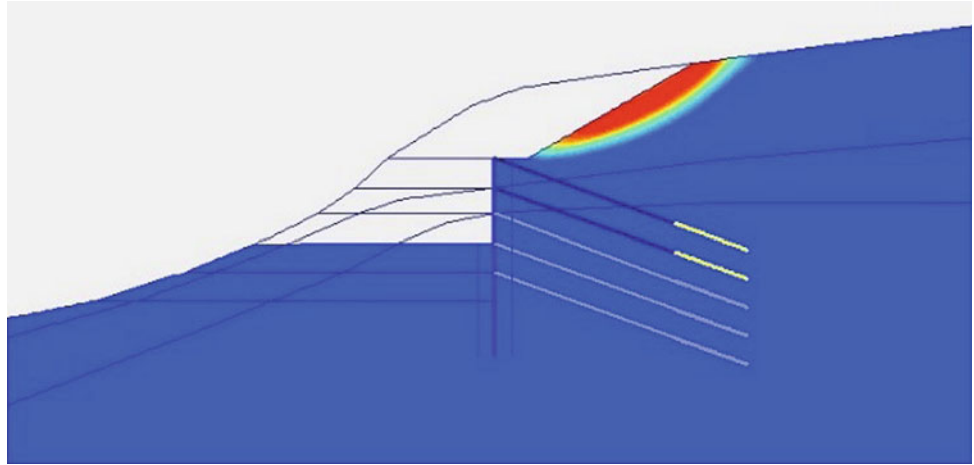


**Fig. 12** Critical failure surface for the next excavation stage and installing the next anchor
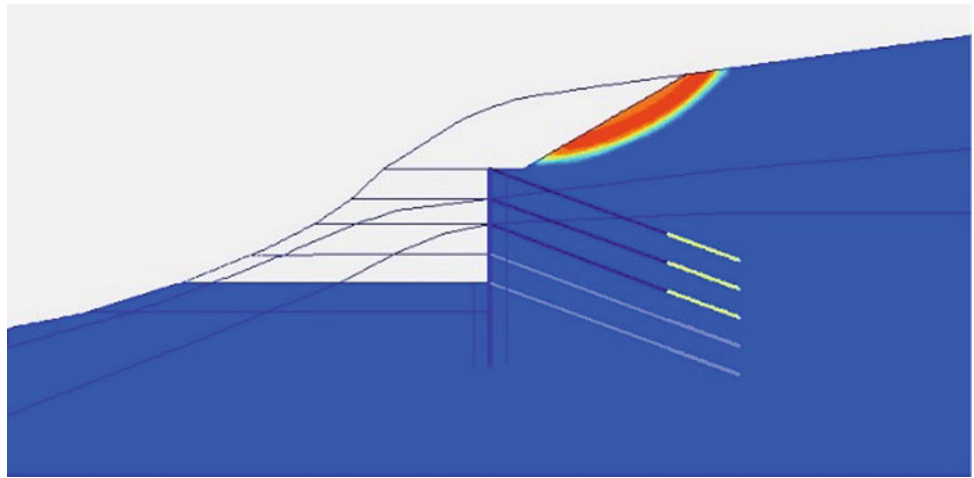


**Fig. 13** Critical failure surface for the last excavation stage and installing the next anchor
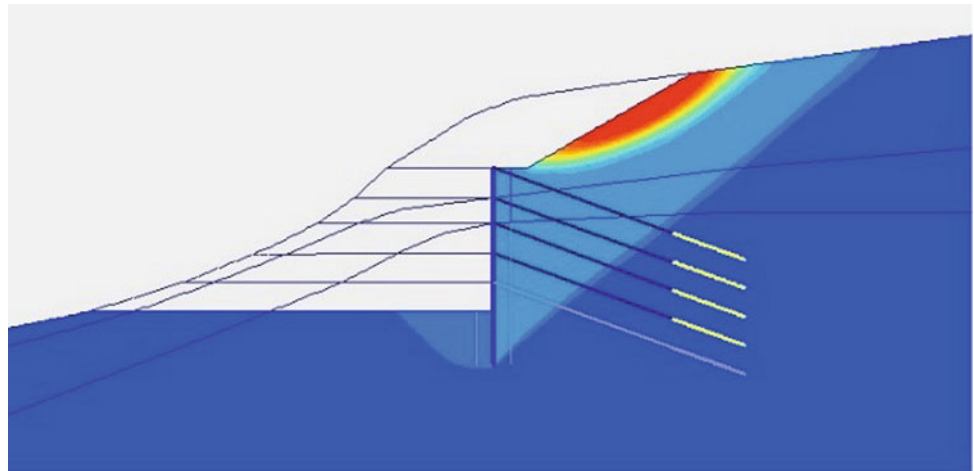
**Fig. 14** Critical failure surface installing the lowest anchor
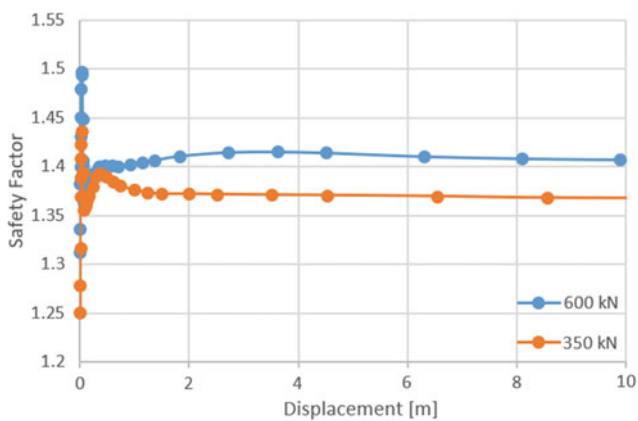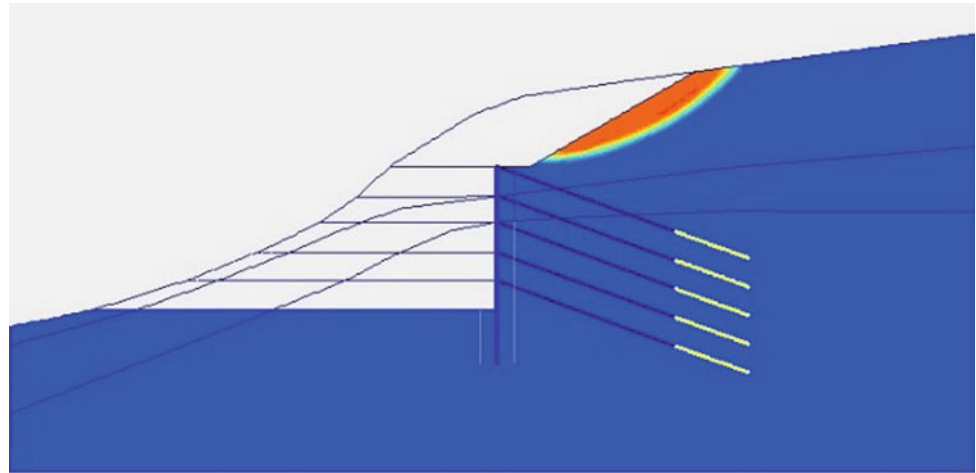




**Fig. 15** Safety factor of the pile wall reinforced by anchors

technique we used has successfully raised the safety factor. Considering this solution, the slope is stable with safety factors larger than the required value 1.25 above the Eurocode requirements.

## 4 Conclusion

The analysis described in this paper is about the reinforcement study of a slope which the East–West Highway in Algeria passes on. The analysis related computations were performed using a finite elements program. To define the

potential slip surface and calculate the factor of safety, various construction stages are defined. The model consists of one initial reference stage, followed by six construction stages going from "first excavation stage (work platforms are made for the execution of the concrete piles)" to "last excavation stage and installing the fourth anchor" and finally one stage for the verification of safety factor after installing the lowest anchor. The main criterion is that the safety against sliding failure has to be at least 1.25, which is imposed by the Eurocode requirements. Reinforcing the Slope by using pile wall and prestressed anchor cable has successfully raised the safety factor. Considering this reinforcement, safety factors larger than the required value 1.25 above in all stage of the work's execution.

## References

Askri, H., et al.: Géologie de l'Algérie, Contribution de SONATRACH Division Exploration, Centre de Recherche et Développement et Division Petroleum Engineering et Développement (1995)

Brinkgreve, R.B.J.: PLAXIS, finite element code for soil and rock analyses, user manual. Balkema, Rotterdam (2002)

Comité Européen de Normalization (CEN), 1997-1:2007, Soil Eurocode 7: Geotechnical Design—Part 1: General Rules (1997)

Hamza, K., Djaafar, C.L.: Slope stability analysis—a case study. In: De Graff, J.V., Shakoor, A. (eds.) Landslides: Putting Experience, Knowledge and Emerging Technologies into Practice, pp. 931–936. AEG Special Publication No. 27 (2017)

# A Short History of Engineering Geology and Geophysics at the British Geological Survey—Part 2: Engineering Geological Mapping

M. G. Culshaw, K. J. Northmore, and D. M. McCann

## Abstract

The British Geological Survey (BGS) formally incorporated engineering geology as one of its key activities by creating the Engineering Geology Unit (EGU) in 1967. From 1968 an engineering geological survey of the proposed site of the new town of Milton Keynes in the south Midlands of England was carried out, as part of a government initiative to build new towns to accommodate an increasing population. This involved analysis of extensive site investigation data and the production of an engineering geological map and a table of summarized geotechnical data for each geological formation. This work led to a much more extensive project for the then proposed Third London Airport in the estuary of the River Thames in South Essex, in south east England and two further mapping projects in development areas adjacent to the Firth of Forth and Cromarty Firth in Scotland. These projects were completed during the 1970s and early 1980s. The experience gained on these projects was then used in a series of urban geological/engineering geological mapping projects in urban areas of England, Scotland and Wales. The paper discusses the engineering geological mapping techniques developed in the first two decades of engineering geological survey and research at the BGS and where this work led in subsequent years.

### Keywords

History of engineering geology • Engineering geological mapping • British geological survey

M. G. Culshaw (✉) · K. J. Northmore · D. M. McCann
British Geological Survey, Keyworth, Nottingham, NG12 5GG, UK
e-mail: martin.culshaw2@ntlworld.com

M. G. Culshaw
School of Civil Engineering, University of Birmingham, Edgbaston, Birmingham, B15 2TT, UK

## 1 Introduction

Culshaw et al. (2014) described how engineering geology began as a formal 'activity' at the British Geological Survey (BGS) with the formation of the Engineering Geology Unit (EGU) under the leadership of Roger Cratchley. There were four main areas of research and survey: engineering geological mapping, geotechnical/geophysical property determinations, slope stability studies and the application of geophysical methods to engineering geology and geotechnical engineering. Over time, these evolved into: urban geology mapping, geotechnical/geophysical property research, geohazard investigations and research, and applied geophysical research. This paper discusses the early engineering geological mapping work and how it evolved into an extensive programme of urban geological mapping. Space does not allow the presentation of examples of the output from the various maps and reports. However, reference is made to a number of examples and to publications arising from some of the maps and reports.

## 2 Mapping for New Town Projects—Milton Keynes

The EGU's first engineering geological mapping project began in 1968 in the designated area for the new city of Milton Keynes, some 50 miles (80 km) NW of London (Fig. 1). At that time, little engineering geological mapping had been carried out in the UK, one of the earliest being the engineering geological map of Belfast (Northern Ireland) that was begun in 1967 and published in 1971 (Bazley 1971; Wilson 1972). The Belfast map was produced by the Geological Survey of Northern Ireland (GSNI). Although staffed by British Geological Survey (then called the Institute of Geological Sciences, IGS) geologists, the GSNI was, and is, an independent organization funded by the Northern Ireland Government.

**Fig. 1** UK location map of the
main places mentioned in the text
(not to scale)



A projected population of 250,000 (a total reached in the last ten years) was to be accommodated in Milton Keynes in a completely new urban area set in a rural environment. From the geological point of view the disadvantage of this mostly rural setting was the lack of existing subsurface data in the form of geological borehole logs. Initially, the EGU became involved as part of the IGS special geological mapping programme for the Milton Keynes area and not, specifically, to produce an engineering geology map of the area. The revised terms of reference (ToR) for the work (after the first ToR had been rejected by the Milton Keynes Development Corporation as too expensive) were:

1. To investigate rock properties (particularly those of engineering significance) and their variations within the Milton Keynes designated area and to show these variations in map form.
2. To carry out trial geophysical surveys in an attempt to delineate buried channels beneath the wide valley through which the River Ouzel (the major river in the area) flows.

EGU engineering geologists sited, supervised, and logged 30 light cable percussion boreholes drilled by a commercial firm. The U4 (undisturbed, 4 in. [100 mm] diameter) cores

taken were tested in commercial laboratories and the results were collated. All the data were eventually published in a report (EG/69/1) (Cratchley et al. 1969) and this was originally intended to accompany the new published geological map of the area. The report was in three volumes, a preliminary report that discussed the engineering geology of the area and summarised some of the geotechnical properties, a second volume that included the borehole logs (and summary geotechnical data) from the initial 30 light cable percussion boreholes for the project paid for by the Milton Keynes Development Corporation and a third volume that included borehole logs and summary geotechnical data for a large number of Minuteman auger, 4 in. (100 mm) auger and B40 hollow stem auger boreholes.

The report is described as 'preliminary' and was produced around October 1969. A final report was scheduled for December 1969 but does not seem to have been produced. The figures are not bound into the Volume 1 of the surviving copies of the report. On page 3 of the report reference is made to Figs. 1, 2 and 3. Two of the three have been identified and are available separately in Cratchley and Denness (1972):

- Figure 1. Trend of selected engineering index properties in one zone of Oxford Clay at Milton Keynes (Fig. 2 of Cratchley and Denness 1972).
- Figure 2. Distribution of selected index parameter ratios showing engineering property trends in Oxford Clay (Lower Middle) at Milton Keynes, Bucks. (Fig. 3 of Cratchley and Denness 1972).
- Figure 3 has not been definitely identified but it may be a sketch map of Engineering Indices of Oxford Clay at Milton Keynes (Site 1) found in the BGS archives.

The same Figs. 2 and 3 are also referred to on page 8 of the report and in Appendix 1 (page 18). A table of selected engineering properties is included in Appendix 2 (page 20).

Between 1970 and 1972 new research was carried out using the EGU's own research funds. This project was able to give guidance on the best routes for a sewer tunnel, on the main drainage line (so as to avoid running sands) and on general foundation conditions in the different rock and soil types in the area (Cratchley and Denness 1972). The study also enabled the EGU to develop the principles on which later engineering geological maps were produced. According to a memo from Roger Cratchley to Geoff Kellaway (a BGS mapping geologist working in Milton Keynes) on 23 June 1971, the study seems to have been then scaled back because of impending EGU involvement in a study of the Third London Airport site in South Essex (see below).

The report was accompanied by an 'engineering geological map' and a detailed table of engineering characteristics, though only indirect reference is made to them. Only three copies of the map exist. Two copies of the table, which is very detailed, survive, including the original. It was probably intended to incorporate the map and table into the final report in more detail.

The table of geotechnical properties and engineering behaviour is one of the earliest examples of its type for a quite extensive geographical area (a whole urban area). The mapped geological units are shown on the engineering geological map, and listed in the table, in terms of their uniqueness from an engineering geological point of view. Consequently, several lihostratigraphic units may be shown as part of a single engineering geological unit. For example, the Jurassic Oxford Clay, Kellaways Clay and Upper Lias are all classified as 'Bedrock—uniform silty clay'. Similarly, Quaternary River Terrace deposits are grouped together as 'Superficial—Interbedded silt, sand and gravel'. However, while the vast majority of the engineering geological units are defined in terms of lithology together with reference of such aspects as structure (jointing, for harder rocks; lamination etc. for soils) or plasticity (for softer clay-rich rocks), the Holocene lithostratigraphic units Alluvium and Head (poorly sorted and poorly stratified deposits formed mostly by solifluction and/or hillwash and soil creep) are, strangely, not classified in these terms.

For each engineering geological unit, the following information is provided: (i) qualitative description and thickness, topographic form and surface relief, degree of weathering (but pre-dating formal weathering classifications), workability (excavatability, compaction, drilling/boring methods), surface drainage and erosion, groundwater conditions, suitability for waste disposal, foundation stability, slope stability, use as a mineral resource and finally, a summary of the main engineering problems associated with the engineering geological unit.

It is now hard to know how much use of the map and table was made by engineers at the Milton Keynes Development Corporation. However, from a research point-of-view, the outputs contributed to the development of appropriate methodologies for providing information suitable for understanding the 'far-field' of De Freitas (2009).

Into the early 1970s, Jon Hallam (EGU, BGS), continued to plot new borehole data sent by the Milton Keynes Development Corporation and to carry out some interpretation (see below) but much of the work was never published. The site investigation reports containing the borehole logs were passed to the BGS archives and the borehole logs were digitally scanned in the early 2000s and entered into the National Borehole Database.

Research focused mainly on Suggestion 4 of the 1969 preliminary report (Cratchley et al. 1969) for further general investigations: "The amplitude of trends of engineering

properties in the Lower Oxford Clay." A series of manual plots for various properties were produced on film and paper (mainly concerning the Jurassic strata and focusing, particularly, on the Upper Athleta zone of the Oxford Clay) but these have not been retained because the source of the original data is not known and so the data that the plots rely on are not available. Roger Cratchley and Bruce Denness published a paper on the research at Milton Keynes in 1972 at the 24th International Geological Congress (Cratchley and Denness 1972). That paper is a better written version of the 1969 report. Bruce Denness completed research into the scale of variation of engineering properties in the Boulder Clay (glacial till) (Denness 1974). Much later, the variation in index properties of the Oadby Till was compared with additional new data by Culshaw et al. (2017) to show that properties at the various scales were very similar. The research was extended by Dave Russell (a University of Reading Ph.D. student) looked at the effect of weathering on the physical and chemical properties of some Mesozoic clays across southern England (Russell 1977). Some of Russell's research was later published.

The geological remapping of the Milton Keynes New Town area was published as a special 1:25,000 scale sheet together with a report (Horton 1974).

## 3 South Essex Engineering Geological Mapping for the Proposed Third London Airport

In the early 1970s, IGS was commissioned by the UK Department of the Environment (DoE) to undertake a regional geological and geotechnical study of an area of some 450 km$^2$ at Foulness/Maplin Sands between the Crouch and Thames estuaries in South Essex (Fig. 1). The area was designated for urban and industrial development, associated with the then proposed new Third London Airport. The research was completed in 1977 and published as a twelve part report with a wallet of over 50 maps. The twelve reports, together with the four principal maps (Engineering Geology Map of South Essex, Sheet 1 [western part] and Sheet 2 [eastern part], Landslip and Slope Map and Engineering Planning Map) were made available for a price of £120 (around £700 today). For £10, the four principal maps could be purchased separately. This project gave the opportunity for experimentation with different ways of presenting the three dimensional geology, particularly emphasising the variations in physical, lithological and geotechnical characteristics of the sediments and sedimentary rocks of the area. It also gave the EGU the opportunity

to set up a major database from existing and new boreholes put down to sample the various strata, which ranged from soft alluvial clays, sands, gravels of Quaternary age to the stiff, fissured Eocene London Clay. Of particular interest and some engineering significance were the loessic Pleistocene deposits called 'Brickearth' that occur as terrace deposits in the centre of the area and which have the characteristic of collapsing under foundation loads when saturated with water. Determination of the characteristics of these deposits, of the disposition and nature of the alluvial deposits, with their very poor foundation and tunnelling properties, and of the whereabouts of landslides enabled the EGU to produce a suite of maps at 1:25,000 scale illustrating the three dimensional stratigraphy, lithology and engineering behaviour, together with an engineering planning map at the same scale. This map subdivides the area into 25 zones each having its own engineering characteristics in terms of foundations, excavation, tunnelling, suitability for fill, drainage, etc. The results of this survey gave significant guidance to land-use planners on the best geological/geotechnical options for the proposed rapid transit route to the airport, areas for heavy industry, etc. The complete data set was also organised in such a way that very rapid appraisals could be made by civil engineering consultants of the feasibility of undertaking certain engineering operations such as bridge/tunnel crossings of buried channels infilled with alluvium. Finally, guidance on site investigation and laboratory testing requirements for deposits such as the uncommon loessic Brickearth were given (Cratchley et al. 1979). Other research papers were published on the engineering geology of the brickearth (Northmore et al. 1996), the Eocene Claygate Member and Bagshot Formation (Northmore et al. 1999) and on the summary engineering planning map (Culshaw and Northmore 2002).

The curtailment of the airport project meant that the survey was not utilised for its original purpose. However, it has obvious relevance to other development in South Essex. Eventually, the information may come to fulfill its original purpose: in early 2009, the government decided to go ahead with a third runway at London Heathrow airport. However, opposition to this was at a high level and the then Mayor of London was in favour of building a new airport in the Thames Estuary, rather than expanding Heathrow. A third runway at Heathrow received final approval in 2016 but the South Essex area remains an area for potential development given its proximity to London.

Attempts were made to encourage other New Towns to collaborate with the EGU in the carrying out of engineering geological mapping but without success. However, mapping work was carried out for the Telford New Town Corporation (Fig. 1) but on slope stability issues.

## 4 Foundation Conditions for Industry

Further ideas for engineering geological mapping were developed by Paul Gostelow during the next major phase of engineering geological mapping by the EGU in the Scottish estuaries (called 'Firths' in Scotland), which began in 1977. This project was related to the requirements of the Scottish Development Department (SDD) to plan and offer the most suitable sites for industrial and petrochemical development in estuaries such as the Forth, Cromarty and Tay on the East Coast of Scotland (Fig. 1) where it was thought likely that gas-gathering pipelines from the North Sea oilfields to the east would be brought ashore. The studies were intended to "*equip the planning machine with the necessary knowledge.*" (Quote from a SDD paper dated 25 June 1979 [probably drafted by Malcolm Rutherford] entitled: "*Engineering geology in the UK: proposals for 1981+. Planning for UK oil related developments: The Scottish Coast*"). The paper also listed the objectives "*for a rolling programme of systematic work on the engineering geology of the broad east coast areas most likely to be involved in development:*"

(a) *to assess geological conditions affecting heavy industrial structures;*
(b) *to identify geological hazards to development and the areas favourable and unfavourable to development and to describe the characteristics of particular strata;*
(c) *to give guidance for the detailed site investigations to be made by developers;*
(d) *to give guidance for land use planning at national and local levels and in particular to provide a basis for advice to Ministers on the best use of limited resources of land and infrastructure.*

These objectives were similar to those given in an earlier paper (26 October 1977) entitled: "*Engineering geology. Scottish Development Department interest 1978–79 onwards*" also by Malcolm Rutherford.

In mid-1978 Paul Gostelow produced a costed, prioritised proposal that identified the areas on the east coast of Scotland to be investigated between 1978 and 1984. The estimated cost was £200,000 per year (around £1.1 m at 2017 prices). Priority 1 was the Upper Firth of Forth, Bandeath to Forth Road Bridge (Fig. 1). Priority 2 was (a) Cromarty Firth, north side (Fig. 1) and (b) Outer Forth, north side. Priority 3 was the Peterhead area (Fig. 1) and Priority 4 the Tay Estuary, north side (Barry Buddon) (Fig. 1). In the event, Priorities 1 and 2a were completed, but not the rest.

Whereas in South Essex the EGU was required to present data relevant to a variety of possible engineering operations, in the Scottish estuaries specific information on the suitability, or otherwise, of the subsoil to withstand the heavy foundation pressures (in excess of 200 kPa) associated with petrochemical development was required and necessitated a different approach. The initial work took place at Bothkennar, in the Firth of Forth estuary area, where the main study was on the engineering geology of the superficial deposits, particularly the highly compressible Holocene Carse Clay.

Out of the Firth of Forth work came the concept of the 'geotechnical profile' and the mapping of this area in terms of these profiles that take into account the geological and geotechnical history of the deposits, their resulting consolidation characteristics and hence the overall bearing capacities and settlement that each profile can accommodate. The area is complicated by the presence of past and (and then) present mineworkings, both for coal and oil shales in the bedrock beneath the Forth Estuary, leading to the necessity to have two categories of foundation conditions (E and F) at the low end of the scale to take into account the mineworkings, and A to D for the superficial sediments as already established for the Cromarty Firth (Gostelow and Tindale 1980; Gostelow and Browne 1986). These two studies were more-or-less completed by the end of March 1981 and the programme ended.

Other surveys overseas include the Geotechnical Map of Nicosia, Cyprus (Hobbs 1982), where particular problems arise with shrinking and swelling clays and an engineering geological map and geotechnical study of Banda Aceh, Northern Sumatra, Indonesia (Culshaw et al. 1979). The latter project was modelled on the South Essex engineering geological mapping project and ran from 1976 to 1978. A digital geotechnical database was developed (though computer hardware and software were rather rudimentary compared with today's standards) and a series of engineering geological maps were produced for the Banda Aceh basin. The project reports, maps and data are held in the BGS archives. The project also had a large training element and around half a dozen Indonesian engineering geologists were involved. The outputs of the project would probably have vanished into obscurity had it not been for the 2004 Indian Ocean tsunami. Banda Aceh was completely destroyed and in the aftermath the German Federal Institute for Geosciences and Natural Resources (BGR) carried out a new engineering geological survey of Banda Aceh (Anon 2010). The data held by the BGS was incorporated into the BGR's outputs.

## 5 Regional and Urban Planning

By the late 1970s/early 1980s, the engineering geological mapping research evolved into a programme of work funded by the Department of the Environment (DoE), the Welsh Office (WO) and the Scottish Development Department

(SDD). This programme continued for some 15 years till 1996. Staff shortages limited EGU inputs. Indeed, initially, there was little enthusiasm in the DoE for the type of engineering geological work pioneered by the EGU. Roger Cratchley argued in a paper dated 11 June 1981 that "*It is thus clear that most of the EGU expertise in sound scientifically based engineering geological mapping, built up over the last 12 years is not appropriate to the new style of mapping required by DOE which is essentially simplistic and based on limited and partial data…*" Not all the EGM projects were led by the BGS (a few were contracted to private consultants) and most of the BGS contracts were led by mapping geologists. However, Roger Cratchley was ultimately proved right as the later EGM projects had significant engineering geological inputs and the last two (for Wigan and Bradford, [Fig. 1]) were led or co-led by EGU staff (see below).

A series of more than 60 studies of the applied geology/environmental geology of British urban areas was carried out. The philosophy behind the research was discussed by Brook and Marker (1987). For each area a report and a series of maps were produced. An initial study (Nickless 1982) was commissioned for the Glenrothes area of Fife, Scotland (Fig. 1). This was followed by five further studies in Scotland.

Some of the studies were fairly basic but later ones were much more sophisticated and comprehensive and included quite a lot of engineering geology. No two studies were the same as geological conditions obviously vary but as the work was labelled 'research' each study had to do something new! Some of the reports ended up being published, or part published, in the scientific literature (for example, Forster et al. 1987, 2004). However, most were not, though the library of the British Geological Survey has a complete set of reports and most, if not all, of the maps have been digitally scanned. The research programme was discussed, in part, in a paper by Culshaw et al. (1990) and more completely by Smith and Ellison (1999). The latter paper contains reference to all the reports for England and Wales. More reports exist for Scotland (see Culshaw et al. 1990) but by the time of the Smith and Ellison paper devolution had taken place and Scotland was no longer part of the DoE's remit. Environmental (or applied, or thematic) geological mapping reached the conclusion of fifteen years of evolution with the production by survey geologists and engineering geologists of a set of maps and reports of Bradford, a major city in the West Yorkshire region of northern England (Fig. 1) (Waters et al. 1996). The major engineering geological input to the Bradford project was summarized by Culshaw and Northmore (2014).

The Bradford study had four main objectives:

- To collect and collate earth science information of relevance to planners, developers, engineers and conservation interests (although the primary audience was planners);
- To produce a set of thematic maps on applied geological topics to assist planning of land use, development and conservation;
- To produce a summary map showing the main earth science factors relevant to planning and development;
- To provide *two* reports, one for non-specialists and the other for those with specific technical knowledge in the fields of geology, hydrogeology, engineering geology and mineral resources.

In around 1999, Martin Culshaw formed the Urban Geoscience Section (first managed by Richard Ellison, then Dave Bridge, then Kate Royse, then Simon Price and most recently by Stephanie Bricker) with a remit to re-examine how urban areas should be mapped (that is, information gathered) and how information should be presented for a range of users (extending beyond planners). However, Brian Marker and Dave Brook of the Department of the Environment should be credited with being the midwives!

The recommendations of the initial review of how urban geoscience should be carried out at the BGS were discussed by Culshaw and Ellison (2002). However, events moved very quickly with the development of digital 3D modelling techniques and by 2005 the emphasis had changed (Culshaw 2003, 2005). New research in urban areas is now firmly, but not exclusively, based around 3D modelling and the development of the provision of environmental information for land-use planning has moved on to cover all/most types of environmental scientific information (for example, Culshaw et al. 2006). Culshaw and Price (2011) have provided a comprehensive overview of developments in urban geology and urban geological mapping up to that date.

Little or no research is currently going on in British universities in urban geoscience. Rather, a broader canvas is being painted on which geology covers only a small corner, so to speak. The emphasis is now on developing sustainable cities; what that means, how it can be achieved for the future and how we know when we are being sustainable are key questions. However, a major project, called 'Urban Futures,' started in 2008 and led by Professor Chris Rogers of the School of Civil Engineering, the University of Birmingham was funded by the UK Engineering and Physical Sciences Research Council. The project sought to answer these questions and others. Engineering geologists from the BGS were involved as co-researchers.

## 6 Concluding Comments

The Engineering Geology Unit of the BGS was created at a time when engineering geology, as a geological sub-discipline, was expanding rapidly in the UK following the 1966 Aberfan (South Wales) landslide disaster in which 144 people, mostly children, were killed. The development of engineering geological mapping was part of this evolution. At the start, engineering geological maps were seen as helping at the desk study stage of site investigation for construction projects. However, over time, their application broadened to include land-use planning, particularly for urban areas and, more broadly, for most aspects of urban development. Applications for site investigation are now reasonably standardised but for urban development research continues at the BGS with the latest involving collaboration with the Geological Office of Singapore's Building and Construction Agency to provide better understanding of the subsurface in relation to groundwater and thermal resources, waste disposal, underground storage and transport facilities. Elsewhere in the world, similar requirements exist, so it is probable that engineering geological mapping will continue to develop to meet the varying needs.

Finally, it is sad to record that relatively few of the maps described here were ever published in the academic literature, though all are available in the BGS library and archives. In part, this was because of the difficulty of adequately publishing maps at an understandable size in journals published on paper (the medium of the time). However, with the help of Professor Bill Dearman (formerly University of Newcastle, UK), engineering geological maps of the UK were published in 2011 (British Geological Survey 2011a, b, c). Though at a small scale (1:1 million) they contain extensive information and were particularly aimed at younger members of the profession in higher education and early career training (Culshaw et al. 2010; Dobbs et al. 2012).

## References

Anon: Indonesia—Management of Georisks, Province Nanggroe Aceh Darussalam (MANGEONAD). https://www.bgr.bund.de/EN/Themen/Zusammenarbeit/TechnZusammenarb/Projekte/Abgeschlossen/Archiv/Asien/indonesien_georisiken_mangeonad_en.html;jsessionid=A816D19F23048EB3613550F172B3BE6E.2_cid284 Hannover: German Federal Institute for Geosciences and Natural Resources (BGR) (website site visited 31.01.18) (2010)

Bazley, R.A.B.: A map of Belfast for the engineering geologist. Q. J. Eng. Geol. **4**, 313–314 (1971)

British Geological Survey: Engineering geology (bedrock) map of the United Kingdom. British Geological Survey, Keyworth, Nottingham (2011a)

British Geological Survey: Engineering geology (superficial) map of the United Kingdom. British Geological Survey, Keyworth, Nottingham (2011b)

British Geological Survey: Extended key for the engineering geology maps of the United Kingdom. British Geological Survey, Keyworth, Nottingham (2011c)

Brook, D., Marker, B.R.: Thematic geological mapping as an essential tool in land-use planning. In: Culshaw, M.G., Bell, F.G., Cripps, J. C., O'Hara, M. (eds.) Planning and Engineering Geology, pp. 211–214 Engineering Geology Special Publication No. 4, Geological Society, London (1987)

Cratchley, C.R., Denness, B.: Engineering geology in urban planning with an example from the new town of Milton Keynes. In: Crawford, C.B., Scott, J.S. (eds.) Proceedings of the 24th International Geological Congress, Montreal, Section 13, pp. 13–22, Geological Society of Canada, Ontario (1972)

Cratchley, C.R., McCann, D.M., Denness, B., Conway, B.W., Hallam, J.H.: Regional geotechnical investigation of the Milton Keynes area (in 3 volumes). (Volume 1: Preliminary Report; Volume 2: Borehole results nos 1–30; Volume 3: 32-351). Institute of Geological Sciences Technical Report EG/69/1. Accompanied by: 'Engineering Geology Map of Milton Keynes'. Hand-coloured on a topographical 1:25,000 scale special sheet for the area and a Table of Engineering Geology Characteristics to accompany the map (1969)

Culshaw, M.G.: Bridging the gap between geoscience providers and the user community (Keynote paper). In: Rosenbaum, M.S., Turner, A. K. (eds.) Proceedings of the Euroconference on "New paradigms in subsurface prediction," Spa, Belgium, 7–12 July 2001. Lecture Notes in Earth Sciences 99, pp. 7–26. Springer, Berlin (2003)

Culshaw, M.G.: From concept towards reality: developing the attributed 3D geological model of the shallow subsurface. Q. J. Eng. Geol.Hydrogeol. **38**, 231–284 (2005)

Culshaw, M.G., Ellison, R.A.: Geological maps: their new importance in a user driven digital age (Keynote paper). In: Van Rooy, J.L., Jermy, C.A. (eds.), Proceedings of the 9th International Association for Engineering Geology and the Environment Congress, Durban, 16–20 September 2002. Keynote Lectures and Extended Abstracts Volume, 25–51. South African Institute of Engineering and Environmental Geologists, Pretoria, ISBN: 0-620-28560-5. Also 67–92 on CD-ROM, ISBN: 0-620-28559-1 (2002)

Culshaw, M.G., Northmore, K.J.: An engineering geological map for site investigation planning and construction type identification. In: Van Rooy, J.L., Jermy, C.A. (eds.), Proceedings of the 9th International Association for Engineering Geology and the Environment Congress, Durban, 16–20 September 2002, pp. 423–431. South African Institute of Engineering and Environmental Geologists, Pretoria. On CD-ROM only, ISBN: 0-620-28559-1 (2002)

Culshaw, M.G., Northmore, K.J.: Urban engineering geological maps for Bradford, UK. In: Lollino, G., Manconi, A., Guzzetti, F., Culshaw, M., Bobrowsky, P., Luino, F. (eds), "Urban Geology, Sustainable Planning and Landscape Exploitation." Proceedings of the 12th Congress of the International Association for Engineering Geology and the Environment on "Engineering Geology for Society and Territory." Torino, Italy. Volume 5, Part 1, Paper 67, 351–354. Springer, Cham (Switzerland) (2014)

Culshaw, M.G., Price, S.J.: The contribution of urban geology to the development, regeneration and conservation of cities. Bull. Eng. Geol. Env. **70**, 333–376 (2011). https://doi.org/10.1007/s10064-011-0377-4

Culshaw, M.G., Sutarto, N.R., Duncan, S.V.: Engineering geological mapping of the Banda Aceh alluvial basin, Northern Sumatra, Indonesia. Bull. Eng. Geol. Env. **19**, 40–47 (1979)

Culshaw, M.G., Forster, A, Cripps, J.C., Bell, F.G.: Applied geology maps for land-use planning in Great Britain. In: Price, D.G. (ed.) Proceedings of the 6th International Congress of the International Association of Engineering Geology, Amsterdam, August 1990, A. A. Balkema, Rotterdam 1, 85–93 (1990)

Culshaw, M.G., Nathanail, C.P., Leeks, G.J.L., Alker, S., Bridge, D., Duffy, T., Fowler, D., Packman, J.C., Swetnam, R., Wadsworth, R., Wyatt, B.: The role of the Environmental Information System for Planners in an urban context. Sci. Total Environ. **360**(1–3), 233–245 (2006)

Culshaw, M.G., Dobbs, M.R., Northmore, K.J., Reeves, H.J., Entwisle, D.C.: A tribute to Professor William Dearman: New small-scale engineering geological maps of the United Kingdom. In: Williams, A.L., Pinches, G.M., Chin, C.Y., McMorran, T.J., Massey, C.I. (eds.), 'Geologically active.' Proceedings of the 11th Congress of the International Association for Engineering Geology and the Environment, Auckland, New Zealand, September 2010, pp. 187–198. CRC Press/Balkema, Leiden, The Netherlands (2010)

Culshaw, M.G., Northmore, K.J., McCann, D.M.: A short history of engineering geology and geophysics at the British Geological Survey. In: Lollino, G., Arattano, M., Giardino, M., Oliveira, R., Peppoloni, S. (eds.), "Education, Professional Ethics and Public Recognition of Engineering Geology." Proceedings of the 12th Congress of the International Association for Engineering Geology and the Environment on: "Engineering Geology for Society and Territory", Torino, Italy. Volume 7, Paper 51, pp. 257–260. Springer, Cham (Switzerland) (2014)

Culshaw, M.G., Entwisle, D.C., Giles D., Berry, T., Collings, A. Banks, V.J., Donnelly, L.J.: Material properties and geohazards—engineering group working party report. In: Griffiths, J.S., Martin, C.J. (eds.), "Engineering Geology and Geomorphology of Glaciated and Periglaciated Terrains." Geological Society, London, Engineering Geology Special Publication 28, pp. 599–740. https://doi.org/10.1144/EGSP28.6 (2017)

De Freitas, M.H.: Geology: its principles, practice and potential for geotechnics. Q. J. Eng. Geol.Hydrogeol. **42**, 397–441 (2009)

Denness, B.: Engineering aspects of the chalky boulder clay at the new town of Milton Keynes in Buckinghamshire. Q. J. Eng. Geol. **7**, 297–309 (1974)

Dobbs, M.R., Culshaw, M.G., Northmore, K.J., Reeves, H.J., Entwisle, D.C.: A methodology for creating national engineering geological maps of the UK. Q. J. Eng. Geol. Hydrogeol. **45**, 335–347. https://doi.org/10.1144/1470-9236/12-003 (2012)

Forster, A., Hobbs, P.R.N., Wyatt, R.J., Entwisle, D.C.: Environmental geology maps of Bath and the surrounding area for engineers and planners. In: Culshaw, M.G., Bell, F.G., Cripps, J.C., O'Hara, M (eds.) "Planning and Engineering Geology," Engineering Geology Special Publication No. 4, Geological Society, London, pp. 221–235 (1987)

Forster, A., Lawrence, D.J.D., Highley, D.E., Cheney, C.S., Arrick, A.: Applied geological mapping for planning and development: an example form Wigan, UK. Q. J. Eng. Geol. Hydrogeol. **37**, 301–315 (2004)

Gostelow, T.P., Browne, M.A.E.: Engineering geology of the upper Forth Estuary. Report of the British Geological Survey, 16, 8. Her Majesty's Stationery Office, London (1986)

Gostelow, T.P., Tindale, K.: Engineering geological investigations into the siting of heavy industry on the east coast of Scotland. 1. The north side of the Cromarty estuary. Engineering Geology Report 80/51. Institute of Geological Science, Edinburgh (1980)

Hobbs, P.R.N.: Geotechnical map of Nicosia. British Geological Survey Technical Report EG/82/10. British Geological Survey, Keyworth, Nottingham (1982)

Horton, A.: Geology of the new town of Milton Keynes: explanation of 1:25,000 special geological sheet SP83 with parts of SP73, 74, 84, 93, and 94. British Geological Survey, Keyworth (1974)

Nickless, E.F.P.: Environmental geology of the Glenrothes district, Fife region: description of 1:25,000 Sheet NO 20. Report of the Institute of Geological Sciences 82/15. Her Majesty's Stationery Office, London (1982)

Northmore, K.J., Bell, F.G., Culshaw, M.G.: The brickearth of South Essex. Q. J. Eng. Geol. **29**, 147–161 (1996)

Northmore, K.J., Bell, F.G., Culshaw, M.G.: The engineering geology of the Claygate Beds and Bagshot Beds of South Essex. Q. J. Eng. Geol. **32**, 215–231 (1999)

Russell, D.J.: The effect of weathering on physical and chemical properties of some Mesozoic clays. Unpublished Ph.D. thesis, University of Reading (1977)

Smith, A., Ellison, R.A.: Applied geological maps for planning and development. A review of examples from England and Wales, 1983 to 1996. Q. J. Eng. Geol. **32**, S1–S44 (1999)

Waters, C.N., Northmore, K.J., Prince, G., Bunton, S., Butcher, A., Highley, D.E., Lawrence, D.J.D., Snee, C.P.M.: A geological background for planning and development in the City of Bradford Metropolitan district. In: Waters, C.N., Northmore, K.J., Prince, G., Marker, B.R. (eds.) British Geological Survey Technical Report, No. WA/96/1 (1996)

Wilson, H.E.: The geological map and the civil engineer. In: Crawford, C.B., Scott, J.S. (eds.) Proceedings of the 24th International Geological Congress, Section 13, pp. 83–86. Geological Survey of Canada, Ontario (1972)

# Factors Contributing to Rockfall Occurrence and the Associated Risk in Rockville, Utah

Carl Jacklitch and Abdul Shakoor

## Abstract

The east-west trending, south-facing slope in Rockville, Washington County, Utah is well known for experiencing large-size rockfalls, including the fatal rockfall of December 2013 that destroyed a home and killed two people. The stratigraphic units present in the area include the well-indurated, Upper Triassic, Shinarump Conglomerate Member (cliff-forming unit) of the Chinle Formation that caps the less-resistant, Lower Triassic, Moenkopi Formation (slope-forming unit). We performed a detailed study to investigate the factors that contribute to rockfall occurrence and the associated risk in the Rockville area. To accomplish this objective, we selected four representative sites along the slope and a few supplemental sites for additional data. The results of our study indicate that the main factors contributing to rockfall occurrence include unfavorable orientation of discontinuities, differential weathering resulting in undercutting, and regional climate (infrequent, high precipitation events; freeze-thaw cycles) whereas those contributing to rockfall risk include high slopes, presence of gullies that channelize rockfall debris, and proximity of homes to the toe of the slope. The results also show that the western portion of the study area poses the highest risk due to the presence of higher slopes, larger exposure of the Shnabkaib Member (the weaker rock unit) resulting in undercutting, higher number of deep gullies, and the higher number of residences closer to the slope toe.

## 1 Introduction

The town of Rockville in Washington County, Utah (Fig. 1), is known for frequent, large, hazardous rockfalls. There have been at least six large rockfalls within the past 38 years (1976; October, 2001; October, 2002; spring, 2007; February, 2010; November, 2010), with five of the six occurring in the past 14 years (Knudsen 2011). The rockfall on December 12, 2013, destroyed a house (Fig. 2) and resulted in the deaths of its two inhabitants (Dalrymple and Piper 2013; Mabbutt 2013; Lund et al. 2014). The rock mass, weighing approximately 2450 tonne fell from a 122 m high slope.

The stratigraphic units present in the area include the well-indurated Upper Triassic Shinarump Conglomerate Member (cliff-forming unit) of the Chinle Formation that caps the less-resistant Lower Triassic Moenkopi Formation (slope-forming unit). The Shinarump Conglomerate Member is 18–41 m thick, dips 1° to 2° to the east, and contains widely spaced vertical joints (Knudsen 2011). It is a medium- to coarse-grained pebbly sandstone and conglomerate. The Moenkopi Formation is a reddish-orange to reddish-brown siltstone, mudstone, and fine-grained sandstone. It generally thins to the northeast from about 122–183 m thick, west of St. George, to 61–85 m thick in the Zion National Park area (Utah Geological Survey 2013). The Moenkopi Formation slopes are covered with thick (14 m) talus deposits, derived from the Shinarump Conglomerate (Knudsen 2011). The Moenkopi Formation consists of two members: the Upper Red member and the Shnabkaib Member (Fig. 3). The Upper Red member consists of shallow marine and mudflat deposits whereas the Shnabkaib Member represents a sabkha environment (Graham 2006). An unconformity is present between the Chinle Formation and the

C. Jacklitch
Gannett Fleming, Inc., Foster Plaza 8, Suite 400, 730 Holiday Drive, Pittsburgh, PA 15220, USA
e-mail: cjacklitch@GFNET.com

A. Shakoor (✉)
Department of Geology, Kent State University, Kent, OH 44242, USA
e-mail: ashakoor@kent.edu

**Fig. 1** Location of Rockville in Washington County, Utah
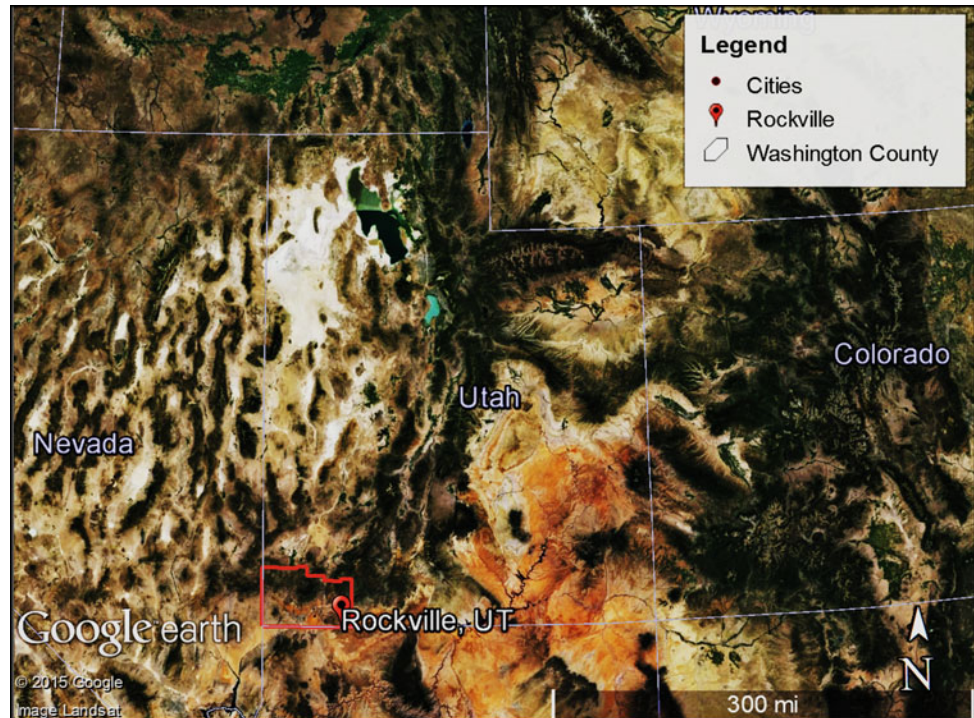


**Fig. 2** The house after the December, 2013 rockfall (Lund et al. 2014)



Moenkopi Formation. A stratigraphic cross-section of the study area can be found in Jacklitch et al. (2018).

The purpose of this research was to evaluate the factors that contribute to rockfall occurrence and evaluate the potential risk from rockfalls to residences in Rockville, Utah.

## 2 Methods

We selected four primary sites along the Rockville slope for detailed investigations and several supplementary sites for additional data. Figure 4 shows the locations of the selected

**Fig. 3** An overview of the stratigraphy of Rockville slope near the fatal rockfall site



**Fig. 4** Location of the four primary sites and the supplemental data sites on a USGS topographic map overlay (Google Earth). *Note* 1 mile = 1.6 km
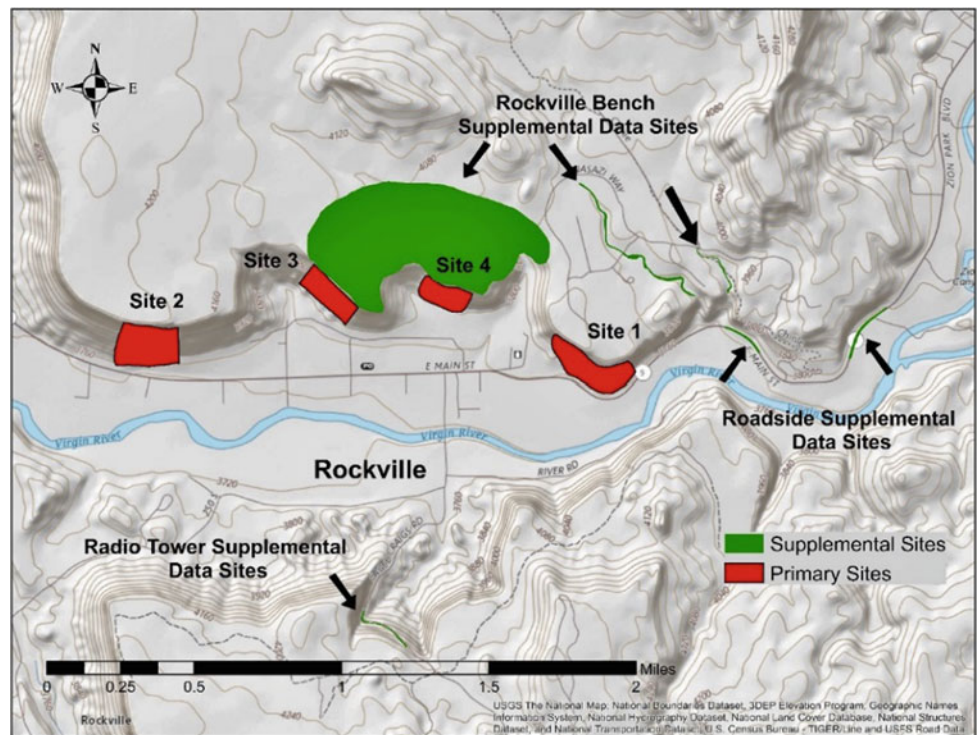
sites. We conducted field investigations to evaluate factors contributing to rockfall occurrence and rockfall risk as well as to determine slope geometry (strike and dip, slope height, slope length), establish slope stratigraphy, collect discontinuity data, evaluate modes of failure, and obtain samples for laboratory testing. For collecting discontinuity data, we used the window mapping and random mapping methods (Wyllie

and Mah 2004) to record the following aspects of discontinuities: geometry, continuity (extent), spacing, aperture, infilling material (if present), surface irregularities, and presence or absence of water. The modes of failure affecting the slopes in Rockville were evaluated using both field observations and results of kinematic analysis. We collected block samples of various rock units for laboratory testing.

The rock blocks were cored in the laboratory to prepare NX-size (54 mm) cores.

We performed laboratory investigations to determine density (mass/volume), basic friction angle, and second-cycle slake durability index values for various rock units comprising the slopes in the study area. We used density and friction angle for rockfall simulations and kinematic analysis, respectively, and slake durability index to evaluate the potential for undercutting of the resistant rock units (Shinarump Conglomerate Member) by the less resistant rock units (Moenkopi Formation). We determined the density values for different rock units by dividing the mass of a core sample from a particular unit by the volume of the sample. We used the Stimpson (1981) method to determine the basic angle of friction. We stacked three cores from each rock unit on a tilting table such that two cores were fixed in place side-by-side and the third core was placed on top, free to slide. The table was tilted until the top core slid over the lower two cores. We measured the tilt angle of the table using a Brunton compass. We used the tilt angle in the following equation to calculate the basic friction angle—$\phi = tan^{-1}(1.155 \tan \alpha)$, where $\phi$ is the internal angle of friction and $\alpha$ is the tilt angle (Stimpson 1981). We used ASTM method D-4644 (ASTM 2010) to determine the second cycle slake durability index ($Id_2$) of the Moenkopi Formation. Six samples collected from two of the sites (four samples from Site 1 and two samples from Site 2) were used for the test.

The data analyses for this study consisted of: (1) stereonet analysis; (2) kinematic analysis; and (3) rockfall analysis. We used Dips software (Rocscience 2014) to perform stereonet and kinematic analyses and RocFall software (Rocscience 2015) to conduct rockfall analysis. The purpose of the stereonet analysis was to determine the principal joint sets. The kinematic analysis was used to evaluate the potential for planar failures, wedge failures, and toppling failures. We used the principal joints, the slope angles, and the basic friction angle for kinematic analysis. The rockfall analysis was conducted to determine the trajectories and the rollout distances of rock blocks of specific sizes. Slope profiles were developed for each of the four sites using USGS topographic maps and aerial imagery from Google Earth and Bing Maps. We entered the slope profiles into RocFall and selected the parameters for the slope material from the suggested values in the RocFall software manual (Rocscience 2015). The parameters included the coefficient of normal restitution, the coefficient of tangential restitution, the dynamic friction coefficient, and the rolling resistance.

In order to calibrate the parameters to ensure accuracy of the model, the parameters were tested with the known block shape, density, mass, and rollout distance of the largest block at the fatal rockfall site. The block shape, density, and mass are the three parameters that can be altered for the rollout distance analysis. As the density remains constant for a given lithology, we altered the block shape and mass at each site to find the combination that yielded the greatest rollout distance. There are 22 shape options available for the general shape of the rock block. Our field observations indicated that rockfall-block sizes and shapes were highly variable. Therefore, in order to accommodate maximum variability, we let the computer program select all 22 shape options. With all 22 shapes selected, 11,000 rock blocks were selected for each run. This provided 500 blocks of each of the 22 block shapes. With the block shape and density fixed, the mass of the block was manually altered for each run until the maximum rollout distance was determined. This process was repeated for all four sites.

## 3 Results of Field and Laboratory Investigations

The average slope angle is 40° for Sites 1 and 2 and 35° for Sites 3 and 4, slope height ranges from 79 m for Site 1 to 131 m for Site 2, and slope length ranges from 137 m for Site 2 to 457 m for Site 1. The average extent of discontinuities for the Shinarump Conglomerate Member and the Upper Red member, respectively, are 5 and 3 m, average spacing 1.8 and 1.7 m, and average aperture 0.25 and 0.5 cm. Most discontinuities are moderately smooth to moderately rough, have no infilling material, and were dry during the field investigation stage. The Shinarump Conglomerate Member has an average density of 2.27 g/cm$^3$, and the Upper Red member has an average density of 2.64 g/cm$^3$. The $Id_2$ values range from 9% for the weaker units to 97% for the stronger units.

## 4 Factors Contributing to Rockfall Occurrence

Field observations revealed that factors contributing to rockfall occurrence in the Rockville area include discontinuities, differential weathering, and climate.

### 4.1 Discontinuities

Among the various aspects of discontinuities recorded in the field, orientation is the most important factor contributing to rockfalls. If the orientation of discontinuities present at a given site does not indicate the potential for a kinematically possible failure, the other aspects of discontinuities become irrelevant. The primary mode of failure for the Shinarump Member, as indicated by the kinematic analysis, is wedge failures. The potential for wedge failures exists at all four

sites. Planar failures within the Shinarump Member are a possible mode of failure at Site 4 and toppling failures are possible at Sites 2 and 3. Within the Upper Red member, all three modes of failure are possible at Sites 1 and 3. Sites 2 and 4 did not show the potential for any mode of failure within the Upper Red member. This does not mean that a slope failure will not occur in the future within the Upper Red member at these sites as undercutting of the Upper Red member, due to differential weathering, may induce rockfalls or other modes of failure. It should be noted that regardless of the mode of failure, all failures end up as rockfalls because of the high slopes in Rockville.

Continuity (extent) and spacing of discontinuities are other important aspects of discontinuities with respect to rockfall hazard as, together, they define the size of the rock block that may detach and fall. Most discontinuities extended the full thickness of the rock unit. Although the average spacing of the discontinuities is approximately 1.8 m, some blocks were continuous for a lateral distance of as much as 46 m. At many locations, a spacing of 5–9 m was observed. The continuous nature and wide spacing of discontinuities are responsible for the frequent large-size rockfalls in the Rockville area such as that of December 12, 2013.

The majority of the discontinuities at the sites were closed and had little or no aperture; however, some discontinuities were open with nearly 0.3 m of separation. The presence of aperture at some locations contributed to the potential for failures.

Most discontinuities at the study sites were moderately rough to moderately smooth. We observed that the valley stress relief joints were predominately smooth whereas the other discontinuities were moderately rough. With the relatively low roughness of the discontinuities, there is less resistance to failure from the rock-to-rock contact. Because of the low roughness, we believed that adjustments to the basic friction angle, as determined by the Stimpson (1981) method, for use in the kinematic analysis, were not warranted. Using the basic friction angle represented the worst case scenario for the analysis and evaluation of the rockfall hazard.

## 4.2 Differential Weathering

Results of the slake durability test show that there is a very high potential for differential weathering within the Moenkopi Formation. The weaker units had $Id_2$ values between 9 and 25% whereas the stronger, more resistant units, had $Id_2$ values ranging from 94 to 97%. The rock units within the Moenkopi Formation that exhibited the lowest slake durability index values were those that contained lenses and seams of gypsum and were more clayey in nature. The large

difference in slake durability index values between the stronger and weaker rock units within the Moenkopi Formation indicates a high potential for differential weathering and the associated undercutting of stronger rock units by the weaker rock units (Fig. 5). The amount of undercutting between the Shinarump Conglomerate Member and the Moenkopi Formation (Fig. 6) is variable across the study area. The primary factors that contribute to the variability in the potential for undercutting between the two rock units is whether the portion of the Moenkopi Formation unit that is in contact with the Shinarump Conglomerate Member consists of more resistant or less resistant rock, or whether the cream to maroon colored silty mudstone lenses are present (Fig. 7). The silty mudstone lenses that exist beneath the Shinarump Member, throughout the study area, promote differential weathering because of their moderate to low durability ($Id_2 = 69\%$). Within most of the study area, the contact between the Shinarump Conglomerate Member and the Moenkopi Formation is covered with colluvium, protecting it from undercutting. However, the mudstone lenses are not protected by colluvial soil because of continual weathering.

## 4.3 Climate

The climate seems to be an important factor in contributing to rockfall occurrence in the Rockville area. It played a significant role in the rockfall that occurred on December 12, 2013, and some of the other recorded major rockfalls. During the end of November and the beginning of December, 2013, there was a total of 6.6 cm of precipitation. Within the same period of time, the temperatures fell below freezing at night and rose above freezing during the day. The lowest temperature for the year (−20 °C), and the lowest temperature in a ten year span, occurred three days prior to the incident. Yet, the daily highs were still in the 10–15 °C range. This freeze-thaw activity likely contributes to all rockfalls in the area, including the rock blocks that fell on December 12, 2013.

## 5 Factors Contributing to Rockfall Risk

Field observations indicated that the following factors contribute to rockfall risk:

## 5.1 Slope Height

Slope height adds to rockfall occurrence and the associated risk in two ways. A higher slope is typically less stable as it

**Fig. 5** Undercutting of the cliff-forming resistant rock unit within the Upper Red member of the Moenkopi Formation by the less resistant slope-forming rock unit at Site 1



**Fig. 6** Undercutting of the Shinarump Conglomerate Member by the Moenkopi Formation between Site 3 and Site 4, resulting in potentially unstable blocks of the Shinarump Conglomerate Member

**Fig. 7** One of the lenses of red to gray mudstone that separates the Shinarump Conglomerate Member from the Moenkopi Formation at several locations

cannot support its own mass. Also, the material that falls from higher slopes gains more momentum as it travels down the slope. This, in turn, creates a greater risk for any object in the pathway of the travelling rock mass. For the Rockville slope, the height decreases from 131 m in the west to 61 m in the east. This suggests a higher potential for rockfall occurrence as well as a higher degree of rockfall risk for the western portion of the study area.

## 5.2 Gullies

While the gullies do not induce rockfalls, they can channelize the rockfalls and debris released from the slope. Therefore, a structure built near the mouth of a gully would have a higher risk of damage from rockfalls. Figure 8 shows examples of gullies at the field sites. Gullies, some of which are fairly deep (>1.8 m), are most prevalent within the western slope, but become less extensive toward the east. This is probably because the Shnabkaib member (the weaker rock unit) is below the ground surface in the eastern portion of the study area.

## 5.3 Proximity of Homes to Slope Toe

Most homes in the town of Rockville are located very close to the slope toe (Fig. 3). This obviously increases the risk from rockfalls.

In summary, field observations revealed that the western portion of the study area poses the highest risk from rockfalls due to the presence of higher slopes, higher number of deep gullies, and higher number of residences closer to the slope toe.

## 6 Modified Rockfall Hazard Rating System for Rockville

The Oregon Department of Transportation (ODOT) rockfall hazard rating system (RHRS) (Pierson 1991) is frequently used to evaluate rockfall hazard. However, the original system was developed for slopes under 33 m in height and rock block sizes under 1.1 m.

Considering the size of the blocks and the height of the slopes in the study area, the ODOT RHRS cannot be used effectively to evaluate the hazard (risk) for the Rockville slopes. Therefore a modified version of RHRS was developed for Rockville that focusses on the risk associated with a rockfall (i.e. the term "hazard" is used here as a synonym for "risk"). The modifications included: "Roadway" was changed to "House," "Annual Maintenance Frequency" was changed to "Annual Frequency", and "Average Daily Traffic" was changed to "Potential for Property Damage/Injury or Fatality". The "Potential for Property Damage/Injury or Fatality" evaluates the possible damage to facilities that are within the rollout distance, as well as the possibility that an injury or fatality may
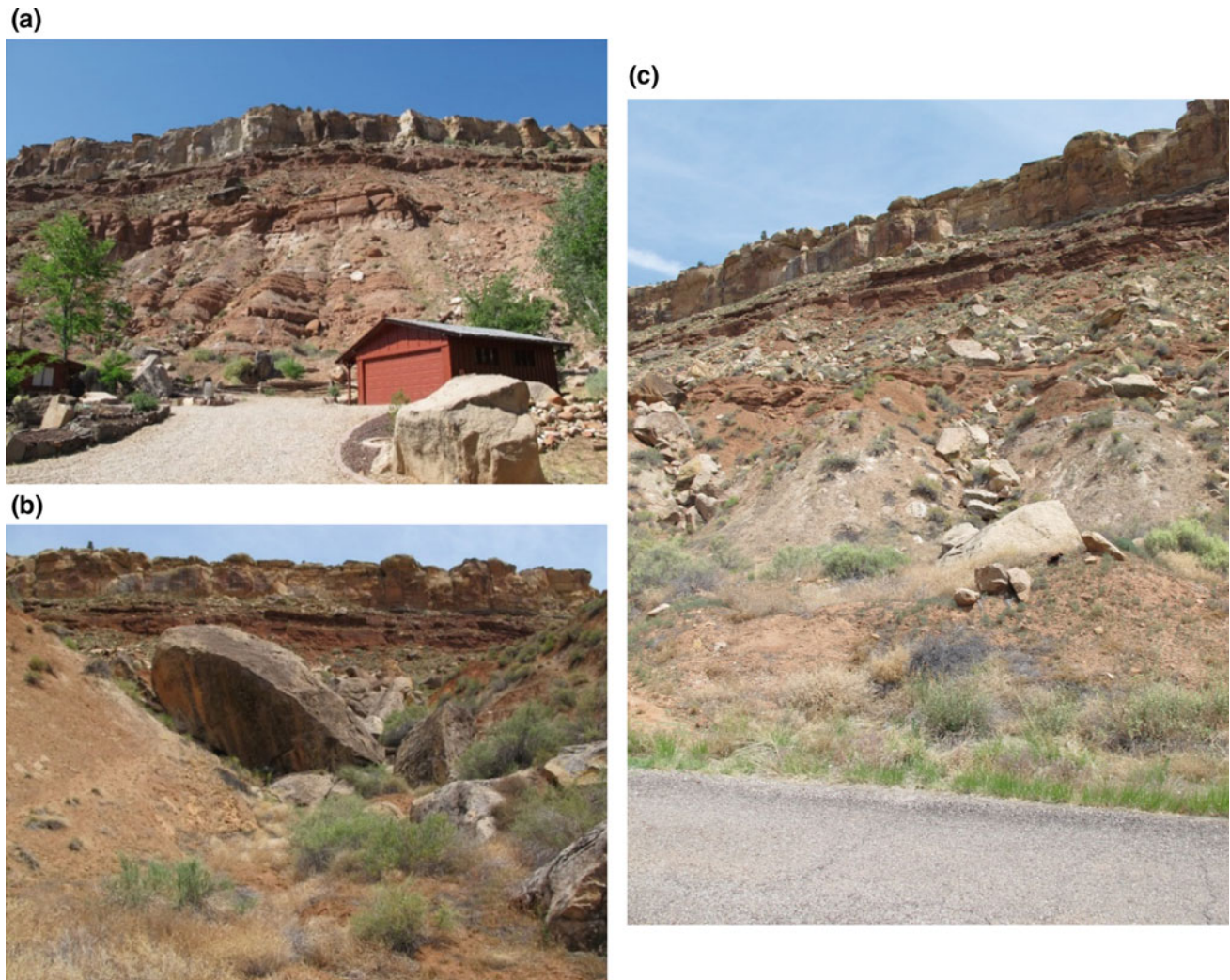
**Fig. 8** **a** Gullies at Site 2 with varying sizes of rock blocks; **b** gullies near the base of the slope at Site 3 with large rock blocks; and **c** a large gully at Site 4 with large rock blocks

**Table 1** Results of the modified ODOT RHRS for the four study sites

| Factor | Site 1 | Site 2 | Site 3 | Site 4 |
|---|---|---|---|---|
| Failure type/hazard | 9 | 100 | 100 | 27 |
| House impact | 3 | 81 | 27 | 27 |
| Annual frequency | 25 | 25 | 25 | 25 |
| Potential for property damage/injury or fatality | 30 | 100 | 100 | 100 |
| Accident history | 3 | 100 | 9 | 9 |
| Sum | 70 | 406 | 261 | 188 |
| Rating (%) | 14 | 81 | 52 | 38 |

occur. In the modified system, the scoring method is the same as the initial ODOT RHRS, with low values representing a low hazard potential and high numbers representing a high hazard potential. A high hazard ranges from 100 to 66%, a moderate hazard ranges from 65 to 33%, and a low hazard ranges from 32 to 0%. The percentages are derived by dividing the score of the slope by the total possible score of 500 (a maximum of 100 for each of the five factors). Table 1 shows the results of the modified version of the RHRS for the four Rockville sites, with Site 2 exhibiting the highest risk and Site 1 the lowest risk from rockfalls.
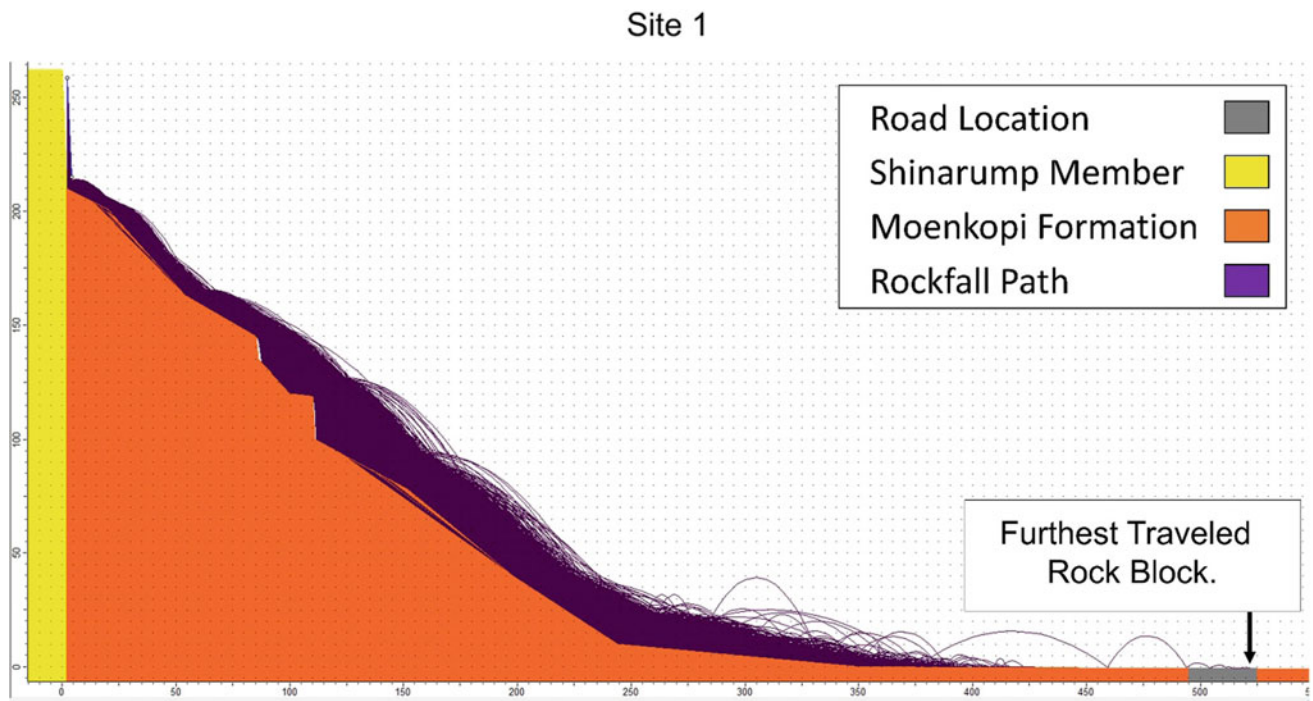
## Site 1



**Fig. 9** Rockfall simulation plot for Site 1 using RocFall software (Rocscience 2015). The rock block weighed 41 kg. After 11,000 simulated rockfalls with variable random block sizes and initiation points along the face of the Shinarump Conglomerate Member, the furthest rollout distance from the point of release was 159 m. This distance represents the furthest distance a rock block can travel at Site 1 for the various block sizes tested

## 7 Rockfall Simulations and Rollout Distances

Using RocFall software (Rocscience 2015), rockfall rollout distances were determined for all four sites. Figure 9 shows an example of such analysis for Site 1. The analysis indicated that the rollout distances for Sites 1, 2, 3, and 4 were 159, 253, 167, and 154 m, respectively. These rollout distances were used to establish the hazardous zones for different portions of the Rockville slope. As long as homes are located within these rollout distances, they are subject to rockfall hazard.

## 8 Conclusions

The conclusions of this study can be summarized as follows:

1. The factors contributing to rockfall occurrence in the Rockville, Utah, area include unfavorably oriented discontinuities, differential weathering, and climate whereas the factors contributing to risk associated with rockfalls include slope height, gullies, and proximity of homes to toe slope.

2. According to the modified RHRS, three categories of rockfall hazard or risk can be used for the Rockville area with the following scores: high hazard—100 to 66%; moderate hazard—65 to 33%; and low hazard—32 to 0%. Site 2 falls in the high hazard category, Sites 3 and 4 in the medium hazard category, and Site 1 in the low hazard category.

3. The rollout distances for the four sites range from 154 to 253 m. Any current and future homes built within 253 m of the slope toe are exposed to potential risk from rockfalls. However, the extent of risk lessens from the western toward the eastern part of the slope.

## References

American Society for Testing and Materials (ASTM): Standard test method for slake durability of shales and similar weak rocks, D644-08, ASTM International, vol. 1 (2010). https://doi.org/10.1520/D4644-08

Dalrymple, J., Piper, M.: Rock slide destroys home, kills two in Rockville. Salt Lake City: The Salt Lake Tribune. Retrieved from http://archive.sltrib.com/story.php?ref=/sltrib/news/57256787-78/amp-rockville-slide-wright.html.csp (2013)

Graham, J.: Zion National Park geologic resource evaluation report: NPS/NRPC/GRD/NRR-2006/014. National Park Service, Denver, Colorado (2006)

Jacklitch, C., Shakoor, A., Lund, W.R.: Evaluation of Rockfall-hazard potential for Rockville, Utah, following a 2013 Fatal Rockfall. Environ. Eng. Geosci. **XXIV**(2) (in press) (2018)

Knudsen, T.R.: Investigation of the February 10, 2010 Rock Fall at 274 west main street, and preliminary assessment of Rock Fall Hazard, Rockville, Washington County, Utah. Report of investigation 270, Utah Geological Survey, pp. 1–17 (2011)

Knudsen, T.R., Lund, W.R.: Geologic hazards of the state route 9 corridor, La Verkin city to town of Springdale, Washington County, Utah. Utah geological survey special study 148, 13 p. 9 plates, scale 1:24,000, DVD (2013)

Lund, W.R., Knudsen, T.R., Bowman, S.D.: Investigation of the December 12, 2013, Fatal Rock Fall at 368 west main street, Rockville, Utah. Report of investigation, 273 Utah geological survey, p. 20 (2014)

Mabbutt, D.: Rockslide in Rockville, one home destroyed, 2 fatalities. St. George: St. George News, Retrieved 8 Feb 2014 from (2013)

Pierson, L.A.: The Rockfall hazard rating system. Oregon department of transportation technical report FHWA-OR-GT-92-05, pp. 1–11 (1991)

Stimpson, B.: A suggested technique for determining the basic friction angle of rock surfaces using core. Int. J. Rock Mech. Min. Sci. Geomech. Abstr. **18**(1), 63–65 (1981)

Rocscience Inc.: Dips version 6.016. University of Toranto, Toronto, Ontario (2014)

Rocscience Inc.: RocFall version 5.014. University of Toranto, Toronto, Ontario (2015)

Utah Geological Survey.: Interactive Utah geologic map. Retrieved 8 Feb 2014 from Utah Geological Survey Geologic Maps, http://geology.utah.gov/maps/geomap/interactive/viewer/index.html (2013)

Wyllie, D.C., Mah, C.W.: Rock slope engineering, 4th ed. Spon Press, New York, p. 431 (2004)

# Weathered Rock Slope Stability Assessment and Risk Mitigation Measures—A Case Study from UKM Campus, Bangi, Selangor, Malaysia

Mohammad Feruj Alam, Animesh Talukder, and Tajul Anuar Jamaluddin

## Abstract

A cut slope, located in front of the Faculty of Social Sciences and Humanity (FSSK) building, Universiti Kebangsaan Malaysia (UKM), Bangi, Selangor failed after a heavy rainfall in November 2012. The main objectives of this study are to assess and characterize the landslide hazards to identify the geological parameters contributing towards the hazards and to recommend suitable risk mitigation measures. The study has been carried out by discontinuity survey, soil and rock testings and kinematic stability analysis. The studied slope is made up of predominantly of highly to completely weathered phyllite, graphitic phyllite and quartzite. The phyllite is generally weak rock and has very low durability, while graphitic phyllite and quartzite are generally medium strong rocks with low durability. The slope is dissected by at least 5 sets of discontinuities (mainly joints and foliations), which exerted profound control on the geometry of the slope failure. Kinematic stability analyses indicated that the slope is unstable and have undergone planar, wedge and/or combined modes of failure. To mitigate the risk for retrogressive failure, the slope has been stabilized with active netting (wire mesh with soil nails). The slope is also equipped with sufficient drainage system to control surface runoff and vegetation cover by applying hydroseeding method. This study has shown a typical example of the importance of geological studies in identifying the root causes for a failure of weathered cut slope and recommended methods for stabilization and remediation of a failed weathered cut slope in a wet tropical country such as Malaysia.

## 1 Introduction

The studied cut slope is situated in front of the Faculty of Social Sciences and Humanity (FSSK), Universiti Kebangsaan Malaysia (UKM), Malaysia. The UKM campus area situated in Bangi, Selangor is encompassing the Kuala Lumpur International Airport, Kuala Lumpur—the main commercial centre, and Putrajaya—the administrative capital. This studied slope area is located about 35 km south of Kuala Lumpur city, 45 km from Kuala Lumpur International Airport (KLIA) and 20 km from Putrajaya. The coordinate of this slope is 02° 55′ 40.94″ N and 101° 46′ 51.48″ E (Fig. 1).

This research lies on its specific focus to assess the stability of the slope and to identify the existing and to predict likely mode of instabilities or slope failures and then assess/recommend to the suitable stabilization/protection measures. This research involves identification of landslide hazards, geological structures, identification of discontinuity, measurement of discontinuity orientation and delineation of weathering grade. This slope is sensitive to landslide hazard aspect due to two landslide occurrences in this slope.

In this slope, first landslide occurred in the 1990s (actual date unknown) and second landslide occurred in 09 November 2012. The residual soil, phyllite, graphitic phyllite, quartzite, oxidized layer/band and quartz vein is exposed in cut slope. Most part of the hill is covered by residual soil but some part of the hill is covered by

M. F. Alam (✉)
Urban & Engineering Geology Branch, Geological Survey of Bangladesh (GSB), Dhaka, Bangladesh
e-mail: ferujgsb@yahoo.com

M. F. Alam
Engineering Geology, Geotechnics and Geohazards Research Group, Department of Geological Sciences, Jahangirnagar University, Dhaka, Bangladesh

A. Talukder
Geological Survey of Bangladesh (GSB), Dhaka, Bangladesh

T. A. Jamaluddin
Geology Programme, Universiti Kebangsaan Malaysia (UKM), Bangi, Malaysia
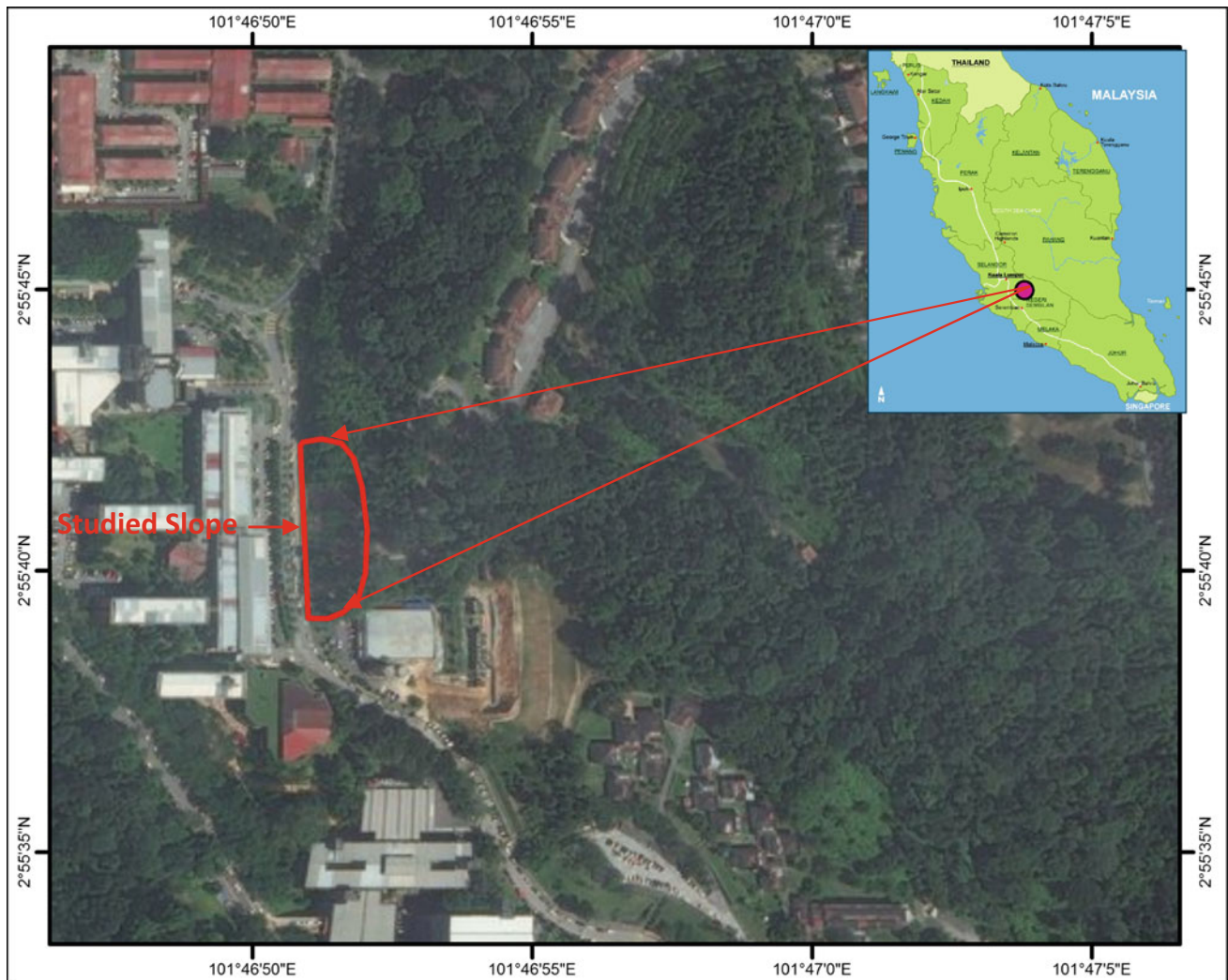
**Fig. 1** Location map of the study area, UKM campus, Malaysia

weathered phyllite and quartzite. The residual soil, completely weathered phyllite, highly weathered phyllite and quartzite belongs to weathering grade VI, V and IV respectively. The graphitic phyllite and quartzite are generally medium strong rocks and low durability, while the phyllite is generally weak rock and very low durability. The slope mass is moderately to heavily jointed. The slope face appeared rough and planar. Two fault line and one recumbent fold was exposed in studied slope.

## 2 Methods

In order to assess the stability of the slope, analyzing a satellite image of the area, followed by slope mapping, soil and rock testings, discontinuity survey, data have been plotted into stereographic plot, kinematic stability analysis of

the slope and finally assess the risk mitigation measures. The slope orientation and slope geometry has been measured by Brunton compass during field work. The lithology and weathering grade have determined by walkover survey and some laboratory testings. The discontinuity survey has conducted by scan line method and randomly at three sections (A, B and C) from five sections because different types of discontinuity have been exposed at three sections of studied cut slope in accordance with I.S.R.M. (1978).

The collected discontinuity and slope orientation data compiled and analyzed statistically by plotting onto equal area net and lower hemisphere projections e.g. pole plot, contour plot, and mean great circle plot. Then interpretation and identification of major and minor discontinuity sets were done and calculated their mean orientations. This work has been done by Stereo 32 software. Friction circle ($\phi$ = friction angle) has been plotted. The friction angle along the major joints in

the saturated completely to highly weathered phyllite is about 32° is assumed for this research case (Xu et al. 2012). This value is considered reasonable, since some of the major joints are normally wavy, tight, dry and have rough surface. The area bounded by the friction circle and slope face (the shaded area in the stereoplots) is considered as critical area. If any discontinuity plane or an intersection between two or more discontinuity planes fall within this area, the rock block or slab bounded by that particular discontinuity planes is likely to be unstable. The potential mode of failure can either be one or combination of the modes of failure e.g. Circular failure, Planar failure, Wedge failure and Toppling failure which have been determined in accordance with Hoek and Bray (1981).

The average great circle was plotted on stereogram and a hypothetical profile line were drawn perpendicular to the slope face on stereogram at three sections of studied slope for further analysis. Along X–Y section calculate the true dip and apparent dip of major discontinuities on stereogram.

Then draw a cross section based on apparent dip and shown potential slope failure direction.

For discontinuity survey and detail study this studied slope was dissected by following five sections those are shown on the Table 1. Three sections have been selected from five sections of studied slope for the purpose of kinematic stability assessment.

## 3 Results and Discussions

### 3.1 Discontinuity Survey

During field work, three types of discontinuity (joint, foliation and fault) have been measured. All discontinuity parameters e.g. types, orientation, length, aperture, filling, roughness and water have measured. Discontinuity sets and average orientation of the discontinuities are shown on the Table 2.

**Table 1** The summary of the slope sections of the studied slope in UKM campus

| Section name | Range of length (m) | Slope length (m) | Thickness of cut slope (m) | Slope strike | Slope dip direction | Slope amount of angle | Remarks |
|---|---|---|---|---|---|---|---|
| Section A | 0–24 | 24 | 2–2.75 | N 10° E to S 10° W | S 80° W | 56° | Cut slope section |
| Section B | 24–58 | 34 | 1.5–2.0 | N 12° E to S 12° W | N 78° W | 51° | Cut slope section |
| Section C | 58–94.5 | 36.5 | 0.8–1.5 | N 12° E to S 12° W | N 78° W | 51° | Cut slope section |
| Section D | 94.5–112.4 | 17.9 | | N 10° E to S 10° W | N 80° W | 46° | Failure slope section |
| Section E | 112.4–141.0 | 28.6 | 1–2.3 | N 05° E to S 05° W | N 85° W | 56° to 35° | Cut slope section |

**Table 2** The summary of discontinuity data from different section of the studied slope

| Sections | Discontinuity sets | Average orientation of the discontinuities | Remarks |
|---|---|---|---|
| A | F | 128/54 | Foliations |
| | J1 | 269/41 | Joints |
| | J2 | 233/83 | Joints |
| | J3 | 197/80 | Joints |
| | J4 | 295/71 | Joints |
| B | F | 162/42 | Foliations |
| | J1 | 183/08 | Joints |
| | J2 | 226/36 | Joints |
| | J3 | 306/43 | Joints |
| | J4 | 060/71 | Joints |
| C | F | 136/48 | Foliations |
| | J1 | 232/40 | Joints |
| | J2 | 243/84 | Joints |
| | J3 | 310/51 | Joints |

## 3.2 Slope Stability Assessment

The slope stability assessment adopted in this study is to highlight any potential danger and mode of weathered rock cut slope failure. Therefore the kinematic slope stability assessment is most suitable. The use of stereographic projection allows the three dimensional orientation data to be represented and analyzed in two dimensions. The stereographic analyses consider only angular relationships between lines, planes and both of lines and planes. Based on this stereographic analysis, the potential mode of slope failures can be determined and assisting the engineer to design or planning the suitable stabilization measures.

The result of the kinematic stability analysis indicates that the three sections of this slope are considered unstable as shown on Fig. 2. The summary of kinematic stability analysis from different section of the studied slope is shown on the Table 3. Field observation indicates that a number of loose/unstable wedges and blocks are readily bounded by dilated/opened up joints, suggesting subtle movements which need urgent attention and stabilization or protection works.

The result of cross section showing the likely structural discontinuities orientation and the potential sliding plane and mechanism of major failure in the different sections of studied slope in UKM. X–Y profile line has been drawn on stereogram and cross sections and the interpreted failure modes are shown on Fig. 3.

## 4 Risk Mitigation Measures

The studied slope is stabilized by steel-wire mesh coupled with active soil nails to stabilize and reinforce the slope. A retaining wall is constructed along the toe of the slope and a drainage control system is installed to intercept and divert surface runoff from flowing over the slope. A hydroseeding method is also applied to the slope for soil improvement to support vegetation growth on poor sub-soil conditions. Details of the recommended stabilization and protection measures for the slope are given below.

### 4.1 Wire Mesh with Soil Nail

The high tensile strength steel-wire mesh is laid down to cover the entire slope face. The wire mesh panels are then tied back and secured to the slope face with steel rope or cable net, system spike plates specially adapted to the net cover, border steel ropes or cables as well as an adequate nailing adapted to the site specific situation. Border ropes have to be able to transfer the load from the net onto the nails in the border sections. The soil nails can provide deeper stabilization by holding the mesh to the surface throughout. These designs are largely dependent on the ability of the system to transfer forces from the facing material to the anchor points.

This method is preferred compared to shotcrete or other impermeable slope protection structures mainly because it allows the groundwater and surface runoff to percolate in and drain out freely through it, thereby permitting healthy and lasting surface vegetative cover. The flexibility and 3D characteristics of the wire mesh and cable netting system allow the mesh to be installed on undulating slope surface and to wrap around existing big trees without removing or cutting down the trees (Jamaluddin 2010; Fatzer et al. 2006).

The wire mesh is used in combination with the active soil nails, provides a flexible and strong surface protection and stabilization cover by being able to lay taut against the rock surface. Soil nailing is in situ reinforcement technique (internally stabilized system) which consists of long steel rods inserted into less disturbed bedrock to stabilize the slope mass. Soil nails are normally installed with perpendicular to the potential failure plane (Fig. 4).

### 4.2 Retaining Wall

A retaining wall is usually provided at the toe of a slope to prevent downslope movement. Guide to retaining wall design by GEO (1993), recommended a retaining wall with level backfill. The top 0.04 m layer of fill should be a suitable material of relatively low permeability and the ground surface should be formed with an adequate gradient in order to avoid ponding which can result in continuous infiltration into the backfill. For retaining wall less than 2 m high, drainage (weep hole) is usually vertically positioned against the back face of the wall.

### 4.3 Drainage Control System

Surface runoff is controlled by installing different types of drain; i.e. cut-off drain, cascading drain and toe drain. Cut-off drain intercept surface flow at the top of the slope, and are normally placed at the crest. Cascading drain connects the cut-off drain and toe drain. This drain network is constructed to intercept and divert surface runoff from flowing over the slope and to prevent surface erosion as well as to minimize infiltration into the slope mass.

Above all the planning and implementation of the proposed slope stabilization measures described above should be supervised by an experienced engineering geologists/geotechnical engineers.
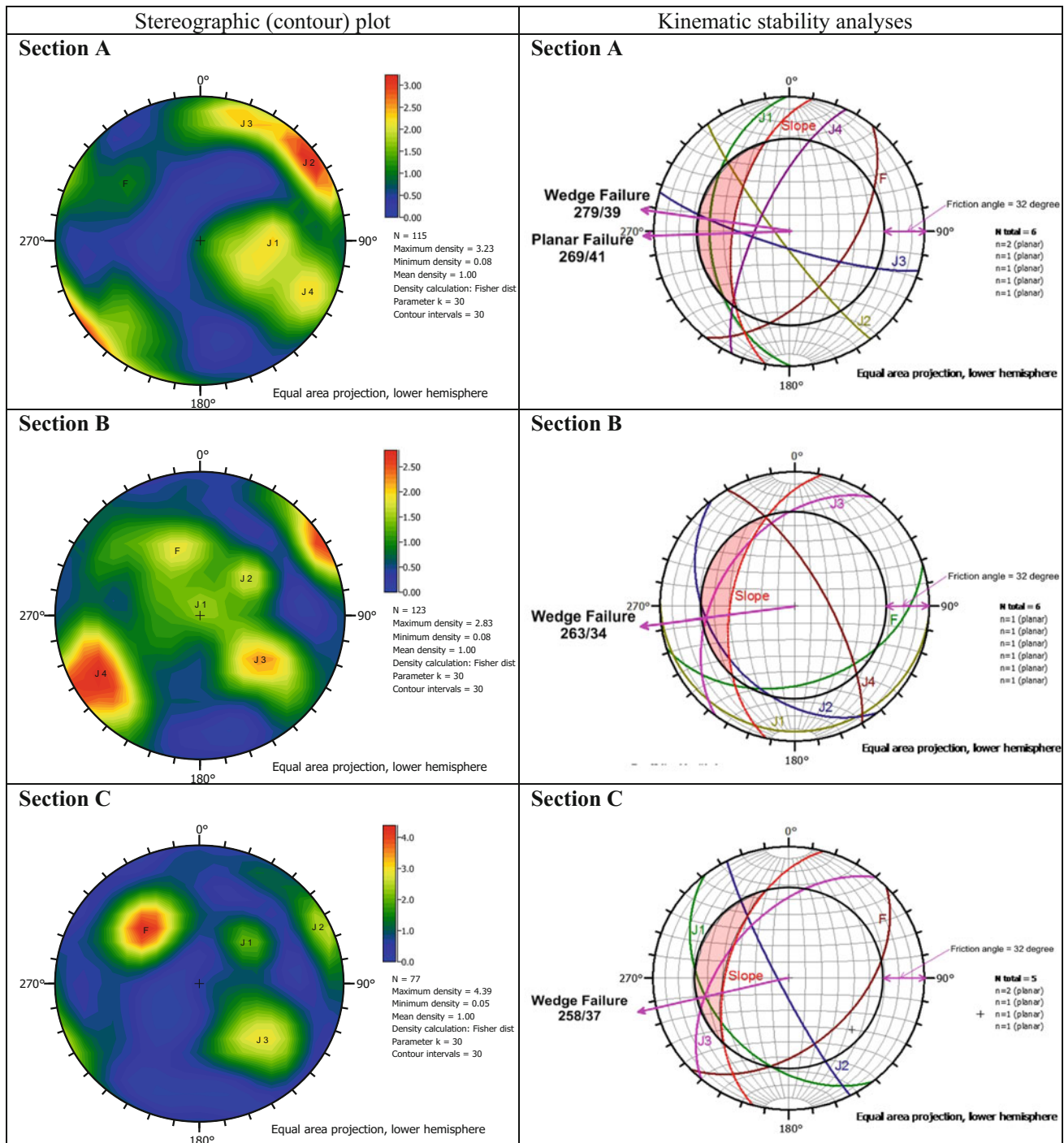
**Fig. 2** The stereographic (contour) plot of discontinuity data and kinematic stability analysis of section A, B and C of the studied slope

**Table 3** The summary of kinematic stability analyses from different sections of the studied slope

| Sections | Mode of potential failure | Joint sets intersection | Direction of potential failure | Description |
|---|---|---|---|---|
| A | Wedge | J1 and J3 | 279° | Potential wedge failure. Joint set J2 act as the release plane |
| | Planar | J1 | 269° | Potential planar failure. Joint set J3 and foliation plane act as the release plane |
| B | Wedge | J2 and J3 | 253° | Potential wedge failure. Joint set J4 act as the release plane |
| C | Wedge | J1 and J3 | 258° | Potential wedge failure. Joint set J2 act as the release plane |
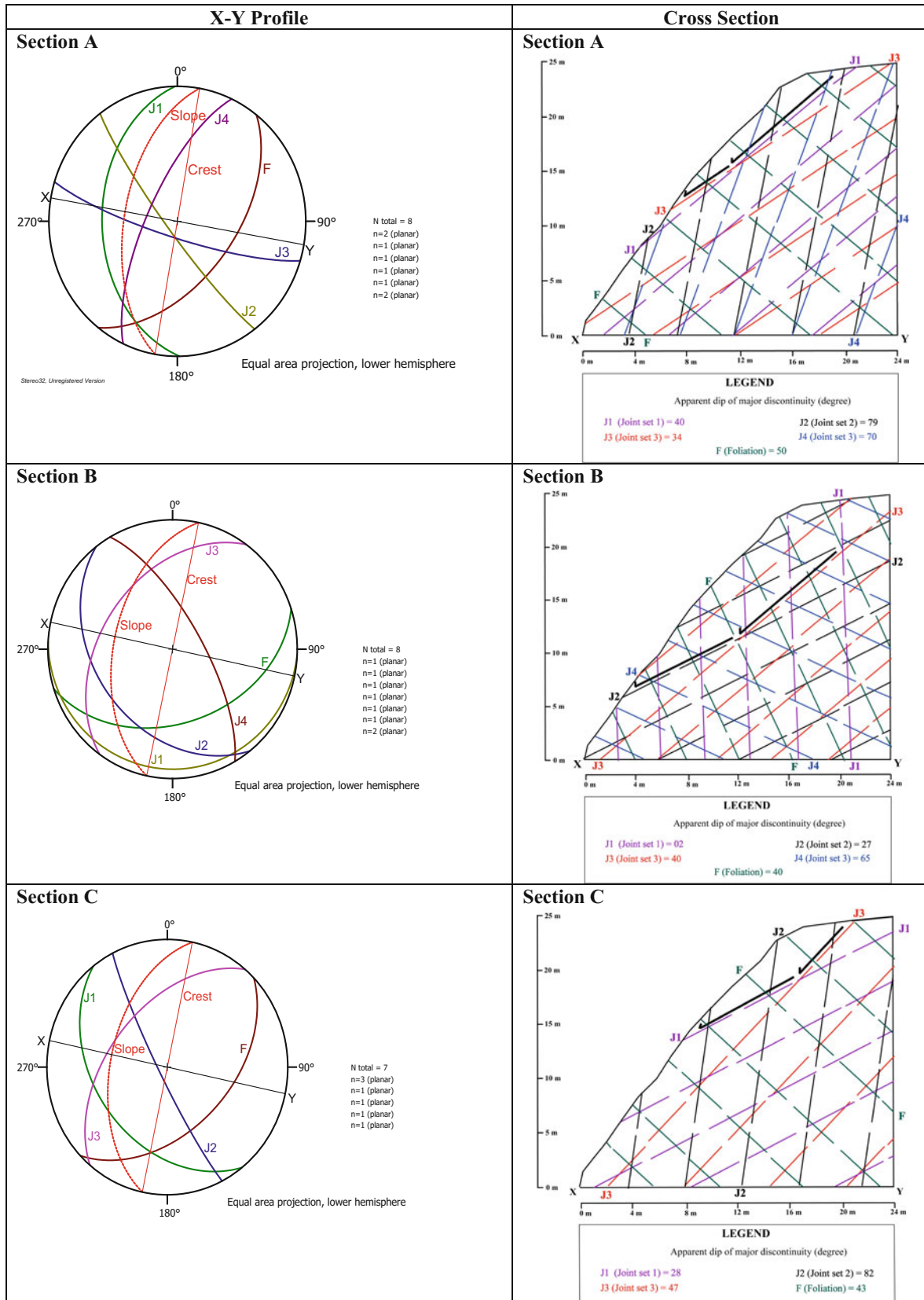
**Fig. 3** The X–Y profile of stereographic projection of major discontinuities and cross sections showing the likely mechanism of major failure in the section A, B and C of the studied slope

**Fig. 4** Proposed conceptual design of a recommended method for slope stabilization showing soil nails orientation, wire mesh and retaining wall at section C of the studied slope
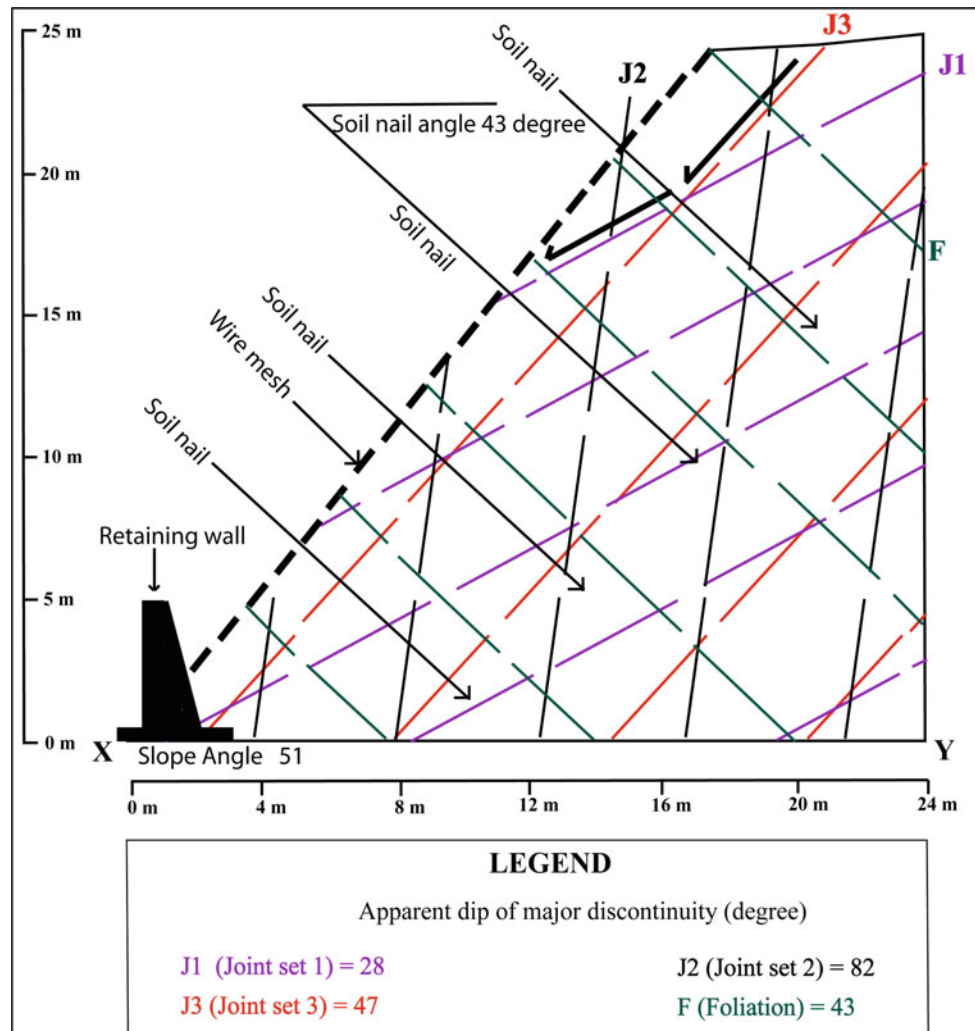
## 5 Conclusion

Results of the discontinuity survey indicate phyllite and quartzite rock mass is moderately to heavily jointed, well foliated and is dissected by 2–5 sets of discontinuities. The slope failure geometry is largely controlled by discontinuities (joints) in the slope masses. The fallen blocks or debris are generally very small to small scale, measures at several tens of cm and generally less than 1.5 m in length or width because the joint spacings are relatively small (several cm to 0.5 m apart). Results of the kinematic stability analysis showed that the studied slope is unstable. The slope shows high potential for planar, wedge and/or combined modes of failure. Based on this study, the main causing factors for the landslide are unfavorable discontinuity orientation, lithology of slopes, highly weathered materials and heavy rainfall. The studied slope has stabilized with steel wire mesh coupled with active soil nails. The toe of the slope is further supported with retaining wall and surface drainage system. A hydroseeding method has also applied to the slope for soil improvement and to support vegetation growth on poor sub-soil conditions. This study showed a typical example of the importance of geological studies in identifying the root causes for a cut slope failure in weathered rocks and the recommended methods for slope stabilization and remediation of a failed weathered cut slope in a wet tropical country such as Malaysia.

# References

Fatzer, A.G., Flum, D., Salzmann, H.: Kiara condominium, Sri Damansara, Selangor, Malaysia, Protection of the rock slope with the SPIDER system—General proposal, 25 Aug 2006. Geobrugg protection systems, Switzerland. Unpublished draft report (2006)

GEO: Guide to retaining wall design, 2nd edn. Geotechnical Engineering Office, Hong Kong (1993)

Hoek, E., Bray, J.W.: Rock Slope engineering. Institution of mining and metallurgy. E & FN Spon press, London (1981)

I.S.R.M.: International society for rock mechanics commission on standardization laboratory and field tests. Suggested methods for the quantitative description of discontinuities in rock masses. Intl. J. Rock Mech. Min. Sci. Geomech. Abstr. **15**, 319–368. Pergamon Press Ltd., Great Britain (1978)

Jamaluddin, T.A.: Engineering geological mapping report for stability assessments of Cheras Quarry phase 3 (Lot PT 1495/1, 1495/2, 1495/3 and 1495/4), p. 15. Mukim Cheras, Daerah Hulu Langat, Selangor (2010)

Stereo32: Software for geoscientists, Ruhr University of Bochum, Endogenous Geology, Institute of Geology and Mining, Germany, http://www.ruhr-uni-bochum.de/hardrock/downloads.html

Xu, L., Han, Z., Chen, S., Chen, H.: Research on the triggering factors analysis and relevant countermeasures of fating mountain landslide induced by Wenchuan earthquake. Earthquake—induced landslides. In: Proceedings of the international symposium on earthquake—induced landslides, Kiryu, Japan. Springer science and business media, p. 362 (2012)

# Landslide Prevention Costs in Road Construction Projects: A Case Study of Diezma Landslide (Granada, Spain)

E. Bergillos, J. Garrido, J. Ordóñez, J. Delgado, and J. M. Bueno

### Abstract

During the construction of many roads, slope stability problems can occur, resulting in a delayed completion of the construction as well as an increased final budget. However, there is still limited data collected that reveals the actual costs of geotechnical issues. The Diezma landslide, affecting the A-92 highway (Granada, SE Spain), is a great example of this situation. The construction project, which was started in 1988, did not identify the geotechnical instabilities of this zone, thus no preventive measures were recommended. The landslide-induced disruption of the highway involved economic losses related to the implementation of corrective measures and to indirect costs. In this paper, an evaluation of direct and indirect costs induced by the landslide is developed, and as a result, the potential cost savings of an adequate geotechnical survey are obtained.

E. Bergillos (✉) · J. Garrido
Dpto. Ingeniería Civil, Universidad de Granada, Campus de Fuentenueva s/n, 18071 Granada, Spain
e-mail: eduardobergillos@correo.ugr.es

J. Ordóñez
Dpto. Ingeniería de la Construcción y Proyectos de Ingeniería, Universidad de Granada, Campus de Fuentenueva s/n, 18071 Granada, Spain

J. Delgado
Dpto. Ciencias de la Tierra y Medio Ambiente, Universidad de Alicante, Po. Box: 99 03080 Alicante, Spain

J. M. Bueno
Consejería de Fomento y Vivienda, Junta de Andalucía, Avda. Joaquina Eguaras 2, 18071 Granada, Spain

## 1 Introduction

Landslides affecting linear infrastructures usually occur on mountainous terrain, where cuttings and embankments are very high and steep. When these landslides happen during the construction stage, they result in delays and excessive costs, as well as in modifications of the construction projects. However, when they happen during the operation stage, damages may require the closure of traffic lanes or even the whole highway, in order to make repairs. In both cases, the resulting costs are substantial for the Administration as well as for the users, and these costs could have been avoided with an adequate geotechnical survey during the planning stage.

One infrastructure notably affected by this issue is the A-92 highway in Granada, (SE Spain). Cuttings and embankments of up to 40 m high had to be undertaken due to the geometric and width requirements of a highway, and due to the hilly terrain. However, these huge earthworks were not supported by an adequate geotechnical survey; therefore, many cuts and landfills were affected by landslides. After the landslide events, numerous emergency works and stabilization projects were initiated to repair the damage, to reinforce slopes and road pavements, and in some places the highway had to be closed during these repairs. The Diezma landslide on the A-92, located 3 km west of the Diezma village (Fig. 1), has been selected for this analysis due to its huge impact. Construction works in this section started in October 1989 and ended in December 1992. Since then, additional works have been undertaken due to landsliding, including three projects under emergency conditions and two stabilization projects (Delgado et al. 2015).

Geotechnical surveys are usually carried out at minimal costs, which does not achieve the thoroughness required to avoid future issues. However, if the costs of later investment in repairs and indirect costs were taken into account, the need to give greater importance to geotechnical studies when

**Fig. 1** Location of the study area in Granada, (SE Spain)



assigning budgets in projects could be clearly justified. A cost/benefit analysis has proven that economic losses cost more than preventive measures (Salbego et al. 2015), and that even the economic losses suffered by the users match or surpass the repair costs (Zêzere et al. 2007; Vranken et al. 2013).

## 2 Geological Setting and Background

Geologically, the area is characterized by the tectonic contact between the Maláguide and the Dorsal domains of the Betic Cordillera chain, where the Numidoide Formation also outcrops. The materials which constitute the Maláguide are red silt, green clay, and black schist with phyllites as bedrock. The Numidoide Formation is composed of a silty-clay silo-clastic matrix with heterometric blocks of limestones and the upper part of the area consists of the limestones of the Dorsal Domains outcrop (Rodríguez-Peces et al. 2011). These limestones have been thrust over the Numidoide Formation and give rise to an accumulation of water over the impermeable layer, forming several springs.

Since its construction, this area has suffered from instabilities (Fig. 2), but applied solutions were at most re-shapes of the slopes. However, on 18 March 2001, a period of intense rainfall triggered the main landslide, with a depth of 10–30 m and an approximate volume of 1,250,000 $m^3$ mobilized. Its toe coincided with the bottom of the

highway's trench, so this landslide collapsed over the highway entirely burying one roadway and partially burying the other.

As a temporary solution, during emergency works and the first stabilization project, a provisional roadway was built in order to restore traffic. However, it required 20 days to complete this road and traffic had to be detoured. Between March 2001 and February 2002, the main constructed corrective measures were: 5 barriers of 89 drainage wells (6–25 m deep), a superficial drainage system composed of ditches and 31 French drains, and a retaining barrier founded by 36 piles (cross-section of 5.70 $m^2$), 12–37 m deep, anchored with 35 anchors (Fig. 3). Later in 2008, a new stabilization project was needed because of the damage that this landslide, which was still in motion, caused to the previous structures upslope of the retaining wall. It consisted of repair works on the ditches, and the drilling of 14 new wells in order to restore broken drainage connections between affected wells (Delgado et al. 2015).

## 3 Methodology

The methodology applied in this study consisted of assessing two scenarios and applying a post-event cost/benefit analysis. Scenario 0 is the actual situation, considering the costs of geotechnical surveys and stabilization projects, all the aforementioned works done so far to stabilize the landslide,

**Fig. 2** Damages: **a** landslide (October 1991), **b** landslide (May 2000), **c, d** main landslide (March 2001), **e** broken drainage well (May 2006), **f** crack near the landslide crown (November 2009)

and the traffic disruption. Scenario 1 is a hypothetical situation where a thorough geological-geotechnical survey would have allowed the design of preventive measures. This would have resulted in most of the works being done during the actual highway construction (some of them would not have been necessary because the landslide would not have happened) and would have avoided remedial work and traffic interruption.

Both direct and indirect costs have been considered. Direct costs are those directly caused by the landslide, and in this study were the costs derived from construction, reconstruction, repairs or maintenance of the affected infrastructure, with their corresponding data acquisition surveys, studies and projects. Indirect costs are those caused by not being able to use the affected infrastructure due to a landslide (Schuster and Highland 2001).

**Fig. 3** Countermeasures: **a** provisional roadway (April 2001) **b** anchors (October 2001) **c** retaining barrier (August 2001) **d** drilling new wells (October 2009)

In order to estimate direct costs, an analysis of projects and studies developed in the area of the Diezma landslide has been made. This analysis resulted in an inventory of all work construction units, measurements and prices, that composed the corrective measures, and has been represented in 2017 monetary units to facilitate comparisons. Project redaction and geotechnical survey (boreholes, laboratory tests, etc.) costs have also been considered, and they added up to 446,744.64 € (being 270,315.78 € for project

redaction and 176,428.86 € for geotechnical surveys). This way, overall direct costs of Scenario 0 have been obtained. Then, to assess direct costs in Scenario 1, all work construction units regarding repairs (such as resurfacing or re-drilling wells, and construction of the provisional roadway) have been removed since the landslide would not have occurred and remedial work would not have been needed. The rest of the remaining work construction units have been considered as preventive measures being part of the initial

construction project designed in 1988. To estimate the value that each work construction unit would have had in 1988, unitary prices for machinery, materials and salaries have been adopted from the initial project whenever possible and those that were not in the project have been extracted from a construction price base from 1988 (Fundación Codificación y Banco de Precios de la Construcción 1988).

In order to estimate indirect costs, we identified the alternative path of the A-92 highway and compared it to the original route. The most direct and used route was the A-308 road (Fig. 1), which was 18 km longer. Applying the methodology suggested by the Ministry of Civil Works (MOPU 1990; Ministerio de Fomento 2014), together with route geometry (length, travel time, average speed, average gradient) and traffic characteristics [daily light and heavy mean traffic and fuel type data from the Traffic General Directorate (DGT)] gathered (see Table 1), different types of costs endured by users have been assessed for both routes and converted to 2017 monetary units. Finally, once all these costs of vehicle depreciation, maintenance, fuel and oil consumption, tyre usage and time loss were obtained, the difference between the two routes was calculated, and is the total of indirect costs induced by the landslide.

## 4 Results and Discussion

The outcomes obtained (Table 2) indicate that the application of preventive measures in Scenario 1 are 5,094,503.87 € (2017 monetary units) cheaper than the current works considered in Scenario 0. This difference is due to avoidable costs, being 1,262,837.15 € of construction direct costs (Fig. 4a), 446,744.64 € of project redaction and geotechnical surveys, and 3,384,922.08 € of indirect costs (Fig. 4b). Therefore, these avoidable costs can be interpreted as the available margin for boreholes and laboratory tests without surpassing the cost already spent.

However, there are certain parameters that could not be considered in this methodology and that would have greatly affected these results. Firstly, economy of scale would be the most important. Applied to construction works, the greater the magnitude of the works, machinery and methods employed, the less their unitary prices because of higher performance, making the difference even higher. Some construction units such as reshapes of the slope were done several times over. So, if all these earthworks and measures had been made once during construction stage, economy of scale would have taken place and this efficiency would have reduced the costs.

On the other hand, if preventive measures had been performed before the landslide happened, geotechnical parameters used in the countermeasures design would not have been residual ones. This greater shear strength of the ground would have allowed the definition of cheaper and less impacting measures than the ones implemented. Therefore, direct costs difference could have been even higher. Regarding indirect costs, it must be considered that all the traffic redirected from A-92 highway was sent through the A-308, a conventional road not prepared for such traffic. If it was proven that this detour increased the number of car accidents, indirect costs would have risen hugely. Moreover, this study considered the vehicle occupation rate as only the

**Table 1** Parameters considered in the analysis of indirect costs

| Section characteristics | Length (km) | Travel time (h) | Average speed (km/h) | Average gradient (%) |
|---|---|---|---|---|
| Scenario 0 (reroute by A-308) | 59 | 0.82 | 72 | 0.64 |
| Scenario 1 (A-92) | 41 | 0.43 | 95 | 0.91 |
| Affected vehicles per day | Total | | Gasoline vehicles (%) | Diesel vehicles (%) |
| Light vehicles (LV) | 13,106 | | 72.71 | 27.29 |
| Heavy vehicles (HV) | 1235 | | 20.31 | 79.69 |
| *Fuel prices* | | | | |
| Gasoline (€/liter without taxation in 2001) | | | 0.55 | |
| Diesel (€/liter without taxation in 2001) | | | 0.56 | |
| *Tyre prices* | | | | |
| Light vehicle (€/4 tyres) in 2001 | | | 327.76 | |
| Heavy vehicle (€/6 tyres) in 2001 | | | 4491.98 | |
| *Oil prices* | | | | |
| Light vehicle oil (€/liter) in 2001 | | | 3.58 | |
| Heavy vehicle oil (€/liter) in 2001 | | | 4.00 | |

**Table 2** Construction direct costs and indirect costs obtained

|  | Scenario 0 | Scenario 1 |
|---|---|---|
| *Direct costs (€)* | | |
| Preventive measures 1992 | | 11,431,169 |
| Settlement 1992 | 167,273 | |
| Emergency works 1998 | 755,380 | |
| Emergency works 2001 | 1,858,745 | |
| Stabilization 2001 | 9,189,061 | |
| Stabilization 2008 | 723,546 | |
| *Indirect costs (€)* | | |
| Depreciation | 853,084 | 592,821 |
| Maintenance | 679,456 | 424,059 |
| Fuel consumption | 938,179 | 770,444 |
| Oil consumption | 65,194 | 51,862 |
| Tyres | 316,406 | 219,876 |
| Time loss | 5,449,141 | 2,857,476 |
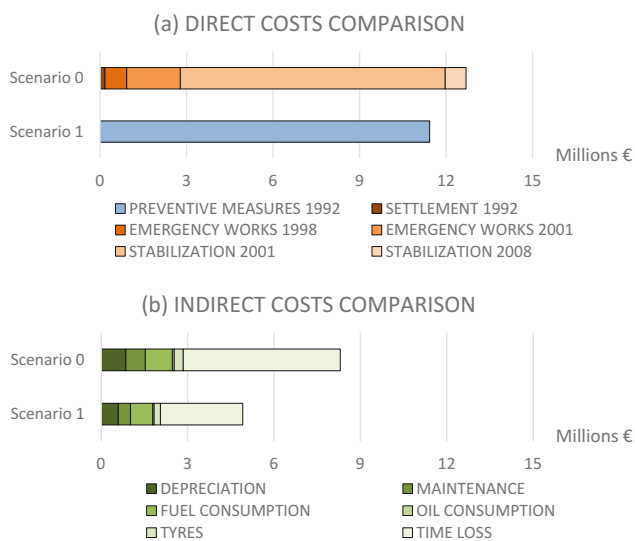


**Fig. 4** Comparison of total direct and indirect costs

driver, due to lack of available data. So, taking into account more passengers would have multiplied indirect costs related to time lost. There are also more types of indirect costs such as loss of value of affected land or economic losses of business in the area. However, this cost assessment has not been considered due to the lack of available data. But despite them being underestimated, indirect costs constitute 66.44% of the total difference in costs, highlighting the economic importance of the traffic interruption to a critical highway such as the A-92.

## 5 Conclusions

This study analysed all projects and corrective measures focused in the area of the Diezma landslide in order to assess the direct costs it caused. Then, it employed traffic data and the methodology suggested by the Ministry of Civil Works to estimate economic losses caused to users of the A-92 highway (indirect costs). These costs have been compared with an assessment of how much it would have taken to make these stabilization works as part of the initial construction project in July 1988 (only direct costs, because there would not have been traffic interruption). This way, an approximation of the potential cost savings of doing a correct geological-geotechnical survey during the planning stage were obtained. Both direct and indirect costs demonstrate that an adequate geotechnical survey at the start of the project would have been economically beneficial, saving up to 5,094,503.87 € (2017 monetary value), 30.83% of total costs. That survey would have disclosed the potential for landslide occurrence and its derived costs during the planning stage, so it could have meant developing better and cheaper solutions or even choosing an alternative route with better geotechnical characteristics. Either way, these economic costs plus the costs of time and resources spent on additional works and projects after the triggering of the Diezma landslide could have been focused on the construction of new infrastructure and/or conservation works on older roads, rather than on repairing a recently constructed highway.

# References

Delgado, J., Garrido, J., Lenti, L., López-Casado, C., Martino, S., Sierra, F.J.: Unconventional pseudostatic stability analysis of the Diezma landslide (Granada, Spain) based on a high-resolution engineering-geological model. Eng. Geol. **184**, 81–95 (2015)

Fundación Codificación y Banco de Precios de la Construcción: Precios 88 (1988)

Ministerio de Fomento: Prescripciones y recomendaciones técnicas relativas a los contenidos mínimos a incluir en los Estudios de Rentabilidad de los Estudios Informativos de la Subdirección General de Estudios y Proyectos (2014)

MOPU: Recomendaciones para la evaluación económica, coste-beneficio de estudios y proyectos de carreteras. Actualización del valor del tiempo y costes de accidentes y combustibles (1990)

Rodríguez-Peces, M.J., Azañón, J.M., García-Mayordomo, J., Yesares, J., Troncoso, E., Tsige, M.: The Diezma landslide (A-92 motorway, Southern Spain): history and potential for future reactivation. Bull. Eng. Geol. Environ. **70**, 681–689 (2011)

Salbego, G., Floris, M., Busnardo, E., Toaldo, M., Genevois, R.: Detailed and large-scale cost/benefit analyses of landslide prevention vs. post-event actions. Nat. Hazards Earth Syst. Sci. **15**, 2461–2472 (2015)

Schuster, R.L., Highland, L.M.: Socioeconomic and environmental impacts of landslides in the Western Hemisphere. US Department of the Interior, US Geological Survey, Open-File Report 01-0276 (2001)

Vranken, L., Van Turnhout, P., Van Den Eeckhaut, M., Vandekerckhove, L., Poesen, J.: Economic valuation of landslide damage in hilly regions: a case study from Flanders, Belgium. Sci. Total Environ. **447**, 323–336 (2013)

Zêzere, J.L., Oliveira, S.C., García, R.A.C., Reis, E.: Landslide risk analysis in the area North of Lisbon (Portugal): evaluation of direct and indirect costs resulting from a motorway disruption by slope movements. Landslides **4**, 123–136 (2007)

# Analyzing the Sensitivity of a Distinct Element Slope Stability Model: A Case Study on the Influence of Permafrost Degradation on Infrastructure Stability

Regina Pläsken, Michael Krautblatter, and Markus Keuschnig

## Abstract

Since the 19th century, the warming rate in the European Alpine region has been twice as high as the average global rate. Warming-related permafrost degradation has been shown to cause a reduction of bedrock bearing capacities, potentially leading to the destabilization and eventually to the failure of high-alpine infrastructure. The presented study investigates permafrost-related changes of bedrock properties and their stability-relevant effects on high-alpine infrastructures. The Kitzsteinhorn summit and its highly frequented cable car station (3029 m a.s.l., Austria) is home to the interdisciplinary Open Air Lab Kitzsteinhorn (OpAL), where the consequences of climate change, based on a long-term monitoring of surface, subsurface and atmospheric parameters are investigated. In a rock-ice mechanical model, degradation of permafrost causes changes in rock fracture toughness and rock friction, affects ice fracturing and creep as well as the behavior of rock-ice interfaces. A first numerical distinct element model of the mechanical behavior of rock slope and the infrastructure was set up, based on OpAL datasets and a civil engineering assessment of the cable car setup. By conducting a thorough rock mechanical model sensitivity analysis, it was tested how individual model parameters affect the rock slope stability below the cable car summit station. The accurate knowledge of the most sensitive parameters and their empirical variation range generates a better process understanding of destabilisation in permafrost-affected rock walls. This facilitates efficient stabilization measures for affected high-alpine infrastructures. Here we show, that the stability of infrastructure on permafrost-affected bedrock is not only passively determined by mechanical changes in the underlying frozen rock mass, but infrastructure also actively affects thermal conditions and rock stability in a relevant way.

## 1 Motivation

Alpine regions have shown twice the warming rate compared to the global average since the 19th century (European Environment Agency 2009). Furthermore, high alpine environments are particularly sensitive to changes in system temperature. Thus, infrastructure built in permafrost-affected environments frequently experiences changes of bedrock properties and resulting stability-relevant effects. While most studies so far have focused on the anticipated thermal changes in permafrost environments, few studies have investigated the mechanical consequences of permafrost degradation (Fischer et al. 2006). Recently, different mechanical controls have been combined into a rock-ice-mechanical model accounting for changes in rock fracture toughness and rock friction, ice fracturing and creep as well as the behavior of rock-ice interfaces. While all these factors are known to decrease stability in thawing permafrost rock walls, their importance varies with different temperature and stress conditions (Krautblatter et al. 2013). However, these attempts have neither explicitly included the impact of infrastructure nor the related thermal and stress impacts of the degrading permafrost rock walls (Bommer et al. 2010). Therefore, this parameter study explicitly combines changes resulting from degrading permafrost rock-walls with infrastructure related impacts. The overall aim of this study is to identify the most sensitive parameters within the chosen distinct element model and to thereby generate a better process understanding of slope stability in permafrost-affected rock walls.

R. Pläsken (✉) · M. Keuschnig
GEORESEARCH Forschungsgesellschaft mbH,
Wals-Siezenheim, Austria
e-mail: regina.plaesken@tum.de

R. Pläsken · M. Krautblatter
Chair of Landslide Research, Technical University Munich,
Munich, Germany

## 2 Study Site and Infrastructure

The designated study site is located around the summit station of the Kitzsteinhorn cable car (3029 m a.s.l., Austria, Fig. 1). It encompasses the north-oriented rock wall of the Kitzstein-horn, which consists of calcareous micaschists. The foliation of the micaschists is inclined roughly parallel with the slope, at angles between 39° and 52°. Until the mid-20th century most parts of the rock wall were covered permanently by the glacier. However, its current surface is located approximately 100 m lower. The exposed rock wall between the summit station and the glacier is affected by permafrost and shows significant seasonality in rock fall activity (Hartmeyer et al. 2016). The summit station was first built in 1965/66 and refurbished in 1981 and 2010. The associated cable car station is anchored to the rock face with pre-stressed rock anchors.

## 3 Data and Methods

### 3.1 Laboratory Testing

Samples of calcareous micaschist were taken and tested by Voigtländer et al. (2014) who carried out >70 tests on



**Fig. 1** View on summit station and rock slope

uniaxial compressive strength, tensile (Brazilian) strength and nondestructive tests (such as Schmidt-hammer tests). All tests were conducted on frozen and unfrozen samples in order to get mechanical characteristics of the rock samples in permafrost as well as non-permafrost conditions. Elastic moduli, compressive and tensile strength (Fig. 2) were all derived from that raw data and used as input data for the model.

### 3.2 Field Testing

Near-surface properties of the rock wall were investigated during the geological mapping of the study site (Geoconsult ZT GmbH 2010). Data on the subsurface properties were collected at two deep boreholes (30 m, direction of drilling roughly perpendicular to slope), situated right at the study site: one immediately adjacent to the summit station, the other one about 45 m below the station. In both boreholes data on discontinuity orientation and condition were derived by means of optical borehole scans (Geoconsult ZT GmbH 2014).

In November 2015, two additional rows of overall 15 pre-stressed rock anchors were installed directly beneath the summit station. The 25 m long anchors are drilled with an inclination of around 3° and a grouted section of 7 m length. Drilling data enhanced the data on joint sets.

### 3.3 Modelling

A distinct element model in UDEC™ (Universal Distinct Element Code, Itasca Consulting Group, Inc.), comprising the rock wall from above the station down to the glacier, was set up (Fig. 3). The model of the rock wall consists of rock blocks which follow a linear-elastic material model. These blocks are interconnected by joints which follow the mohr-coulomb material model.

One central parameter set (frozen rock, mean value of parameters) was assembled. Consequently, model runs were performed with variation of temperature conditions (frozen, unfrozen), individual block (rock) and joint parameters in the range of standard deviation (Table 1). Results were compared to the initial (central) parameter set.

The Factor of Safety (FoS) was chosen as model parameter to be contrasted on a comparative basis. The distinct element model set up in UDEC is utilized to investigate the influence of the different model parameters. Values for geometric, elastic and plastic model parameters were derived based on the lab and field data described above. Where no lab or field data were available the dataset was supplemented with data from literature in close linkage to the conditions at the study site. The estimation of the joint
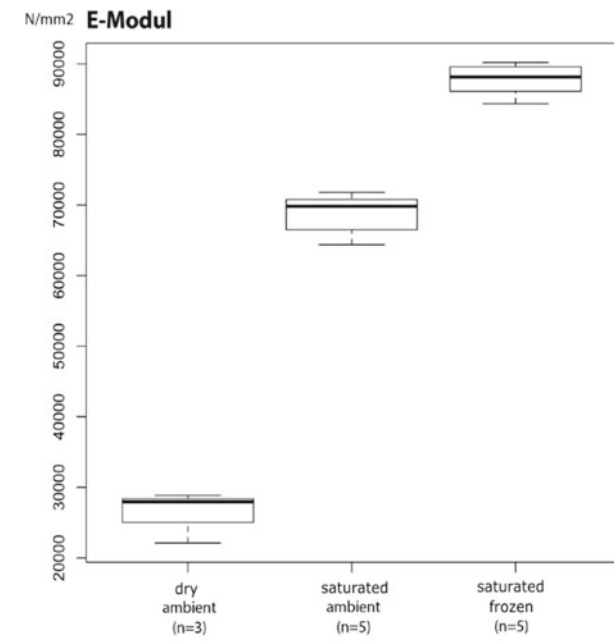
(a) Young's modulus of calcerous micaschists
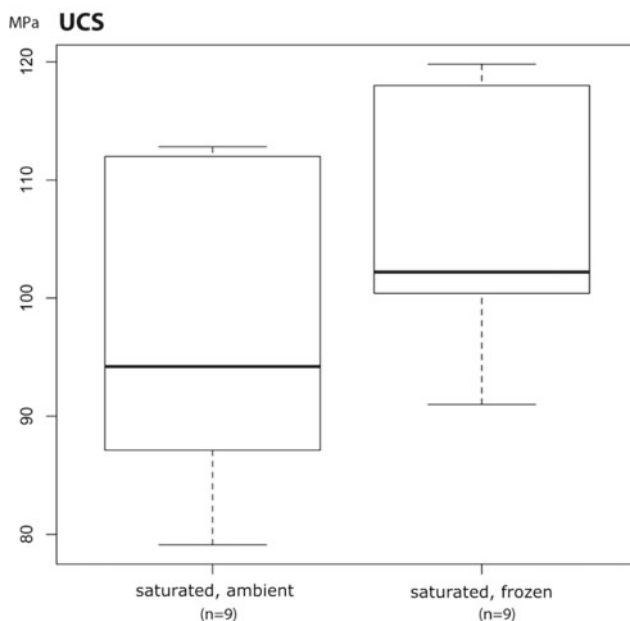


(b) compressive strength of calcerous micaschists

**Fig. 2** Rock parameters of calcerous micaschists in frozen and unfrozen conditions, after Voigtländer et al. (2014)

normal and shear stiffness was derived from the elastic modulus and the condition of the rock after Barton (1972) in conjunction with the assumption of similar stiffness characteristics with a physically possible value range of E (Young's modulus)/G (shear modulus) between 2 to 3. Figure 4 shows parameters used in the distinct element model and their origin. The relations were used for the evaluation of model behavior.

For load values, planning documents were used, the missing information on building infrastructure was collected on-site.

## 4 Results

Variation of parameters resulted in a total of 12 datasets. Six selected datasets are illustrated in Fig. 5 to show the influence of temperature, elastic as well as fracture parameters of rock and joints on model behavior. For each set the central parameter set is contrasted with the varied one in terms of FoS of friction angle and cohesion for both rock and joints. Overall system FoS is the smallest one of the four values. Temperature state only influences FoS in friction of both joint and rock (Fig. 5a). The ambient (unfrozen) state is characterized by a slightly higher FoS. Changes in joint parameters vary in their impact on system behavior: The reduction of friction angle (Fig. 5b) results in a reduction in all FoS of rock and joint parameters. A reduction of joint tensile strength (Fig. 5c) significantly influences FoS of rock cohesion. In contrast, variation of elastic rock parameters (Fig. 5d) have no visible impact on FoS of rock and joint parameters. Higher loads (factor 1.5), shown in Fig. 5e, result in a significant reduction of FoS, particularly in terms of friction angles whereas rock cohesion shows hardly any reaction to the variation. Changes in friction of rock (Fig. 3f) influence FoS significantly except the FoS cohesion of joints, which shows no response to changes.

## 5 Discussion

The factor of safety is apparently influenced only to very small degree by parameters of intact rock, especially by elastic rock parameters (E- and G-modulus). The fracture criteria of rock have a significant impact on the safety margin of the mechanical system. Among changes in the rock mechanical system, the impact of changing friction and degrading fracture toughness in the range of rock bridges (parts of a joint, where rock remained unbroken yet) connecting fracture walls, appear to be the most important ones. There are significant change patterns which can be traced to straightforward physical or model relationships. Examples include the increase of FoS for friction angle when increasing the friction angle in the model or a decrease of FoS when introducing higher loading (Fig. 5e). Deviating from that are some effects which cannot easily be explained. Some of these seem to occur due to numerical reasons and not so much due to conclusive model behavior like the effect

**Fig. 3** Distinct element model in UDEC: rock blocks, joints and infrastructure components
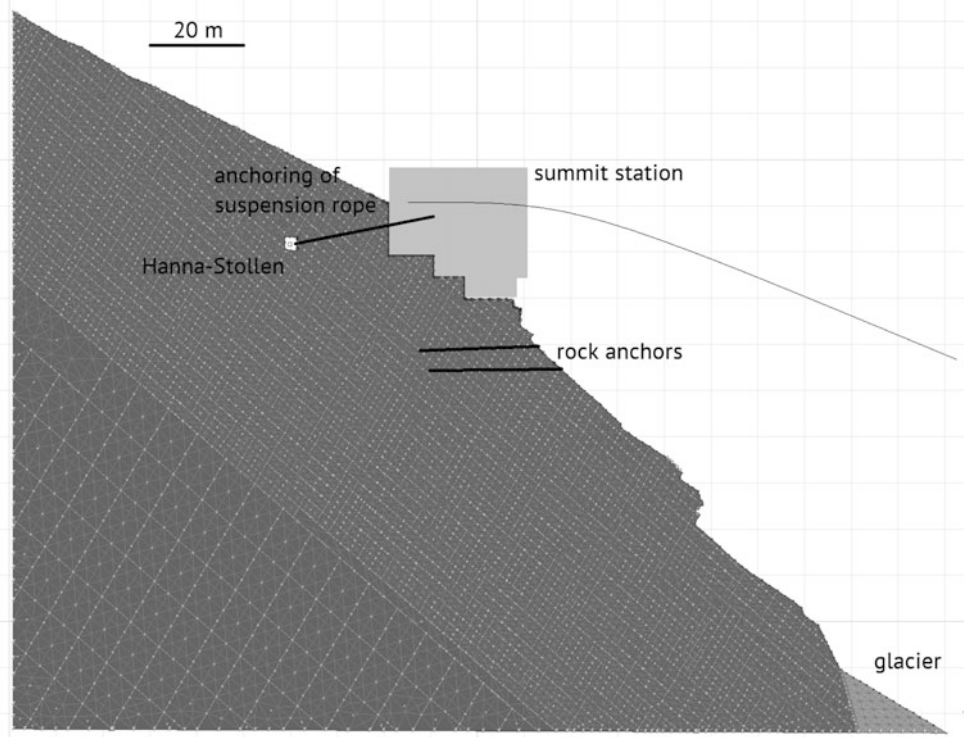


**Table 1** Core (mean) data set (left) and varied model parameters (right)

| | | Saturated, frozen | |
|---|---|---|---|
| | | Mean | Varied |
| Young's modulus | [MPa] | 80,426 | 76,000 |
| ν | [–] | 0.2 | 0.2 |
| UCS | [MPa] | 107 | 88 |
| Tensile strength | [MPa] | 6.8 | 4.7 |
| c | [MPa] | 2.0 | 2.2 |
| $\phi_{tot}$ | [°] | 40.6 | 32.3 |

**Fig. 4** Parameter set for blocks and joints in distinct element model and their data sources

(a) frozen and unfrozen conditions

(b) reduced friction in joints

(c) reduced tensile strength joints

(d) reduced elastic parameters rock

(e) 1.5fold load

(f) reduced friction rock
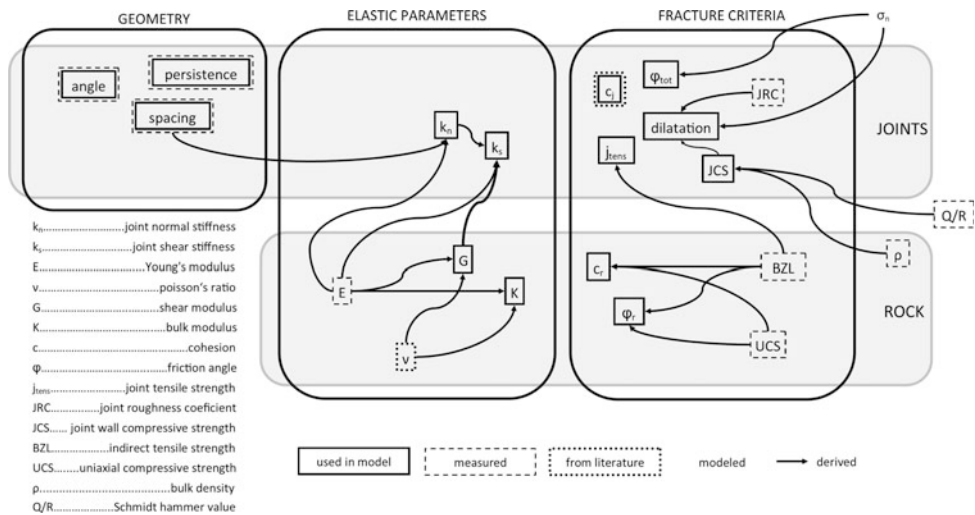
**Fig. 5** Factor of safety of core dataset (frozen, solid line) and for varied parameters (dashed line) regarding rock and joint fracture criteria

of reducing the joint tensile strength (Fig. 5c). The data sets to be further evaluated are chosen by examining visual results and planes of failure.

These described observations lead to the presumption that the mechanical behavior of joints is more important for the whole system than the behavior of the rock itself. Furthermore, changes in joint parameters (Fig. 5b, c) affect the FoS significantly. That strengthens the presumption of joint dominant behavior of the rock mechanical model.

Furthermore, thermal state influences mechanical system behavior. As higher values for FoS are reached in the unfrozen state, one may first conclude that permafrost degradation results in a more stable mechanical system. However, it is important to note that this study compares two states (frozen and unfrozen) and not the mechanical behavior in course of system warming. Studies like Günzel (2008) and Davies et al. (2001) show, that the state between −2 and 0 °C is mechanically most relevant. Systems, which are currently in a frozen state will undergo such temperatures before reaching a completely unfrozen state.

## 6 Conclusion and Outlook

Especially in extreme environments such as the Austrian Alps, it is not always possible to conduct extensive investigations and measurements on site. This parameter study shows that by choosing the right dataset for a measurement network as well as by selecting the most relevant parameters, time and money can efficiently be invested and better results may be generated with less effort.

Furthermore, this study suggests that joints are dominant and thus further effort is to be focused on investigating parameters of joint fracture criteria (lab testing, field evaluation). Until now elastic joint parameters are derived indirectly; more detailed evaluation of joint stiffness is required. Depending on the physical effects occurring in the upper tens of meters beneath the rock surface, the anchor loads may later be used for model validation.

Thermal state affects the mechanical system behavior, thereby thermal impacts from infrastructure and environmental changes also influence slope stability in permafrost-affected rock walls. In addition to the results presented in this study, further modelling of mechanical impact of water and ice should be conducted. Furthermore, closer considerations of different temperature steps around 0 °C are needed in order to cover the scope of potential warming related changes in mechanical system behavior.

## References

Barton, N.: A model study of rock-joint deformation. Int. J. Rock Mech. Min. Sci. Geomech. Abstr. **9**, 579–582 (1972)

Bommer, C., Phillips, M., Arenson, L.: Practical recommendations for planning, constructing and maintaining infrastructure in mountain permafrost. Permafrost Periglac. Process. **21**(1), 97–104 (2010)

Davies, M., Hamza, O., Harris, C.: The effect of rise in mean annual temperature on the stability of rock slopes containing ice-filled discontinuities. Permafrost Periglac. Process. **12**(1), 137–144 (2001)

European Environment Agency: Regional climate change and adaption. The Alps facing the challenge of changing water resources. Luxembourg (2009)
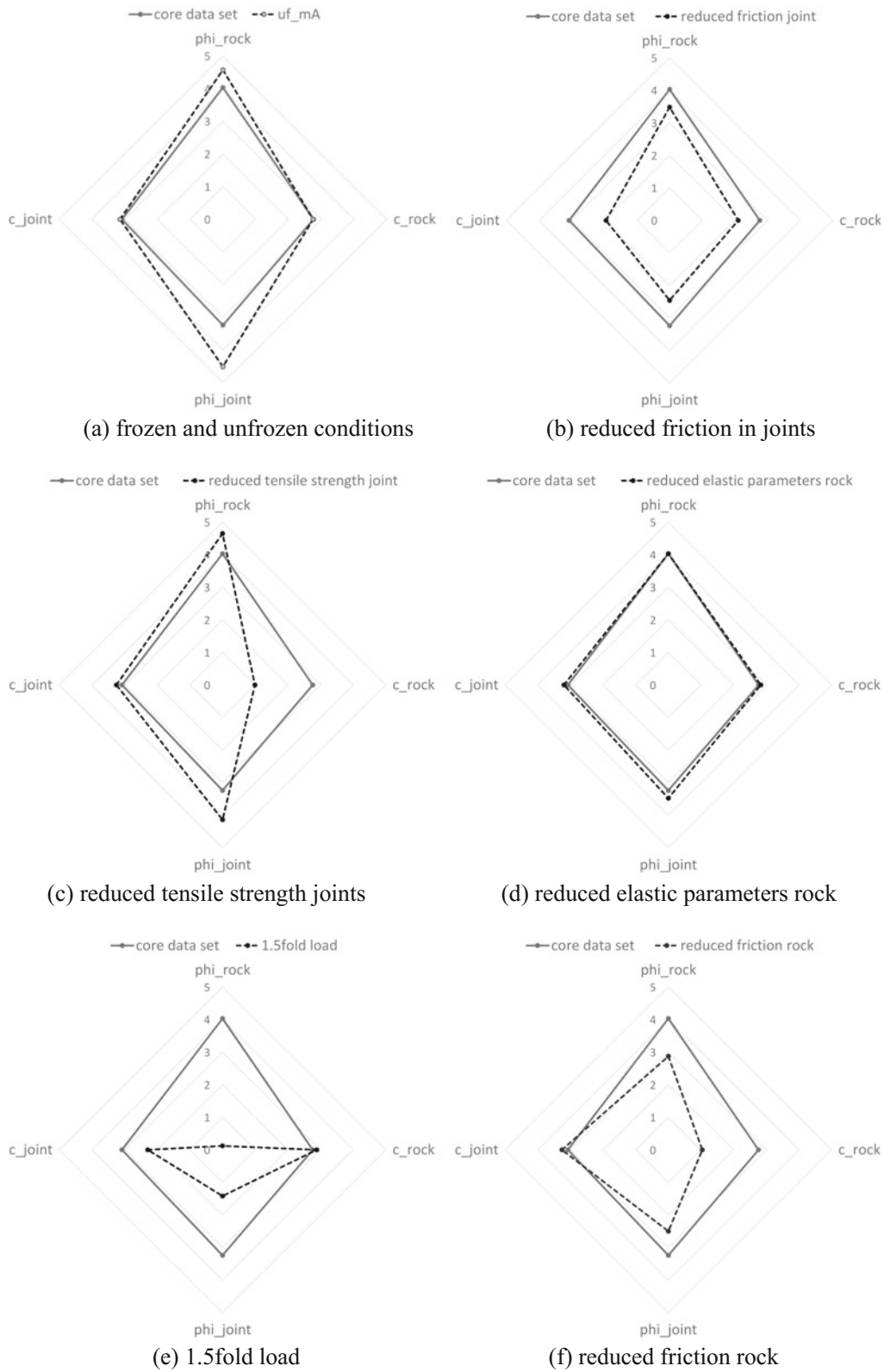
Fischer, L., Kääb, A., Huggel, C., Noetzli, J.: Geology, glacier retreat and permafrost degradation as controlling factors of slope instabilities in a high-mountain rock wall: the Monte Rosa east face. Nat. Hazards Earth Syst. Sci. **6**, 761–772 (2006)

Geoconsult ZT GmbH (12.12.2010): Kartierung Gipfelstation. Salzburg, Austria (2010)

Geoconsult ZT GmbH (20.03.2014): Sicherungsplanung der Felsflanke unterhalb der Gipfelbahn. Salzburg, Austria (2014)

Günzel, F.: Shear strength of ice-filled rock joints. In: Kane, D.L., Hinkel, K.M. (eds.) Proceedings of the 9th International Conference on Permafrost, Fairbanks, Alaska, pp. 581–586 (2008)

Hartmeyer, I., Keuschnig, M., Delleske, R., Schrott, L.: Rockfall in permafrost-affected Cirque Walls: new insights on spatial variability and potential causes derived from a 4-year LiDAR monitoring campaign. Kitzsteinhorn. Austria. In: Speech at 11th International Conference on Permafrost, 20–24 June 2016. Potsdam, Germany (2016)

Krautblatter, M., Funk, D., Günzel, F.: Why permafrost rocks become unstable. A rock-ice-mechanical model in time and space. Earth Surf. Process. Land. **38**(8), 876–887 (2013)

Voigtländer, A., Scandroglio, R., Krautblatter, M.: Entwicklung geotechnischer Felsparameter des Kitzsteinhorner Kalkglimmerschiefers – Abschlussbericht zum Forschungs - und Entwicklungsvertrag der TU München und AlpS-GmbH. München, Germany (2014)

# Rockfall Hazard Assessment at the World Heritage Site of Giant's Castle Reserve, Drakensberg, South Africa

Maria Ferentinou

## Abstract

Drakensberg is a steep, mountainous terrain, where rockfalls widely occur along the slopes of the V-shaped valleys. Rockfall events, often responsible for casualties and fatalities, have occurred in the past and occur sporadically in that mountain range. In this study rockfall accumulation zones were mapped, and a data set of 208 rockfall boulders was developed. The falling blocks' measured size range from 1 m$^3$ to 4 × 10$^3$ m$^3$ and the shape for the majority of the blocks is either cube or prism. A good agreement between the measured cumulative distribution and a fit by a power-law distribution, for volumes larger than 20 and 50 m$^3$ is noticed. The rockfall trajectory paths, maximum run-out distances, involved kinetic energies, and rockfall velocities were estimated, based on rockfall analysis. A pseudo 3D rockfall analysis based on the shadow angle principle was applied to account for the lateral disperse of the falling blocks. The outcome of the rockfall analysis revealed that Giant's Castle Main Camp is susceptible to rockfall hazard.

## Keywords

Rockfall • Hazard • Risk • Drakensberg

## 1 Introduction

Drakensberg is the highest mountain range in southern Africa. Since 2000, it is proclaimed a combined natural and cultural World Heritage site. The majority of the mountainous area is on the western border of the province of KwaZulu Natal. Giant's Castle reserve (Fig. 1), is considered a valuable natural (hosts a wide biodiversity) and economic resource. The Main Caves approximately 1.5 km away from Giant's Castle main camp are decorated with San rock art onto sandstones of the Clarens Formation, and they serve as a major tourist and cultural heritage attraction. According to Ezemvello KwaZulu Natal Wildlife, (EZNW), who manages the reserve, the camp served to accommodate for the period of 2013–2014 around 2500 visitors.

In the campsite, there are rock blocks of medium size, which are older than the development of the camp, in 1902. Widespread blocks along the slopes of the valley are signs of rockfall activity, (Fig. 2), however there is lack of recent evidence of the rockfall events. Sporadic events have occurred in the past along the whole extent of the Drakensberg escarpment, mainly reported by mountaineers near the tourist centres. Thus, there is an identified threat for lives of hikers, climbers, for property, parking lots, tent cabins, wooden cabins and residences.

Since there was lack of information on previous rockfalls in the area, an investigation took place through historic questionnaires submitted to the staff, newspaper articles, and local archives; however, it was difficult to construct a complete record of previous events. There were no available databases reporting reliable information that concerns previous rockfall (such as the number, magnitude and possible related damages), that would enable towards a quantitative risk assessment study.

A number of studies related to rockfall hazard identification and modelling in historical sites exist in the literature. Among others, (Evans and Hungr 1993; Canselli and Crosta 1993; Wieczorek et al. 1995; Turner and Schuster 1996; Guzzetti et al. 2002; Crosta and Agliardi 2003; Dorren 2003; Frattini et al. 2008; Alejano et al. 2010, Binal and Ercanoglu 2010; Saroglou et al. 2012; Topal et al. 2012; Mineo et al. 2018).

In order to investigate the rockfall hazard in the study area, field mapping of rockfall accumulation zones, the talus zone boundary, and outlying boulders was carried out. The volume of the boulders was measured in the field and the cumulative distribution was produced. Critical profiles

M. Ferentinou (✉)
Civil Engineering Science, University of Johannesburg,
Johannesburg, South Africa
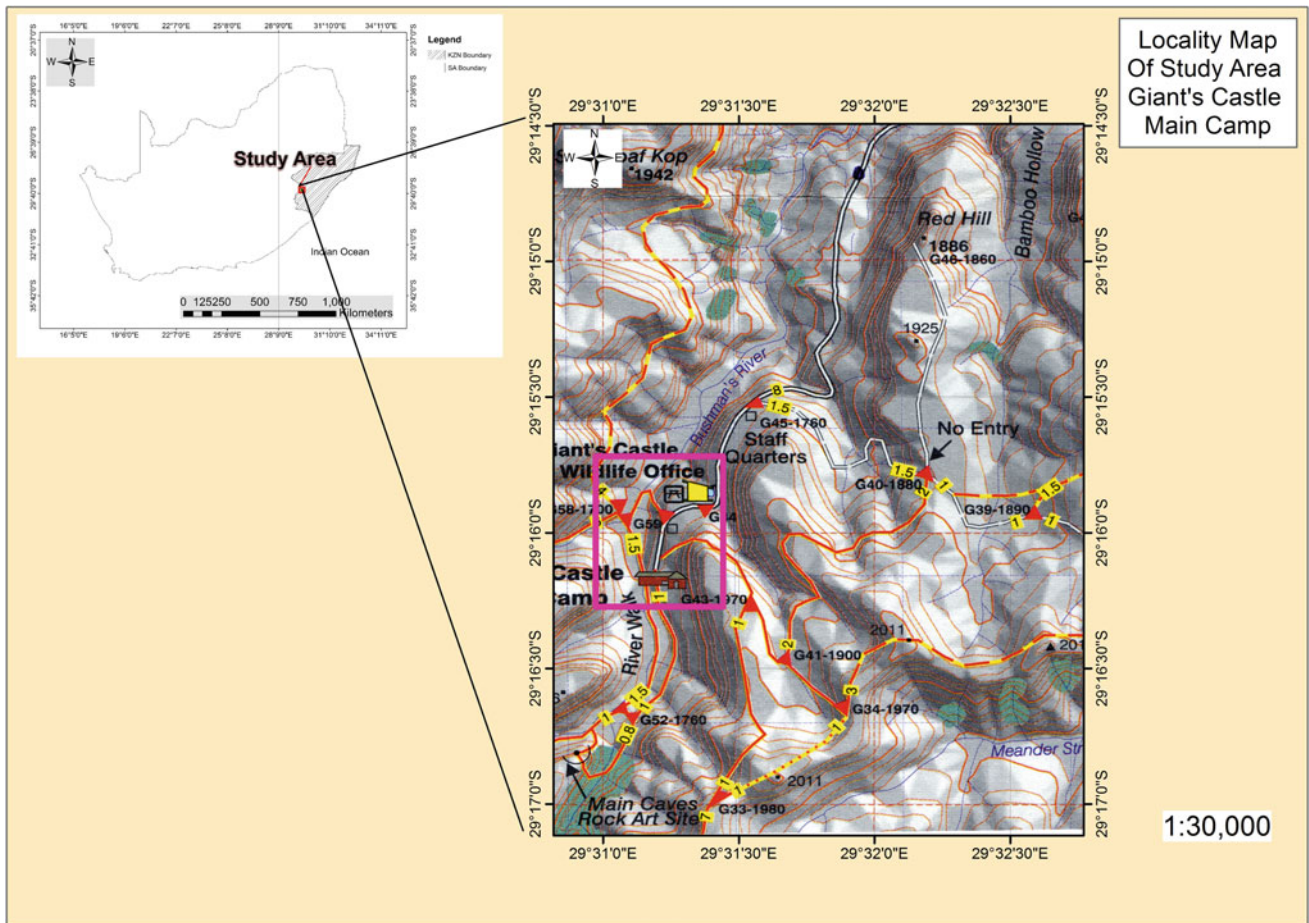e-mail: mferentinou@uj.ac.za

**Fig. 1** Study area of the Giants Castle Nature Reserve, Drakensberg, South Africa

**Fig. 2** Example of rockfall in Giant's Castle Main Camp

were analysed using rockfall analysis, and a qualitative risk assessment was performed to map the anticipated rockfall hazard.

## 2 Study Area

Giant's Castle takes its name from the massive ramparts of rock rising above the lodge. In past studies, there has been an appreciable amount of data collected on the climatological, hydrological and ecological aspects of the Drakensberg region, however, in comparison, very little is known about the geomorphology of the region and there has only been limited studies on weathering processes in this region (Sumner et al. 2009). The stratigraphy of the Drakensberg forms part of the Karoo Supergroup and is characterized by a sequence of horizontally bedded fine sandstones and silt-stones strata overlain by basalt and intruded by a network of dolerite dykes and sills. The general stratigraphy is described by Du Toit (1954), as the Molteno, Elliot and Clarens Formations.

## 3 Methodology

### 3.1 Field Studies

Rockfall accumulation zones, the upper boundary of the talus slope and outlying boulders were mapped, by means of digital orthophoto maps (South African National Geo-Spatial Information, 2009), Google Earth® satellite imagery for the years 2008–2016, and field mapping, (Fig. 3). Fieldwork was undertaken to validate remote sense mapping and to confirm the location of the rockfall source areas with the use of a Garmin eTrex® portable GPS. Measurements took place on approximate boulder length, width, and height. Approximate boulder volumes based on the exposed dimensions, were calculated. The mean boulder volume for the boulders beyond the base of talus is 150 m$^3$. Following Wieczorek et al. (1999), the term outlying boulders is obtained as any rockfall generated debris of substantial size (> 0.5 m$^3$) that travels beyond the limits of the talus deposits. The spatial and temporal distribution of the outlying boulders beneath the different cliffs and talus slopes, and their temporal frequency, was used to proceed with quantifying the rockfall hazard that was identified within the study region.

### 3.2 Rockfall Inventory Development

Determining the age of outlying boulders is important for assessing the timing of boulder deposition in this colluvial

cover zone. It is also important to estimate whether the outlying boulder represent an individual rockfall event or they are the product of fragmentation of a bigger rock. Considering that Drakensberg was deglaciated ∼ 17–16 ka years ago (Gasse 2000; Mills et al. 2012), there is potential for many boulders to have fallen many thousands of years ago. In this study, the assumption was made that maximum accumulation time in the study region is close to the timing of deglaciation. However, it could be assumed that the ages of all the mapped boulders span from this time to the present, with at least some of the mapped outlying boulders deposited historically (past ∼ 150 years).

Several authors (Dussauge-Peisser et al. 2002) have studied the distribution function of the rockfall volume. Most of them found that the complementary cumulative distribution function well fits a power law:

$$N = aV^{-b} \qquad (1)$$

Where V is the rockfall volume, N is the number of rockfalls larger than a threshold value V occurring in a given rock wall during an investigation period, $a$ and $b$ are constants. The constant $a$, represents the number of rockfalls whose volume is greater than 20 m$^3$ (assuming the law is valid for this volume range). According to the same authors, $a$ coefficient value depends on the size of the cliff, the length of the investigation period and the geological and geomorphological context. On the contrary, the exponent $b$ only depends on the geological and geomorphological context. Its value has been determined for some different contexts (Dussauge-Peisser et al. 2002). For the particular contexts studied up to now, the exponent is b = 0.60, and a = 0.95.

The dataset that was developed refers to 208 rock blocks with a volume ranging from 1 m$^3$ to $4 \times 10^3$ m$^3$, and the shape for the majority of the blocks is either cube or prism. The distribution was statistically tested in order to find out the best fit over the wider range of volume distribution (Fig. 4). It fits it up to 200–300 m$^3$ only.

### 3.3 Rockfall Simulations

Critical profiles were selected for the 2-D rockfall analysis by considering unfavourable geometry of the slope and high rockfall accumulation zones (Fig. 5). Eight profiles (Fig. 6) were chosen to analyse the rockfall hazard. These profiles were chosen for the campsite, the staff houses and two profiles were selected for the hiking trail to analyse the rockfall hazard potential for day and night hikers that use the hiking trail. The simulations were tested with 8000 rocks being projected. Restitution coefficients normal R$_n$ and tangential R$_t$ were selected based on back analysis calibration
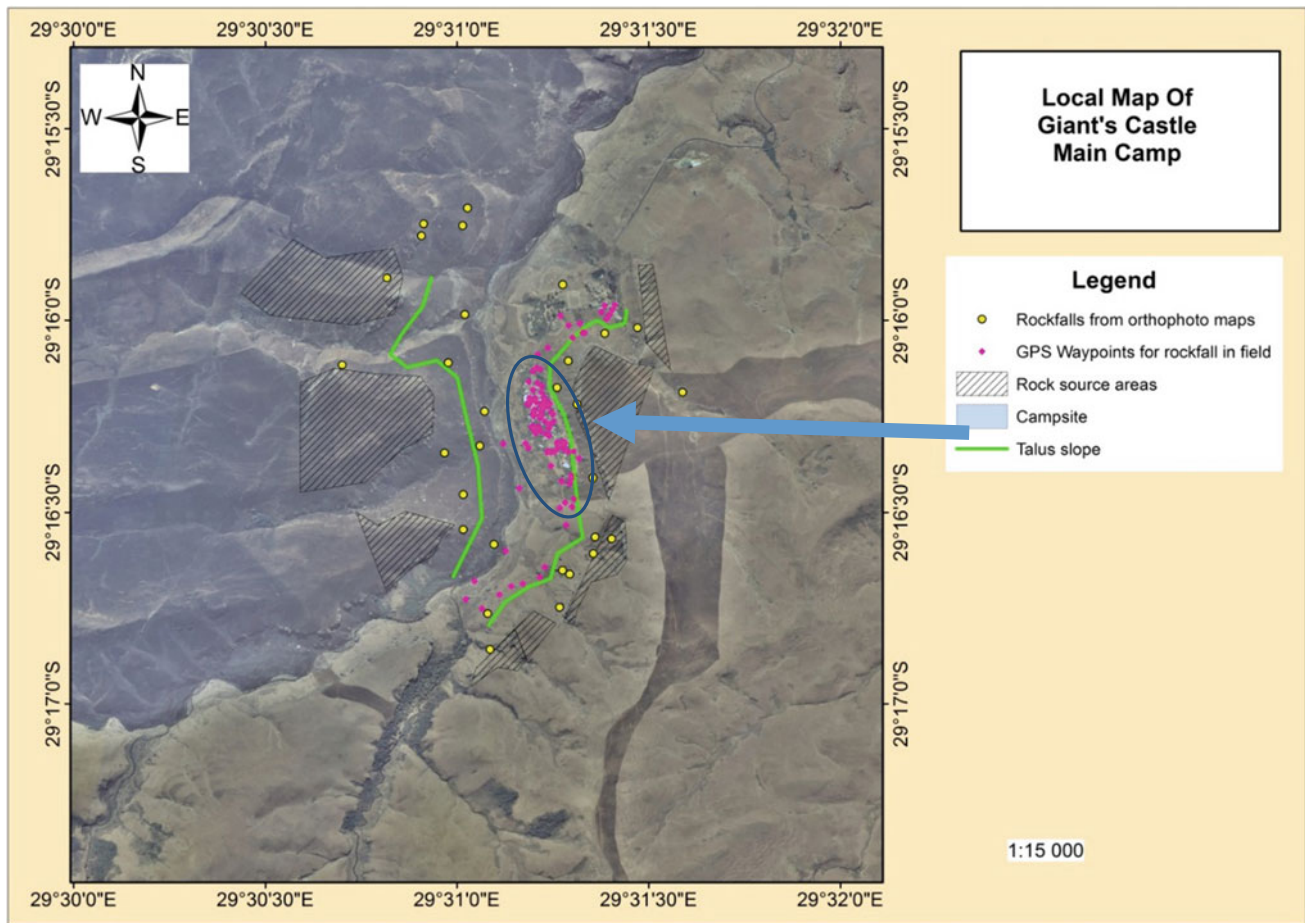
**Fig. 3** Locations of rockfall source areas (hatch), rockfalls mapped from orthophoto maps (yellow dots), rockfalls from field mapping (magenta dots)
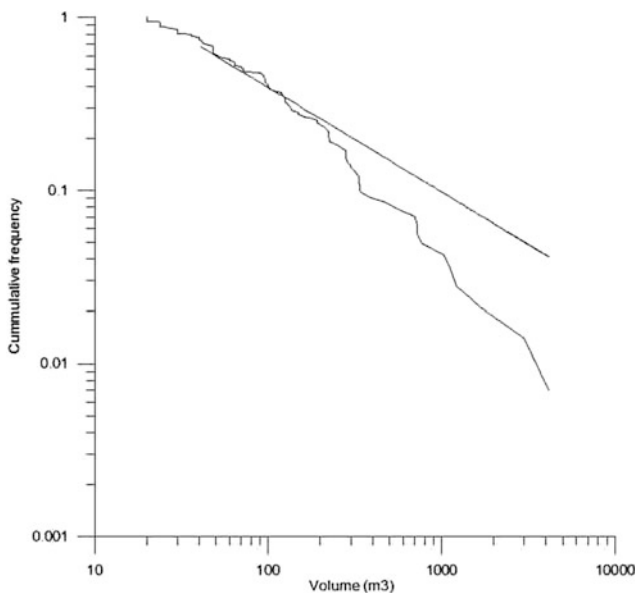


**Fig. 4** Cumulative volume distribution for the studied rockfall boulders. The power law fits up to 200–300 m³ only with the equation f = 0.95 V$^{-0.60}$

and literature review, Table 1. For all the profiles, a friction angle of 25° was used. This value was determined from the UCS strength results from sandstone samples from the Elliot Formation, and with a Geological Strength Index (GSI) rating of 70.

The simplest method describing rockfall propagation zone, is based on the shadow angle approach, (Evans and Hungr 1993). According to shadow angle approach the maximum travel distance of blocks is defined by the intersections of the topography with energy line having an empirically—estimated inclination (Evans and Hungr 1993). CONEFALL estimates the potential rockfall propagation area using a digital elevation model and a grid file comprising all the rockfall source areas as input data. Preliminary estimation of rockfall reach susceptibility is based on kinetic energy. The results of the simulation are presented in (Fig. 6), and are illustrating the estimated potential rockfall prone areas from the mapped rock fall source areas. The campsite added in as a black polygon, and the hiking trails are with the dashed line.

**Fig. 5** Rock fall simulation, at the Camps site
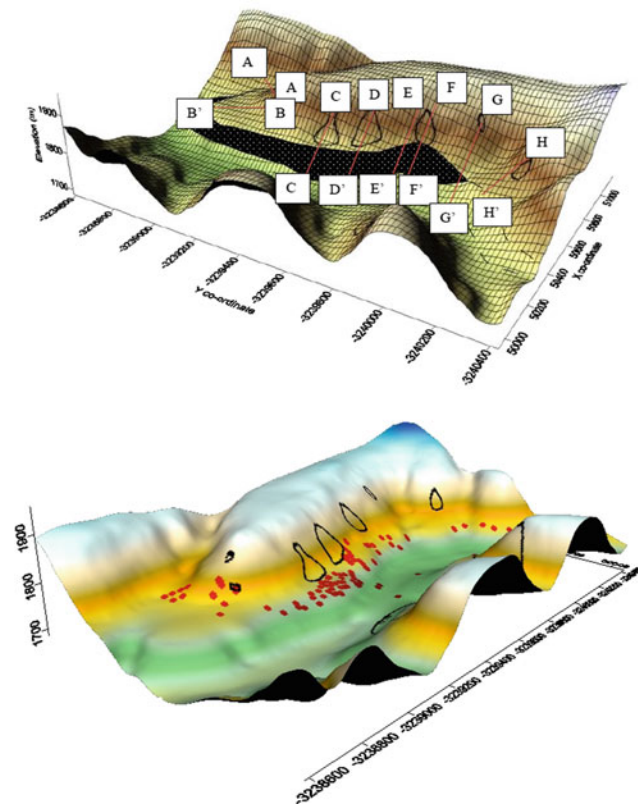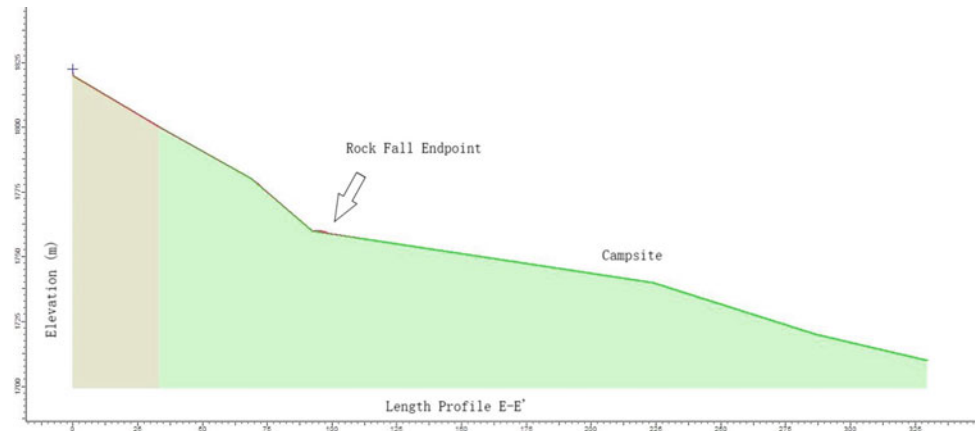


**Fig. 6** Resulting propagation zones (cones), after pseudo 3D analysis, rockfalls with red dots

## 4 Risk Assessment

Qualitative risk analysis is using descriptors to define the frequency of hazardous events and the consequences. This may comprise tools such as risk rating systems, risk scoring schemes, and risk ranking matrices (Fell et al. 2005). In this paper, a qualitative risk analysis was performed giving descriptive rating scales to define the magnitude of potential consequences and the likelihood that these consequences

will occur due to a rockfall event. Qualitative risk estimations are used where both the likelihood and adverse consequences are expressed in qualitative terms. It is a widely used methods, and is used to combine the qualitative scoring of adverse consequences and the qualitative scoring of likelihood/probability of hazard. In Table 2 a risk matrix is developed for consequences to people and property, based on Van Dine et al. (2002).

Van Dine et al. (2002) risk matrix was applied to assess rockfall risk at Giant's Castle Main Camp. The area was subdivided in nine zones. For hazard, a rating of 'high' (H), 'moderate' (M), 'low' (L) and 'very low' (VL) was adopted. The rating was based on the 2-D analysis simulations, considering factors such as the bounce height, the kinetic energy of the rocks, the translational velocity, as well as the ends. The 3-D simulation was used to assess the hazard based on the rockfall propagation zones considering how close the 'cones' were to the campsite. Then, the different potential consequences were determined, to people and the consequence to property. There are approximately 2500 visitors on an annual basis and there are 50 buildings in Giant's Castle Main Camp. ArcGis was used in order to produce the qualitative risk maps, (Fig. 7).

## 5 Discussion and Conclusions

Rockfall accumulation zones and the talus zone in medium and local scale were mapped in the Giants castle camp site. An inventory of 208 rockfall boulders was developed. The falling blocks' measured size range from of $1 \text{ m}^3$ to $4 \times 10^3 \text{ m}^3$ size, and the shape for the majority of the blocks is either cube or prism. The volume distribution function for the rockfalls mapped in this study using a threshold of $20 \text{ m}^3$, well fits by a power law for volumes greater than $20 \text{ m}^3$, with an exponent of 0.60 and a correlation coefficient of 0.983. The volumes lower than $20 \text{ m}^3$, are underrepresented, probably by under sampling. These results seem to

**Table 1** Restitution coefficient R_N and R_T values from literature and back analysis

| Case studies | Back analysis | | Literature | |
|---|---|---|---|---|
| | $R_N$ | $R_T$ | $R_N$ | $R_T$ |
| Sandstone from Kastamonu Castle, Turkey (Topal et al. 2012) | Talus material: 0.35 | Talus material: 0.62 | | |
| Sandstone in Lubango, Angola (Andrade and Goncalves 2014) | Bedrock: 0.5 | Bedrock: 0.9 | | |
| Mardin Castle, Turkey (Dadashzadeh et al. 2014) | Talus material: 0.32 Bedrock: 0.53 | Talus material: 0.8 Bedrock: 0.99 | Talus material: 0.22 Bedrock: 0.53 | Talus material: 0.8 Bedrock: 0.99 |
| Giant's Castle Main Camp | Talus material: 0.35 Bedrock: 0.48 | Talus material: 0.82 Bedrock: 0.86 | | |

**Table 2** Risk matrix developed for different elements at risk (after Van Dine et al. 2002)

| Hazard | Consequence to people | | | Consequence to property | | |
|---|---|---|---|---|---|---|
| | High | Moderate | Low | High | Moderate | Low |
| High | VH | H | M | VH | H | M |
| Moderate | H | M | L | H | M | L |
| Low | M | L | VL | M | L | VL |
| Very low | L | VL | | L | VL | |



**Fig. 7** Risk assessment map for people and buildings, based on qualitative analysis

be consistent with previous studies, (Dussauge-Peisser et al. 2002). The application of the distribution law would allow for estimations of a mean recurrence interval for events in the examined volume range.

2-D rockfall modelling was performed along critical profiles. The rockfall trajectory paths, maximum run-out distance, total kinetic energy, bounce height, and translational velocity were obtained from the analyses. The analyses on certain profiles posed a potential rockfall hazard to visitors as the run-out zones extended very close to the camp. 3-D rockfall analysis showed that the maximum run-out distance was further than that estimated by the 2-D

analyses. This run-out distance variation in the models may be attributed to the inherent resolution of the terrain models used in both analyses.

The outcome of the rockfall analyses performed indicated that there is potential rockfall hazard associated with Giant's Castle Main Camp, and hence, a qualitative risk assessment was undertaken whereby rockfall susceptibility maps were developed, delineating the most susceptible rockfall hazard zones within the study area.

After undertaking the risk assessment, an aspect of risk management needs to be implemented for Giant's Castle Main Camp. The risk shows that Zone 5 is at very high risk

to people and for buildings and therefore needs to have some form of risk management. It is suggested that monitoring through laser scanning techniques, can give further insight into calculating recurrence intervals.

Such quantification can assist the provincial authorities to make decisions with respect to existing and potential future infrastructure in the Giant's castle Campsite. Further in-depth studies dealing with the assessment of the resulting risk, would assist onto acceptable risk levels.

# References

Alejano, L.R., Ordóñez, C., Armesto, J., Rivas, T.: Assessment of the instability hazard of a granite boulder. Nat. Hazards **53**(1), 77–95 (2010)

Andrade, P.S., Goncalves, G.: Rock fall analysis on the city of Lubango, SW Angola. Eng. Geol. Soc. Territory **2**, 2027–2034 (2014)

Binal, A., Ercanoğlu, M.: Assessment of rockfall potential in the Kula (Manisa, Turkey) Geopark Region. Environ. Earth Sci. **61**(7), 1361–1373 (2010)

Cancelli, A., Crosta, G.B.: Hazard and risk assessment in rockfall prone areas. In: Skipp, B.O. (ed.) Risk Reliability in Ground Engineering, pp. 177–190. Inst. Civ. Eng., Thomas Telford (1993)

Crosta, G., Agliardi, F.: A methodology for physically based rockfall hazard assessment. Nat. Hazards Earth Syst. Sci. **3**, 407–422 (2003)

Dadashzadeh, N., Aras, C., Yesiloglu-Gultekin, N., Bilgin, A., Duzgun, H.S.B. (2014). Analysis of potential rockfalls and protection measures for the Mardin castle, Turkey. In: Alejano, Perucho, Olalla, Jiménez (eds.) Rock Engineering and Rock Mechanics: Structures in and on Rock Masses. Taylor & Francis Group, London

Dorren, L.K.A.: A review of rockfall mechanics and modelling approaches. Prog. Phys. Geogr. **27**(1), 69–87 (2003)

Dussauge-Peisser, C., Helmstetter, A., Grasso, J.R., Hantz, D.R., Desvarreux, P., Jeannin, M., Giraud, M.: Probabilistic approach to rock fall hazard assessment: potential of historical data analysis. Nat. Hazards Earth Syst. Sci. **2**, 15–26 (2002)

Du Toit, A.L.: The geology of South Africa. Oliver and Boyd, Edinburgh (1954)

Evans, S.G., Hungr, O.: The assessment of rockfall hazard at the base of talus slopes. Can. Geotech. J. **30**, 620–636 (1993)

Fell, R., Ho, K.K.S, Lacasse, S., Leroi, E.: A framework for landslide risk assessment and management. In: Hungr, O., Fell, R., Couture, R., Eberhardt, E. (eds.) Landslide Risk Management. Taylor & Francis Group, London, ISBN 041538043 X (2005)

Frattini, P., Crosta, G., Carrara, A., Agliardi, F.: Assessment of rockfall susceptibility by integrating statistical and physically-based approaches. Geomorphology **94**(3–4), 419–437 (2008)

Gasse, F.: Hydrological changes in the African tropics since the Last Glacial Maximum. Quat. Sci. Rev. 189–211 (2000)

Guzzetti, F., Malamud, B.D., Turcotte, D.L., Reichenbach, P.: Power-law correlations of landslide areas in central Italy. Earth Planet. Sci. Lett. **195**(3–4), 169–183 (2002)

Mills, S., Grab, S., Rea, B., Carr, S., Farrow, A.: Quat. Sci. Rev. **55**, 145–159 (2012)

Mineo, S., Pappalardo, G., Mangiameli, M., Campolo, S., Mussumeci, G.: Rockfall analysis for preliminary hazard assessment of the cliff of Taormina Saracen Castle (Sicily). Sustainability **10**(2), 417 (2018). https://doi.org/10.3390/su10020417

Saroglou, H., Marinos, V., Marinos, P., Tsiambaos, G.: Rockfall hazard and risk assessment: an example from a high promontory at the historical site of Monemvasia, Greece. Nat. Hazards Earth Syst. Sci. **12**, 1823–1836 (2012)

Sumner, P.D., Hall, K.J., van Rooy, J.L., Meiklejohn, K.I.: Rock weathering on the eastern mountains of southern Africa: review and insights from case studies. J. Afr. Earth Sci. **55**(5), 236–244 (2009)

Topal, T., Akin, M.K., Akin, M.: Rockfall hazard analysis for an historical Castle in Kastamonu (Turkey). Nat. Hazards **62**, 255–274 (2012)

Turner, A.K., Schuster, R.L.: Landslides Investigation and mitigation: National Research Council, Transportation Research Board Special Report 247. National Academy Press, Washington, D.C. (1996)

Van Dine, D.F., Jordan, P., Boyer, D.C.: An example of risk assessment from British Columbia, Canada. In: McInnes, R.G., Jakeways, J. (eds.) Instability—Planning and Management, pp. 399–406. Thomas Telford, London (2002)

Wieczorek, G.F., Nishenkod, S.P., Varnes, D.J.: Analysis of rockfalls in the Yosemite Valley, California. In: Daemen, J.J.K., Schultz, R.A. (eds.) Rock Mechanics: Proceedings of the 35th US Symposium, pp. 85–89. Balkema, Rotterdam (1995)

Wieczorek, G.F., Morrissey, M.M., Iovine, G., Godt, J.: Rock-fall potential in the Yosemite Valley, California. U.S. Geol. Surv. Open File Rep. **99**(578) (1999). http://greenwood.cr.usgs.gov/pub/open-file-reports/ofr-99-0578/

# Assessment Proposal for Definition of Slope Stabilization Measures in Urban Areas: The Fontaínhas Scarp, Oporto (Portugal)

Rute Ramos and Filipe Telmo Jeremias

## Abstract

The Fontaínhas scarp, located on the right bank of the Douro River between D. Luis and D. Maria Pia bridges, presents an historical record of slope failures since 19th century is extremely important for risk management of that area as well as for the surrounding streets. In order to help future decision-making processes related to interventions on the escarpment, a study was performed, in 2011, to characterize the stability conditions of the scarp, based on existing bibliographic information, detailed field inspections and identification of risk situations. Aiming to systematize the problems identified in the field, the study area was subdivided in five sectors, considering the existence of important stabilization works, the type and distribution of the constructions (residential areas and ruins), the slope morphology and the vegetation (type and distribution) as criteria. Taking into account the characterization carried out for each sector, a remedial measures proposal for the risk situations identified in the field was suggested to the city council of Oporto, with the least possible impact on the landscape. Thus, this paper focuses on the characterization carried out on the escarpment as well as the description of the respective proposal.

## Keywords

Stability conditions • Scarp • Remedial measures

## 1 Introduction

The Fontaínhas scarp, located in Oporto (Portugal), has been suffered several slope failures, mainly rockfall and landslides, since at least 1879 (date of the oldest record).

Following the occurrence of major events related with periods of intense rainfall, some stabilization measures were executed. The most important stabilization work was performed next to the D. Luis Bridge, in 2002, and comprised the execution of 321 anchors, 4178 m of nailing, 1.65 ton of injections, 3150 m of internal drains and the removal of 25,000 m$^3$ of soil/blocks (Borges and Correia 2003).

In order to study the global problem and to help future decision-making processes related to interventions in the study area, the characterization of the stability conditions of the escarpment was carried out, in October and November of 2011 (LNEC 2011).

To achieve these objectives, a study was carried out which included the following tasks: (i) collection, analysis and interpretation of data (bibliography and cartographical documents); (ii) visual observations for characterization of the reference situation (date of the studies), in which the information about the geological and geotechnical aspects of the rock mass, the stabilization interventions preformed on the escarpment, the type of urban occupation and the distribution and type of the vegetation cover were recorded; and finally, (iii) definition of a proposal with the remedial measures for the risk situations identified in the study area, as well as the geological–geotechnical constraints to be considered in the different scenarios of the use of the scarp.

## 2 Study Area

### 2.1 General Setting

The Fontainhas scarp is located in the urban area of Oporto, on the right bank of the river Douro, between D. Luis and D. Maria Pia bridges (Fig. 1). It was carved by the Douro River and extends along 1200 m, developing between elevations of 8 and 72 m. The average height is about 50 m and the average slope is 35–45° dipping south.

The scarp occupies a total area of 76,900 m$^2$ and is limited at west and east by the bridges D. Luis and D. Maria Pia,

R. Ramos (✉) · F. T. Jeremias
National Laboratory for Civil Engineering, Lisbon, Portugal
e-mail: rramos@lnec.pt
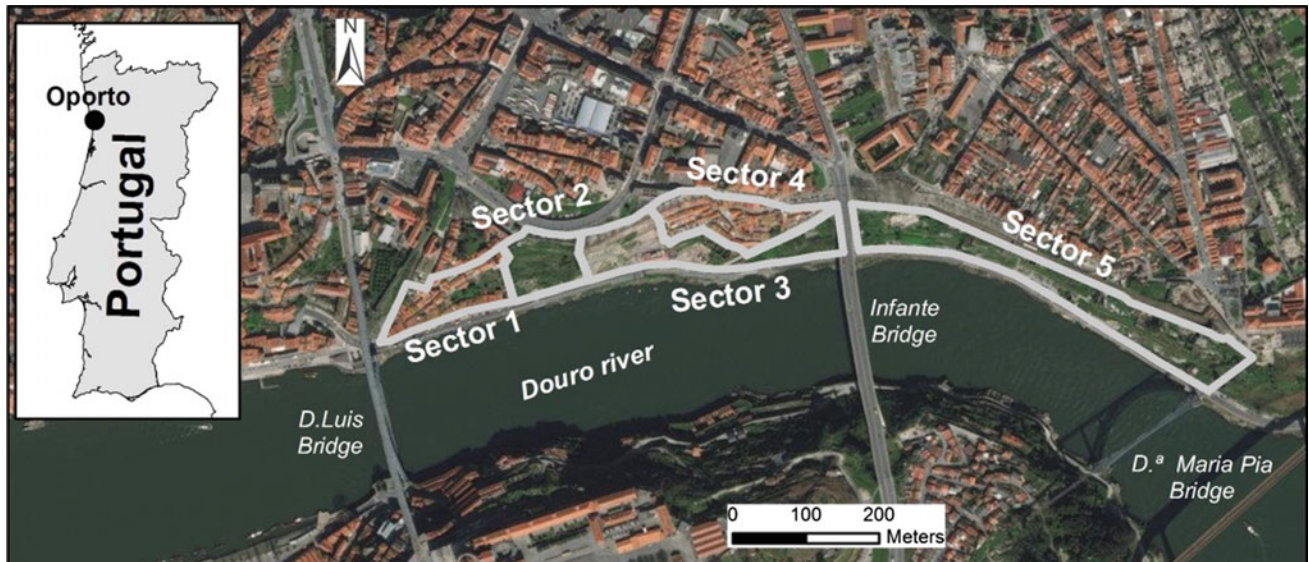
**Fig. 1** Location of the study area
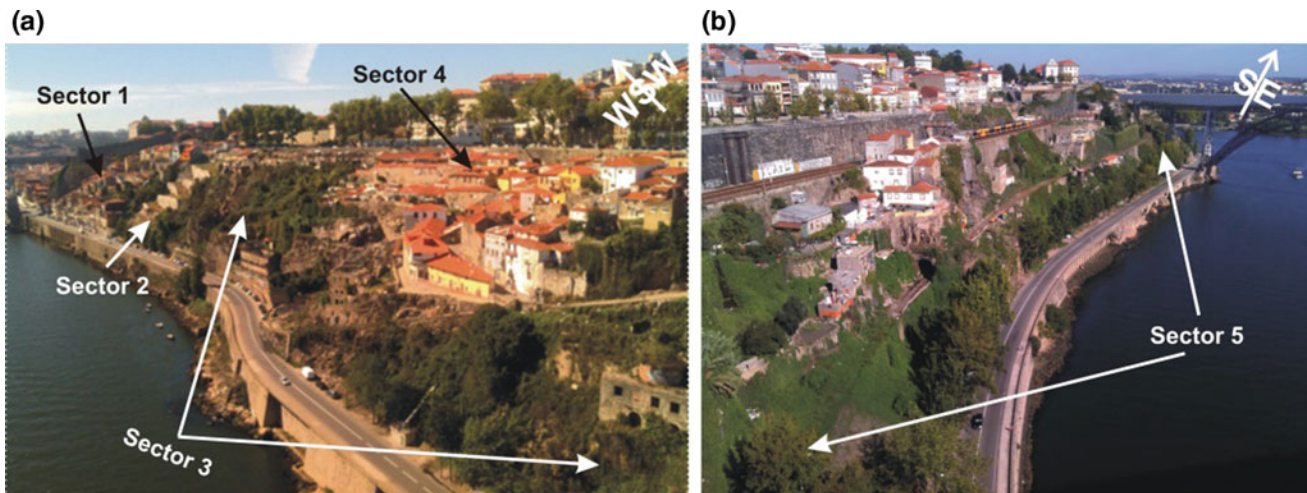


**Fig. 2** General view of the scarp. **a** Perspective for sectors 1–4; **b** Perspective for sector 5

respectively, at south by an important avenue (Gustavo Eiffel) and at north by streets and a railway (Fig. 2).

In the eastern half, the transverse profile is characterized by the presence of one or two small platforms (4–5 m wide), related with an ancient railway line and residential areas (Fig. 2b).

There are three residential complexes (neighborhoods) build on the study area, the Guindais (located next to the D. Luis bridge) and the Fontaínhas and the Nicolau (both located next to the Infante bridge). Some scattered or crowded ruins with variable sizes are also observed.

The study area is densely colonized by undergrowth and shrub vegetation. The arboreal vegetation is sparse and occurs, in general, in small gardens and in the vicinity of the main streets.

## 2.2 Geological and Geotechnical Conditions

In the study area occurs granites, locally called by Oporto granite, which corresponds to an alkaline, autochthonous, leucocratic, medium to coarse grain, two-mica granite. These granites resulted from an intrusion contemporaneous of the 3rd phase of the Hercynian deformation (syntectonic), being genetically related with migmatites and parautochthonous anatexis granites (Coba and FCUP 2003).

The granite outcrop defines a NW-SE alignment, due to the existence of Hercynian structures, bounded by metamorphic lithologies such as schists and greywackes (Coba and FCUP 2003). The geological contact between these different types of lithologies is materialized by migmatitic aureoles created during the schist metamorphic process, which matched with the granite intrusion that occurred 310–315 m.y. ago [Pinto et al. 1987 in (Neves 1999)].

Regarding the discontinuities, the granitic mass is moderately fractured ($F_3$) at the surface by four main facture systems according to (Coba and FCUP 2003) and (Neves 1999): (1) N50–65°W, 76–90°NE; (2) N38–56°E, 75–89°SE; (3) N52–80°W, 21–50°SW and (4) N9–10°E, 43–72°WNW.

The residual soils are poorly developed due to the steep slope morphology of the study area, being characterized by a maximum thickness of about 4 m. However, the landfill deposits can reach up to 20 m thick, mainly in the back side of masonry walls.

The groundwater flow in granites is controlled by discontinuities and, as a result, some runoffs are visible along the slopes which can generate small waterfalls with important flows during winter.

## 3 Methodology

The reference situation of the scarp was characterized between October and November of 2011, using a set of parameters, previously defined and adjusted to bibliographical information collected (reports) and to detailed field observations.

In order to improve the analysis of the information regarding the characterization of the Fontaínhas escarpment, the study area was subdivided in five sectors (Fig. 1), considering the existence of important stabilization works, the type and distribution of the constructions (residential areas and ruins), the slope morphology and the vegetation (type and distribution) as criteria.

The characterization of each sector was based on the following information: (a) identification (identification of the sector, location map and date of field observations), (b) geometric parameters (mean direction, length, mean height, transverse profile); (c) geological and geotechnical setting (geological data, geotechnical data, types of slope failures, hydrogeology, vegetation), and (d) interventions/constructions (stabilization works and type and distribution of the constructions).

Subsequently, a qualitative analysis of the risk constrains for the use of the escarpment and the surrounding streets, such as slope failures and structural collapse, was realized. This analysis included, on the one hand, the identification of sites with slope failures identified (based on bibliography), as well as the susceptible sites to the occurrence of these events (through field observations) and, on the other hand, the recognition of the vulnerable sites which may result in consequences for humans and/or heritage.

In addition, a qualitative analysis of the risk situations, associated to the resulting instability hazards at the rock mass and/or buildings, and of its consequences for the use of the escarpment and the surrounding streets was realized.

Finally, the combination of all information allowed defining a proposal with the remedial measures required to implement for the identified risk situations, as well as the geological–geotechnical conditions to be taken into account in the different scenarios of the use of the scarp.

## 4 Characterization of Each Sector and Identification of the Risk Situations

### 4.1 Sector 1

This sector is located at the western limit of the escarpment, circumscribing the residential complex of Guindais, whose western boundary matches with a funicular. In this sector, the scarp developed between elevations of 3 and 57 m, with an average slope of about 35°. It presents very dense and consolidated constructions along the main streets.

In what concerns to geological and geotechnical conditions, it is characterized by soil deposits with 3–4 m thick and a moderately weathered rock mass ($W_3$) up to 22 m deep that changes to slightly weathered ($W_2$) at greater depths, which is moderately to highly fractured ($F_3$–$F_4$) up to 16.5 m deep and slightly fractured ($F_2$) below this depth.

The type of instabilities identified on the field was rockfall near the funicular and some of the buildings. However, some stabilization measures were formerly executed for their control, such as masonry walls, nailed walls, nails, wire mesh and drains.

Therefore, the loss of functionality and breakage of the Guindais funicular, building damage and injuries and/or loss of lives were identified as potential risk situations.

Figure 3 presents the location and identification of the slope instabilities, stabilization works and risk situations identified in this sector.

### 4.2 Sector 2

Sector 2 matches with the area that underwent significant stabilization works in 2002, having no constructions and developing between elevations of 11 and 72 m. In the western part, the transversal profile of the scarp is characterized by an average slope of 38° and by the presence of several slope steps related with the containment solution.

**Fig. 3** Characterization of the reference situation and the risk situations of sectors 1 and 2
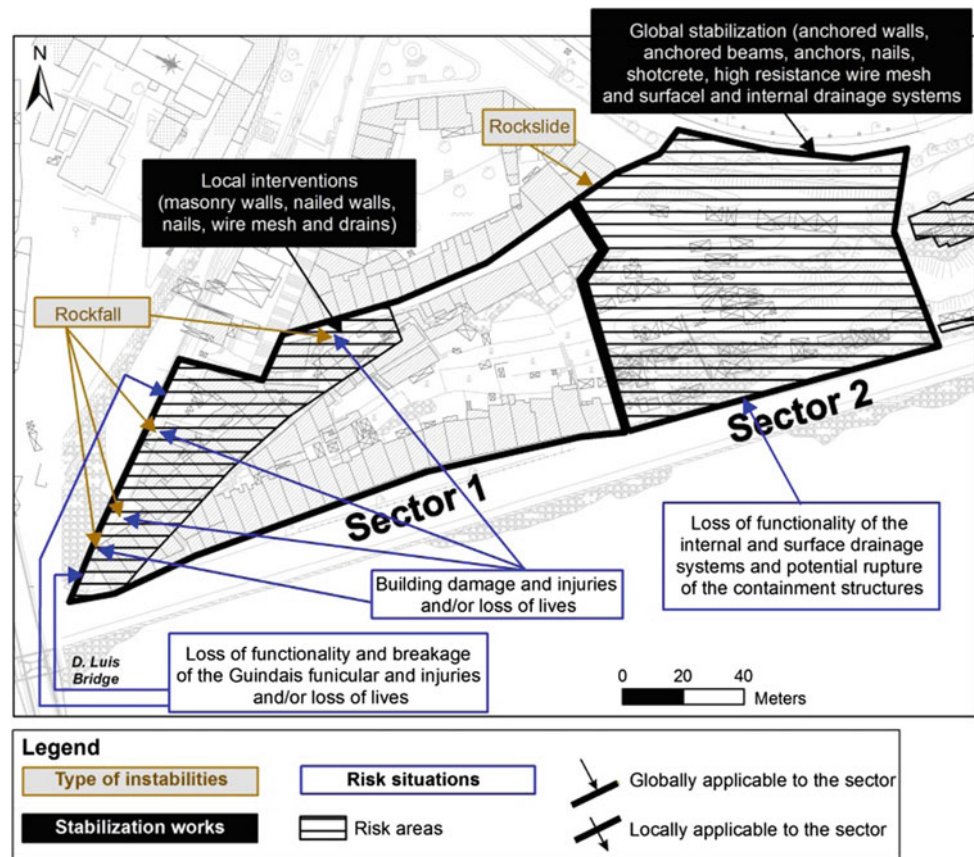
In the eastern part, the scarp presents an average slope of 53° and has no slope steps.

Regarding the geological and geotechnical conditions, the soil deposits attain 4 m thick and the rock mass is moderately to strongly weathered ($W_3$–$W_5$) up to 13-19 m deep and slightly to moderately weathered ($W_{1-2}$–$W_3$) at greater depths, with moderately spaced to very close discontinuities ($F_3$–$F_5$) up to 18–19 m deep and widely to moderately spaced discontinuities ($F_2$–$F_3$) at greater depths.

Several water appearances are visible along of the stabilization walls, which are drained and captured by the internal and superficial drainage systems. Two piezometric levels were recorded at elevations of 32 and 52 m, respectively.

The stabilization works carried out after the slope failure of 2001 included anchored walls (in the western zone), anchored beams, anchors and nails (on mass), shotcrete, high resistance wire mesh (in the eastern zone) and surface and internal drainage systems.

As risk situations, it was recognized in this sector the loss of functionality of the internal and surface drainage systems and the possibility of rupture of the containment structures.

The location and identification of the slope instabilities, stabilization works and risk situations identified in this sector are represented in Fig. 3.

## 4.3 Sector 3

This sector is situated at East of the previous sector, corresponding to an area occupied by ruins. The scarp presents an average slope of 39° and sub-vertical slopes in the surroundings of the main avenue (Gustavo Eiffel). It develops between elevations of 12.5 and 63 m and comprises several platforms at elevation levels of 42, 50, 59 and 63 m.

The geological and geotechnical conditions are characterized by soil deposits up to 2.0 m thick and a moderately weathered ($W_3$) rock mass up to 37 m deep, which changes to slightly weathered ($W_2$) at greater depths, moderately fractured ($F_3$). The groundwater drainage is visible along the slopes confining with the Gustavo Eiffel Avenue.

There is a great probability of instabilities occurrence in this sector such as rockfall and landslides and, therefore, like in sector 1, some stability measures were previously implemented for their control, like a dynamic retaining barrier at the foot of the slope (at the western part). Other interventions observed include masonry walls for delimitation of the properties.

Concerning the type of constructions, this sector has a building in poor stability conditions placed at the top of the western limit and some scattered ruins.

**Fig. 4** Characterization of the reference situation and the risk situations of sectors 3 and 4
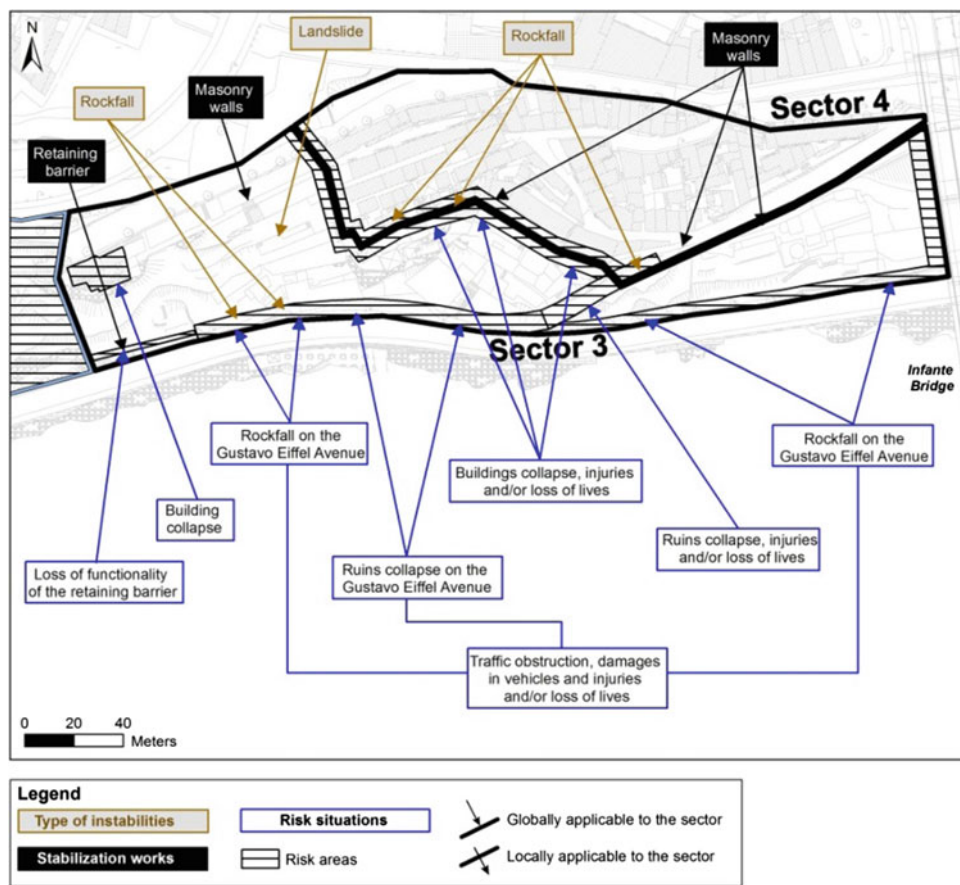


The identified risk situations included the possibility of collapse of existing constructions (building and ruins), mainly in the vicinity of streets, the loss of functionality of the retaining barrier, rockfall on the Gustavo Eiffel Avenue, traffic obstruction, damages in vehicles and injuries and/or loss of lives.

Figure 4 presents the location and identification of the slope instabilities, stabilization works and risk situations identified in this sector.

## 4.4 Sector 4

Sector 4 comprises the residential complex of Fontaínhas and develops between elevations of 29 and 71 m, with an average slope of about 26°.

In what concerns to geological and geotechnical conditions, the sector is characterized by soil deposits with a maximum thickness of 4 m and a moderately to strongly weathered ($W_3$–$W_4$) rock mass, with moderately spaced to closed discontinuities ($F_3$-$F_4$).

Groundwater drainage occurs along some of the slopes confining with the streets, at elevations of 23, 36 and 47 m.

In this sector, the instabilities identified are also related with rockfall. The built area is dense and consolidated. The observed interventions comprise only masonry walls for delimitation of the properties.

The collapse of constructions (buildings and terraces), in particular in the vicinity of the natural and cut slopes, and the possibility of injury and/or loss of life were identified as risk situations.

The location and identification of the slope instabilities, stabilization works and risk situations identified in this sector are represented in Fig. 4.

## 4.5 Sector 5

This sector is located between the Infante and D. Maria Pia bridges and comprises three different areas. In the western zone, the scarp develops between elevations of 10 and 65 m, with an average slope of 44°, and includes two platforms at elevations of 26 and 55 m, which are related with an ancient railway line and to the Nicolau residential complex, respectively. In the central zone, this sector develops between elevations of 8.5 and 53 m, with an average slope of 53°, and contains a platform at an elevation of 31 m, that

matches with an ancient railway line. Finally, in the eastern zone, the scarp is defined by elevations between 9 and 57 m, an average slope of 41° and a platform at an elevation of 35 m, which also corresponds to the ancient railway line. In all zones, the slopes contiguous to the platforms are sub-vertical.

Regarding the geological and geotechnical conditions, this sector is characterized by cover deposits up to 18 m thick (especially in the back side of the masonry walls), and a moderately fractured ($F_3$) and weathered granitic mass ($W_3$).

Groundwater drainage is observed along the slopes confining with the residential complex, as well as in the vicinity of the Gustavo Eiffel Avenue. The water level ranges between elevations of 18 and 23 m.

In this sector, the stabilization actions identified in the field included the reinforcement of the rock mass existing over the ancient railway tunnel, using shotcrete, nails, wire mesh and drains, and at the base of the slope next to the Infante bridge with wire mesh, as well as masonry walls delimiting the railway platform and the properties.

The constructions are concentrated in small clusters (in the Nicolau residential complex), occurring also some disseminated buildings, partially in ruins.

As risk situations, it was recognized the rockfall on the slopes confining with the residential complex and the Gustavo Eiffel Avenue, the uncontrolled groundwater flows on the slopes, the structural collapse (buildings and/or ruins), traffic obstruction, damages in vehicles and injuries and/or loss of lives.

The location and identification of the slope instabilities, stabilization works and risk situations identified in this sector are represented in Fig. 5.

## 5 Geotechnical Solutions Proposal

Based on analysis and interpretation of the information already available and collected in the field, a set of remedial measures was recommended to perform in each sector, in order to control the identified risk situations and, at the same time, to generate the least possible impact on the landscape. The geological and geotechnical conditions to be taken into account in future scenarios of the use of the scarp, namely requalification as *non aedificandi* area (area where it is forbidden to build) or replanning of the area, were also suggested for sectors 3 and 5.

Given the risk situations identified in the field, it was proposed as suitable remedial activities for all sectors visual inspections, monitoring, reinforcement and maintenance of the observation system installed in structures and/or mass rock and analysis of the observation data. Nevertheless, each sector has its singularities and, therefore, other specific measures were recommended.

Thus, in case of Sector 1, the additional measures include slope sanitation and, in particular areas, the execution of stabilization works like shotcrete, wire mesh and nails.

In Sector 2, it was also considered as important measures to carry out the assessment of the conservation status of the containment structures, the rehabilitation of the drainage system and other components of the containment solution, deforestation, cleaning and maintenance of the surface and internal drainage systems and the potential reinforcement of the stabilization solution.

Regarding Sector 3, the demolition of buildings, the analysis of the retaining barrier functionality, the study of streets protection measures (removal of unstable blocks, wire mesh, nails, shotcrete, global/partial ruins demolition,



**Fig. 5** Characterization of the reference situation and the risk situations of sector 5
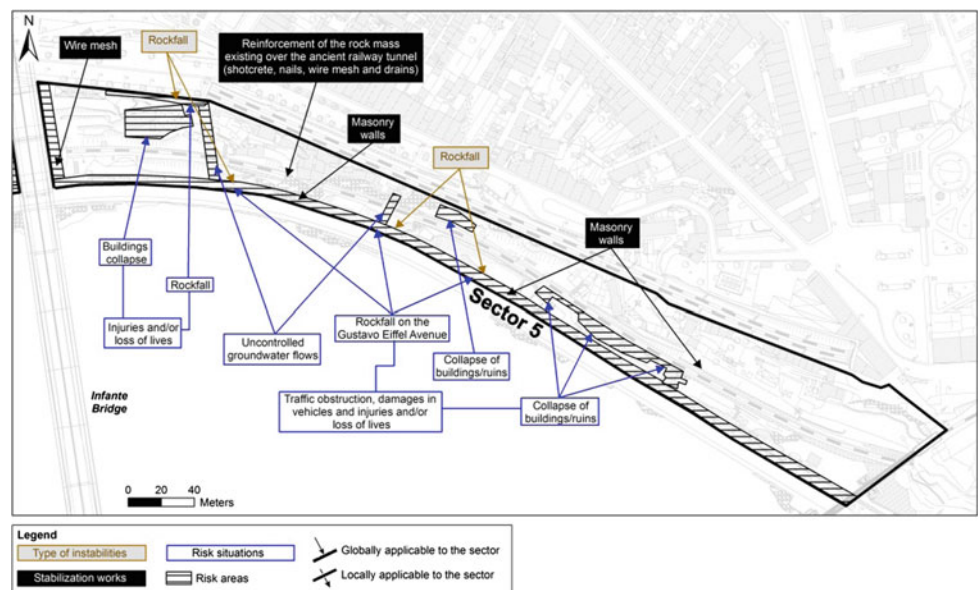
containment/reinforcement of walls, among others) and the definition of a protection perimeter on the western slopes confining with the Infante bridge were also recommended.

In Sector 4, the remedial measures also comprise stabilization works on the rocky slopes bordering this sector and buildings demolition at the western and southwestern areas.

Finally, in what concerns to sector 5, the proposal also considered the stabilization of the upper slopes confining with the Nicolau residential complex (removal of unstable blocks, wire mesh, nails, shotcrete, drains, among others), installation of surface and internal drainage systems, constructions demolition (buildings/ruins), stabilization of the rocky slopes and the masonry walls located between the Gustavo Eiffel Avenue and the ancient railway platform (with wire mesh, nails, shotcrete and reinforcement of existing walls) and the definition of a protection perimeter on the eastern slopes confining with the Infante bridge.

Moreover, for the future scenarios of the scarp use in sectors 3 and 5, it was recommended for the requalification as *non-aedificandi* area the demolition of constructions, deforestation, rubble removal, slopes sanitation, execution of complementary site investigations and tests, adjustment of the slopes geometry and the use of complementary stabilization measures adjusted to the landscape. In case of the replanning of the area, it was suggested the execution of a technical-economic study of an urban design that comprises the stabilization solution of the rock mass supported by complementary site investigations and tests. Regarding Sector 4, no geological and geotechnical constrains were identified for the development of solutions for future uses of space.

## 6   Final Remarks

Aiming the definition of homogeneous areas, the Fontaínhas escarpment was subdivided into 5 sectors for the characterization of the stability conditions. The subdivision of the study area was based on a set of criteria such as the existence of stabilization works, type and distribution of the constructions (buildings and ruins), slope morphology and vegetation (type/distribution).

Based on a set of parameters, addressing identification, geometry, geological and geotechnical conditions and presence of interventions/buildings, the reference conditions and the risk situations of each sector were characterized.

Taking into account the risk situations identified in each sector, a remedial measures proposal was suggested to the city council of Oporto, with the least possible impact on the landscape. However, during the design it should be studied in detail for its proper implementation.

The geological and geotechnical information updated with field observations and observation data analysis was considered sufficient for the definition of the remedial measures suggested.

Sectors 1 and 2, located in the western part of the escarpment, correspond to an urban area with historical and patrimonial value and an area with significant stabilization works, respectively. Therefore, for these sectors only the implementation of measures that ensure the stability of the escarpment was recommended.

In the remaining sectors (sectors 3 to 5), the suggested approach was slightly different. It was recommended the priority measures for the control of the identified risk situations, as well as the geological and geotechnical constrains to be taken into account in the different scenarios of the use of the scarp.

These recommended measures have been designed and applied in the study area since late 2013.

## References

Borges, L., Correia, A.: Escorregamentos de terra e queda de blocos – O exemplo do passeio das Fontaínhas (Porto). Seminário "Riscos Geológicos", pp. 35–46, Associação Portuguesa de Geólogos (2003)

Coba, S.A.: FCUP: Oporto geotechnical map, vol. I, 2nd edn., Porto (2003)

LNEC: Caracterização das condições de estabilidade da escarpa da margem direita do rio Douro, entre as pontes de D. Luís e D.ª Maria Pia. Report 393/2011–NGEA, Lisbon (2011)

Neves, J.: Geomorfologia e geotecnia da zona das Fontaínhas (Porto): uma contribuição para o seu ordenamento. Master Thesis, 106 p (1999)

# The Use of JBlock in the Analysis of Potential Rock Falls at the Magdalena Colliery, Dundee, South Africa

Khethani Reason Khoza, Egerton Daniel Christian Hingston, Sihle Mtshali, Cebolenkosi Khumalo, and Nomonde Mabogo

## Abstract

Rock falls are a major cause for concern at the Magdalena Colliery, where mining of bituminous coal has been going on for the past twelve years. Potential keyblocks are the result of numerous joint intersections that result in many unstable blocks that fall off the roof, when the weight exceeds the support capacity. Several attempts have been made in the past to accurately predict rock fall occurrence. This paper describes the use of the computer program JBlock to simulate keyblocks in the roof at Section 1, Panel 417 at the Magdalena Colliery and to predict the probability of occurrence of rock falls. Scanline mapping was undertaken in the roof followed by cluster analysis in DIPS to determine the major joint sets for input into the JBlock program in order to identify potentially unstable keyblocks. Laboratory tests were also conducted on selected samples in order to determine the geotechnical properties of the material and also to carry out a rock mass classification. The program tested the generated keyblocks for the current support system and a proposed support system, which was based on the rock mass classification. Results obtained show that the current support system is inadequate at Section 1, Panel 417.

## Keywords

Rock fall • Discontinuities • Keyblocks
JBlock

K. R. Khoza · E. D. C. Hingston (✉)
University of KwaZulu-Natal, Private Bag 54001, Durban, 4000, South Africa
e-mail: hingstone@ukzn.ac.za

S. Mtshali · C. Khumalo · N. Mabogo
Buffalo Coal, Dundee, South Africa

## 1 Introduction

Rock falls are a major hazard in South African underground collieries. The damage ranges from minor injuries caused by small pieces of rocks, to severe and sometimes fatal injuries, caused by large keyblocks. Despite attempts to reduce the number of injuries, statistics show that the injury rate still remains unacceptably high. The driving factors of these statistics are the presence of discontinuities in the rock mass and the inability to select appropriate support systems (Gumede and Stacey 2007). Buffalo Coal currently operates two collieries in Dundee, South Africa; the Magdalena Colliery and the Aviemore Colliery, which are hosted within the Klip River coalfield. The Aviemore Colliery extracts high-grade anthracite coal while the Magdalena Colliery extracts high-grade bituminous coal (Muller et al. 2013). The focus of this study was the Magdalena Colliery, which has been mining bituminous coal since 2005.

Two coal seams, which are referred to as the Alfred seam and the Gus seam of the Vryheid Formation, are currently being mined at the Magdalena Colliery. Mining is by the bord and pillar method, also referred to as the room and pillar method, whereby a continuous miner is used to extract bituminous coal from the Alfred seam and the Gus seam. The bord and pillar mining method involves the extraction of the ore from relatively flat-lying deposits, whereby the excavation is carried out to produce a network of rooms between pillars of ore (in this case coal) that are left behind to support the overlying strata (Brady and Brown 2006; Clemente et al. 2013). The rooms that are produced as a result of excavation of the coal act as access openings, haul roads, and ventilation.

The intersection of numerous joints and other fractures exposed on the rock surface as a result of mining operations contribute to the formation of keyblocks. The objective of the support system is to stabilize as many of these keyblocks as possible (Esterhuizen and Streuders 1998). The Magdalena Colliery has been experiencing large incidence of

rock falls over the years, which in one instance has led to the temporary closure of an entire section. Most of the joint/slip related falls occur around areas intersected by dolerite dykes and/or sills near where there is an increase in joints and slip in the roof. An investigation of the potential keyblock failure has been undertaken in Section 1, Panel 417 of the Magdalena colliery. Since it is impractical to map every discontinuity and accurately estimate the rock fall potential, a computer program, JBlock (Esterhuizen et al. 1996) was used to determine the probability of failure of potential keyblocks. The program uses the measured joint data (length, spacing and orientation) to estimate the probability of occurrence of potentially unstable blocks and rock falls. Discontinuity survey was conducted using scanline mapping and the data obtained was then evaluated to determine the major joint sets using DIPS 7.0. Furthermore, the JBlock program was used to assess the efficiency of the implemented support system and to propose new support system.

## 2 Location

The study area is located within the Magdalena Colliery, which is approximately 22 km north of the central town of Dundee, in the KwaZulu-Natal Province (27° 58′ 24″ S and 30° 11′ 51″ E) South Africa (Fig. 1). The towns of Glencoe, Dannhauser and Hattingspruit lie to the south, west-southwest and southwest respectively of the Magdalena Colliery.

## 3 Geology of the Study Area

The study area lies within the Vryheid Formation of the Ecca Group, a subdivision of the Karoo Supergroup, which is of Carboniferous age (320–180 Ma) (Johnson et al. 1997). The Vryheid formation comprises feldspathic sandstone, grey micaceous shale and mudstone (Fig. 2) (Muller et al. 2013). The Vryheid Formation contains five coal seams that persist throughout the Formation (Johnson et al. 1997). The seams are fairly flat-lying with a gentle dip towards the southwest (Greenshields 1986). The coal seams currently located at the collieries belong to the Klip River coalfied, which is hosted in the Vryheid Formation (Muller et al. 2013). The Klip River coalfield contains two economic seams, the Upper Alfred seam and the lower Gus seam, which are currently being mined (Muller et al. 2013). The Alfred seam is more developed than the Gus seam, as it ranges in thickness from 1.5 m in the south to 3.3 m in the north, whereas the less developed Gus seam ranges in thickness from 0.5 m in the south to 1.3 m in the north (Muller et al. 2013). The rank of both seams ranges from bituminous to anthracite (Muller et al. 2013). Both seams have a parting towards the north

consisting of an intermediate, coarse- to medium-grained sandstone, which ranges in thickness from approximately 1 to 10 m (Cronje et al. 2007).

A series of dolerite intrusions is present in the Magdalena area, represented by the Ingogo dolerite sill as well as a network of widely spaced dolerite dykes (Clemente et al. 2013; Muller et al. 2013). At Panel 417, Section 1, which is the focus of this study, a dolerite intrusion spanning 13.88 m resulted in both replacement and a 13.3 m displacement of the Alfred seam (Fig. 3). The dolerite intrusion caused a significant delay in the mining schedule, and also instability in the roofs particularly so in the contact zones between the dolerite and the micaceous sandstone. Roof support is by tendon roof bolts with a length of 1.8 m and a 1 m × 1.5 m spacing. However, the density of the roof bolts is increased where there are slips and joints with additional roof bolts of 1.5 m long and 0.6 m long with osro straps (i.e. a type of steel strap extensively used in underground support to prevent slabs from loosening). Spot bolting is also done on the dolerite at targeted locations because the holes for the roof bolts could not be drilled to required depth.

## 4 Methodology

### 4.1 Scanline Mapping

Determination of the major joint sets is very crucial in analyzing the probability of failure of keyblocks in JBlock. Thus, a discontinuity survey was undertaken using scanline mapping. Priest (1993) described scanline mapping as an ideally suitable method of determining discontinuity orientation and other large-scale geometrical properties at exposed faces and also it is statistically rigorous. Scanline mapping was conducted on the exposed rock surface in Section 1 using a 30 m interval. Discontinuities were recorded taking into account the dip and dip direction with the aid of a Clar type geological compass manufactured by Breithaupt Kassel, as well as the discontinuity characteristics including range, length and spacing. The range is the difference between the maximum and minimum values of the measured dips and dip directions. In this case, the dip direction range was used, as stipulated by the JBlock manual. The fractures created by blasting activities were ignored from the mapping exercise in order to avoid contamination of the data and confusion in determining the major joint sets. A total of 120 discontinuity datasets, where rock mass exposure allowed, were recorded on a total scanline distance of 65 m. The data obtained from the discontinuity survey was analyzed using Rocscience DIPS 7.0. The data was plotted as poles, and cluster analysis, which uses fuzzy clustering, reveal three major joint sets; J1, J2 and J3, with an average dip and dip direction of 89°/354°, 65°/237° and
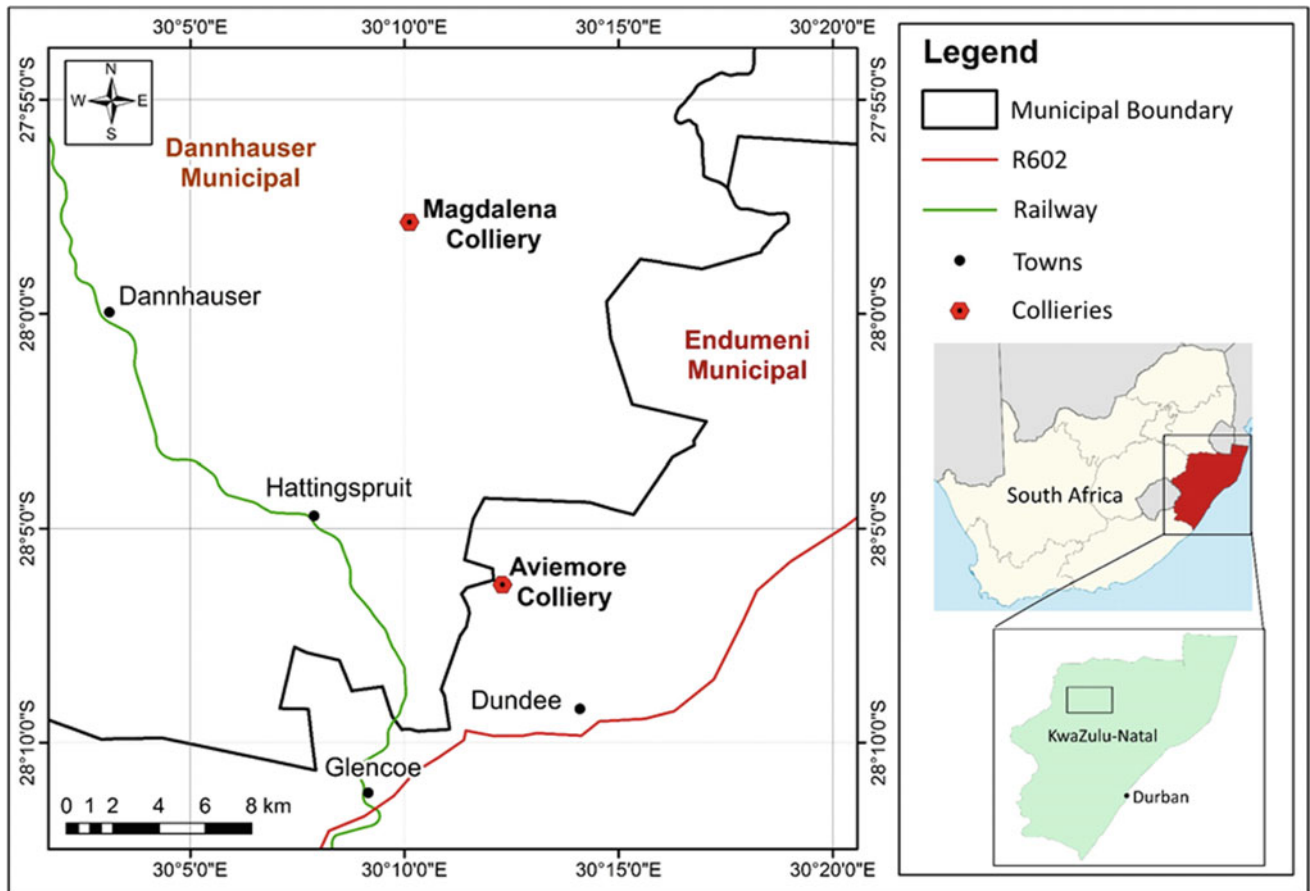
**Fig. 1** Location map of Magdalena Colliery

**Fig. 2** Local geology of the study area (modified after Council for Geoscience 1997)
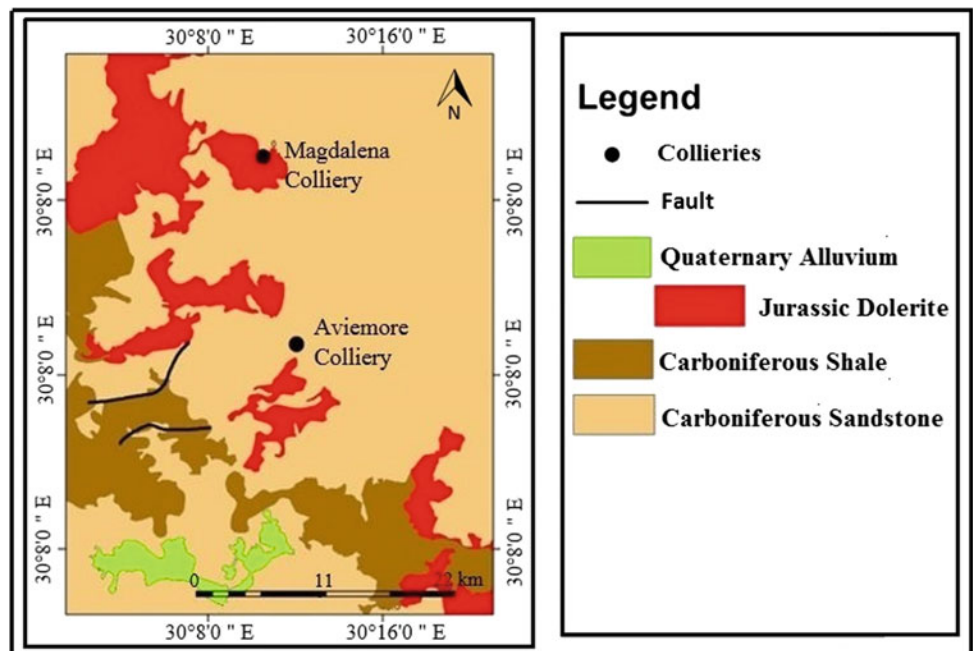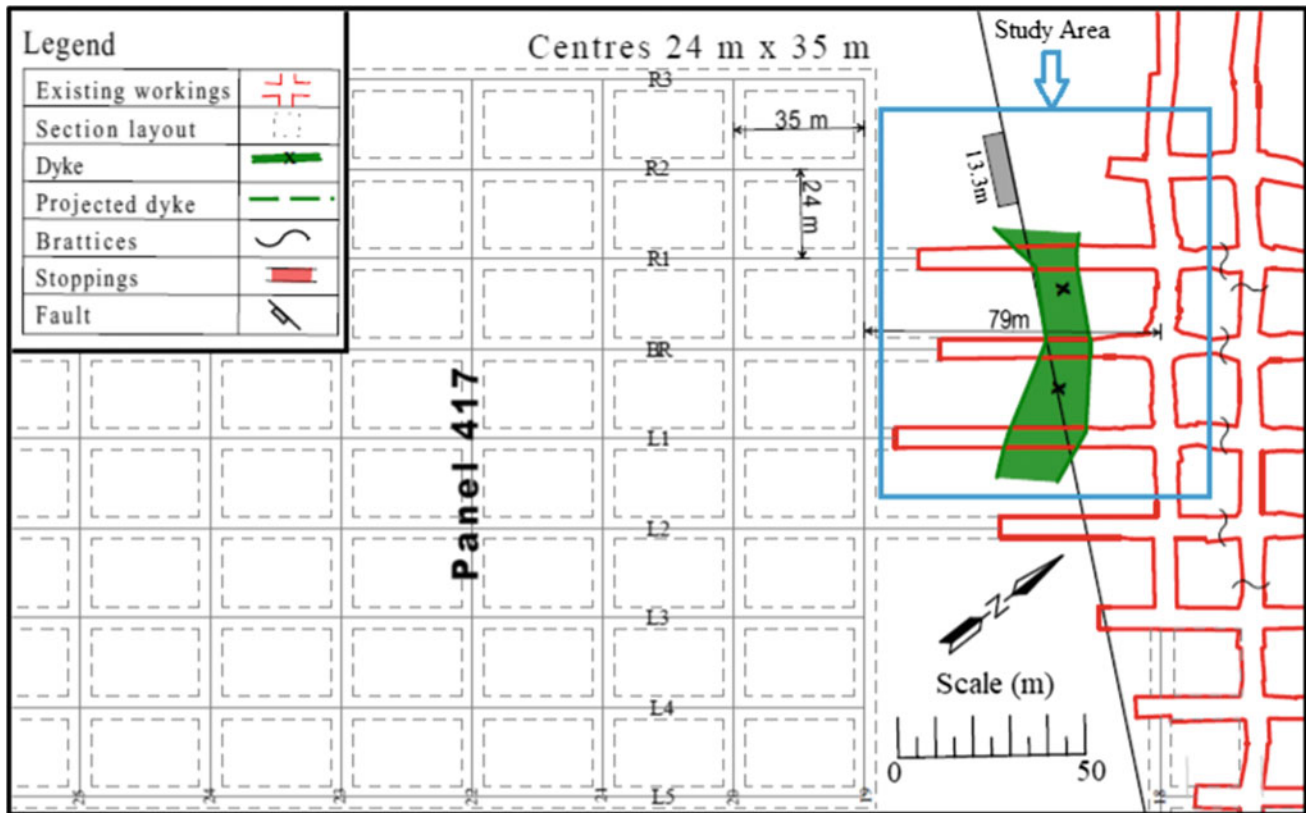
**Fig. 3** Section plan indicating the study area, Section 1, Panel 417

65°/107° respectively (Fig. 4). A summary of the major joint sets and their properties, which were subsequently used in JBlock, are shown in Table 1.

## 4.2 Laboratory Testing and Rock Mass Classification

Laboratory tests were conducted on selected samples of the sandstone and dolerite in order to determine their geotechnical properties. The tests conducted include dry density, Brazilian Disc test, point load test and uniaxial compressive strength test (UCS). The tests were conducted in accordance with the ISRM (1981) procedures for rock testing. The results obtained from the laboratory tests conducted are summarized in Table 2. The understanding of the rock strength was crucial in this investigation before proposing the new support system. Thus, the parameters obtained from mapping, field and laboratory testing were processed into three rock mass classification systems: Rock Mass Quality Designation (RQD) (Deer 1964), Rock Mass Rating (RMR) (Bieniawski 1989) and the Q-System (Barton et al. 1974). Based on the three classification systems used, the dolerite rock mass and the sandstone rock mass could be classified as good rock (Table 3).

## 4.3 JBlock Simulation

In order to represent realistic situations, JBlock requires many simulations to be run. In this study, a total of 10,000 simulations were run, creating more than 10,000 keyblocks. The simulation was first run for the current support system operating in the colliery in order to evaluate its effectiveness, and then run for a proposed system which was based on the rock mass rating.

In the case of the current support system, 1.8 m long tendon fully grouted roof bolts of 20 mm diameter with a support capacity of 200 kN were used with a spacing of 1 m × 1.5 m. In specific areas, such as contact zones, slips and faults, which require more stringent measures, an additional 1.5 m long and 0.6 m long tendon roof bolts with osro straps were added. The area of interest includes the contact zone between the sandstone and the dolerite dyke. The area simulated is 65 m by 6 m excavation, which is supported with one support system, with no additional support to obtain presented block failure results. A total of 10,000 removable blocks were generated and occurrence of unstable keyblocks were obtained. An example of the panel dimension used in the simulation is shown in Fig. 5.

In the new support system simulation, the spacing of the roof bolts was changed from the standard current system of
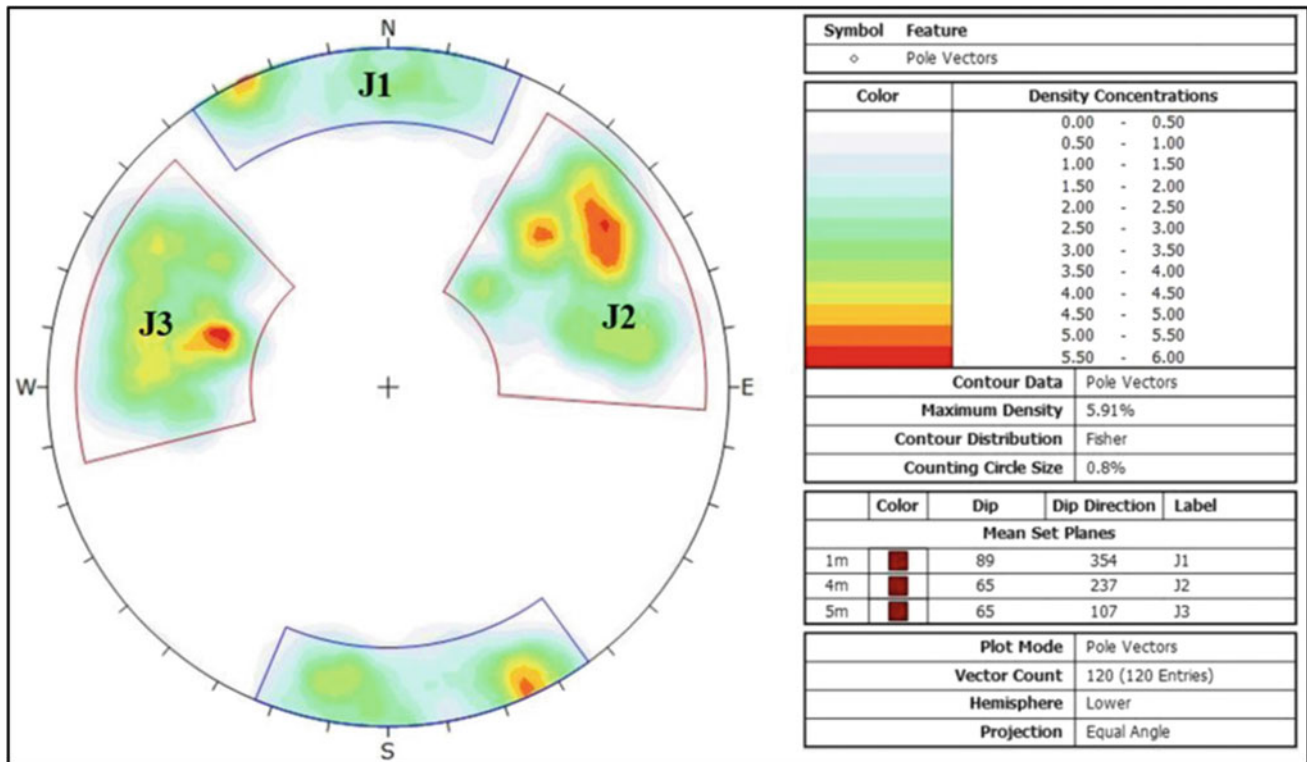
**Fig. 4** Stereoplot showing the contoured plot of the three joint sets

**Table 1** Summary of the major joint sets used as input parameters in JBlock

| Joint set | Orientation | | Range | Spacing (m) | | | Length (m) | | |
|---|---|---|---|---|---|---|---|---|---|
| | Dip (°) | Dip Direction (°) | | Min | Mean | Max | Min | Mean | Max |
| J1 | 89 | 354 | 15 | 0.5 | 1.0 | 1.8 | 3 | 7 | 15 |
| J2 | 65 | 237 | 26 | 0.8 | 1.2 | 2.1 | 4.5 | 8 | 17 |
| J3 | 65 | 107 | 23 | 0.3 | 1.0 | 4.0 | 2.3 | 6 | 11 |

1 m × 1.5 m to 1.2 m × 1.2 m. The length of the roof bolt was increased from 1.8 to 2.1 m and the diameter remains unchanged (20 mm). The roof bolts have capacity of 200 kN with a shear stress capacity of 500 kN/m² grout. Along the special areas, the 1.5 and 0.6 m long tendon roof bolts with osro straps were implemented by spot bolting.

## 5 Results and Discussion

A total of 10,000 keyblocks were generated and the probability of failure of unstable keyblocks was obtained (Fig. 6). It should be noted that there was no additional wire mesh support installed in obtaining the results. It could be seen that the probability of keyblock failure for 1 m³ blocks is 62% and the highest support failure value of 8% with the overall probability of rock fall of 17.41%. South African code of practice insists that the probability of rock falls must be reduced as low as

possible by identifying and stabilizing special areas. As a result, the probability of block failure obtained is high, thus indicating that the support is inadequate.

The area of the contact zones has little to no cohesion, hence it brings about a reduction in the effectiveness of the current support system. As a result, this area experienced high keyblock failures. During section planning, this area has been already classified as a special area as a result of the contact and its related joints and slips. However, extensive support must be employed based on the rock fall results. This means that the successful employment of extensive support in these special areas would reduce the incidences of keyblock failures while promoting the profitability of the colliery. The implementation of longer roof bolts and reduced spacing intervals would improve safety.

The simulations obtained for the proposed support system, are shown in Fig. 7. It could be seen that the proposed system resulted in a reduction of the probability of rock falls. The probability of block failure for 1 m³ blocks reduced

**Table 2** Geotechnical properties of the sandstone and dolerite

| Sample | | Dolerite | Sandstone |
|---|---|---|---|
| Dry density (kg/m$^3$) | Average | 2700 | 2373 |
| | Range | 2620–2730 | 2308–2414 |
| | Number of samples | 6 | 6 |
| UCS (MPa) | Average | 160.49 | 33.85 |
| | Range | 156.86–162.78 | 30.60–37.74 |
| | Number of samples | 6 | 6 |
| Point load index Is$_{50}$ (MPa) | Average | 6.46 | 1.53 |
| | Range | 5.34–7.34 | 0.59–2.15 |
| | Number of samples | 6 | 6 |
| Brazilian disc strength (MPa) | Average | 13.38 | 5.40 |
| | Range | 11.60–16.78 | 2.66–5.70 |
| | Number of samples | 6 | 6 |
| Correlated UCS by Broch and Franklin (1972) (MPa) | Average | 155.04 | 36.72 |
| | Range | 128–176 | 14.16–51.6 |
| | Number of samples | 6 | 6 |

**Table 3** Rock mass classification for the sandstone and dolerite

| Rock type | Rock mass classification | | | | | |
|---|---|---|---|---|---|---|
| | Q-system | | RMR | | RQD | |
| Sandstone | 14 | Good rock | 63 | Good rock | 79 | Good rock |
| Dolerite | 15 | Good rock | 71 | Good rock | 83 | Good rock |

from 62% for the current support to 11% for the proposed support system. The highest support failure also reduced from 8 to 2% and the overall probability of rock fall reduced from 17.41 to 6.07%. Much work is required in evaluating the proposed support system as the reduced spacing of the roof bolts and the 2.1 m long roof would be more expensive and time consuming to install than the current 1.8 m bolt. However, it could be concluded that implementation of the new support system would improve safety and promote, in the longer term, the profitability of the colliery as less rock falls would occur.
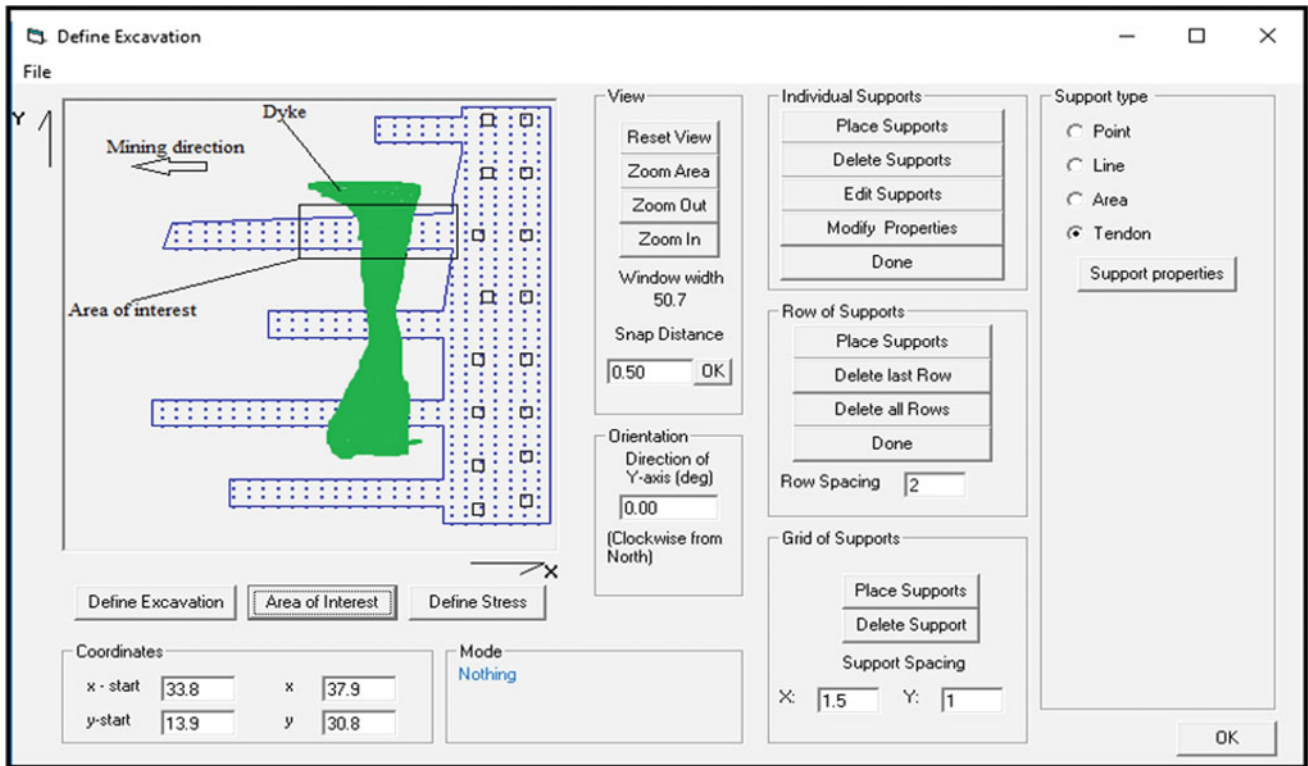
**Fig. 5** Panel dimension used in JBlock
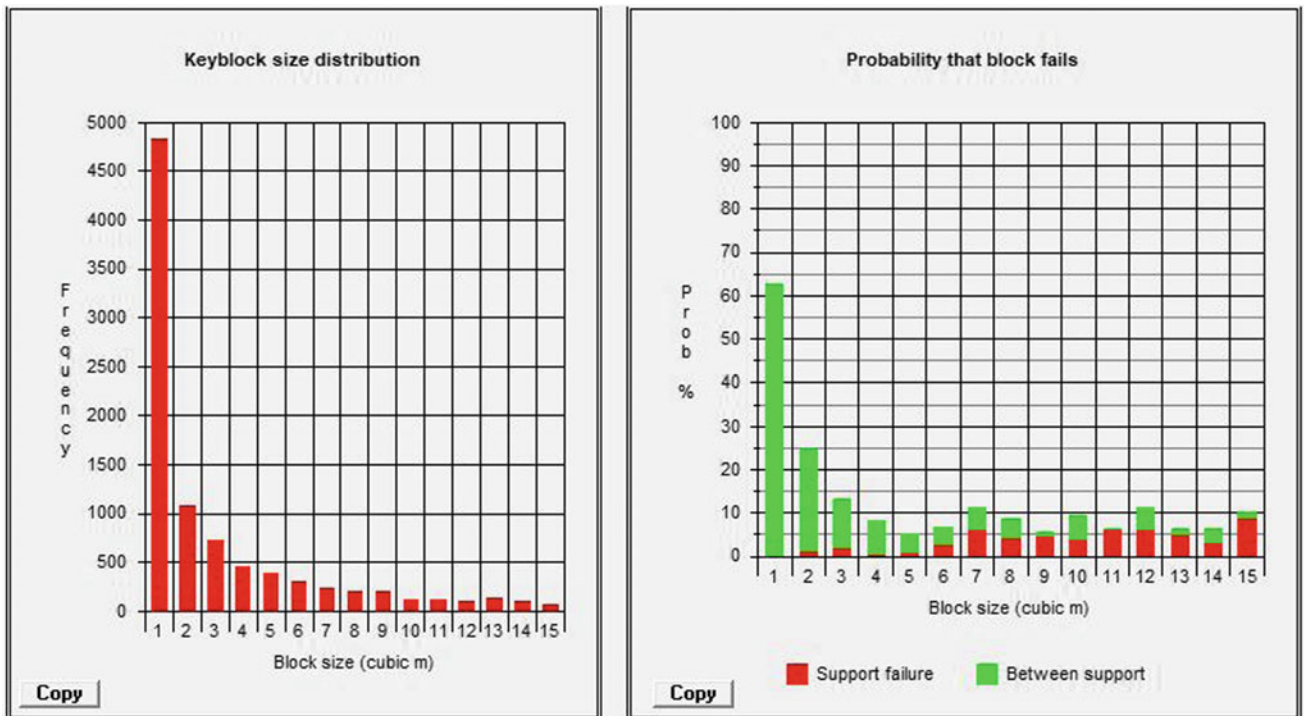


**Fig. 6** Probability of block failure based on the current support system
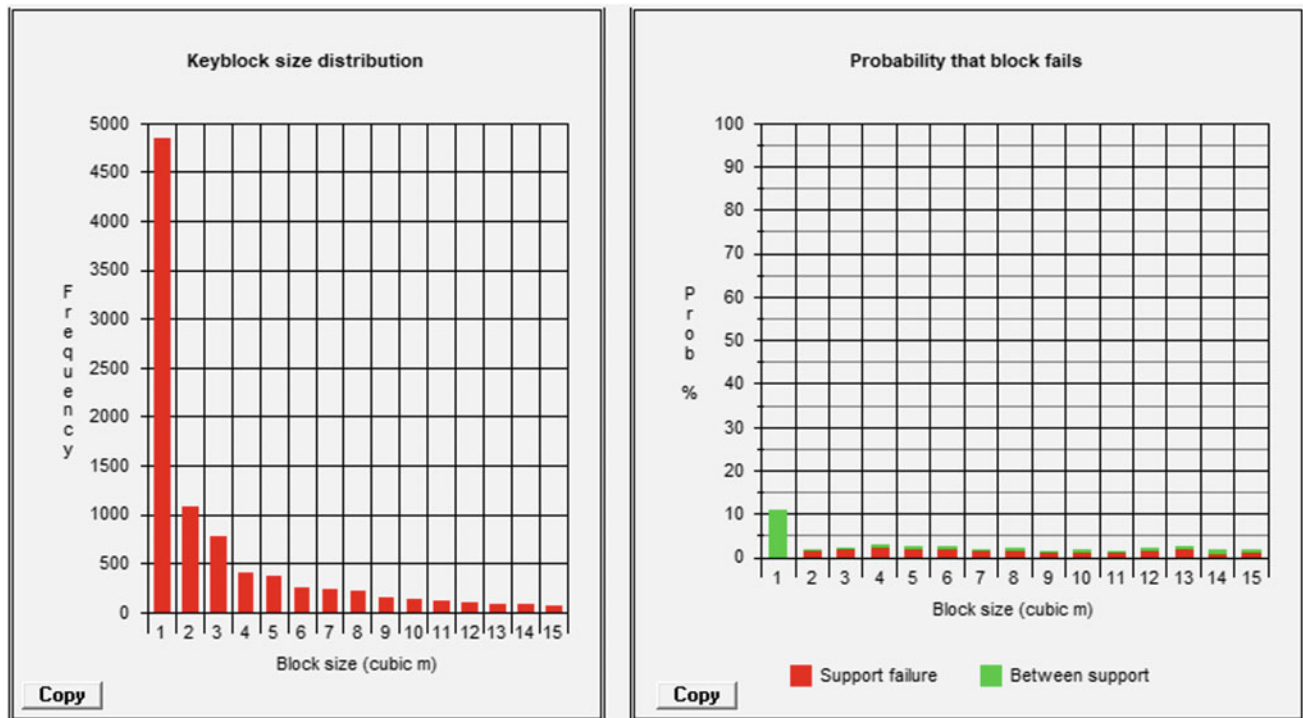
**Fig. 7** Probability of block failure for proposed support system

## 6 Conclusion

The JBlock results showed that the current support system used in Section 1, Panel 417 dolerite contact zone is inadequate. The contact zones showed cracks, which resulted in higher probabilities of rock falls, thus indicating the inability of 1.8 m roof bolts to stabilize the roof. As a result, a new support system, which shows a reduction in the probability of rock fall, was proposed using JBlock. The increase in the length of roof bolt by 0.3 m and a rearrangement in the spacing, resulted in more than 40% reduction in the probability of keyblock failure for a 1 $m^3$ block. Although the proposed support system is more expensive than the current support system and time consuming to install, the benefits would far outweigh the costs in the long term and also create a safer working environment. This study has assisted the colliery in improving the support system in this section.

## References

Barton, N., Lien, R., Lunde, J.: Engineering classification of rock masses for the design of tunnel support. Rock Mech. **6**(4), 189–236 (1974)

Bieniawski, Z.T.: Engineering Rock Mass Classifications: A Complete Manual for Engineers and Geologists in Mining, Civil, and Petroleum Engineering. Wiley, Canada (1989)

Brady, B.H.G., Brown, E.T.: Rock Mechanics for Underground Mining, 3rd edn. Springer, Netherlands (2006)

Brown, E.T. (ed.): ISRM: Rock Characterization, Testing and Monitoring, ISRM Suggested Methods. Pergamon Press, Oxford (1981)

Clemente, D., Muller, C.J., Odentdal, N.J., van Heerden, D.: An Independent Qualified Person's Report on Forbes Coal Dundee Operations in the KwaZulu-Natal Province. Minxcon, South Africa (2013)

Council for Geoscience: 1:250,000 Geological Series Sheet, 2830 Dundee. Government Printer, Pretoria (1997)

Cronje, P.: Parting, Gus and Alfred. Report No. 0704-005Mag. Big C Rock Engineering, Bronkhorstspruit, South Africa (2007)

Deere, D.U.: Technical description of rock cores. Rock Mech. Eng. Geol. (1964)

Esterhuizen, G.S.: JBlock User's Manual and Technical Reference (1996)

Esterhuizen, G.S., Streuders, S.B.: Rockfall hazard evaluation using probabilistic keyblock analysis. J. S. Afr. Inst. Min. Metall. **98**, 59–64 (1998)

Greenshields, H.D.: Eastern transvaal coalfield. Min. Deposits Southern Afr. **2**, 1995–2010 (1986)

Gumede, H., Stacey, T.R.: Measurement of typical joint characteristics in South African gold mines and the use of these characteristics in the prediction of rockfalls. J. S. Afr. Inst. Min. Metall. **107**(5), 335–344 (2007) (submitted for publication)

Johnson, M.R., Van Vuuren, C.J., Hegenberger, W.F., Key, R.: Stratigraphy of the Karoo supergroup in Southern Africa: an overview. J. Afr. Earth Sci. **23**(1), 3–15 (1997)

Muller, C.J., van Heerden, D., Odendaal, N.J., Clemente, D.: An Independent Qualified Persons' Report on Forbes Coal Dundee Operations in the KwaZulu-Natal Province, South Africa, Minxcon (2013)

Priest, S.D.: The collection and analysis of discontinuity orientation data for engineering design, with examples. Compr. Rock Eng. **3**, 167–192 (1993)

# Geomechanical Behavior Changes of Bunter Sandstone and Borehole Cement Due to scCO$_2$ Injection Effects

Flora F. Menezes, Christof Lempp, Kristoff Svensson, Andreas Neumann, and Herbert Pöllmann

## Abstract

Geomechanical behavior changes caused by supercritical (sc) CO$_2$ in an analogue reservoir formation and in borehole cement are described after physical and mechanical evaluations. To simulate reservoir conditions, rock and cement specimens were conditioned during 5 weeks with scCO$_2$ at 333 K, brine at 16 MPa of hydrostatic pressure. Geomechanical experiments, such as traditional triaxial compression test and Brazilian tests, were executed with untreated and treated samples. First, results of the effects of CO$_2$ injection are presented through changes in physical and mechanical properties, as well as visual evaluations of the sandstone matrix and pore structure.

## Keywords

Geological CO$_2$ storage • Bunter sandstone • Geomechanical

## 1 Geological Storage of Carbon Dioxide

As described by the Intergovernmental Panel on Climate Change (IPCC), carbon dioxide capture and storage (CCS) is a process consisting of the separation of carbon dioxide (CO$_2$) from industrial and energy-related sources, transport to a storage location and a long-term isolation from the atmosphere. Geological storage of CO$_2$ has been considered as a transitional option to reduce CO$_2$ emissions in the atmosphere (IPCC 2005).

Funded by the German Federal Ministry for Economic Affairs and Energy (BMWi), the research project Cluster

F. F. Menezes (✉) · C. Lempp · K. Svensson · A. Neumann
H. Pöllmann
Institute for Geosciences and Geography,
Martin-Luther-University Halle-Wittenberg,
Von-Seckendorff-Platz 3, 06120 Halle, Germany
e-mail: flora.menezes@geo.uni-halle.de

(www.bgr.bund.de/CLUSTER) investigates the impacts of CO$_2$ streams and mass flow for different scenarios along the CCS chain. Therefore, this work focuses on the physical and mechanical property changes of rock and borehole cement on the basis of triaxial experiments. Those experiments simulate conditions of a saline aquifer under compressive stress regime, especially after a long-term CO$_2$ injection.

This work presents the first part of an investigation on the geomechanical behaviour changes in a potential reservoir rock and in borehole cement caused by scCO$_2$ by taking into consideration the variability of boundary conditions in storage locations (e.g. effective stress changes, storage period, and directional anisotropy). After a brief geological overview and textural description of the Bunter Sandstone, the methodology to evaluate the physical properties of rock and cement is given. Strength and deformability of short and long-term experiments on rock and cement specimens are presented and discussed, illustrated by microscopic pictures before and after CO$_2$-treatment. Preparation of mortar mixtures, sample conditioning and short and long-term mechanical experiments were carried out at the Martin-Luther-University in Halle (Germany).

## 2 Materials and Methods

### 2.1 The Trendelburg Beds

The Trendelburg beds corresponds to a sandy, braided river deposit from the middle Bunter Sandstone which, together with the Wilhelmshausen Formation, belongs to the Lower Solling Formation deposited in the central part of the Reinhardswald basin (Weber and Ricken 2005).

Rock blocks from the Trendelburg beds were collected from the Fa. Bunk quarry located in Bad Karlshafen (51° 38′ 36.932″ N 9° 27′ 22.953″ E), Germany. The greyish Trendelburger beds from Bad Karlshafen consist of a fine to medium grained sandstone, compact, clearly layered and therefore with a pronounced direction of planar anisotropy.

A very characteristic feature of the Trendelburg beds is the presence of rounded or rather elliptical lenses, filled by slightly loose grain aggregates, mainly of feldspar. They discern from the sandstone fabric in their lightly rose coloured and friable texture, which makes them identifiable with the naked eye. The diameter of those structures varies from 5 to 20 mm, and in there, opaque minerals occur more often than in the fabric.

Other isolated structures of interest observed in rock blocks at times are dendritic veins of opaque mineral phases, light greenish layers of maximal 1 cm and some minor joints. Rock fragments were characterised by using Powder X-ray Diffraction (PXRD). The Trendelburg beds consist of quartz ($\sim$64 to 72 wt%), K-feldspar ($\sim$11 to 17 wt%), muscovite ($\sim$10 to 12 wt%) and Na-feldspar ($\sim$1 to 12 wt%) and was classified as subarkose after Folk's sandstones classification (Weber and Ricken 2005).

## 2.2 Evaluation of Physical Properties

Physical properties were mostly evaluated by using core samples with edge lengths of about 14 cm and a diameter of 7 cm, precisely plane-parallel and with flat lateral surfaces, after recommendations of the German Geotechnical Society (DGGT) (Deutsche Gesellschaft für Erd- und Grundbau e.V. 1987). In order to analyse rock's directional anisotropy, core samples were drilled transverse and parallel to bedding. The effective porosity after German standards (DIN 1936) is determined by the difference between dry and wet densities, where the amount of water in the pore space corresponds to the effective porosity (connected pore space). For a double determination of effective porosity, a buoyancy technique was executed (Tavallali and Vervoort 2010). The grain density (or specific gravity) was evaluated for each rock block twice, with helium gas- and water pycnometry methods by using rock powder. The total porosity was then determined through the ratio between dry and grain density.

To analyse physical and mechanical properties of borehole cement, circular cylindrical specimens were produced with identical size as rock specimens. They were made of Portland slag cement (CEM III/A 52,5 N HS/NA), a cement type made of 50% ground granulated slag. Considering the $CO_2$ injection scenario, CEM III was selected as a borehole cement by virtue of being well resistant against acids. The production of the specimens was executed after German standards (DIN EN 2005).

## 2.3 Geomechanical Experiments and Sample Conditioning

Traditional triaxial compression tests were carried out in order to characterize the geomechanical behaviour of host rock and borehole cement, by simulating reservoir stress changes due to $scCO_2$ injection under a compressive stress regime. The scenario of an $scCO_2$ injection corresponds to a saline aquifer at 1600 m depth and at 333 K. A synthetic formation brine with kNaCl, $MgCl_2$ and $CaCl_2$ (salinity: 250 g/L) was prepared to fully saturate core samples. Accepting 2.65 $g/cm^3$ as a mean density of a sediment basin crust, and assuming a linear relation between depth and pressure (after Euler's formula), a horizontal stress gradient of 0.025 MPa/m and a hydrostatic pore pressure gradient of 0.01 MPa/m was considered. Therefore, the initial state of stress in this saline aquifer should have 16 MPa of pore pressure and 40 MPa of confining pressure.

A conventional triaxial compression system consists of a radial, isotropic confining pressure ($\sigma_3 = \sigma_2$), an axial pressure ($\sigma_1$) and an internal, resistance fluid pressure ($pf$) acting in the pore spaces of the specimen. Such compression tests were performed as multistage tests, where several peaks and residual strengths can be obtained for a single rock specimen (Deutsche Gesellschaft für Erd- und Grundbau e. V. 1987). Triaxial tests were performed from 10 to 70 MPa of confining pressure using the same rate of deformation ($\dot{\varepsilon} = 5.7 \times 10^{-6}$ s$^{-1}$). Water (at room temperature) or $scCO_2$ (at 323 K) was used as saturating fluid for the pore fluid pressure.

Before starting triaxial tests, rock specimens had been saturated with water or brine. Some rock specimens were mechanical investigated just after a long-term $scCO_2$-treatment, in which the sample was exposed to hydrostatic reservoir conditions (333 K and 16 MPa of $scCO_2$) in an autoclave system for five weeks. To illustrate the effects of this $scCO_2$-treatment, micrographs from rock specimens were taken with a 3D-microscope before and after $scCO_2$-treatment (Fig. 8).

To complete mechanical experiments, uniaxial tensile strength was indirectly determined by the Brazilian tensile method with diametrical loading, modified after German standards (DIN 22024 1958). Cylindrical specimens with 5 cm length and two different diameters were used (7 or 5 cm diameter). Tensile strength could be determined in dry, water-saturated and $scCO_2$-treated specimens, regarding their directional anisotropy in a similar approach as by Tavallali and Vervoort (2010).

## 2.4 Geomechanical Evaluation

The mechanical failure of sandstone due to triaxial loading leads to the formation of shear fractures caused by brittle deformation. In geological and engineering applications, it is usual to apply the Mohr-Coulomb failure criterion in the field of brittle deformation to evaluate shear parameters with effective stresses by using the data obtained from triaxial compression tests. Once shear parameters for different degrees of pore pressure and/or different confining pressures were calculated it was possible to use them for calculating back unconfined compressive strength ($\beta_d$), which is used here as a comparison parameter. Furthermore, it was possible to determine a proportionality factor from the linear slope between axial stress and axial deformation, mentioned here as deformation modulus ($V$). This deformation modulus was evaluated between 30 and 60% of the peak stress from the stress-strain curve, in order to prevent machine-dependent influence and early failure behaviour (Erikson et al. 2015).

## 3 Results and Discussion

Density and porosity values for 95 rock specimens of Trendelburg beds are shown on Fig. 1. A linear relationship between dry density (from 2.27 to 2.34 $g/cm^3$) and effective porosity (from 9 to 13%) has been observed, and in ca. 80% of the samples the effective porosity corresponds to at least 80% from total porosity. This relationship between effective and total porosity is useful to figure out to what extent pore pressure acts in connected pore spaces during the triaxial test. Samples with low porosity ratio may not react properly to $CO_2$ as others samples do.

Results from water saturation and buoyancy techniques show an acceptable coefficient of correlation r (0.99 after Pearson), which suggests that both methods are reliable for determining effective porosity (Fig. 2, right). However, special attention is required when testing different specimen's sizes. It was observed that small specimens, such as those used for the Brazilian-Test ($v_o = 98$ $cm^3$) or suction tension ($v_o = 11$ $cm^3$), show a large scattering on porosity and density values which dissociate from porosity values of bigger specimens ($v_o = 540$ $cm^3$) and of rock blocks ($v_o > 540$ $cm^3$) (Fig. 2, left).

Figure 3 shows a box-chart of tensile strengths evaluated with specimen from all investigated rock blocks, organised after saturation conditions and structural anisotropy. Next to it, the bar chart compares tensile strengths for saturated and treated specimens concerning results from a single block (WG 5). Tensile strength has been evaluated from 2.3 to 12 MPa, where the biggest resistance was found when applying the force perpendicular to samples bedding. Due to

the weakening effect of pore fluids, tensile strength has been higher in dry conditions than under water saturation. Specimens treated with $scCO_2$ have shown the lowest tensile strength values in both directions, especially when considering untreated samples from the same block (−30%).

Physical properties of mortar specimens were determined after a hydration period of at least 28 days after the cement production, under water and brine saturation conditions. The density varies from 2.19 to 2.3 $g/cm^3$ and the longitudinal ultrasonic wave varies from 3.55 to 3.69 km/s. An increase in density of ca. 1% was observed after the $scCO_2$ treatment in the autoclave system, which was related to the development of a new greenish mineral phase. This finding is still under investigation.

## 3.1 $CO_2$ Content and Long-Term Effects

The content of $scCO_2$ corresponds to a factor between the minimum in $scCO_2$-volume (in $cm^3$), which is storage in sandstone pore spaces during triaxial test, and the specimen porosity (in $cm^3$). The $scCO_2$-volume was determined by a difference of volume in two positions during triaxial test: at its beginning, under sub-hydrostatic conditions ($\sigma_1 = 10$ MPa, $\sigma_3 = 8$ MPa and $Pf = 6$ MPa), and at its first load-step, before reaching mechanical failure. As the beginning of a triaxial test is always being performed as the same, one can associate $CO_2$ factor change with the pressure conditions of the load-step.

$CO_2$ content is a parameter (1) to qualify directional anisotropy, (2) to estimate the influence of pressure on the gas content and (3) to evaluate long-term $scCO_2$ effects. Figure 4 shows that the content of $scCO_2$ increases when pore pressure flows parallel to bedding (blue square over red triangle), and after a long-term $scCO_2$-treatment (yellow triangle over red triangle). In an isotropic stress field, the content of $scCO_2$ on the intact sandstone ranges between 0.5 and 2.9 and is linearly described as a function of confining and pore pressures (Fig. 4, right). There are three pressure curves with different ratios of pore- and confining pressures (40, 60 and 80%), so that a 40% ratio has a lower gas consumption than 60 or 80% and stays stable after 30 MPa of confining pressure. Considering the closed system in the triaxial cell, $scCO_2$-content values >1 refer to several causes, such as porosity change due to pressure, due to a continuing reaction between $scCO_2$ and brine, or due to stabilising pore pressure. This last instance would explain why the lowest pressure curve (0.4) is the first which reaches a stable state.

Stress-strain curves for the first load-step (continuous) for treated and untreated specimens are shown in Fig. 5 (parallel and transverse to bedding). Under triaxial stress, compressive strength and modulus of deformation were higher by arranging the bedding parallel to the major stress axis
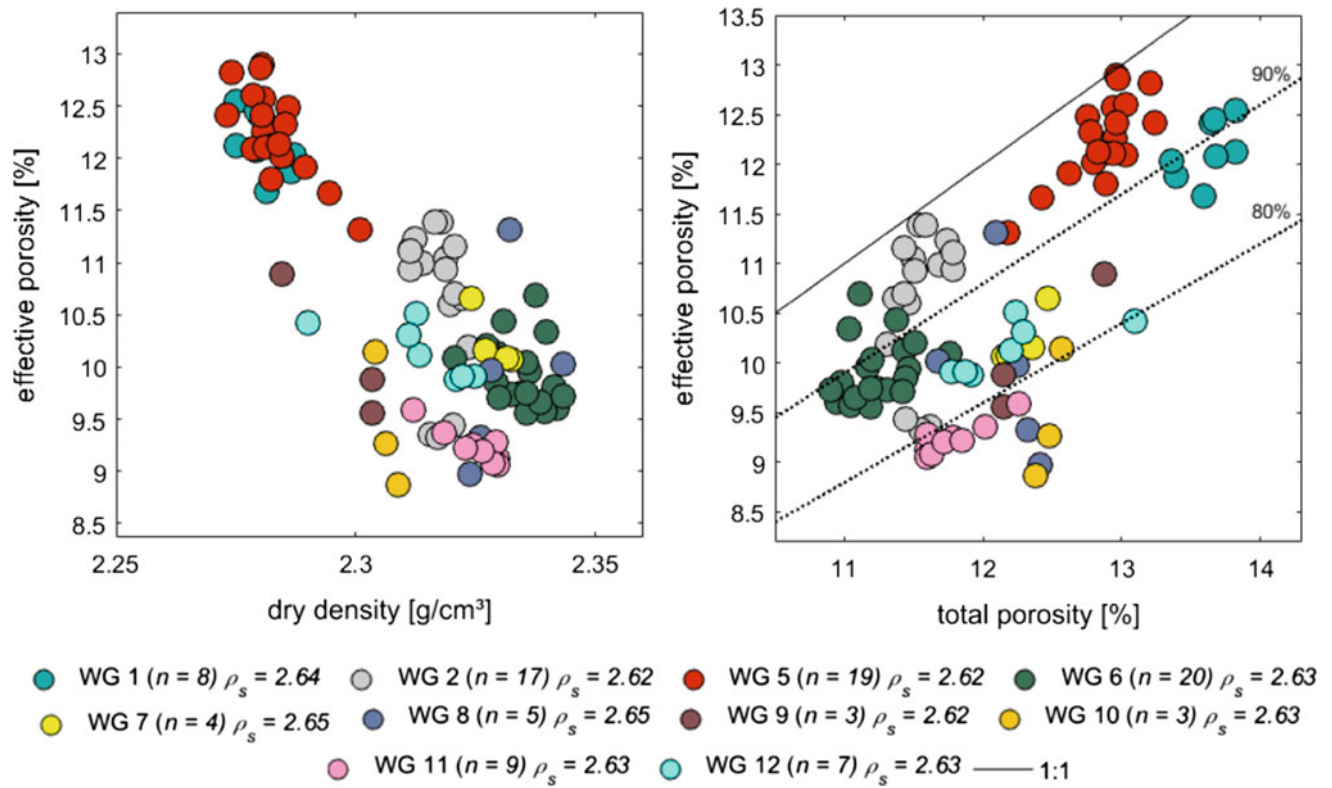
**Fig. 1** Physical properties were determined with 95 cylindrical samples (7 × 14 cm) from 10 different rock blocks of Trendelburg beds, which explains the observed scattering. However, a linear relationship between density and porosity has been observed. Total porosity was evaluated using grain density ($\rho_s$ in g/cm$^3$). The black line (on the right) shows where all pore spaces are connected
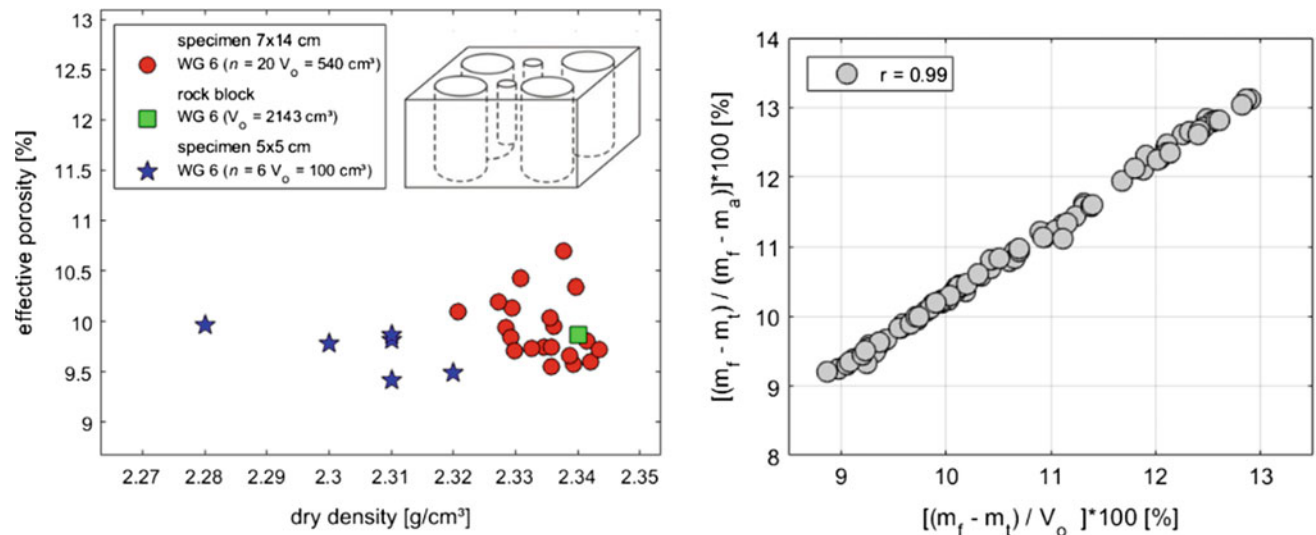




**Fig. 2** Different geomechanical experiments require different specimen shapes. Due to sandstone contrasting layers, small specimens (5 × 5 cm) may not represent physical properties of a whole rock block. On the right side, the comparison of effective porosity determined with water saturation (on the abscissa) and after buoyancy (on the ordinate). Coefficient of correlation after Pearson. $V_o$ = volume of the body, $m_a$ = mass of immersed body, $m_t$ = dry mass and $m_f$ = water saturated mass

(Fig. 5, left). The influence of a long-term scCO$_2$-treatment could be understood as an anisotropy, which therefore could be maximised when bedding is arranged parallel to $\sigma_1$.

Triaxial tests for residual strength are represented as Mohr-Coulomb failure criterion in Fig. 6. The residual compressive strength, calculated back as uniaxial strength
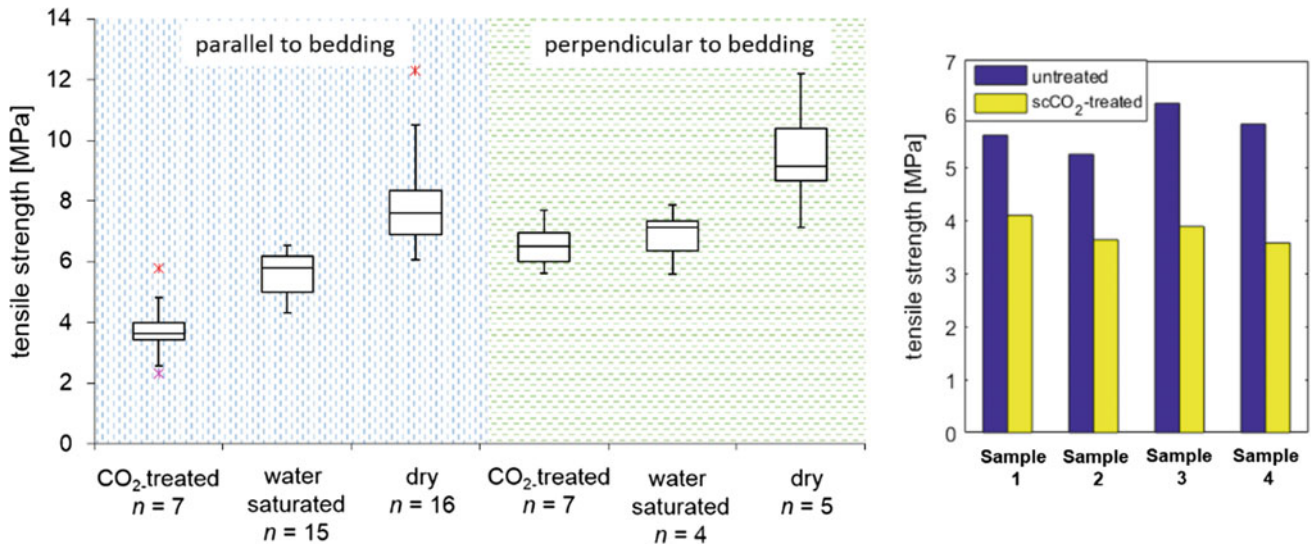
**Fig. 3** Uniaxial tensile strength was indirectly determined by the Brazilian-Test with cylindrical rock specimens. Results from block 5 are separately presented on the right side. Tensile strength is a direction-dependent property and decreases after 5 weeks scCO$_2$-treatment in the autoclave system (BoxPlot © Vertex 2017)
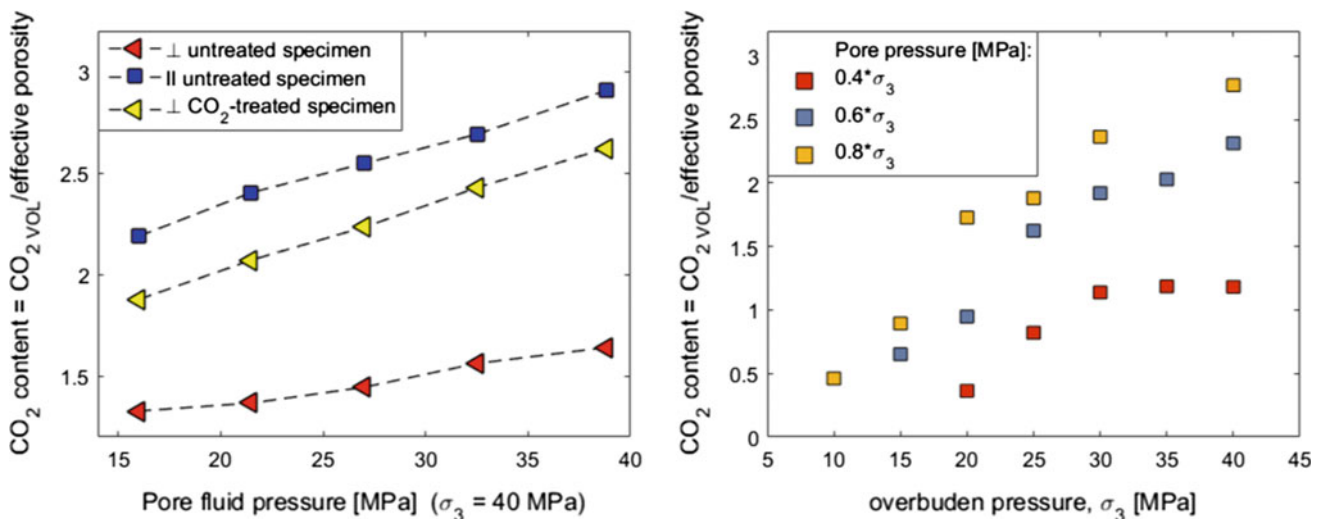


**Fig. 4** CO$_2$-content is here presented as a factor to quantify CO$_2$-volume regarding stress conditions and pore space. It depends on material properties, such as porosity, permeability and directional anisotropy, as well as on confining- and pore-pressures

($\beta_d$), had decreased after a long-term scCO$_2$-treatment in both experiments (−15 and −35%). For a better comparison of shear parameters and modulus of deformation between treated and untreated specimens, specimens were collected from the same block of rock.

Compressive strength and modulus of deformation were determined for cement specimens at reservoir stress conditions ($\sigma_3 = 40$ MPa and $pf = 16$ MPa) and presented on Fig. 7. As we can see, the uniaxial strength of cement varies from 196 (28 days) to 207 MPa (161 days), which reflects the property of cement of getting harder with time. Stress-strain curves clearly show two domains of

deformation. The first one is brittle, where stress and strain were quickly increased with a high deformability rate (represented by V$_b$).

After reaching a considerable compressive strength ($\sigma_{1max} = 140$ MPa), they underwent a plastic behaviour where the axial pressure increased at a very low rate and the deformation took place predominantly in a radial direction (V$_p$). As expected, a previously damaged specimen showed lower compressive strength compared to untested core samples (29 days, ca. −16%). The influence of scCO$_2$-treatment on cement specimens can be seen by an increased hardness ($\sigma_1 = 217$ MPa) and decreased deformability (V$_b = 21$ GPa).
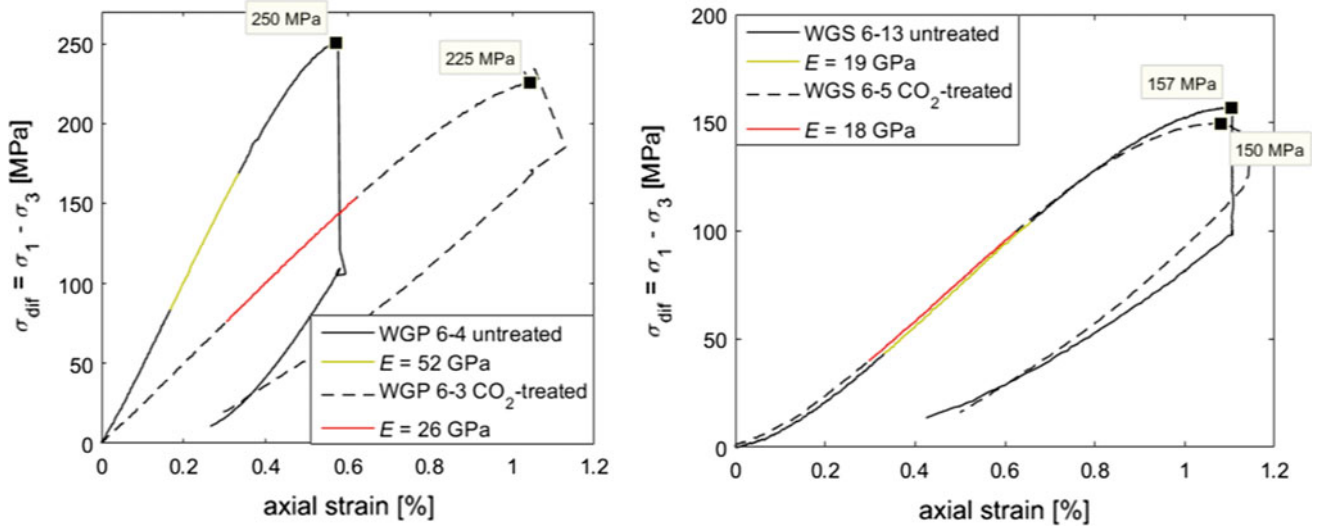
**Fig. 5** Stress-strain curves from triaxial compression tests for untreated and treated rock specimens. On the left side, mechanical load ($\sigma_1$) is applied parallel to bedding. On the right side, mechanical load is applied perpendicular to bedding, the difference on strength and deformability are minimal. At conditions of $\sigma_3 = 40$ MPa, $pf = 16$ MPa
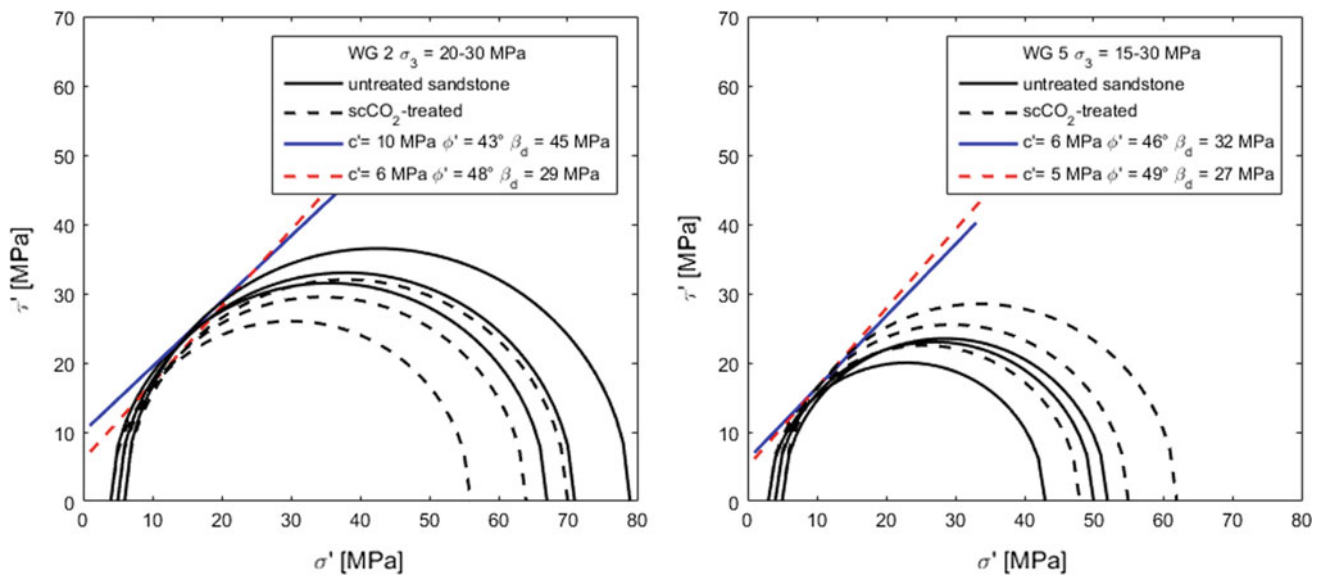


**Fig. 6** Effective residual compressive strength ($\beta d$) for treated and untreated sandstones from $\sigma_3 = 20$ to 30 MPa (left) and from $\sigma_3 = 15$ to 30 MPa (right). For both experiments at two rock blocks $\beta d$ clearly decreases after a five week $scCO_2$-treatment

On rock samples, micrographs from rock specimens were taken before and after $scCO_2$ treatment with a 3D-Digital-microscope under reflected light as an illustration of the influence of $scCO_2$. Those micrographs show how mineral phases were dissolved and therefore how pore spaces became connected (Fig. 8). Visual evaluation of effects of $scCO_2$ are described as an opening of pore spaces (1) through mineral phase dissolution (3) and rounding grain corners (2).

**Fig. 7** Stress-strain curves from triaxial compression tests for cement specimens at 40 MPa confining pressure and 16 MPa pore pressure (using water as pore pressure medium). The hardening process time is significant to develop a pronounced brittle or ductile behavior, as we can see by comparison of the moduli of deformation ($V_b$ = brittle, $V_p$ = ductile)
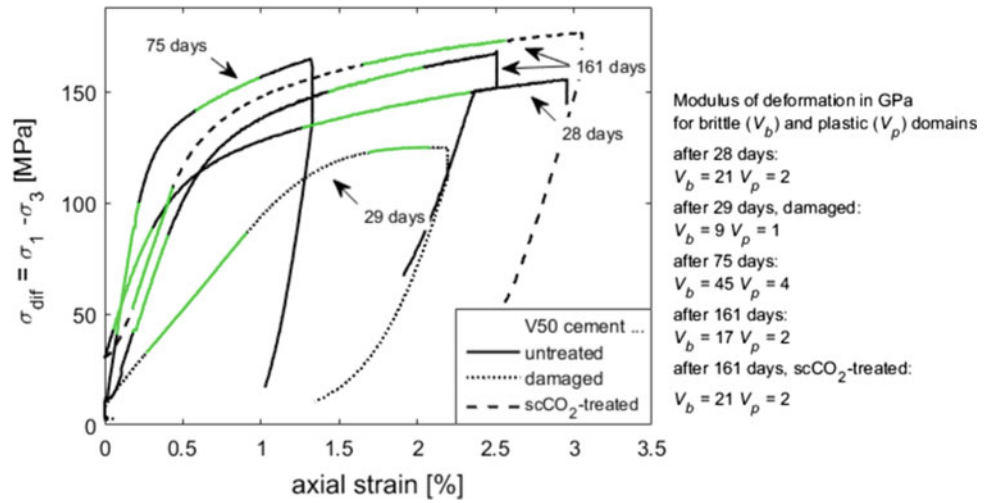


**Fig. 8** Visual evaluation of effects of scCO$_2$ are described as an opening of pore spaces (1) through mineral phase dissolution (3) and rounding grain corners (2)
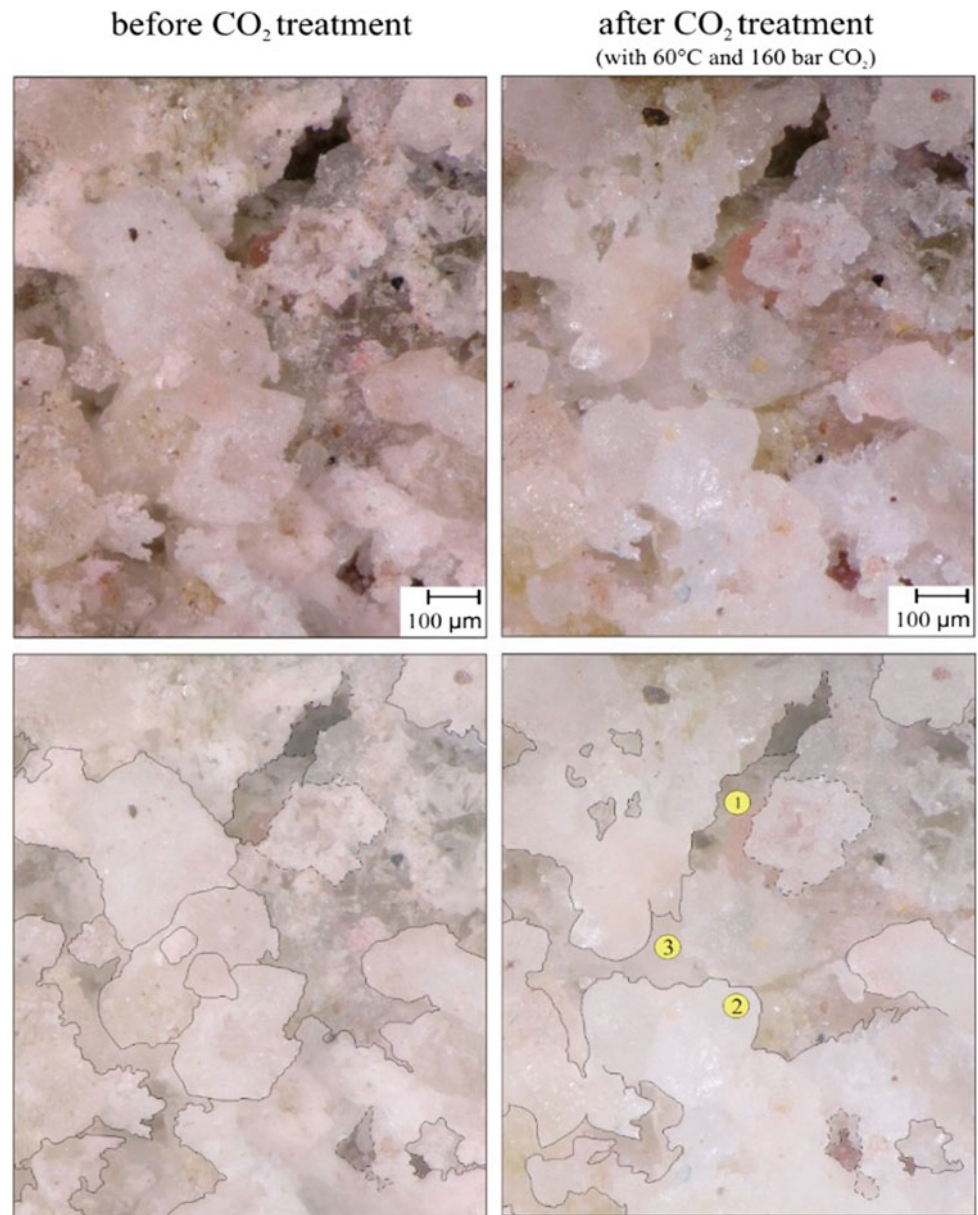
## 4 Conclusion

Considering a reservoir under an isotropic stress field, where vertical stress is slightly above horizontal stress, the adsorption of $scCO_2$ by the host rock will depend on its porosity, permeability (as flow direction), as well as on the relationship between pore- and confining pressures, as illustrated in Fig. 4. The influence of a long-term $scCO_2$ treatment observed in rock specimens could be downgraded from neutral to negative: experiments done at high pressures ($\sigma_3 = 40$ MPa) with transverse specimens, found there was a slight decrease in strength and an increase in deformability observed, as shown in Fig. 5. The negative effect of $scCO_2$ on the deformability of the Trendelburger bed is reflected by a decrease in compressive, tensile and residual strength (10, 30 and 15% respectively), an increase in deformability and in permeability due to an increase in the $scCO_2$-volume consumed during triaxial tests. Moreover, dissolution effects and pore structure changes could be detected through before-and-after micrographs. The long-term influence of $scCO_2$ enhances mechanical and chemical alterations in the sandstone, which could be recognized as a new induced anisotropy. These influences were better identified by the samples where the load was applied parallel to its bedding. The scattering of results may also reproduce the variability in mineralogical and physical properties of the Trendelburger beds, particularly for the rock blocks in which effective and total porosity mismatches were more than 20%. Further investigations in the mineralogical variety of the Trendelburger beds, on the structural anisotropy and on the mechanics of long-term chemical treated specimens are currently being carried out to provide more reliable information about mechanical changes due to $scCO_2$ injection in sandstone reservoirs.

## References

Deutsche Gesellschaft für Erd- und Grundbau e.V.:Mehrstufentechnik bei dreiaxialen Druckversuchen und direkten Scherversuchen, Empfehlung Nr. 12 des Arbeitskreises 19 – Versuchstechnik Fels. In: Technische Prüfvorschriften für Boden und Fels im Straßenbau (TP BF-StB) (1987)

DIN 22024:1958-10, Investigations of the raw material in hard-coal-mining; indirect tensile strength determination on solid rocks

DIN EN 1936:2007-02, Natural stone test method - Determination of real density and apparent density, and of total and open porosity; German version EN 1936:2006

DIN EN 196-1:2005-05, Methods of testing cement – Part 1: Determination of strength; German version EN 196-1:2005

Erikson, K., Lempp, C., Pöllmann, H.: Geochemical and geomechanical effects of $scCO_2$ and associated impurities on physical and petrophysical properties of Permotriassiac Sandstones (Germany): an experimental approach. Environ. Earth Sci. (2015)

IPCC: IPCC Special Report on Carbon Dioxide Capture and Storage. Prepared by Working Group III of the Intergovernmental Panel on climate change [Metz, B. O. Davidson, H. C. de Coninck, M. Loos, and L. A. Meyer (eds.)]. Cambridge University Press, Cambridge, UK and New York, NY, USA, 442 pps (2005)

Tavallali, A., Vervoort, A.: Effect of layer orientation on the failure of layered sandstone under Brazilian test conditions. Int. J. Rock Mech. Min. Sci. **47**(2), 313–322 (2010)

Weber, J., Ricken, W.: Quartz cementation and related sedimentary architecture of the Triassic Solling Formation, Reinhardswald Basin, Germany. Sed. Geol. **175**(1–4), 459–477 (2005)

# The Behavior of the Highly Weathered and Partially Decomposed Flysch in the Reactivation of Landslide Phenomena in Greece

S. Anagnostopoulou, V. Boumpoulis, P. Lampropoulou, A. Servou, N. Depountis, and N. Sabatakakis

## Abstract

Some of the most serious landslide movements in Greece are often observed in the upper zone of weathered flysch and can be classified as composite landslides. This paper describes the landsliding behavior of highly weathered and tectonically decomposed flysch in a characteristic landslide in Western Greece, focusing on its physical and mechanical parameters, such as moisture content, clay percentage and shear strength. Back analysis was carried out in order to estimate the cohesion and angle of friction at the time of failure. The behavior of the flysch formation was also examined with the use of shear-related tests. All results were cross-examined, and it was concluded that weathered flysch in Western Greece is a landslide-prone material with small amounts of clay minerals, and its sliding behavior is mainly controlled by the rising of the water table and the tectonic activity.

## 1 Introduction

Many landslides occurring in Greece are observed in the weathered and decomposed flysch. During the last decade, for example, an increase of 25% of landslide phenomena has been recorded in the country, as a result of human activities, increasing urbanization and uncontrolled use of land areas that are vulnerable to landslides (Sabatakakis et al. 2012). Many of these landslides involving weathered flysch, a critical landslide-prone geological formation, have been reactivated in recent decades due to intense and prolonged rainfall. In this study, a representative landslide, i.e., the Panagopoula landslide, is examined, focusing on the behavior of the weathered flysch on its reactivation.

The research area comprises an extensive instability zone located in the Gulf of Corinth, where periodically induced landslide events have been interspersed with creep activity (Koukis et al. 2009; Kavoura et al. 2016). In 1971 and 1972, translational and rotational slides occurred, affecting the transportation lines over about 250 m. The slides took place on structurally sheared and weathered flysch sediments and are still active in smaller areas (Sabatakakis et al. 2015). The examined landslide is a representative composite fault-related slide, and its plan along with the surrounding geology is illustrated in Fig. 1.

The flysch sediments include different lithological units, such as sandstones, clays, conglomerates and siltstones, and they are closely related to the Alpine orogenesis. Due to the high percentage of coarse grained material, testing of representative specimens of the flysch's weathered zone using conventional laboratory apparatuses, without any knowledge of the shear failure parameters, is quite difficult. For this purpose, an initial back analysis was carried out on the assumed failure surface in order to estimate the flysch's shear strength parameters at the time of failure.

Borehole samples that were collected in the field were later used for laboratory testing. The laboratory tests were conducted to determine moisture content, grain size distribution, Atterberg limits, shear strength parameters and the quality/quantity of clay minerals in the shear zone. A ring shear test was conducted to determine the residual angle of friction in the finer material of the flysch's weathered zone (<0.075 mm). Large shear tests were also conducted to determine the apparent shear strength parameters of the flysch's weathered zone, as it is more convenient to extrapolate the in-situ state and model its behavior with the use of a large shear box apparatus (Christoulas et al. 1988).

S. Anagnostopoulou (✉) · V. Boumpoulis · P. Lampropoulou
A. Servou · N. Depountis · N. Sabatakakis
Department of Geology, Patras University, 26504 Patras, Greece
e-mail: geo09008@upnet.gr
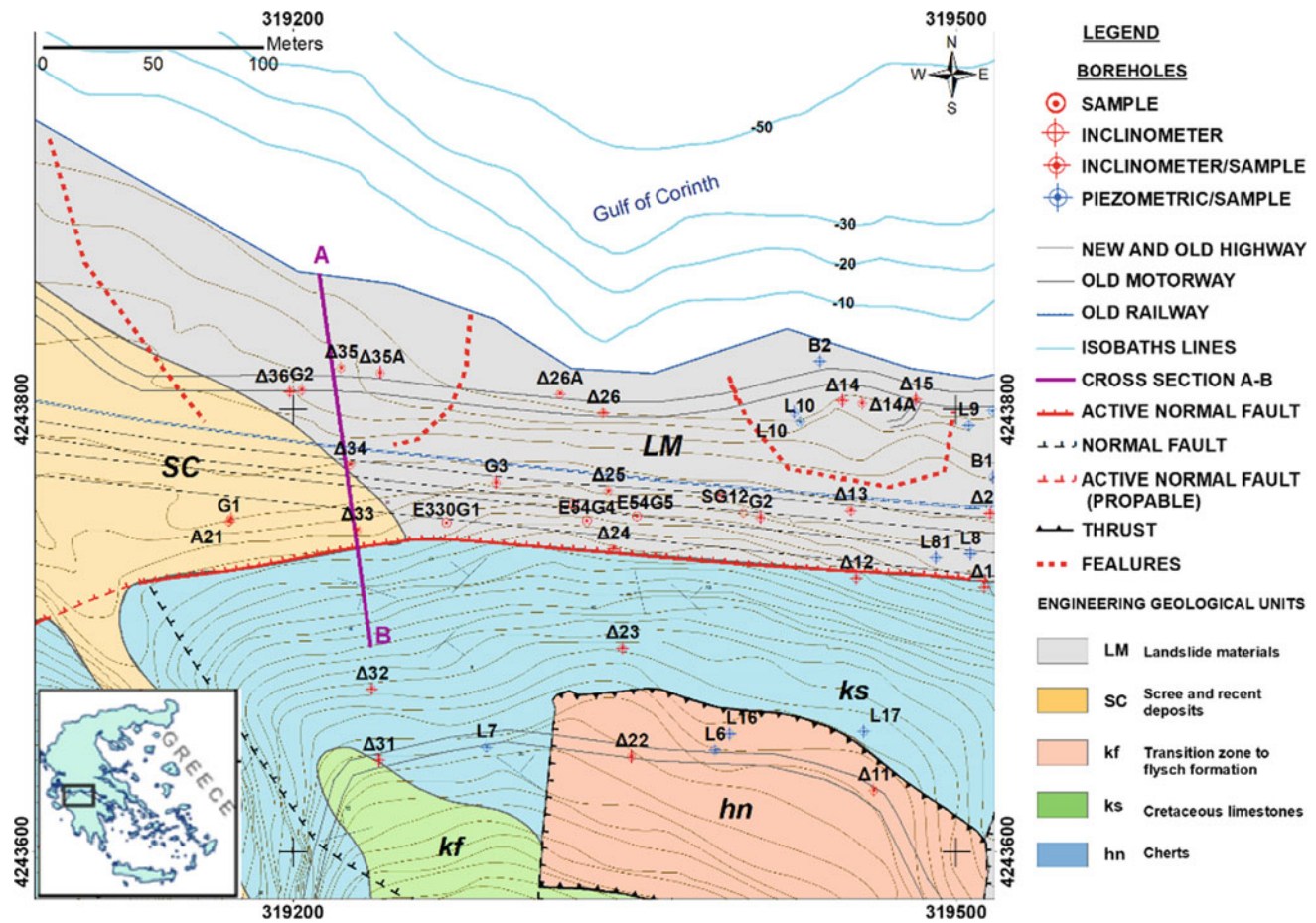
**Fig. 1** Simplified engineering geological map of Panagopoula, Greece

## 2 Slope Stability Back Analysis

Various parameters contribute to the reactivation of landslides. High moisture content is one of the most critical parameters, especially when a weathered and partially decomposed formation exists (Koukis et al. 2009; Tsiambaos et al. 2015).

For the purposes of this study, a long-term survey was carried out in the Panagopoula area. Horizontal displacements as well as water table measurements were derived from several monitoring boreholes in order to correlate the water level change with landslide movements. The interaction of the water table's variation to the horizontal displacement variations recorded at a depth of 21.5 m, where the assumed failure surface of the weathered flysch exists, is shown in Fig. 2. Moreover, from these measurements that were derived from a monitoring borehole (BH_2), it can be seen, that the critical water table level that triggered the reactivation of landslide along the failure surface was found to be at 1.3 m AOD (above ordnance datum).

From the evaluation of all geological information that was derived from a long-term survey in the surrounding area, a geotechnical model was designed in order to estimate the shear strength parameters of flysch at the time of failure, by performing back analysis (Fig. 3). The model contains a weak weathered zone (WZ) representing the partially decomposed and weathered flysch, a water table at 1.3 m AOD and a non-circular failure surface with an inclination of 27°. The SLIDE 6.0 software program was used to perform back analysis on the geotechnical model by considering a non-circular failure surface along the soil-bedrock contact. By performing this analysis in the suggested model, the estimated shear strength parameters for the weak zone of flysch were found to be $c' = 0$ kPa and $\varphi' = 15°$.

All parameters used in the model, except the parameters of the weak zone that were calculated from back analysis, were derived from the mean values of laboratory tests of a geotechnical investigation that took place for the construction of the new national road from Patras to Athens (Table 1).

**Fig. 2** Correlation of the water table's variation with horizontal displacements as recorded in the Panagopoula landslide
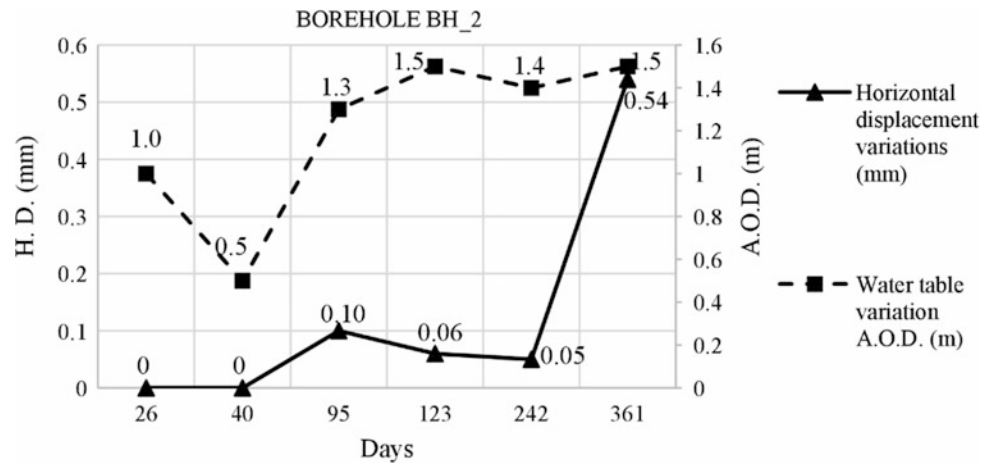


**Fig. 3** Geotechnical model for slope stability analysis in the Panagopoula landslide (cross section AB from Fig. 1)
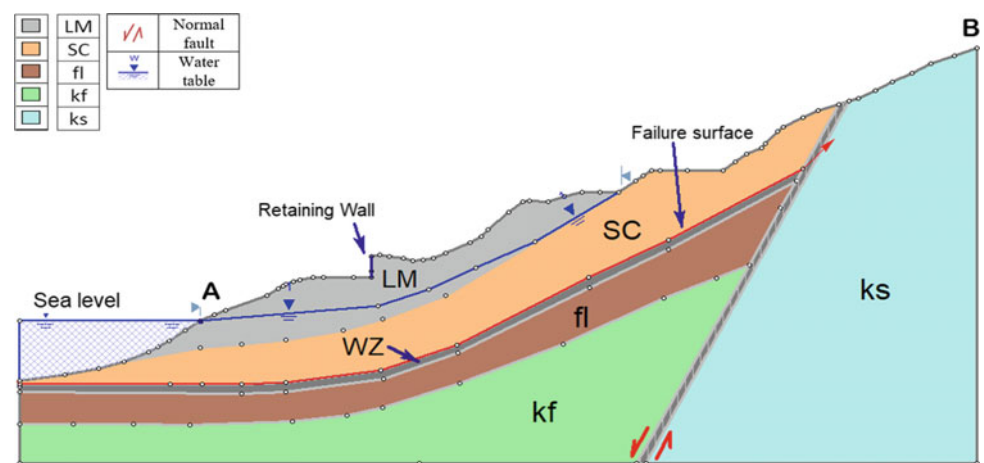


**Table 1** Parameters used for stability analysis scenarios

| Geological formations | Cohesion (c′, kPa) | Angle of internal friction ($\varphi'$, °) |
|---|---|---|
| LM (landslide materials) | 10 | 20 |
| SC (scree and recent deposits) | 10 | 25 |
| WZ (weak zone of flysch) | 0 | 15 |
| fl (flysch formation, mainly siltstones) | 80 | 30 |
| Kf (transition zone to flysch) | 150 | 35 |
| Ks (cretaceous limestone) | 250 | 35 |

## 3 Laboratory Tests on Weathered Flysch Samples

An extensive approach to laboratory tests on flysch samples (ring and large shear tests) was followed the slope stability back analysis, emphasizing on flysch's residual strength parameters. The moisture content varied throughout the tests in order to observe the behavior of the weathered flysch with different moisture contents. Additionally, X-ray diffraction analysis was performed in order to determine the quantity and quality of clay minerals in the shear zone.

### 3.1 Physical Properties of the Weathered Flysch

The weathered flysch samples collected from the failure zone (weak zone) were classified according to USCS as

**Table 2** Physical properties of the weathered flysch

| Depth (m) | Grain size analysis (Passing %) | | | | Atterberg limits | | | USCS classification | Moisture content(%) |
|---|---|---|---|---|---|---|---|---|---|
| | No. 4 | No. 10 | No. 40 | No. 200 | LL | PL | PI | | |
| 21.5–22.6 | 94 | 90 | 87 | 41 | 21 | 12 | 9 | SC | 16 |
| 22.9–23.8 | 86 | 61 | 48 | 21 | 26 | 11 | 15 | SC | |
| 25.2–26.2 | 37 | 20 | 12 | 5 | – | – | – | GW-GC | |

clayey sands (SC) of medium plasticity with a strong presence of well-graded gravels and a moisture content of 16%. All physical properties of the weathered flysch are shown in Table 2.

### 3.2  Ring Shear Tests on the Weathered Flysch

A laboratory test was also carried out by using the ring shear apparatus developed by Bromhead (1979, 1986) under four different normal stresses σ′ (50, 100, 300 and 400 kPa). For the test, it was used the fine-grained portion of flysch that passed through ASTM sieve No. 200 (<0.075 mm) with a moisture content of 16%. The consolidation stage was preceded by shearing for 100 min, due to the small drainage path of the specimen, as it has been suggested by Bromhead (1979). The results of the test are shown in Fig. 4 and indicate that the residual angle of friction of the weathered flysch along the failure surface varies from 19.5° to 21.5° (a mean value of around 20°), which is higher compared the angle of 15° that was derived from the back analysis scenario, because of the increased wall friction that develops along the inner and outer circumferences of the specimen when using the ring shear apparatus.

Furthermore, the tested flysch specimen was compared with other types of weathered flysch that exist in Greece as they were derived by Christoulas et al. (1988) (Fig. 5). It is clear that the values of the brown flysch from the village of



**Fig. 5** Variation of residual effective angle of friction as a function of normal load in weathered flysch in Greece

Elati are almost the same with the tested flysch specimen of the current research.

### 3.3  Large Shear Test
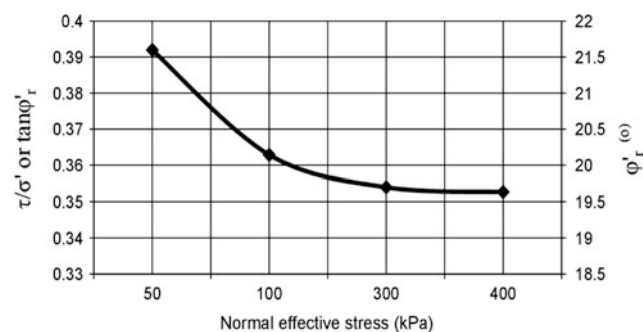
The Large Shear Box 300 (VJT2780A) apparatus is used to calculate apparent shear strength parameters in soil samples. Direct tests were performed with this apparatus on flysch samples in accordance with ASTM standards (2004). Two different samples were tested with different moisture contents (8 and 10%, respectively), passing through the sieve No. 4 (<4.75 mm). For each of the samples, three varying normal stresses were applied in order to determine the effects upon shear resistance and displacement.

The different consolidation loads were left for one day, and the shearing rate of the samples was very low (1 mm/min) in order to assure that no significant amount of pore water pressure would be developed at any stage of the test. Both tests were regulated with the criteria to stop when the accumulated shear strain (γ) reached 10%. The results showed that while increasing the percentage of moisture by 20%, the apparent shear strength parameters of flysch were also reduced by an equal percentage (Table 3). The moisture content of 16% of the in-situ weathered flysch could not be achieved due to the plastic behavior of flysch at this amount of moisture.



**Fig. 4** Variation of residual angle of friction of the weathered flysch as a function of normal effective stress

**Table 3** Apparent shear strength parameters of flysch correlated to different moisture contents in a large shear box

| Test No. | Moisture content (%) | Normal stress_1 | Normal stress_2 | Normal stress_3 | Apparent cohesion = c' (kPa) | Angle of Shearing Resistance = $\varphi'$ (°) |
|---|---|---|---|---|---|---|
| 1 | 8 | 100 | 200 | 300 | 199.5 | 47 |
| 2 | 10 | 100 | 200 | 400 | 157.3 | 37 |

**Table 4** Semi-quantitative mineralogical analyses of sheared flysch in Greece

| Type of flysch | Minerals (%) | | | | |
|---|---|---|---|---|---|
| | Quartz | Calcite | Plagioclaste | Smectite and chlorite | Illite and/or muscovite |
| Brown flysch from the Livadia-Delphi road | 20 | 7 | 20 | 5 | 8 |
| Grey flysch from the Livadia-Delphi road | 34 | – | 24 | 20 | 22 |
| Brown flysch from the village of Elati | 40 | – | 25 | 10 | 10 |
| Grey flysch from Panagopoula | 35 | 39 | 10 | 8 | 6 |

## 3.4 X-Ray Diffraction Analysis on the Weathered Flysch

Several soil samples taken from the weathered zone of flysch were used for an X-ray diffraction analysis. The results showed a dominant presence of quartz and calcite and small amounts of smectite, chlorite and mica, while lower amounts of feldspars were also present in most of the samples (Table 4).

Smectite can expand significantly under high moisture content and is a potential triggering factor in combination with others for landslide events (Duzgoren-Aydin et al. 2002; Regmi et al. 2014). Due to its minor presence and the great thickness of overburden above the failure zone (20 m), it is obvious that smectite did not contribute to the landslide event in the Panagopoula area. Table 4 shows the results of X-ray analyses by comparing the grey flysch of Panagopoula with other flysch landslide areas in Greece, as they were derived by Christoulas et al. (1988). It is clearly noticeable that the brown flysch from the village of Elati is closer to the results of the Panagopoula site.

## 4 Conclusions

Instability phenomena are very common in the weathered and tectonically highly sheared flysch and cause serious problems in many places in western Greece. Back analysis and laboratory tests in the weathered zone of flysch of a representative flysch-prone landslide, e.g., the Panagopoula landslide, resulted in the following conclusions:

1. The sudden rising of the water table above the weathered flysch zone triggered the reactivation of the landslide, due to its tendency to slide along a pre-existed failure surface, when overcoming its equilibrium state.

2. Slope stability back analysis along the failure surface estimated that the shear strength parameters of the weathered flysch at the time of failure, had a cohesion c' = 0 and an angle of friction $\varphi'$ = 15°.

3. The residual angle of friction along the failure surface for the finer material, with the use of a ring shear apparatus, calculated to be $\varphi'$ = 20°, higher than the overall angle of friction ($\varphi'$ = 15°), because of the increased wall friction that develops along the inner and outer circumferences of the specimen when using the ring shear apparatus.

4. Large shear box tests performed under a variety of different moisture contents showed that the apparent shear strength parameters of the weathered flysch were reduced by about 20% under an increase of an equal percentage in moisture content. This result needs further investigation with different moisture contents before drawing conclusions about the importance of the increased moisture in the shear strength parameter decrease.

5. The minor presence of clay minerals, as estimated by X-ray analyses, proved that clay minerals did not contribute to the reactivation of this landslide. On the contrary it was proved that the weathered flysch behaves mostly as a frictional material controlled by the slope inclination and water level changes.

## References

ASTM: Standard Test Method for Direct Shear Test of soils Under Consolidated Drained Conditions D3080-04 (2004)

Bromhead, E.N.: A simple ring shear apparatus. Ground Eng. **12**(5), 40–44 (1979)

Bromhead, E.N.: The Stability of Slopes, p. 373. Surrey University Press, London (1986)

Christoulas, S., Kalteziotis, N., Gassios, E., Sabatakakis, N., Tsiambaos, G.: Instability phenomena in weathered flysch in Greece. In: Proceedings of the 5th International Symposium on Landslides, pp 103–108. A A Balkema, Publication Rotterdam, Lausanne (1988). https://doi.org/10.1016/0148-9062(89)90314-8

Duzgoren-Aydin, N.S., Aydin, A., Malpas, J.: Distribution of clay minerals along a weathered pyroclastic profile, Hong Kong. CATENA **50**(1), 17–41 (2002). https://doi.org/10.1016/s0341-8162(02)00066-8

Kavoura, K., Sabatakakis, N., Tsiambaos, G.: Long term ground displacements due to a large landslide in western Greece. In: Aversa et al. (eds.) Landslides and Engineered Slopes. Experience, Theory and Practice, pp. 1177–1181. CRC Press (2016) https://doi.org/10.1201/b21520-142

Koukis, G., Sabatakakis, N., Ferentinou, M., Lainas, S., Alexiadou, X., Panagopoulos, A.: Landslide phenomena related to major fault tectonics: rift zone of Corinth Gulf, Greece. Bull. Eng. Geol. Environ. **68**(2), 215–229 (2009). https://doi.org/10.1007/s10064-008-0184-8

Regmi, A.D., Yoshida, K., Dhital, M.R., Pradhan, B.: Weathering and mineralogical variation in gneissic rocks and their effect in Sangrumba Landslide, East Nepal. Environ. Earth Sci. **71**(6), 2711–2727 (2014). https://doi.org/10.1007/s12665-013-2649-8

Sabatakakis, N., Koukis, G., Vassiliades, E., Lainas, S.: Landslide susceptibility zonation in Greece. Nat. Hazards **65**(1), 523–543 (2012). https://doi.org/10.1007/s11069-012-0381-4

Sabatakakis, N., Tsiambaos, G., Rondoyianni, R., Papanakli, St., Kavoura, K.: Deep-seated structurally controlled landslides of Corinth Gulf rift zone, Greece: the case of Panagopoula landslide. In: Proceedings of 13th ISRM Congress Innovations of Applied and Theoretical Rock Mechanics. ISBN: 978-1-926872-25-4, paper 651 (2015)

Tsiambaos, G., Sabatakakis, N., Rondoyanni, T., Depountis, N., Kavoura, K.: Composite landslides affecting flysch and neogene weak rock formations induced by heavy rainfalls. In: 13th ISRM International Congress of Rock Mechanics. International Society for Rock Mechanics. ISBN: 978-1-926872-25-4 (2015)

# Integration Between Physiographic Compartmentation and Geomechanical Characterization of Rock Masses Applied to Landslide Susceptibility at the Rio-Santos Highway (BR-101) in São Sebastião (SP)—Brazil

Debora Andrade Targa and Fabio Augusto Gomes Vieira Reis

## Abstract

The purpose of this paper is to assess the areas that are most susceptible to landslide occurrence along the Rio-Santos Highway in São Sebastião—SP (Brazil) based on the integration of the physiographic compartmentation and the geomechanical characterization of the study area. To produce physiographic compartmentation, the study area was subjected to photointerpretation to identify areas with homogenous textures and similar geomorphologic features. Moreover, DEM, slope maps and landslide scar mapping were used to complement the geomorphologic characterization of the region. A geological and geotechnical survey was used to obtain the parameters to classify rock masses according to the RMR classification and Q-System. Four units were delineated and described based on their geological, geotechnical and geomorphologic aspects. The units considered to be the most susceptible to the occurrence of shallow landslides are III and IV.

## Keywords

Susceptibility • Highway • Landslides • Geomechanical classification

## 1 Introduction

### 1.1 Introduction to the Subject

The Rio-Santos Highway (BR-101) is a heavy traffic corridor and is thus one of the most important roads in Brazil. It is located in the geomorphologic context of the Serra do Mar, a region known by its mountainous terrane and escarpments along the road. Due to the peculiar geomorphologic features of the area and the tropical weather that is prevalent in Brazil, shallow landslides are very frequent and cause a great number of road accidents every year. Thus, to guarantee the safety of those who travel on the highway, a geomorphologic and geomechanical study of the rock slopes was developed in an attempt to understand and quantify geotechnical problems. A geotechnical investigation consists of the quantification of the rock mass quality to predict its behavior in an engineering design, provide guidelines for an engineering design and reduce infrastructure failure (Bieniawski 1989).

The definition of a landslide is described as the fast movement of soil and/or rock towards the base of a slope, which has a defined geometry and rupture surface (Guidicini and Nieble 1984). These phenomena are classified based on their rupture surfaces and include shallow landslides, which are the focus of this paper. The movement is deflagrated when shear stresses overcome the mechanical resistance of the rock mass and friction is not capable of holding the geological material in place (Gerscovich 2013). Weathering, anthropic interference and the geomorphologic setting can destabilize the slope and trigger shallow landslides. Thus, in order to promote the safety of the population and highway infrastructure, this paper combines geomechanical and geomorphologic characterization in order to study the susceptibility of landslide occurrence along the Rio-Santos Highway (BR-101) in São Sebastião—SP (Brazil).

### 1.2 Study Area Characterization

The study area is a 40-km track of the Rio-Santos Highway between Maresias Beach (km 155) and Enseada Beach (km 115) in São Sebastião city, which is located on the northern coast of the State of São Paulo—Brazil (Fig. 1).

The geologic and geomorphologic context corresponds to the Serra do Mar complex, an orogenic lineament trending NE–SW which formed during the Neoproterozoic Era (Janasi et al. 2003). The main lithologies are gneiss complexes, granites, micaceous schists and quartzites, which

D. A. Targa (✉) · F. A. G. V. Reis
São Paulo State University, Rio Claro, Brazil
e-mail: debora.targa@gmail.com

**Fig. 1** The location of São
Sebastião city and the study area
contour
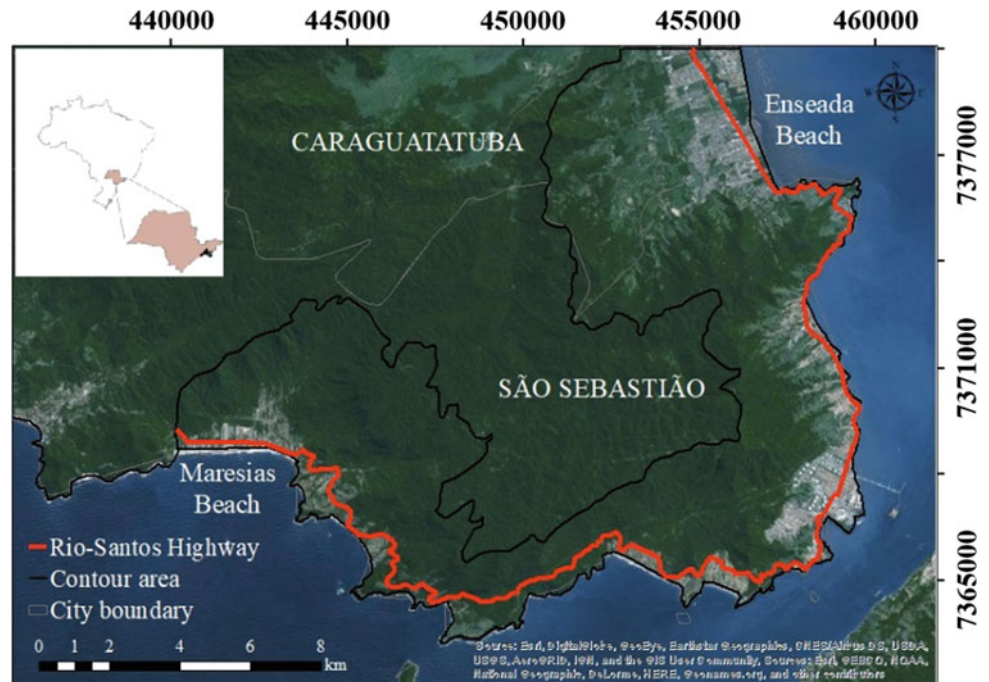


range from medium to high metamorphic grade, and Quaternary sedimentary deposits associated with coastal dynamics. The study area is delimited by the Cubatão, Taxaquara and Camburu Faults, which are NE–SW-trending and are associated with the Transcurrent Zone of São Paulo (Campanha et al. 1994; Hasui 2010). There are two main geomorphologic units: The Juqueriquere Hill and the coastal plains, which form a steep escarpment between them.

## 2 Materials and Methods

### 2.1 Geoprocessing Data

The Digital Elevation Model (DEM) was produced from the 1:50.000 topographic maps of Caraguatatuba (SF-23-Y-D-VI-1), Maresias (SF-23-Y-D-V-4), Pico do Papagaio (SF-23-Y-D-V-2) and São Sebastião (SF-23-Y-D-VI-3) obtained from the IBGE (Brazilian Institute of Geography and Statistics) 1974 database. The DEM provided a basic map and spatial database to produce a slope map at a scale of 1:50.000, which was organized into 5 classes. The landslide scars were identified based on the visual analysis of orthophotos of São Sebastião City from 2012 provided by EMPLASA (Empresa Paulista de Planejamento Metropolitano SA) at a scale of 1:20.000 with a spatial resolution of GSD (Ground Sample Distance). All these procedures were performed using the ArcGis 10.3 Software using the SIRGAS 2000 Zone 23S datum.

### 2.2 Geological and Geotechnical Survey

To obtain the geological and geotechnical parameters required by Bieniawski (1989) and Barton et al. (1974) for classifying rock mass quality, fieldwork was necessary to describe the geological context, structural aspects and dynamic slope processes. To test the uniaxial compressive strength of the rock masses, the Schmidt Hammer provided measures of hardness that were converted to resistance using an abacus (Deere and Miller 1966). To validate this method, it was necessary to obtain 20 values of resistance, specifying each kind of material tested, according to ISRM (1981). In addition to the rock masses, the profile soils were also included in the analysis.

### 2.3 Physiographic Compartmentation

The study area was divided into homologous zones, which are areas that possess similar landscape features and geological contexts. They were discerned by textural analysis, the density of geomorphologic elements and drainage network patterns according to the method proposed by Zaine (2011). Each delimited unit had its own characterization based on the declivity, amplitude, and geometry of its slope and drainage channel, as well as its number of landslide scars, geology and type of relief. The physiographic compartmentation consisted of compiled data acquired from the maps, fieldwork observations and aerial images obtained from EMPLASA at a scale of 1:20.000.

## 2.4 Geomechanical Classification

The Rock Mass Rating (RMR) (Bieniawski 1989) and the Q-System (Barton et al. 1974) were used to obtain the geomechanical classification of the study area. The RMR classification was proposed by Bieniawski (1989), who considered six parameters to predict the behavior of rock masses, attributing weights to each one and a sum of all the values to define the quality class, ranging from 0 to 100. These six parameters consist of uniaxial compressive strength, Rock Quality Designation (RQD), discontinuity conditions, water influence and discontinuity orientations, which are applied to homogenous parts of each rock mass where the spacing between discontinuities is equally distributed.

Like the RMR, the Q-System is composed of six parameters: the RQD, the joint set number ($J_n$), the joint roughness number ($J_r$), the joint alteration number ($J_a$), the joint water reduction factor ($J_w$) and the SRF (stress reduction factor). Each parameter receives a weight according to its importance, and the result obtained by Eq. 3 corresponds to the rock mass quality. The Q-System value varies from 0.001 to 1000.

$$Q = \frac{RQD}{Jn} \times \frac{Jr}{Ja} \times \frac{Jw}{SRF} \tag{1}$$

To calculate the RQD index, the fractures were analyzed in situ rock masses instead of drill cores. When a drill core is unavailable, the RQD may be estimated from the number of joints per volume of the rock mass (Palmstrom 1982). It was necessary to calculate the volumetric joint index ($J_v$) from the number of families of discontinuities (S) using the following equation:

$$Jv = \sum_{i=1}^{n} \frac{1}{Si} \tag{2}$$

Then, the $J_v$ index is used to obtain the RQD using Eq. 2:

$$RQD = 115 - 3.3 \times Jv \tag{3}$$

## 3 Results

## 3.1 Landslide Scars and Auxiliary Maps

A total of 80 shallow landslides were delimited, which were concentrated in the southwestern and southern regions of the study area near the steepest rock slopes. The landslides were found at concave and rectilinear profile slopes with medium declivity (15°–30°). Their geologic context includes biotite-gneisses, migmatites and leucogranites. Overlying the landslide scars and the DEM (Fig. 2), the scars are more frequent in the 10–90 m range of altitude.

The slope map was organized into five classes of declivity, varying from very low (0°–5°) to very high (45°<) (Fig. 3). The dark green color corresponds to flat surfaces near the coastline. The majority of the study area is yellow, which represents an intermediary range of slope angles (15°–30°) where most of the landslides scars were found. The orange color represents the escarpment regions of Juqueriquere Hill, where the steepest slopes (with angles over 45°) are found, but no scars were identified.

## 3.2 Physiographic Compartmentation

The physiographic compartmentation divided the study area into four units (Fig. 4).

Unit I represents coastal plains near the road where no shallow landslides were observed. The geologic context corresponds to sandy deposits and fluvial sediments where large drainage channels are located at a low declivity and low local amplitude terrain. Because it is near the beach, this area is overly populated, which causes problems such as the improper disposal of garbage, deforestation on the slopes and inappropriate slope profiling when building houses, which has increased the rate of erosion on the slopes.

Unit II consists of escarpments that sustain Juqueriquere Hill with a rectilinear slope profile and the highest slope angles. The escarpment rock consists of leucogranites and gneisses. Due to the slope geometry, soil profiles are almost nonexistent, and only thin layers of sandy soils have formed due to gneissic weathering. Furthermore, no shallow landslides were identified at this location.

Unit III consists of hills that are characterized by a high declivity of over 45° and medium amplitude. The slope profile is rectilinear and drainage channels are narrow and oriented, providing conditions for intense water percolation and rock mass degradation. The geological context is leucogranites and micaceous gneisses that are mostly fractured and show an advanced alteration stage. The sandy soils are well developed, extending to 2 m of thickness, and offer a substrate for vegetation which promotes weathering and intensifies water flow accumulation. Along the road, some rock falls, topples and landslide processes were recorded. There are 29 landslide scars (32%) identified in unit III.

Unit IV is characterized by relief with a low to medium slope angle and medium amplitude. The slope geometry is concave, which allows drainage convergence and the mobilization of geological material downwards to this region. The lithology in unit IV consists of granites,

**Fig. 2** DEM and the spatial distribution of landslides along the altitude classes
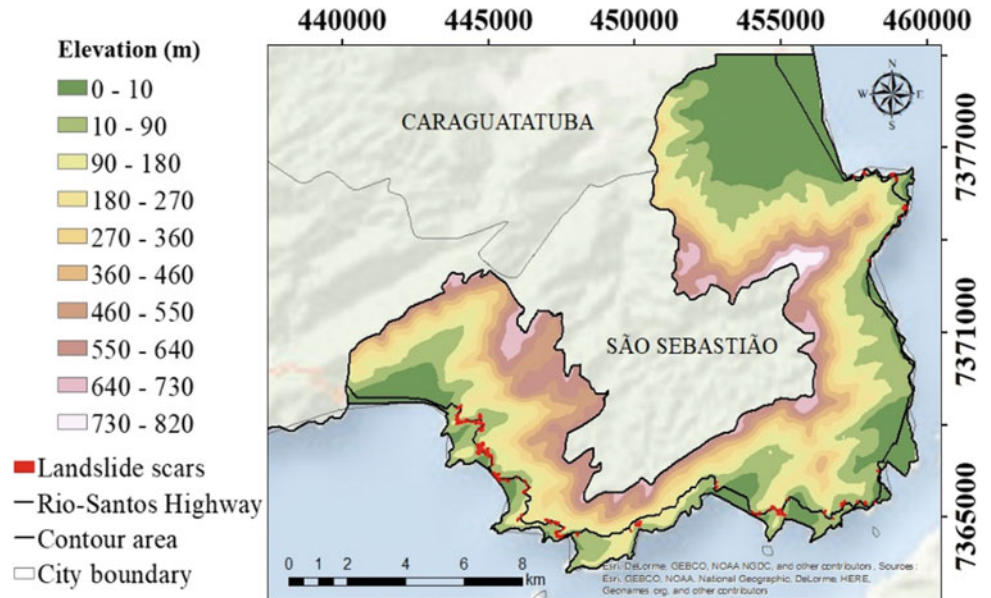


**Fig. 3** Slope map of study area organized into 5 classes of declivity
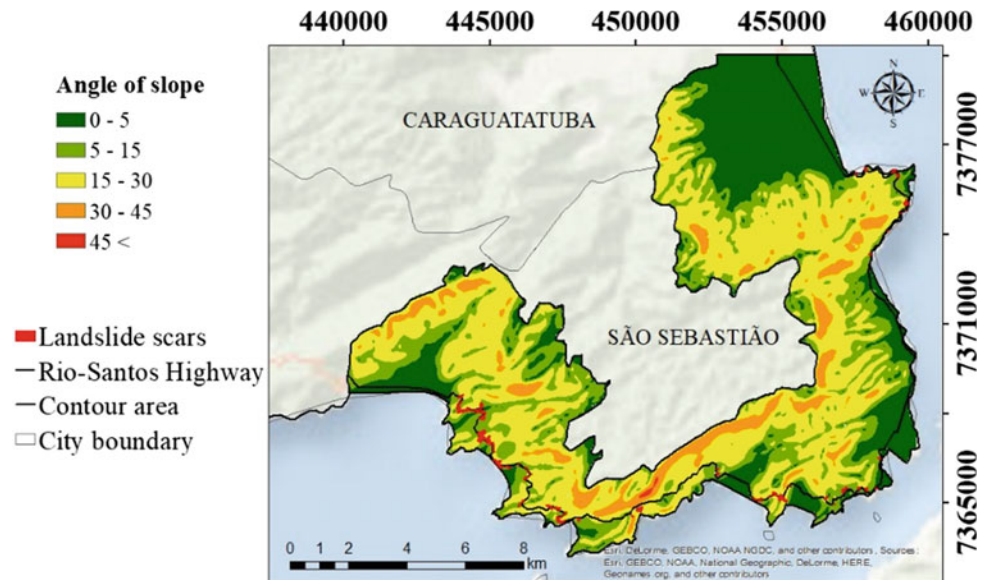


migmatites, gneissic complexes and soils composed of sand and clay sediments that are 1 m thick. The rocks are fractured and slightly altered due to the flow of water through discontinuities, forming channels and causing percolation. Near km 136 and km 137, talus and colluvial deposits have amassed a considerable volume of geological material towards the highway. A debris flow was deposited on drainage channels; it is composed of metric boulders and tree trunks and characterized by high declivity where a continuous stream flows towards the highway. This unit has the highest percentage of landslide incidence, approximately 64% or 51 landslides scars.

### 3.3 Geomechanical Classification

During fieldwork, 59 outcrops were visited, including 29 rock masses and 30 soils (Fig. 5). The slopes are mainly composed of granites and gneisses with extensive amounts of discontinuities. Two types of soils were described; one is a sandy, yellowish soil that promotes water percolation, while the other is a red clay with a higher cohesion index. In some outcrops, the percolation of water is noticeable through the joints, which degrades the rock and creates a thin layer of clay that promotes the development of vegetation at the top of the slopes.

**Fig. 4** Spatial distribution of the four physiographic units
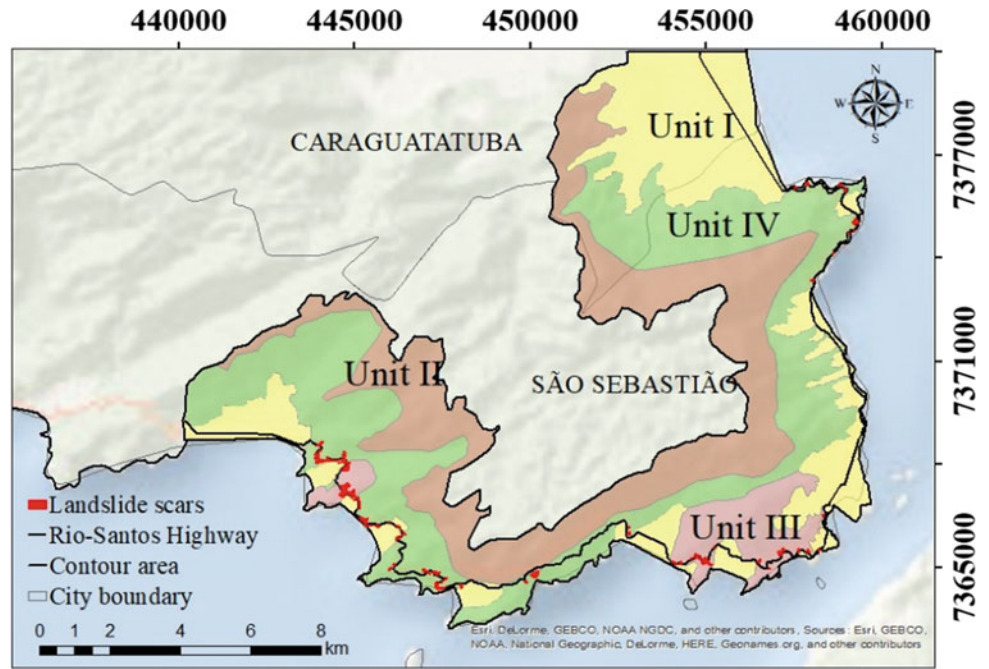


**Fig. 5** Outcrops visited along the Rio-Santos Highway (BR-101)
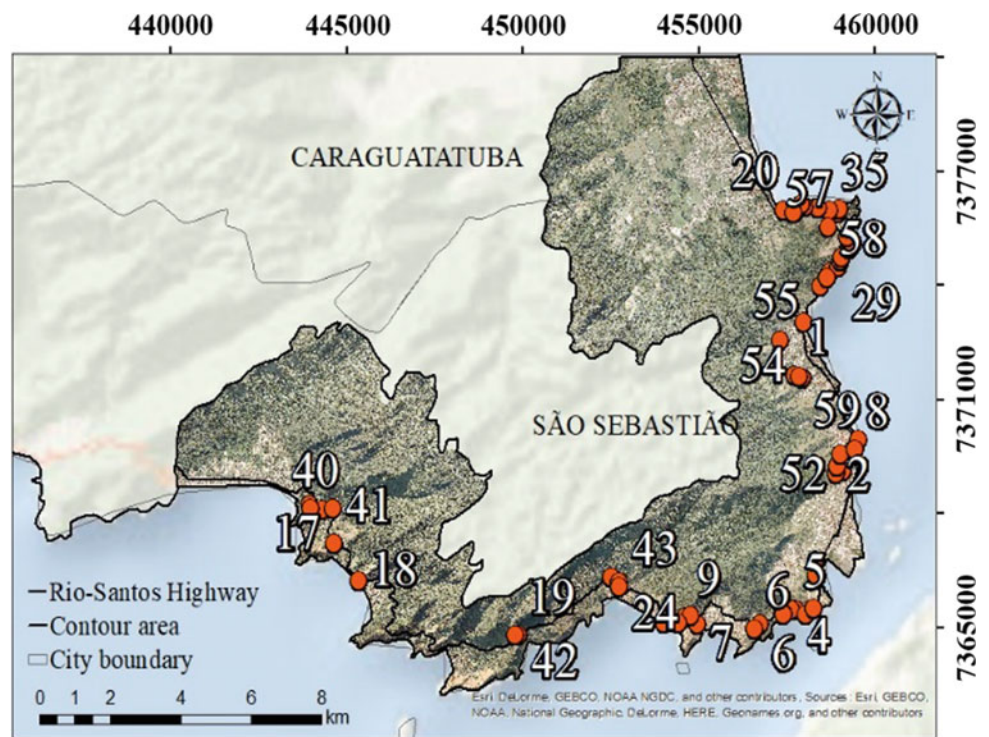


The discontinuities are characterized by slightly rough and weathered walls, irregular to undulating surfaces and separations between 1 and 6 mm where almost no filling was observed. The spacing of discontinuities extends to 1 m in rocks classified as good and very good, whereas that in fair rocks was less than 200 mm. The discontinuity orientation projects into the rock masses, providing greater stability for the slope and less risk of landslide incidence toward the highway.

The RQD resulted in values ranging from 55.6% in rocks of fair quality to 95.2% in rocks of excellent condition. In fair-quality rock masses, the number of joint sets varied from one joint set to multiple joint sets. The Stress Reduction Factor used in the analysis was 2.5, corresponding to single

weakness zones containing clay or chemically disintegrated rock. The values obtained by Schmidt Hammer varied from 210 MPa on rock masses in better geomechanical conditions to 25 MPa on rocks in precarious conditions.

The RMR classified the rock masses from class I (Very good) to class III (Fair). However, the Q-System classification indicated an apparent decline in the quality of rock masses when compared to the RMR, with classes ranging from Good (D) to Poor (F). The majority of rock masses classified as Fair or Poor were found in Unit III. The classes of Very good/Good or Good/Fair represent almost all the rock masses visited in Unit IV. The geomechanical data collected from the study area is summarized in Table 1.

Some divergent results comparing the RMR and Q-System demonstrated that the two methods are not completely equivalent. The intermediary values showed a great correlation, while the extreme values (the highest and lowest results) did not match. This occurred because the Q-System uses a logarithmic scale, whereas RMR is based on a linear equation (Christofolleti 2014). Additionally, the Q-System considers 9 parameters to classify rock masses, which can interfere with the final result.

## 4 Discussion

According to IPT (1988), a rectilinear slope profile tends to form the highest slope angles because it is more susceptible to shallow landslide occurrence. Furthermore, concave geometry is a geomorphologic feature that can concentrate water flow and improve soil saturation (Tominaga 2007). It decreases the friction between sedimentary particles, which causes geological material to be easily transported and deposited at the slope base as talus or colluvial deposits. This scenario was verified at Units II, III and IV. However, the steep slopes (over 45°) of unit II do not allow a well-developed soil profile to form and reduces the chances of landslide occurrence from soils. Instead, for slopes mainly composed of rock masses, these zones offer a high risk of rock falls and topples. However, the soils from units III and IV are mature and basically sandy. Sand has a natural low cohesion index and can be easily transported by gravity and water flows (Wolle and Carvalho 1994), providing conditions to deflagrate shallow landslides.

Unit I is particularly flat and overpopulated. Many houses and communities have been built without an appropriate technical investigation, usually in peripheric zones with steep slopes close to the edges of units III and IV. Situations such as the improper disposal of garbage, deforestation on slope areas and inappropriate slope reprofiling can increase the potential for landslide occurrence. Inappropriate slope reprofiling can interfere with the superficial drainage system and the base level of the terrain, increasing erosion processes and, consequently, contributing to geological material transport (Amorim and Oliveira 2007). Vegetation affects the hydrologic cycle and interferes with groundwater levels, slowing soil saturation and reducing the chances of landslide occurrence (Selby 1993). Without this natural protection, soil can be easily transported, which compromises community infrastructure and public safety. Thus, shallow landslides were not observed because once the relief consists of flat surfaces without unevenness to cause morphodynamic processes, it cannot deflagrate landslides. Instead, only erosional features could be identified at unit I.

Although unit IV has a favorable combination of geomorphologic parameters to deflagrate landslides, the geomechanical classifications established classes of good quality to the rock masses. Thus, landslides are more likely to occur due to geomorphologic parameters and soil depth, whereas morphodynamic processes linked with rock slopes, such as topples and rock falls, are not a threat to the highway. However, unit III combined the geomorphologic parameters required to form landslides with the fair quality classification of rock masses from the geomechanical study. This means that the region is favorable for both shallow landslides at soil profiles and mass movement involving rock masses. Comparing the two units, unit III was considered the most susceptible to landslide occurrence.

**Table 1** Classes of rock mass quality represented in the study area

| Outcrops | RMR | | Q-System | |
|---|---|---|---|---|
| | Class | Quality | Class | Quality |
| 29, 31, 33, 35, 36 | I | Very Good | D | Good |
| 4, 7, 8,16, 17, 22, 25, 26, 27, 28, 30, 32, 34, 37, 38, 39 | II | Good | E | Fair |
| 5, 10, 11, 12, 13, 19, 21, 23 | III | Fair | F | Poor |

## 5  Conclusions

The most susceptible area to landslide occurrence is unit III, whose integration of geomorphologic parameters and geomechanical classification represented the best combination to deflagrate these phenomena. Moreover, steep slope areas occupied inappropriately by the population can also contribute to erosional processes and can indirectly interfere with the community infrastructure, as is seen in unit I. The geomechanical classifications provided a good estimation of the rock mass quality along the Rio-Santos Highway. Because most rock masses were classified as good or very good, this guaranteed the stability of the road infrastructure.

The integration of physiographic compartmentation and a geotechnical survey is a very effective method to understand the relationship between landslides and local to regional triggering factors, such as geomorphologic settings and geotechnical behavior. Thus, these tools may be beneficial in further studies performed along the Rio-Santos Highway at a more detailed scale.

## References

Amorim, R.R., Oliveira, R.C.: Geographic environmental analysis of hillside sections in the urban area of São Vicente—SP. Soc. Natureza **19**(2), 123–138 (2007)

Barton, N., Lien, R., Lunde, J.: Engineering classification of rock masses for the design of tunnel support. Rock Mech. **6**, 189–236 (1974)

Bieniawski, Z.T.: Engineering Rock Mass Classification: A Complete Manual for Engineers and Geologists in Mining, Civil and Petroleum Engineering. Wiley, USA (1989)

Campanha, G.A.C., Ens, H.H., Ponçano, W.L.: Morphotectonic analysis of the Juqueriquerê—Plateau, São Sebastião (SP). Rev. Bras. Geociências **24**(1), 32–42 (1994)

Christofolleti, C.: The RMR and Q correlation and its geological significance. Dissertação de mestrado em geoquímica e geotectônica, University of São Paulo, São Paulo (2014)

Deere, D.U., Miller, R.P.: Engineering classification and index properties of intact rock. Air Force Laboratory Technical Report no AFNL-TR-65-116 (1966)

Gerscovich, D.M.S.: Slope Stability, 1st edn. Oficina de Texto, São Paulo (2013)

Guidicini, G., Nieble, C.M.: Estabilidade de taludes naturais e de escavação, 2nd edn. Blucher Editor, São Paulo (1984)

Hasui, Y.: The great Precambrian collision of the Southeastern Brazil and the regional structure. Geociências **29**(2), 141–169 (2010)

Instituto de Pesquisas Tecnológicas do Estado de São Paulo (IPT): Estudo das instabilizações de encostas da Serra do Mar na região de Cubatão objetivando a caracterização do fenômeno de corrida de lama e da prevenção de seus efeitos. IPT, São Paulo (1988)

ISRM: Suggested methods for determining hardness and abrasiveness of rocks. In: Brown (ed.) Rock Characterization, Testing and Monitoring. ISRM Suggested Methods. Pergamon, Oxford (1981)

Janasi, V.D.A., Alves, A., Vlach, S.R.F., Leite, R.J.: Peraluminous granites of the central portion of the Ribeira Fold Belt, São Paulo State: recycling events of the Neoproterozoic continental crust. Série Científica **3**, 13–24 (2003)

Palmstrom, A.: The volumetric joint count—a useful and simple measure of the degree of rock jointing. In: Proceedings of the 4th International Congress on International Association of Engineering Geology, Dehli, pp. 221–228 (1982)

Selby, M.J.: Hillslope Materials and Processes. Oxford University Press, Oxford (1993)

Tominaga, L.K.: Avaliação de metodologias de análise de risco a escorregamentos: Aplicação de um ensaio em Ubatuba, SP. Tese de doutorado em Geografia física. University of São Paulo, São Paulo (2007)

Wolle, C.M., Carvalho, C.S.: Taludes Naturais. In: Falconi, F.F., Junior, A.N. (eds.) Solos do litoral de São Paulo, pp. 180–203. ABMS, São Paulo (1994)

Zaine, J.E.: Metodologia de fotogeologia aplicado a estudos geológico-geotécnicos: ensaio em Poços de Caldas, MG. Tese (Livre docência em Geociências e Meio Ambiente). University of São Paulo State University, Rio Claro (2011)

# Landslide Susceptibility and Soil Loss Estimates Impacting Streams in the Drift Creek/Siletz Watershed, Lincoln County, Oregon

David Korte and Abdul Shakoor

## Abstract

This study models landslide susceptibility on a watershed scale and estimates soil loss resulting from landslide derived sediment within 30 m of Strahler 3rd order or higher streams in the Drift Creek/Siletz watershed. Landslide derived sediment has been suspected of decreasing water quality, suspending water treatment plant operations, and degrading ecology in the Drift Creek/Siletz watershed by the Oregon Department of Environmental Quality (DEQ). The watershed has been designated as "Impaired by Unknown Stressors" by the MidCoast Watersheds Council Biological Monitoring Results Survey (2013). Logistic regression was used to determine the most significant variables contributing to landslide occurrence and to create a watershed scale landslide susceptibility map with area under the ROC curve of 0.8761. The most significant variables are slope angle, terrain elevation, soil erodibility factor, and plan curvature (curvature perpendicular to slope direction). Soil loss estimates were made by using the U.S. Department of Agriculture RUSLE 2 equation in ArcGIS to accommodate the many different spatial factors in the calculation. The watershed wide average annual soil loss estimate agrees with published findings for watersheds of similar size and physiographical location. Four Upper Drift Creek landslide deposits within 30 m of the stream network showed the highest average annual soil loss estimates (281.5 tons/acre/year combined). These landslide deposits coincide with recent logging activity. Logging activity and the time for forest re-growth appears to substantially influence soil loss in the Drift Creek/Siletz watershed.

## Keywords

Landslide susceptibility • Soil loss

## 1 Introduction

This study models landslide susceptibility on a watershed scale and estimates soil loss from landslide deposit sediment impacting Strahler 3rd Order and higher streams in the Drift Creek/Siletz watershed. Landslides tend to increase sediment bedload resulting in loss of pools, and/or fish habitat, habitat connectivity, and diversity. Suspended landslide sediment increases temperature, turbidity, and exceedance of Total Maximum Daily Load (TDML) targets established by the United States Environmental Protection Agency (EPA) and the DEQ. In addition to providing habitat and diversity, the streams in the Drift Creek/Siletz watershed are a source of drinking water for the Confederated Tribes of Siletz Indians and Lincoln City.

Sediment influxes, possibly associated with landslide activity, are suspected by the DEQ of decreasing water quality, affecting water treatment plant operations, and impacting ecology in the Drift Creek/Siletz watershed. During this study, we evaluated landslide susceptibility and estimated soil loss for landslide deposits mapped in a previous study (Korte and Shakoor 2017). In the previous study, the Oregon Department of Geology and Mineral Industries (DOGAMI) provided light detection and ranging (lidar) imagery and the mapping methodology (Burns and Madin 2009). In this study, lidar DEM derived slope angle, curvature (plan, profile, and standard), flow direction, landslide deposit aspect, USDA NRCS (2017) sourced soil erodibility factors and USGS MRLCC (2017) land cover were used to calculate the probability of landslide occurrence and estimate potential sediment delivery to streams. Precipitation was not used in sensitivity analysis because there are no recording stations in this watershed and interpolation from nearby stations results in uniform precipitation across the study area.

D. Korte (✉) · A. Shakoor
Department of Geology, Kent State University,
Kent, OH 44242, USA
e-mail: dkorte@kent.edu

A. Shakoor
e-mail: ashakoor@kent.edu

The Drift Creek/Siletz watershed does not have active USGS stream monitoring stations. The Schooner Creek station (14303950), located near the northwest boundary of the Lower Drift Creek watershed, monitors only flow. The Confederated Tribes of Siletz Indians have monitored Boulder Creek, Warnick Creek, and the North Fork Siletz River for temperature and Cedar, Euchre, and Sams Creeks for both temperature and turbidity. Temperature, turbidity, flow and stream geometry are needed to draw any meaningful water quality correlations with the streams in the Drift Creek/Siletz watershed. Therefore, this study will estimate soil loss to determine the most likely areas of stream impact by landslide-derived sediment.

## 1.1 Problem and Significance

The United States Forest Service (USFS) has designated the Drift Creek/Siletz watershed as a Tier 1 Key Watershed. A Key Watershed is defined by the National Forest and Bureau of Land Management District as a watershed containing: (a) habitat for potentially threatened species or stocks of anadromous salmonids or other potentially threatened fish, or (b) greater than six square miles with high-quality water and fish habitat. Coho Salmon (*Oncorhynchus kisutch*) and Steelhead Trout (*Oncorhynchus mykiss*) populations are severely depressed in Drift Creek watersheds. The watershed is listed by the Oregon Department of Fish and Wildlife (ODFW) as a "source area" for Steelhead. The MidCoast Watersheds Council has designated the watersheds as a high priority for protection and enhancement.

The DEQ is concerned about the TDML (the maximum amount of a pollutant that a waterbody can receive and still meet water quality standards and an allocation of that load among various sources of that pollutant) found in the watershed (DEQ 2013; Michie, Personal Communication 2014). Suspected sediment influxes of unknown origin are changing the ecology of the watershed by stressing fish habitat through increasing turbidity, increasing conductivity, increasing temperature, reducing stream flow, decreasing dissolved oxygen concentrations, and decreasing general water quality. The pH of Devil's Lake has exceeded alkaline standards during winter/spring seasons since 2003 (Salmon-Drift Creek Watershed Council 2006). In addition, the Confederated Tribes of Siletz Indians obtain their drinking water from the watershed. Water treatment operations in the watershed are sometimes shut down due to turbidity resulting from excessive sedimentation, particularly below 3rd order (Strahler) streams (van de Wetering, Personal Communication, 2014). The DEQ needs to know if these sediment influxes are the result of natural or anthropological phenomena to properly plan and direct funding for

remediation. The DEQ and the Oregon Department of Mineral and Geologic Industries (DOGAMI) suspect that landslides may be responsible for some of the deterioration of the Drift Creek/Siletz watershed (Michie, personal communication 2014).

## 1.2 The Drift Creek/Siletz Watershed

The Drift Creek/Siletz watershed is a combination of 2 Hydrologic Unit Code 6 watersheds, Upper and Lower Drift Creek, located within the Siletz watershed. The area of the Drift Creek/Siletz watershed is approximately 107 km$^2$. Elevation ranges from 1 to 975 m and slope angles range from 0° to 85°. The area is heavily dissected with no preferred direction of ridgelines. Major streams trend from northeast to southwest and east to west. The 30-year annual average precipitation in the watershed is 310.6 cm; about half is rainfall and half snowfall. Fall and winter are the wettest seasons. Autumn receives 83.1 cm and winter receives 140 cm. Spring receives 72 cm of precipitation and summer is the driest season with 15.5 cm precipitation (National Weather Service 2016). Rainfall and snowfall are not differentiated by season in the in the precipitation records. However, the overall marine temperate climate and seasonal precipitation concentration leads to most landslides occurring during the winter months (Smith 1978) as bedrock erosion increases and soil strength decreases due to the flow and infiltration of water.

Douglas fir, western red cedar, western hemlock, big leaf maple, and red adler are abundant in the watershed. The understory and floor are covered with ferns and shrubs. The watershed is in its 3rd or 4th forest harvest (van de Wetering, personal communication 2014). Logging is currently active in the eastern region of the watershed (Upper Drift Creek). Foresters are required to reclaim logged areas with conifers per the Forest Practices Act (Oregon Department of Forestry 2014). Some of the logging bounds and/or crosses Strahler 3rd order or higher streams.

### 1.2.1 Geology

The watershed has variable lithology consisting primarily of Siletz River Volcanics and Tyee Formation, with minor areas of Yamhill and Nestucca Formations (Fig. 1). The watershed is heavily forested and geomorphic expressions of landslides are difficult to interpret from aerial orthophotographs. Temporal landslide data is limited because there is only one detailed digital elevation model (DEM) and little observational history.

The dominant bedrock in the watershed is Siletz River Volcanics (74.6 km$^2$) and the Tyee Formation (16.1 km$^2$). The Yamhill Formation, Nestucca Formation, Intrusive Formations, Depot Bay Basalt, Alsea Formation, and alluvial deposits (listed in order of age) make up the remaining
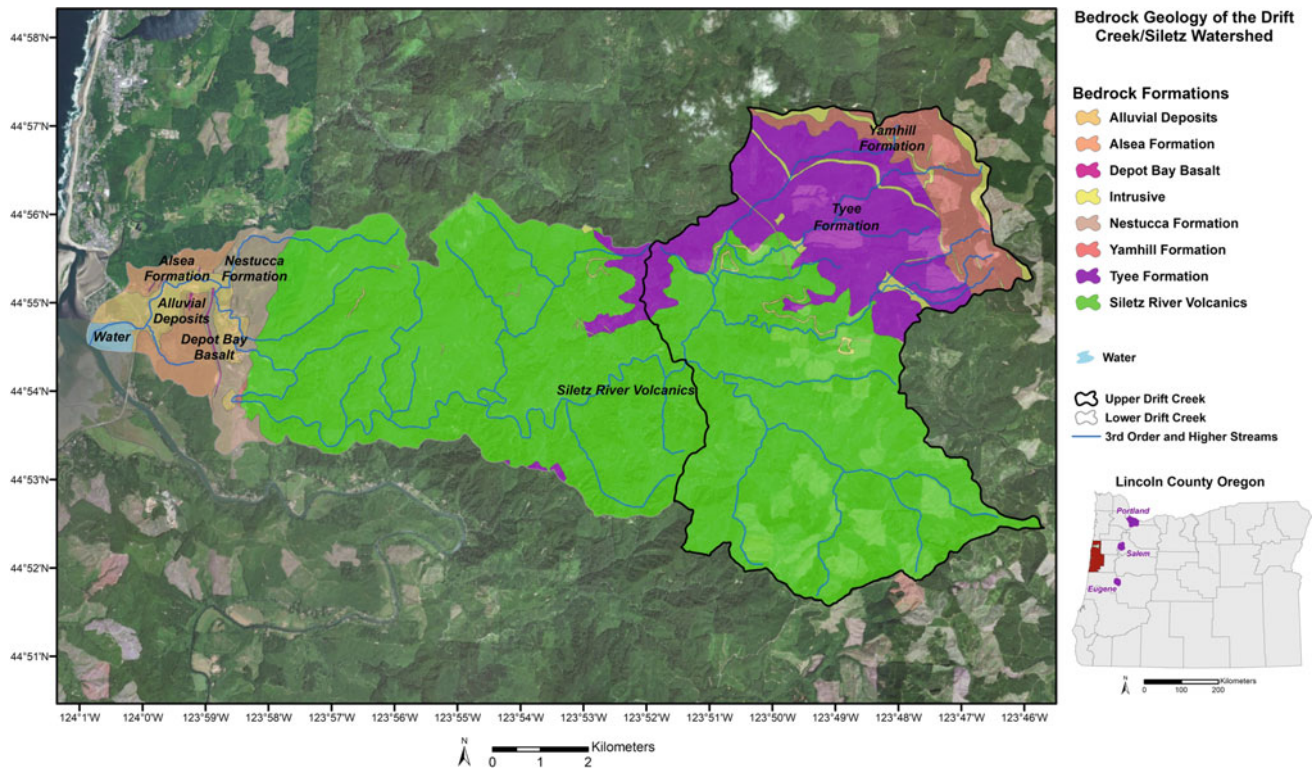
**Fig. 1** Bedrock units for the Drift Creek/Siletz Watershed

107 km² area. The Yamhill Formation, Nestucca Formation, and Alsea Formation are generally constrained to the eastern and western edges of the watershed. These units have eroded away from the interior of the watershed, leaving exposures of Siletz River Volcanics as the dominant bedrock by area.

The Siletz River Volcanics consist of aphanitic to porphyritic vesicular pillow flows, tuff-breccias, massive lava flows, and sills of tholeiitic and alkalic basalt (Fig. 2). The upper part of the sequence contains numerous interbeds of basaltic siltstone and sandstone, basaltic tuff, and locally derived basalt conglomerate. Zeolitization of the rocks and presence of calcite veins are pervasive within the unit (USGS MROSD, 2017). These rocks are of marine origin and have been interpreted as oceanic crust and seamounts, an off-shore terrain named "Siletzia", that was accreted onto the Oregon coast 55–50 million years ago (Wells et al. 1998). Siletzia basalts (Siletz River Volcanics) form the basement of the Oregon Coast Range (OCR) and therefore compose the core of the OCR anticline. The age of the Siletz River Volcanics spans the Paleocene to Eocene Epochs.

The Tyee Formation has been interpreted as a deep-water submarine fan complex that formed on top of the Siletzia terrane in a fore-arc basin 49–48 million years ago. The fore-arc basin was created by the collision of Siletzia with the North American continent. Later uplift of the OCR displaced the fore-arc basin to what is now the Williamette Valley which separates the Cascades from the OCR (Wells et al. 1998) and tilted the Tyee Formation slightly (<20°) to the east. Groove and flute casts indicate deposition by north-flowing turbidity currents. The proximal end of the fan complex is to the south and the distal end to the north. Therefore, the Tyee Formation is thickest to the south and thinnest in the north. The Drift Creek/Siletz watershed is at the very distal end of the fan complex, the end of the Tyee Formation. The Tyee Formation in this watershed is a sequence of thin rhythmically bedded, medium to fine grained micaceous, feldspathic, lithic, or arkosic marine sandstone and micaceous, carbonaceous siltstone containing minor interbeds of dacite tuff in the upper part (Fig. 3). Probable provenance of the unit is the southwest Idaho batholith (Heller et al. 2016). The Tyee Formation is Middle Eocene in age.

In addition, there are 37 different soil types derived from extrusive, intrusive, and sedimentary bedrock parents mapped in the Drift Creek/Siletz watershed. The top five soil types with landslide deposits vary in depth to bedrock from 51 to 203 cm (USDA NRCS 2017). Runoff potential varies from moderately low to moderately high. Erodibility varies

**Fig. 2** Siletz River Volcanics showing faint pillow basalt features from Korte and Shakoor (2017)



**Fig. 3** Tyee formation showing interbedded marine sandstone and micaceous carbonaceous siltstone from Korte and Shakoor (2017)
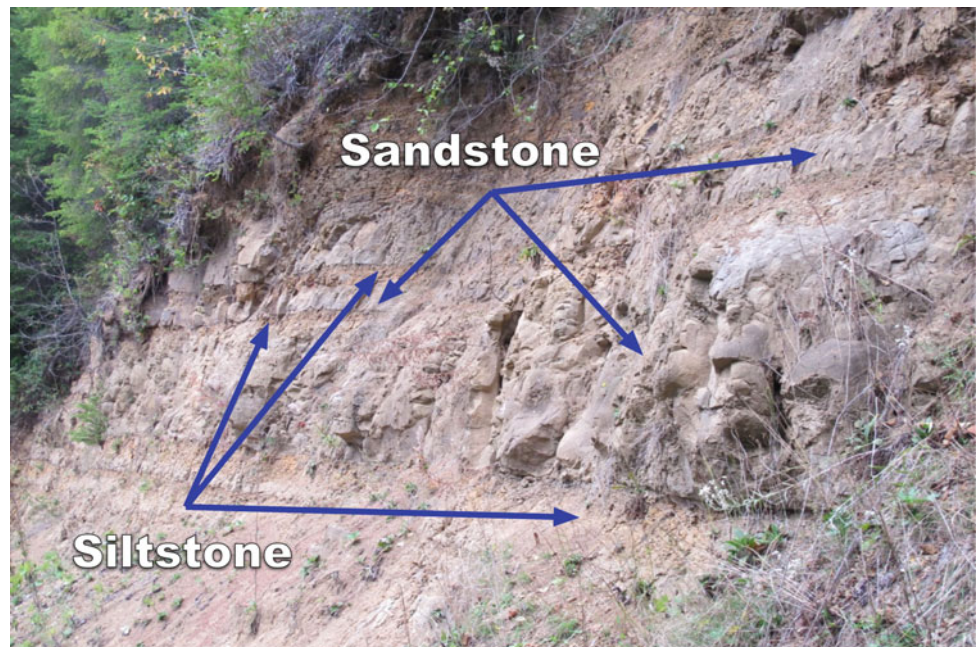


from moderate to high. The textures of these top five soils are silt loam—very gravelly loam, silt loam—gravelly loam, and gravelly silt loam. Grains > 0.075 mm classify as SM for Siletz River Volcanics and SP-SM for the Tyee Formation. Fines classify as ML for both Siletz River Volcanics and the Tyee Formation per USCS (ASTM D2487) classification. The average slope angle in the watershed is 25°.

## 2 Methods

### 2.1 Landslide Susceptibility Map

A landslide inventory map for the Drift Creek/Siletz watershed was prepared using the protocol for inventory mapping

of landslide deposits from lidar imagery developed for DOGAMI by Burns and Madin (2009). The protocol was developed to provide consistent methodology for collecting and visualizing data, to minimize mapping errors, and to enhance the reliability of landslide hazard maps (Ardizzone et al. 2002; Haneberg 2006; Burns and Madin 2009). The inventory map was created by manually digitizing 570 landslide deposits, associated scarps and scarp flanks, and fans at 1:24,000, 1:10,000 and 1:4000 scales, over an area of 107 km$^2$ (Korte and Shakoor 2017). Inventory mapping was limited to slope movements within 30 m of a third order or higher stream channel which is where sediment issues have been problematic (van de Wetering, personal communication 2014). The database model used to create the inventory map was sourced from DOGAMI and the Oregon Geospatial Enterprise Office. The inventory map was verified where possible on the ground through direct observation and serves as the basis for the landslide susceptibility map.

A new database for the landslide susceptibility map was created by adding the DEM derived variables of curvature (plan and profile), slope aspect, terrain elevation, flow direction, soil erodibility factors, and land cover designations to the DOGAMI database. Plan curvature is defined as curvature perpendicular to slope, profile curvature is the curvature in the direction of slope. Soil type and erodibility were sourced from a Custom Soil Resource Report for Lincoln County, Oregon generated by the United States Department of Agriculture Natural Resources Conservation Service and added to the database (USDA NRCS 2017). Land cover was sourced from the National Land Cover Database 2011 and added to the database (USGS MRLCC 2017).

Statistical methods have been shown to accurately predict the likelihood of landslide occurrence e.g. (Haneberg 2004; Guzzetti et al. 2005; Guzzetti 2006; van Westen et al. 2008). The data set in this study includes non-normally distributed data, continuous data, categorical data, and binary data (presence or absence of a landslide). Logistic regression analysis can accommodate non-normally distributed data, continuous data, categorical data, and binary data (Costanzo et al. 2014; Budimir et al. 2015; Zhang et al. 2016; Raja et al. 2017). A logistic regression model would use occurrence of a landslide as a binary dependent variable. For example, a value of (1) would indicate presence of a landslide and a value of (0) would indicate absence of a landslide. Values between (0) and (1) indicate the likelihood (probability) of landslide occurrence. Independent variables in the model are the factors contributing to landslides based on the data from the study area. Logistic regression calculates coefficients (weight factors) and significance (p) of each independent variable through an iteration process where each independent variable is evaluated on its own, in combination with other independent variables, and with all independent variables. The significance level defined for each individual independent variable in this study is 0.05. The null hypothesis is that each independent variable has no effect on the overall model. If $p < 0.05$, then the null hypothesis is rejected, and the variable is significant to the model. The process used in this study then creates an equation that maximizes the area under a Receiver Operating Characteristic (ROC) curve, which is a plot of sensitivity versus specificity (Eng 2005). The maximum area under the curve is 1. The model with area under the ROC curve closest to 1 was chosen as the most valid model. Quantitatively the regression equation can be written as:

$$P = 1/(1 + e^{-z}) \tag{1}$$

where P is the probability of landslide occurrence and z is the combination of coefficients and independent variables responsible for landslide occurrence. The parameter z can be written as:

$$z = \beta_0 + \beta_1 V_1 + \beta_2 V_2 + \cdots + \beta_n V_n \tag{2}$$

where $\beta_0$ is a constant and $\beta_n$ is the coefficient for each respective independent variable $V_n$. The parameter z ranges from $-\infty$ to $\infty$; therefore, the range of P is from 0 to 1. Landslide non-occurrence was added to the database by randomly selecting 570 points within 30 m of stream channels where landslides did not occur. These points were then tagged with the same attributes as landslide occurrence. The process tests for P = 0 and P = 1 while generating coefficients $\beta_n$ and significance of the independent variables in the model. Variables with high significance ($p < 0.05$) were then used in the model which maximized the area under the ROC curve. The model was then rasterized to create a 10 m$^2$ resolution landslide susceptibility map of the study area. 10 m$^2$ pixel size was chosen because the mean area of the landslide deposits in the landslide inventory is 150 m$^2$ and none of the landslide deposits mapped were less than 10 m$^2$ in area. For mapping purposes, susceptibility was classified as Very High (P = 0.76–1), High (P = 0.51–0.75), Medium (P = 0.26–0.50), and Low (P = 0.01–0.25).

## 2.2 Estimating Average Annual Soil Loss

Soil loss in the Drift Creek/Siletz watershed was calculated by using the U.S. Department of Agriculture RUSLE 2 equation in ArcGIS (USDA ARS 2017). The equation calculates average annual soil loss in tons per acre per year. ArcGIS was used instead of the United States Department of Agriculture National Resource Conservation Service (USDA NRCS) RUSLE 2 v 2.6.8.4 program because of the variable soil erodibility factors and land cover designations in the watershed. This allowed for more accurate estimation of soil

loss by accounting for spatial variations of these variables. The RUSLE equation is:

$$A = R * K * Ls * C * P \qquad (3)$$

where A = average annual soil loss, R = rainfall-runoff erosivity factor, K = soil erodibility factor, Ls = slope length and steepness factor, C = cover management factor, and P = support practice factor.

The R factor is measure of the erosive force and intensity of rain in a normal year. R was calculated using the U.S. EPA rainfall erosivity factor calculator for a 30-year period from January 1, 1987 to October 20, 2017 (R = 4260) and for January 1, 2016 to December 31, 2016 (R = 151) for Lincoln County, Oregon to approximate rainfall erosivity in the watershed because the calculator does not use watershed shapes (polygons) for input extent.

The K factor varies by soil type. There were 37 different K factors in this study. K factors are included in custom soil reports from the USDA NRCS but not included in the NCRS SSURGO databases used in GIS mapping. A table of the soil types and respective K factors was created and joined to the SSURGO database.

The Ls factor quantifies the combined effect of slope length and steepness. Ls factors for different slope angles and slope lengths can be found in summarized tables or calculated from the lidar DEM. For this study, the Ls factors for each 1 m$^2$ pixel were calculated (Pelton et al. 2007) because of the many different slope lengths and slope angles in the study area. The equation for Ls uses a flow accumulation ("flowacc") and slope ("slope") raster multiplied together. The individual equations for L and s are:

$$L = (\text{``flowacc''} * [resolution]/22.1)^{0.4} \qquad (4)$$

$$s = (\sin(\text{``slope''} * 0.01745)/0.09)^{1.4} * 1.4 \qquad (5)$$

The C factor reduces the soil loss estimate according to how effective vegetation is at preventing detachment and transport of soil particles. C factors were rasterized to 10 m$^2$ using a table generated from RUSLE 2 guidelines for the state of Oregon and land cover data sourced from the Multi-Resolution Land Characteristics Consortium National Land Cover Database 2011 (NLCD 2011).

The P factor is the ratio of soil loss with a given surface condition to soil loss with up-and-down hill plowing. P is greater than 1 for compacted conditions and less than one for loose conditions. The control condition, P = 1, was used in this study.

Estimated average annual soil loss was then calculated and mapped at 10 m$^2$ resolution over a 30-year period and for year 2016. Overall mean soil loss statistics were calculated for the entire watershed. The relationship between estimated average annual soil loss, mapped landslide
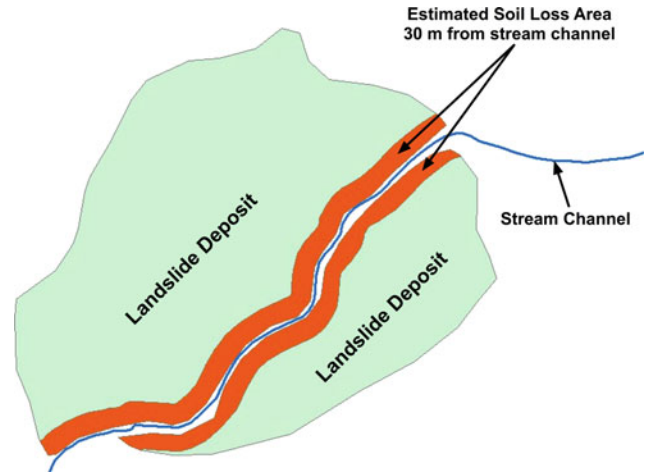


**Fig. 4** Zone of landslide deposits used for average annual soil loss estimates

deposits, and a 30 m stream buffer was investigated by intercepting the respective map layers and using zonal statistics to quantify how much soil sediment is delivered to the stream network by landslide deposits (Fig. 4).

## 3 Results

### 3.1 Landslide Susceptibility

Table 1 summarizes the significance of the independent variables from most significant to least significant used in the logistic regression model.

Running the model using only the independent variables with $p < 0.05$ (the most significant contributors to landslide occurrence) maximizes the area under the ROC curve and calculates the parameter z as:

$$z = -15.383 + (0.096 * SlopeAngle) + (0.003 * TerrainElevation) \\ + (36.536 * SoilErodibilityFactor) + (-0.063 * PlanCurvature)$$

The area under the ROC curve is 0.8761. For scale, a value of 1 would be a perfect prediction and a value of 0.5 would be random chance. Adding insignificant variables to the model only increased the area under the ROC curve by a maximum of 0.0033. The model was exported as an Excel spreadsheet which allows sensitivity analysis by varying the values of all the independent variables and observing the effect on predicted chance of landslide occurrence.

The equation $P = 1/(1 + e^{-z})$ was used to create a landslide susceptibility map thematically displaying the chance of landslides occurrence (Fig. 5). Thirty-three percent of the watershed has a high to very high probability of landslide susceptibility. The high and very high probability areas of landslide occurrence are primarily above 390 m

**Table 1** Results of independent variable significance in the logistic regression model

| Independent variable | Significance ($p$) |
|---|---|
| Slope angle | <0.001 |
| Terrain elevation | <0.001 |
| Soil erodibility factor | <0.001 |
| Plan curvature | 0.034 |
| Bedrock | 0.127 |
| Land cover | 0.281 |
| Slope aspect | 0.330 |
| Flow direction | 0.478 |
| Profile curvature | 0.881 |
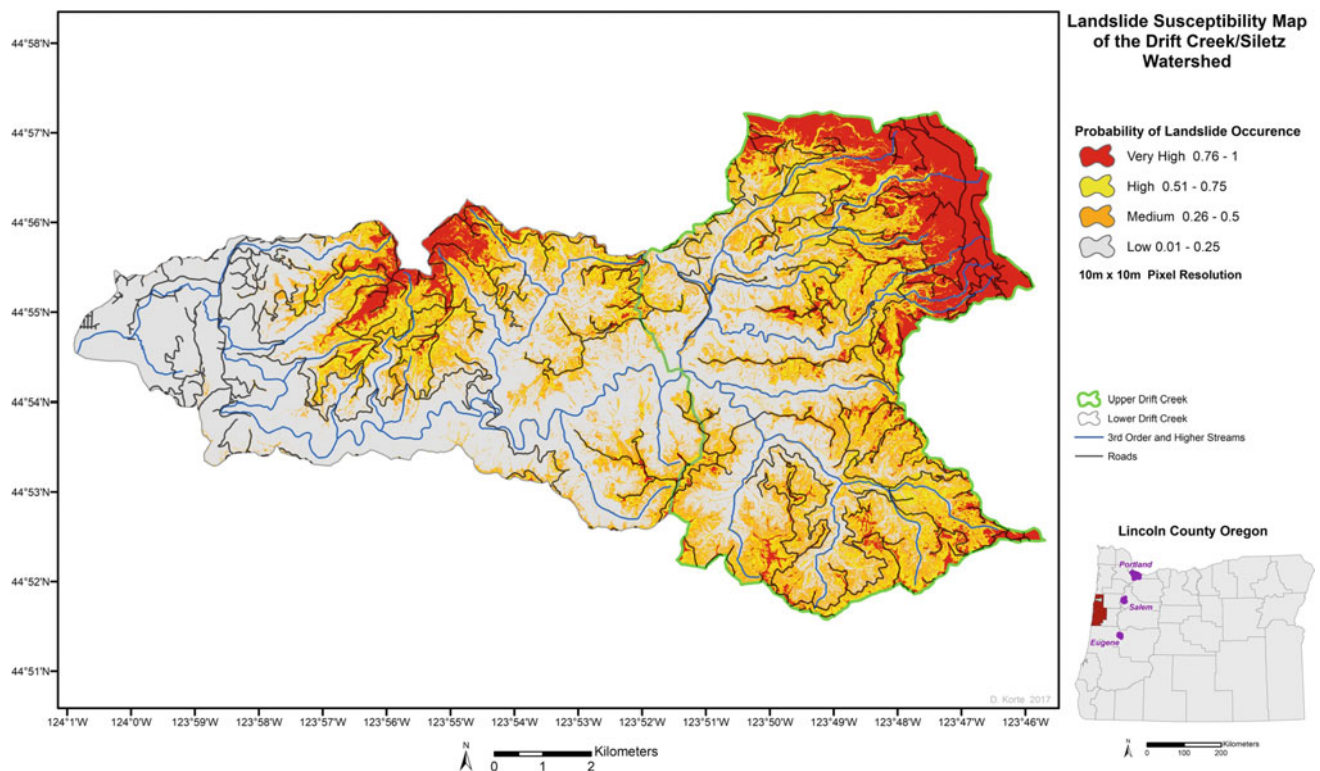


**Fig. 5** Landslide susceptibility map of the Drift Creek/Siletz watershed showing probability of landslide occurrence

terrain elevation, with slope angles >25° (which is above the 25° average slope angle for the watershed), along stream channels where landslide deposits were mapped, logging areas and along roads leading to those logging areas.

### 3.2 Estimated Average Soil Loss

The estimated average annual soil loss over a 30 period was 27 tons/acre/year over the entire extent of the watershed. The estimated average annual soil loss for 2016 was 28 tons/acre/year. The result of using the RUSLE equation

in this study to estimate average annual soil loss is within 5% of Milliman and Syvitski's (1992) result of 29.5 tons/acre/year for a watershed of similar area and physiographic location. However, watershed scale soil loss can only be used to characterize the watershed. Sediment yield increases with the size of a watershed. Larger watersheds generate more sediment than smaller watersheds. Specific sediment yield (average annual soil loss, tons/acre/year) decreases with increasing watershed size because of the increase in watershed area.

The average annual soil loss model in this study allows examination of small area/large scale areas of interest.
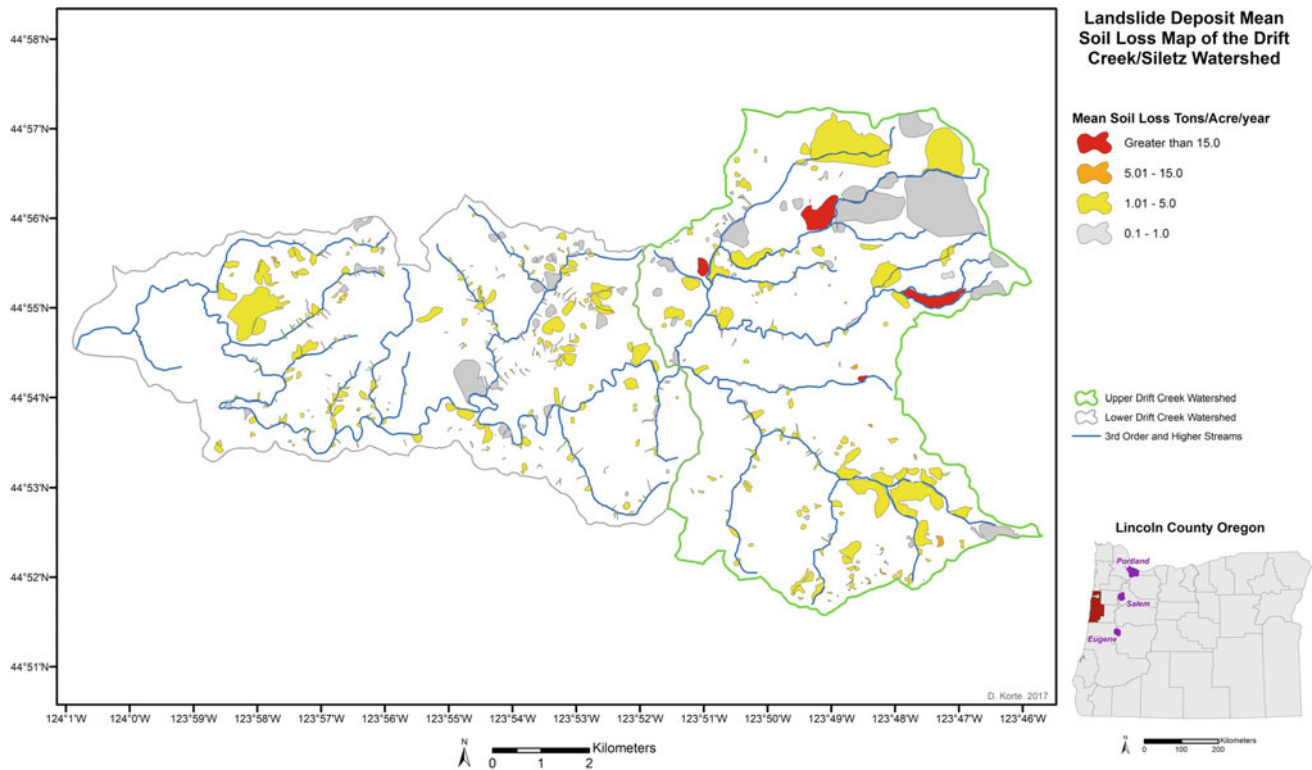
**Fig. 6** Estimated average annual soil loss per landslide deposit

This makes the soil loss model particularly valuable because it can be used for a number of different scenarios. Average annual soil loss anywhere in the watershed, at any distance from the stream network, at any specific landslide deposit, any specific land cover condition, near any road, etc., can now be easily estimated in the Drift Creek/Siletz watershed.

Figure 6 shows the estimated average annual soil loss per landslide deposit. There were 4 landslides out of 570 that individually lost greater than 15 tons/acre/year. They are located within recent logging areas in Upper Drift Creek. The soil types in these areas have soil erodiblity factors that range from 0.37 to 0.4, which are among the highest in the watershed. The estimated average annual soil loss within 30 m of the stream network for these 4 landslides combined is 281.5 tons/acre/year. Other than previous logging, none of these four high soil loss landslides show any nearby human related activity.

The area of the landslide deposits within 30 m of the stream network in Upper Drift Creek is 128 acres and the total estimated annual soil loss for those 128 acres is 65 tons/acre/year. Lower Drift Creek has 85 acres of landslide deposits within 30 m of the stream network and the estimated annual soil loss is 29 tons/acre/year. The soil loss estimates show that landslide deposits contribute substantially more sediment to streams in Upper Drift Creek where there is more logging activity than in Lower Drift Creek.

## 4 Conclusions

This research was undertaken to provide a better understanding of landslide susceptibility and sediment loading to Strahler 3rd order or higher streams in the Drift Creek/Siletz watershed. The two dominant rock types, Siletz River Volcanics and Tyee Formation, have low strength and weather into poorly graded sandy and silty soils (Korte and Shakoor 2017). While this study cannot determine the effects of landslide sediment on water quality and ecological habitat, it does advance our knowledge of where landslides are likely to occur and estimates how much soil loss occurs in the Drift Creek/Siletz watershed.

The landslide susceptibility model exhibited a high degree of statistical validity. In addition, the model highlighted areas away from the stream network where landslides appear in the lidar DEM. Therefore, it will be useful in mapping a watershed wide landslide inventory. The most important omission in the model is water. There is no detailed precipitation variation data across the 107 km$^2$ area of the watershed. Also, there have been no pore pressure studies in the study area. Precipitation and pore pressure could be used to further refine the regression model.

The Revised Universal Soil Loss Equation was used as a mapping technique to accommodate 37 different soil types and

13 different land cover factors. Upper Drift Creek had the highest average annual soil loss estimates in the Drift Creek/Siletz watershed. Current logging activity is prevalent to Upper Drift Creek. Logging activity, including roads and the time needed to re-grow logged areas appears to substantially affect soil loss in Upper Drift Creek by compacting soils, loading slopes, and removing established vegetation.

# References

Ardizzone, F., Cardinali, M., Carrara, A., Guzzetti, F., Reichenbach, P.: Impact of mapping errors on the reliability of landslide hazard maps. Nat. Hazards Earth Syst. Sci. **2**, 3–14 (2002)

Budimir, M.E.A., Atkinson, P.M., Lewis, H.G.: A systematic review of landslide probability modelling using logistic regression. Landslides **12**, 419–436 (2015)

Burns, W.J., Madin, I.P.: Protocol for Inventory Mapping of Landslide Deposits from Light Detection and Ranging (Lidar) Imagery: Oregon Department of Geology and Mineral Industries Special Paper 42, 36 p (2009)

Costanzo, D., Chacon, J., Conoscenti, C., Irigaray, C., Rotigliano, E.: Forward logistic regression for earth-flow landslide susceptibility assessment in the Platani river basin (southern Sicily, Italy). Landslides **11**, 639–653 (2014)

Eng, J.: Receiver operating characteristic analysis: a primer. Acad. Radiol. **12**(7), 909–916 (2005)

Guzzetti, F., Reichenbach, P., Cardinali, M., Galli, M., Ardizzone, F.: Probabilistic landslide hazard assessment at the basin scale. Geomorphology **72**, 272–299 (2005)

Guzzetti, F.: Landslide hazard and risk assessment. Ph.D. thesis, University of Bonn, Bonn (2006). http://hss.ulb.uni-bonn.de/2006/0817/0817.htm

Haneberg, W.C.: A rational probabilistic method for spatially distributed landslide hazard assessment. Environ. Eng. Geosci. **10**(1), 27–43 (2004)

Haneberg, W.C.: Effects of digital elevation model errors on specially distributed seismic slope stability calculations: an example from Seattle, Washington. Environ. Eng. Geosci. **XII**, 247–260

Heller, P.L., Peterman, Z.E., O'Neil, J.R., Shafiqullah, M.: Isotopic provenance from the eocene tyee formation, oregon coastal range. Geol. Soc. Am. Bull. **96**(6), 770–780 (2016)

Korte, D., Shakoor, A.: Landslide distribution and material properties in the Drift Creek Watersheds, Lincoln County, Oregon. In: 3rd North American Symposium on Landslides 2015. Association of Environmental and Engineering Geologists, Roanoke (2017)

Michie, R.: Oregon Department of Environmental Quality (2014) (700 NE Multnomath Street, Suite 600, Portland, OR 97232)

MidCoast Watersheds Council. 23 North Coast Highway, Newport, OR, 97365 (2013). www.midcoastwatersheds.org

Milliman, J.D., Syvitski, J.P.M.: Geomorphic/tectonic control of sediment discharge to the ocean: the importance of small mountain rivers. J. Geol. **100**, 525–544 (1992)

National Weather Service. (2016). http://www.srh.noaa.gov/ridge2/RFC_Precip/. Accessed 29 Aug 2017

Oregon Department of Environmental Quality (DEQ): Construction of Stormwater Erosion and Sediment Control Manual: Water Quality Division Surface Water Management, 22pp (2013)

Oregon Department of Forestry: Forest Practice Administrative Rules and Forest Practices Act: Chapter 629: Forest Practices Administration, 94pp (2014)

Pelton, J., Frazier, E., Pckiligis, E.: Calculating slope length factor (LS in the Revised Universal Soil Loss Equation (RUSLE). Indian Acad. Sci. Reson. **12**(7), 7p (2007)

Raja, N.B., Cicek, I., Turkoglu, N., Aydin, O., Kawasaki, A.: Landslide susceptibility mapping of the Sera River Basin using logistic regression model. Nat. Hazards **85**, 1323–1346 (2017)

Salmon-Drift Creek Watershed Council: Volunteer water quality monitoring Salmon-Drift Creek Watershed Council. Final sport and accounting Oregon Watershed Enhancement Board grant # 204-074, 21pp (2006)

Smith, E.: Determination of coastal changes in Lincoln County, Oregon using aerial photographic interpretation. Master's thesis, The Department of Geography at Portland State University, 29pp (1978)

United States Department of Agriculture Agricultural Research Service (USDA ARS). https://www.ars.usda.gov. Accessed 15 Aug 2017

United States Department of Agriculture National Resources Conservation Service (USDA NCRS). https://websoilsurvey.sc.egov.usda.gov/App/HomePage.htm. Accessed 15 Feb 2017

United States Department of the Interior, United States Geological Survey. Mineral resources on-line spatial data (USGS MROSD) (2017). http://mrdata.usgs.gov/geology/state/fips-unit.php?code=f41041

United States Department of the Interior, United States Geological Survey, Multi-Resolution Land Characteristics Consortium (MRLCC). https://www.mrlc.gov/. Accessed 21 June 2017

van Westen, C.J., Castellonos, E., Kuriakose, S.L.: Spatial data for landslide susceptibility, hazard, and vulnerability assessment: an overview. Eng. Geol. **102**, 241–255 (2008)

van de Wetering, S.: Confederation tribes of siletz indians, personal communication (2014)

Wells, R.E., Weaver, C.S., Blakely, R.J.: Fore-arc migration in Cascadia and its neotonic significance. Geology **26**(8), 759–762 (1998)

Zhang, M., Cao, X., Peng, L., Niu, R.: Landslide susceptibility mapping based on global and local logistic regression models in the three Gorges reservoir area, China. Environ. Earth Sci. **75**, 958–969 (2016)

# Large-Scale Rockslide Inventory of the Central Asia Region: Data and Analysis

Alexander Strom

## Abstract

Database of large-scale bedrock landslides of the Central Asian region embracing the Pamir, the Tien Shan, and the Dzungaria mountain systems has been compiled. Collected rockslides range in volume from nearly $1 \times 10^6$ m$^3$ to ca. $10 \times 10^9$ m$^3$ with the affected areas from several hectares to more than 100 km$^2$. More than 950 landslide features have been identified and quantitative parameters (area of the deposits, total area affected, volume, runout, height drop, etc.) of about 62% of them have been measured up to now. Most of case studies are prehistoric. Statistical analysis of this database with regard to the confinement conditions demonstrates that total affected area and its ratio with height drop characterize rockslide mobility better than runout and angle of reach. Higher mobility of secondary rock avalanches associated with momentum transfer within rockslide debris in comparison with rock avalanches of other types is confirmed statistically. These results can be useful for landslide hazard assessment both in Central Asia and in other mountainous regions.

## 1 Introduction

Large-scale catastrophic bedrock landslides (rockslides) are among the most hazardous natural phenomena endangering people in mountainous regions. Simultaneous catastrophic failure of millions and, sometimes, billions of cubic meters of rocks can devastate vast areas and form natural dams which subsequent breach could be even more destructive.

The Central Asian region embracing the Pamir, the Tien Shan, and the Dzungaria mountain systems located in Afghanistan, China, Kazakhstan, Kyrgyzstan, Tajikistan and

A. Strom (✉)
Geodynamics Research Center—Branch of JSC "Hydroproject Institute", Moscow, Russia
e-mail: strom.alexandr@yandex.ru

Uzbekistan (Fig. 1), is one of the global "landslide hotspots". However, case studies from this part of the world are poorly known to the international community of landslide researchers, except very few features such as the 1911 Usoi rockslide and the 1949 Khait rock avalanche. More than 950 bedrock landslides ranging in volume from slightly less than $1 \times 10^6$ m$^3$ to ca. $10 \times 10^9$ m$^3$, with the affected areas from several hectares to 144 km$^2$ have been identified in this region. Most of them are prehistoric.

Quantitative parameters such as area of the deposits (A), total affected area ($A_{total}$), volume (V), runout (L), height drop (maximal—$H_{max}$, and to the deposits tip—H), width of the deposits ($W_{max}$) and of the headscarp base ($W_0$), etc., have been measured up to now for about 62% of case studies identified. For eastern (Chinese) and north-eastern (Kazakh) parts of the study region percentage of the quantified case studies is higher and reaches 90%. Rockslides included in the database can be ascribed to almost all known types of these phenomena—falls, topples, slides, flows, spreads and deep seated gravitational slope deformations (DSGSD) (Hungr et al. 2014). Due to the large number of case studies, correlation analysis of various quantitative parameters characterizing these features could be performed, both for the entire database and for different data samples considering various factors predetermining debris motion, such as the presence or absence of the frontal and/or lateral confinement and rock avalanche type (Strom 1996, 2006, 2010; Strom and Abdrakhmatov 2018). This paper presents some results of such analysis that can be applied for landslide hazard assessment both in Central Asia and in other mountainous regions. More detailed analysis can be found in (Strom and Abdrakhmatov 2018).

## 2 Size-Frequency Distribution

As it was mentioned in the previous section, quantitative parameters have been measured for about 62% of more than 950 cases identified within the entire study region, while at
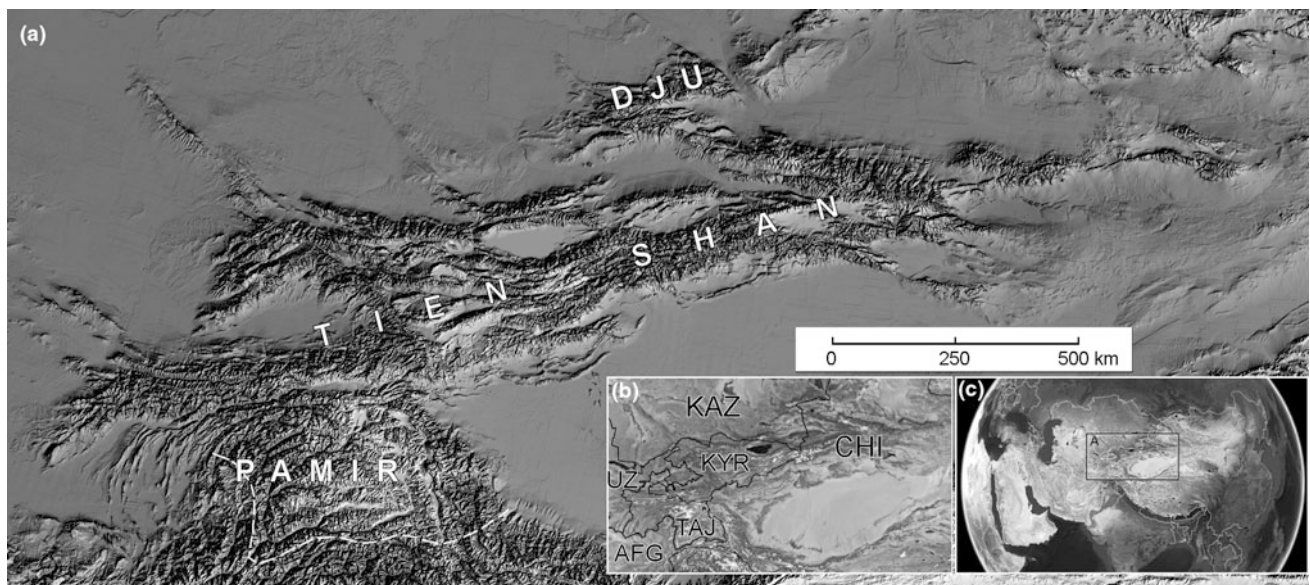
**Fig. 1** A—the 30″ SRTM DEM of the study region; B—political boundaries in the Central Asia region (from Google Earth); C—location of the study region (outlined) in Asia. DJU—the Dzungarian Range, AFG—Afghanistan, CHI—China, KAZ—Kazakhstan, KYR— Kyrgyzstan, TAJ—Tajikistan, UZ—Uzbekistan. Dashed line—the conventional western and southern boundaries of the Pamir. After (Strom and Abdrakhmatov 2018), with permission of Elsevier

some part of it the percentage of the quantified case studies reaches 90%. Comparison of size-frequency distributions of rockslides of the entire region and of its better and worse characterized parts (Fig. 2) shows that they are nearly similar indicating that the selection of case studies, whose quantitative parameters have been measured, was, basically, random, though for the worse characterized areas maximum of the quantified case studies is slightly shifted to larger features. Thus, the results of the statistical analysis of the incomplete general database can be considered as more or less representative. I have to notice that not all parameters could be measured for all landslide features identified; that is why number of data samples used for compiling different plots presented hereafter is not similar. Areas and runouts were measured directly on Google Earth images; volumes were estimated individually for each case study.

Considering relatively poor accuracy of rockslide volume estimates (sometimes up to ±50%; volume of each rockslide body included in the database was estimated individually) due to irregularity of the deposits' shape and absence of data on the preceding relief, overlapping volume ranges were used (see x-axis of a plot on Fig. 2). It allowed obtaining smoother and, likely, more realistic distributions.

Size-frequency distribution of landslides based on various inventories have been analyzed in numerous publications (Hadjigeorgiou et al. 1996; Hovious et al. 1997; Pelletier et al. 1997; Stark and Hovious 2001; Malamud et al. 2004a, b; Turcotte and Malamud 2004; Hovious and Stark 2006; Guzzetti et al. 2008, 2012; Corominas and Moya 2008; Chen

et al. 2011; Korup et al. 2012; Li et al. 2012, 2014, 2016; Mavrouli and Corominas 2015; Corominas et al. 2017).

Rockslide size can be characterized also by the deposits' area—parameter measured with much higher accuracy than volume. Area-frequency distribution of the Central Asian large-scale rockslides, which deposits' area ranges from $\sim 10^4$ to $\sim 10^8$ m$^2$, is shown in Fig. 3. Different number of cases represented in Figs. 2 and 3 appeared because for some case studies where deposits have been eroded significantly, volume estimates were based on the source zone volume.

## 3 Parameters Characterizing Rockslide and Rock Avalanche Mobility

Most of researchers used horizontal projection of runout distance measured from the headscarp crown to the deposits tip (L) and ratio of vertical difference between these points (height drop—H, measured as the altitude difference between headscarp crown and deposits' front tip) to L (angle of reach or fahrböschung—term proposed by A. Heim) as a measure of rockslide mobility (Sheidegger 1973; Hsü 1975; Davies 1982; Li 1983; Shaller 1991; Corominas 1996; Kilburn and Sorrencen 1998; Legros 2002). Indeed, increase of rockslide volume corresponds to increase of runout and to decrease of the H/L ratio. The same was found for the Central Asian rockslides, considering their confinement conditions. In this research it was noticed that the correlation

**Fig. 2** Size (volume)—frequency distributions for the entire Central Asia region (All—595 cases), for its Chinese and Kazakh parts (251 cases) and for the remaining parts of the region (Other—344 cases). Modified from (Strom and Abdrakhmatov 2018), with permission of Elsevier
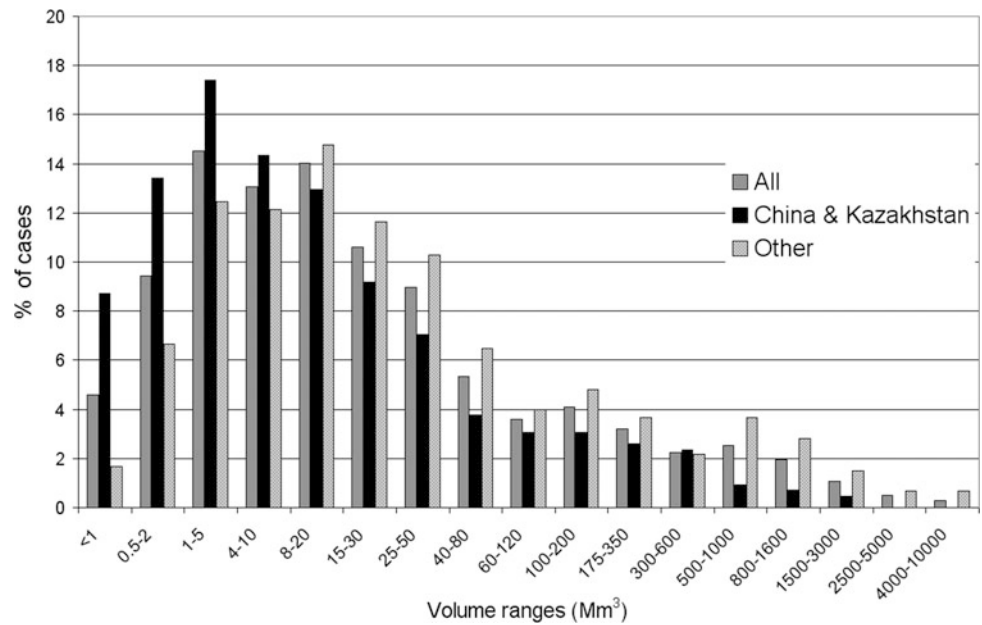


**Fig. 3** Deposits' area—frequency distribution of 577 Central Asian rockslides. Modified from (Strom and Abdrakhmatov 2018), with permission of Elsevier
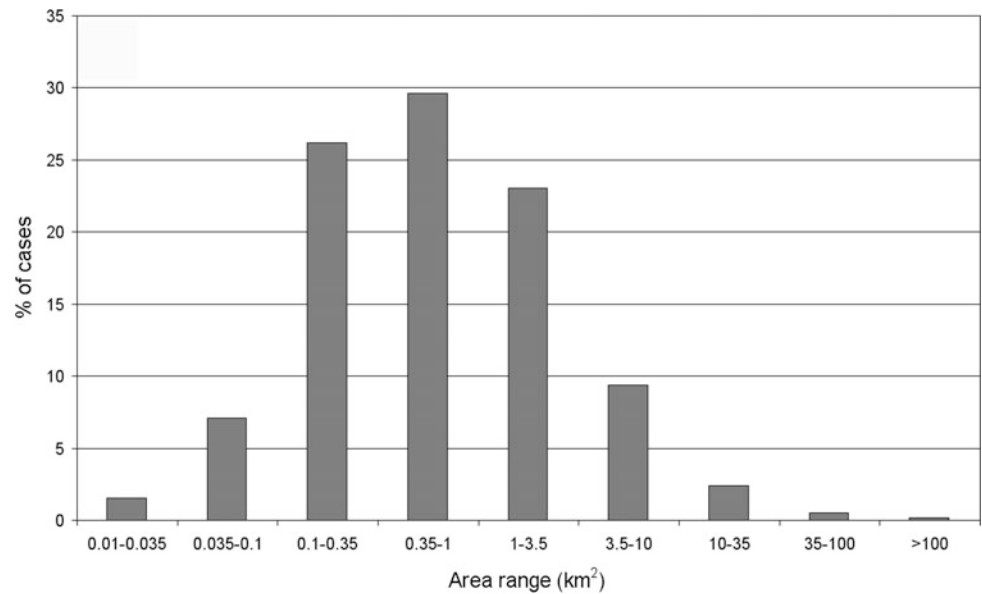


coefficients for L ÷ V relationships are much higher than those for H/L ÷ V, where V—deposits volume (compare Figs. 4 and 5). Relationship between runout and product of rockslide volume and maximal height drop (parameter, reflecting the potential energy available better than V or H separately) was analyzed as well (Fig. 6). Here $H_{max} = H$ for unconfined and laterally confined rockslides, while for frontally confined landslide features, $H_{max}$ was measured as vertical distance between headscarp crown and the deposits' lowermost base that can be much lower than their front tip.

It is interesting to note that on L ÷ V plot runout distance for laterally confined features exceeds that of frontally confined and unconfined rockslides (see Fig. 4), while the relationship between runout and the product of rockslide volume and maximal height drop for laterally confined features is characterized by extremely large scatter and very poor correlation (see Fig. 6).

Rockslide debris, however, moves not only forward but sidewise as well, especially in frontally confined and in unconfined conditions, when they often form fan-shaped or the pancake-shape bodies (Fig. 7). Even if rockslide debris would not move as far as when it moves straightly forward, it could affect larger area, thus increasing the exposure—one of the basic parameters used for landslide risk assessment (Corominas et al. 2015). Thus, it seems more logical to characterize rockslide mobility by the total affected area

Fig. 4 Relationships between runout and rockslide volume for rockslides with different confinement: 301 frontally confined, 135 laterally confined and 78 unconfined cases. Here and hereafter, corresponding $R^2$ values are added to the legend. After (Strom and Abdrakhmatov 2018), with permission of Elsevier
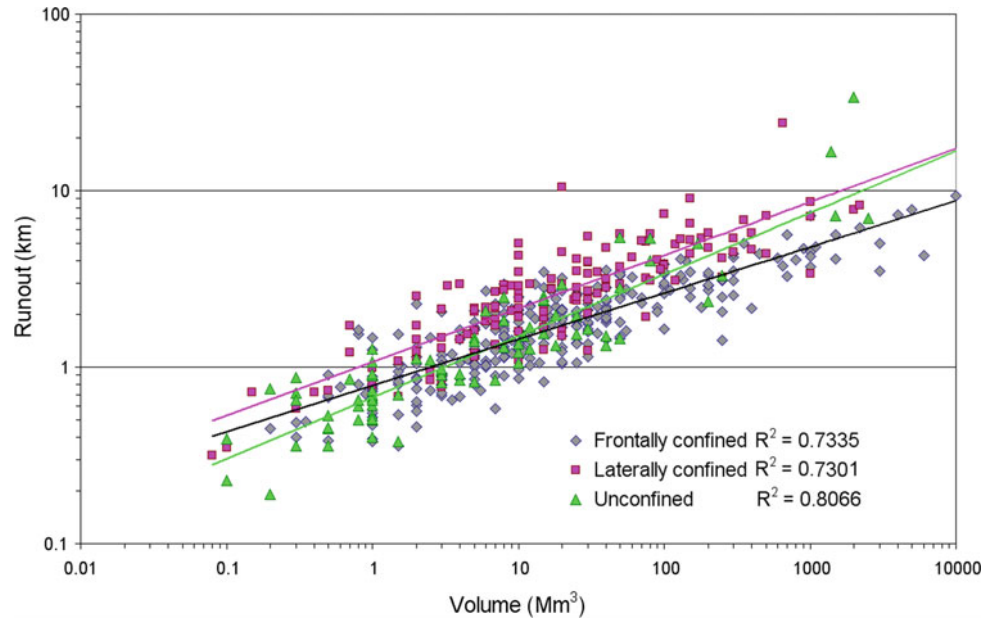


Fig. 5 Relationships between H/L ratio and rockslide volume for rockslides with different confinement. 289 frontally confined, 134 laterally confined and 74 unconfined cases. After (Strom and Abdrakhmatov 2018), with permission of Elsevier
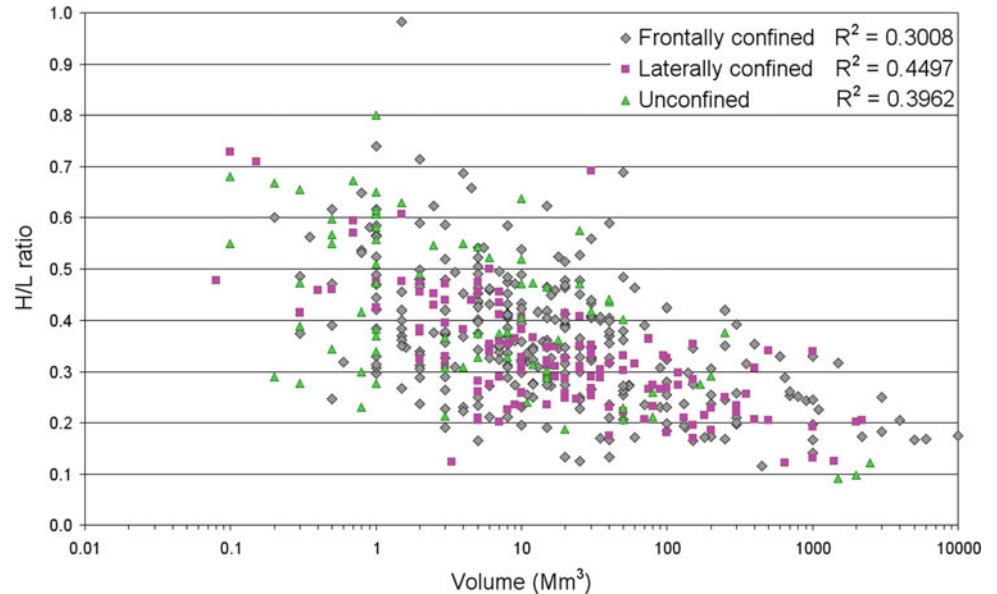


($A_{total}$). Runout length can be treated as its axial dimension. Relationship between rockslide volume and area was analyzed in Li (1983).

Relationships between total affected area and rockslide volume follow power law distribution with a scatter of about half order of area magnitude and high correlation coefficients. Unconfined rockslides, whose volume exceeds ca. 10 mm³, affect larger areas than confined ones (Fig. 8). It differs from the relationship between runout and volume of the collapsed rock mass (compare with Fig. 4) that clearly shows larger runout of the laterally confined features. I have to mention that plots on Figs. 8 and 9 were compiled for

**Fig. 6** Relationships between runout and product of rockslide volume and maximal height drop for rockslides with different confinement. 289 frontally confined, 134 laterally confined, and 74 unconfined cases. After (Strom and Abdrakhmatov 2018), with permission of Elsevier
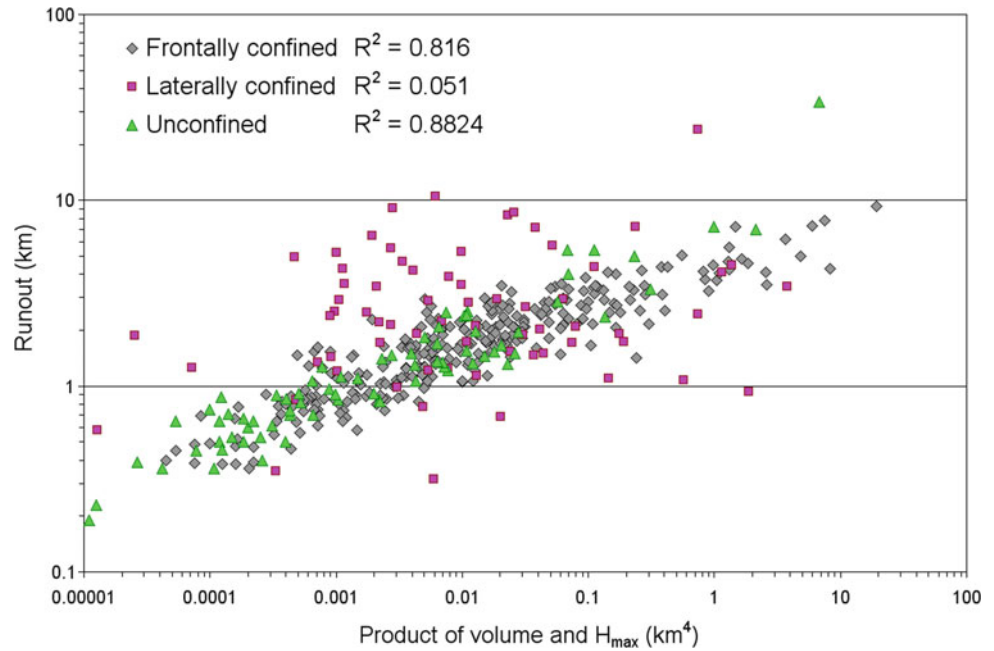


**Fig. 7** Main types of rock avalanche deposits' shape in unconfined conditions. A—monodirectional, B—fan-shaped, C—pancake-shaped, L—runout, $W_0$—headscarp base width, $W_{max}$—maximal width of the deposits. After (Strom and Abdrakhmatov 2018), with permission of Elsevier
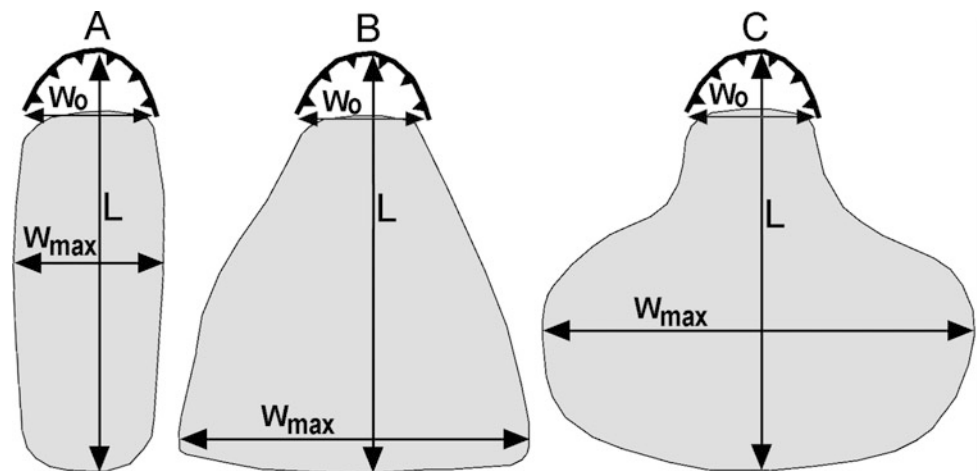


case studies where type of confinement could be defined clearly, which is less than total number of events with measured volume.

Best correlations were found for the relationships between $A_{total}$ and product of rockslide volume and maximal height drop better related to the potential energy (Fig. 10). High correlation coefficients ($R^2 > 0.925$) are typical of all confinement types, unlike similar ratio with runout that correlates well for rockslides in frontally confined

($R^2 = 0.816$) and unconfined ($R^2 = 0.8824$) conditions only (compare with Fig. 6).

Summarizing data presented above we can conclude that affected area reflects rockslide debris mobility better than its runout. Such conclusion is supported by higher correlation coefficients of the relationships between both total affected area and $H/A_{total}$ ratio and parameters like rockslide volume, height drop and their product than those between these parameters and runout and $H/L$ ratio.

**Fig. 8** Relationships between total affected area and rockslide volume for features with frontal confinement (337 cases), lateral confinement (94 cases) and in unconfined conditions (79 cases). After (Strom and Abdrakhmatov 2018), with permission of Elsevier
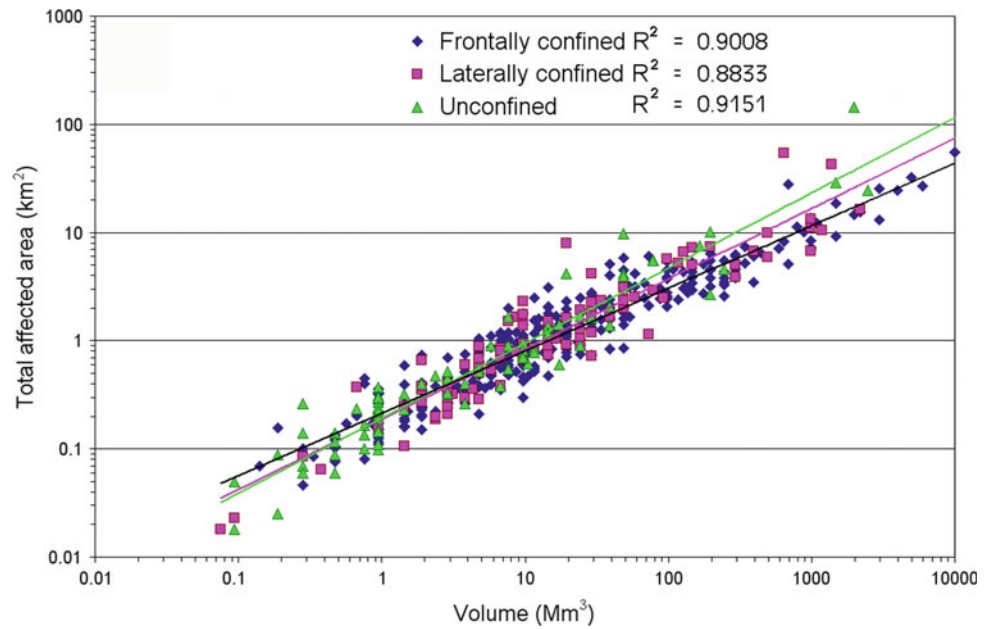


**Fig. 9** Relationships between H/A$_{total}$ ratio and rockslide volume for rockslides with frontal confinement (332 cases), lateral confinement (92 cases) and in unconfined conditions (76 cases). After (Strom and Abdrakhmatov 2018), with permission of Elsevier
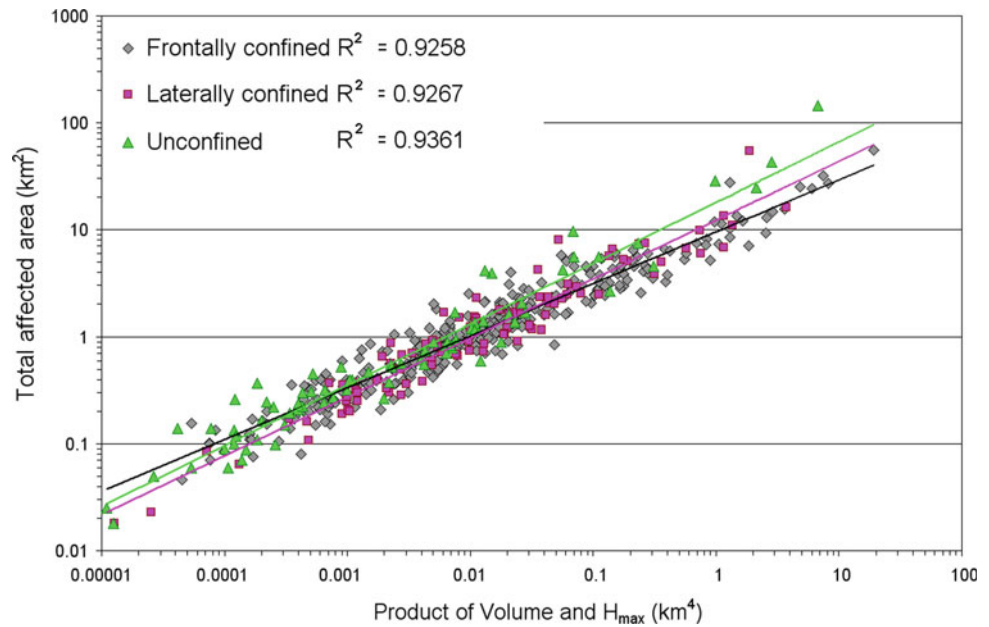
## 4 Excessive Mobility of Secondary Rock Avalanches

When rapidly moving rockslide that gained its momentum during initial descend, strikes either the slope base or the opposite slope of the valley at a sharp angle or passes through a sharp valley constriction, part of the sliding mass accumulates at the foot of a headscarp forming a compact body, while part of debris converts into long runout Secondary rock avalanche (Strom 1996, 2006). It was hypothesized that from the mechanical point of view, formation of Secondary rock avalanches is caused by momentum transfer from the rapidly decelerating portion of debris that accumulates at the proximal part of the deposition zone to its portion retaining possibility of further motion. The latter accelerates causing its extra-mobility (Strom 2010; Strom and Abdrakhmatov 2018).

This assumption was supported by comparison of the relationships between runout of the avalanche-like parts of such features (measured as the horizontal distance from the secondary rock avalanche crown on the slope of a compact body to the deposit tip) with their volume, height drop and product of these parameters with similar relationships revealed for the entire database described above (Fig. 11)—in all cases Secondary rock avalanches appeared to be more mobile on average.
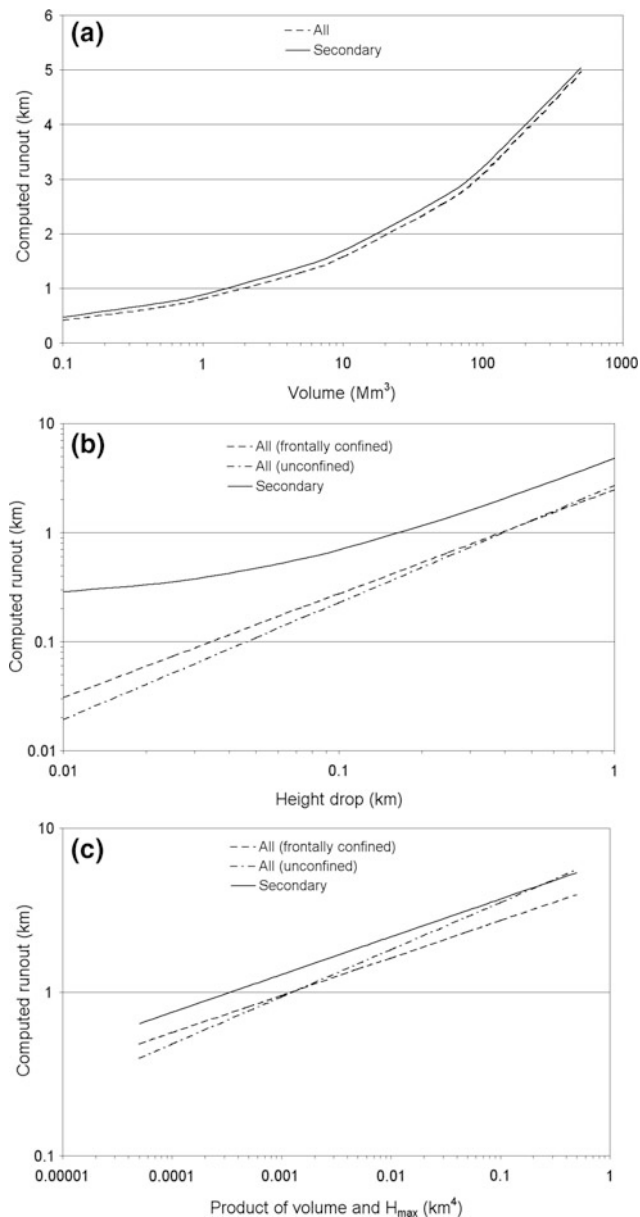
**Fig. 11** Relationships of the runout values (L) calculated according to regression equations for the entire database and for the secondary rock avalanches. A—for the specified volume (V); B—for the specified height drop (H); C—for the specified V × H value. After (Strom and Abdrakhmatov 2018), with permission of Elsevier

# 5 Conclusions

Compilation of the representative large-scale bedrock landslides database of the Central Asia region provided valuable data for their statistical analysis. Large number of features, for which quantitative parameters are available, allows the selection of samples considering confinement conditions and other additional parameters.

Comparison of relationships between rockslide volume (V), height drop (H) and their product (V × H), which is somehow proportional to the potential energy available, with runout (L), angle of reach (H/L), total affected area ($A_{total}$) and $H/A_{total}$ ratio shows that the two latter bidimensional parameters characterize rockslide mobility better than unidimensional ones.

Analysis of the Secondary rock avalanche sample and its comparison with general relationships supports the assumption on the excessive mobility of such type of highly mobile rockslides.

These results can be useful for landslide hazard assessment both in Central Asia and in other mountainous regions.

## References

Chen, C.C., Telesca, L., Lee, C.T., Su, Y.S.: Statistical physics of landslides: new paradigm. EPL **95**(4), 49001 (2011)

Corominas, J.: The angle of reach as a mobility index for small and large landslides. Can. Geotech. J. **33**, 260–271 (1996)

Corominas, J., Moya, J.: A review of assessing landslide frequency for hazard zoning purposes. Eng. Geol. **102**, 193–213 (2008)

Corominas, J., Einstein, H., Davis, T., Strom, A., Zuccaro, G., Nadim, F., Verdel T.: Glossary of terms on landslide hazard and risk. In: Lollino, G., et al. (eds.) Engineering Geology for Society and Territory, vol. 2, pp. 1775–1779. Springer International Publishing, Switzerland (2015)

Corominas, J., Mavrouli, O., Ruiz-Carulla R.: Rockfall occurrence and fragmentation. In: Sassa, K., et al. (eds.) Advancing culture of living with landslides, pp. 75–97 (2017)

Davies, T.R.: Spreading of rock avalanche debris by mechanical fluidization. Rock Mech. **15**, 9–24 (1982)

Guzzetti, F., Ardizzone, F., Cardinali, M., Galli, M., Reichenbach, P., Rossi, M.: Distribution of landslides in the Upper Tiber River basin, central Italy. Geomorphology **96**(1–2), 105–122 (2008)

Guzzetti, F., Mondini, A.C., Cardinali, M., Fiorucci, F., Santangelo, M., Chang, K.T.: Landslide inventory maps: new tools for an old problem. Earth Sci. Rev. **112**, 42–66 (2012)

Hadjigeorgiou, J., Couture, R., Locat, J.: In-situ block size distributions as tools for the study of rock avalanche mechanisms. In: Proceedings of the 2nd North American Rock Mechanics Symposium, vol. 1, Montreal (1996)

Hovius, N., Stark, C.P., Allen, P.A.: Sediment flux from a mountain belt derived by landslide mapping. Geology **25**, 801–804 (1997)

Hovius, N., Stark, C.P.: Landslide-driven erosion and topographic evolution of active mountain belts. In: Evans, S.G., Scarascia Mugnozza, G., Strom, A., Hermanns, R.L. (eds.) Landslides from Massive Rock Slope Failure. NATO Science Series: IV: Earth and Environmental Sciences, vol. 49, pp. 573–590. Springer, Berlin (2006)

Hsü, K.J.: Catastrophic debris streams (sturzstroms) generated by rock falls. Geol. Soc. Am. Bull. **86**, 129–140 (1975)

Hungr, O., Leroueil, S., Picarelli, L.: Varnes classification of landslide types, an update. Landslides **11**, 167–194 (2014)

Kilburn, C.R.J., Sørensen, S.A.: Runout length of sturzstroms: the control of initial conditions and of fragment dynamics. J. Geophys. Res. **103**(B8), 17877–17884 (1998)

Korup, O., Görüm, T., Hayakawa, Y.: Without power? Landslide inventories in the face of climate change. Earth Surf. Process. Landforms **37**, 92–99 (2012)

Legros, F.: The mobility of long-runout landslides. Eng. Geol. **63**, 301–331 (2002)

Li, T.: A mathematical model for predicting the extent of a major rockfall. Z. für Geomorphol. N.F. **27**, 473–482 (1983)

Li, L.P., Lan, H.X., Wu, Y.M.: Comment on "Statistical physics of landslides: New paradigm" by Chen C.-C. et al. EPL **100**(2), 29001 (2012)

Li, L.P., Lan, H.X., Wu, Y.M.: The volume-to-surface-area ratio constrains the rollover of the power law distribution for landslide size. Eur. Phys. J. Plus **129**(5), 89 (2014)

Li, L.P., Lan, H.X., Wu, Y.M.: Effect of sample size on exploiting landslide size distribution. Geoenviron. Disasters **3**, 18 (2016)

Malamud, B.D., Turcotte, D.L., Guzzetti, F., Reichenbach, P.: Landslides inventories and their statistical properties. Earth Surf. Proc. Land. **29**, 687–711 (2004a)

Malamud, B.D., Turcotte, D.L., Guzzetti, F., Reichenbach, P.: Landslides, earthquakes and erosion. Earth Planet. Sci. Lett. **229**, 45–59 (2004b)

Mavrouli, O., Corominas, J.: Comparing kinematically detachable rock masses and rockfall scar volumes. In: International Symposium on Geohazards and Geomechanics (ISGG2015). IOP Conference Series: Earth and Environmental Science, vol. 26 (2015)

Pelletier, J.D., Malamud, B.D., Blodgett, T., Turcotte, D.L.: Scale-invariance of soil moisture variability and its implications for the frequency–size distribution of landslides. Eng. Geol. **48**(3–4), 255–268 (1997)

Shaller, P.J.: Analysis and implications of large Martian and Terrestrial landslides. Ph.D. thesis, California Institute of Technology, 569pp (1991)

Sheidegger, A.E.: On the prediction of the reach and velocity of catastrophic landslides. Rock Mech. **5**, 231–236 (1973)

Stark, C.P., Hovius, N.: The characterization of landslide size distributions. Geophys. Res. Lett. **28**, 1091–1094 (2001)

Strom, A.L.: Some morphological types of long-runout rockslides: effect of the relief on their mechanism and on the rockslide deposits distribution. In: Senneset (Ed.) Landslides. Proceedings of the Seventh International Symposium on Landslides, pp. 1977–1982. Balkema, Trondheim (1996)

Strom, A.L.: Morphology and internal structure of rockslides and rock avalanches: grounds and constraints for their modelling. In: Evans, S.G., Scarascia Mugnozza, G., Strom, A., Hermanns, R.L. (eds.) Landslides from Massive Rock Slope Failure. NATO Science Series: IV: Earth and Environmental Sciences, vol. 49, pp. 305–328 (2006)

Strom, A.L.: Evidence of momentum transfer during large-scale rockslides' motion. In: Williams, A.L., Pinches, G.M., Chin, C.Y., McMorran, T.G., Massei, C.I. (eds.) Geologically Active. Proceedings of the 11th IAEG Congress, Auckland, New, pp. 73–86, 5–10 Sept 2010. Tailor & Frensis Group, London (2010)

Strom, A., Abdrakhmatov, K.: Rockslides and rock avalanches of Central Asia: distribution, morphology and internal structure, p. 459. Elsevier, New York (2018)

Turcotte, D.L., Malamud, B.D.: Landslides, forest fires, and earthquakes: examples of self-organized critical behavior. Phys. A **340**, 580–589 (2004)

# Application of a Statistical Approach to Landslide Susceptibility Map Generation in Urban Settings

Ciro Sepe, Pierluigi Confuorto, Anna Claudia Angrisani, Diego Di Martire, Mariano Di Napoli, and Domenico Calcaterra

## Abstract

Landslide susceptibility maps are effective tools for the mitigation of risks caused by such geological events. In line with recent scientific trends and thanks to the availability of detailed geological data, landslide susceptibility modeling, by means of statistical methodologies, has gained increasing consideration. The present work is based on a methodology widely employed in the field of ecology to draw prediction maps for the occurrence probability of certain species (MaxEnt). The study area is located in Palma Campania, a town sited in the peri-vesuvian area (in the province of Napoli, southern Italy) and characterized by a significant presence of pyroclastic soils, affected by several landslide events, one of which killed eight people in 1986. In this work, eleven geomorphological and geological predisposing factors were selected, based on previous experiences of landslides in peri-vesuvian areas and following several field surveys. Results were critically evaluated using a validation dataset (Receiver Operating Characteristic—ROC curves), by means of Sensitivity-Specificity graphs estimating Area Under Curve (AUC), and other tests such as the Jackknife and response curves, which highlighted the major role played by a number of factors. The consistent agreement between our results and the existing official map demonstrates the validity of the adopted procedure for emergency and land planning.

## 1 Introduction

Landslides are one of the most common geohazards in Italy which cause severe damage each year; in fact, slope instabilities represent the primary cause of death due to natural hazards (Guzzetti et al. 2012). To minimize damage and economic loss (both in emergency and post-emergency phases), as well as the number of casualties caused by landslides, developing valuable comprehension of the factors predisposing to landslide susceptibility is essential (i.e. the likelihood of a landslide occurring in an area based on local terrain conditions), so as to forecast their occurrence. Statistical approaches considering the combination of predisposing factors related to landslide triggering allowed the achievement of a number of improvements in risk management and land planning (e.g. Zizioli et al. 2013; Conforti et al. 2014; Carratù et al. 2015; Finicelli et al. 2016; Hussin et al. 2016). In this paper, a probabilistic approach widely used in ecology for the occurrence probability of species has been applied to the landslide susceptibility assessment of Palma Campania (in the province of Napoli, Italy), a town located in the peri-vesuvian area. Applications of such an approach dealing with "hazards" instead of species occurrence have been suggested by Felicisimo et al. (2013), Convertino et al. (2013), Davis and Blesius (2015), Carotenuto et al. (2017), for the analysis of landslide susceptibility. Such methodologies consist of different procedures named Species Distribution Modeling (SDM) and include

C. Sepe · P. Confuorto · A. C. Angrisani · D. Di Martire
M. Di Napoli · D. Calcaterra (✉)
Department of Earth, Environmental and Resources Science,
Federico II University of Napoli, Largo San Marcellino, 10,
80138 Naples, Italy
e-mail: domenico.calcaterra@unina.it

C. Sepe
e-mail: ciro.sepe@unina.it

P. Confuorto
e-mail: pierluigi.confuorto@unina.it

A. C. Angrisani
e-mail: annaclaudia.angrisani@unina.it

D. Di Martire
e-mail: diego.dimartire@unina.it

M. Di Napoli
e-mail: marianodinapoli@yahoo.it

several statistical approaches (mainly Bayesian) to predict the occurrence of an event in unsampled locations. In a multinomial logistic regression via the MaxEnt algorithm (Maximum Entropy—Philips et al. 2006), geomorphological, geological and anthropic layers (landslides, lithology, slope, aspect, cover thickness, land use, planform curvature, fire-affected areas, distance to rocky scarps, distance to roads and type of road surface) are considered predictors, where locations of detected events and modeled background points are used as response variables. The outcome is a susceptibility map, which also includes the evaluation and the confirmation of model results by means of success and prediction curves. Furthermore, the output susceptibility map has been compared to the existing official one, included in the Municipal Emergency Plan (MEP 2016). The official map was created on the basis of a different semi-probabilistic approach (Calcaterra et al. 2003), which considers fewer parameters with respect to those used in this study. Such a comparison revealed a similar areal pattern with, however, a slight difference in the distribution of susceptibility classes. Our findings showed promising outcomes, highlighting the reliability of a not yet widespread method for landslide distribution susceptibility, which can be useful for land planning purposes and fundamental for the generation of alert systems in MEPs.

## 2 Geological and Geomorphological Setting

Palma Campania is located on the eastern border of the Campanian Plain (Fig. 1). The municipality of Palma C. covers an area of 20.78 km$^2$, of which 78% is flat land (slope angle < 15°), while the residual portion of territory (22%) is occupied by hills or mountains (slope angle > 15°), reaching the highest elevation at 840 m a.s.l., and with a mean elevation of ca. 165 m a.s.l.

From a geological point of view, the territory consists of two main lithological formations represented by (1) Mesozoic carbonate rocks and (2) pyroclastic deposits deriving from the volcanic complex of Somma-Vesuvius and the Campi Flegrei caldera; moreover, debris deposits, sometimes intercalated with pyroclastic materials, are also present. The Mesozoic complex is constituted mainly of Jurassic and Cretaceous limestones belonging to the stratigraphic-structural unit of the Picentini-Taburno Mountains. In particular, it is present along the northwestern slope of Monte Sant'Angelo (762 m a.s.l.), which is part of Mount Pizzo d'Alvano, and is located to the east of the town of Palma Campania. The stratigraphic sequence is completed by incoherent pyroclastic deposits (cinerites, lapilli and

volcanic scoriae), essentially resulting from the explosive activity of Somma-Vesuvius over the past 22,000 years, found both on the mountainous reliefs as well as on the plain; pyroclastic deposits are essentially related to fall out mechanisms. Such pyroclastic deposits, mantling the mountainous slopes, have produced extremely rapid landslides under certain lithostratigraphic and morphometric conditions, and more generally under occurrence of and/or following intense rains. In fact, on the basis of the Southern Apennine Hydrographical District (SAHD) database, and a field survey, the recognized landslides are scattered in the mountainous areas of the communal territory and can be classified as rotational/translational slides, debris flows and complex phenomena (Cruden and Varnes 1996). A relevant case (out of a total of 35 inventoried landslides), occurred on February 22, 1986, in the "Crocelle" locality, when a rapid landslide of about 15,000 m$^3$ destroyed two buildings at the footslope, resulting in the loss of eight lives. (Guadagno et al. 1988).

## 3 Materials and Methods

### 3.1 Methodology: MaxEnt Model

In order to generate the landslide susceptibility map, the MaxEnt method was used.

MaxEnt (Maximum Entropy, Philips et al. 2006) is a general automatic machine-learning method developed to handle missing data issues. It was conceived for species distribution predictions, regardless of the biological details of the species considered. It is a method which does not consider absent information, allowing researchers to include recorded data in their predictions, rather than working with direct sampling. Such an aspect makes this algorithm well suited to drawing probability map distributions of events like landslides (Carotenuto et al. 2017). Entropy is a value which measures the importance of choosing a parameter or an environmental variable within a model. More precisely, entropy is a measure of information content unpredictability, which, if the outcome of an event is unknown, should give us more information and consequently larger entropy (Kornejady et al. 2017). By maximizing the entropy, MaxEnt takes into account variables with the highest information value in order to predict landslide occurrence. Thus, the purpose of MaxEnt is to detect the driving set of variables which cause a pattern to occur. Hence, this set of variables creates the most "susceptible" conditions of the considered process, where susceptibility is a spatially dependent variable (Convertino et al. 2013).

**Fig. 1** Geological map of the south-western portion of the Campanian plain. (1) Alluvial deposits; (2) Travertine; (3) Incoherent ash-fall deposits; (4) Mainly coherent ash-flow deposits; (5) Lavas; (6) Debris and slope talus deposits; (7) Miocene flysch; (8) Middle Jurassic-Upper Cretaceous limestones; (9) Lower Triassic–Middle Jurassic dolomites and calcareous limestones; (10) Outcropping and buried fault; (11) Total isopach lines (m) of the most important Mt. Somma-Vesuvius explosive Plinian and sub-Plinian eruptions. Modified from De Vita et al. (2006)
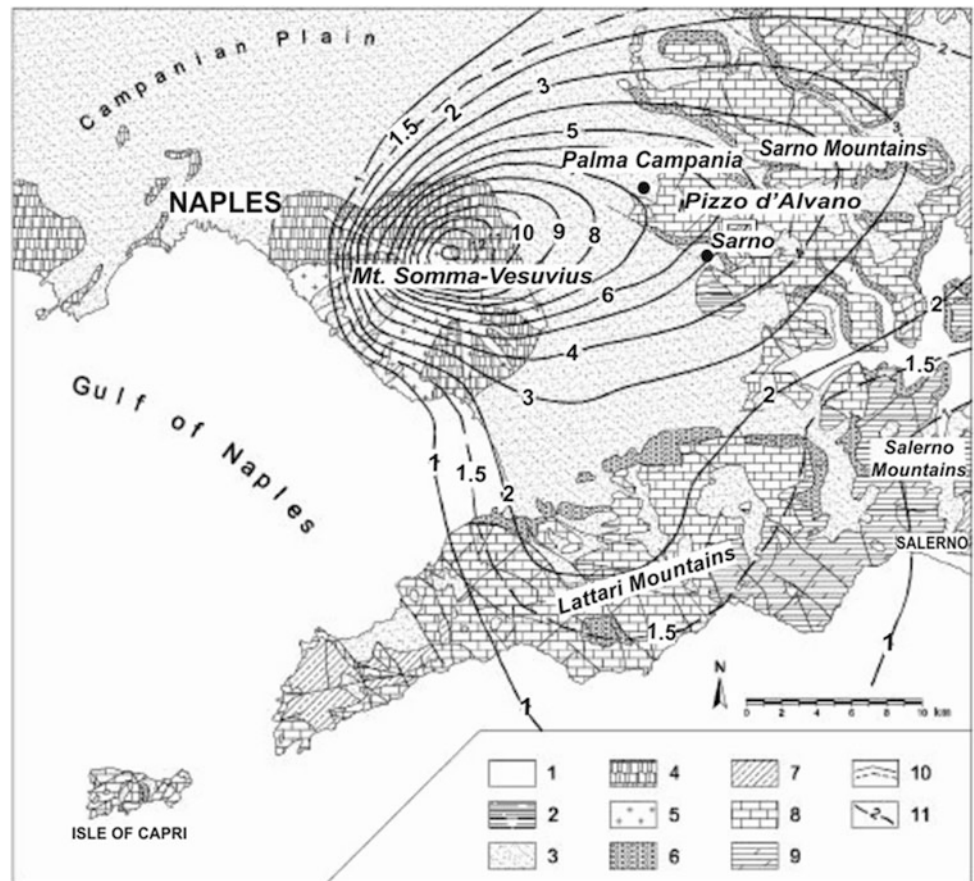


Maximized entropy provides information to predict desired patterns with the highest accuracy. The co-occurrence of environmental variables and their values is what determines landslide susceptibility. Slope stability, in fact, is not ruled by only one variable, and failure conditions are commonly attained through a combination of mutually interacting relevant factors.

Landslide susceptibility assessment (ranging between 0 and 1) is dependent on registered events and environmental variables. The higher the susceptibility, the greater the likelihood of landslide occurrence. The final outcome of the MaxEnt model is an event occurrence probability map, in which each cell expresses a probability value.

The Area Under Curve (AUC) can be used to evaluate the model's performance. AUC is strongly advised for the comparison of two-class classifiers because it summarizes the performance across all possible decision thresholds. Furthermore, MaxEnt determines the ROC curve, plotting the sensitivity (i.e. true positives) versus the specificity (true negative), and also provides statistical tests such as Jackknife. The latter is a useful way to identify the most important variables in the model and to calibrate the parameters of said model.

More details on the MaxEnt approach can be found in Phillips and Dudík (2008).

## 3.2 Materials: Predisposing Factors

The first step towards obtaining a valuable landslide susceptibility map by means of the MaxEnt model is the preparation of a landslide inventory map and the selection of Landslide Predisposing Factors (LPF). The former has been created by SAHD and updated with several field surveys performed in 2016 and 2017, whose photo report is presented in Fig. 2. The study area has been selected excluding most of the flat area of Palma Campania, covering about 8.6 km². The landslide inventory map is composed of 35 landslides, mainly rotational/translational slides, flows and complex landslides, covering ca. 0.2 km² of the territory (corresponding to 2% of the study area), these are represented by points, which refer exclusively to the initiation zone, so to be more suitable for the model.

A Digital Elevation Model (DEM), extracted from the Technical Regional Map (1:5.000) by means of the Topo to Raster interpolation method (available in GIS environment),

**Fig. 2** Field surveys photos:
**a** Landslide main scarp and
deposit; **b** burnt trees and stream;
**c** burnt trees and Palma Campania
inhabited area in the background;
**d** burnt vegetation and limestone
outcrop in the background;
**e** pyroclastic deposit



with a cell resolution of 5 × 5 m (suitable for the scale of
analysis and for the size of landslides here discussed), has
provided the basis for most of the LPFs, namely:

– Slope: a slope map has been obtained from DEM in GIS
  environment. 6 classes were determined, following
  instructions from SAHD: (1) 0°–15°, (2) 16°–27°,
  (3) 28°–35°, (4) 36°–45°, (5) 46°–55°, (6) 56°–90°.
– Aspect: an aspect map has been derived from DEM in
  GIS environment. It is subdivided in 9 classes, every 45°,
  except for the first class, corresponding to flat areas:
  (1) flat areas, (2) N–NE (0°–45°), (3) E–NE (46°–90°),
  (4) E–SE (91°–135°), (5) S–SE (136°–180°), (6) S–SW
  (181°–225°), (7) W–SW (226°–270°), (8) W–NW
  (271°–315°), (9) N–NW (316°–360°).
– Distance from rocky scarps: rocky scarps correspond to
  areas where slope > 55°. A buffer zone of 5 m has been
  set to highlight them.
– Distance to roads: a map highlighting the distance to
  roads and pathways has been obtained considering a
  buffer zone of 5 m.
– Road typology: 3 classes have been considered, based on
  the type of soil on which they are sited. The types are:

(1) road in pyroclastic cover, (2) road in bedrock, (3) not
specified.
– Distance to streams: a distance to stream map has been
  created considering a buffer zone of 5 m along the main
  streams.
– Planform curvature and profile curvature: these two
  features have been obtained with the "curvature" tool, in
  GIS environment.

Moreover, other thematic maps have been added to the
model:

– Lithology: the official geo-lithological map has been
  acquired from the MEP. Six different lithological units
  have been considered for the study area: (1) Pyroclastic
  deposits, (2) Recent detrital-alluvial fan deposits,
  (3) carbonate bedrock, (4) Slope detrital deposits,
  (5) Paleo-fan deposits, (6) Piedmont glacis.
– Cover thickness: the official map of the cover thickness
  of Palma Campania has been created by SAHD and
  further updated during field operations. Five classes have
  been discretized: (1) <0.5 m, (2) 0.5–2 m, (3) 2–5 m,
  (4) 5–20 m, (5) no cover.

- Land use: a land cover map has been obtained by the Corine Land Cover project in 2012. Five different types of cover have been here recognized: (1) Fruit trees and berry plantations, (2) Discontinuous urban fabric, (3) Complex cultivation patterns, (4) Broad-leaved forest, (5) Land principally occupied by agriculture, with significant areas of natural vegetation.
- Burnt areas: a map of burnt areas has been obtained from the MEP and integrated with field observations. Therefore, a thematic map relating to fires between 2000 and 2009 (MEP) has been generated. In addition, field surveys highlighted that 2016 and 2017 fires occurred within previously identified areas, thus confirming the existing data.

## 4   Results

A susceptibility map referring to the initiation zones of landslides over the entire hilly area of Palma Campania (Fig. 3a) has been generated using the MaxEnt software. Training and test data were selected randomly by the software, which took into account 25% of landslides for the test and all landslides for the training dataset. The susceptibility map consists of $5 \times 5$ m cells, derived from the available Digital Elevation Model (DEM) of the area. The MaxEnt mean prediction map has a mean probability of 22%, with the lowest corresponding to 0% and the highest to 96%. The susceptibility map has been divided into 4 classes, using the natural breaks methodology, based on the optimization method (Jenks 1967). Classes range from "null", corresponding to absence of probability of occurrence, to $I_3$, which refers to the highest level of susceptibility. Furthermore, the number of landslides occurring in each considered class and the areal distribution of the different susceptibility classes were calculated. An increasing trend of landslide events towards the higher susceptibility classes has been recognized: class null, class I1, class I2 and class I3, which refer to 5, 15, 23 and 56% of landslides, respectively. As for the areal distribution, this shows a decreasing trend, from 44% in the lowest class (null) to 9% in the highest class of susceptibility ($I_3$). The MaxEnt software is also able to provide statistical-based tests which prove the reliability of the prediction. The first is the ROC curve, which is useful for evaluating the correspondence between the model results and the examined data. The value of the ROC/AUC curve is equal to 0.86 for the training data, while AUC = 0.80 for the test data (Fig. 3b).

Additionally, the Jackknife test, another automatic output of the software, is shown in Fig. 4. It can estimate the importance of each variable in the computation of the probability of occurrence. The result of the Jackknife test consists of histograms, each composed of three colored bars: light blue, dark blue and red. The light blue bar expresses the AUC of the model removing one factor at a time. Similarly, the dark blue bar represents the AUC model using each factor individually. The red bar stands for the model results using all factors together (Kornejady et al. 2017). Therefore, according to the graph, when factors are used one at the time, the slope factor scores the highest AUC value, followed by land use and cover thickness. This means that such factors have the most valuable information when compared to others, and therefore can be considered more predisposing than others. In contrast, profile curvature and distance to streams produced the lowest AUC, highlighting their limited role in landslide probability of occurrence. The largest reduction in AUC, when considering the removal of factors one-by-one (green bar), mainly occurs when excluding lithology and aspect factors. Other outputs of the MaxEnt software are response curves. They show how each environmental variable affects the model prediction. In particular, such curves refer to the marginal effect of changing exactly one variable, whereas the model may take advantage of sets of variables changing together. Burnt areas appear to have a certain role in landslide susceptibility, when compared to areas not affected by fires; aspect response curves show that higher susceptibility is obtained in slopes oriented toward SW, W and NW; rocky scarps do not influence the model. Even though lithology doesn't bear a great weight on the model, the first two classes (pyroclastic deposits and recent detrital-alluvial fan deposits) seem to have greater importance; the distance to streams has a certain impact, as well as the road cut in the bedrock; the slope classes which majorly affect the prediction are the third and the fourth (between 26° and 45°); the most important class of cover thickness is the first, corresponding to values between 0.5 and 2 m of thickness. Finally, the first class of land use (fruit trees and berry plantations) has a higher influence on the model. Our susceptibility map was then compared to the official one, included in the MEP, showing a similar pattern, but with a significant decrease in the areal extension of the highest susceptibility classes: for instance, class $I_3$ went from 15% on the MEP to 9% on the MaxEnt map, therefore decreasing from 1,300,000–780,000 m$^2$ ca.

## 5   Discussion

In this work, a statistical approach has been used to draw a landslide susceptibility map. The analysis of the final map and of the validation tests (e.g. Jackknife) highlights that the factors which bear a major role in the predisposition tolandslide activation are slope and pyroclastic cover thickness, confirming a well-known trend already evidenced in other works on peri-vesuvian landslides (e.g. De Vita et al.
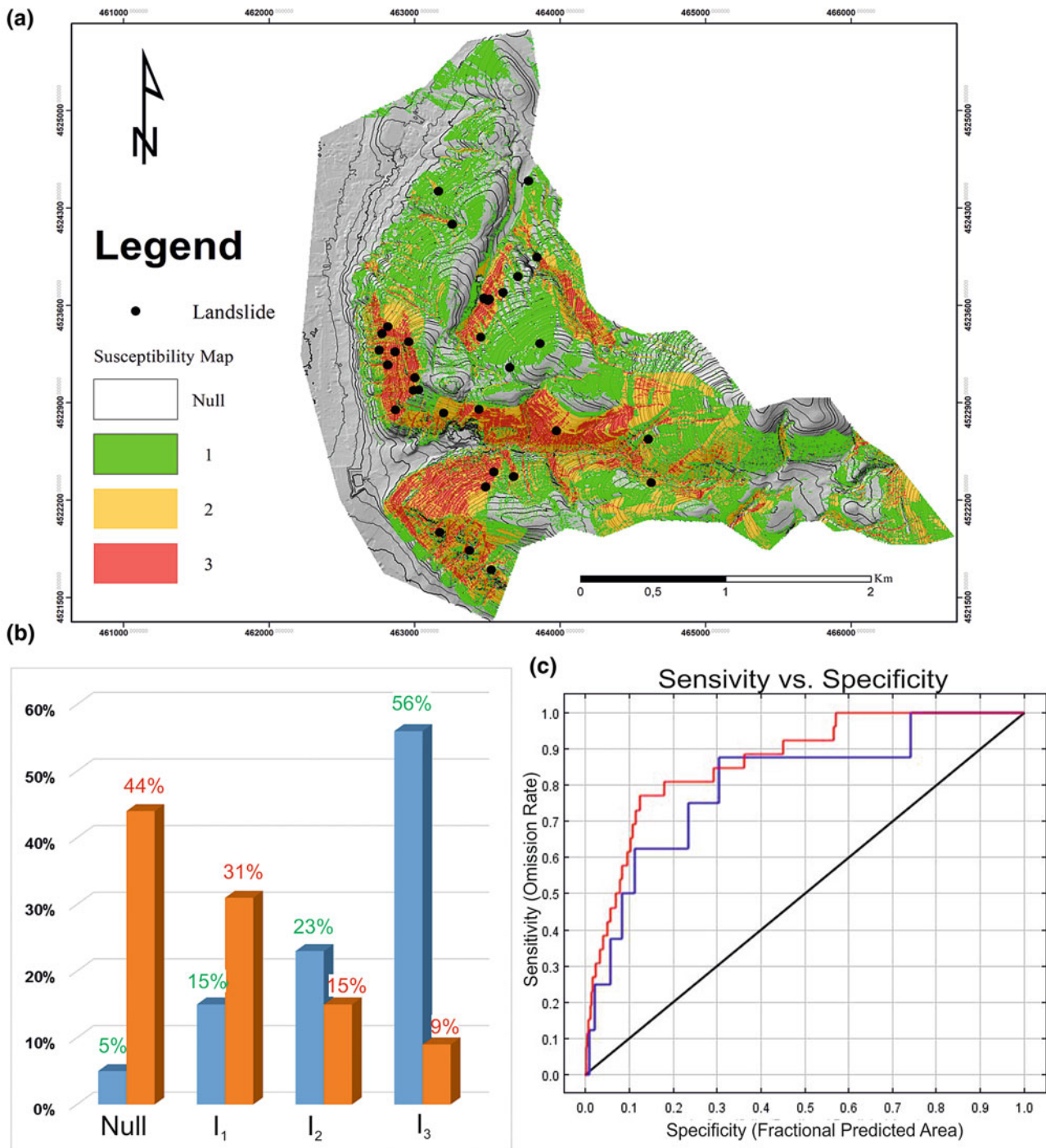
**Fig. 3** **a** Susceptibility map obtained through MaxEnt; **b** histogram showing the areal distribution of susceptibility classes (in orange) and landslides within each class (in blue); **c** sensitivity versus specificity graph

2006). However, land use seems to gain considerable value, as never before because of the coincidence of wildfires with fruit trees, where most of the landslides are located. This is a significant finding, explained by the accelerated alteration of soils due to fires, which can foster slope instability. The positive contribution of slope orientation, instead, is mostly correlated to solar radiation, which determines lower rates of evapotranspiration and thus different values of soil suction. Among the parameters characterized by a lower weight, a certain role is played by road typology. When roads and paths are built on rocky outcrops, cutting the slope profile and therefore interrupting the cover continuity and exposing

**Fig. 4** Jackknife test of AUC for Palma Campania
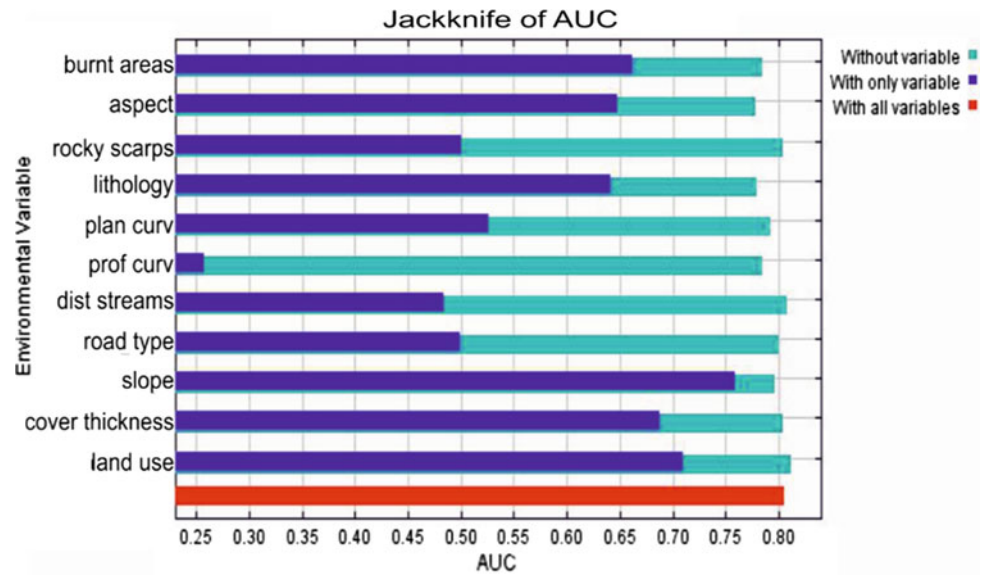


the substrate to weathering, favorable conditions to instability may arise. Profile curvature and distance to streams have the lowest weight, demonstrating that landslides in Palma C. are less dependent on hydrography.

Moreover, the distribution of recorded landslides within the areas classified as susceptible (I1, I2 and I3), points out and demonstrates the suitability of the MaxEnt model as a forecasting tool, testified by 95% of landslides falling within those classes. Comparison with the official susceptibility map, shows a similar areal pattern, demonstrating the value of statistical models such as MaxEnt. In this case, the use of a higher number of parameters makes the susceptibility scenario closer to reality and thus less cautionary, as the MEP is supposed to be.

Thus, the benefits of applying a statistical model such as MaxEnt lie not only in the analysis of each predisposing factor, but also in its capability of working with small datasets, as well as in its ease of use. However, some drawbacks have to be pointed out, mostly due to the fact that landslides have to be treated separately, according to their typology. Here, indeed, only slides, flows and complex landslides have been considered. Such an aspect reduces the size of the database, influencing the reliability of results. Therefore, further field surveys are required to enrich a landslide database. This work further highlights the importance of field activities: many parameters considered in our susceptibility analysis are very peculiar to the study area and thus can only be obtained with an accurate knowledge of the territory. This might also help develop a better understanding of landslide generation processes for specific areas, improving the accuracy of landslide prediction.

## 6 Conclusions

Landslide susceptibility maps are fundamental tools for urban planning and for the generation of alert systems in municipality emergency plans. The use of statistical-based susceptibility maps has become increasingly widespread, and MaxEnt, a model derived from ecology, has been successfully implemented for such purpose in recent years. Here, in the Palma Campania case, 11 landslide-controlling factors were taken into account. Such an amount of information was obtained either thanks to the availability of ancillary data or, most of all, by means of accurate field survey, which enabled a richer knowledge of the territory and of landslide generation. Utilizing MaxEnt showed valuable results, testified by the AUC value of 0.86, as well as by the 95% of inventoried landslides falling within the susceptibility classes. Moreover, MaxEnt was useful to understanding the greater importance of some predisposing factors, such as slope gradient, land use and cover thickness, over others. Comparison with the official susceptibility map showed similarities but also a slight difference in the areal extension of the highest class. This might be due to the fact that the official map considers slope and cover thickness main predisposing factors (Hydrogeomorphological Setting Plan 2015), whilst the present study adds other parameters, obtained through a deeper knowledge of the territory gained by performing field surveys. The latter could thus represent a significant boost to a susceptibility evaluation which is better suited to very local settings and therefore more useful for civil protection purposes, in order to plan mitigation works

with more accuracy, to reduce run-out areas and consequently limit the damage to inhabited areas.

# References

Calcaterra, D., Parise, M., Palma, B.: Combining historical and geological data for the assessment of the landslide hazard: a case study from Campania, Italy. Nat. Hazards Earth Syst. Sci. **3**(1/2), 3–16 (2003)

Carotenuto, F., Angrisani, A.C., Bakthiari, A., Carratù, M.T., Di Martire, D., Finicelli, G.F., Raia, P., Calcaterra, D.: A new statistical approach for landslide susceptibility assessment in the urban area of Napoli (Italy). In: Proceedings of the 4th World Landslide Forum, Ljubljana, Slovenia, vol. 2, pp. 881–889, May 29–June 2, 2017. Springer International Publishing, switzerland (2017). https://doi.org/10.1007/978-3-319-53498-5_100

Carratù, M.T., Di Martire, D., Finicelli, G.F., Calcaterra, D.: Comparison of bivariate and multivariate analyses for landslide susceptibility mapping in the Phlegraean district: the case study of Camaldoli hill (Napoli, Italy). Rend. Online Soc. Geol. It. **35**, 50–53 (2015). https://doi.org/10.3301/ROL.2015.61

Conforti, M., Pascale, S., Robustelli, G., Sdao, F.: Evaluation of prediction capability of the artificial neural networks for mapping landslide susceptibility in the Turbolo River catchment (northern Calabria, Italy). Catena **113**, 236–250 (2014). https://doi.org/10.1016/j.catena.2013.08.006

Convertino, M., Troccoli, A., Catani, F.: Detecting fingerprints of landslide drivers: a MaxEnt model. J. Geophys. Res. Earth Surf. **118**, 1367–1386 (2013). https://doi.org/10.1002/jgrf.20099

Cruden, D.M., Varnes, D.J.: Landslide types and processes. In: Turner, A.K., Schuster, R.L. (eds.) Landslides: Investigation and Mitigation, vol. 247, pp. 36–75. Transportation Research Board, National Research Council, National Academy Press, Washington, DC, Special report (1996)

Davis, J., Blesius, L.: A hybrid physical and maximum-entropy landslide susceptibility model. Entropy **17**, 4271–4292 (2015). https://doi.org/10.3390/e17064271

De Vita, P., Agrello, D., Ambrosino, F.: Landslide susceptibility assessment in ash-fall pyroclastic deposits surrounding Mount Somma-Vesuvius: application of geophysical surveys for soil thickness mapping. J. Appl. Geophys. **59**(2), 126–139 (2006). https://doi.org/10.1016/j.jappgeo.2005.09.001

Felicísimo, Á.M., Cuartero, A., Remondo, J., Quirós, E.: Mapping landslide susceptibility with logistic regression, multiple adaptive regression splines, classification and regression trees, and maximum entropy methods: a comparative study. Landslides **10**(2), 175–189 (2013). https://doi.org/10.1007/s10346-012-0320-1

Finicelli, G.F., Confuorto, P., Carratù, M.T., Di Martire, D.: Multivariate statistical approach vs. deterministic physically-based model for landslide susceptibility assessment. Rend. Online Soc. Geol. It. **41**, 151–154 (2016). https://doi.org/10.3301/ROL.2016.116

Guadagno, F.M., Palmieri, M., Siviero, V., Vallario, A.: The Palma Campania landslide. Geol. Tec. **4**, 18–29 (1988). (in Italian)

Guzzetti, F., Mondini, A.C., Cardinali, M., Fiorucci, F., Santangelo, M., Chang, K.T.: Landslide inventory maps: new tools for an old problem. Earth Sci. Rev. **112**(1), 42–66 (2012). https://doi.org/10.1016/j.earscirev.2012.02.001

Hussin, H.Y., Zumpano, V., Reichenbach, P., Sterlacchini, S., Micu, M., van Westen, C., Bălteanu, D.: Different landslide sampling strategies in a grid-based bi-variate statistical susceptibility model. Geomorphology **253**, 508–523 (2016). https://doi.org/10.1016/j.geomorph.2015.10.030

Hydrogeomorphological Setting Plan: Update year 2015, Naples, Italy (2015) (in Italian)

Jenks, G.F.: The data model concept in statistical mapping. Int. Yearb. Cartography **7**, 186–190 (1967)

Kornejady, A., Ownegh, M., Bahremand, A.: Landslide susceptibility assessment using maximum entropy model with two different data sampling methods. Catena **152**, 144–162 (2017). https://doi.org/10.1016/j.catena.2017.01.010

Municipality Emergency Plan of Palma Campania town (2016)

Phillips, S.J., Anderson, R.P., Schapire, R.E.: Maximum entropy modeling of species geographic distributions. Ecol. Model. **190**(3), 231–259 (2006). https://doi.org/10.1016/j.ecolmodel.2005.03.026

Phillips, S.J., Dudík, M.: Modeling of species distributions with Maxent: new extensions and a comprehensive evaluation. Ecography **31**, 161–175 (2008). https://doi.org/10.1111/j.0906-7590.2007.5203.x

Zizioli, D., Meisina, C., Valentino, R., Montrasio, L.: Comparison between different approaches to modeling shallow landslide susceptibility: a case history in Oltrepo Pavese, Northern Italy. Nat. Hazards Earth Syst. Sci. **13**(3), 559–573 (2013). https://doi.org/10.5194/nhess-13-559-2013

# Multitemporal Landslide Mapping and Quantification of Mass Movement in Red Beach, Santorini Island Using Lidar and UAV Platform

Efstratios Karantanellis, Vassilis Marinos, and George Papathanassiou

## Abstract

Santorini Island constitutes one of most unique geological structures as it compromises a distinctive Miocene volcano. Rockfalls and landslides are widespread phenomena in Santorini due to orientation and steepness of the cliffs which are mainly formed as high elevated lava domes with loose material inside, extruded by sticky, slow-flowing dacite lava. Especially, landslide events in high vulnerable areas can cause significant environmental and socioeconomic impacts. Following a landslide hazard, comprehensive and reliable information on the geotechnical and geometric properties but also on the actual consequences of the phenomenon is mandatory. Today, the evolution of geoscience enables the use of innovative tools such as Unmanned Aerial Vehicles (UAVs) to address emergency response in disastrous situations. As a result, landslide identification and monitoring of large areas can be accomplished economically and timely. During the last decade, the UAV platform has become a useful and reliable research tool in emergency situations such as landslide monitoring. The current research performs a semi-automated method to evaluate and quantify site-specific landslide hazard in the area of Red Beach on the island of Santorini, Greece. Red Beach shows very high tourist activity during the whole year, so it is mandatory for safety reasons to establish guidance to eliminate landslide hazard in prone areas. Considering the availability of high spatial and spectral datasets, multitemporal change detection techniques were performed between two different datasets acquired in February and September of 2017 with a UAV platform. The methodology implemented in the current research revealed the accumulation area of failure, flow direction but also allowed the quantification of the mass movement in the area of interest. The outcome of the current research aims to highlight the usefulness of photogrammetry and UAV platforms to assess and mitigate the potential negative consequences of landslide hazard.

## 1 Introduction

In recent times, natural hazards are posing major trouble in many regions of world and they can cause crucial economic dislocation, environmental impacts and fatal injuries. Human and material losses caused by natural disasters are a significant obstacle to sustainable development for a healthy society (Jaedicke et al. 2014). According to official statistics, Europe is seated in the second place of overall casualties over a period of 100 years with a number of 16,000 losses due to landslide phenomena (EM DAT 2017). More individually, landslides constitute one of the most widespread geo-hazards which take places every year in the territory of Greece and it has terrible consequences in the sustainability (Civil Protection Organization 2016). In most of the cases, those failures are linked as indirect post-events after heavy rainfall or seismic events had occurred locally and the majority has considerable losses (Popescu 2000). The tremendous effects of landslides have serious impacts in the anthropogenic environment and most of the times the event is abrupt with no warning sign of failure. Especially for areas with high touristic activity such as the island of Santorini where every year nearly the 20% of the total number of tourist arrivals for the whole country are concentrated there. As a result, Santorini island has emerged as one of the top island destinations worldwide.

The last decades, Remote Sensing (RS) techniques and Geographical Information Systems (GIS) have been undergone rapid developments investigating the field of landslide

E. Karantanellis (✉) · V. Marinos · G. Papathanassiou
Aristotle University of Thessaloniki, 54124 Thessaloniki, Greece
e-mail: skarantanellls@gmall.com

hazard management. The combination of efficiency and precision acquiring data and analyzing in a time effective manner made the RS and GIS applications integral parts of landslide investigations (Miller et al. 2012). More individually, the use of a low-cost remote sensing approach based on Unmanned Aerial Vehicles (UAVs) and Structure-from-Motion (SfM) techniques were followed to assess and evaluate a specific area on the island of Santorini. Last years, UAVs have shown tremendous growth in the field of landslide management due to their effectiveness and efficiency in gathering valuable data in affected areas (Ahmad et al. 2011). Moreover, in post-emergency situations it can pose an important tool for search and rescue teams and mapping purposes in dangerous locations to avoid direct human interaction (Choi and Lee 2012). It has to be highlighted that the details of SfM and the principles of close-range photogrammetry will not be covered in great extent as it is the application of the platform in slope monitoring and its products which is the main focus.

## 2 Study Area

Santorini Island is located in the south region of the Cyclades Archipelago in the Mediterranean Sea. It is formed completely from volcanic material of the Pre-Minoan eruption era, dacitic and andesitic composition (Antonopoulos 1992). The extrusion of these lavas from sea floor is dated almost 2 million years ago and caused various pyroclastic flows and deposits. It must be mentioned that Santorini Island has a unique morphology with very steep cliffs susceptible to erosion processes (Antoniou and Lekkas 2010).

As a result, many regions in the west part of the island set to be prone in landslide events. The specific area of research is named as "Red Beach" due to the oxidation of the lava composition which gives the characteristic red colour of the scoria formation (Fig. 1). It is situated at the southeastern part of the active volcanic island in "Akrotiri" and the area extends for 1.5 ha with very high touristic activity during the year. The landscape is very steep with the volcanic slopes generally dipping up to 80° and up to 40–45 m in height. The length of the beach is approximately 200 m and its width ranges between 4 and 10 m and it is strongly dependent by the seasonally sea erosion.

In addition, geomaterial of Red Beach is considered as medium to well cemented scoria and compact lavas in the sown parts. In details, it is formed from coarse grained medium cemented volcanic breccia and thin grained well cemented volcanic breccia. Scoria formation has particular, low tensile strength with large open tension fissures and cracks along the area which their development has been monitored during the study period. Moreover, discontinuities of N–S and NE–SW orientation are present in the area perpendicular to the slope direction (Mountrakis et al. 1996). A conceptual model of the engineering geological conditions is presented in Fig. 2. The island of Santorini is a great example of the Quaternary volcanism activity in the wide area of the Aegean. As a consequence, the study area is fully structured from high elevated steep lava domes with loose material inside which constitutes the area prone to landslide phenomena due to erosion processes. In last 20 years, more than 5 rock fall and landslide events caused the local authorities to be emerged and propose further investigations.



**Fig. 1** Location of "Red Beach" and the 3D model of the area
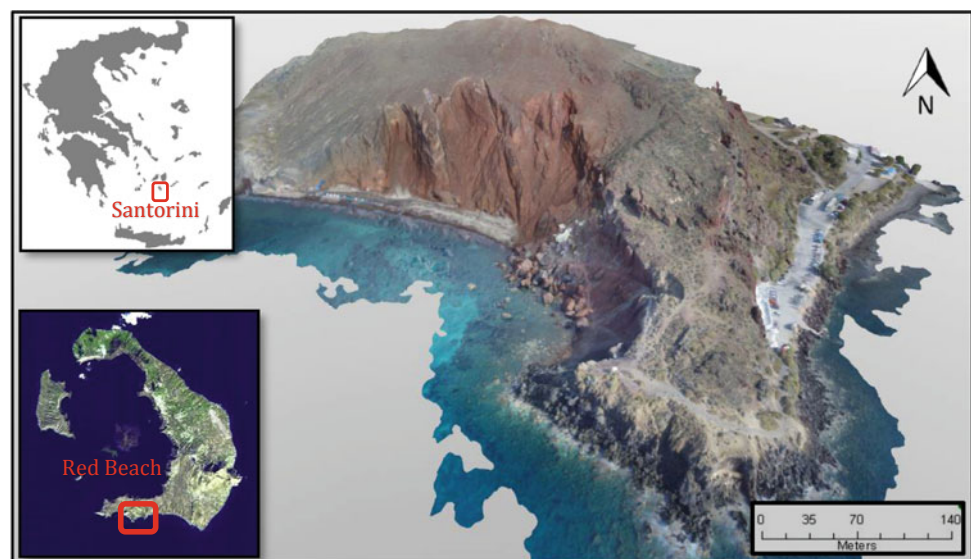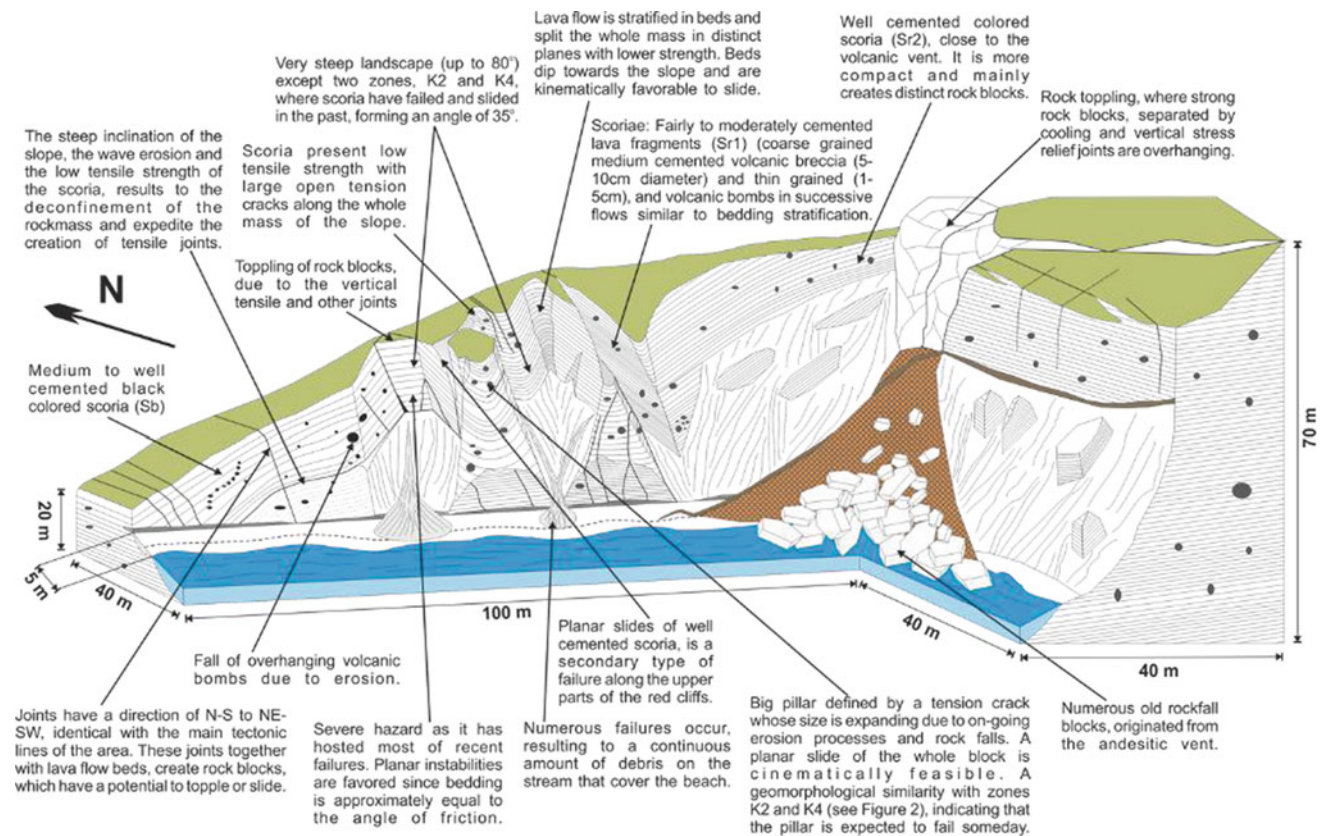
**Fig. 2** Conceptual model on the engineering geological condition along the Red Beach (Marinos et al. 2017)

## 3  Background & Methodology

### 3.1  UAV Background

During last years, the use of UAVs in landslide monitoring has shown an extreme growth (Colomina and Molina 2014) and the future seems more promising. Those platforms are able to fly and collect datasets over disastrous areas where human interception is inevitable for in situ studies (Bendea et al. 2008). Most of the studies are focusing in the delineation of the affected area from UAV orthophotos and the classification of the hazardous area based on a number of factors (Tahar et al. 2016). In contrary, some researchers choose to follow a more topographic approach by using as main input a high resolution Digital Surface Model (DSM) of the landslide area in order to identify the affected area based on topographic factors such as slope and aspect. In late years, Niethammer et al. (2010) has executed several flights using a micro-UAV to investigate the DSM generation in the Super-Sauze landslide in France which costed several human lives. Moreover, Murphy et al. (2016), showed the usefulness of UAVs in landslide monitoring by performing machine vision techniques in 3D reconstruction

of Oso mudslide in Washington. In addition, D'Oleir-e-Oltmanns et al. (2012) used a fixed-wing UAV mounted with a compact camera to collect data to produce detailed DSMs to monitor gully erosion in the area of Morocco. Also, Rau et al. (2012) performed several flights over large area to delineate landslide displacements with a fixed-wing platform. In contrary, Lidar sensors for landslide studies are dealing with the characterization of the affected area and they are characterized with the advantage of mitigating the influence of vegetation. In most of the landslide cases, months or years after the event the vegetation is well re-structured and slide characteristics such as scarp and/or the flanks are not visible from a passive sensor (Sui et al. 2008). Therefore, Lidar constitutes a valuable tool in monitoring and detecting unstable vegetated slopes. In addition, a great example is presented in Koma et al. (2014) where both active and passive sensors are compared in extraction of geomorphic and geological characteristics in a case study occurred in Vorarlberg, Austria.

A principal objective of the current project was to exploit the advantage of using a UAV platform to acquire precise data in hazardous areas. In the current case, datasets were compromised from three different epochs. The first was collected with a Lidar sensor in 2013 as a post-event

capturing and it will be used as α validation dataset. The initial visit begun when the local authorities were emerged after a heavy rainfall which resulted in a huge landslide and transformed Red Beach area inaccessible for couple of months. Till nowadays, the area is characterized in "red alert" and people enter the area on their own risk. The second dataset was collected with a UAV platform in February 2017, 4 years after the initial event, followed by another flight six months later in late September. The details and specifications of flight campaigns are presented in Table 1.

## 3.2 UAV Mapping

In the current case study, we used a commercial mini-UAV quadrotor platform with a stabilized built-in camera (Sony EXMOR—12.4 Megapixel) mount on to capture and collect images for the generation of the 3D model and the respective orthophoto of Red Beach in Santorini island (Fig. 3). The platform uses onboard the GPS/GLONASS navigation system. Moreover, it has been used black & white paper targets as Ground Control Points (GCPs) distributed along the area to create an arbitrary coordinate system. The latter was performed based on manual identification of natural and/or artificial objects identified on the images and surveyed during the field trip. During the creation of the 3D model, a small number of GCPs were used in image processing step to correctly calibrate the resulted model. The remaining points were used to acquire a verification of model scaling and an estimation of the model error propagation. Each of the campaigns' details are presented in Table 1 with the respective Ground Sampling Distance (GSD) and the respective Root Mean Square Error (RMSE).

The magnitude of the Red Beach declivity, about 300 m in length and around 50 m in height, as well as the inaccessible and dangerous environment due to the continuous rock falls and slides, requires meticulous measurement management by using classical and up- to- date surveying documentation methods. To achieve the best available coverage of the area but in the same way to keep resolution in high standards (submeter) the flights were performed with a predefined flight path with 75% of sidelap and nearly 80% frontlap. The 3D point cloud generation and the image

processing step were performed using a commercial available software, Pix4D (2017). Ground control points were distributed along the area where was accessible. The distances among the targets were measured manually in order to facilitate an arbitrary coordinate system to correctly scale the 3D model. On each acquisition time, 30–35% of the GCPs were used as points to verify the model error propagation. Furthermore, to derive the final 2D and 3D products, any inconvenient noise due to moving objects (people on the beach) and shadows from the sun angle of the acquisition time had been removed. Next step was to generate the dense point cloud as it constitutes the basis for the image analysis stage.

## 4 Analysis

A successful identification and characterization of slope instability processes relates directly to the temporal and spatial quality of the 2D and 3D products. Essential factor in this process forms the precise and accurate alignment between the compared epoch datasets to minimize any inconvenient noise. Once the model is generated the following critical steps are feature extraction and surface measurements (Remondino et al. 2011). In the current study, the initial step was to perform a quantitative analysis based on change detection techniques to extract the volume of the displaced material between the studied epochs. Based on the extracted result, a scenario-based analysis of the rate of movement with the respective flow direction has been extracted and presented. The areas of Red Beach with high potential risk are visualized in Fig. 4, as they were presented in a previous research of Marinos et al. (2017). Following the aforementioned research a more detailed approach of the quantification of the mass movement is attempted in the current study.

The initial step in post-image processing was to detect any changes based on the 3D point cloud. The alignment between the two datasets resulted in an acceptable RMS error below 1 as a result the map constitutes a reliable information for further analysis (Castagnetti et al. 2014). In, the result of the change detection analysis is visualized after the alignment and co-registration between the two clouds

**Table 1** Flight campaigns specification

| Campaign (month/year) | Images | GCPs | GSD | Mean reprojection error (pixel) | RMSE vertical | RMSE planimetric | Orthophoto resolution | DSM resolution |
|---|---|---|---|---|---|---|---|---|
| Feb-2017 | 232 | 5 | 2.50 | 0.215 | 0.51 | 0.94 | 2.5 | 4 |
| Sept-2017 | 207 | 5 | 2.96 | 0.223 | 0.42 | 0.86 | 2.9 | 4 |

**Fig. 3** Orthophotos and respective DSMs—February 2017 (**1a–2b**) and September 2017 (**2a–2b**)
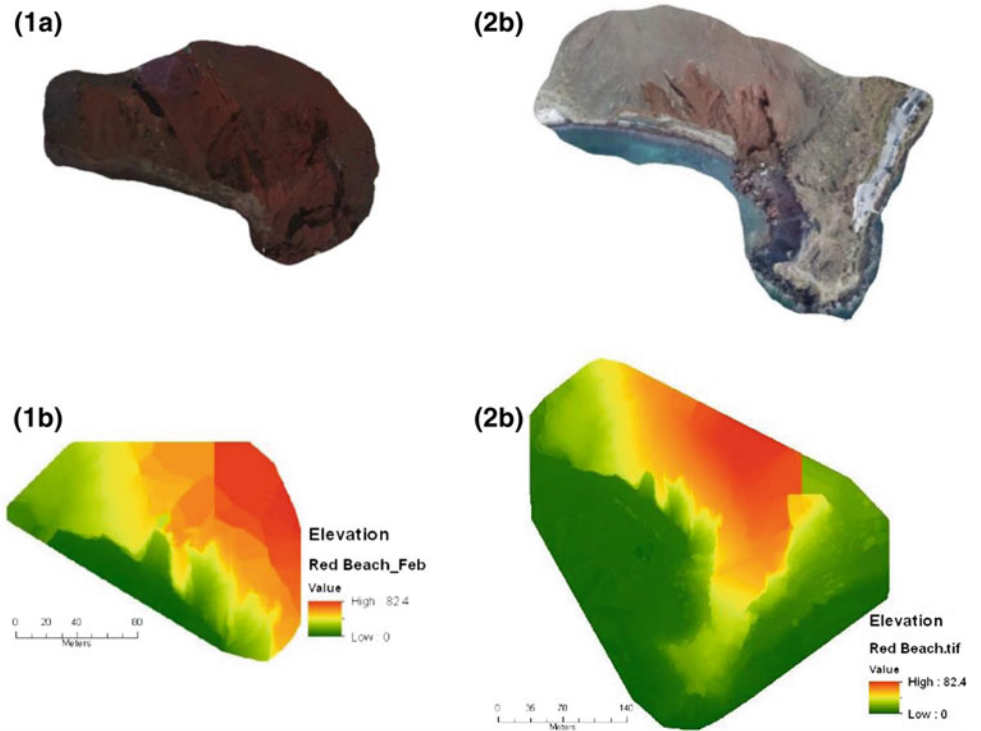


**Fig. 4** Close-up of the areas of interest at Red Beach in oblique view
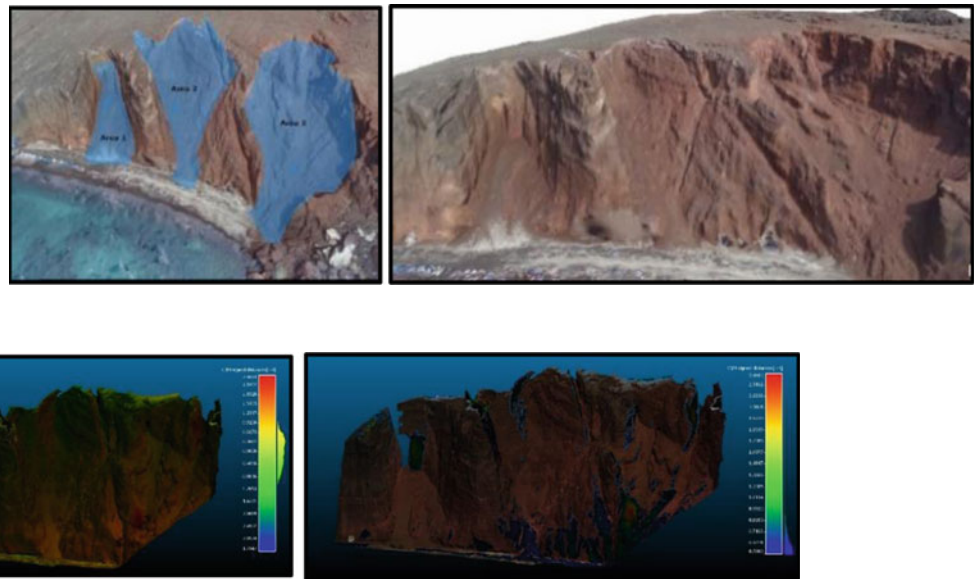




**Fig. 5** Change detection analysis between January and September 2017. Left overall changes are presented and on the right the significant changes in the displaced material

where the areas with significant change are colorized with the "blue-yellow-red" colour ramp in Fig. 5. Significant changes are highlighted in the right image. Both image comparison stages took account the resulted RMS error before executing any further analysis as a result it is integrated in the image analysis. As a result, the mentioned differences between the studied epochs represent the displacements as accumulated material in the study period.

The following step includes the estimation of volume displacements during the 6-months period. Quantitative analysis has been performed on the 3D point cloud and mesh. The volume of the displaced material in each region

**Table 2** Displaced material with the respective Area of Interest

| Area of interest | Area extent (m²) | Displaced volume |
|---|---|---|
| Area 1 | 778 m² | 152 m³ ± 1 |
| Area 2 | 1693 m² | 39 m³ ± 1 |
| Area 3 | 2122 m² | 58 m³ ± 1 |

respectively is illustrated in Table 2 for the 6-month study period (Feb 17–Sept 17) with the respective area extent in square meters. Area 1 is shown the most significant movement as more than 150 m³ material has been displaced on the toe of the region posing great danger for the swimmers and for the visitors. In contrary, Area 2 and Area 3 are shown smaller movements with 39 and 58 m³ of displaced material respectively, accumulated on the toes of slopes.

Most of the morphological changes is represented as toppling due to stress relief and in second place, due to erosion and weathering processes such as superficial erosion which are related to serial precipitation events or extreme ones. Furthermore, the study area is characterized strongly for rare rainfall events but most of them are short and extreme which result in fluctuations in the water saturation in the clay-rich topsoil layer. In the same way the engineering characteristics of the study area are in poor condition such as the soil cohesion. Toppling of rock blocks, due to the vertical tensile and other joints, is the main failure mechanism along the rock cliffs in the area of Red Beach. Rock toppling is also the principal mechanism along the old volcanic vent, where strong rock blocks, separated by cooling and vertical stress relief joints are overhanging. In addition, planar slides of mentioned scoria, is the other type of failure along the upper parts of the Red Beach cliffs. The planes of lava flow dip with the same dip direction of the main slope of the area 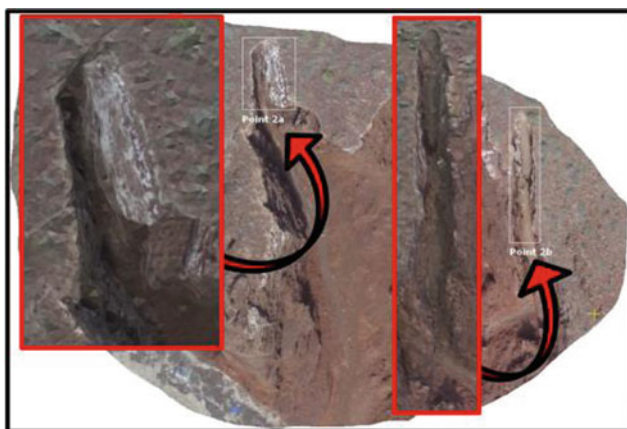and daylight to the slope surface Moreover, the development of two fissures were monitored during the study period above the scarp of Area 2 visualized in Fig. 6. First, 2A a

studied fissure which has been imitated since 2013 showed extreme growth during the 6-month period. The 2A fissure has been initiated around 2013 and it was estimated that between the 6 month period showed a growth of 70 cm in length and 25 cm in width. Its openness is calculated around 50 cm and total length in 120 cm. In addition, 2B fissure has shown smaller changes. Its openness was estimated at 35 and 10 cm in width. The resulted changes are adds-on that erosion shows great influence on the landslide dynamics of Red Beach.

## 5 Conclusion

In conclusion, the use of UAV platforms presents an extreme increase in the field of landslide monitoring. UAV constitute an effective tool to acquire rapidly and with no danger data from inaccessible areas. The aim of this work was to indicate the use of a UAV to monitor any displacements in a hazardous area and to determine the volume of and flow accumulation of the displaced material between a 6-month period. Results have shown that overlapping imagery can be adopted as an effective tool for landslide mapping and identification. Also, a significant challenge was to test the effectiveness of collecting accurate measurements against any critical issues such as bad weather conditions, occlusions, and exposure issues. In terms of accuracy of the derived products, 3D point deviation was compared based on the z-axe against a TLS-based DSM. The RMSE was estimated below 1 in all our cases. The three hazardous areas where examined individually by using the 3D point cloud of February 2017 as a baseline to measure any displacements. As it is illustrated in it can be extracted that specific areas show critical displacements even if the study period looks short (6 months). As a result, most of the material is concentrated on the toe of each of the three slides where it is accumulated since the initial event.

## 6 Future Work

Further research is needed, to develop a novel automated approach for multi-sensor and multi-resolution data fusion based on RS techniques and close-range photogrammetry. In addition, future research has to establish a framework within the adopted method to assess the transferability and



**Fig. 6** Fissure development above the scarp in area 2

efficiency in different landslide scenarios. Furthermore, continuous datasets will be gathered in time periods of 6-months to 1-year in Red Beach area, Santorini to establish a standard velocity of the mass movement in the region of interest. In the end, there is need to propose adaptive strategies for multi-hazard assessment of the region to prevent further environmental degradation and negative consequences for the local society.

# References

Ahmad, A., Tahar, K.N., Aziz, W.A.: Unmanned aerial vehicle technology for large scale mapping. Buletin Gis Geomatik Jabatan Ukur dan Pemetaan Malaysia **2**, 98–108 (2011)

Antoniou, A.A., Lekkas, E.: Rockfall susceptibility map for Athinios port, Santorini Island, Greece. Geomorphology **118**, 152–166 (2010). https://doi.org/10.1016/j.geomorph.2009.12.015

Antonopoulos, J.: The great Minoan eruption of Thera volcano and the ensuing tsunami in the greek archipelago. Nat. Hazards **5**, 153–168 (1992). https://doi.org/10.1007/BF00127003

Bendea, H., Boccardo, P., Dequal, S., et al.: Low cost UAV for post-disaster assessment. In: Proceedings of the XXI Congress: International Society for Photogrammetry and Remote Sensing, Beijing, China, vol. XXXVII, pp. 1373–1380, 3–11 July 2008

Castagnetti, C., Bertacchini, E., Corsini, A., Rivola, R.: A reliable methodology for monitoring unstable slopes: the multi-platform and multi-sensor approach. 92450 J (2014). https://doi.org/10.1117/12.2067407

Choi, K., Lee, I.: A UAV based close-range rapid aerial monitoring system for emergency responses. In: ISPRS—The Interantional Archives of the Photogrammetry and Remote Sensing and Spatial Information Sciences, vol. XXXVIII-1, pp. 247–252 (2012). https://doi.org/10.5194/isprsarchives-xxxviii-c22-247-2011

Civil Protection Organization: Greek Civil Protection (2016). http://civilprotection.gr/el

Colomina, I., Molina, P.: Unmanned aerial systems for photogrammetry and remote sensing: a review. ISPRS J Photogramm Remote Sens **92**, 79–97 (2014). https://doi.org/10.1016/j.isprsjprs.2014.02.013

D'Oleire-Oltmanns, S., Marzolff, I., Peter, K.D., Ries, J.B.: Unmanned aerial vehicle (UAV) for monitoring soil erosion in Morocco. Remote Sens **4**, 3390–3416 (2012). https://doi.org/10.3390/rs4113390

EM DAT: The International Disaster Database (2017). http://www.emdat.be/

Jaedicke, C., Van Den Eeckhaut, M., Nadim, F., et al.: Identification of landslide hazard and risk "hotspots" in Europe. Bull. Eng. Geol. Environ. **73**, 325–339 (2014). https://doi.org/10.1007/s10064-013-0541-0

Koma, Z., Székely, B., Dorninger, P., et al.: Comparison of UAV and TLS DTMs for acquisition of geological, geomorphological information for Doren landslide, Vorarlberg Austria. **16**, 11513

Marinos, V., Prountzopoulos, G., Asteriou, P., et al.: Beyond the boundaries of feasible engineering geological solutions: stability considerations of the spectacular Red Beach cliffs on Santorini Island. Environ. Earth Sci., Greece (2017). https://doi.org/10.1007/s12665-017-6823-2

Miller, P.E., Mills, J.P., Barr, S.L., et al.: A remote sensing approach for landslide hazard assessment on engineered slopes. IEEE Trans. Geosci. Remote Sens. **50**, 1048–1056 (2012). https://doi.org/10.1109/TGRS.2011.2165547

Mountrakis, D., Pavlides, S., Chatzipetros, A., Meletlidis, S.: Active deformation of Santorini European commission volcanic risk. In: Proceedings of the Second Workshop on European Laboratory Volcanoes (1996)

Murphy, R.R., Duncan, B.A., Collins, T., et al.: Use of a small unmanned aerial system for the SR-530 mudslide incident near Oso. Washington, DC **33**, 476–488 (2016). https://doi.org/10.1002/rob

Niethammer, U., Rothmund, S., James, M.R., et al.: Nav-based remote sensing of landslides. Int. Arch. Photogramm. Remote. Sens. Spat. Inf. Sci. ISPRS Arch. **38**, 496–501 (2010)

Pix4D: Pix4D (2017)

Popescu, M. E.: Landslide causal factors and landslide remediatial options. Landslides and related slope instability phenomena plague many parts of the world. A wealth of experience has been accumulated in recent years in understanding, recognition and treatment of land, pp. 1–21 (2000)

Rau, J.Y., Jhan, J.P., Lo, C.F., Lin, Y.S.: Landslide mapping using imagery acquired by a fixed-wing UAV. ISPRS Int. Arch. Photogramm. Remote Sens. Spat. Inf. Sci. **XXXVIII-1**, 195–200 (2012). https://doi.org/10.5194/isprsarchives-xxxviii-1-c22-195-2011

Remondino, F., Barazzetti, L., Nex, F., et al.: UAV photogrammetry for mapping and 3D modeling. Curr. Status Future Persp. **XXXVIII**, 14–16 (2011). https://doi.org/10.5194/isprsarchives-xxxviii-1-c22-25-2011

Sui, L., Wang, X., Zhao, D., Qu, J.: Application of 3D laser scanner for monitoring of landslide hazards. Int. Arch. Photogramm. Remote Sens. Spat. Inf. Sci. **XXXVII**, 277–282 (2008)

Tahar, K.N., Ahmad, A., Papamichail, D., et al.: International conference on recent trends in physics 2016 (ICRTP2016). J. Phys. Conf. Ser. **755**, 11001 (2016). https://doi.org/10.1088/1742-6596/755/1/011001

# Extreme Flood and Landslides Triggered in the Arroscia Valley (Liguria Region, Northwestern Italy) During the November 2016 Rainfall Event

Giacomo Pepe, Andrea Mandarino, Emanuele Raso, Andrea Cevasco, Marco Firpo, and Nicola Casagli

## Abstract

From November 20th, 2016, to November 25th, 2016, Liguria Region (northwestern Italy) experienced prolonged and intense rainfall. The rainfall sequence occurred following two main phases. The second phase mainly hit the western sector of the region, reaching its peak on November 24th. Rainfall was particularly abundant within the Arroscia valley, where the 5–days cumulative rainfall locally exceeded 50% of the mean annual precipitation. In this paper, we document the rainstorm magnitude, presenting a first inventory of the rainfall–induced ground effects within the Arroscia Valley. The mapping was performed by means of extensive field work that was partly supported by satellite imageries. More than 250 landslides affected the upper sector of the valley, while in the downstream reach, widespread flood-related forms and processes resulting from the abundant precipitation were mapped. The results of this study are expected to be helpful for future research on both landslide– and flood–related channel change susceptibility and risk scenarios evaluation.

## Keywords

Extreme flood • Heavy rainfall • Landslide mapping • Liguria

## 1 Introduction

In the last decades, Liguria Region (northwestern Italy) has often experienced considerable Damaging geo–Hydrological Events (DHEs) (Cevasco et al. 2015) leading to important environmental, social and economic consequences. Due to its geographical, geological and geomorphological settings, this region is prone to landslides and floods. Because of severe weather conditions, which are mainly characterized by intense and sometimes very localized rainfall, DHEs were recently recorded in the eastern (Cevasco et al. 2014, 2017), central (Silvestro et al. 2012; Faccini et al. 2015) and western (Guzzetti et al. 2004; Segoni et al. 2009) sectors of this region. During the autumn of 2016, a severe rainstorm hit northwestern Italy, and rainfall was particularly abundant in western Liguria, where widespread landslides and flood peaks seriously damaged infrastructure, private homes and agricultural activities. The rainfall-induced consequences were particularly severe within the Arroscia Valley. In this paper, we analyzed this rainfall event and present a first inventory of the rainfall–induced ground effects within the Arroscia Valley. The main purposes of this paper are as follows: (i) to describe the type and the abundance of the rainfall–induced ground effects and (ii) to study the rainfall conditions that triggered both landslides and fluvial processes.

## 2 Study Area

The Arroscia Valley is situated in the western part of the Liguria Region (Fig. 1), and it is an east-west trending valley whose drainage basin area is approximately 290 km². The main stream is the Arroscia Torrent that rises from Mt. Frontè (2151 m), which represents the highest elevation of the basin. The Arroscia Torrent flows approximately eastward, receiving several tributaries. Both the upper and the intermediate segments of the valley are characterized by

G. Pepe (✉) · A. Mandarino · E. Raso · A. Cevasco · M. Firpo
Department of Earth, Environmental and Life Sciences,
University of Genova, Corso Europa 26, 16132 Genoa, Italy
e-mail: giacomo.pepe@unige.it

N. Casagli
Department of Earth Science, University of Florence,
Via La Pira 4, 50121 Florence, Italy

mountainous landscapes while the downstream reach shows gentle slopes and a somewhat wide floodplain. From a geological point of view, the study area is characterized by the tectonic units involved in the front of the Ligurian Alps that belong to the Piedmontese continental margin Domain and the Piedmontese–Ligurian oceanic Domain. The former includes the alternation of carbonate and siliciclastic successions, and the latter is mainly composed of carbonate flysch (Decarlis et al. 2013; Pepe et al. 2015).

## 3  The November 20th–25th, 2016, Event

From November 20th, 2016, to November 25th, 2016, prolonged and intense rainfall affected a wide portion of Liguria. The rainfall sequence occurred in two main phases. The first phase (November 20th–22nd) mainly hit the central zone of the region. On the other hand, during the second phase (November 23rd–25th), rainfall was abundant in the western sector. Additionally, due to also orographic effects brought by the Western Ligurian Alps, the rainfall magnitude was higher in the inland territories located close to the watershed separating the southern side of the region from the northern side. From the early hours of November 23rd, significant rainfall episodes repetitively affected the Arroscia Valley. The largest cumulative daily rainfall magnitudes were reached at Mendatica (206 mm), Poggio Fearza (168 mm), Pornassio (164 mm) and Pieve di Teco (134 mm). The rainstorm reached its peak on November 24th and was particularly concentrated in the upper portion

of the basin, where prolonged rainfall occurred, some of which occurring in bursts. As seen from the rainfall diagrams (Fig. 2a), inside the most affected area, rainfall followed a similarly temporal trend; it was strongly localized and characterized as high-magnitude in terms of cumulated rainfall. The highest cumulative rainfall values were recorded at Pieve di Teco, where up to 364.6 mm in 24 h was measured. Slightly lower values were recorded at Pornassio and Poggio Fearza. The highest cumulative values during the 5–days rainfall period were measured at Mendatica (800.4 mm). Rainfall was less intense and abundant both in the middle and the lower section of the basin. However, in response to the rainfall that fell in the inland territories during the late evening of November 24th, the hydrometric level of the Arroscia Torrent rose up to 5.56 m (Fig. 2b), overflowing its banks. With reference to the Pieve di Teco station, the cumulative rainfall measured during the November 20th–25th, 2016, event (i.e., 661.4 mm) was 30 and 56% higher than the mean monthly (196.4 mm) and the mean annual precipitation (1176.6 mm) values, respectively.

## 4  Rainfall–Induced Ground Effects

After the rainfall event, we performed field surveys to prepare an inventory of the rainfall–induced ground effects. Landslides and flood–related forms (e.g., bank erosions, overbank deposits and undercut and damaged bank protections) were identified and mapped in the field using topographic base maps (at 1:5000 scale) and a common GPS
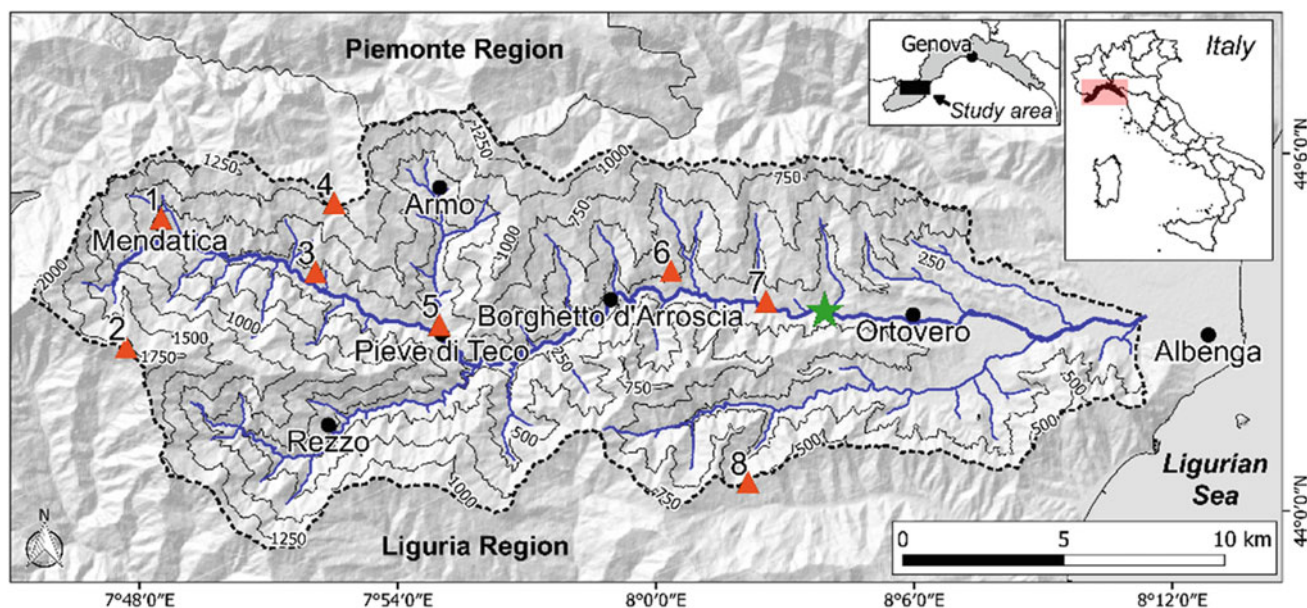


**Fig. 1** Location of the study area. Dotted black line: Arroscia basin; black circles: main villages; red triangles: rain gauge stations (1 Mendatica, 2 Poggio Fearza, 3 Pornassio, 4 Colle di Nava, 5 Pieve di Teco, 6 Ranzo, 7 Onzo Ponterotto, 8 Testico); green star: Pogli d'Ortovero hydrometer

Fig. 2 **a** Cumulative rainfall and **b** hydrometric level recorded by the rain and the stream gauges (see Fig. 1 for location) from November 20th, 2016, to November 25th, 2016
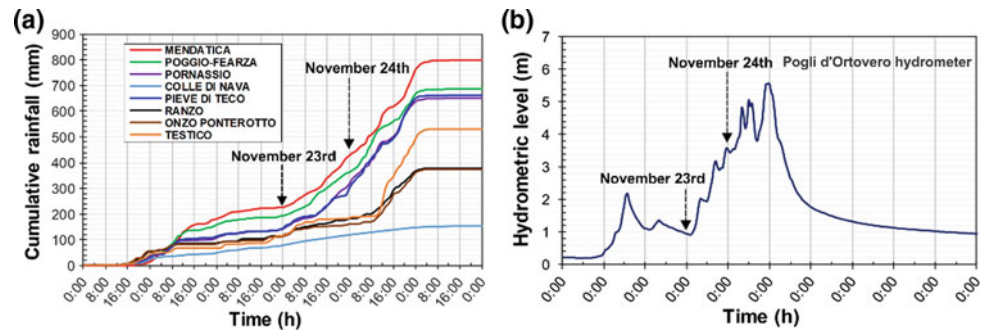


Fig. 3 **a** Spatial distribution of the cumulative rainfall for the November 20th–25th rainfall event and related rainfall–induced landslides. Continuous blue lines: isohyets in millimeters; black triangles: rain gauges (1 Mendatica, 2 Poggio Fearza, 3 Pornassio, 4 Colle di Nava, 5 Pieve di Teco); orange dots: landslides. **b**, **c** Examples of rainfall–induced shallow landslides
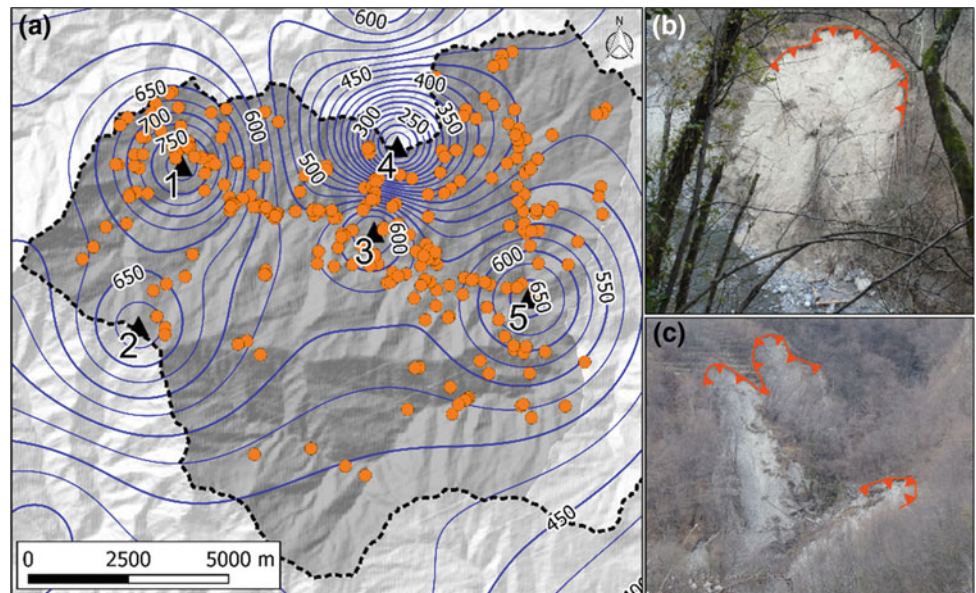


device. The mapping activity was undertaken along main, secondary and farm roads. At panoramic points of view, we took photographs of inaccessible slope areas to accurately map the landslides on topographic maps and to help identify the landslide type. Subsequently, mapped elements were manually digitized in GIS environment. Digital mapping was aided by analyzing satellite imageries acquired from the Emergency Management Service (E.M.S. emergency.-copernicus.eu), realized with the support of the European Spatial Agency (E.S.A.) just a few days after the event, and from post–event Google Earth satellite images.

## 4.1 Landslides

We mapped a total of 280 landslides. As can be seen from Fig. 3a, the landslide spatial distribution is not homogeneous throughout the affected area, and there is no clear agreement concerning cumulative rainfall values.

The map was constructed using the 5–days cumulative rainfall values recorded by 43 rain gauges (eight located

within the study area and thirty-five in the surrounding areas) and applying the inverse distance weighting (IDW) interpolation method. The landslide inventory map covers an area of 127 km$^2$ (40% of the Arroscia total drainage basin area), and the resulting average landslide density was 2.2 slope failures/km$^2$. Rainfall-induced landslides were mainly located in the northwestern sector of the upper Arroscia catchment. Most of the rainfall–induced landslides were shallow (Fig. 3b, c), whereas only a few cases of deep–seated failures were recognized. Landslides were classified according to the classification proposed by Hungr et al. (2014) (Table 1).

Generally, shallow landslides were mainly triggered as debris slides involving eluvial–colluvial and anthropically reworked deposits directly overlying the bedrock. Subsequently, many shallow landslides evolved into debris–avalanches and less frequently into debris–flows. The rupture surface was mostly planar and parallel to the topographic surface and corresponded to the interface between the slope deposits and the weathered or fresh bedrock. In a few cases, sliding of a mass of soil on a rotational rupture surface was

**Table 1** Summary of the landslides inventoried after the November 20th–25th rainfall event in the upper Arroscia Valley

| Landslide type | N | % | Involved material |
|---|---|---|---|
| Debris slide | 128 | 45.7 | Eluvium, colluvium, reworked soils |
| Debris avalanche | 123 | 43.9 | Eluvium, colluvium, reworked soils |
| Debris flow | 29 | 10.4 | Eluvium, colluvium, weathered bedrock |
| Total | 280 | 100 | |

observed. Damage was particularly severe at Lavina di Rezzo, where a debris flow travelled long distances, overran private houses and damaged a main road.

## 4.2 Flood-Related Forms and Processes

In the upper and middle segments of the Arroscia Torrent, the flood remained confined in the fluvial channel, and only a few mass movements due to slope undercutting were observed. In the downstream part of the mountainous reach, small, flat areas adjacent to the bank edge were flooded and covered by overbank deposits. Downstream of the Ortovero village up to the outlet, most flood–related fluvial processes were recognized, even if this reach was almost completely channelized (mainly using longitudinal gabions and groynes). Here, the flood caused intense and pre-existing bank erosions and triggered new consistent bank retreats due to the collapse of bank protections (Fig. 4). Furthermore, a general condition of undercutting affected most of the longitudinal and cross defenses. Because of lateral erosion processes and the reactivation of stabilized surfaces located between groynes, an increase in the active channel width was mapped. In the floodplain reach, no relevant flooding occurred. The whole discharge remained between bank protections, highlighting that the channel was somewhat incised.

## 5 Final Remarks

In this paper, we analyzed the effects of a severe 5–days rainfall event that hit the Arroscia valley in November 2016. More than 250 landslides and widespread flood–related forms and processes were mapped. The preliminary observations revealed that the landslide distribution can be strongly related to the occurring of localized rainfalls.

**Fig. 4** Flood-related forms and processes. **a** flooded areas covered by overbank deposits; **b** bank retreats; **c** active channel widening (Google Earth images, March 2017)
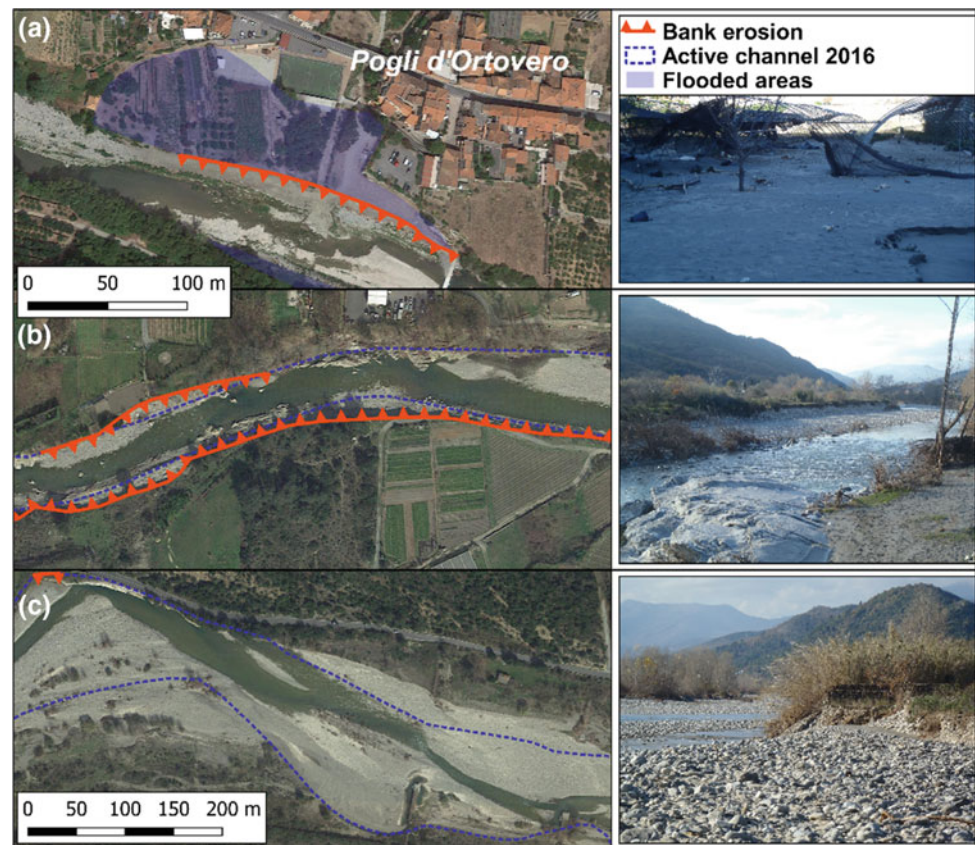
However, considering the high variability in the local morphological and geological features, the objectives of future investigations should be to understand the other rainfall–induced landslide-controlling factors that could have played a significant role in landslide occurrence. Simultaneously, fluvial processes should be analyzed to identify other triggering factors and to assess the short–term channel evolution. These factors will be the basis of both landslide– and flood–related channel change susceptibility analysis and risk scenario evaluation. Eventually, the results of this study may contribute to improve local forecasting and warning systems.

## References

Cevasco, A., Pepe, G., Brandolini, P.: The influences of geological and land use settings on shallow landslides triggered by an intense rainfall event in a coastal terraced environment. Bull. Eng. Geol. Env. **73**, 859–875 (2014). https://doi.org/10.1007/s10064-013-0544-x

Cevasco, A., Diodato, N., Revellino, P., Fiorillo, F., Grelle, G., Guadagno, F.M.: Storminess and geo-hydrological events affecting small coastal basins in a terraced Mediterranean environment. Sci. Total Environ. **532**, 208–219 (2015). https://doi.org/10.1016/j.scitotenv.2015.06.017

Cevasco, A., Pepe, G., D'Amato Avanzi, G., Giannecchini, R.: Preliminary analysis of the November 10, 2014 rainstorm and related landslides in the lower Lavagna valley (eastern Liguria). It. J. Eng. Geol. Env. Spec. (5–15) (2017). https://doi.org/10.4408/ijege.2017-01.s-01

Decarlis, A., Dallagiovanna, G., Lualdi, A., Maino, M., Seno, S.: Stratigraphic evolution in the Ligurian Alps between Variscan heritages and the Alpine Tethys opening: A review. Earth-Sci. Rev. **125**, 43–68 (2013). https://doi.org/10.1016/j.earscirev.2013.07.001

Faccini, F., Luino, F., Sacchini, A., Turconi, L., De Graff, J.V.: Geohydrological hazards and urban development in the Mediterranean area: an example from Genoa (Liguria, Italy). Nat. Hazards Earth Syst. Sci. **15**, 2631–2652 (2015). https://doi.org/10.5194/nhess-15-2631-2015

Guzzetti, F., Cardinali, M., Reichenbach, P., Cipolla, F., Sebastiani, C., Galli, M., Salvati, P.: Landslides triggered by the 23 November 2000 rainfall event in the Imperia Province, Western Liguria, Italy. Eng. Geol. **73**, 229–245 (2004). https://doi.org/10.1016/j.engeo.2004.01.006

Hungr, O., Leroueil, S., Picarelli, L.: The Varnes classification of landslide types, an update. Landslides **11**, 167–194 (2014). https://doi.org/10.1007/s10346-013-0436-y

Pepe, G., Piazza, M., Cevasco, A.: Geomechanical characterization of a highly heterogeneous flysch rock mass by means of the GSI method. Bull. Eng. Geol. Env. **74**, 465–477 (2015). https://doi.org/10.1007/s10064-014-0642-4

Segoni, S., Leoni, L., Benedetti, A.I., Catani, F., Righini, G., Falorni, G., Gabellani, S., Rudari, R., Silvestro, F., Rebora, N.: Towards a definition of a real-time forecasting network for rainfall induced shallow landslides. Nat. Hazards Earth Syst. Sci. **9**(6), 2119–2133 (2009). https://doi.org/10.5194/nhess-9-2119-2009, https://doi.org/10.5194/nhess-9-2119-2009

Silvestro, F., Gabellani, S., Giannoni, F., Parodi, A., Rebora, N., Rudari, R., Siccardi, F.: A hydrological analysis of the 4 November 2011 event in Genoa. Nat. Hazards Earth Syst. Sci. **12**, 2743–2752 (2012). https://doi.org/10.5194/nhess-12-2743-2012

# Landslide Risk Assessment, Management and Reduction for Urbanized Territories

Valentina Svalova

## Abstract

The problem of geological and landslide risk management is viewed as a series of events leading to risk reduction, including risk analysis, risk assessment, risk mapping, vulnerability evaluation, concept of acceptable risk, monitoring organization, engineering-technical methods, insurance and others. The methodology for landslide risk assessment and mapping for urban areas is developed. The construction of a landslide risk map in the territory of Moscow is suggested.

## 1 Introduction

The problem of landslide risk management is viewed as a series of events leading to landslides risk reduction. Natural risk is a relatively new and not fully explored concept. There are many definitions of natural risk. And often a scientific study or a scientific approach to the problem begins with a presentation of the author's position and the choice of the definition of natural risk for the problem.

If one of the main systematic approaches to hazards research is their classification, so now also the concept of Risk Management can be considered as a new step in science development and new basement for systematic hazards investigation.

Development of the Risk concept demands the promotion of the methods for the Risk Assessment and calculation. It makes the Risk Theory the scientific discipline with good mathematical background. It is necessary to elaborate common approaches to the risk calculation for various types of natural hazards. The methods for seismic risk assessment as the most advanced ones must be spread to landslides, karst, suffusion, flooding, pollution and other types of natural hazards and risks and also to complex and multi-risk.

Arising from everyday life, gambling, finance, business and building, the Risk Concept became the subject of scientific research and basement for systematic investigations of natural and man-made hazards and disasters.

In common sense the Risk is a potential possibility to gain or lose something (life, health, property, money, environment etc.). The risk situation can arise at meeting with uncertainty resulting from action or inaction. Risk is a consequence of unpredictable outcome.

In the risk-analysis science the Risk is considered as a measure of the probability of damage to life, health, property, money or the environment. The Risk is defined as a probability of the natural hazard event multiplied by the damage from possible consequences.

The Risk Analysis is a use of available information for hazard identification and vulnerability evaluation.

Vulnerability is a degree of loss of a given element or a set of elements exposed to the occurrence of a natural or man-made hazard. It is expressed on a scale of 0 (no loss) to 1 (total loss).

The Risk Assessment is considered as the process of making decision on whether the existing risk is acceptable or non-acceptable and implies the risk analysis and risk evaluation processes (Corominas et al. 2014).

Sometimes the Risk Assessment is considered as Risk calculation based on selected parameters and establishment of ranking risk criteria.

The acceptable risk is defined by a level of human and property loss that can be tolerated by an individual or community. The probability of acceptable risk is very small. The concept of acceptable risk arises from the understanding that absolute safety is an unattainable goal.

V. Svalova (✉)
Sergeev Institute of Environmental Geoscience RAS, Ulansky per., 13, PB 145, 101000 Moscow, Russia
e-mail: inter@geoenv.ru

The Risk Management is considered as a complete process of the Risk Assessment and the Risk Reduction (Corominas et al. 2014).

The risk reduction implies some methods and measures, including legislative, organizing, economic, engineering, information and other.

Sometimes the Risk Management is considered as measures for the Risk Reduction.

And in this sense the problem of the Landslide Risk Management is viewed as a series of events leading to landslides risk reduction and avoiding. It includes landslides monitoring, landslide forecast, engineering work, slopes strengthening, insurance and other.

Summarizing the systematic approach to the natural hazards research based on the Risk concept it is possible to present the next steps and scheme to establish criteria for ranking risk posed by different types of natural or man-made hazards and disasters, to quantify the impact that a hazardous event or process may have on population or structures and to enhance strategies for risk reduction and avoiding (Table 1).

## Risk Management

1. Hazard Identification;
2. Vulnerability evaluation;
3. Risk analysis;
4. Concept of acceptable risk;
5. Risk assessment;
6. Risk mapping;
7. Measures for risk reduction:
   (a) legislative;
   (b) organizational and administrative;
   (c) economic, including insurance;
   (d) engineering and technical;
   (e) modeling;
   (f) monitoring.
   (g) information.

According to the most common definition, the Risk is the probability of the natural hazard event multiplied by the possible damage:

$$R = P \times D,$$

where R—risk, P—probability, D—damage.

For the multi-risk assessment it is possible to use a sum of risks of different hazards:

$$R = \sum R_i$$

For Risk Maps construction it is necessary to use Natural Hazards maps and maps of possible damage. These maps can be of local, regional, federal (sub global) and global levels.

Landslide is a major geological hazard, which poses serious threat to human population and various other infrastructures like highways, rail routes and civil structures like dams, buildings and others.

Landslides occur very often during other major natural disasters, such as earthquakes, floods and volcanoes.

The word 'landslide' represents only a type of movement that is slide.

However, it is generally used as a term to cover all the types of land movements, including falls, creep, spreads, flows and other complex movements.

A correct term to represent all these movements may be 'mass movement' or 'mass wastage'. However, the term 'landslide' has been accepted and is being used commonly around the world as a synonym of 'mass wastage'.

Some main aspects of the landslides risk management are considered.

## 2 Landslides Risk Assessment and Mapping

The geological risk mapping is an important step towards solving the problem of natural risk management. (Corominas et al. 2014; Kazeev et al. 2014) Due to the complexity and diversity of the problem, the combination of probabilistic and deterministic approaches and expert estimates arises.

The probability of landslide process depends on the stability of the landslide slope, trigger mechanisms (precipitation, earthquakes), technological factors. The first step is studying the physical and mechanical sliding process at

**Table 1** Relationship between the main items of the risk concept for systematic approach to natural hazards and disasters research

**Risk Management structure**
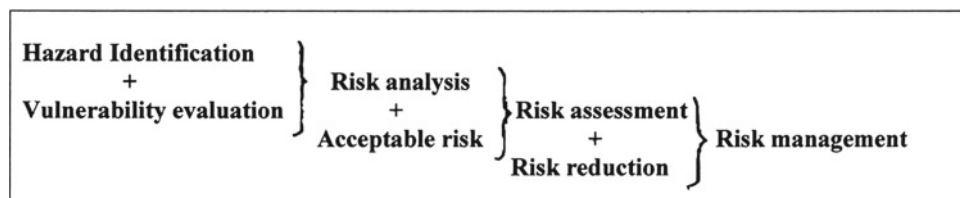
different conditions. Nevertheless, the landslide process mechanics is still not fully understood. Landslide prediction is not always possible. Even statistical frequency of landslides activation for a particular area varies widely.

As an example, we will consider the approach to the construction of the landslide risk map in the territory of Moscow.

### 2.1 Study Area

Landslide processes in Moscow are well investigated (Kutepov et al. 2002, 2004; Nikolaev et al. 2011; Osipov 1997; Osipov et al. 2002, 2010; Postoev et al. 1989; Postoev and Svalova 2005; Ragozin 2003; Keh-Jian et al. 2009; Svalova 2001, 2011a, b, 2012, 2013, 2014a, b, c, d, 2016a, b, c, d, e, f, g, 2017, 2008; Zubko 2009). Landslides cover about 3% of the city, where there are 15 deep and a lot of small landslides, and the landslide hazard is mapped. Last years in Moscow there has been a significant activation of landslide processes. To assess the landslide hazard, the height of a slope, the landslide body volume, mass velocity, rock properties, topography of the surrounding area, the range of possible promotion landslide masses, hydrogeological conditions and trigger mechanisms have to be taken into account. Selection of taxons (special areas) varying degrees of landslide hazard in the city is completely solvable task. And gradation is possible by the three degrees of danger (high, medium, low) as well as by five degrees (very high, high, medium, low, not dangerous), depending on the details of the task.

The most expensive land and buildings in Moscow are located in the city center, where also the oldest historic buildings, the most vulnerable to natural hazards, and the most expensive new ground and underground construction, subway lines, complex traffic, and technical communications of high density are located. There is an increased density of population. We can assume that the closer to the center of Moscow, the greater the potential damage from possible landslide process.

The hazardous industrial production has been moved to the Moscow's periphery. But the protected zone of Moscow in the Vorobyovy Gory and in Kolomenskoye also has high cultural value, and the potential damage there is highly evaluated. So a first approximation map of landslide risk in Moscow may be an overlay of landslide hazard maps and population density, building density, land prices, density of roads and infrastructure maps. Areas with the highest degree of landslide hazard and the highest damage are the areas of the highest landslide risk in the territory of Moscow.

The methodology for risk evaluation and mapping is suggested in the following paragraph.

### 2.2 Methodology for Landslide Risk Mapping

For the automated analysis of the factual material and the risk maps construction it is needed to find the intersection of the landslide hazard map and integrated map of possible damage t.e. for each i—th fragment $R_i$ of the risk map to find the product of probability $P_i$ of landslide event to the amount of different j—th possible damages from landslides that could cause damage to land, buildings, transport, communications, people and others:

$$R_i = P_i \sum_j D_{ij}$$

The maps of landslide hazard are necessarily calibrated from 0 to 1 to reflect the probability of landslide events ($0 \leq P \leq 1$). Thus, gradation, for example, is possible on a scale of (0; 0.25; 0.5; 0.75; 1), where 0 corresponds to no danger of landslides, 0.25—low, 0.5—average 0.75—high and 1—a very high probability of the landslide process. This assessment is expert in nature. In principle, it is possible to construct the landslide hazard maps as the intersection of maps of factual material, such as map of relief contrast, rock strength, slope stability, speed of motion of the surface, density of rainfall, seismicity, etc. Of course, this will require additional research and evaluation.

For a comprehensive assessment of the damage in each region it is suggested that the possible damage of each option be calibrated on a three-point system (0, 1, 2), where 0 means no damage, 1—middle damage, 2—high damage. The parameters here are, for example, (1) cost of land, (2) cost of housing, (3) density of buildings, (4) population density, (5) density of roads and communications. The higher the value (the value of land, housing, etc.), the greater the damage in case of a hazardous event (Svalova 2016f, g, 2017).

Then, the possible damage to 5 parameters for each element varies from 0 to 10.

The risk also in each element ranges from 0 to 10. This is the risk in relative terms (high–low) on a 10-point scale.

$$D_i = \sum_j D_{ij}, \; j = 1 - 5, \; D_{ij} = (0, 1, 2), 0 \leq D_i \leq 10,$$

$$0 \leq R_i \leq 10.$$

After defeating the map of the area into squares and calculating the risk for each square, you can get a map of the area at risk on the 10-point scale (Svalova 2016f, g, 2017).

**Fig. 1** Andronievskaya Embankment with Svjato-Andronikov monastery

**Fig. 2** Cracks near
Svjato-Andronikov monastery
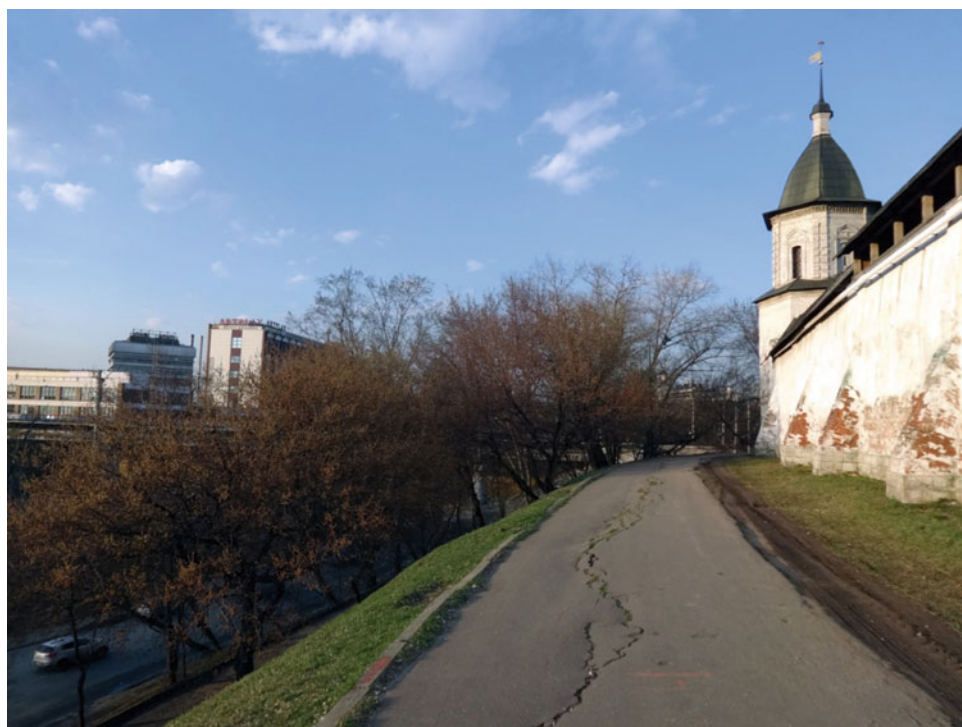


On the basis of preliminary expert estimates, it will be the areas in the vicinity of the Moscow River and the Yauza River, as well as in the areas of contrasting relief along riverbeds of paleorivers in the city center.

The places of high landslide risk are Andronievskaya Embankment (Figs. 1 and 2), Nikolo-Yamskaya Embankment (Fig. 3), Kotelnicheskaya embankment (Fig. 4), Samotechnaya Street (Fig. 5) in the center of Moscow.

**Fig. 3** Nikolo-Yamskaya Embankment

**Fig. 4** Kotelnicheskaya
Embankment

**Fig. 5** Samotechnaya street

The places of highest landslide risk are Vorobyovy Gory (Hills) (Figs. 6, 7, 8 and 9) and the Kremlin Hill (Figs. 10 and 11). They are shown as white circles in the map of geological danger in Moscow (Fig. 12).

These areas may be considered as the "hot spots" on the risk map. And even thought in some of these areas, the population density is not so high, the other components (cost of land, historical importance of the object, density of

**Fig. 6** Vorobyovy gory with the Moscow state university, ski-jumps and metro-bridge

underground utilities and others) contribute greatly to the high risk assessment.

These areas must be measured in terms of risk management and reduction at the first place. It means monitoring organization, slope strengthening, ban of extra buildings and activities.

As an additional fact, it is interesting to use the Metro scheme and the night cosmic photo of Moscow, which reflect the density of communications and possible damage (Figs. 13 and 14).

**Fig. 7** Vorobyovy gory with building of the presidium RAS (Russian Academy of Sciences), Andreevsky monastery and new living houses

**Fig. 8** Destroyed escalator in Vorobyovy gory

**Fig. 9** Place of landslide activation in Vorobyovy gory
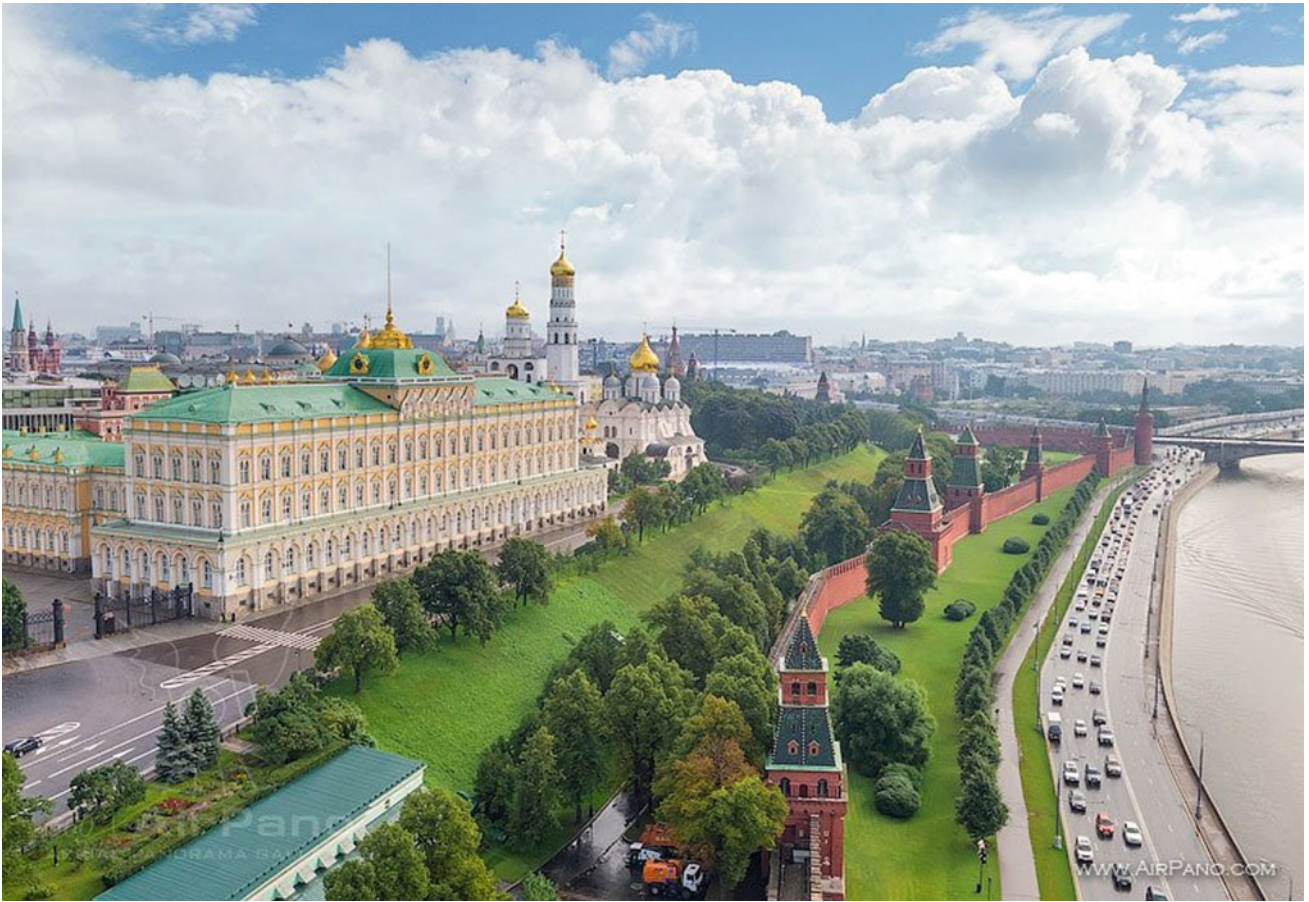
**Fig. 10** Kremlin Embankment

**Fig. 11** Center of Moscow with the Kremlin hill and the Moscow river

**Fig. 12** Map of geological
danger in Moscow. landslides,
karst, underflooding.
(V. I. Osipov., V. M. Kutepon,
O. K. Mironov) (Kutepov et al.
2002). Landslides are near rivers
in semi-dark (red and pink).
1—very high danger, 2—high,
3—middle, 4—low, 5—no.
White circles—risk "hot spots".
Kremlin hill (center) and
Vorobyovy gory (South–West)
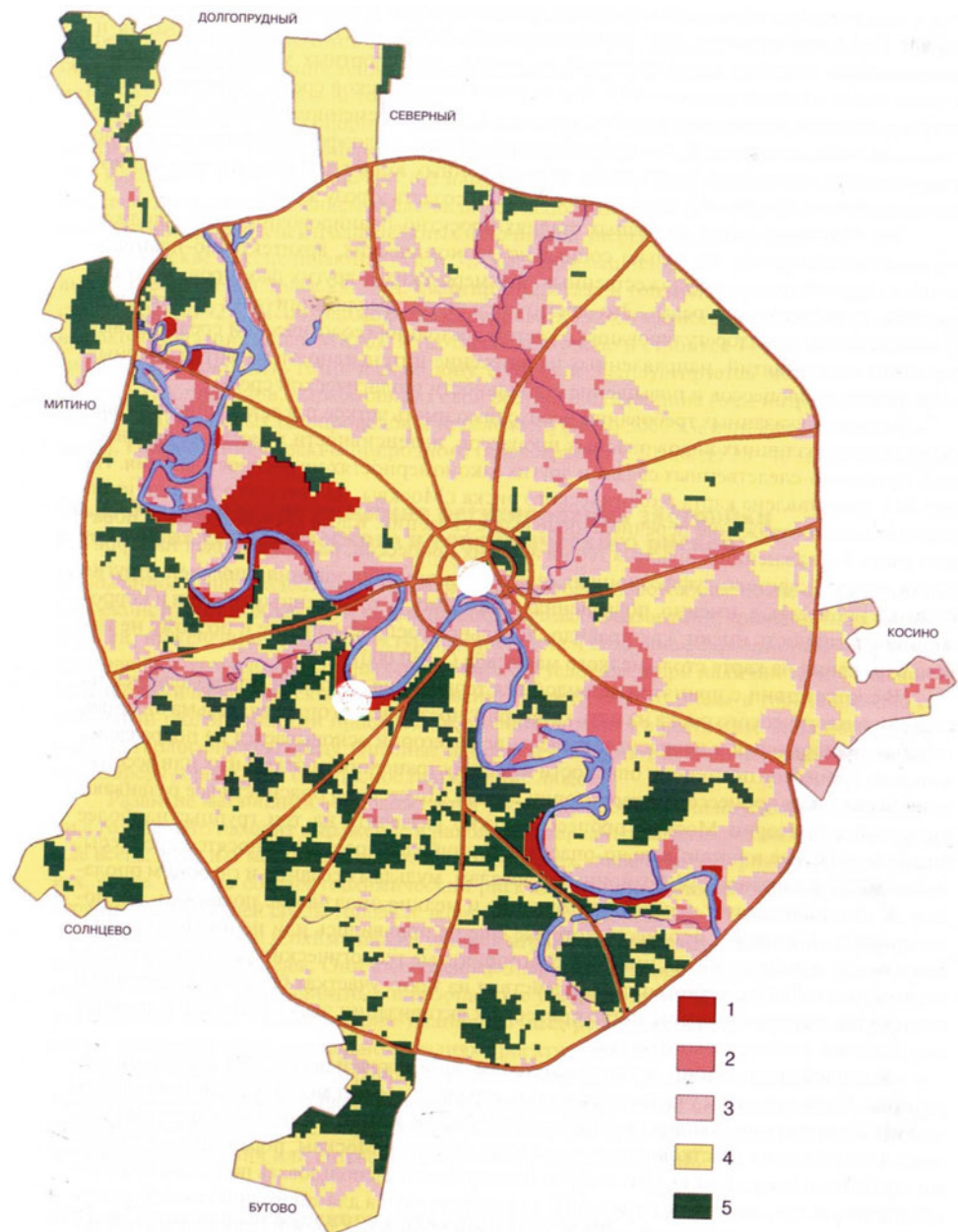
**Fig. 13** Metro-scheme of Moscow. http://www. rosmetrostroy.ru/
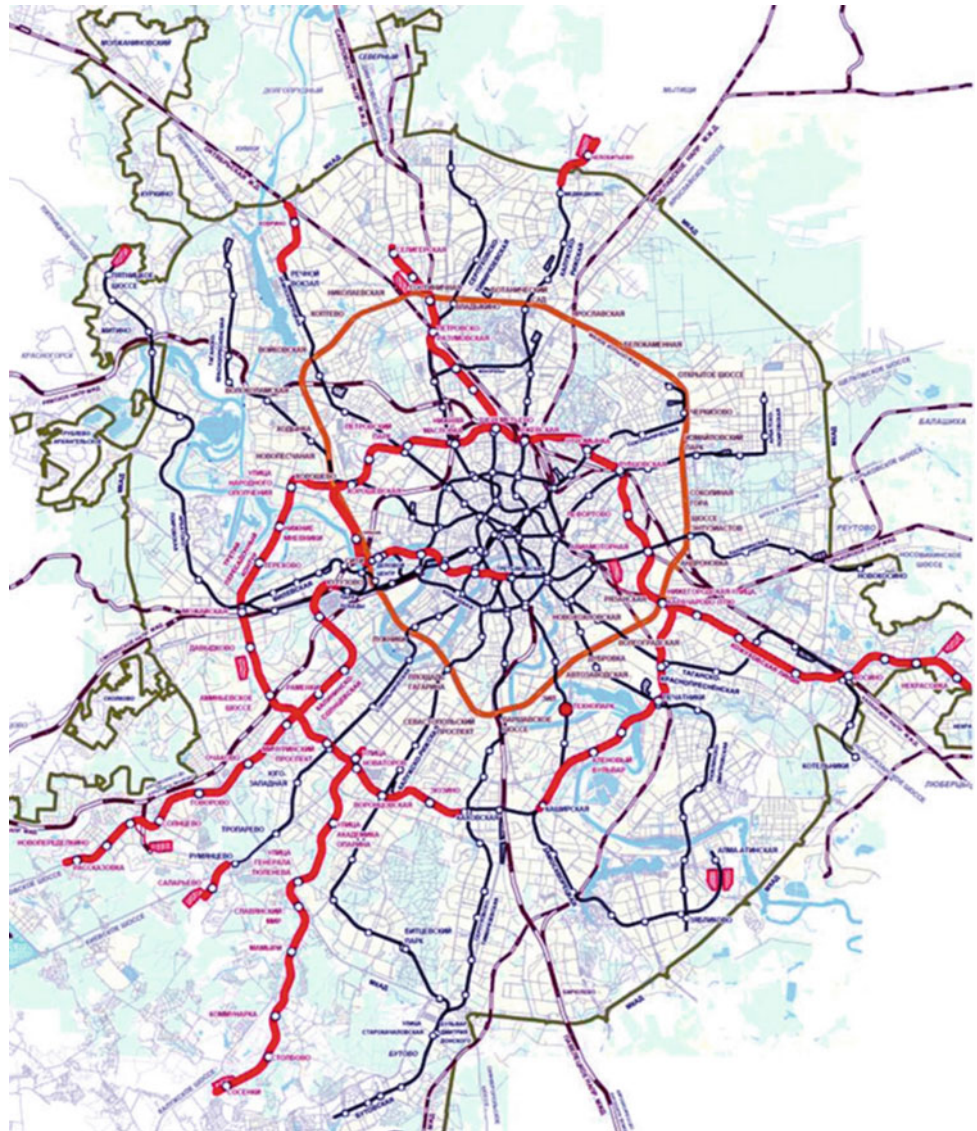
**Fig. 14** Cosmic photo of Moscow at night

# References

Corominas, J., van Westen, C., Frattini, P., Cascini, L., Mallet, J.-P.: Recommendations for the quantitative analysis of landslide risk. Bull. Eng. Geol. Environ. **73**(2), 209–263 (2014)

Kazeev, A.I., Postoev, G.P., Fedotova, K.Y.: Landslide hazard criteria for transportation safety of the 2014 Olympics in Sochi. In: 14th GeoConference on Science and Technologies in Geology, Exploration and Mining. Conference Proceedings. Volume II. International Multidisciplinary scientific GeoConference, 17–26 June 2014, pp. 567–572. Bulgaria (2014)

Keh-Jian, S., Nikolaev, A.V., Bashilov, I.P., Svalova, V.B., Lin, C.C., Song, S.T.: Theory and methods of earthquake early warning systems for underground pipelines and hazardous slopes. In: Abstracts of International Conference Geohazards. Taiwan (2009)

Kutepov, V.M., Sheko, A.I., Anisimova, N.G., Burova, V.N., Victorov, A.S., et al.: Natural Hazards in Russia. Exogenous Geological Hazards. Moscow, "KRUK", 345 pp (2002)

Kutepov, V.M., Postoev, G.P., Svalova, V.B.: Landslide hazards estimation on sites of modern and historical constructions in Moscow. In: Proceedings of 32 IGC, Italy, Florence (2004)

Nikolaev, A.V., Bashilov, I.P., Shou, K.-J., Svalova, V.B., Manukin, A.B., Zubko, Y.N., Behterev, S.V., Kazantseva, O.S., Rebrov, V.I.: Some directions of works on maintenance of geological safety of engineering constructions. In: Proceedings of ENGEOPRO, 7 pp. Moscow (2011)

Osipov, V.I., Medvedev (ed.): Moscow. Geology and Town. M., Moscow Textbooks and Kartolitografiya, 400 p (1997)

Osipov, V.I., Shojgu, S.K., Vladimirov, V.A., Vorobjev YuL, A.V.P., et al.: Natural Hazards in Russia. Natural Hazards and Society. Moscow, "KRUK", 245 pp (2002)

Osipov, V.I., Ginzburg, A.A., Novikova, A.V.: Systems of guarding seismic monitoring for potentially dangerous objects. Geoecology Eng. geol. Hydrogeol. Geocryology **5**, 458–461 (2010)

Postoev, G.P., Erysh, I.F., Salomatin, V.N., et al.: Artificial Activation of Landslides, 134 p. Russia. M: Nedra (1989)

Postoev, G.P., Svalova, V.B.: Landslides risk reduction and monitoring for urban territories in Russia. In: Proceedings of the First General Assembly of ICL (International Consortium on Landslides), "Landslides: Risk Analysis and Sustainable Disaster Management, pp. 297–303. Washington, USA, Springer (2005)

Ragozin, A.L. (ed.): Natural Hazards of Russia. Evaluation and Management of Natural Risk, 316 p. Moscow, KRUK (2003)

Svalova, V.B.: Mechanical-mathematical modeling and monitoring for landslide processes. J. Environ. Sci. Eng. **5**(10), 1282–1287 (2001)

Svalova, V.B.: Monitoring and modeling of landslide processes. Monit. Sci. Technol. **2**(7), 19–27 (2011a)

Svalova, V.B.: Landslide process simulation and monitoring. In: Proceedings of ENGEOPRO, Moscow, 7 pp (2011b)

Svalova, V.B.: Mechanical-mathematical modeling and monitoring for landslides. In: Proceedings of IPL (International Program on Landslides) Symposium, UNESCO, Paris, pp. 63–68 (2012)

Svalova, V.B.: Risk reduction for landslide hazards. Modeling and monitoring. In: Proceedings of The International Conference Natural Risks: Analysis, Estimation, Mapping, Moscow, MSU, pp. 157–163 (2013)

Svalova, V.B.: Modeling and monitoring for landslide processes. In: Linwood, K. (ed.) Chapter in Book: Natural Disasters—Typhoons and Landslides—Risk Prediction, Crisis Management and Environmental Impacts. Nova Science Publishers, NY USA, pp. 177–198 (2014a)

Svalova, V.B.: Mechanical-mathematical modeling and monitoring for landslide processes. In: IPL 163 Project. Proceedings of the World Landslide Forum 3, vol. 4, pp. 24–27. Beijing, China (2014b)

Svalova, V.B.: Modeling and monitoring for landslide processes: case study of Moscow and Taiwan. In: Proceedings of the World Landslide Forum 3, vol. 4, pp. 628–632. Beijing, China (2014c)

Svalova, V.B.: Mechanical modeling and geophysical monitoring for landslide processes. In: Proceedings of IAEG XII Congress

"Engineering Geology for Society and Territory", vol. 2, pp. 345–348. Torino-2014, Italy, Springer (2015)

Svalova, V.B.: Monitoring and modeling of landslide hazard in Moscow. Eng. Prot. **1**(12), 34–38 (2016a)

Svalova, V.B.: Monitoring and reducing the risk of landslides in Taiwan. Monit. Sci. Technol. **3**, 13–25 (2016b)

Svalova, V.B.: Analysis of landslide risk in Taiwan. "Commonwealth", Russia-China Sci. J. **4**, 136–141 (2016c)

Svalova, V.B.: Analysis and management of risk of landslides. Sci. Phys. Math. **2**, 28–31 (2016d)

Svalova, V.B.: Reducing the risk of landslides. Uniform All-Russia Sci. Bull. **2**(Part 3), 79–83 (2016e)

Svalova, V.B.: Landslides modeling, monitoring, risk management and reduction. EESJ (East Eur. Sci. J., Pol.) **7**(11), 43–52 (2016f)

Svalova, V.B.: Risk analysis, evaluation and management for landslide processes. Sci. Europe (Praha, Czech Republic) **4** 6 (6), 15–25 (2016g)

Svalova, V.: Landslide Risk: Assessment, Management and Reduction. Nova Science Publishers, NY, 253 p (2017)

Svalova, V.B., Postoev, G.P.: Landslide process activization on sites of cultural heritage in Moscow, Russia. In: Proceedings of the First World Landslide Forum 2008, 4p. Tokyo, Japan (2008)

Zubko, Y.N., Nikolaev, A.V., Bashilov, I.P., Svalova, V.B.: Autonomous portable seismic receiver with digital registration for seismological studies. In: Abstracts of International Conference Geohazards. Taiwan (2009)

# Monitoring and Risk Management for Landslide Hazard in Taiwan

Svalova Valentina

### Abstract

High frequency of landslides in Taiwan area is affected by its geography and geology background. Landslide hazard was significantly affected by the 1999 Chi-Chi earthquake (921 earthquake), as this event changed the geomaterial conditions. A sustainable urban development plan is essential for the landslide hazard management. It should consider political and economical factors except technical factors. Besides, the climate change impact to natural hazard becomes more and more significant in Taiwan area. The rainfalls are more concentrated and the temperature increased about 1.5° during last 100 years. The concentrated rainfalls might more significantly affect the landslides in the futures. The problem of landslide and debris flow risk management is seen as series of events leading to risk reduction, including Risk analysis, Risk assessment, Risk mapping, Vulnerability evaluation, Concept of acceptable risk, Monitoring organization, Engineering-technical methods, Insurance and others. The problem of monitoring organization for landslides and debris flow in Taiwan is considered and analyzed.

### Keywords

Landslide • Risk • Risk management • Risk assessment • Risk reduction • Monitoring

## 1 Introduction

Risk management is considered as the complete process of Risk assessment and Risk reduction.

Risk reduction implies some methods and measures, as legislative, organizing, economic, engineering, information and others. (Corominas et al. 2014; Ragozin 2003).

S. Valentina (✉)
Sergeev Institute of Environmental Geoscience RAS, Ulansky per., 13, PB 145, 101000 Moscow, Russia
e-mail: inter@geoenv.ru

Sometimes in narrow sense Risk Management is considered as measures for Risk Reduction.

And in this sense the problem of Landslide Risk Management is seen as a series of events leading to landslides risk reduction and avoiding. It includes landslides monitoring, landslide forecast, engineering works, slopes strengthen, insurance and others.

Summarizing systematic approach to natural hazards research on the base of the Risk concept it is possible to present the next steps and scheme to establish criteria for ranking risk posed by different types of natural or man-made hazards and disasters, to quantify the impact that hazardous event or process have on population, structures and to enhance strategies for risk reduction and avoiding.

**Risk Management**

1. Hazard Identification;
2. Vulnerability evaluation;
3. Risk analysis;
4. Concept of acceptable risk;
5. Risk assessment;
6. Risk mapping;
7. Measures for risk reduction:
   (a) legislative;
   (b) organizational and administrative;
   (c) economic, including insurance;
   (d) engineering and technical;
   (e) modeling;
   (f) monitoring.
   (g) information.

## 2 Monitoring Organization for Debris Flow. Case Study of Taiwan

Taiwan is located on the edge of Eurasian Sea Plate and Philippine Sea Plate. The maximum length and the average width of Taiwan is about 395 and 144 km respectively. And

the total area is about 36,000 km$^2$. The mountains in Taiwan are high and steep, and the terrain is highly variable, as well as the elevations. (Taiwan's highest point is Yu Shan, also called Jade Mountain, which is at 3952 m) In Taiwan, the plains are narrow, which is only occupied with one-third of Taiwan. Earthquakes occur frequently in Taiwan. The rainy season in Taiwan is caused by rainfall along a persistent stationary front between spring and summer; and typhoons are influencing Taiwan mostly in the summer and autumn. The annual average rainfall is more than 2500 mm.

There is abundant rainfall in Taiwan. Variable rainfall duration and intensity leads to floods and debris flow disasters (Fig. 1).

Since the 1999 Chi-Chi earthquake (ML = 7.3) occurred (earthquake 921), the frequency of the disasters, which are caused by landslides, complex landslides, debris flows and soil erosion, has increased more than before.

The 921 earthquake (ML = 7.3) took place in central Taiwan on September 21, 1999. A 195-ha slopeland was devastated by a gigantic rock avalanche, called the Chiu-Fen-Erh-Shan (Chiufengershan) landslide, near the Nankang village of Kouhsing in Nantou County during the earthquake; the slid materials blocked the confluence of two streams leading to the formation of two landslide dams (Figs. 2 and 3).

Further monitoring and hydrology studies on landslide area became necessary for landslide management (Geology et al. 1997; Kutepov et al. 2002, 2004; Postoev et al. 1989; Postoev and Svalova 2005; Svalova 2001, 2011a, b, 2012, 2013, 2014a, b, c, 2015, 2016a, b, c, d, e, f, g, 2017; Svalova and Postoev 2008; Osipov 2002; Kazeev 2014; Osipov 2010; Shou et al. 2009; Nikolaev et al. 2011; Zubko et al. 2009). Thus, a project for monitoring the Chiu-Fen-Erh-Shan landslide began in 2003. It includes:

1. Landslide dams water level monitoring
2. Post-failure behavior simulation
3. Morphological fluctuation using LiDAR (Light Detection and Ranging)
4. Long-term monitoring using photogrammetry images.

The post-failure behavior and impact area of Chiu-Fen-Erh-Shan slope along the inferred sliding surface were investigated by using the method of Discontinuous Deformation Analysis (DDA).

In order to prevent life and economic losses due to landslide, complex landslide, debris flows and soil erosion, the Soil and Water Conservation Bureau (SWCB) has aimed at debris flow disaster management and early warning operations and begun the construction of debris flow monitoring station and Formosa Emergency Management Action System (FEMA) since 2000. Satellite imagery, geographic information, high-end communications and sophisticated monitoring technologies have been implemented and



**Fig. 1** Landslide after rain in 2010, Taiwan

**Fig. 2** USGS ShakeMap for the 921 earthquake



USGS ShakeMap : Chi-Chi, Taiwan

Mon Sep 20, 1999 17:47:18 GMT  M 7.7  N23.82 E120.88  Depth: 21.0km  ID:199909201747

Map Version 1.1 Processed Sat Nov 8, 2008 08:25:56 PM MST
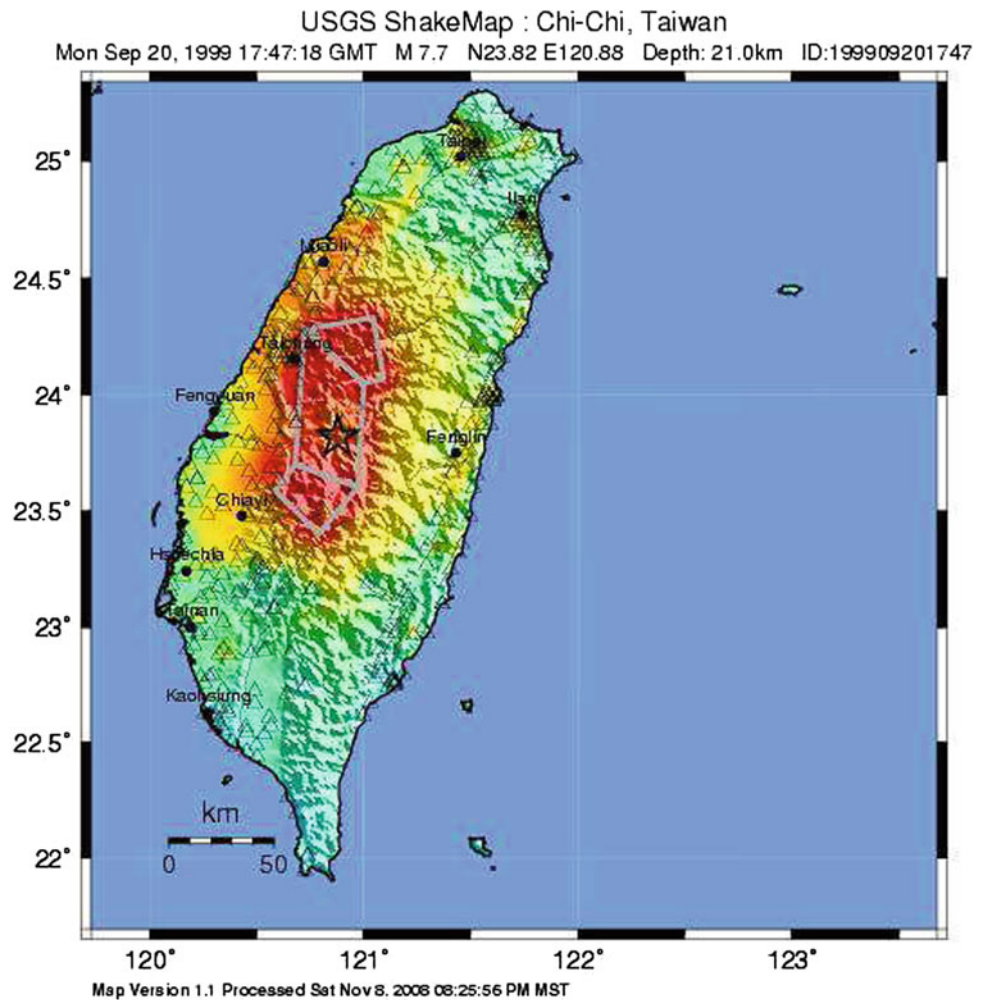
| PERCEIVED SHAKING | Not felt | Weak | Light | Moderate | Strong | Very strong | Severe | Violent | Extreme |
|---|---|---|---|---|---|---|---|---|---|
| POTENTIAL DAMAGE | none | none | none | Very light | Light | Moderate | Moderate/Heavy | Heavy | Very Heavy |
| PEAK ACC.(%g) | <.17 | .17-1.4 | 1.4-3.9 | 3.9-9.2 | 9.2-18 | 18-34 | 34-65 | 65-124 | >124 |
| PEAK VEL.(cm/s) | <0.1 | 0.1-1.1 | 1.1-3.4 | 3.4-8.1 | 8.1-16 | 16-31 | 31-60 | 60-116 | >116 |
| INSTRUMENTAL INTENSITY | I | II-III | IV | V | VI | VII | VIII | IX | X+ |

integrated in the system (Figs. 4, 5 and 6). SWCB is keen on the international exchanges for debris flow disaster prevention.

## 3 Engineering and Technical Methods. Debris Flow Management

### 3.1 Source Management

To reduce the amount of sediment material, source management is very important. Different engineering methods are utilized according to the terrain and its recent history.

Large amounts of water is one of the main factors that cause debris flows, so excess water must be eliminated to the fullest extent possible. This can be done using inbuilt drainage pipes in stream beds or in slopes to divert groundwater.

Runoff with a thick deposition layer can easily induce debris flow. Often, rocks are set in stream beds to capture sediment from the water and prevent further sediment from being lifted, reducing the risk of debris flows.

Cleaning unstable depositions in and around streams such as rocks and logs as well as overhanging braches prevents the obstruction of a debris flow, which can cause the debris to build up and then burst, creating a more dangerous situation.

**Fig. 3** Chiufengershan landslide after 921 earthquake in Taiwan



**Fig. 4** The equipment at the Fengqiu Debris flow monitoring station include 1 rain gauge, 2 CCD cameras, 2 geophones, 4 wire sensors and 1 water level meter

## 3.2 Transportation Stage Management

Engineering and re-vegetation can lower the velocity of debris during the transportation stage of debris flow, and thus to reduce the damage caused by debris flow.

The velocity of debris flow is closely related to the slope degree. In order to lower the velocity, check dams or submerged dams are used to increase the roughness of the streambed. This allows accumulation of sediments, making the slope gentler, decreasing the velocity of debris flow.

Debris flows contains a lot of water that allows it to move fluidly. If the water and sediments are separated, the debris flow will slow down. Check dams can reduce the velocity of debris flow while horizontal grates allow sediment and water to be separated, stopping the debris flow (Fig. 7).

**Fig. 5** The equipment at the Shang'an debris flow monitoring station includes 1 rain gauge, 1 CCD camera, 1 geophone, 2 wire sensors and 1 water level meter



**Fig. 6** The equipment at the Songhe Debris flow monitoring station includes 1 rain gauge, 2 CCD cameras, 2 geophones and 8 wire sensors

**Fig. 7** The debris flow dehydration



In order to prevent the accumulation of debris in valleys, check dam are used to accumulate sediments more efficiently.

## 3.3 Deposition Stage Management

When the debris flow comes to flat areas, the accumulation of sediments often causes riverbed siltation, elevating the riverbed. It is necessary to dispose of this sediment effectively.

The velocity of debris flow will slow when it reaches a gentler slope. Check dams are set in broad, flat terrain to form deposition areas, adjusting the slope and stabilizing the streambed.

Using debris or concrete cofferdams to form deposition areas allows safe debris accumulation. They are often located on flat, broad areas such as alluvial fans, usually about 30–40 m wide and located close to valleys.

Setting forest buffer zones in outlets help stop debris flow and contribute to debris accumulation.

If the outlet is not wide enough for debris flow accumulation, diversion dams or artificial channels are used to lead debris flow to a safer place to discharge.

## 4 Conclusions

Risk management is important way to risk reduction. The main aspects of landslides risk management could be considered as landslides risk assessment and mapping, landslides monitoring and engineering methods for slope strengthen, water discharge and rational land use.

## References

Corominas, J., van Westen, C., Frattini, P., Cascini, L., Mallet, J.-P., et al.: Recommendations for the quantitative analysis of landslide risk. Bull. Eng. Geol. Environ. **73**(2), 209–263 (2014)

Moscow. Geology and town: Ed. by Osipov and Medvedev. M., Moscow textbooks and kartolitografiya, 400 p (1997)

Kazeev, A.I., Postoev. G.P., Fedotova, K.Y.: Landslide hazard criteria for transportation safety of the 2014 Olympics in Sochi. In: 14th GeoConference on Science and Technologies in Geology, Exploration and Mining. Conference Proceedings. Volume II. International Multidisciplinary scientific GeoConference, pp. 567–572, 17–26 June 2014. Bulgaria (2014)

Kutepov, V.M., Sheko, A.I., Anisimova, N.G., Burova, V.N., Victorov, A.S. et al.: Natural hazards in Russia. Exogenous geological hazards. Moscow, "KRUK", 345 pp (2002)

Kutepov, V.M., Postoev, G.P., Svalova, V.B.: Landslide hazards estimation on sites of modern and historical constructions in Moscow. In: Proceedings of 32 IGC, Italy, Florence (2004)

Nikolaev, A.V., Bashilov, I.P., Shou K.-J., Svalova, V.B., Manukin, A. B., Zubko, Y.N., Behterev, S.V., Kazantseva, O.S., Rebrov, V.I.: Some directions of works on maintenance of geological safety of engineering constructions. In: Proceedings of ENGEOPRO, 7 pp. Moscow (2011)

Osipov, V.I., Ginzburg, A.A., Novikova, A.V.: Systems of guarding seismic monitoring for potentially dangerous objects. Geoecology Eng. Geol. Hydrogeol. Geocryology **5**, 458–461 (2010)

Osipov, V.I., Shojgu, S.K., Vladimirov, V.A., Vorobjev YuL, A.V.P., et al.: Natural Hazards in Russia. Natural Hazards and Society, pp. 245 pp. Moscow, "KRUK" (2002)

Postoev, G.P., Erysh, I.F., Salomatin, V.N. et al.: Artificial activation of landslides, 134 p. Russia. M: Nedra (1989)

Postoev, G.P., Svalova, V.B.: Landslides risk reduction and monitoring for urban territories in Russia. In: Proceedings of the First General Assembly of ICL (International Consortium on Landslides), "Landslides: Risk Analysis and Sustainable Disaster Management", pp. 297–303. Washington, USA, Springer (2005)

Ragozin, A.L. (ed.): Natural Hazards of Russia. Evaluation and Management of Natural Risk, 316 p. Moscow, KRUK (2003)

Svalova, V.B., Postoev, G.P.: Landslide process activization on sites of cultural heritage in Moscow, Russia. In: Proceedings of the First World Landslide Forum 2008, 4p. Tokyo, Japan (2008)

Shou, K.-J.,Nikolaev, A.V., Bashilov, I.P., Svalova, V.B., Lin, C.C., Song, S.T.: Theory and methods of earthquake early warning systems for underground pipelines and hazardous slopes. In: Abstracts of International Conference Geohazards 2009. Taiwan (2009)

Svalova, V.B.: Mechanical-mathematical modeling and monitoring for landslide processes. J. Environ. Sci. Eng. **5**(10), 1282–1287 (2001)

Svalova, V.B.: Monitoring and modeling of landslide processes. Monit. Sci. Technol. **2**(7), 19–27 (2011a)

Svalova, V.B.: Landslide process simulation and monitoring. In: Proceedings of ENGEOPRO, Moscow, 7 pp (2011b)

Svalova, V.B.: Mechanical-mathematical modeling and monitoring for landslides. In: Proceedings of IPL (International Program on Landslides) Symposium, UNESCO, Paris, pp. 63–68 (2012)

Svalova, V.B.: Risk reduction for landslide hazards. In: Modeling and monitoring, Proceedings of The International Conference Natural risks: analysis, estimation, mapping, Moscow, MSU, pp. 157–163 (2013)

Svalova, V.B.: Modeling and monitoring for landslide processes. In: Linwood, K. (ed.) Chapter in Book: Natural Disasters—Typhoons and Landslides—Risk Prediction, Crisis Management and Environmental Impacts, pp. 177–198. Nova Science Publishers, NY USA (2014a)

Svalova, V.B.: Mechanical-mathematical modeling and monitoring for landslide processes. IPL 163 Project. In: Proceedings of the World Landslide Forum 3, vol. 4, pp. 24–27. Beijing, China (2014b)

Svalova, V.B.: Modeling and monitoring for landslide processes: case study of Moscow and Taiwan. In: Proceedings of the World Landslide Forum 3, vol. 4, pp. 628–632. Beijing, China (2014c)

Svalova, V.B.: Mechanical modeling and geophysical monitoring for landslide processes. In: Proceedings of IAEG XII Congress "Engineering Geology for Society and Territory", vol. 2, pp. 345–348. Torino-2014, Italy, Springer (2015)

Svalova, V.: Landslide Risk: Assessment, Management and Reduction. Nova Science Publishers, NY, 253 pp (2017)

Svalova, V.B.: Monitoring and modeling of landslide hazard in Moscow. Eng. Prot. 1(12), 34–38 (2016a)

Svalova, V.B.: Monitoring and reducing the risk of landslides in Taiwan. Monit. Sci. Technol. 3, 13–25 (2016b)

Svalova, V.B.: Analysis of landslide risk in Taiwan. "Commonwealth" Russia-China Sci. J. 4, 136–141 (2016c)

Svalova, V.B.: Analysis and management of risk of landslides. Scientia. Phys.Math. 2, 28–31 (2016d)

Svalova, V.B.: Reducing the risk of landslides. Uniform All-Russia Sci. Bull. 2 (Part 3), 79–83 (2016e)

Svalova, V.B.: Landslides modeling, monitoring, risk management and reduction. EESJ (East Eur. Sci. J., Pol.) 7(11), 43–52 (2016f)

Svalova, V.B.: Risk analysis, evaluation and management for landslide processes. Sci. Eur. (Praha, Czech Republic). 4(6), 15–25 (2016g)

Zubko, Y.N., Nikolaev, A.V., Bashilov, I.P., Svalova, V.B.: Autonomous portable seismic receiver with digital registration for seismological studies. In: Abstracts of International Conference Geohazards 2009, Taiwan (2009)

# Landslide Inventory of the Cinque Terre National Park, Italy

Emanuele Raso, Andrea Mandarino, Giacomo Pepe, Diego Di Martire, Andrea Cevasco, Domenico Calcaterra, and Marco Firpo

## Abstract

Landslide inventory maps are effective and easily understandable products both for experts, such as engineering geologists, and for nonexperts, including decision-makers, planners, and civil protection managers. At present, the Cinque Terre landscape suffers from the massive abandonment of cultivations on the terraces, with negative consequences for slope stability due to the increasing erosional processes. Each landform was digitized as a polygon using a GIS platform. Landslide detection was performed by a two-step method. The first step consisted of mapping landslides using orthophotos provided by Liguria Region, together with Google Earth imagery; the second step was a field verification study carried out between September and November 2015. Four hundred and five landslides were then identified and grouped into seven main typologies: a percentage distribution analysis of the different landslide types detected in Cinque Terre was then performed. A large number of debris slides (33.3%) indicates the vulnerability of dry-stone walls after large amounts of rainfall. Rockfalls (18.5%) are also frequent and especially concentrated along the eastern sector of the coastline. In addition, debris flows (12.6%) are widely distributed, especially along the western sector of Cinque Terre, among the Monterosso and Vernazza municipalities; these landslides were mainly triggered by the October 25th, 2011, meteorological event (382 mm of rainfall in 24 h recorded by the Monterosso al Mare weather station). Many landslides with complex evolutions (7% of the total) were detected along the coastline between Vernazza and Manarola; these events are historically well-known and extensively described in the literature.

## 1 Introduction

Landslides are the most frequent geomorphological hazard in Italy, and despite causing casualties and economic losses, they cause fewer losses than earthquakes. In the third millennium, there has been a higher frequency of events detected. Landslides can involve flowing, rotational/translational sliding, toppling or falling movements, and many landslides exhibit a combination of different types of movements (Varnes 1978; Hungr et al. 2014).

Landslide inventories are essential to understand the evolution of landscapes and to ascertain landslide susceptibility and hazard (Lari et al. 2014; Di Martire et al. 2016). Despite landslide maps being compiled worldwide every year at distinct scales, limited efforts have been made to critically compare landslide maps prepared using different techniques or by separate investigators (Guzzetti 2005). In this work, the identification and mapping of landslide type and size within the Cinque Terre National Park (Liguria Region, northwestern Italy) is presented. The processing and management of collected data through an open source geographic information system (QGIS) software was carried out and a landslide inventory map was created (Conforti et al. 2014).

The geomorphological data acquired in this work contribute to understanding the influence of landslide processes on the landscape evolution of the area and the consequent land management and hazard assessment activities.

E. Raso (✉) · A. Mandarino · G. Pepe · A. Cevasco · M. Firpo
Università degli Studi di Genova, Genoa, Italy
e-mail: emanuele.raso@edu.unige.it

D. Di Martire · D. Calcaterra
Università degli Studi di Napoli Federico II, Naples, Italy

## 2 Study Area

The Cinque Terre (The Five Lands) is a 38 km² wide coastal region of eastern Liguria (northwestern Italy), which encompasses five small towns that represent an important national tourist attraction. The landscape mainly consists of steep rocky slopes shaped by wave action in the basal portion and by geomorphological processes and human activities in the upper portion.

In 1999, this area became a national park for its environmental, naturalistic and cultural relevance. The landscape is characterized by terraces, supported by dry-stone walls, mainly for the cultivation of vineyards.

These terraces are not only an important cultural heritage but also a complex system of landscape engineering (Canuti et al. 2004). However, the recent abandonment of farming and the neglect of terraced structures have led to a rapid increase in land degradation problems, with serious threats to human settlements located along the coast (Conti and Fagarazzi 2005; Cevasco et al. 2014; Galve et al. 2015; Raso et al. 2016a; Brandolini et al. 2017). The instability of the dry-stone walls and the clogging of drainage channels are now the main causes behind the most frequent landslide mechanisms within the Cinque Terre (Canuti et al. 2004; Cevasco et al. 2013).

The geological setting of the study area (Fig. 1) was formed by tectonic phases related to the opening, evolution and closure of the Ligurian-Piedmont oceanic basin (Abbate et al. 1970). This sector of the Eastern Liguria Apennines also experienced Quaternary surface uplift with the subsequent formation of unstable marine terraces.

The Cinque Terre National Park is characterized by four overlapping tectonic units: Tuscan Nappe, Internal Ligurids Unit, External Ligurids Unit and Canetolo Complex. The Tuscan Nappe outcrops on the western side of Monterosso bay and, in particular, along the thick turbidites of the Macigno Formation (Upper Oligocene). The latter is largely outcropping along most of the Cinque Terre coast. The Internal Ligurids consist of a Jurassic ophiolite basement with pelagic cover, followed by a Late Cretaceous turbidite sequence. This lithological sequence outcrops along the entire NE-SW dipping slope of the Mesco Promontory, the westernmost point of the national park. The geological structure heavily influences the slope stability, especially along the littoral zone: the main feature is an anticline recumbent fold with Thyrrenian (SW) vergence, dipping gently towards the NNW; the general framework is characterized by several short wavelength parasitic folds.

The tectonic pattern is defined by several major faults trending NW-SE, along which the actual coastline was formed; a minor faults system perpendicular to the NE-SW fault system has also influenced the direction of short rivers draining into the Thyrrenian Sea.

**Fig. 1** Geological map of the Cinque Terre National Park (overlay on a relief map)
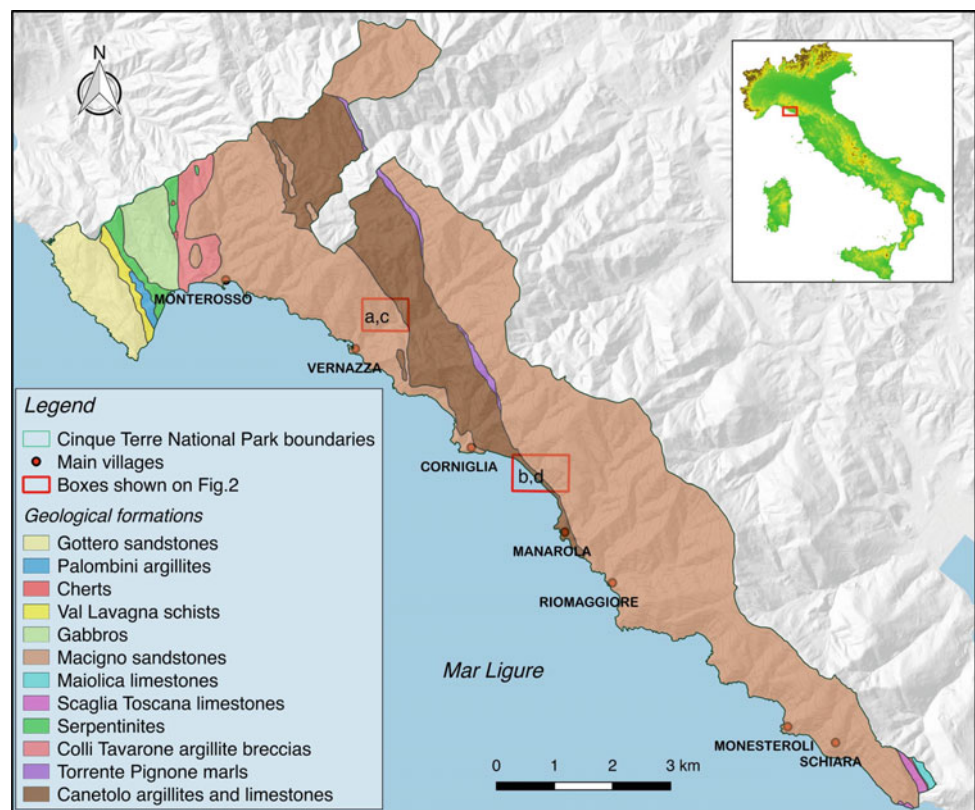
## 3  Methods

In this study, landslides larger than 25 m$^2$ were mapped in the analyses. In the landslide inventory mapping, for each landslide, the polygon feature was drawn from Landsat$^{TM}$ and Google$^{TM}$ 2012 and 2015 satellite images, 1:25.000 aerial photographs (obtained from Friuli-Venezia-Giulia geological service in November 2011), field verification, and eventually converted to the raster format (Fig. 2).

The landslide detection was performed by a two-step method. The first step focused on mapping the scarps over the slopes, using orthophotos and satellite imageries (2012 and 2015).

Each landform was digitized as a polygon using QGIS software. This cartographic base was referenced during a geomorphological campaign carried out between September and November 2014. The field verification produced a 1:25.000 landslide inventory map within the entire Cinque Terre National Park.

## 4  Results

The landslides considered in the present paper can first be distinguished by phenomena triggered before and after the extreme rainfall event that occurred on October 25th, 2011, when significant rainfall started a few hours before a total of 159 landslides were triggered between Monterosso al mare and Vernazza. In a few hours, approximately 382 mm of rainfall was recorded by the rain gauge at Monterosso al Mare (ARPAL 2012).

The landslides triggered during the October 25th, 2011 event were mainly distributed along the western sector of the study area, severely affecting the Monterosso al Mare and Vernazza municipalities (Cevasco et al. 2015) (Fig. 3).

A total of four hundred and five landslides (Fig. 4) were identified and grouped into seven main typologies, referring to the classification proposed by Hungr et al. (2014).

A percent distribution analysis of the different landslide types detected in Cinque Terre was then performed (Fig. 5): a large number of debris slides (135–33.3%) indicates the vulnerability of dry stone terraces after large amounts of rainfall. Rockfalls (75–18.5%) are also frequent and especially concentrated along the eastern sector of the coastline, where the Macigno sandstone and siltstone and the Scaglia Toscana limestones widely outcrop along >50 m high cliffs.

Debris flow deposits (51–12.6%) are also widely distributed, especially along the western sector of Cinque Terre, in the Monterosso al Mare and Vernazza municipalities; these landslides were mainly triggered by the October 25th, 2011 meteorological event.

Other landslide types are less abundant and, except for coastal debris avalanches, dated before the 2011 flooding event. Many landslides with complex evolutions (Guvano, Rodalabia, Macereto) are detected along the coastline between Vernazza and Manarola; these events are historically well-known and extensively described in the literature (Terranova 1984; Raso et al. 2016b; Brandolini et al. 2017).



**Fig. 2** Example of landslide digitization using aerial photos and subsequent validation through field survey—boxes location shown on Fig. 1. **a** and **c** Portion of the Vernazza catchment, badly hit by extreme rainfall events in 2011. **b** and **d** Coastal sector between Corniglia and Manarola. Landslide type:
1. Debris/gravel/soil slip;
2. Complex; 3. Rockfall;
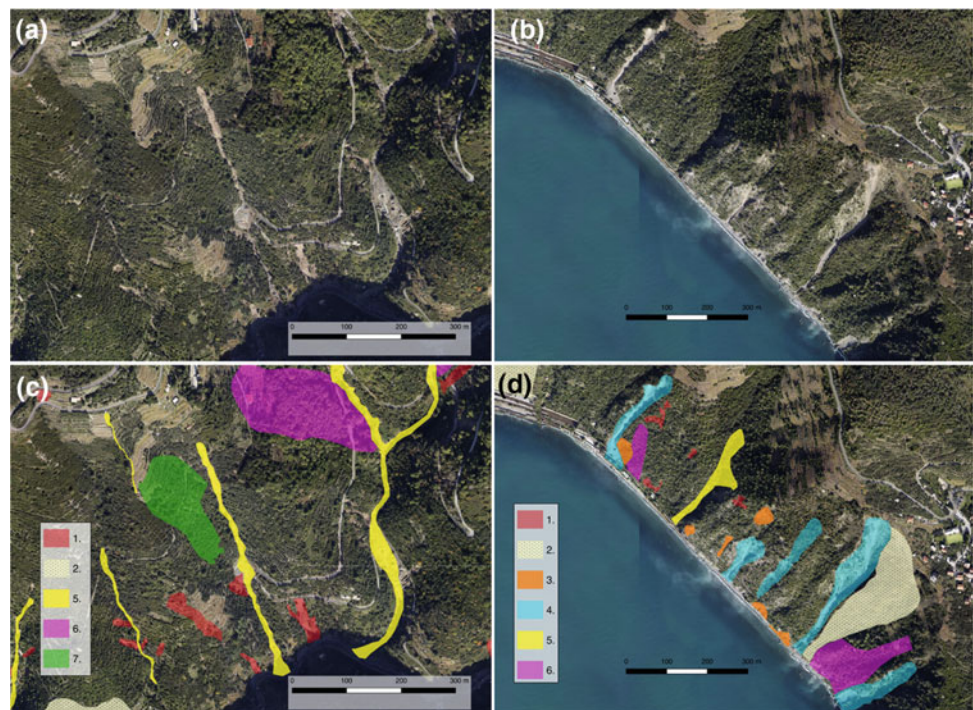4. Debris avalanche; 5. Debris flow; 6. Planar slide; 7. Rotational slide

**Fig. 3** Landslide triggered before and after the October 25th, 2011 flooding event affecting the western sector of the National Park. **a**, **b**: Pictures taken in the surroundings of the village of Vernazza during and after the flooding event
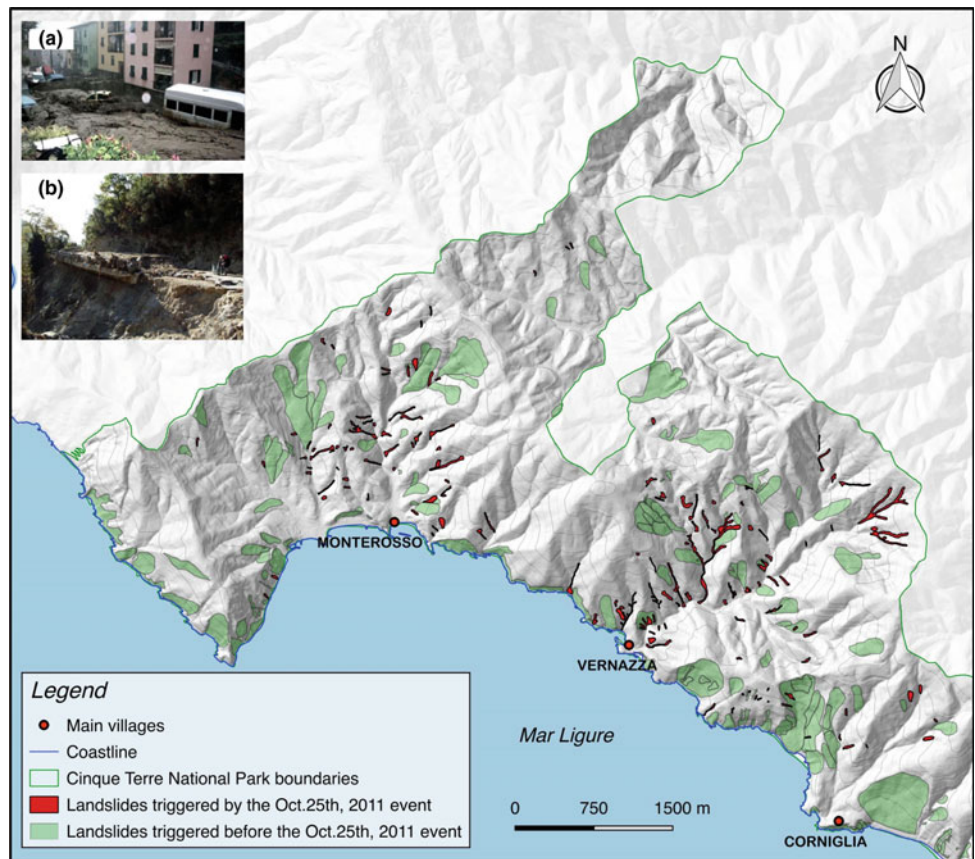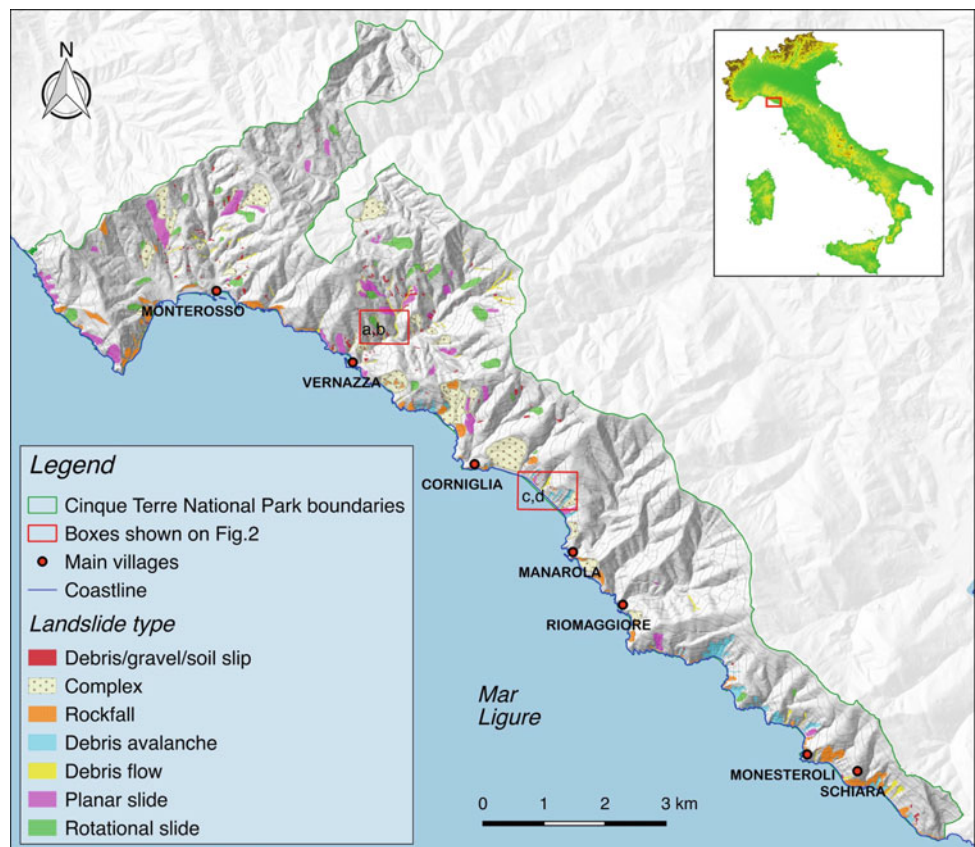


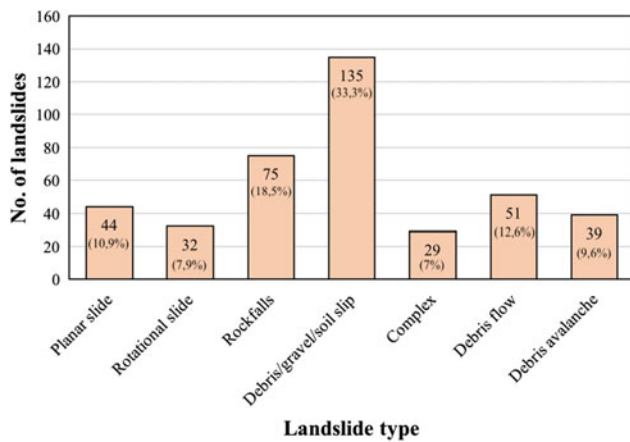**Fig. 4** Landslide inventory of the Cinque Terre National Park

**Fig. 5** Histogram showing the number of catalogued landslides for each typology (% in parenthesis); total no. of catalogued landslides: 405 (Hungr et al. 2014)

## 5 Final Remarks

The landslides mapped in this inventory occurred in a territory prone to slope failures, due to the local geological and geomorphological setting. Many debris flows and debris slides were related to the presence of roads lacking adequate drainage and to the reduction in river and creek cross-sections. The abandonment of terraced slopes has caused a lack of maintenance on dry-stone walls and a consequent increase of local collapses that often evolve to major landslides. Accurate landslide mapping provides crucial information for further analysis, such as susceptibility, hazard and risk evaluation. At the moment, mapping been only partially performed along the Cinque Terre National Park area, an area that incurs a high number of visitors all year long and, therefore, needs analyses to further understand the prevention of risk scenarios.

## References

Abbate, E., Bortolotti, V., Passerini, P., Sagri, M.: The Northern Apennines geosyncline and continental drift. Sed. Geol. **4**(3–4), 637–642 (1970)

A.R.P.A.L.-C.F.M.I.-P.C. (Agenzia Regionale per la Protezione dell'Ambiente Ligure-Centro Funzionale Meteoidrologico di Protezione Civile della Regione Liguria): "Uno tsunami venuto dai monti"—Provincia della Spezia 25 ottobre 2011 rapporto di evento meteo- idrologico. Quaderni ARPAL, 1–96 pp (2012)

Brandolini, P., Cevasco, A., Capolongo, D., Pepe, G., Lovergine, F., Del Monte, M.: Response of terraced slopes to a very intense rainfall event and relationships with land abandonment: a case study from Cinque Terre (Italy). Land Degrad. Dev. (2017). https://doi.org/10.1002/ldr.2672

Canuti, P., Casagli, N., Ermini, L., Fanti, R., Farina, P.: Landslide activity as a geoindicator in Italy: significance and new perspectives from remote sensing. Environ. Geol. **45**, 907–919 (2004)

Cevasco, A., Brandolini, P., Scopesi, C., Rellini, I.: Relationships between geo-hydrological processes induced by heavy rainfall and land-use: the case of 25 October 2011 in the Vernazza catchment (Cinque Terre, NW Italy). J. Maps **9**, 289–298 (2013)

Cevasco, A., Pepe, G., Brandolini, P.: The influences of geological and land use settings on shallow landslides triggered by an intense rainfall event in a coastal terraced environment. Bull. Eng. Geol. Env. **73**, 859–875 (2014)

Cevasco, A., Diodato, N., Revellino, P., Fiorillo, F., Grelle, G., Guadagno, F.M.: Storminess and geo-hydrological events affecting small coastal basins in a terraced Mediterranean environment. Sci. Total Environ. **532**, 208–219 (2015)

Conforti, M., Muto, F., Rago, V., Critelli, S.: Landslide inventory map of north-eastern Calabria (South Italy). J. Maps **10**(1), 90–102 (2014)

Conti, G., Fagarazzi, L.: Forest expansion in mountain ecosystems: "environmentalist's dream" or societal nightmare? Driving forces, aspects and impacts of one of the main 20th century's environmental, territorial and landscape transformations in Italy. Planum, Eur. J. Plann. **11**, 1–20 (2005)

Di Martire, D., Novellino, A., Ramondini, M., Calcaterra, D.: A-differential synthetic aperture radar interferometry analysis of a deep seated gravitational slope deformation occurring at Bisaccia (Italy). Sci. Total Environ. **550**, 556–573 (2016)

Galve, J.P., Cevasco, A., Brandolini, P., Soldati, M.: Assessment of shallow-landslide risk mitigation measures based on land use planning through probabilistic modelling. Landslides **12**, 101–114 (2015)

Guzzetti, F.: Landslides hazard and risk assessment, Unpublished Ph.D. Thesis, University of Bonn (2005)

Hungr, O., Leroueil, S., Picarelli, L.: The Varnes classification of landslide types, an update. Landslides **11**, 167–194 (2014)

Lari, S., Frattini, P., Crosta, G.B.: A probabilistic approach for landslide hazard analysis. Eng. Geol. **182**, 3–14 (2014)

Raso, E., Faccini, F., Brandolini, P., Firpo, M.: The lovers' lane ("Via dell'Amore") rockfall events: a history of dangerous collapses. In: Rock Mechanics and Rock Engineering: From the Past to the Future, vol. 2, pp. 1287–1292 (2016a)

Raso, E., Brandolini, P., Faccini, F., Firpo, M.: The Guvano complex landslide in the Cinque Terre National Park, Italy: Geomorphological characterization, GNSS monitoring and risk management. In: Rock Mechanics and Rock Engineering: From the Past to the Future, vol. 1, pp. 607–612 (2016b)

Terranova, R.: Aspetti geomorfologici e geologico-ambientali delle Cinque Terre: rapporti con le opere umane (Liguria orientale) Studi e Ricerche di. Geografia **7**, 39–90 (1984)

Varnes, D.J.: Slope movement types and processes. In: Schuster, R.L., Krizek, R.J. (eds.) Landslides, Analysis and Control. Special Report, 176. Transportation and Road Research Board, National Academy of Science, Washington D.C., pp. 11–33 (1978)

# Landslide Susceptibility Mapping in Tegucigalpa, Honduras, Using Data Mining Methods

Anika Braun, Elias Leonardo Garcia Urquia, Rigoberto Moncada Lopez, and Hiromitsu Yamagishi

## Abstract

Being located in a mountainous area in the heart of Central America, with a young and partially very soft volcanic geology under the influence of a humid tropical climate with high rainfall during the rainy season, the area of the Honduran capital city, Tegucigalpa, is highly prone to landslides. Due to rapid and uncontrolled urbanization, especially on the slopes that surround the city, there is a strong interaction between human activities and landslides, further increasing landslide occurrences and causing a high vulnerability of the poorest part of the population. We here employed a landslide inventory, a geological map, and a dataset of landslide related factors, generated from data that is freely available for the analysis of landslide susceptibility with the help of data mining techniques. An input dataset of 21 variables, such as lithology, landform and drainage characteristics, and road density, was pre-processed, explored, coded in the IBM SPSS Modeler software, and implemented for the prediction of landslide occurrences with Artificial Neural Networks (ANN), Bayesian Networks (BN), and Decision Trees (DT). Different techniques were applied to enhance the performance of the model predictions by preparing the dataset to make it mathematically more accessible. The models with the balanced dataset yielded promising overall correct predictions of landslide and non-landslide cases of 85% (ANN) to 90% (DT) and correct predictions of landslides of 35% (BN) to 63% (ANN).

## 1 Introduction

As a first step in a landslide risk management strategy, the assessment and mapping of the spatial probability of landslide occurrence, or landslide susceptibility, can be useful and simple to perform, as it requires only basic input data (Corominas et al. 2013). This is probably why, in the past three decades, an abundance of landslide susceptibility studies has been published, first using simple bi- and multivariate statistical methods (e.g. Van Westen et al. 1997; Lee et al. 2003), and recently, with the progress in the field of "machine learning", increasingly complex data mining methods (Hong et al. 2015). Data mining is understood as the exploration of large or complex datasets for patterns and dependencies by the application of statistical and machine learning techniques. The numerous studies have been reviewed recently in Chen et al. (2017).

One advantage of data mining methods compared to more simple techniques that require discrete data, is their ability to handle continuous data, which can contain information that would otherwise get lost during the classification through the user. The slope angle is an example that is commonly being used as a variable in landslide susceptibility analysis. Often it is arbitrarily classified, e.g. into 5° or 10° classes. More subtle trends within these classes are disguised by this procedure. Moreover, data mining techniques are robust regarding noisy and incomplete data. They also allow for

A. Braun (✉)
Department of Engineering Geology, Institute of Applied Geology, Technische Universität Berlin, Berlin, Germany
e-mail: anika.braun@rwth-aachen.de

E. L. Garcia Urquia
Department of Civil Engineering, National Autonomous University of Honduras, Tegucigalpa, Honduras
e-mail: elias.urquia82@gmail.com

R. Moncada Lopez
Departamento de Ingeniería Civil, Facultad de Ingeniería y Arquitectura, Universidad Tecnológica Centroamericana (UNITEC), Tegucigalpa, 11101, Honduras
e-mail: rigoberto.moncada@unitec.edu

H. Yamagishi
Shin Engineering Consultant Co. Ltd, Sapporo, Japan
e-mail: hiromitsuyamagishi88@gmail.com

certain techniques to enhance a dataset for modeling by making its features mathematically more favorable, for instance, by balancing an imbalanced dataset. Imbalanced distributions of the prediction target class are a common problem in data mining of real-world datasets (Chawla 2009), that can be overcome by dataset balancing (Pyle 2003).

Tegucigalpa, the capital and largest city in Honduras, is one of the most exposed areas of a country very prone to natural hazards. For the past 20 years, according to Germanwatch reports (Kreft 2016), Honduras has been on the global top three of countries most affected by natural disasters. The urban area of Tegucigalpa is currently expanding at an exponential rate and in a disorderly manner. In terms of landslide disasters, extreme events have been triggered by hydro-meteorological events such as Hurricane Fifi in 1974, Hurricane Gilbert in 1988, Hurricane Mitch in 1998 (Harp et al. 2002), and Tropical Storm No. 16 in 2008. Also, a 7.3 magnitude earthquake in 2009 is evidence of the threat of seismic events (PNUD 2010). Most landslides can be attributed to triggering by intense rainfall and most rainy seasons present abundant yearly material and human losses due to this phenomenon. However, Garcia-Urquia and Axelsson (2015) and Garcia-Urquia (2016) showed that many landslide events documented in the written media and occurring between 1980 and 2005 had connections with low amounts of rainfall. This finding suggests that the urban nature of these landslides makes them harder to predict with rainfall thresholds, since anthropogenic actions such as deforestation, uncontrolled loading of slopes and poor water management significantly contribute to slope destabilization.

While Tegucigalpa has been subject of different landslide studies, these have often been limited in area and scope. Research developed immediately after Hurricane Mitch, such as USGS report by Harp et al. (2002) and JICA's Master Plan (2002), all focused close to River Choluteca Area. As the city has increased in size, a lot of this information is not applicable to a greater extent of new settlements. DIPECHO project by UNDP (2010) and DesInventar (Rosales 1998) have contributed with landslide inventory mapping, but have not been exclusively focused to susceptibility.

Most recently, UNDP developed a Mass Movement Hazard Map adjusted by heuristic methods, and applying factors such as slope angle, with assistance of Colombian consultants CI AMBIENTAL (last update on 2013). However, several susceptibility factors, such as geology, geomorphology, landslide inventory, are not implemented in the model. Thus, even for the region that has been most studied in Honduras, landslide information is very limited. For other very vulnerable rural areas, information is extremely scarce and mostly non-existent. As a result, a reliable method of susceptibility mapping would be of great value for prevention and planning. For a larger extent in Tegucigalpa,

landslide susceptibility mapping has recently been carried out with the bivariate statistical matrix method (Garcia-Urquia and Yamagishi 2017). Another susceptibility map has been produced in the aftermath of Hurricane Mitch using the Mohra and Vahrson method (Pineda 2004).

We here for the first time introduce three data mining methods, Artificial Neural Networks (ANN), Bayesian Networks (BN), and Decision Trees (DT), for landslide susceptibility mapping of the entire urban area of Tegucigalpa. The objectives were first the enlargement of a basic factor dataset through a geomorphometric analysis, then the enhancement of the dataset for modeling using balancing and coding techniques, and finally the optimization of the models themselves. The focus in this publication is on the enhancement of the dataset through balancing.

## 2 Setting

Tegucigalpa´s physiography is the result of a combination between river valley topography (Choluteca River), where most of the city was located since 1578 until its accelerated growth during the 20th Century, and a mountainous topography extending outward along its periphery, with elevations ranging from 900 to 1300 m above sea level (Fig. 1). Urban growth to these steep parts has resulted in a dramatic increase of landslide events (PNUD 2010). Rainfall has an annual average range of 1075–1175 mm (IHCIT 2012); although for some extreme events, such as Hurricane Mitch, 281 mm of rainfall were recorded in only one week (Harp et al. 2009). Garcia-Urquia and Axelsson (2014) showed that between 1980 and 2005, May, June and September were the wettest months, while landslide occurrence was highest in the latter part of the rainy season (August, September and October).

From a geological standpoint, the main groups and formations of Tegucigalpa are of volcanic and sedimentary origin (Rogers and O'Conner 1993). The Padre Miguel Group, which covers the greatest percentage of the site, has rhyolitic, dacitic and andesitic tuffs, lahars, ignimbrites and other Tertiary pyroclastic sediments, some highly vulnerable to saturation during the rainy season (IHCIT 2014). Other volcanic units are Matagalpa Formation, Tertiary mafic basalt and andesite flows, and Quaternary dark basalt flows; at their lithological boundary, slope failures have been identified as a common occurrence (Quezada-Román et al. 2018). On the other hand, the Valle de Angeles Group, located at the center, east and southeast of the city, consists of conglomerates, mudstone and sandstone. At the riverside, which crosses the city and splits it from north to south, fluvial terraces and Quaternary alluvial sediments can be found (IGN 1987). These sediments are also very susceptible to erosion and loss of resistance due to saturation.

**Fig. 1** Location map of Tegucigalpa, Honduras, the outlines of the study area and Fig. 2, and the outlines of Fig. 3
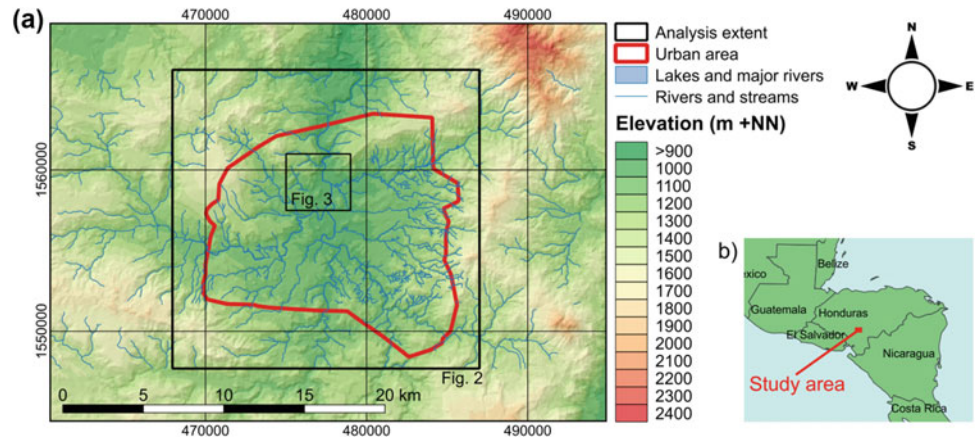


## 3   Methodology

### 3.1   Input Data

The data used in this analysis is based on a landslide inventory, a digital elevation model, a geological map, and the river and road network in the urban area of Tegucigalpa. All input data was converted into grids with a 30 m cell size.

The landslide inventory (Fig. 2) was mapped in 2013 in collaboration with the Japan International Cooperation Agency (JICA) through aerial image interpretation in combination with field surveys performed by UNAH a relevant and susceptible zones. It contains a total number of 3051 polygons covering an area of 25.24 km², of which 71.78% are landslide bodies, 16.82% landslide scarps, 11.74% rock creep,

and 0.65% failures. "Rock creep" is here referring to slow moving rock slides over large periods of time, while "failure" refers to superficial failures of debris. All of the polygons were included in the analysis as landslide events (positive).

A 30 m digital elevation model (DEM), from the ALOS world digital surface model (JAXA 2016), was downloaded free of charge. Since it contained some no data areas, additional elevation data was obtained from the 30 m Shuttle Radar Topographic Mission (SRTM) DEM that is also provided free of charge (USGS 2016).

A geological map with nine major lithological units in the analysis area was provided by JICA and extended in the NE with the help of the geological map by Rogers and O'Connor (1993) (Fig. 2). For the NW no reliable information on the geology was available, so this area was not considered in the analysis. Shapefiles for the road and river network were also

**Fig. 2** Geological map of the study area with the polygons of the landslide inventory
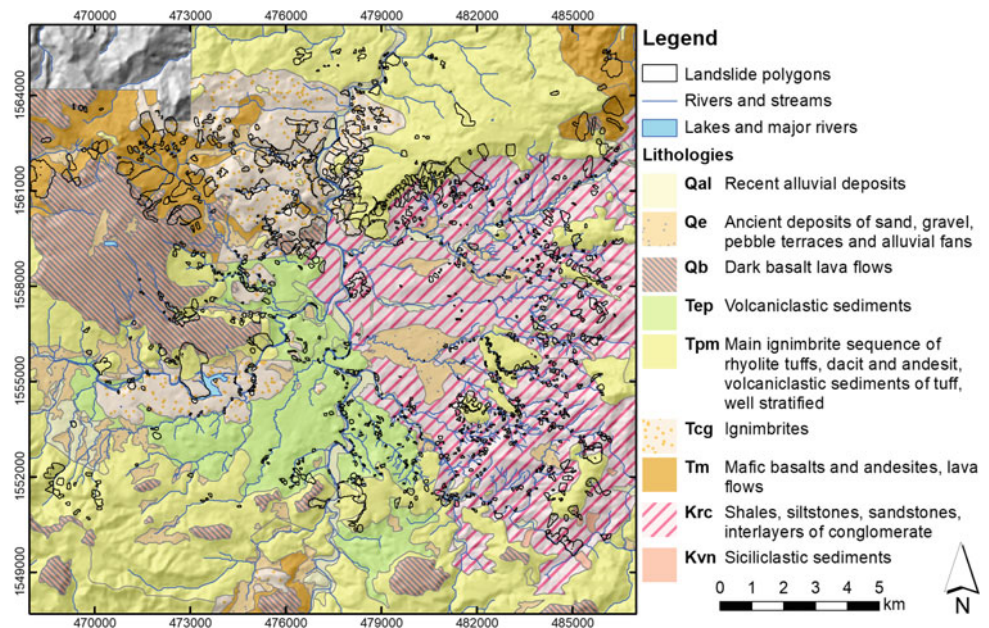
provided by JICA, whereas the road network was extended with data downloaded from the OpenStreetMap project (OpenStreetMap contributors 2016) and the river network was extended with the stream network generated during a hydrological analysis of the DEM in ArcGIS.

## 3.2 Data Processing

In order to account for anthropogenic activities that could favor the destabilization of slopes, roads were implemented as a proxy for human activities. Two parameters were derived from the road network in ArcGIS, Euclidean distance to roads and road density (No. 2 and 3 respectively in Table 1).

In a hydrological analysis of the low-pass filtered, void filled, and depressionless DEM in SAGA GIS, the catchment area, topographic wetness index (TWI), and stream power index (SPI) (Moore et al. 1993) were derived (No. 18, 20

and 21 respectively in Table 1). Moreover, a grid with the Euclidean distance to rivers was calculated in ArcGIS (No. 19 in Table 1).

In a geomorphometric analysis, first the primary terrain parameters slope angle, slope aspect, slope curvature, and relative relief were derived. Then the secondary terrain parameters, curvature derived landforms (Dikau 1988), slope length, the sky view factor (SVF), and the topographic position index (TPI) for landforms within a 300 and 2000 m radius, respectively, were derived from the DEM (No. 4–11 and 12–17 in Table 1, respectively). The TPI was also classified into 9 landform classes after Weiss (2001). The SVF is a measure for the area of unobstructed sky visible from each cell in the terrain raster and it is thus a measure for the solar irradiation (Kokalj et al. 2011). With the TPI, simply for each cell the elevation is compared to the mean elevation within a defined neighborhood radius (Weiss 2001). More descriptions of these parameters are given in Table 1.

**Table 1** List of input parameters and their description, indication of the platform with which they were generated and their role in the different input datasets for predictive modeling

| No. | Parameter and description | Platform | Type d: discrete c: continuous |
|---|---|---|---|
| 1 | Lithological units | | d |
| 2 | Euclidean distance to roads (m), continuous or classified into <30, 30–120 m, and >120 m | ArcGIS | c |
| 3 | Road density within a radius of 500 m (km/km$^2$) | ArcGIS | c |
| 4 | Elevation (m) | ArcGIS | c |
| 5 | Slope angle in degrees, continuous or classified with break values 5°, 15°, 25°, 35°, 45°, and 55° | ArcGIS | c |
| 6 | Slope angle in radian calculated after Zevenbergen and Thorne (1987) | SAGA | c |
| 7 | Slope aspect in degrees, coded into N and S sector respectively with cosine function, or classified into 8 sectors | ArcGIS | c |
| 8 | Slope curvature (negative = concave, positive = convex, 0 = flat) | ArcGIS | c |
| 9 | Planar curvature (negative = concave, positive = convex, 0 = flat) | ArcGIS | c |
| 10 | Profile curvature (negative = concave, positive = convex, 0 = flat) | ArcGIS | c |
| 11 | Relative relief, range between minimum and maximum elevation within a 5 × 5 cell neighborhood | ArcGIS | c |
| 12 | Curvature classified into landforms after Dikau (1988) | SAGA | d |
| 13 | Slope length (m) | SAGA | c |
| 14 | Sky view factor (−), measure for the area of unobstructed sky (Kokalj et al. 2011) | SAGA | c |
| 15 | Topographic position index (−) (negative = valleys, positive = ridges), within 300 m radius for individual landforms (Weiss 2001) | SAGA | c |
| 16 | Topographic position index (−) (negative = valleys, positive = ridges), within 2000 m radius for major landforms (Weiss 2001) | SAGA | c |
| 17 | Classification of TPI into 9 landforms (Weiss 2001) | SAGA | d |
| 18 | Catchment area (m$^2$), area of cells draining into the respective cell | SAGA | c |
| 19 | Euclidean distance to rivers (m), continuous or classified into <30, 30–120 m, and >120 m | ArcGIS | c |
| 20 | Topographic wetness index (m$^2$ m$^{-1}$), characterizes spatial distribution of zones of surface saturation and soil water contents (Moore et al. 1993) | SAGA | c |
| 21 | Stream power index, measure of the erosive power of overland flow (Moore et al. 1993) | SAGA | c |

## 3.3 Data Preparation and Exploration

All parameter grids were gathered in ArcGIS and transferred into a table with the tool "Sample". The table was then imported into the modeling software IBM SPSS Modeler 17.0. Here the dataset was further processed and explored prior to the actual modeling.

While the parameters lithology, classified curvature, and TPI landforms were of a nominal data type or measurement level, and the parameter landslides was binary, all other parameters were of continuous measurement level. The distribution of the continuous parameters was examined and the log10 function was applied to transform the distribution of the parameters TWI and SPI into a normal distribution. All continuous parameters were normalized to a range from 0 to 1 with a linear normalization function in order to avoid scale effects. Some continuous parameters however, such as the curvature and TPI, are distributed in the negative and positive number space, where 0 is marking a distinct change. In order to maintain this mathematical switch, these parameters were normalized between −1 and 0, and 0 and 1, respectively.

One particularly complex parameter is the slope aspect. It is generated in ArcGIS in azimuthal degrees, whereas 0° and 360° both correspond to the north sector. This is mathematically not clear. To overcome this problem, very often it is transformed into a discrete parameter by classifying it according to the eight main ordinal directions N, NE, E, SE, S, SW, W, and NW. However, with the continuity maybe some relevant information gets lost. Especially since the N and the S exposure of slopes are believed to be related to their degree of stability, the parameter aspect was here coded with the cosine function into two new variables, a N aspect, where 1 corresponds to a N exposure and 0 to an E or W exposure, and a S aspect, where 1 corresponds to a S exposure and 0 to an E or W exposure respectively.

## 3.4 Modeling

As a further preparation for the modeling, the dataset was randomly partitioned into a training and a test dataset containing 50% of the data, respectively. The models were developed with the training partition, while their performance is evaluated with the test partition.

One major problem in data mining of real-world problems is the imbalance of the classification categories, particularly with an underrepresentation of the modeling target in such datasets (Chawla 2009). In our dataset only 7.14% of the records are representing a landslide, or in other words 7.14% of the study area is covered by landslides. It is

assumed that a well-balanced dataset should be distributed at least 70/30 (Pyle 2003). One way to overcome this problem is to balance the training dataset through artificially increasing the number of landslide records by multiplying them with a factor. However, care has to be taken that the distribution of the training dataset is not getting distorted compared to the test dataset. In order to examine how balancing the training dataset can affect the modeling performance, we here simply tested different multiplication factors 3, 6, 10, and 14, for increasing the percentage of landslide cases in the training dataset, resulting in landslide positive to negative ratios of 19, 32, 44, and 52% respectively, to cover and go beyond the range of 20/80 and 30/70 balancing ratios that are recommended as optimal by Pyle (2003).

In the field of data mining, the prediction of landslide occurrence is a binary classification problem. Among the most commonly used data mining algorithms for classification problems are Decision Trees, Artificial Neural Networks, and Bayes Networks, which are also implemented in our study. Decision Trees are algorithms that recursively separate the dataset into smaller subsets on the basis of statistical tests performed at each node, to form a hierarchical, tree-like structure (Friedl and Brodley 1997). Artificial Neural Networks simulate information processing in the biological nervous system. They consist of interconnected processing units carrying a transfer function that are trained to predict an expected output by adapting weights between the processing units (Lee et al. 2003). Bayesian Networks are directed acyclic graphs representing a set of random variables and their probabilistic dependencies that are intended to simulate human reasoning (Pearl 1985).

In general, during the training phase of the modeling process, the algorithms learn to recognize patterns in the data that are related to one of the two possible outcomes of the classification, respectively. During the test phase, the trained model is then applied to an unknown dataset to test its performance. It is worth noting that the prediction is not based on causality, but solely relies on the information found in the data. This is referring to the fundamental nature of the data mining procedure as opposed to general statistical methods that are based on hypothesis testing or heuristic methods based on expert knowledge. However, the conversion of the real-world problem into a virtual data model and the evaluation of the ability of the virtual world to reflect the real world have to be based on expert knowledge on the landslide processes in the study area.

In a first step, we here developed default models of the three types Decision Trees, Artificial Neural Networks, and Bayesian Networks, respectively. Then we modified the input dataset by applying different balancing factors to the records representing landslides in the training partition.

## 4 Results and Discussion

### 4.1 Model Evaluation

For the evaluation the prediction outcomes, different performance indicators can be consulted. The four basic indicators in binary prediction problems are the numbers or percentages of hits (true positives), correct rejections cr (true negatives), false alarms fa (false positives), and misses (false negatives). Derived performance indicators are the hit rate H, which is the rate of predicted positives, and the proportion correct PC, which is the overall rate of correct predictions. The most important skill of a model is the prediction of positives, which is particularly challenging when the positives are underrepresented in the training data. For example, in our case a model that would just reject all landslides and predict the absence of the event in all cases would still have a PC of 92.86, but a hit rate H of 0%. Moreover, a well balanced model should have low numbers of false alarms and misses, whereas the costs of a false alarm and a miss may vary depending on the nature of a prediction problem. Basically, a miss can be considered as more dramatic than a false alarm. Repeated false alarms can however lead to a decrease in the acceptance or trust in the model.
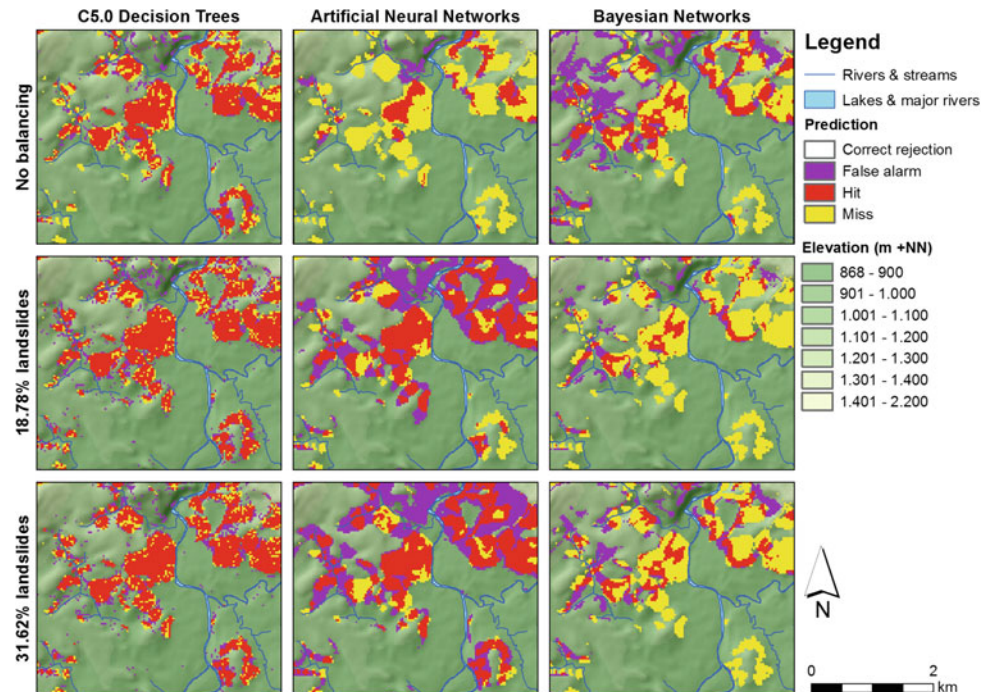
### 4.2 Effect of Balancing

Different multiplication factors, resulting in landslide positive to negative ratios of 19, 32, 44, and 52% of landslides were applied with default models in order to analyze the effect on model performance and error generation.

For the C5.0 Decision Trees, the balancing had almost no effect on the overall performance expressed through PC, and only a little effect on the hit rate H in the beginning (Table 2). Relatively large discrepancies between the model performance in training and test, especially after balancing, indicate a general over fitting of the model to the training dataset, as expressed by the difference of PC and H in test and training, and thus a poor ability of the models to generalize the learned patterns for unknown areas. Looking at the prediction in their spatial context in the left column in Fig. 3, it becomes obvious that the C5.0 Decision Trees produce a relatively good susceptibility map even without balancing the data. When a balancing factor is applied, there is an increased number of isolated, randomly scattered false alarm and miss cells, which is probably because they only occur in the test dataset, while the distribution between test and training is random. In future research, it seems to be most promising to further develop the C5.0 Decision Trees without data balancing.

**Table 2** Results for C5.0 decision trees, artificial neural networks (ANN) and Bayes networks in terms of the rate of correctly detected events (hit rate H), the proportion of overall correct classifications (PC), the proportion of false positives (type I error), and proportion of false negatives (type II error) for different levels of dataset balancing in the test run. Also, the difference of H and PC between training and test run are displayed. It should be low for a well balanced model with a good ability to generalize

| | Test | | False | False | Training—test | |
|---|---|---|---|---|---|---|
| | H (%) | PC (%) | Positive (%) | Negative (%) | $\Delta$H (%) | $\Delta$PC (%) |
| *Comparison of C5* | | | | | | |
| 7.14% landslides | 40.22 | 93.68 | 2.04 | 4.28 | 15.62 | 2.08 |
| 18.78% landslides | 55.53 | 91.89 | 4.93 | 3.19 | 34.39 | 5.02 |
| 31.62% landslides | 53.69 | 91.90 | 4.78 | 3.32 | 37.12 | 5.39 |
| 43.53% landslides | 53.65 | 90.36 | 6.32 | 3.32 | 36.73 | 5.37 |
| 51.9% landslides | 52.62 | 90.35 | 6.26 | 3.39 | 38.16 | 5.64 |
| *Comparison of ANN* | | | | | | |
| 7.14% landslides | 7.20 | 92.71 | 0.43 | 6.86 | −0.21 | 0.04 |
| 18.78% landslides | 35.43 | 90.99 | 4.23 | 4.77 | -0.12 | 0.08 |
| 31.62% landslides | 63.44 | 85.16 | 12.14 | 2.70 | 0.34 | 0.16 |
| 43.53% landslides | 76.64 | 79.69 | 18.58 | 1.73 | 1.36 | 0.26 |
| 51.9% landslides | 83.15 | 72.21 | 26.54 | 1.25 | 1.53 | 0.48 |
| *Comparison of Bayes* | | | | | | |
| 7.14% landslides | 7.91 | 92.94 | 0.77 | 6.28 | 0.42 | 0.10 |
| 18.78% landslides | 21.30 | 91.05 | 3.58 | 5.37 | 0.69 | 0.11 |
| 31.62% landslides | 35.88 | 87.44 | 8.18 | 4.38 | 1.42 | 0.20 |
| 43.53% landslides | 46.75 | 82.94 | 13.42 | 3.63 | 1.29 | 0.20 |
| 51.9% landslides | 54.92 | 79.38 | 17.54 | 3.08 | 0.48 | 0.22 |

**Fig. 3** Matrix with spatial distribution of prediction results for C5.0 decision trees (left), artificial neural networks (middle), and bayesian networks (right) at different levels of data balancing. Extent indicated in Fig. 1

For the ANN, with increasing balancing, the hit rate H increased significantly. At the same time, the number of misses went down, while the number of false alarms increased, which is why there is almost no effect on the PC. The Bayesian Networks showed a similar behavior with increasing balancing as the ANN, but their performance was in general below that of the ANN (Table 2). Both model types are most balanced regarding false alarms and misses at a balancing ratio of about 80/20. However, their hit rates H reach more interesting levels at a balancing ratio of about 70/30. In the middle column of Fig. 3 it can be seen that with increasing balancing, the Artificial Neural Networks develop better skills of recognizing landslides also in spatial context. They produce already more coherent landslide bodies at a balancing ratio of around 80/20, while they even detect the landslides around the hill in the center of the city, which is in the SE corner of the map excerpt. Interestingly, here the false alarms also build spatially relatively coherent patterns that seem to be geologically plausible, and thus, they might actually be valuable for pointing out highly susceptible areas. The Bayesian Networks show no significant alteration of landslide detection skills in the spatial context (right column in Fig. 3). Overall, they seem to be a less favorable method to model our particular dataset, while the Artificial Neural Networks show potential for further development on a balanced dataset.

Which level of balancing can be considered appropriate in the end? Actually, Pyle (2003) considers a ratio of 70/30 as relatively optimal, but recommends to stick to an 80/20 ratio to keep distribution distortion effects low, and also take into account the related costs of errors. In general, both, the costs of false alarms and misses are relevant. Although a miss seems to be more dramatic, false alarms can also turn out to be dramatic when the elements at risk start losing faith in the prediction system. Anyway, in landslide susceptibility mapping, costs of false alarms are probably less than in predictions of more disastrous natural hazards, such as hurricanes. In our particular case, higher balancing factors resulted also in higher numbers of false alarms, and here a balance between the costs of false alarms and the benefit of the balancing has to be ruled out. For the C5.0 Decision Trees, the gain through the balancing is not very significant, weighed against the costs of over fitting and false alarms. For the ANN, it might be worth accepting higher costs through false alarms for the sake of better landslide recognition skills.

## 5 Conclusions

A dataset composed of 21 variables, which was derived from very basic data sources, and a landslide inventory, were implemented for developing C5.0 Decision Trees, Artificial Neural Networks, and Bayesian Networks for the predictive modeling of landslide susceptibility in Tegucigalpa, Honduras. To address the general problem of imbalanced real-world datasets, different levels of dataset balancing were implemented to increase the data density of positives, and their effect on the prediction performance was examined.

It can be concluded that while the C5.0 Decision Trees do not significantly react to the balancing, the ANN and

Bayesian Networks clearly improve their ability to detect landslides as reflected by their increasing hit rates. The improvement comes at the cost of increased numbers of false alarms that have to be weighed against the gain through the enhanced detection skills. Generally speaking, negative to positive ratios of 80/20 to 70/30 appear to be an ideal range.

The models with the 70/30 balanced dataset yielded promising overall correct predictions of 85% (ANN) to 90% (DT) and correct predictions of landslides of 35% (BN) to 63% (ANN). While the performance of the Bayesian Networks was clearly less promising than that of the other two models, the Decision Trees showed extraordinarily good performances that came at the cost of high discrepancies between test and training and thus a poor ability to generalize, and the Artificial Neural Networks showed satisfying performances with relatively high numbers of false alarms. Depending on potential deployments of the models, the Decision Trees might be interesting for the employment in an early warning system as they are more accurate, for example by coupling the resulting landslide susceptibility maps with rainfall thresholds or real-time rainfall data, or by using them to identify locations for the installation of monitoring instruments. The Artificial Neural Networks might be useful for identifying future endangered areas by considering the false alarms.

The general approach of applying data mining techniques to an extended dataset seems to be promising and it could, in the future, be further developed for Tegucigalpa by examining the composition of the dataset considering the particular challenges of data scarcity, and then also implemented for other areas with similar characteristics that struggle with data scarcity.

# References

Chawla, N.V.: Data mining for imbalanced datasets: an overview. In: Maimon, O., Rokach, L. (eds.) Data Mining and Knowledge Discovery Handbook, pp. 875–886. Springer, US (2009)

Chen, W., Pourghasemi, H.R., Panahi, M., Kornejady, A., Wang, J., Xie, X., Cao, S.: Spatial prediction of landslide susceptibility using an adaptive neuro-fuzzy inference system combined with frequency ratio, generalized additive model, and support vector machine techniques. Geomorphology **297**, 69–85 (2017)

CI AMBIENTAL S.A.S.: Producto No. 2 Actualización del Mapa de Amenazas por deslizamientos de la Ciudad de Tegucigalpa. Informe Final y Mapa. Programa de las Naciones Unidas para el Desarrollo-PNUD y GOAL. Proyecto Honduras (2013)

Corominas, J., Westen, C., Frattini, P., Cascini, L., Malet, J.-P., Fotopoulou, S., Catani, F., Van Den Eeckhaut, M., Mavrouli, O., Agliardi, F., Pitilakis, K., Winter, M.G., Pastor, M., Ferlisi, S., Tofani, V., Hervás, J., Smith, J.T.: Recommendations for the quantitative analysis of landslide risk. Bull. Eng. Geol. Env. **73**, 209–263 (2013)

Dikau, R.: Entwurf einer geomorphographisch-analytischen Systematik von Reliefeinheiten, Band 5 der Reihe Heidelberger Geographische Bausteine, 37p (1988)

Friedl, M.A., Brodley, C.E.: Decision tree classification of land cover from remotely sensed data. Remote Sens. Environ. **61**, 399–409 (1997)

Garcia-Urquia, E.: Establishing rainfall frequency contour lines as thresholds for rainfall-induced landslides in Tegucigalpa, Honduras, 1980–2005. Nat. Hazards **82**(3), 2107–2132 (2016)

Garcia-Urquia, E., Axelsson, K.: The use of press data in the development of a database for rainfall-induced landslides in Tegucigalpa, Honduras, 1980–2005. Nat. Hazards **73**(2), 237–258 (2014)

Garcia-Urquia, E., Yamagishi, H.: Landslide susceptibility mapping based on aerial photograph interpretation inventory for Tegucigalpa, Honduras: an application of the matrix method. In: Yamagishi, H., Bhandary, N.P. (eds.) GIS Landslide. Springer Japan, pp. 163–181 (2017)

Garcia-Urquia, E., Axelsson, K.: Rainfall thresholds for the occurrence of urban landslides in Tegucigalpa, Honduras: an application of the critical rainfall intensity. Geogr. Annaler: Ser. A, Phys. Geogr **97**(1), 61–83 (2015)

Harp, E.L., Held, M.D., Castañeda, M.R., McKenna, J.P., Jibson, R.W.: Landslide hazard map of Tegucigalpa, Honduras. U.S. Geological Survey Open-File Report 02-219, 9 pp (2002)

Harp, E., Reid, M., McKenna, J., Michael, J.: Mapping of hazard from rainfall-triggered landslides in developing countries: examples from Honduras and Micronesia. Eng. Geol. **104**, 295–311 (2009)

Hong, H., Pradhan, B., Xu, C., Bui, D.: Spatial prediction of landslide hazard at the Yihuang area (China) using two-class kernel logistic regression, alternating decision tree and support vector machines. Catena **133**, 266–281 (2015)

Instituto Geográfico Nacional-IGN: Mapa Geológico de Tegucigalpa, Lepaterique y San Buenaventura. Tegucigalpa, Honduras **1**(50), 000 (1987)

Instituto Hondureño de Ciencias de la Tierra-IHCIT: Atlas Climático y de Gestión de Riesgo de Honduras. Universidad Nacional Autónoma De Honduras, 161 pp (2012)

Instituto Hondureño de Ciencias de la Tierra-IHCIT: Estudio Hidrogeoquímico de la parte alta de la cuenca del Río Choluteca. Subproducto 2.4, Actualización del inventarío de recursos de aguas subterráneas. Universidad Autónoma de Honduras. Proyecto Fondo de Adaptación, 159 pp (2014)

Japan Aerospace Exploration Agency-JAXA: ALOS Global Digital Surface Model 'ALOS World 3D—30 m' (AW3D30 DSM Ver. 1.0), data available from the JAXA web interface (2016). http://www.eorc.jaxa.jp/ALOS/en/aw3d30/data/index.htm, downloaded in Nov 2016

Japanese International Cooperation Agency-JICA: The Study on Flood Control and Landslide Prevention in the Tegucigalpa Metropolitan Area of the Republic of Honduras. Prepared by Pacific Consultants International and Nikken Consultants Inc, Tegucigalpa, Honduras (2002)

Kokalj, Ž., Zakšek, K., Oštir, K.: Application of sky-view factor for the visualisation of historic landscape features in lidar-derived relief models. Antiquity, **85**(327), 263–273. (2011)

Kreft, S., Eckstein, D., Melchior, I.: Global Climate Risk Index 2017. Who Suffers Most From Extreme Weather Events? Weather-related Loss Events in 2015 and 1996 to 2015. Germanwatch Briefing Paper (2016)

Lee, S., Ryu, J.-H., Lee, M.-J., Won, J.-S.: Use of an artificial neural network for analysis of the susceptibility to landslides at Boun, Korea. Environ. Geol. **44**, 820–833 (2003)

Moore, I.D., Gessler, P.E., Nielsen, G.A., Peterson, G.A.: Soil attribute prediction using terrain analysis. Soil Sci. Soc. Am. J. **57**(2), 443–452 (1993)

OpenStreetMap contributors: Planet dump, retrieved from https://planet.openstreetmap.org on 11/03/2016 (2016)

Pineda, M.A.: Identificación y análisis de las áreas susceptibles de los procesos de remoción en masa, en la cuenca alta del rio Grande o Choluteca, en Tegucigalpa, Honduras.C.A. (Masters Degree Thesis), Universidad de Costa Rica (2004)

Pearl, J.: Bayesian networks: a model of self-activated memory for evidential reasoning. In: Proceedings of the 7th Conference of the Cognitive Science Society, University of California, Irvine, pp. 1–22 (1985)

Programa de las Naciones Unidas para el Desarrollo-PNUD: Informe de Línea Base: Proyecto DIPECHO VII UNDP. 14 Barrios Vulnerables a Deslizamientos y Sismos en la Ciudad de Tegucigalpa, 42 pp (2010)

Pyle, D.: Business Modeling and Data Mining. Morgan Kaufmann, San Francisco (2003)

Quezada-Román, A., Moncada, R., Paz Tenorio, J.A., Espinoza Jaime, E.: La información geográfica institucional en las investigaciones sobre movimientos de laderas en Costa Rica, Honduras, p. 7p. México y Nicaragua, Revista Geográfica de América Central (2018)

Rogers, R.D., O'Conner, E.A.: Mapa Geológico de Honduras: Hoja de Tegucigalpa (segunda edición). Inst. Geográfico Nac., Tegucigalpa, Honduras **1**(50), 000 (1993)

Rosales, C.: Asistencia técnica para la evaluación de los efectos del huracán Mitch en Honduras, 17nov—8dic, 1998. Reporte. Red de Estudios Sociales en Prevención de Desastres en América Latina —LA RED/ Comité Permanente de Contingencias—COPECO (1998)

United States Geological Survey-USGS: SRTM 1 Arc-Second Global elevation data, data available from the USGS via the EarthExplorer web interface. https://earthexplorer.usgs.gov/, downloaded in (Nov 2016)

Van Westen, C.J., Rengers, N., Terilen, M.T.J., Soeters, R.: Prediction of the occurrence of slope instability phenomena through GIS-based hazard zonation. Geol. Rundsch. **86**, 404–414 (1997)

Weiss, A.: Topographic position and landforms analysis. In: Poster Presentation, ESRI User Conference, San Diego, CA, vol. 200 (July 2001)

# Landslide Inventory and Susceptibility Models, Prestonsburg 7.5-min Quadrangle, Kentucky, USA

Hannah Chapella, William Haneberg, Matthew Crawford, and Abdul Shakoor

### Abstract

The Cumberland Plateau of eastern Kentucky is a forested and landslide prone area dominated by narrow ridges, steep slopes, and, in many places, terrain disturbed by past and current coal mining. The bedrock geology of the region comprises flat-lying Paleozoic shales, sandstones, siltstones, and coals; the vegetation is temperate deciduous forest sustained by average annual precipitation of about 125 cm. We undertook a pilot project to develop an extensible airborne LiDAR based landslide mapping protocol and create landslide inventory maps of the Prestonsburg, Kentucky, 7.5-min quadrangle, which we will ultimately use to support landslide susceptibility models of the areas. Arcuate head scarps, bulging toes, displaced drainage paths, and hummocky topography define landslides throughout the study area. Supplementary topographic roughness, topographic curvature, and bedrock geology maps, along with aerial photographs and a focused program of field checking, helped to confirm mapped features as landslides. We will collect samples for geotechnical testing and combine the results with a LiDAR based DEM to create susceptibility maps using both the physics-based probabilistic computer code PISA-m and empirical logistic regression models. If successful, our protocol may be implemented statewide and the results made available through an online database, serving as a resource for residents and professionals.

## 1 Introduction

Landslides are one of the most common natural disasters around the globe, causing destruction of infrastructure and loss of life. In the United States, landslide related deaths average 25–50 per year, and economic losses (adjusted for inflation) likely average $2.8 billion per year (Schuster and Highland 2001).

The state of Kentucky averages direct economic losses of approximately $10–20 million per year from landslide-related events. In an ongoing landslide inventory project, the Kentucky Geological Survey is compiling landslide information from a variety of sources to understand the extent of landslide hazard and to provide a standardized database (Crawford 2014). A pilot project is underway to develop a landslide mapping protocol using airborne LiDAR in an attempt to standardize the process of landslide mapping, identification, and characterization to aid in the overall understanding of these hazards.

### 1.1 Geologic Setting

Our study focuses on the Prestonsburg 7.5-min quadrangle, located in Floyd County and a small portion of southern Johnson County, Kentucky (Fig. 1). The topography is typical of a mature unglaciated plateau, with narrow ridges, steep-sided valleys, and an average vertical relief of 213 m. The bedrock geology comprises flat lying packages of Paleozoic shales, sandstones, siltstones, and coals. Past coal mining has disturbed the terrain as a consequence of deep mining, contour stripping, auger mining, mountaintop removal, and valley fill (Waters and Abney 2000).

H. Chapella (✉) · A. Shakoor
Kent State University, Kent, OH, USA
e-mail: hchapell@kent.edu

A. Shakoor
e-mail: ashakoor@kent.edu

W. Haneberg · M. Crawford
Kentucky Geological Survey, Kentucky University, Lexington, KY, USA
e-mail: bill.haneberg@uky.edu
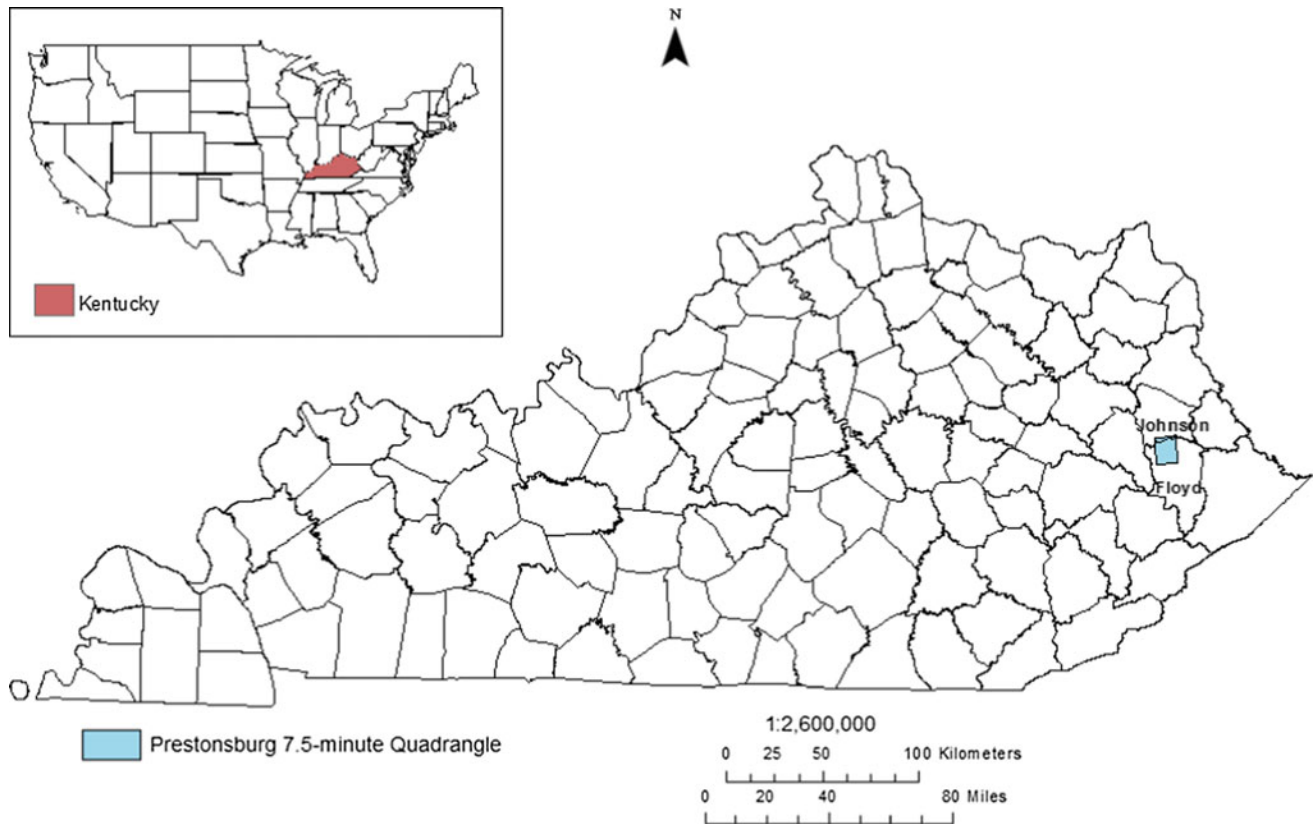
M. Crawford
e-mail: mcrawford@uky.edu

**Fig. 1** The location of the State of Kentucky with respect to the contiguous United States, shown in the upper left corner, and a county map of Kentucky illustrating the location of the Prestonsburg 7.5-min quadrangle

Mountainous regions of Kentucky are susceptible to a variety of slope movements as the result of steep slopes, unfavorable geologic conditions, precipitation, and slope modifications by humans. Slides are the prevailing mode of slope movement in the Prestonsburg area, and can be attributed to the failure of colluvial soils. Landslides within this region are triggered primarily by rain during winter and spring seasons (Crawford et al. 2015).

### 1.2 LiDAR

LiDAR, an acronym for Light Detection and Ranging, is a laser-based remote sensing technique used to obtain topographic data that support creation of high resolution digital elevation models (DEMs). In their simplest form, DEMs are grids of elevation values representing Earth's topography. LiDAR data can be processed to create high resolution bare-earth DEMs in which infrastructure and vegetation are computationally removed. DEMs are particularly useful for landslide analyses in rugged and highly forested areas. In order to make DEMs useful in landslide studies, the DEMs can be visualized as shaded relief renderings, topographic contours, or other DEM derivatives within a geographic information system (GIS) software environment (Haneberg 2017).

Airborne LiDAR DEMs have become increasingly available during the past 20 years. Burns (2007) conducted a pilot project that researched the best remote sensing dataset to use as a primary tool for systematically mapping landslides in Oregon, and found that LiDAR data resulted in the identification of 3–200 times more landslides with more accurate spatial extents than would have been possible using conventional aerial photographs and topographic maps.

## 2 Methods

We first created a landslide inventory to illustrate the spatial distribution of past landslides. Our landslide inventory separated landslides into two main feature classes based on how landslide features were mapped. Landslides digitized from the LiDAR DEMs and derivative maps were recorded in a landslide polygon feature class, whereas landslides that occurred after the acquisition of LiDAR were recorded as points in a separate feature class.

To further understand the landslide hazard within the Prestonsburg quadrangle, we used the slope stability model PISA-m (e.g., Haneberg et al. 2009) to identify potential landslide areas. PISA-m requires specific input layers and geotechnical parameters to determine problematic areas.

PISA-m and variations of the first-order, second-moment approach upon which it is based have been used to assess static and seismic slope stability on land and in deepwater marine environments (Haneberg 2004, 2012, 2016; Weppner et al. 2008; Haneberg et al. 2009; Bruce et al. 2013; Cole 2013). We used our landslide inventory to evaluate the PISA-m results for the Prestonsburg quadrangle.

## 2.1 Landslide Inventory

To begin building a landslide inventory, we compiled LiDAR, aerial imagery, bedrock geology, soil, hydrological, and previous landslide inventory data using ESRI ArcMap 10.4.1. The LiDAR DEM was used to create a suite of shaded relief renderings, using hillshade and slopeshade techniques to create a pseudo-3D depiction of the topographic surface. To support our interpretation of shaded relief renderings, we also created contour maps, topographic curvature maps, and topographic roughness maps. Topographic curvature maps were prepared using the output curvature raster, a combination of profile curvature and planform curvature, to emphasize terracing, ridges and valleys, and convex/concave surfaces. Topographic roughness has no single definition; however, within the context of geomorphology, we use roughness as an expression of the variability of a topographic surface using the standard deviation of slopes method and a $5 \times 5$ floating window (Grohmann et al. 2011).

We mapped landslide features in a systematic manner, using a LiDAR point cloud tile index as reference. To familiarize ourselves with the typical morphology of landslides found within the Prestonsburg area, we conducted a preliminary round of mapping followed by a focused program of field checking.

We used polygons to delineate landslides and define spatial extents based on morphological characteristics visible in the LiDAR-based maps. Morphological feature used to identify landslides included headscarps, side scarps or flanks, hummocky topography, bulging toes, mid-slope terraces, offset drainages, and drainages whose courses have been controlled by landslide features (Schulz 2004). We visually evaluated a combination of the shaded relief renderings, contour lines, topographic curvature and roughness maps, and aerial imagery to qualitatively classify the type of slope movement, using Cruden and Varnes (1996) classification. Additionally, we used Soeters and Van Westen (1996) image characteristics of slope movement types that describe the typical morphology, vegetation, and drainage aspects visible on stereo imagery for interpreting and classifying the type of slope failure, as shown in Table 1. Landslides that occurred after the LiDAR data were collected are designated as points and termed AD landslides.

AD landslide points were determined by examining aerial imagery for denuded areas and clear vegetational contrast with the surroundings.

We created a confidence rating system, a modified version of Burns and Madin (2009), as shown in Table 2, which qualitatively describes our confidence that a landslide was interpreted correctly from remotely sensed data. We assigned points based on the clarity of the feature in the LiDAR. When a feature was not visible, a point value of 0 was assigned. Likewise, when a feature was clearly visible, a point value of 9 or 10 was assigned depending upon agreement within supporting layers. Supporting layers are those that suggest the presence of a landslide, such as aerial imagery, slope profile graphs, topographic curvature and topographic roughness. Defining features as slightly visible and moderately visible is not straightforward and, ultimately, depended upon our judgement. We differentiated slightly visible from moderately visible based on the proportion of the landslide area that was inferred, providing a range of point values to account for the degree of uncertainty during the digitizing process.

## 2.2 Landslide Susceptibility

PISA-m is a physics-based probabilistic slope stability model that utilizes a first-order, second-moment approximation of the infinite slope stability equation used by the U.S. Forest Service LISA and DLISA programs (Haneberg 2004, 2005). The model incorporates an element of probability to account for uncertainties within input geotechnical variables, such as bulk density ($\gamma_{moist}$), saturated density ($\gamma_{saturated}$), angle of internal friction ($\varphi$), cohesive strength ($c_{soil}$), pore pressure coefficient ($h_w$), soil thickness (d), tree root cohesive strength ($c_{roots}$), and tree surcharge (q). PISA-m requires three input rasters: a DEM, a geologic or soil unit map, and a forest cover unit map.

We reduced the resolution of our DEM to 3 m to use as the DEM input raster. The geologic unit raster comprised three units: colluvium, alluvium, and shale. Shale was included as an individual unit because during the inventory process we found that approximately 70% of landslides occurred near or at a shale arc. Shale arc is a polyline of shale units in the stratigraphic column, which were digitized from older geologic maps. Our shale unit in the unit raster was obtained from creating a 36-m buffer around shale arcs to account for shale thickness and possible error during the digitizing process. Our tree unit raster was created using the National Land Cover Database (NLCD) map for the quadrangle containing two units, temperate deciduous forest and non-forested. The values for geotechnical parameters, as shown in Table 3, were obtained from Kentucky Transportation Cabinet geotechnical reports and previous

**Table 1** Elements used within ArcGIS that illustrate image characteristics for interpreting and classifying the type of slope failure based on Soeters and Van Westen (1996) stereo imagery characteristics
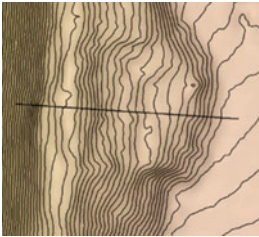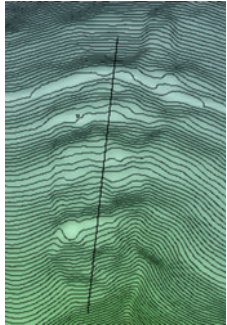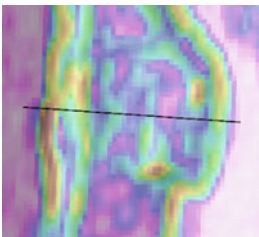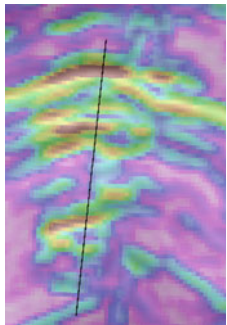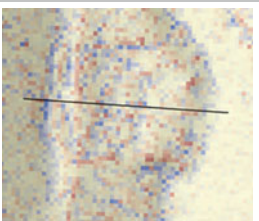
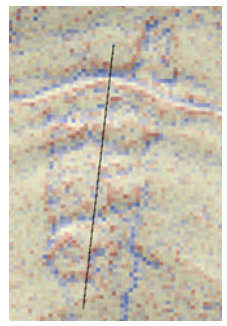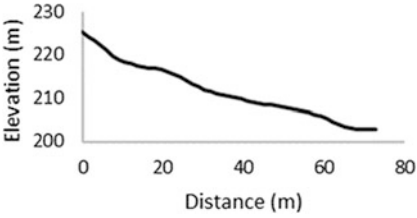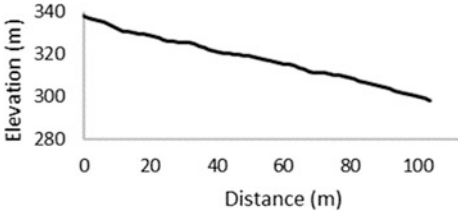| Element | | Rotational | Translational |
|---|---|---|---|
| Contours (0.6 m) | Contour derivative maps overlaid on shaded relief renderings further enhance our ability to locate and define landslides and features such as headscarps, toes, and fans |  |  |
| Topographic roughness | Topographic roughness is a visual aid to indicate the degree of chaotic relief upon a slope |  |  |
| Topographic curvature | Topographic curvature maps emphasize concave and convex forms within rotational landslides, while terracing, and block size is enhanced for translational landslides |  |  |
| Profile graph | Profile graphs taken through the center of a slide mass can illustrate concave/convex forms, back-tilting slope facets, or relatively planar surfaces |  |  |

**Table 2** Confidence rating system, a modified version of Burns and Madin (2009)

| Feature | Not visible | Slightly visible | Slightly visible + support | Moderately visible | Moderately visible + support | Clearly visible | Clearly visible + support |
|---|---|---|---|---|---|---|---|
| Headscarp | 0 | 1–2 | 2–3 | 4–6 | 6–8 | 9 | 10 |
| Flanks | 0 | 1–2 | 2–3 | 4–6 | 6–8 | 9 | 10 |
| Toe | 0 | 1–2 | 2–3 | 4–6 | 6–8 | 9 | 10 |
| Additional characteristics | 0 | 1–2 | 2–3 | 4–6 | 6–8 | 9 | 10 |

| Confidence | Score |
|---|---|
| Low | $\leq 10$ |
| Moderate | 11–29 |
| High | $\geq 30$ |

**Table 3** PISA-m geotechnical parameters and distribution type

| Geotechnical map unit | Variable | Distribution | Minimum | Maximum | Mean $\pm$ SD |
|---|---|---|---|---|---|
| *Alluvial soil* | | | | | |
| | $\varphi$ (degrees) | Uniform | 20 | 36 | |
| | $c_{soil}$ (kPa) | Uniform | 7.10 | 48.06 | |
| | d (m) | Uniform | 6.1 | 12.2 | |
| | $h_w$ (dimensionless) | Uniform | 0.12 | 0.43 | |
| | $\gamma_{saturated}$ (mg/m$^3$) | Uniform | 1.93 | 2.13 | |
| | $\gamma_{moist}$ (mg/m$^3$) | Uniform | 1.87 | 2.28 | |
| *Colluvial soil* | | | | | |
| | $\varphi$ (degrees) | Uniform | 25 | 36 | |
| | $c_{soil}$ (kPa) | Uniform | 5.64 | 22.55 | |
| | d (m) | Uniform | 1.5 | 18.3 | |
| | $h_w$ (dimensionless) | Uniform | 0.24 | 0.59 | |
| | $\gamma_{saturated}$ (mg/m$^3$) | Uniform | 1.79 | 2.25 | |
| | $\gamma_{moist}$ (mg/m$^3$) | Uniform | 1.48 | 2.36 | |
| *Shale unit* | | | | | |
| | $\varphi$ (degrees) | Uniform | 20 | 27 | |
| | $c_{soil}$ (kPa) | Uniform | 9.58 | 95.76 | |
| | d (m) | Uniform | 0.61 | 43.9 | |
| | $h_w$ (dimensionless) | Uniform | 0.01 | 0.47 | |
| | $\gamma_{saturated}$ (mg/m$^3$) | Uniform | 2.08 | 2.27 | |
| | $\gamma_{moist}$ (mg/m$^3$) | Uniform | 2.05 | 2.61 | |
| *Temperate deciduous forest* | | | | | |
| | $c_{roots}$ (kPa) | Uniform | 5.70 | 6.99 | |
| | q (kPa) | Normal | | | 2.51 $\pm$ 0.5 |

studies of similar geologic lithology (Drnevich et al. 1974; Sainju and Kalisz 1990; Waters and Abney 2000; Haneberg 2004; Shakoor and Smithmyer 2005).

## 3   Results

A landslide inventory map provides information about past landslides in an area of interest. Assessing the types of landslides within a landslide inventory and examining the spatial distribution with respect to the underlying geology can help to understand the causes of instability. An inventory map does not specify the probability that a landslide will occur; however, it can provide useful information for comparison with the results of a susceptibility model.

Within our landslide inventory area, we mapped 431 landslide polygons, as shown in Fig. 2, comprising 293 translational slides, 76 rotational slides, and 62 complex slides. Additionally, we have identified 22 landslides with the use of aerial imagery, thus far, occurring after the acquisition of our LiDAR in 2012. The dominant mode of sliding is translational, which we infer to occur along the colluvium-bedrock contact as pore pressures increase after rainfall.

The susceptibility model, PISA-m, calculates the probability that the factor of safety is less than or equal to 1 (Prob [FS $\leq$ 1]) for the given ranges of input variables under conditions simulated by the infinite slope approximation. According to the PISA-m results (Fig. 3), the potential for landsliding is greater in the southern portion of the quadrangle where dissection has produced steeper slopes and 19 of the 22 aerial derived (post-LiDAR) landslides occurred in areas that were calculated to have Prob[FS $\leq$ 1] $\geq$ 0.50. The general agreement between our PISA-m map and landslide inventory is encouraging; however, we will be collecting samples of each soil unit and conducting laboratory testing to validate parameters used in the PISA-m simulations. Additionally, we will create an empirical logistic regression susceptibility model within ArcGIS to compare our inventory and PISA-m results.

## 4   Discussion

Both landslide inventory and susceptibility maps can be useful resources to engineers, contractors, land-use planners, first responders, and others. Landslide inventory maps not only document landslide phenomena but can also be used to investigate landslide distributions, types, and patterns with respect to geomorphology and geological characteristics, and are a preliminary step toward determining susceptibility, hazard, and risk (Guzzetti et al. 2012). Over the last decade, large contributions have been made to improve methods and techniques for producing landslide inventory, susceptibility, and hazard zonation, and in return, there has been significant improvement in acquisition and processing of remotely sensed data (Guzzetti et al. 2012; Hervas et al. 2013; Haneberg 2017).

The degree to which inventory and susceptibility maps are successful and effective depends upon LiDAR quality, which can be highly variable. Datasets with poor ground strike densities can make it difficult to interpret landslide features from DEM derivative maps and potentially affect the output results of a stability model if they do not accurately represent the topography. We found that ground strike density varied considerably from north to south within the Prestonsburg quadrangle (Fig. 4). Thus, it is important to examine ground strike density maps to ensure that differences in landslide density are real and not artifacts of LiDAR data collection and processing.
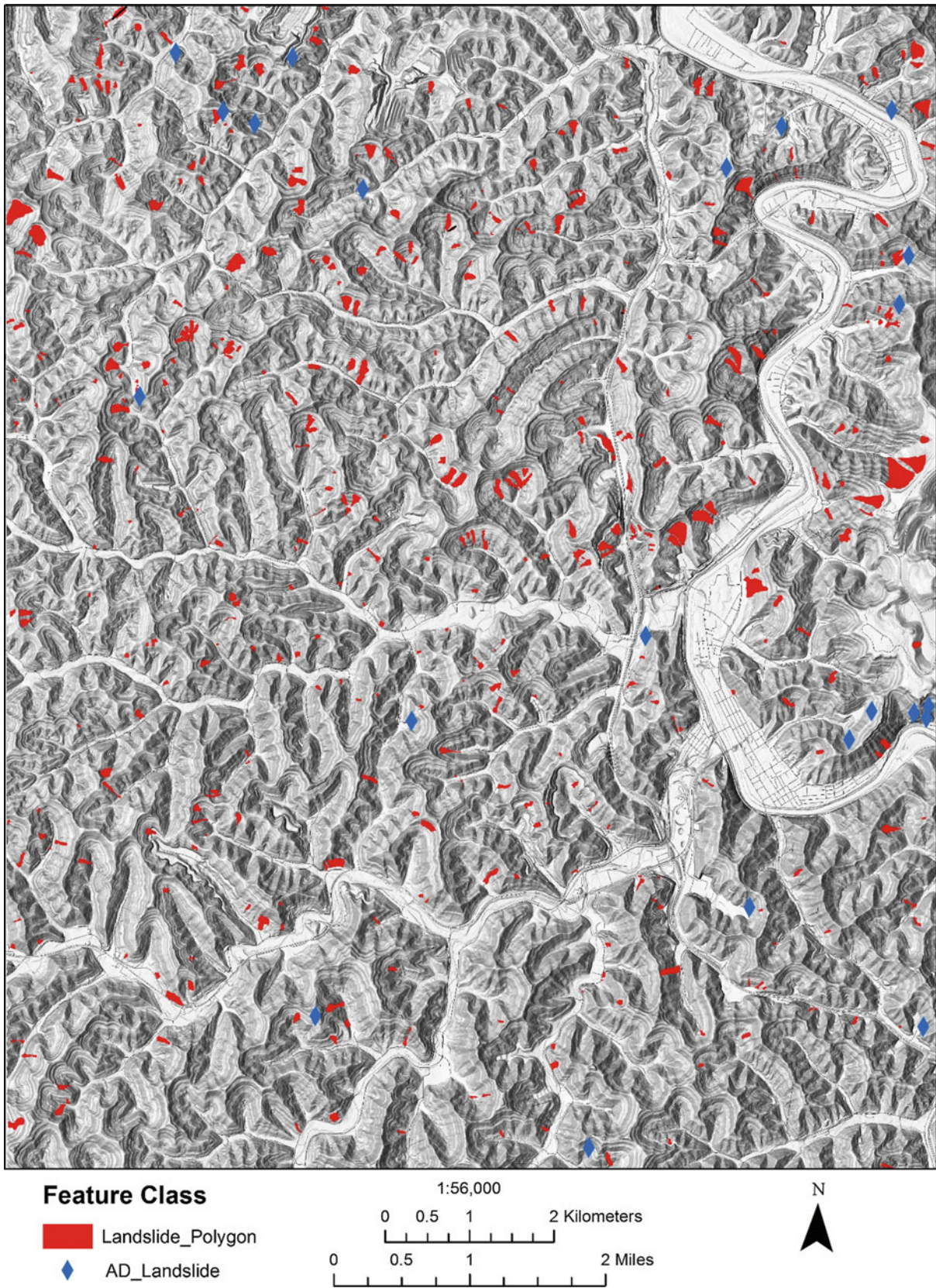
**Fig. 2** Prestonsburg 7.5-min quadrangle landslide inventory map. Landslide polygons were mapped using the airborne LiDAR DEM and the AD landslide points were reported after the LiDAR data were collected
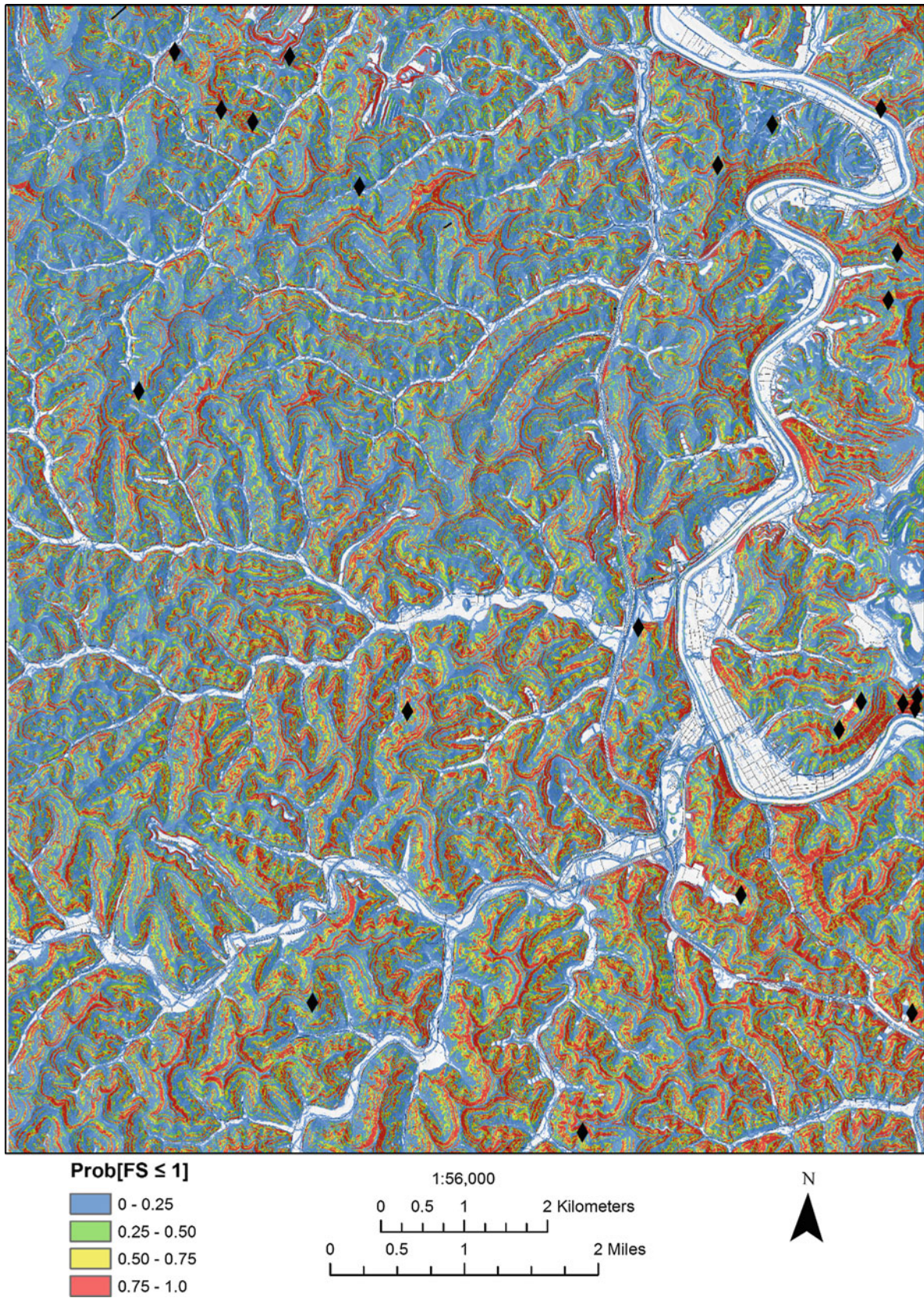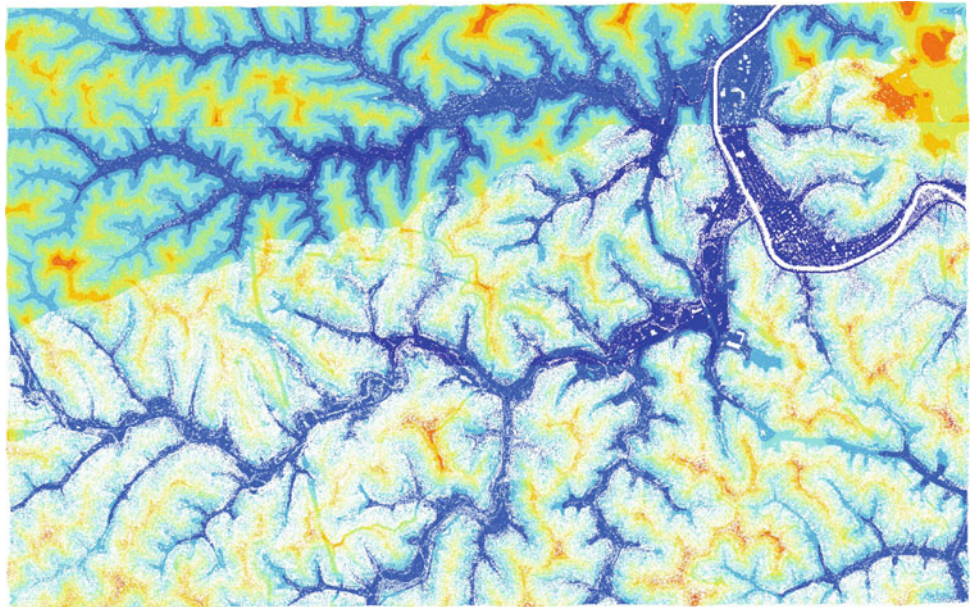
**Fig. 3** Preliminary PISA-m landslide susceptibility map and locations of landslides that occurred after LiDAR acquisition

**Fig. 4** LiDAR ground strike map illustrating the distinct differences in ground strike density between the northern and southern portion of the quadrangle. At least three different levels of ground strike density are apparent



## 5 Conclusions

The conclusions of this study are as follows:

1. Among the 431 landslides mapped using LiDAR, 293 are translational slides, 76 rotational slides, and 62 complex slides.
2. Twenty-two additional landslides have occurred in the study area since the acquisition of LiDAR in 2012.
3. Majority of the translational landslides tend to occur along the colluvium-bedrock contact.
4. The potential for landsliding is greater in the southern portion of the quadrangle, as indicated by PISA-m.

## References

Bruce, B., Haneberg, W., Drazba, M.: Using qualitative slope hazard maps and quantitative probabilistic slope stability models to constrain least-cost pipeline route optimization. In: Offshore Technology Conference (2013). https://doi.org/10.4043/23980-ms

Burns, W.J.: Comparison of remote sensing data-sets for the establishment of a landslide mapping protocol in Oregon. AEG Special Publication 23: Vail, Colo., Conference Presentations, 1st North American Landslide Conference (2007)

Burns, W.J., Madin, I.P.: Protocol for inventory mapping of landslide deposits from light detection and ranging (LIDAR) imagery. Oregon Department of Geology and Mineral Industries Special Paper 42 (2009)

Cole, R.A.: Map-based probabilistic infinite slope analysis of the Stephens Creek Watershed, Portland, Oregon. Dissertations and thesis. Paper 625 (2013). https://doi.org/10.15760/etd.625

Crawford, M.M.: Kentucky geological survey landslide inventory: from design to application. Kentucky Geological Survey Information Circular IC_31_12 (2014)

Crawford, M.M., Zhu, J., Webb, S.E.: Geologic, geotechnical, and geophysical investigation of a shallow landslide, Eastern Kentucky. Kentucky Geological Survey, Report of Investigations 29 (Series XII) (2015)

Cruden, D.M., Varnes, D.J.: Landslide types and processes. In: Turner, A.K., Schuster, R.L. (eds.) Landslides, Investigation and Mitigation Special Report 247, pp. 36–75. Transportation Research Board, National Academy Press, Washington, D. C. (1996)

Drnevich, V.P., Gorman, C.T., Hopkins, T.C.: Shear strength of cohesive soils and friction sleeve resistance. Kentucky Transportation Center Research Report 1447 (1974)

Grohmann, C.H., Smith, M.J., Riccomini, C.: Multiscale analysis of topographic surface roughness in the Midland Valley, Scotland. IEEE Trans. Geosci. Remote Sens. **49**(4), 1200–1213 (2011)

Guzzetti, F., Mondini, A.C., Cardinali, M., Fiorucci, F., Santangelo, M., Chang, K.: Landslide inventory maps: New tools for an old problem. Earth Sci. Rev. **112**, 46–66 (2012). https://doi.org/10.1016/j.earscirev.2012.02.001

Haneberg, W.C.: A rational probabilistic method for spatially distributed landslide hazard assessment. Environ. Eng. Geosci. **X**, 27–43 (2004)

Haneberg, W.C.: PISA-m: Probabilistic Infinite Slope Analysis, User Manual, Version 1.0, Haneberg Geoscience (2005)

Haneberg, W.C.: Spatially distributed probalistic assessment of submarine slope stability. In: Offshore Site Investigation and Geotechnics: Integrated Technologies-Present and Future. Society of Underwater Technology (2012)

Haneberg, W.C.: Incorporating correlated variables into GIS-based probabilistic submarine slope stability assessments. In: Submarine Mass Movements and their Consequences. Springer, Cham, pp. 529–536 (2016)

Haneberg, W.C.: Emerging trends and technologies in spatially distributed landslide hazard assessment. Association of Environmental & Engineering Geologists (2017)

Haneberg, W.C., Cole, W.F., Kasali, G.: High-resolution lidar-based landslide hazard mapping and modeling, UCSF Parnassus Campus,

San Francisco, USA. Bull. Eng. Geol. Environ. **68**, 263–276 (2009). https://doi.org/10.1007/s10064-009-0204-3

Hervas, J., Eeckhaut, M.V.D., Legorreta, G., Trigila, A.: Inroduction. In: Magottini, C., Canuti, P., Sassa, K. (eds) Landslide Science and Practice; Volume 1: Landslide Inventory and Susceptibility and Hazard Zoning, pp. 1–2. Springer, Berlin (2013). https://doi.org/10.1007/978-3-642-31325-7

Sainju, U.M., Kalisz, P.J.: Characteristics of "coal bloom" horizons in undisturbed forest soils in eastern Kentucky. Soil Sci. Soc. Am. J. **54**, 879–882 (1990)

Schulz, W.H.: Landslides mapped using LIDAR imagery. U.S. Geological Survey Open-File Report 2004-1396, Seattle, Washington, 1 sheet, scale 1:31,680, with 11 p. text (2004)

Schuster, R.L., Highland, L.M.: Socioeconomic and environmental impacts of landslides in the western hemisphere. U.S. Geological Survey Open-File Report 01-0276 (2001)

Shakoor, A., Smithmyer, A.J.: An analysis of storm-induced landslides in colluvial soil overlying mudrock sequences, southeastern Ohio, USA. Eng. Geol. **78**(2005), 257–274 (2005). https://doi.org/10.1016/j.enggeo.2005.01.001

Soeters, R., Van Westen, C.J.: Slope instability recognition, analysis, and zonation. In: Turner, A.K., Schuster, R.L. (eds) Landslides, Investigation and Mitigation Special Report 247, pp. 129–177. Transportation Research Board, National Academy Press, Washington, D. C. (1996)

Waters, B.A., Abney, M.G.: Soil survey of Floyd and Johnson counties, Kentucky. Natural Resources Conservation Service (2000)

Weppner, E., Hoyt, J., Haneberg, W.: Slope stability modeling and landslide hazard in Freshwater Creek and Ryan Slough Humboldt County, California. Pacific Watershed Associates Report No. 08076901 (2008)

# Total Landslide Susceptibility Modelling

Phil Flentje, David Stirling, Darshika Palamakumbure,
and Carlie Martin

## Abstract

This paper outlines the status of the landslide susceptibility modelling of the Sydney Basin region within the state of NSW, Australia. This area extends from Newcastle in the north to Batemans Bay in the south and west to include the Blue Mountains, an area of approximately 31,000 km$^2$. The University of Wollongong NSW Landslide Inventory includes 1863 landslides (134 falls, 278 flows and 1451 slides) to date. The region supports approximately one quarter of the population of Australia. Individual susceptibility models for both slide category and flow category landslides have been developed for the entire Sydney Basin region. Rockfall Susceptibility has also been developed for portions of the Wollongong Local Government Area. The susceptibility models are suitable for use at local scale, Advisory level Local Government Area Development Control Plans. As the models cover the three dominant landslide types identified within the inventory, a trial Total Landslide Susceptibility model has now been developed. As each landslide susceptibility model is a 10 m pixel resolution numerical grid, with values ranging from 0 to 1, the total susceptibility model has been developed, quite simply, by summing the three individual models producing a Total Susceptibility numerical grid. However, classifying this grid into zones is not simple. Furthermore, the Australian regulatory requirements are varied and the outcomes often complex involving a spatial query of the total susceptibility grid and its three contributing landslide susceptibility grids.

## Keywords

Landslide • Susceptibility • Zoning

P. Flentje (✉) · D. Stirling (✉) · D. Palamakumbure
University of Wollongong, Wollongong, NSW 2522, Australia
e-mail: pflentje@uow.edu.au

C. Martin
AECOM, Sydney, NSW 2000, Australia

## 1 The Sydney Basin Region of Australia

The southern Sydney Basin region of NSW on the east coast of the Australian mainland covers an area of 30,902 km$^2$ and when extended by a 3 km wide buffer, it's an area of 36,225 km$^2$ (Fig. 1). The basin contains (and is defined by the extent of) Permian to Triassic age mostly conformable near horizontal sediments with some syn-depositional and post depositional tectonic structuring that rest on a Paleozoic basement of granites and metamorphic rocks of Devonian age from the Lachlan Fold Belt Orogen. The sedimentary sequence has been subject to some uplift with gentle folding and small magnitude faulting during the late stage development of the Great Dividing Range. Fluvial erosion and slope instability has developed a landscape of gorges and plateaus, wide expansive coastal plains with coastal cliffs, prominent deep mature estuaries and abundant beaches. Experiencing a cool temperate climate the region has year round rainfall with annual totals ranging from less than 1 m up to almost 2 m with a gradient generally increasing to the west, up to the crest of the Great Dividing Range, before dramatically dropping further westward. The region is blanketed with eucalypt forests, woodlands and coastal heaths superimposed by anthropogenic modifications including farming, urban development and transport infrastructure.

The region includes the city of Sydney, the largest capital city in Australia, together with the cities of Newcastle and Wollongong and a number of smaller regional centers. The Australian Bureau of Statistics 2016 census data reports that the population within this area is 5.87 million people, approximately one quarter of the population of Australia. Clearly, in this mature and highly governed nation, proper land-use planning is considered essential to cope with the increasing pressure to develop marginal land. In local government areas where landslides have occurred repeatedly, Landslide Risk Assessment and Management is recognized as an important factor in effective land-use zoning practices.

**Fig. 1** Southeastern Australia location plan highlighting the shaded extent of the Sydney Basin region
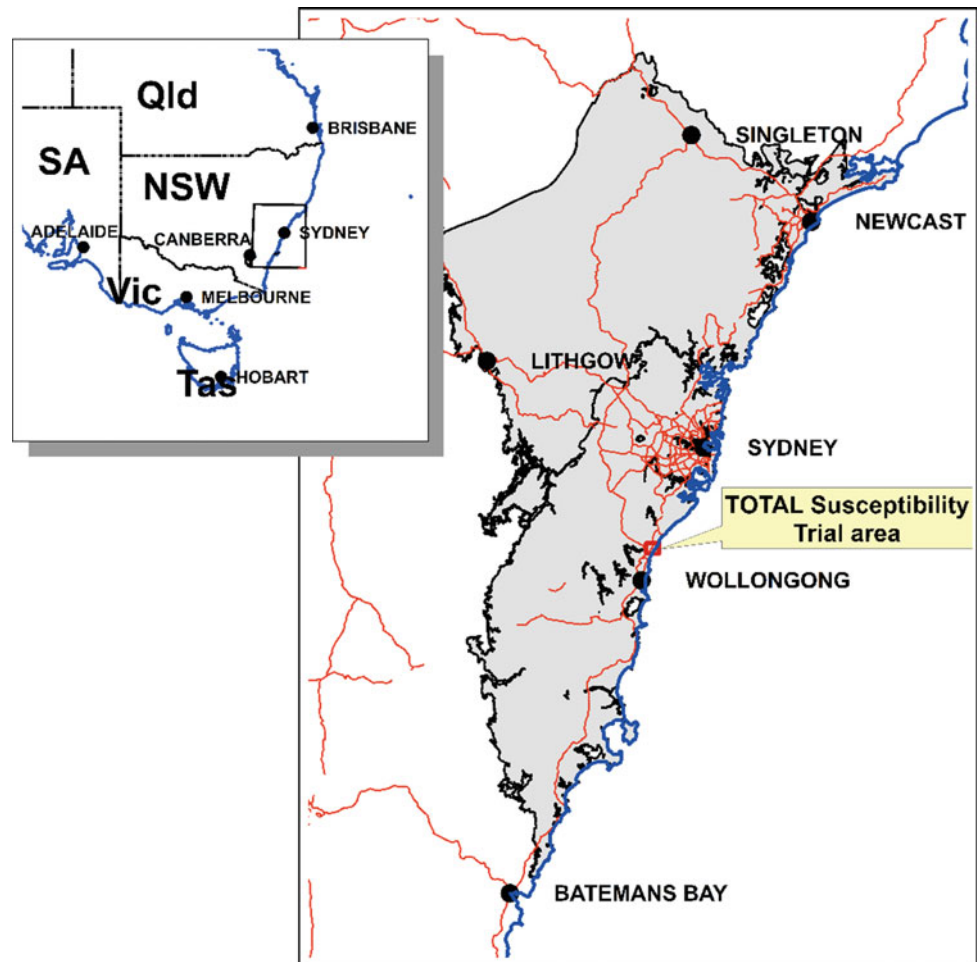


The Landslide Risk Management Guidelines (AGS 2007) and JTC-1 2008 (Fell et al. 2008) state the development of Landslide Inventories and then Landslide Susceptibility Zoning as the first step of landslide risk assessment for effective land use planning.

## 2    The Sydney Basin Landslide Inventory

Landslide inventories play a crucial role in modelling landslide susceptibility and hazard zoning for land use planning since the historic landslide records are a guide towards assessing the future possibility of landsliding (Fell et al. 2008). Furthermore, the JTC-1 Landslide Risk Management guidelines emphasize that landslide inventories are a vital component of any landslide zoning programs and essential to be included in landslide zoning reports (Fell et al. 2008). The quality and comprehensiveness of a landslide inventory directly affect the reliability of the evaluations derived from it (Galli et al. 2008).

Developed since 1993, a recent doctoral research program has expanded and redesigned the NSW landslide inventory to a comprehensive level and suitable for growth over the next 10 years (Flentje et al. 2012; Palamakumbure 2015; Flentje et al. 2016). The database structure has been developed in MS Access 2007 to facilitate the effective storing and analysis of landslide alphanumerical data linked with the spatial database, all of which has been compiled as an ArcGIS v10 geo-database. Field mapping and compilation work has been carried out using base maps and on the desktop GIS software at 1:4000 or larger scales, field mapping assisted with GPS and more recently high resolution differential GNSS. Aerial photograph interpretation and in recent years with sub meter resolution Airborne Laser Scan data and derived high resolution hill shade models have also been employed. Each landslide is referenced by a key Site Reference Code which does not change over time. The Inventory includes 1863 landslides (134 falls, 278 flows and 1451 slides) to date and only these three main types of landslides are considered significant in this region.

# 3 Methodology for Developing Total Landslide Susceptibility

As the NSW Landslide Inventory clearly demonstrates the presence of slide, flow and rockfall category landslides, a comprehensive assessment of landslide susceptibility must consider these three fundamentally different mechanisms of failure and landslide processes. The approach taken has been to independently assess these three different mechanisms of failure and landslide processes in individual susceptibility zonings and ultimately sum the results as outlined in Eq. 1:

$$\text{Total Susceptibility} = \Sigma \, \text{Slide, Flow and Fall Susceptibility}$$
(1)

This approach requires, of course, that the individual susceptibility zoning grids are numerically similar. In this project, each of the susceptibility grids (ArcGIS Raster grids) have been reduced to floating point values between 0 and 1. After appropriate enumeration of the individual components, the Total Susceptibility grid can also be expressed in terms of values ranging between the limits of 0 to 1. This modelled grid can then also be classified into zones of Low, Moderate and High Total Susceptibility in the same way as the component susceptibility models have been.

# 4 Software Tools and Grid Resolution Employed

## 4.1 Flow and Slide Susceptibility Modelling

For the model development and multilayer data analysis, the ESRI ArcGIS v.10 software environment was used. The See5 software was used to derive decision tree based rule-sets. The application of decision trees, a knowledge-based data-mining technique (Quinlan 1986; Kohavi and Quinlan 1999) in landslide susceptibility mapping has been gaining attention over past few decades due to its enhanced predictive capabilities and independence from subjective expert judgments (Saito et al. 2009; Miner et al. 2010; Yeon et al. 2010). Data mining (DM) can be described as the science of computer modelling heuristic learning processes. It is a computationally fast and a less cumbersome method which is capable of handling input data from different scales without assuming its frequency distribution (Pal and Mather 2003; Saito et al. 2009). Also, the relationship between landslide occurrence and the causative factors is not required to be known prior to the model development as it is depicted by the tree structure itself (Saito et al. 2009). Decision trees have become a preferable modelling method as it allows a

better compromise between clarity, accuracy and efficiency (Ferri et al. 2003; Yeon et al. 2010). The DM learning process extracts patterns from large databases, whether they are concerned with organizational processes or, as in this case, natural phenomena—landslides. These patterns can be used to gain insight into aspects of the phenomena, and to predict outcomes (in this case, pixels with characteristics matching those of known landslides where no landslides have been identified) as an aid to decision-making (Palamakumbure et al. 2015a, b, c). Hence the critical importance of the Landslide Inventory in this methodology. Early work on this was carried out in collaboration with Geoscience Australia (Chowdhury et al. 2002).

The entire data mining and GIS process for Flow and Slide Susceptibility modelling was automated by developing an ArcGIS Landslide Data Mining (LSDM) add-in toolbar (Palamakumbure et al. 2014). The process is carried out separately for each landslide type. This tool automates a series of tedious manual processes involved in data extraction, preparation, deriving See5 rules as summarised below (Palamakumbure et al. 2015a) and preparation of the ArcGIS Slide and Flow susceptibility grids.

Four example rules from a twenty nine strong rule set summarising Flow type landsliding, are shown in Table 1. The full nested rule sets are applied as "AND/IF/THEN" logical operations in Python scripting. Each rule represents a path from one tree node to another and the predicted class (non-landslide or landslide, 0 or 1) represents the terminal node, depicting the relationship between the Landslide causative factors and the landslide occurrence, and the order of relevance of the Landslide causative factors. The confidence of the prediction made is evaluated and validated using the Laplace ratio $(n - m + 1)/(n + 2)$ where $n$ is the number of training cases that a specific rule covers and $m$, is the number of incorrectly classified cases, $n$ and $m$ being the first two numbers in brackets after the rule number, in Table 1. The confidence value (0–1) is given in square brackets at the end of each rule, after the predicted class in Table 1.

## 4.2 Rockfall Susceptibility Modelling

Following some detailed site mapping of numerous recent rock falls and some two dimensional analysis using the Rocscience Rocfall software, the ESRI ArcGIS compatible Rockfall Analyst software extension V9.3.1 and V10.0.1 beta (Lan et al. 2007) from the University of Alberta team has been employed in the development of rockfall Susceptibility zoning. The spatial extent and a network neighborhood count of the modeled rockfall trajectories provides a useful Susceptibility zoning outcome (Flentje et al. 2015).

**Table 1** Example 2014 data mining rules from the Sydney Basin flow modelling work

| Rule 1: (17741/355, lift 1.2) | Rule 7: (1318/202, lift 4.2) |
|---|---|
| a > 193.797<br>s <= 10.96276<br>-> class 0 [0.980] | a > 83.69223<br>a <= 143.3372<br>rc > 0.333963<br>s > 29.28903<br>w > 3.105168e-007<br>-> class 1 [0.846] |
| **Rule 2: (13887/473, lift 1.2)** | **Rule 8: (509/88, lift 4.1)** |
| pc <= 1.831974<br>rc > −1.831455<br>rc <= 0.333963<br>s <= 13.76796<br>t = 2<br>w > 0.002031242<br>-> class 0 [0.966] | a > 83.69223<br>a <= 143.3372<br>f > 43<br>rc > 0.333963<br>s > 12.21367<br>w > 3.105168e-007<br>-> class 1 [0.826] |
| Attributes | |
| a = aspect<br>f = flow accumulation<br>pc = plan curvature<br>rc = profile curvature<br>s = slope<br>t = terrain 3 classes<br>w = wetness<br>class 0<br>class 1 | Floating point<br>Floating point<br>Floating point<br>Floating point<br>Floating point<br>Classified integer<br>Floating point<br>Non-landslide pixel<br>Landslide pixel |

These four examples include two from the class 0 (non landslide) and two from the class 1 (landslide predicted) rule set (comprises twenty nine rules)

## 4.3 Grid/Pixel Resolution and the Delta (δ) Ratio Parameter

The selection of which pixel resolution is the most beneficial has been considered in some detail (Palamakumbure et al. 2015a). An analysis was conducted for several trial regions with 7 different pixel resolutions varying from 2 m up to 30 m. For the data sets available at that time and examined in that study, and reported herein, a 10 m pixel resolution was considered optimal. The delta (δ) ratio parameter has been developed as one measure of modelling rigor, by taking the ratio of the square root of a representative (mean) landslide area (A) of the inventory and the area of a pixel where P is the pixel size (Eq. 2).

$$\delta = \sqrt{A}/P^2 \qquad (2)$$

In summary, a delta ratio of 1.5 m$^{-1}$ is considered an optimum value for the Sydney Basin work. Delta ratios less than 1 may be considered as lower resolution, regional guidance, whereas Delta ratios of greater than 5 may be considered as highly resolved. However, each project is heavily dependent on the level of detail contained within the Landslide Inventory.

## 5 Slide Category Landslide Susceptibility

Preliminary studies covering the entire Sydney Basin region, which were described as 'proof of concept', were completed (Flentje et al. 2011) up to a decade ago. The GIS data layers employed in the modelling for both Slide and Flow susceptibility, and the respective layer usage in developing the rule sets, are summarised in Table 2. The most recent slide susceptibility modelling outcomes for the Sydney Basin are summarised in Table 3 (Palmakumbure et al. 2015a). The Slide Susceptibility values range from 0.01 up to 0.87.

## 6 Flow Category Landslide Susceptibility

Modelling of Flow category landslides has been conducted using the same See5 methodology as for Slides discussed above (Palmakumbure et al. 2015b). Data from eight different layers derived from the Digital Elevation model was extracted corresponding to the landslide and randomly selected non-landslide pixel locations (Table 4).

It is of note that the Geology data layer was ultimately not used in modelling of the flow category landslides as it has

**Table 2** Attribute usage in data mining rules in flow and slide category modelling

| Attribute/GIS layer | Flow % | Slide % |
|---|---|---|
| Slope | 100 | 38 |
| Plan curvature | 39 | 7 |
| Profile curvature | 26 | 11 |
| Curvature | 26 | 9 |
| Aspect | 16 | 11 |
| Terrain | 14 | 4 |
| Wetness index | 12 | 12 |
| Geology | – | 100 |
| Flow accumulation | <1% | <1% |
| Landslide pixels—training cases | 32,862 | 670,164 |

**Table 3** Statistical summary of the Sydney Basin slide category modelling

| Susceptibility class | % of the study area | % Slide population | Area of slides (km$^2$) | Area (km$^2$) of class | % of area effected by slides |
|---|---|---|---|---|---|
| Very low - 1 | 84 | 1.51 | 0.5 | 25.900 | 0.002 |
| Low - 2 | 6.23 | 4.99 | 1.65 | 1.650 | 0.08 |
| Moderate - 3 | 5.2 | 15.9 | 5.27 | 1.590 | 0.33 |
| High - 4 | 4.8 | 77.55 | 25.64 | 1.480 | 1.73 |

**Table 4** Sydney Basin flow category modelling distribution

| Susceptibility class | % of the study area | % Flow population | Area of flows (km$^2$) | Area (km$^2$) of class | % of area effected by flows |
|---|---|---|---|---|---|
| Very low - 1 | 59 | 9 | 0.15 | 18.233 | 0.0008 |
| Low - 2 | 11 | 5 | 0.08 | 3.399 | 0.0024 |
| Moderate - 3 | 14 | 32 | 0.53 | 4.326 | 0.0122 |
| High - 4 | 16 | 54 | 0.89 | 4.944 | 0.0179 |

been assumed that the occurrence of flows, in the Sydney region, does not largely depend on Geology. Debris flows are generally shallow seated landslides and therefore, underlying geology is less relevant. Our model is based on the mapped location of relatively few (only 267 flows), in 2014, within an area of 30,603 km$^2$. In early trials, with the Geology was included in the modelling, the spatial extent of the modelled Debris Flow susceptibility was limited by the Geology in which they occur, which we considered to be unnecessarily restrictive for the application—developing a debris flow susceptibility map with wide application. If alternatively, say 1000 debris flows had been mapped within

a single local government area, modelling within that small area may be more appropriate using geology.

The Flow category landslide susceptibility results are summarized in Table 4. The Flow Susceptibility values range from 0.01 up to 0.89.

## 7 Rockfall Category Landslide Susceptibility

The rockfall susceptibility was developed quite differently as discussed previously. Trajectories were modelled from a seeder line along the crest of the escarpment, at 1 m spacing

with a high resolution Airborne Laser Scan (Lidar) 2 m pixel DEM. Once modelled, a 'susceptibility grid' was developed using a neighborhood count, counting every trajectory that comes within 5 by 5 neighborhood matrix of 2 m pixels and summing the results of the analysis for every pixel. The process to this point, whilst moderately complex, is completed after considerable field work and then by employing the University of Alberta Rockfall Analyst extension (Flentje et al. 2015) provided the user inputs certain parameters. Simply dividing the numerical value for each pixel by the highest total (5600 in this case) provided a grid with totals ranging from 0 to 1.

A total of only 16 rock falls from the total 134 within the inventory, represented by 6889 10 m pixels, exist within the $\sim 30$ km$^2$ trial area reported herein. The rockfall category landslide susceptibility results with respect to the distribution of rockfalls are summarized in Table 5. The Fall Susceptibility values range from 0.01 up to 0.99.

## 8 Total Landslide Susceptibility

### 8.1 Developing the Model

Once the individual slide, flow and fall susceptibility grids are processed to have value ranges between 0 and 1, it's a simple process of numerically assessing the individual components to produce a grid with values ranging between 0 and 1. The total susceptibility for this $\sim 30$ km$^2$ small trial area ranges from 0.007 up to 0.691. An image showing the stacked grids is included in Fig. 2. The distribution of the 4 zones (Very Low, Low, Moderate and High) within the Total Susceptibility grid together with the distribution of the Slide, Flow and Fall landslides within each of the zones are summarised in Table 6.

### 8.2 Understanding and Using the Model

We have become used to the fact that 'Hazard' models (Susceptibility models should be the fundamental basis of
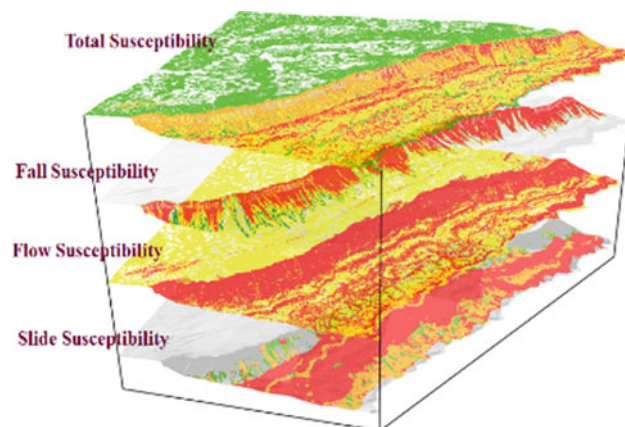


**Fig. 2** Stacked 3D image of the slide, flow and fall susceptibility models that sum to make the total susceptibility zoning

Hazard Models) are composed of traffic light colors demarking the various hazard zones. As such many zoning maps have some areas of red (most susceptible or hazardous), some areas of orange and grade out through yellow and or green to lesser hazard, and hopefully have large tracts of land with little or no susceptibility/hazard. Generally at least that's the intention, to enclose the highest hazards in the smallest areas of land, whilst identifying large portions of any given study area as safe for development, whatever that may be. The three zoning models discussed above certainly follow this trend and logic as summarised in Tables 3, 4 and 5.

To demonstrate the use of the Total Susceptibility model and its contributing Landslide Inventory and Slide, Flow and Fall Susceptibility models, in a land use planning application, Fig. 3, shows 4 separate zoning maps of the same area, each with a central highlighted property parcel. This parcel is large, 55,400 m$^2$ in area. Using a spatial query in ArcGIS, and the Zonal Statistics tool, each layer is queried with respect of the parcel area to determine the actual zoning distribution (area and percentage). The results of these queries are summarised in Table 7.

Table 7 shows the property parcel is classified as 82.5% of its area (44,900 m$^2$) being High Total Susceptibility, 71%

**Table 5** Wollongong $\sim 30$ km$^2$ trial rockfall modelling distribution

| Susceptibility class | % of the study area | % Fall population | Area of falls (km$^2$) | Area (km$^2$) of class | % of area effected by falls |
|---|---|---|---|---|---|
| Not susceptible | 91.96 | 5.03 | 0.01 | 27.28 | 0.04 |
| Very low - 1 | 1.30 | 27.85 | 0.06 | 0.39 | 15.56 |
| Low - 2 | 1.28 | 25.90 | 0.06 | 0.38 | 14.78 |
| Moderate - 3 | 1.40 | 29.89 | 0.06 | 0.42 | 15.53 |

**Table 6** Trial area total susceptibility categories with % area landslide distributions within each zone

| Total susceptibility | | | | Slides | Flows | Falls |
|---|---|---|---|---|---|---|
| Pixel count | class | Min | Max | % | % | % |
| 108788 | Very low - 1 | 0.01 | 0.03 | 0.00 | 0.00 | 0.00 |
| 35721 | Low - 2 | 0.03 | 0.10 | 0.12 | 0.02 | 0.07 |
| 14664 | Moderate - 3 | 0.10 | 0.26 | 0.18 | 0.04 | 0.35 |
| 53868 | High - 4 | 0.26 | 0.69 | 0.10 | 0.40 | 0.21 |

High Slide Susceptibility, 33% High Flow Susceptibility and essentially not susceptible to rockfalls. The one element not actually captured outside of Fig. 3c is the green slide category landslide that does effect the property parcel. This landslide covers approximately 8% of the parcel and details from the Inventory could, if available, be provided as required.
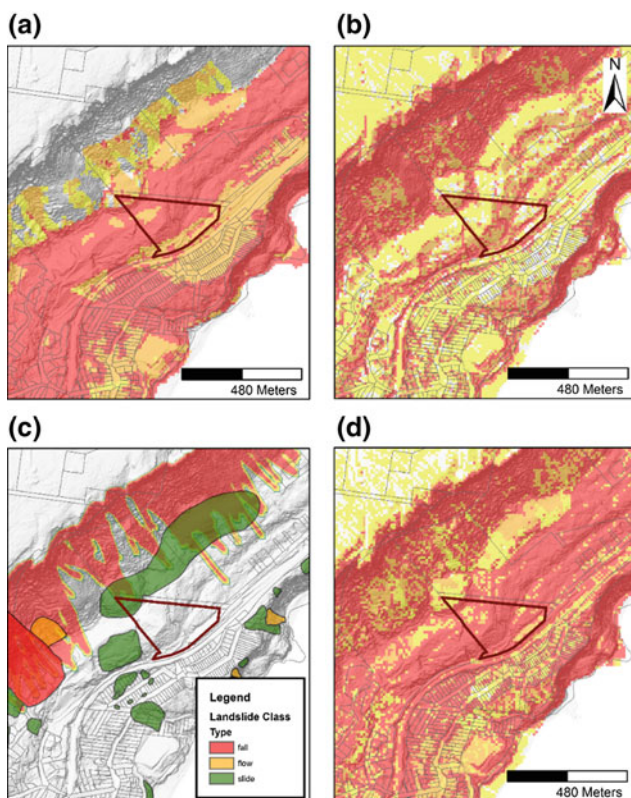


**Fig. 3** Susceptibility grids within the trial area highlighting the query cadastral parcel; **a** slides—legend is Table 3, **b** flows—legend is Table 4, **c** falls—legend is Table 5 and also showing the landslide inventory and **d** total—the legend for the total susceptibility zoning is shown in Table 6. The susceptibility distributions within the highlighted parcel are summarised in Table 7

## 9 Landslide Management

The legislation on land-use planning and development in Australia is different from state to state, and still between different Local Government Councils, within each of the states. The states of NSW, Queensland, Victoria and Tasmania have rules and regulations concerning the constructions on sites that are prone to landside hazard. In NSW, State Environmental Planning Policies (SEPP) provide a framework for the development of planning policies at the local government level. The Local Environmental Plans (LEP) are integral parts of NSW planning system. They are created by local councils in consultation with local communities and guide planning decision for local government areas. The Wollongong Development Control Plan (DCP 2009) outlines planning controls for the Wollongong City and Chapter E12 of this DCP addresses the geotechnical assessment of slope instability. As per these regulations, it is a requirement to assess the area of a proposed development for slope instability.

Some state governments have policies regarding the application of landslide risk management (LRM) concepts while some do not, but this work is generally carried out by local governments. During this process adaptation of AGS (2007) guidelines is essential. It is in part due to these regulatory requirements that the Australian Geomechanics Society developed the Landslide Risk Management (LRM) Guidelines from 1985 (AGS 2007). The AGS 2007 Guidelines are often referenced in the Local Government regulations and the required "Geotechnical Reports" are required to be compliant with these guidelines. To invoke the requirements, some local governments will have paid consultants to develop Susceptibility or Hazard maps (sometimes incorrectly called Risk maps), possibly even with simple landslide inventories, although typically not. These maps will be used as a binary form of capture and if a parcel is zoned as affected then a 'geotechnical report' is required. The process works well enough, if applied

**Table 7** Summary of cadastral parcel query of all susceptibility grids shown in Fig. 3

| Zone | Total susc. m² | Total susc. % | Slide susc. m² | Slide susc. % | Flow susc. m² | Flow susc. % | Fall susc. m² | Fall susc. % |
|------|------|------|------|------|------|------|------|------|
| Very low - 1 | 0 | 0.0 | 0 | 0.0 | 6700 | 12.3 | 54,000 | 99.3 |
| Low - 2 | 4200 | 7.7 | 300 | 0.6 | 14,000 | 25.7 | 200 | 0.4 |
| Moderate - 3 | 5300 | 9.7 | 15,300 | 28.1 | 15,800 | 29.0 | 100 | 0.2 |
| High - 4 | 44,900 | 82.5 | 38,800 | 71.3 | 17,900 | 32.9 | 100 | 0.2 |

correctly and only if the local government has a useful Susceptibility or Hazard zoning map. Unfortunately many do not and of those that do exist, most have been prepared by individual consultants using a unique technique such that comparisons between local government areas is not possible. Hence across the states, and indeed around the Nation there exists an incomplete patchwork of LRM procedures.

Clearly the parcel shown in Fig. 3 would be captured in the quite effective Wollongong City Council Local Government managed Development Application process. Based on the Landslide Inventory and these Susceptibility Zoning maps, which the Local Government may use, any development of the land parcel would require some form of geotechnical investigation to investigate the known landslide and potential for any type of landsliding that may affect the proposed development during its design life. The zonings at some locations, not necessarily at the selected parcel, may even be sufficient to preclude any development at all.

## 10   Summary and Conclusions

The Total Susceptibility modelling and zoning methodology detailed in this paper quite accurately accounts for the presence of slide, flow and rockfall category landslides and the three fundamentally different mechanisms of failure and landslide processes they represent. Whilst they are not independent, but co-related in time and space, this methodology allows a comprehensive management process to be developed. Application of this methodology within local government may well be enhanced with provision of pre-liminary landslide inventories, specific landslide type susceptibility zonings (even if only regional in nature) and possibly even Decision Support Matrices to aid non specialist planning assessment of submitted development applications such that those for moderate or higher susceptibility parcels may need assessment from suitably qualified geo-hazard professionals. This review may be external to the local government organization if in-house geo-hazard

expertise is not available. This is a process the authors hope to see being applied more widely and systematically across Australia into the future.

The authors and several other colleagues have been trying to secure funding to develop large scale landslide inventory and susceptibility tools, similar to those described herein for application across southeastern Australia. Unfortunately, our attempts so far have been unsuccessful although we are still working towards that goal.

## References

Flentje, P., Stirling, D., Chowdhury, R.N.: Landslide inventory, susceptibility, frequency and hazard zoning in the Wollongong and wider Sydney Basin Area. In: Landslide Risk Management Roadshow 2011 National Seminar Series. Aust. Geomech. J. **46**(2), 41–49 (2011)

Flentje, P., Stirling, D., Palamakumbure, D.: An Inventory of landslides within the Sydney Basin to aid the development of a refined susceptibility zoning. Ground engineering in a changing world. In: Proceedings of the 11th Australia New Zealand Conference on Geomechanics. Published by the Australian Geomechanics Society. Melbourne, July 15th–18th (2012)

Flentje, P., Palamakumbure, D., Thompson, J.: Assessing rockfall along the Illawarra escarpment. In: Lollino, G., Giordan, D., Crosta, G.B., Corominas, J., Azzam, R., Wasowski, J., Sciarra, N. (eds.) Engineering Geology for Society and Territory, vol. 2, pp. 2031–2036. Springer International Publishing, Switzerland (2015). http://link.springer.com/chapter/10.1007/978-3-319-09057-3_361

Flentje, P., Miner, A.S., Stirling, D., Palamakumbure, D.: Landslide inventory and susceptibility zoning across South-eastern Australia. In: Eggers, M.J., Griffiths, J.S., Parry, S., Culshaw, M.G. (eds.) Keynote Presentation for Theme 30, Session 30.1 Session 3 (2016)

Lan, H., Martin, C.D., Lim, C.H.: RockFall analyst: a GIS extension for three-dimensional and spatially distributed rockfall hazard modelling. Department of Civil and Environmental Engineering, University of Alberta. Comput. Geosci. **33**, 262–279 (2007). http://doi.org/10.1016/j.cageo.2006.05.013

Miner, A.S., Vamplew, P., Windle, D.J., Flentje, P., Warner, P.: A comparative study of various data mining techniques as applied to the modeling of landslide susceptibility on the Bellarine Peninsula, Victoria, Australia. Paper presented at the 11th IAEG congress of the international association of engineering geology and the environment, Auckland, New Zealand (2010)

Palamakumbure, D.: GIS-based landslide inventory and landslide susceptibility modelling across the Sydney Basin. Ph.D. thesis, Faculty of Engineering and Information Sciences, University of Wollongong, Unpublished, 341 pages (2016)

Palamakumbure, D., Flentje, P., Stirling, D.: Consideration of optimal pixel resolution in deriving landslide susceptibility zoning within the Sydney Basin, New South Wales, Australia. Comput. Geosci. **82**, 13–22 14. Published by Elsevier, and available online via Science Direct (2015a)

Palamakumbure, D., Flentje, P., Stirling, D.: Flow category landslide susceptibility modelling of the Sydney Basin. Changing the Face of the earth: geomechanics and human influence. In: Proceedings of the 12th Australia New Zealand Conference on Geomechanics, February, Wellington, New Zealand (2015b)

Palamakumbure, D., Stirling, D., Flentje, P., Chowdhury, R.: ArcGIS V.10 landslide susceptibility data mining add-in tool integrating data mining and GIS techniques to model landslide susceptibility. In Lollino, G., Giordan, D., Crosta, G.B., Corominas, J., Azzam, R., Wasowski, J., Sciarra, N. (eds.) Engineering Geology for Society and Territory, vol. 2, pp. 1191–1194. Springer International Publishing, Switzerland (2015c). http://link.springer.com/chapter/10.1007/978-3-319-09057-3_208

Saito, H., Nakayama, D., Matsuyama, H.: Comparison of landslide susceptibility based on a decision-tree model and actual landslide occurrence: The Akaishi Mountains, Japan. Geomorphology **109**(3–4), 108–121 (2009). https://doi.org/10.1016/j.geomorph.2009.02.026

Yeon, Y.K., Han, J.G., Ryu, K.H.: Landslide susceptibility mapping in Injae, Korea, using a decision tree. Eng. Geol. **116**(3–4), 274–283 (2010)

# Identification of Mudflow-Prone Areas in Southeastern Brazil

L. de A. P. Bacellar

### Abstract

Mudflow accidents have been described in Southeastern Brazil, some of them involving huge volumes of organic clay, causing economic losses and casualties. Usually, these mudflows occur in amphitheater-like headwaters of hilly areas of basement rocks. These amphitheaters are filled with layers of soft organic clay, characterized by low values of Nspt and UU shear strength, interfingered with or partially or totally covered by colluvium, with higher Nspt. The organic clay layer can reach 6 m in thickness. It overlies thin pebbly sand layers or silt-rich saprolites. This stratigraphy is a natural consequence of climate oscillations that have prevailed since the Upper Pleistocene/Holocene, causing advances or retreats of the fluvial system and, consequently, of the headwater zones. It is not easy to identify the triggering mechanism of these movements, but a retrogressive rupture model is possible, since these clays present some strength sensitivity. Groundwater uplift pressure on the less permeable organic clay is probably an important triggering mechanism for mudflows and it hinders the clay consolidation throughout the geological time. A detailed geomorphological mapping of a hydrographic basin near Belo Horizonte (State of Minas Gerais) helped identify several amphitheater-like headwaters with similar characteristics to those identified at accident sites. The description of outcrops, auger, cable percussion boring samples and geophysical surveys validated the above-mentioned stratigraphy, proving that this configuration is common in basement areas of southeastern Brazil. With the growth of Brazilian cities towards regions with these characteristics, greater care should be taken to prevent the repetition of mudflow accidents.

L. de A. P. Bacellar (✉)
Federal University of Ouro Preto, Minas Gerais, Brazil
e-mail: luisapbacellar@gmail.com

## 1 Introduction

The classification of flows is controversial, because they are members of a continuum spectrum of different kinds of mass movements (Hutchinson 1988). We adopt the term mudflow for mass movements involving saturated plastic soil with high water contents that moves fast (Hungr et al. 2014) for long distances as a high density viscous flow, until it comes to rest with a tongue-like shape.

Some mudflow accidents were reported in basement areas of southeastern Brazil and the best known are those that occurred in Vila Albertina (Amaral and Fuck 1973; Guidicini and Prandini 1974) and Vila Barraginha (CETEC 1992). Vila Albertina mudflow took place in 1972 in the city of Campos do Jordão (State of São Paulo), with 80,000 m$^3$ of earth travelling for more than 700 m and destroying 60 houses and causing 17 casualties (Guidicini and Prandini 1974). The accident of Vila Barraginha occurred in 1992 in the city of Contagem (State of Minas Gerais). A volume of 30,000 m$^3$ of earth was transported for approximately 200 m, causing the destruction of 180 houses and 36 casualties (CETEC 1992).

The sites of these accidents and others not studied in depth have some characteristics in common (Guidicini and Prandini 1974; CETEC 1992; Bacellar 2000; Barel Filho 2002; Meleu 2017), such as: they are located in drainage headwater hollows (zero-order basins of Tsukamoto et al. 1982); many of these hollows tend to have an amphitheater-like form (amphitheater-like headwaters—ALH) that are filled up with alluvial and/or colluvial sediments; the alluvial sediments (mainly pebbly sands and organic clay) occur in the bottom of the ALH, over an erosional surface in saprolite; layers of soft organic clay up to 6 m thick are very common in the alluvial package; this clay, which is usually rich in fibrous organic matter, presents adverse geotechnical properties, such as high liquid limit (up to 67%), low $N_{SPT}$ blow values (0–4), low UU strength ($\sim$17 kPa) and intermediate to high strength sensitivity, between 1 and 23

(Bacellar 2000; CETEC 1992; Meleu 2017); the organic clay presents low hydraulic conductivity (K < $10^{-7}$ cm/s) and it confines groundwater underneath in sand or saprolite (Bacellar 2000); the alluvial sediments are partially or totally covered up by ramps of massive, colluvial sediments composed of sandy clay with pebbles (Bacellar 2000; Bacellar et al. 2004). The colluvium presents higher cohesion and Nspt due to laterization and pedological processes (Bacellar 2000).

The triggering mechanisms of these accidents are controversial, but they are frequently attributed to man-made earthworks on upslope segments (Guidicini and Prandini 1974; CETEC 1992) or downslope cuts. These mechanisms are probably favored by the groundwater under pressure on the organic clay that also hinders its total consolidation. The low consolidation explains the low UU strength, and the organic fibers probably explain the high strength sensitivity (Bacellar et al. 2004).

These ALH are interpreted as a consequence of cut and fill episodes due to climate oscillations (wetter and drier) that occurred in southeastern Brazil since the Upper Pleistocene/Holocene, causing advances or retreats of the fluvial system and, consequently, of the headwater hollows (Bacellar 2000; Bacellar et al. 2004). The depicted configuration in headwater hollows are equally reported in several other basement bed rock regions of Southeastern Brazil (Meis 1977; Meis and Monteiro 1979; Modenesi 1988; Moreira 1992; Augustin 1994; CETEC 1994; Behling and Lichte 1997; Danderfer et al. 2002) and of other parts of the world, especially in tropical zones (Petit and Bourgeat 1966; Shoroder 1976; Thomas 1994; Master and Duane 1997).

However, the ALH present many different topographical forms and inner stratigraphy and some of them are more susceptible to mudflows. The first geomorphological model for headwater areas was proposed by Hack and Goodlet (1960). In this model, the headwaters were divided in noses (convex contours outward, away from the mountain), side slopes (straight contours) and hollows and footslopes (concave contours outward, away from the mountain). The footslope differs from the hollow by a gentler slope.

Two main types of headwater hollows are described in the Paraíba do Sul basin, southeastern Brazil (Moura 1990; Moura et al. 1991): concave-plane hollows (HCP) and concave hollows (HC). According to these authors, the HCP hollow would represent paleogullies, and the HC type was interpreted as the result of several episodes of colluviation. As a consequence, HCP and HC hollows present alluvial-colluvial and colluvial sediments, respectively. The analysis of the data presented by these authors shows that the morphology of HCP differs from HC by a gentler footslope.

These types of hollows were described in other regions of southeastern Brazil, such as in the Maracujá hydrographic basin (Bacellar 2000; Bacellar et al. 2004). In this basin, Bacellar (2000) named headwater hollows ALH to avoid confusion with Moura et al. (1991) models. Some of these ALH present a gentler footslope (hereafter called ALHg) and others a steeper, ramp-form footslope (hereafter called ALHs), corresponding to the HCP and HC of Moura et al. (1991). Bacellar (2000) considered that ALHg and ALHs generate as paleogullies and mass movements (especially slumps), respectively. The ALHg are prone to mudflows, because they usually contain alluvial sediments, with soft organic clay layers.

However, it is not always easy to distinguish between these two types because of the subsequent topographical reshaping throughout the geological time.

The main objective of this work is to study these two types of ALH in order to validate their expected stratigraphy and their susceptibility to mudflow. The study area is the Maracujá Hydrographic Basin (MHB), which is located in the Iron Quadrangle geological province (Door 1969; Alkmim and Marshak 1998). Circa 80% of this basin drains basement rocks of the Archean Bação Complex (Fig. 1), which is composed of tonalitic, trondhjemitic or granodioritic gneisses and migmatites, intruded by granodioritic and granitic granitoids (Door 1969; Alkmim and Marshak 1998; Hippert 1994). Proterozoic metamorphic rocks (schists, phyllites, quartzites and itabirites) of the Rio das Velhas and, mainly, Minas supergroups crop out in the upper part of the basin (Door 1969; Alkmim and Marshak 1998).

## 2 Materials and Methods

This work was carried out in four steps. (i) Initially, a 1:25,000-scale geomorphological map was prepared for MHB. It is an updated version of a previous geomorphological map (Bacellar 2000), and helped characterize two homogeneous geomorphological domains based on the superposition of the following maps: hypsometry, slope gradient, slope heights, and slope index. The map was subsequently checked with extensive fieldwork. (ii) The drainage system was surveyed and the channels were classified according to the hierarchy system proposed by Strahler (1957). ALH (zero-order basin of Tsukamoto et al. 1982) were classified in two main topographical forms, ALHg and ALHs, adapting the classification by Moura (1990). This was done using (1:25,000 and 1:10,000) aerial photographs and subsequent field mapping. (iii) Some of these ALH that were difficult to classify were selected at random for a deeper in situ geotechnical investigation, including field mapping, geophysical surveys (GPR and electrical resistivity), auger and cable percussion drilling and collection of SPT data. (iv) The results were compared with the two ALH conceptual models.

**Fig. 1** Location and geologic sketch map of the Maracujá Hydrographic Basin (MHB). The Rio das Velhas Supergroup crops out as a thin layer between the Minas Supergroup and basement rocks in the southern part of the basin, and cannot be depicted in this scale
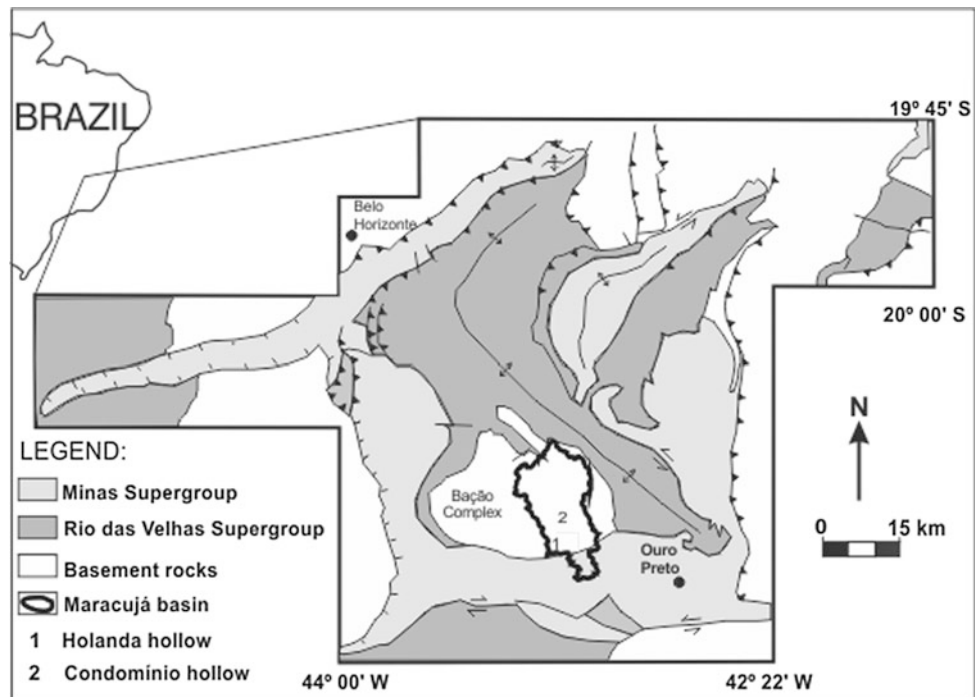


## 3 Results and Discussion

As a consequence of lithological distribution, two main geomorphological domains (and some subdomains) can be distinguished in MHB (Fig. 2). Domain 1 is located in the upper part of MHB, corresponding to the Minas Supergroup. Hillcrests are steep, sharp, follow the rock foliation, and altitudes are higher than 1140 m. The relief presents slope heights between 70 and 140 m, and the drainage system forms a trellis pattern, typical of folded metamorphic rocks. It is separated from the downstream domain by knickpoints. Domain 2 is located mainly on basement rocks (and minor parts on Rio das Velhas Supergroup) in the medium and low portion of MHB. It exhibits a half-orange landscape (Twidale 1982), characterized by gentle hills, with convex tops, low topographic amplitudes (slope heights), and drainage showing an angular-dendritic pattern.

This domain can be divided in three subdomains (Fig. 2). Subdomain 2A shows gently sloping hills (<30%) and slope heights lower than 70 m. Subdomain 2C that encompass basement and Rio das Velhas Supergroup has a steeper relief, with slope heights higher than 140 m. Subdomain 2B presents an intermediate pattern between domains 2A and 2C. The higher slope gradient and slope height of subdomains 2B and 2C in basement areas, similar to the ones found in domain 1, is explained by neotectonic reactivation in the northeastern part of MHB (Bonaccorsi 2006).

The soil profile is thicker (up to 50 m deep) in the flatter areas, like subdomain 2A, with well developed soil profiles and the formation of Oxisols (Bacellar 2000). Thinner and less developed soils (Inceptisols, Ultisols and Entisols) prevail in the steeper terrains, like domain 1 and subdomain 2C. Consequently, deep and large gullies are very frequent in subdomain 2A, as discussed by Bacellar et al. (2004), while in the stepper domains prevail mass movements, especially creeps and slumps.

Both types of ALH were identified (Fig. 3), but their distribution is uneven in MHB (Fig. 4). In flatter areas (subdomain 2A), ALHg prevails (Figs. 2 and 4), with low declivity footslopes (<15%), more circular forms and with higher average widths (230 m). In steep areas (subdomains 2B and 2C) and in the Minas Supergroup rocks (domain 1) ALHs prevails, with more inclined footslopes (>30%) and higher average widths (115 m). Both types are variably connected to the current drainage system. ALHs, however, tends to have this lower end higher than the drainage system.

The topographic forms of ALHg are very similar to the gullies that currently occur in subdomain 2A. These gullies develop not only as a result of superficial erosion, but also with piping and groundwater induced slumps, as demonstrated by Bacellar (2000). These subsurface processes are responsible for the more circular form of these gullies, with higher widths (Bacellar 2000). The ALHg stratigraphy is a result of the stabilization of the gullying processes (Bacellar 2000). Initially, alluvial sediments are deposited in a humid

**Fig. 2** Geomorphological map of Maracujá basin with subdomains defined by hypsometry, slope gradient, slope heights, and slope index
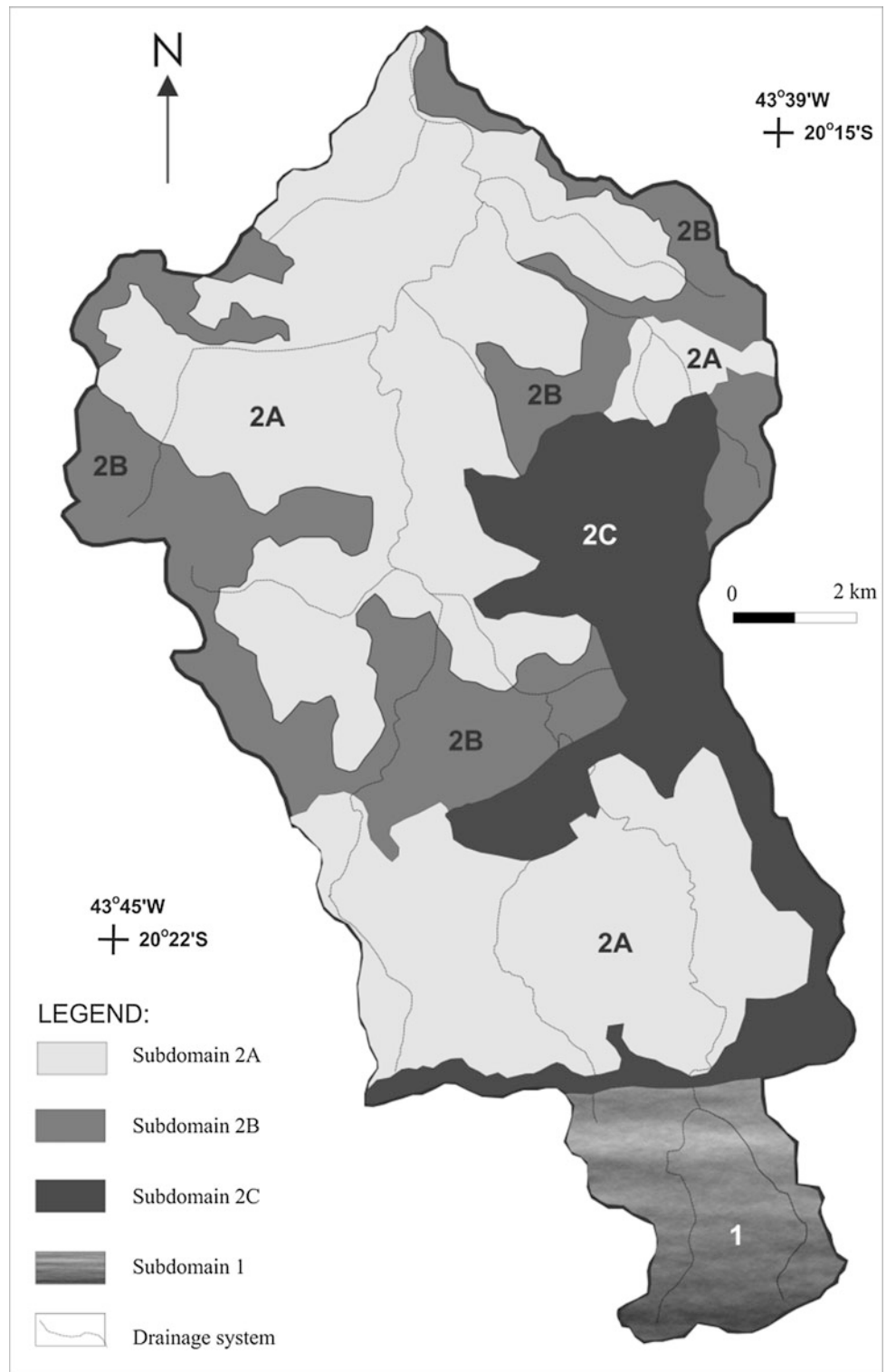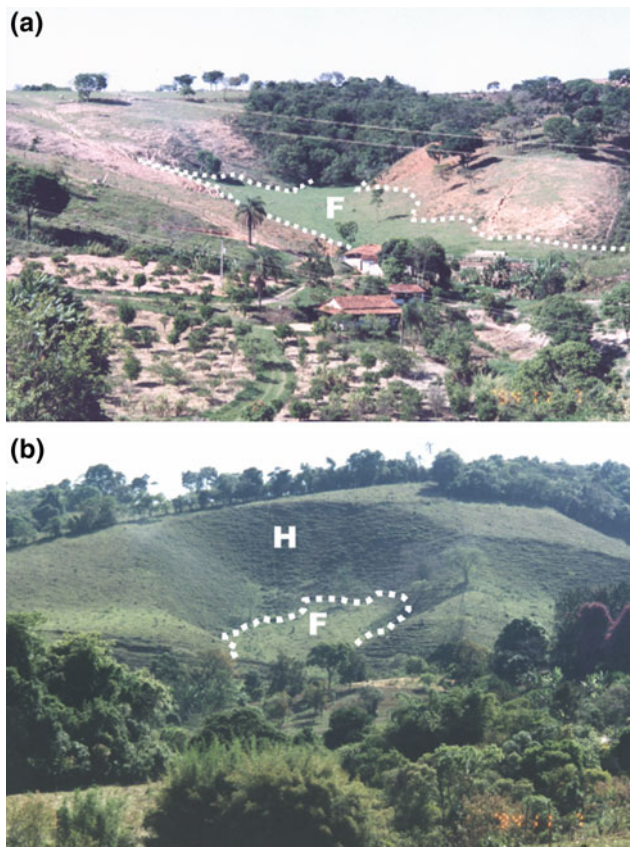
**Fig. 3** Two types of ALH. **a** ALHg, with a gentler footslope, and **b** ALHs, with a steep footslope

environment due to the groundwater collecting, and subsequently colluvial deposition take place in a drier environment. Nowadays, the gentler and wider ALHg footslope favors groundwater recharge and the development of an uplift pressure on the organic clay, which can trigger mudflow, as suggested by previous works (Bacellar 2000; Bacellar et al. 2004).

However, the distinction between ALHg and ALHs is not always easy, due to the progressive reshaping of these hollows by colluvium throughout the Upper Pleistocene/ Holocene. The amount of reshaping depends on several factors, like the hollow width and length, hollow age, the relief characteristics upslope, etc.

As ALHg presents wider footslopes, the reshaping by colluvial ramps is usually not complete. The identification is by means of the analysis of their inner parts, usually deprived of colluvial ramps, where gentle slopes (<15%) can remain. In some specific cases, the ALH nature can only be determined with a detailed geotechnical investigation of the subsurface, including soundings and geophysical surveys.

Therefore, these investigation methods were performed in six hollows that could not be classified in the field or with aerial photograph interpretation. The investigation consisted of direct and indirect methods, such as cable percussion and auger borings and GPR and electrical resistivity surveys. The application of these methods proved that it is possible to define ALH type that could not be properly classified with direct methods. For sake of brevity, only the data of two ALH (Holanda and Condomínio) will be presented here.

The Condomínio hollow (situated between coordinates 20° 19′ 6.16″S/43° 41′ 5.71″W and 20° 19′ 26. 18″S/43° 41′ 1.36″W) is very wide (Figs. 4 and 5), which is typical of ALHg, but it shows a steeper footslope that is more characteristic of ALHs, with a ramp of colluvium. A small topographic step separates the footslope of the side slopes. At first sight, this hollow was interpreted as ALHs, but superficial termite mounds composed of dark organic clay suggest that alluvial sediments could lie underneath. Electrical resistivity surveys detected a very low resistivity layer (100 $\Omega$m) that could be caused by a saturated clay layer. GPR surveys with a 100 MHz antenna, cable percussion (with SPT) and auger borings revealed that under a thick colluvium layer (up to 6 m thick) lies an alluvium with an extensive layer of organic clay (Fig. 5) that dips downslope. Percussive soundings reveal that the organic clay has very low $N_{SPT}$ blows (below 4) and Casagrande piezometers have shown that there is an uplift pressure at the base of the soft organic clay. Therefore, the investigation has proved that this is a typical ALHg, but it is so reshaped by colluvium ramps that it is impossible to detect it with direct methods.

The Holanda hollow (situated between coordinates 20° 22′ 21.32″S/43° 41′ 51.25″W and 20° 22′ 22.94″S/43° 41′ 45.61″W) is located in a tributary of the Maracujá basin (Figs. 4 and 6). Its width and footslope gradient are typical of ALHs, but its outer limits are strongly reshaped and can only be recognized by a subtle topographic step that limits it (Fig. 6). GPR surveys with 100 MHz antenna and cable percussive (with SPT) soundings revealed that this hollow is filled up with massive sandy clay with sparse pebbles that were interpreted as colluvium. Beneath this colluvium there are 4-m thick layers of stratified pebbly sands (Fig. 6) that were interpreted as wash sediments. The topographic form suggested that these ALHs were generated as mass movements, probably slump that were subsequently filled with wash sediments and colluvium, and profoundly reshaped.

The whole study revealed that a solid geomorphologic mapping is able to identify ALHs that are prone to mudflows (ALHg) in hilly areas of basement rocks. In some situations,

**Fig. 4** Map of hollow distribution (ALHs and ALHg) in the Maracujá basin. Note that ALHg are more common in the subdomain 2A and ALHs in the subdomain 2B and 2C and domain 1 (compare with Fig. 2). H—Holanda hollow; C—Condomínio hollow
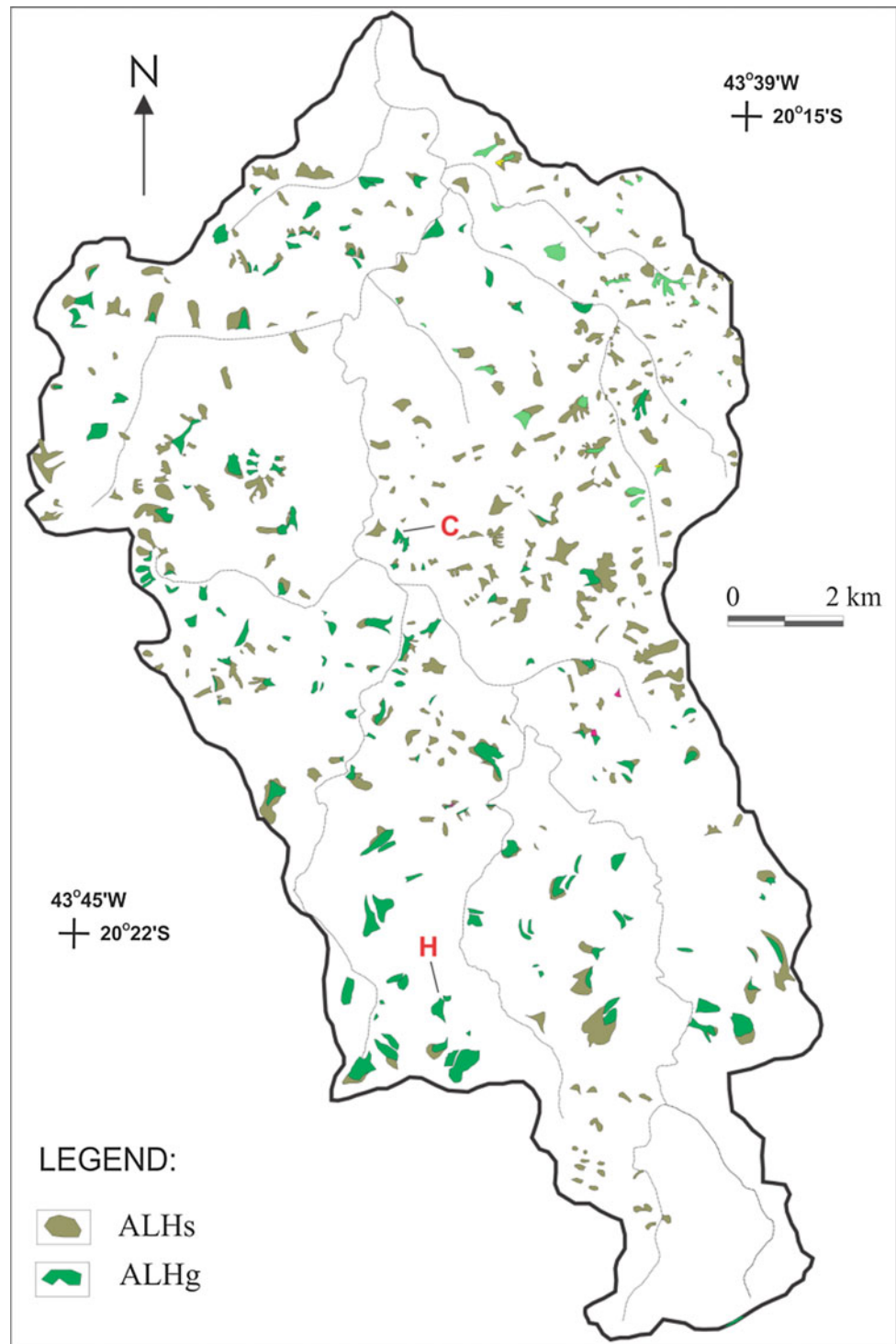


these hollows can only be identified by indirect methods. Among these, GPR proved to be very efficient to determine the extension of the soft clay, since the ALHg depth is usually in the resolution limit of the method, as well as there is a good impedance contrast between the alluvium and colluvium layers. Likewise, cable percussion drilling with Nspt measurements proved to be a cheap and very effective method to determine the consistency of the hidden soft clay, thus helping foresee a hazardous situation involving mud-flows, and even projects of building foundations.
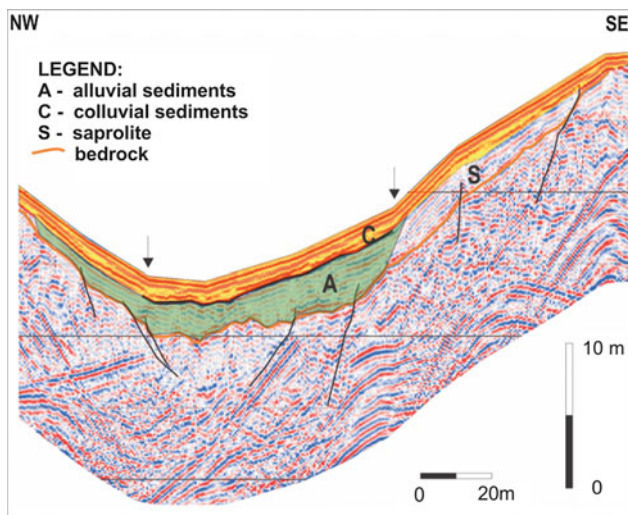
**Fig. 5** Condomínio ALHg. The GPR survey reveals the dimension of the alluvial (green) and colluvial (orange) packages. The ALHg limit (arrows, marking topographic steps) is not easily visible on the surface. The soft organic layer can be identified by a strong radar signal
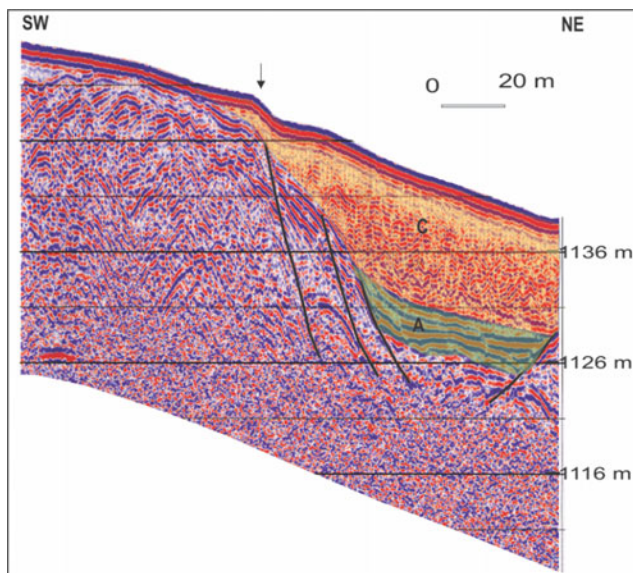


**Fig. 6** Holanda ALHs. Note the thick package of colluvium (c) that overlies stratified sediments, interpreted as wash deposits The ALHs limit is marked by the topographic step (arrow)

## 4 Conclusions

Severe mudflow accidents have occurred in basement rock areas of southeastern Brazil, causing many casualties, economic losses and environmental impacts. These mudflows are usually triggered in a specific type of amphitheater-like headwaters (ALH) that present alluvial sediments, especially soft organic clay layers (ALHg type). These types of features are very common in basement rock areas with specific topographic characteristics, which have a widespread occurrence in southeastern Brazil.

The Maracujá Hydrographic Basin (MHB) was chosen to properly identify these features and to validate the proposed model. The MHB geomorphological mapping proved to be an effective method to identify ALHg. However, in some situations, ALHg are not easily recognized in the field, and other methods, like soundings (with SPT) and geophysical surveys, especially the GPR, are recommended for an efficient identification of these hazardous sites.

Therefore, it is always recommended to carry out a detailed geotechnical investigation in these ALHg sites, even when only light-weight structures—or small cuts—are planned to be built in ALHg, in order to determine the soft clay depth, thickness, extension and bearing capacity.

## References

Alkmim, F.F., Marshak, S.: Transamazonian orogeny in the Southern São Francisco Craton region, Minas Gerais, Brazil: evidence for paleoproterozoic collision and collapse in the Quadrilátero Ferrífero. Precambr. Res. **90**, 29–58 (1998)

Amaral, S.E., Fuck, G.F.: About the landslide of an organic mud from Campos do Jordão, S.P., in August, 1972. Bol. Inst. Geoc. USP. **4**, 21–37 (1973) (in Portuguese)

Augustin, C.H.R.R.: Amphitheatres and hollows with depositional sequences and their significance on the evolution of tropical landscape. In: 14th International Sedimentology Congress Recife, G5–G6 (1994)

Bacellar, L de A.P.: Condicionantes geológicos, geomorfológicos e geotécnicos dos mecanismos de voçorocamento na bacia do rio Maracujá, Ouro Preto, M.G. DSc thesis. COPPE/UFRJ (2000)

Bacellar, L de A.P, Lacerda, W.A., Coelho Netto, A.L.: Amphitheaterlike headwaters: areas of mudflow hazard in southeastern Brazil. In: Proceedings of IX International Symposium on Landslides, Rio de Janeiro, Leiden, Balkema (2004)

Barel Filho, D.: Geological Aspects of Campos de Jordão Region as a Way to Understand Landslides Processes. Graduation Monography. IG-USP, 41 p (2002) (in Portuguese)

Behling, H., Lichte, M.: Evidence of dry and cold climatic conditions at glacial times in tropical Southeastern Brazil. Quatern. Res. **48**, 348–358 (1997)

Bonaccorsi, M.I.: Caracterização da deformação frágil e sua relação com os processos de voçorocamento na porção sudestes do Complexo Metamórfico Bação - Quadrilátero Ferrífero- Minas Gerais. Dissertação. DEGEO. Universidade Federal de Ouro Preto (2006)

CETEC (1992) Geotechnical report on Vila Barraginha landslide—Contagem (MG). Belo Horizonte, vol. 1, pp. 1–57 (in Portuguese)

CETEC (1994) Basic studies for the environmental diagnosis of Betim County, Belo Horizonte, vol. 1, pp. 1–214. Internal report (in Portuguese)

Danderfer, A., Paulo, J.R., Bacellar, L de A.P.: Evaluation of geological risk in Vargem das Flores Basin, Betim and Contagem Counties, M.G. In: XI Brazilian Symposium on Remote Sensing, Belo Horizonte (2002) (in Portuguese)

Door, J.V.N.: Physiographic, stratigraphic, and structural development of the Quadrilátero Ferrífero, Minas Gerais. Brazil. USGS/DNPM professional paper, 641-A, 110 p (1969)

Guidicini, G., Prandini, F.L.: Vila Albertina landslide case and its importance to urban planning. In: Proceedings of Brazilian Congress on Soil Mechanics, pp. 405–411 (1974) (in Portuguese)

Hack, J.T., Goodlet, J.C.: Geomorphology and forest ecology of a mountain region in the Central Appalachians. Geological survey professional paper: 1-347 (1960)

Hippert, J.F.: Structures indicative of helicoidal flow in a migmatitic diapir (Bação Complex, southeastern Brazil). Tectonophysics **234**, 169–196 (1994)

Hungr, O., Leroueil, S., Picarelli, L.: The Varnes classification of landslide types, an update. Landslides **11**, 167–194 (2014)

Hutchinson, J.N.: Morphological and geotechnical parameters of landslides in relation to geology and hydrogeology. General report. In: Proceedings of IV Symposium on Landslides, vol. 1, pp. 3–35. Balkema, Lausanne (1988)

Master, S., Duane, M.J.: The Nyika Plateau structure, Malawi (Central África) rediscovered: not an astrobleme, XXIX. Lunar and Planetary Review (1997)

Meis, M.R.M.: Quaternary morphostratigraphic units in the middle Doce River Valley. In: Proceedings of Brazilian Academy of Sciences, vol. 49, pp. 443–459 (1977) (in Portuguese)

Meis, M.R.M., Monteiro, A.M.F.: Upper quaternary rampas, Doce River Valley, Southeastern Brazil Plateau. Zeitschrift Geomorphol. **23**, 132–151 (1979)

Meleu, D.: Caracterização geológica e geoténica das argilas orgânicas moles do quartenário – estudo de caso Vila Barraginha, Contagem/Minas Gerais. Graduation monography n. 22. DEGEO/UFOP, 69 p (2017) (in Portuguese)

Modenesi, M.C.: Correlative meaning of the quaternary deposits from Campos do Jordão, São Paulo: paleoclimatic and paleoecological implications. Bol. I.G., São Paulo (1988) (in Portuguese)

Moreira, C.R.M.: Controlling factors of gullying in Santo Antônio sub-basin, Rio Grande basin. M.Sc. thesis. IGC, Federal University of Minas Gerais, Belo Horizonte (1992) (in Portuguese)

Moura, J.R.S.: Environmental transformations in upper quaternary in the middle Paraíba do Sul valley (SP/RJ). Ph.D. thesis. UFRJ/CCMN/IG, Rio de Janeiro (1990) (in Portuguese)

Moura, J.R.S., Peixoto, M.N.O., Silva, T.M.: Geometria do relevo e Estratigrafia do Quaternário como base à tipologia de cabeceiras de drenagem em anfiteatro - médio vale do rio Paraíba do Sul. Rev. Bras. Geoc. **21**(3):255–265 (1991)

Petit, M., Bourgeat, F.: Os lavaka malgaches: um agente natural da evolução das vertentes. Bol. Geográf. **25**(190), 29–32 (1966)

Shoroder Jr., J.F.: Mass movement on the Nyika Plateau, Malawi, Zeit. Fur. Geomorph. Berlin **20**(1), 56–57 (1976)

Strahler, A.N.: Quantitative analysis of watershed geomorphology. Trans. Amer. Geophys. Union **38**(6), 913–920 (1957)

Thomas, M.F.: Geomorphology in the Tropics: A Study of Weathering and Denudation in Low Latitudes. Wiley, New York (1994)

Tsukamoto, Y., Ohta, T., Noguchi, H.: Hydrological and geomorphological studies of debris slides on forested hillslopes in Japan. IAHS Pub. **137**, 89–98 (1982)

Twidale, C.R.: Granite Landforms. Elsevier, Amsterdam (1982)

# Slope Stability of Benguela and Lobito Urban Areas, Western Angola, Using RHRS

Pedro Santarém Andrade, Cipriano Lialunga, Rufino Camela, and David Muquepe

## Abstract

A study of slope stability in the Benguela and Lobito areas, in Western Angola, was carried out. Seven slopes are studied. Three of the slopes are located at the urban area of Lobito, the other three are situated at Catumbela and one is located in the Caota's area. The majority of the slopes are essentially composed of intercalations of limestone and marls belonging to the Quissonde Formation of the Cretaceous period. The methodology adopted in this work was useful to identify and characterize the different stability problems of the slopes. The Rockfall Hazard Rating System (RHRS), established by Pierson et al. (1990), was used to define the potential hazard for the roadways users. RHRS permits an analysis of the rockfall on roadways with relative low costs and can be applied in undeveloped countries, where the measurements devices are limited or scarce. Different types of slopes failures have occurred such as rockfalls, flows and landslides. The main causes of the slope movements are rainfall, slope geometric modification, rapid urbanization and roadway construction without the necessary geological and geotechnical characterization. The areas, of the studied slopes belong to dry tropical climate of arid and semi-arid characteristics, nevertheless torrential rainfall episodes can occur and initiate hazardous landslides. The majority of results of RHRS for the different slopes lie between 300 and 500. The results analysis allowed the adoption of mitigation and prevention measures.

P. S. Andrade (✉)
Department of Earth Sciences, Centro de Geociências, University of Coimbra, 3030-790 Coimbra, Portugal
e-mail: pandrade@dct.uc.pt

C. Lialunga · R. Camela · D. Muquepe
Department of Earth Sciences, University of Coimbra, 3030-790 Coimbra, Portugal

## 1 Introduction

In recent years and during the period of the civil war, there was a huge increase in urban populations on the Angolan coast. This led to occupation of areas with slope stability problems. This is a study of seven slopes (S1–S7). Three slopes are located in the urban area of Lobito, while another three are situated at Catumbela and one is located in the Caota area.

The study of landslides in the urban areas of Catumbela and Lobito, and in coastal areas such as Caota (Benguela) is necessary for the successful development of these areas to avoid economic losses and injuries to residents. In the areas studied, rock landslides may occur, causing economic damage or road casualties.

Different types of slope failures, such as rockfalls, flows and slides, have occurred on the slopes. The main causes of slope movements are rainfall, geometry modifications of the slopes, rapid urbanization and road construction where the necessary geological and geotechnical characterization has not been carried out. The most intense rainfall, in the period between January and April, causes erosion and slope movements. In March 2015, in the urban areas of Catumbela and Lobito, over 100 people died due to landslides and floods.

## 2 Methodology

The methodology adopted in this study was used to identify and characterize various stability problems in the areas. The following steps were taken: research and bibliographical review, inquiry and worksheets, field survey, use of Rockfall Hazard Rating System (RHRS) (Pierson et al. 1990), and finally data analysis. The RHRS system has been used by several Transports Departments in the United States of America and other countries and by different authors, sometimes with adaptations (Pack et al. 2007; Russell et al.

2008; Luciano 2008; Li et al. 2009; Gomes et al. 2012; Budetta and Nappi 2013). An assessment of unstable slopes located along the roadways could be performed by using the RHRS system to prioritize possible stabilization interventions.

The RHRS system is used to assess hazards, taking into consideration the following parameters: slope height, ditch effectiveness, average vehicle risk, decision sight distance, roadway dimension, geological characteristics, block size, climate and presence of water, and rockfall history (Table 1). Parameters can assume values between 3 and 81 points.

The slope height corresponds to vertical height. Blocks located at elevated heights present a greater potential energy than blocks of the same weight at a lower height. The rating in this category increases with the slope height.

Slope ditches permit the retention of falling rock material. Ditch effectiveness depends on slope height and dip; ditch morphology, width and depth; the dimension of rock blocks and the presence of slope irregularities.

The average vehicle risk (AVR) corresponds to the probability of a vehicle being affected by slope movements. AVR values increase as *road* traffic increases and diminish with higher speed limits.

Decision Sight Distance is related to the length of the road that a driver has in order to avoid the falling rock material on the road.

Roadway width is determined normal to the roadway centerline and includes the paved shoulders.

Geologic characteristics are defined by a field survey that includes geological and structural features. This parameter is divided into two cases: Case 1 is for slopes made up of rock masses in which discontinuities are prevalent, whereas Case 2 refers to slopes where erosion processes are dominant.

Rockfall dimension is determined by structural condition. Individual block size or the quantity of rockfall defines the volumetric dimension. An increase in rockfall dimension increases the risk associated with slope movements.

The presence of water can increase driving forces and reduce resistance. This can lead to stability problems. The annual rainfall value or existing freeze/thaw cycles, for an identified area, must be defined. If the annual rainfall value is less than 508 mm, the area under consideration is classified as a low precipitation zone. The area is defined as a high precipitation area, if the annual rainfall value is greater than 1270 mm.

Rockfall history is established from visual survey or from maintenance crew records. Although rockfall history of a slope is not frequently registered, it can provide an estimate for the potential type of slope movements that can occur.

## 3 Geology and Slope Description

S1, S2 and S3 correspond to slopes in the urban area of Lobito. S4, S5 and S6 are slopes located at Catumbela and S7 is situated in the Caota area.

**Table 1** Rockfall Hazard Rating System parameters and values

| Category | Rating criteria and score (3–81 points) |
|---|---|
| Slope height | 7.6–30.5 m |
| Ditch effectiveness | Good catchment—no catchment |
| Average vehicle risk | 25% of the time—100% of the time |
| Percent of decision sight distance | Adequate site distance (100% of low design value)—very limited sight distance (60% of low design value) |
| Roadway width including paved shoulders | 13.4–6.1 m |
| Geologic characterization (Case 1) | Structural condition (Discontinuous joints, favorable orientation—continuous joints, adverse orientation) Rock friction (Rough, irregular—clay infilling or slickensided) |
| Geologic characterization (Case 2) | Structural condition (Few differential erosion features—major erosion features) Difference in erosion rates (Small difference—extreme difference) |
| Block size Quantity of rockfall/event | 0.31–1.22 m 2.29–9.18 m$^3$ |
| Climate and presence of water | Low to moderate precipitation, no water on slope—high precipitation or continual water on slope |
| Rockfall history | Few falls—constant falls |

Slopes S1–S6 are composed of limestone, marly limestone and marls, which belong to the Upper Albion Quissonde Formation from the Cretaceous Period in the Benguela Basin. Slope 7 is essentially made up of brownish marls belonging to the lower member of the Quifandongo Formation (Lower Miocene). Slopes S1–S7 also show superficial deposits in the upper parts.

Slope 1 is located in Bandeira Quarter in Lobito showing two sections, of which one is 100 m long and 13 m high (Fig. 1). The slope dip is vertical. Slope 1 is mainly composed of fine-grained, yellow and brown limestone. Superficial deposits of 1–3 m in thickness, which are located on the upper part of the slope. There is building construction on the upper parts of Slope 1, stratification is sub-horizontal with faults sometimes with water percolation. Rockfalls and wedge failures are the most common landslides. Flows occur on superficial deposits.

Slope 2 is situated on Morro da Quileva I and is 179 m long and 22 m high. The slope dip is 70°SW. Slope 2 is constituted of limestone and marl intercalations. The thickness of the superficial deposits varies between 2 and 7 m. Debris deposits with a thickness of up to 0.5 m can be found at the toe of the slope. Stratification is sub-horizontal to 10° SW dip. Some of the layers present dissolution cavities of dm dimension. Various faults are 5–9 m in length. The most common slope movements are rockfalls, generally associated with differential erosion between limestones and marls. Some flows with dimensions of up to 3 m$^3$ can also occur. The main causes of slope movements are water action, overload, erosion processes, root growth, animal presence and vibrations produced by vehicular traffic.

Slope 3 is located on the Bela Vista/Elavoco and is 100 m long and 7 m high. The Slope dip is 75°–85°N. Slope 3 is

situated along one of most important roads in Lobito city. Slope lithology is constituted by a yellow, white, orange and grey limestone and also of grey and brown marls. Stratification is sub-horizontal to 10°SW dip. The upper part of Slope 3 consists of superficial deposits with a thickness of 1–1.6 m. The presence of faults, measuring 7–8 m in length, was observed. The most common instability situation is rockfall, caused by water action, vibrations, erosion processes and overload at the top of the slope. Small dimension flows, caused by soil erosion, disaggregation of rock material and anthropic deposits, were also observed.

Slope 4 is situated in Cambanbi Quarter, along the road linking Catumbela and Lobito (Fig. 2). Slope 4 is 14 m high and 125 m long. The slope dip is 80°NW to sub-vertical. Stratification presents a dip of 10°–15°W. Slope 4 consists of limestone, marls with gypsum, and sometimes with iron oxides and Pleistocene marine terraces on the top of the slope, where there can also be soil or anthropic deposits with a thickness of 0.5–2.0 m. The most frequent type of slope movements are rockfalls, flows which are more seldom, and planar failures.

Slope 5 is located on Poli Quarter, with a height of 9.8 m and a length of 34 m. The slope presents a dip of 75°–80°NW. The slope's lithology includes fine-grained gray, whitish and yellowish limestones, and very fine-grained brownish to yellowish marls. There are several residential buildings at the top of the slope. Soil deposits at the slope crest are less than 0.5 m in thickness. Stratification shows a dip between 15° and 25°W and vegetation is absent or scare. Landslides types that can occur are the rockfall and flow, the latter linked to soil deposits. The external causes of instabilities are the additional loads at the top of the slope, water percolation and superficial erosion. The main internal causes are water stress increase and strength decrease.

Slope 6 is located in Alto Nivo Quarter. The height of the slope is between 6.0 and 7.5 m and its length is approximately 100 m. The lithology corresponds to fine-grained compact yellow and brownish limestones, and very



**Fig. 1** Slope 1, erosional features leading to rockfalls



**Fig. 2** Slope 4, with intercalated layers of limestone and marls

fine-grained grey and brown marls. Stratification dips 20°W. Limestone and marl layers are 3–60 cm thick and 1–40 cm thick, respectively. Vegetation is scarce. Slope movements generally correspond to rockfalls. The main consequences of instability are damage to houses and traffic disruption. The internal causes of landslides are lithology, presence of water and geological structures. The external causes are excavation and increasing load on the top of the slope, vibrations and water percolation.

Slope 7 is located in the Caota area and corresponds to a partially excavated slope. There are 5 sections with extensions of 20–65 m, and heights ranging from 6 to 16 m. The lithology corresponds to siltstones, yellow and whitish marls, flint, gypsum veins, iron oxides and clays. Compact micritic dolomitic limestone is also present. Debris deposits are located at the toe of the slope. Rockfalls are the most common type of instability. Translational landslides can also occur. Rockfall trajectories can reach the roadway adjacent to the slope. The external causes of slope movements are water percolation, vibrations and superficial erosion. Lithology, the presence of geological structures, water pressure and loss of material strength correspond to the internal causes of slope problems.

## 4 Results

The RHRS was applied to all seven slopes to define the potential hazards for road users. Each RHRS parameter was defined as a weighted value (Table 2).

Slope height is lower for Slopes 3, 6 and section 1 of Slope 7, where slope height is lower or equal to 7.5 m. Slope

2 presents a height of 22 m; which is greater than the other slopes and corresponded to a value of 27 points.

Ditch effectiveness was classified as good on slopes 5, 6 and section 5 of Slope 7. There is no catchment of the falling rock material on Slopes 4, 5, 6 and on sections 3 and 4 of Slope 7.

The average vehicle risk for the different slopes had low values. The exceptions were the AVR values for Slopes 2 and 3, which were equal to or greater than 50%.

Decision sight distance was very limited for Slopes 5, 6, 7 and section 2 of Slope 1; with values corresponding to 40% or less of the design value.

Roadway width is generally less than 7.5 m, with values equal to or higher than 54 points.

Geological characterization was established, using Case 2 criteria. The slopes studied demonstrated differential erosion, leading to slope movements.

Slopes 1–6 are mainly composed by limestone and marls intercalations. Some slopes show soil deposits or marine terraces on the upper part of the slopes. Structural conditions for Slopes 1–4 were classified with 54 points. Slopes 5–6 showed frequent erosion features but there was no significant evidence of major erosion, corresponding to a classification of 27 points. The difference of erosion rates of the geological material for Slopes 1–6 was high to extreme, with a classification of 54 points.

Slope 7 presents intercalations of yellowish marls, siltstones, flint nodules and compact dolomitic limestone. Structural conditions showed a classification of 27–54 points, which corresponded to many and to major erosion features. Difference in erosion rates was defined as high, corresponding to 27 points.

**Table 2** Rockfall Hazard Rating System parameters results

| Slope rating/category | S 1 Sect 1 | S 1 Sect 2 | S 2 | S 3 | S 4 | S 5 | S 6 | S 7 Sect 1 | S 7 Sect 2 | S 7 Sect 3 | S 7 Sect 4 | S 7 Sect 5 |
|---|---|---|---|---|---|---|---|---|---|---|---|---|
| Slope height | 7 | 7 | 27 | 3 | 9 | 4 | 3 | 3 | 5 | 7 | 9 | 9 |
| Ditch effectiveness | 9 | 6 | 18 | 18 | 81 | 81 | 81 | 18 | 54 | 81 | 81 | 3 |
| Average vehicle risk | 6 | 6 | 18 | 9 | 8 | 3 | 3 | 3 | 3 | 3 | 3 | 3 |
| Percent of decision sight distance | 54 | 81 | 54 | 54 | 9 | 81 | 81 | 81 | 81 | 81 | 81 | 81 |
| Roadway width | 54 | 54 | 54 | 54 | 5 | 81 | 81 | 54 | 81 | 81 | 81 | 81 |
| Structural condition | 54 | 54 | 54 | 54 | 54 | 27 | 27 | 27 | 27 | 54 | 54 | 27 |
| Difference in erosion rates | 54 | 54 | 54 | 54 | 54 | 54 | 54 | 27 | 27 | 27 | 27 | 27 |
| Block size or quantity of rockfall/event | 9 | 9 | 3 | 3 | 27 | 3 | 9 | 54 | 9 | 9 | 54 | 27 |
| Climate and presence of water | 18 | 18 | 18 | 18 | 18 | 18 | 18 | 18 | 18 | 18 | 18 | 18 |
| Rockfall history | 9 | 9 | 18 | 18 | 18 | 9 | 18 | 9 | 27 | 27 | 27 | 27 |
| Total | 274 | 301 | 381 | 303 | 283 | 361 | 375 | 293 | 332 | 387 | 435 | 303 |

*S* Slope; *Sect* Section

There is a great variation in block dimension. Values were higher for Slope 4 and sections 1, 4 and 5 of Slope 7. Block size was 1.0 m for the sections 1 and 4 of Slope 7, corresponding to 54 points.

The areas of the slopes studied belong to a dry tropical climate with arid and semi-arid characteristics where the average annual rainfall was reported to be approximately 270 mm (Consult 2007), although torrential rainfall episodes can occur and cause hazardous slope movements. The value for the parameter was defined as 18 points.

Rockfall history is linked to periods of rainfall. On Slopes 1 and 5, the rockfall history was recorded as occasional, while for Slopes 2, 3, 4 and 6, it was more frequent. For sections of Slope 7, with the exception of section 1, there were many rockfalls, which corresponded to 27 points.

The majority of RHRS results fell between 300 and 500, only section 1 of Slopes 1 and 7 were lower than 300. Section 4 of Slope 7 scored 435 points, corresponding to the higher value obtained.

The RHRS classification does not suggest what stabilization methods should be adopted. According to Hoek (2017), citing Lawrence Pierson, in the State of Oregon, slopes with a total RHRS rating lower than 300 are classified as low priority, whereas slopes with a rating exceeding 500 are considered for urgent stabilization measures.

## 5 Conclusions

A study of seven road slopes located in the urban areas of Lobito, Catumbela and in the Caota area was carried out. Slopes presented stability problems over the years, leading to vehicular damages with human casualties. Landslides usually occur during periods of rainfall, normally from January to April.

The RHRS permits an analysis of rockfall on roads at relatively low costs and can be used in undeveloped countries, where measurement devices and equipment are limited or scarce. Field survey was useful to define different parameter values and to characterize slope stability, and the use of the RHRS can establish the priority of slopes stabilization measures.

Slopes situated at Lobito and Catumbela are essentially composed of limestone and marls intercalations, belonging to Quissonde Formation of the Cretaceous Period. Slope 7 is mainly composed of marls of the Quifandongo Formation (Lower Miocene age).

The most common slope movements are rockfalls, which were present on all the slopes studied. Flows were verified on Slopes 1–4 and there were landslides on Slopes 1, 4 and

7. All slopes and their respective sections presented RHRS values greater than 300, with the exception of section 1 of Slopes 1 and 4. Section 4 of slope 7 showed a RHRS value greater than 400.

According to the results on the RHRS and considering the causes of slope movements, it was proposed that periodical inspections of all the slopes studied should be conducted. Road users must be informed of slope stability problems and their major consequences.

Remedial measures were adopted to prevent or reduce the consequences of slope movement. For slopes with RHRS values greater than 300, the use of mesh wire, sometimes with rock bolts was recommended. For more weathered slope sections, and also for areas next to unstable soil deposits, it was proposed that scaling should be carried out and/or gabion walls constructed.

## References

Budetta, P., Nappi, M.: Comparison between qualitative rockfall risk rating systems for a road affected by high traffic intensity. Nat. Hazards Earth Syst. Sci. **13**, 1643–1653 (2013)

Consult: Monografia da Província de Benguela/Angola, 1st edn., 86 pp. Sociedade Angolana de Estudos e Consultoria, Lda KAT, Angola (2007) (in Portuguese)

Gomes, T., Andrade, P.S. Cunha, P.P.: Stability study of railway slopes in central Portugal. In: Proceedings of XIII Congresso Nacional de Geotecnia, LNEC, Lisboa, Portugal, pp. 365–366. LNEC, Lisbon (2012) (in Portuguese)

Hoek, E: Practical rock engineering. https://www.rocscience.com/documents/hoek/corner/. Last accessed 2017/10/10

Li, Z., Huang, H., Xue, Y., Yin, J.: Risk assessment of rockfall hazards on highways. Georisk Assess. Manage. Risk Eng. Syst. Geohazards **3**(3), 147–154 (2009)

Luciano, P.: Quantitative Risk Assessment of Rockfall Hazard in the Amalfi Coastal Road. Universitat Politècnica de Catalunya, Barcelona, 90 pp (2008)

Pack, R.T., Farnsworth, C.B., Leonard, B.D.: Development of a rockfall hazard rating system for the State of Utah. In: Proceedings of First North American Landslide Conference, Vail, Colorado, pp. 134–145 (2007)

Pierson, L.A., Davis, S.A., Van Vickle, R.: Rockfall Hazard Rating System Implementation Manual. Federal Highway Administration (FHWA), US Department of Transportation, United States of America, 172 pp (1990)

Russell, C.P., Santi, P.M., Higgins, J.D.: Modification and statistical analysis of the Colorado rockfall hazard rating system, Report CDOT-2008-7. Colorado Department of Transportation DTD Applied Research and Innovation Branch, United States of America, 137 pp (2008)

# Use of Micro-electromechanical Systems Inertial Sensors as a Geotechnical Monitoring Method for Slope Deformation

Cheng Li, Yueping Yin, and Shengwu Song

## Abstract

The rapid growth of performance and cost reduction of micro-electromechanical systems (MEMS) make it possible to apply inertial sensors to slope deformation monitoring. In this paper, we propose a slope deformation monitoring means that measures and tracks displacements and movements without external georeferencing. The inertial measurement unit (IMU) consists of triaxial accelerometers and gyroscopes, which measure linear acceleration and rotational rate, respectively. It can be deployed either on the slope surface or underground. Applying the inertial navigation algorithms, we can achieve not only the velocity but also the attitude and position of the observed target. Unlike most of the existing deformation geotechnical measuring methods, the provided method measures the deformation of a slope until it fails, and allows continuing movement surveillance after the failure, which facilitates the local authorities in the implementation of effective and sustainable mitigation measures. This method can be combined with global navigation satellite system (GNSS) to achieve a monitoring scheme for the whole process of slope deformation. Making use of the measurements appropriately, we can derive the deformation or displacement at different phases of the slope deformation process.

## Keywords

Slope deformation • Inertial sensors • IMU • Data fusion • GNSS

C. Li (✉) · S. Song
Powerchina Chengdu Engineering Corporation Limited, 1 Huanhua North Road, Chengdu, 610072, China
e-mail: licheng@chidi.com.cn

C. Li
Chang'an University, Middle-Section of Nan'er Huan Road, Xi'an, 710064, China

Y. Yin
China Geological Environmental Monitoring Institute, 20A Dahuisi Road, Beijing, 100081, China

## 1 Introduction

Slope deformation monitoring is an essential method aiming at slope stability assessment and landslide early warning. By the formats of the measurements, various measuring devices can be generally classified into two main groups depending on whether external georeferencing is required. Total stations and Global Navigation Satellite System (GNSS) are typical means that measure georeferenced displacements in one, two or three dimensions; and devices like extensometers, tilt meters, accelerometers measure displacements without external georeferencing. The devices in first category can be carried out either at a distance or at the slope, while the equipment in the latter group require an installation of sensors on or under the surface of the slope and measure corresponding parameters at different times.

With the rapid growth of performance of micro-electromechanical systems (MEMS), the low-cost, small-sized, and low energy-consumed MEMS inertial sensors have been progressively implemented into geotechnical monitoring. Scientists from RWTH Aachen university have developed a wireless monitoring network deployed with MEMS accelerometers and inclinometers (Fernández-Steeger et al. 2009; Azzam et al. 2010; May 2013), and has applied it to monitor natural hazards and geotechnical activities, such as tilting of rock towers deformation (Arnhardt 2011), ground subsidence due to ground improvement measures (Fernández-Steeger et al. 2013), tunneling construction (Li et al. 2014), and landslide monitoring (Arnhardt and Neussner 2013; Canli et al. 2015). Measurand company has developed a shape acceleration array (SAA) monitoring device that measures winding angles and direction by cascading a series of MEMS accelerometers, and has implemented this device into slope monitoring (Abdoun et al. 2008). Besides accelerometers, MEMS gyroscopes that measure angular rates are widely applied in wireless mouse, smartphone, digital camera, motion controller, drone, and virtual reality device (Godha and

Cannon 2005; Roberts and Tayebi 2013; Yuan and Chen 2014; Wittmann et al. 2015). Specifically, a triaxial accelerometer and a triaxial gyroscope compose an Inertial Measurement Unit (IMU), substituting the six outputs of IMU into inertial navigation algorithms, then the attitude, velocity and position of the observed object can be deduced. In this paper, we introduce a slope deformation monitoring means that measures and tracks slope deformation without external georeferencing, and propose a process scheme to track slope deformation based on various monitoring methods. In the following we first briefly describe the methodology; then we discuss the processing principles in the using of GNSS and IMU monitoring methods in different moving phases; afterwards, we propose a process scheme for slope deformation monitoring; a conclusion is provided in the end.

## 2 Methodology

Gyroscopes and accelerometers are used to measure rotational rate and linear acceleration respectively. An IMU aims at continuously calculating the orientation, velocity and position of a moving object without external georeferencing. Since the movement of slope differs from that of a flight vehicle, the algorithms should be adapted for slope deformation process. In general, the velocity of the moving target corresponds to the slope deformation rate, while position tracking corresponds to the displacements. The deformation of a slope is relatively slow and small; hence, we provide positional coordinates under a local rectangular coordinate system instead of longitude and latitude coordinates. In the following, the basic algorithm of inertial navigation system is briefly introduced, and the adapted methodology is presented.

### 2.1 Equation of Specific Force

Specific force is defined as the non-gravitational force per unit mass in meters/second$^2$. According to Newton's second law and the theorem of Coriolis, the specific force $\boldsymbol{f}^b$ can be expressed as:

$$\dot{\boldsymbol{v}}_{en}^n = \boldsymbol{C}_b^n \boldsymbol{f}^b - \left(2\boldsymbol{\omega}_{ie}^n + \boldsymbol{\omega}_{en}^n\right) \times \boldsymbol{v}_{en}^n + \boldsymbol{g}^n \tag{1}$$

where direction cosine matrix $\boldsymbol{C}_b^n$ is the coordinate transformation matrix relating the body frame $b$ to geographic frame $n$, which is derived from the output of the gyroscope $\boldsymbol{\omega}^b$. $\boldsymbol{f}^b$ is the output of the accelerometer, and $-\left(2\boldsymbol{\omega}_{ie}^n + \boldsymbol{\omega}_{en}^n\right) \times \boldsymbol{v}_{en}^n + \boldsymbol{g}^n$ denotes harmful acceleration that should be subtracted from the accelerometer output (Savage 1998).

The specific force equation is considered as the basic equation in inertial navigation system. For a better understanding of the specific force equation, a few orthogonal and right-handed reference frames defined in inertial navigation theory are described below.

- Earth frame ($e$ frame; $X_e$, $Y_e$, $Z_e$ axes) is a coordinate frame which has its origin at the earth's center of mass and has axes which fixed in the earth.
- Inertial (operational) frame ($I$ frame; $X$, $Y$, $Z$ axes) is defined as a frame that has its origin at the mass center of the earth and is nonrotating relative to the stars.
- Geographic frame ($n$ frame; $E$, $N$, $U$ axes) is a local navigational frame which has its origin at the system's location and its axes aligned with the east, north, and up directions.
- Body frame ($b$ frame; $R$, $P$, $Y$ axes) has its origin at the vehicle center of mass, and it constitutes Euler angles of $\varphi$, $\theta$, $\psi$ denoted as roll, pitch, and yaw.

### 2.2 Resolving Process

Figure 1 illustrates the flowchart of the resolving algorithm that calculates the attitude, velocity and position of the IMU sensor based on accelerometers and gyroscopes. The procedure can be summarized as following five steps:

(1) Derivation or definition of initial deformation rate $v_0$, position $P_0$ and direction cosine matrix (DCM) $C_0$.
(2) Derivation DCM based on gyroscope output $\omega$ over time.
(3) Further calculation of Euler angles $\varphi$, $\theta$, $\psi$ denoted as the rotation angles around $X$- , $Y$- , $Z$-axis, so that the form of the ground can be derived.
(4) Calculation of deformation rate $v_m$ at $T = \boldsymbol{t}_m$ based on DCM, accelerometer output $f$, gyroscope output $\omega$, and $v_{m-1}(\mathrm{m} \geq 1)$.
(5) Calculation of deformed position $P_m$ at $T = \boldsymbol{t}_m$ based on $v_{m-1}$, $v_m$ and $P_{m-1}(\mathrm{m} \geq 1)$.

Following the flowchart of the resolving algorithm, slope deformation rate and deformed position can be deduced from IMU sensed data. To express concisely, the abbreviations $\boldsymbol{C}_m$ and $\boldsymbol{C}_{m-1}$ are used instead of $\boldsymbol{C}_{b(m)}^{n(m)}$ and $\boldsymbol{C}_{b(m-1)}^{n(m-1)}$ that denote the direction cosine matrix at $T = \boldsymbol{t}_m$ and $T = \boldsymbol{t}_{m-1}$. Likewise, $\boldsymbol{v}_{m-1}, \boldsymbol{v}_m$, $\boldsymbol{P}_{m-1}$ and $\boldsymbol{P}_m$ represent $\boldsymbol{v}_{en(m-1)}^{n(m-1)}$, $\boldsymbol{v}_{en(m)}^{n(m)}$, $\boldsymbol{P}_{en(m-1)}^{n(m-1)}$ and $\boldsymbol{P}_{en(m)}^{n(m)}$ respectively.

The common algorithms that are applied for the computation of DCM are quaternions and Euler angles (Britting 1971). Particularly, the initial DCM $\boldsymbol{C}_0$ can be calculated based on the initial output from the accelerometer and magnetometer (Li et al. 2016), and the initial deformation

**Fig. 1** Flowchart of the resolving algorithm
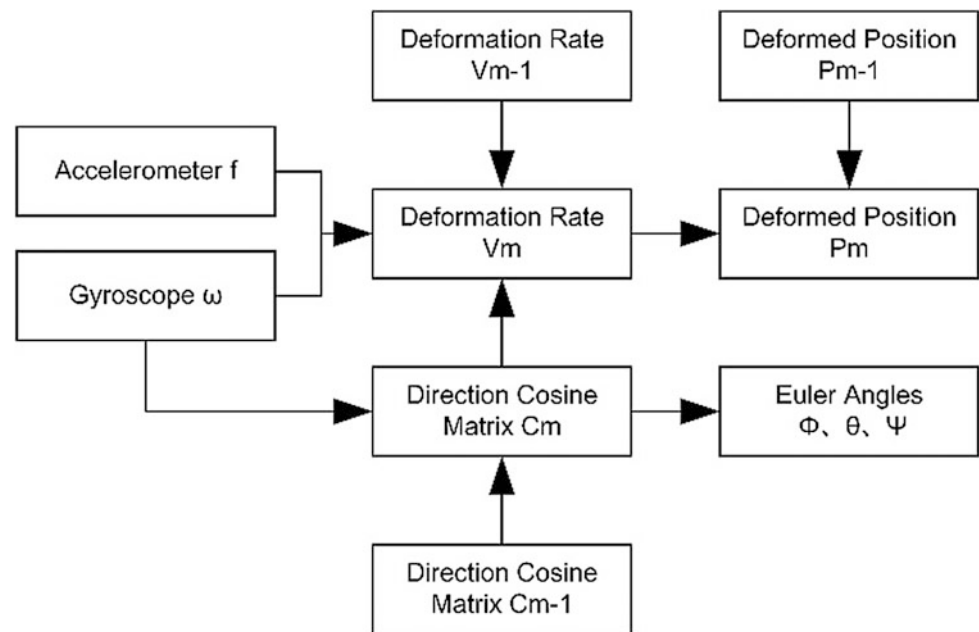


rate $v_0$ and deformed position $P_0$ can be both defined as a three-dimensional vector $[0 \quad 0 \quad 0]^T$.

When measuring slope deformation, the specific force $\dot{v}_{en}^n$ can be deduced by solving the specific force equation, and then the deformation rate and deformed position can be further solved by an integral and a second-time integral successively. When the system requires a relatively low accuracy, some parameters can be omitted for a simple calculation.

## 3 Discussion

The well-known United States' Global Positioning System (GPS) was declared fully operational in 1995 and was opened for civilian use shortly after. Its potential for landslide monitoring was realized quickly by the scientific community and has now been utilized for almost two decades (Gili et al. 2000). Besides GPS, other Global Navigation Satellite Systems (GNSS) have been developed such as the Russian GLONASS, the European Union's GALILEO, and the Chinese BeiDou navigation satellite system (BDS), all of which provide sufficient operational capabilities for global use. GNSS is an all-weather operated space-based system, and the displacement at the monitoring point can be deduced continuously. A GNSS receiver operates passively and records the time of arrival (TOA) for signals from all satellites in view, and its three-dimensional location will then be calculated by a trilateration algorithm (Kaplan and Hegarty 2005).

These years, real-time GNSS monitoring of slope deformation has been achieved, and many scholars are devoting themselves to improving positioning performance based on multi-GNSS observation data. The GNSS measurements are affected by noise and errors from the propagation of signals through atmospheric layers, which makes positioning more complex. With the study of Precise Point Positioning (PPP) these years, the positioning performance has made a significant progress. Even though the kinematic PPP has achieved a centimeter-level accuracy (Lou et al. 2016), such performance usually cannot be guaranteed in field monitoring due to limited computational power and uncertain atmospheric conditions.

As a result, multi-measuring means should be adopted in slope monitoring and a study of how to process multi-measurements is necessary. In this paper, the concept of data fusion is presented. Multi-sensor data fusion is an emerging technology which incorporates data from multiple sensors and related information from associated databases, to reach higher accuracies and more specific inferences than those obtained using a single sensor alone (Hall and Llinas 1997). How to use the measurements from various resources in an appropriate way, is a key issue during data processing and also the main discussion in this paper.

Figure 2 illustrates a sketch of the slope deformation phases based on the experience from several cases of slope monitoring and early warning in recent years (Xu et al. 2008). The slope deformation can be divided into three successive stages: initial deformation stage, constant deformation stage, and accelerated deformation stage. During the initial deformation stage, the displacement is relatively small with mere millimeters per month and the deformation is usually discontinuous. With the constant deformation of the slope, the deformation rate reaches a continuous and more
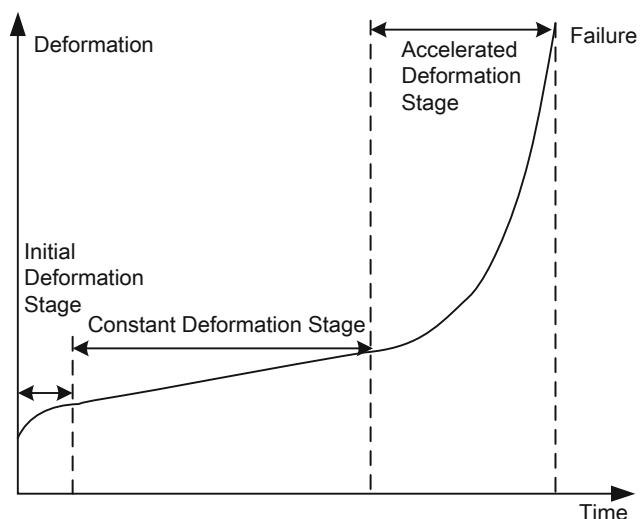
**Fig. 2** Sketch of three phases of slope deformation, after (Xu et al. 2008)

detectable level of several centimeters per day, and eventually accelerates sharply until the slope fails.

Based on our experience of real-time slope monitoring in the Xiluodu reservoir area in Sichuan, China, a millimeter-scale accuracy can only be achieved based on continuous observations. As a result, only one displacement value is solved per day to guarantee the monitoring accuracy. However, in some circumstances, the system has failed to detect fast displacements like bank collapse, which took place suddenly and endangered the safety of residents and their properties. In this case, the IMU method possesses an advantage in measuring the displacement. Its solving accuracy will be unchanged as it does not require external georeferencing. As far as the initial status is given, the deformation rate and updated position can be deduced based on its own measurements. It is worth mentioning that IMU measurements can be used as a supplement to GNSS monitoring but not as a substitution, as the gyroscope in an IMU generates drift that must be corrected by external references periodically, otherwise it would not be able to provide real deformation.

In general, the GNSS monitoring method is more applicable when more observations are available during positioning solving, and IMU monitoring is more reliable when the deformation rate accelerates. When designing the architecture of the data fusion model, the principles below must be considered:

- The GNSS solving frequency can be altered along with the deformation phase. For instance, during the initial deformation stage when the deformation is usually in the range of millimeters per month, a daily positioning from GNSS monitoring would already meet the requirement. With the acceleration of the deformation, a one-day displacement will not be helpful but should be altered to more frequent results. As the accuracy of GNSS solving results will be affected by the number of observations, which drops with the increase of solving frequency. Thus a threshold should be set in advance to ensure the availability of the GNSS displacements.

- The raw data are not equally processed but are prioritized corresponding to the deformation phase. For instance, in the stage of initial deformation, the displacement is relatively small and the deformation rate is slow, and the IMU raw measurements are not going to be processed but considered as training data to optimize the inertial measuring model. Hereby, the GNSS displacement should be used as the main reference in the monitoring analysis, and the values can be used to correct the IMU gyroscope output from time to time. With the acceleration of slope deformation, the time interval of displacement solving decreases until the GNSS displacement cannot provide the required accuracy, the IMU measurements will then be processed prior to GNSS data.

Based on the concept of multi-data fusion and the two principles above, an operational flowchart of the slope deformation processing scheme is drawn below in Fig. 3. After inputting the raw data into the processing unit, the GNSS solving frequency is checked first, if it exceeds a defined threshold that thus cannot provide the required accuracy, the IMU measurements will be used to calculate the deformation. On the contrary, if the GNSS solving frequency is below the threshold, the deformation will be determined based on GNSS measurements. In the next round, the GNSS solving frequency will be increased when the slope deforms faster than a pre-set critical rate, until it surpasses the pre-defined GNSS frequency threshold. As an auxiliary function, the IMU solving model can be updated based on the solved deformation from GNSS monitoring, hereby the updated IMU solving model will be available in the whole monitoring process. At last, the calculated deformation will be exported for a stability analysis or early warning assessment.

**Fig. 3** Flowchart of the slope
deformation processing scheme
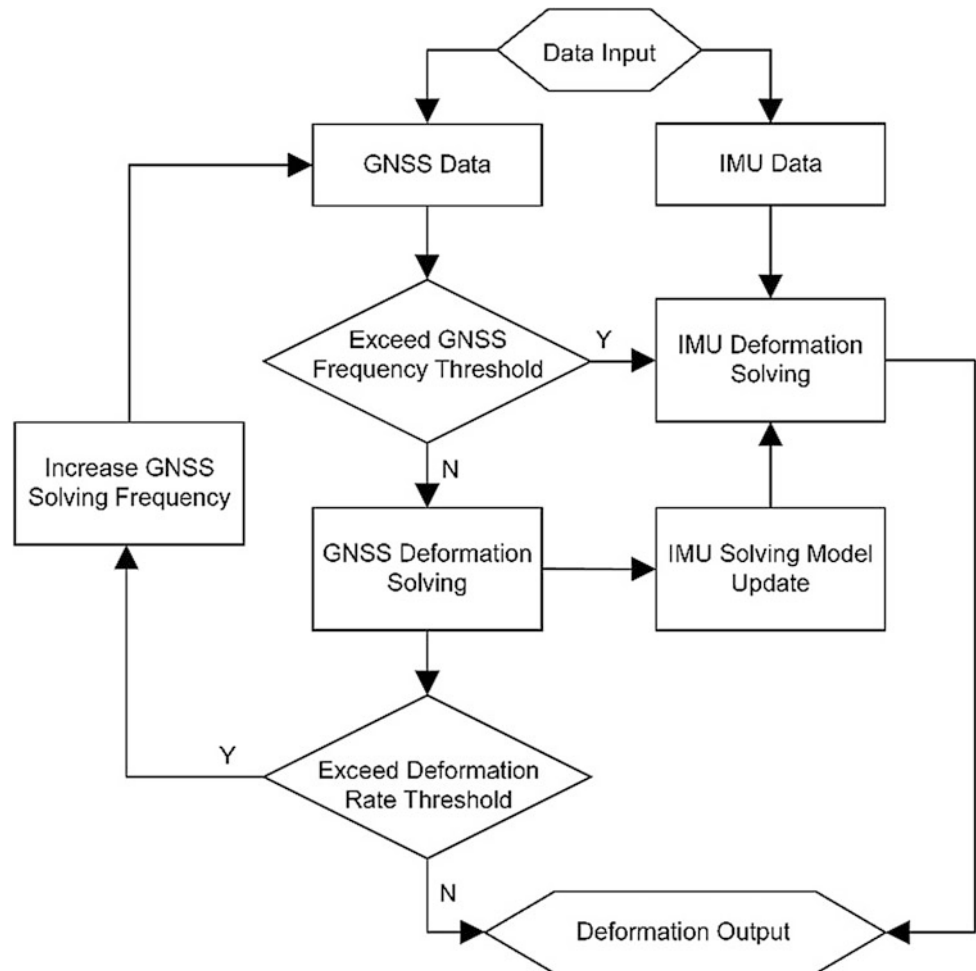


## 4    Conclusion

In this paper, we have introduced a new method for slope
deformation monitoring. Using micro-electromechanical
systems' inertial sensors to measure the rotational rate and
linear acceleration, the deformation rate and displacement
can be deduced using inertial navigation algorithms. Fur-
thermore, we have proposed a monitoring process scheme
for slope deformation based on GNSS and IMU measure-
ments. Following the flowchart, we would be able to provide
the slope deformation during the whole process with high
accuracy by the means of a data fusion of space based GNSS
and in situ based IMU monitoring.

## References

Abdoun, T., Bennett, V., Dobry, R., et al.: Full-scale laboratory tests using
a shape-acceleration array system. In: Proceedings of the 4th Decennial
Geotechnical Earthquake Engineering and Soil Dynamics Confer-
ence IV, Geotechnical Special Publication, Sacramento, 21–29 (2008)

Arnhardt, C.: Monitoring of surface movements in landslide areas with
a self organizing wireless sensor network (WSN). Ph. D. thesis,
RWTH Aachen University, Aachen, Germany (2011)

Arnhardt, C., Neussner, O.: Setup of a landslide monitoring system on
the Philippine Island of Leyte near the village of Malinao
(Municipality of St. Bernard). In: Margottini, C., Canuti, P., Sassa,
K. (eds.) Landslide Science and Practice. Springer, Berlin, Heidel-
berg (2013)

Azzam, R., Arnhardt, C., Fernández-Steeger, T.M.: Monitoring and
early warning of slope instabilities and deformations by sensor
fusion in self-organized wireless ad-hoc sensor networks. J. SE
Asian Appl. Geol. **2**(3), 163–169 (2010)

Britting, K.R.: Inertial Navigation System Analysis. Artech House,
London (1971)

Canli, E., Thiebes, B., Engels, A., Glade, T., Schweigl, J., Bertagnoli,
M.: Multi-parameter monitoring of a slow moving landslide in
Gresten (Austria). In: Proceedings of the European Geoscience
Union General Assembly, Vienna, Austria, 12–17 (2015)

Fernández-Steeger, T., Arnhardt, C., Walter, K., Niemeyer, F., Nakaten,
B., Homfeld, S.D., Asch, K., Azzam, R., Bill, R., Ritter, H., et al.:
SLEWS—a prototype system for flexible real time monitoring of
landslides using an open spatial data infrastructure and wireless sensor
networks. Geotechnol. Sci. Rep. **2009**(13), 3–15 (2009)

Fernández-Steeger, T., Ceriotti, M., Link, J.Á.B., May, M., Hentschel,
K., Wehrle, K.: "And then, the weekend started": story of a WSN
deployment on a construction site. J. Sensor Actuator Netw. **2**, 156–
171 (2013)

Gili, J.A., Corominas, J., Rius, J.: Using global positioning system techniques in landslide monitoring. Eng. Geol. **55**(3), 167–192 (2000)

Godha, S., Cannon, M.E.: Integration of DGPS with a low cost MEMS—based Inertial Measurement Unit (IMU) for land vehicle navigation application. In: Proceedings of International Technical Meeting of the Satellite Division of the Institute of Navigation, vol. 1, pp. 13–16 (2005)

Hall, D.L., Llinas, J.: An introduction to multisensor data fusion. Proc. IEEE **85**(1), 6–23 (1997)

Kaplan, E.D., Hegarty, C.: Understanding GPS: principles and applications, 2nd edn. Artech House, London (2005)

Li, C., Fernández-Steeger, T., Link, J.Á.B., May, M., Azzam, R.: Use of mems accelerometers/inclinometers as a geotechnical monitoring method for ground subsidence. Acta Geodyn. Geomater. **11**, 337–348 (2014)

Li, C., Azzam, R., Fernández-Steeger, T.: Kalman filters in geotechnical monitoring of ground subsidence using data from MEMS sensors. Sensors **16**(7), 1109 (2016)

Lou, Y., Zheng, F., Gu, S., et al.: Multi-GNSS precise point positioning with raw single-frequency and dual-frequency measurement models. GPS Solutions **20**(4), 849–862 (2016)

May, M.: X-SLEWS: developing a modular wireless monitoring system for geoengineering wide area monitoring. Master thesis, RWTH Aachen University, Aachen, Germany (2013)

Roberts, A., Tayebi, A.: A new position regulation strategy for VTOL UAVs using IMU and GPS measurements. Automatica **49**(2), 434–440 (2013)

Savage, P.G.: Strapdown inertial navigation integration algorithm design part 2: velocity and position algorithms. J. Guid. Control Dyn. **22**(2), 384 (1998)

Wittmann, F., Lambercy, O., Gonzenbach, R.R., et al.: Assessment-driven arm therapy at home using an IMU-based virtual reality system. In: IEEE International Conference on Rehabilitation Robotics, IEEE, pp. 707–712 (2015)

Xu, Q., Tang, M., Xu K., et al.: Research on space-time evolution laws and early warning-prediction of landslides. Chin. J. Rock Mech. Eng. **27**(6), 1104–1112 (2008) (in Chinese)

Yuan, Q., Chen, I.M.: Localization and velocity tracking of human via 3 IMU sensors. Sens. Actuators A **212**(6), 25–33 (2014)

# New Technology for Calculation of a Slip Surface Depth of Deep Landslides

Andrey Kazeev and German Postoev

## Abstract

A new approach for identification of critical states of soil masses was elaborated. The mechanism of formation of the limiting state in a soil mass during the initiation of a landslide is considered. The equations for assessment of a soil mass limited state prior to landslide formation were obtained. Also the equation for calculation of a landslide slip surface depth was obtained, using slope morphological and soil strength parameters. The developed limit state criteria were tested on specific landslide slopes. The results of these calculations have shown a good agreement with the actual data. For example, the calculated depths of sliding surfaces for deep landslide sites in Moscow coincide with depths identified by inclinometer measurements with accuracy of 0.5 m. The derived equation is suitable for slopes composed of different soils, from weak loams to very strong lithified Sarmatian limy clays of Balchik (Bulgaria), which are characterized by structural strength equal to 1 MPa.

## Keywords

Deep landslides • Slip surface • New calculation method

## 1 Introduction

Landslides annually cause Russia and other countries huge economic, social and environmental impacts. It's enough to say, that landslides occur in more than 700 cities in Russia.

In researching landslides, the most important is to identify its mechanism, assess possible landslide hazard for engineering constructions and to reveal slip surface depth for designing proper effective protection measures.

There is a great number of landslide classifications, based on certain characteristics: landsliding mechanism (i.e. the process); planar shape; magnitude of an area or volume; landslide age; depth of a sliding plane; occurrence within a certain geologic formation, etc. Mechanism-based classifications are the most common (Petrov 1987; Cruden and Varnes 1996; Fisenko 1965; Demin 1981 etc.). But, as we consider, much more important is to recognize different landslide types on the basis of their formation mechanism which is more important than mechanism of displacement.

Based on mechanism of formation, landslides may fall into three main categories (Postoev 2010, 2013):

- deep-seated compression-extrusion type;
- shear–sliding type;
- liquefaction–induced and flow type.

Deep-seated compression-extrusion landslides represent a major risk to urban infrastructure. They have a complex mechanism of development, have enormous weight, causing a large problem in the implementation of protection measures.

## 2 Regularities of Deep-Seated Compression-Extrusion Landslides

The first category encompasses relatively deep-seated block landslides of compression–extrusion (Fig. 1).

The block-type landslides of compression-extrusion mechanism are the most widespread and can be found in different engineering geological conditions. For example, typical deep landslides can be found in Britain (Bromhead and Ibsen 2007), Ukrain (Odessa, Mariupol), Russia (Moscow, Nizhny Novgorod, Kazan, Ulyanovsk, Volgograd, Cheboksary, Saratov, Saransk, Sochi et al.), etc. Landslide cirques can reach impressive sizes (up to 4.5 km and more, with slip surface depth more than 100 m).

A. Kazeev (✉) · G. Postoev
Sergeev Institute of Environmental Geoscience, RAS,
Ulanskii Street 13/2, Moscow, 101000, Russia
e-mail: kazeev@yandex.ru

**Fig. 1** Schemes of a landslide deformation with compression–extrusion mechanism: **a**, **b**—the compression landslide in cohesive soils; **c**—the subsidence and the spread of landslide blocks in rocks; **d**—bulging of the valley bottom; **e**—gravitational folds: deep creep with the S-shaped deformation of layers; **f**—gravitational deformation of ridges
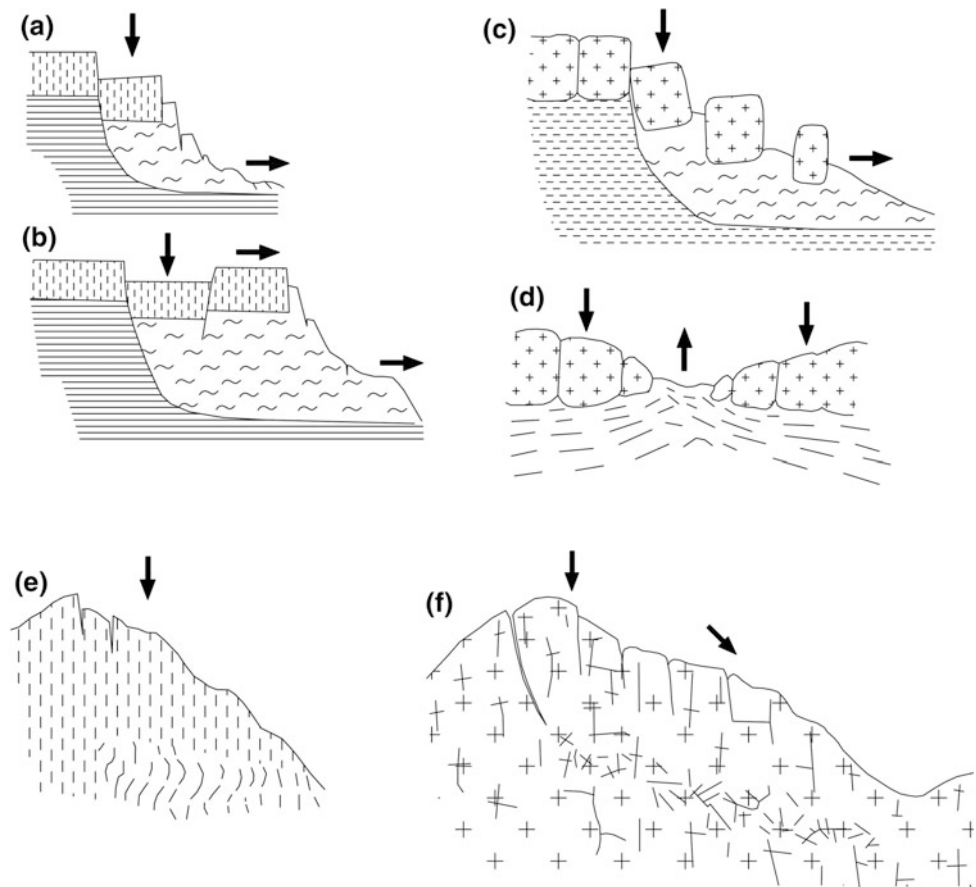


The loss of stability of a slope mass and its progressive deformation take place in accordance with the compression scheme. The horizon characterized by soil strength $\sigma_{str}$ below compressive stress caused by the weight of overlying strata is being deformed. This leads to firstly subsidence and depression in the overlying mass upslope, then increase in tensile stresses in a zone of subsidence and then to the formation and downward propagation of a tension crack. Finally, a landslide block separates along this crack and moves down along a steep curved slip surface. The angle of the slip surface flattens downslope and may become nearly horizontal. The displacement of a new sliding block triggers a displacement of the previously separated blocks located further downslope.

The slip surfaces are typically formed in clayey soils. These landslides usually occur on coastal areas and may develop in slopes of excavations, embankments, and in pit walls. Landslides in fractured and/or weathered rocks are less known, which occur in mountainous and foothill regions. They are characterized by slow development of deformations during the initial developmental stage that may take place for several hundreds of years.

However, very often this stage of the new block formation (with deformation of the mass based on the compression scheme) is not analyzed during investigation of a landslide mechanism. The subsidence of the new block along a steep curved slip surface is mistakenly thought of as a shear process, and a landslide is considered to have a shear–sliding mechanism.

The formation of a long front of these landslide blocks and, moreover, of landslide cirques is an important feature in recognition of this landslide type. As rule, the relief is stepped, reflecting the blocky structure of a landslide mass. This stepped geomorphology may be barely recognized in the relief at the end of the landslide cycle, at which point, as a result of prolonged repeated displacements, the upper blocks, as well as the blocks further downslope, reach the lowest position on the slope and form nearly horizontal landslide terrace.

The appearance of long continuous cracks is the feature of active displacement of landslide blocks. Crown cracks usually occur at the top of the slope on the "plateau", and also on the boundaries between landslide blocks. A scar wall of the cirque is steep, curved and has a maximum height in the central part of the cirque. The slip surface flattens out downslope and meets the nearly horizontal slip surface of previously displaced landslide blocks constituting the landslide body in the existing landslide cirque.

Landslide blocks of the compression—extrusion type can be formed practically **in any type of soil or rock**, if the following condition takes place in the ground mass:

$$\sigma_{str} < \gamma h, \tag{1}$$

$\sigma_{str}$    material strength of a layer in consideration;
$\gamma$    unit weight of overburden material;
$h$    depth of potentially deformable layer.

Displacement of a landslide body is caused by the pressure of the upslope blocks, therefore, a compressional bulge or ridge is formed at the toe. These characteristical bulges often occur in front of each landslide block (in the middle zone of the landslide terrace) that comprises the landslide body. This geomorphic feature is especially prominent during the main displacement stage, when a new landslide block separates from the plateau. In coastal areas when the sliding surface extends into the submerged part of the slope this bulge often resembles an island.

## 3 The Limit-State of a Ground Mass During Landslide Formation

The soil in a groundmass is situated in the conditions of a complex stress state. In this regard, the soil bearing capacity and the deformation behavior of the soil in a groundmass can have significant differences from the appropriate data and regularities obtained during laboratory testing of soil samples.

The first significant criterion of strength of cohesive soils is structural strength ($\sigma_{str}$). Physically the soil structural strength under compression corresponds to extreme pressure, which the structural skeleton of the soil can withstand without destructive deformations. Graphically the structural strength is marked on the x-axis by the Mohr's limit circus, which passes through the coordinate origin, i.e. when the $\sigma_3 = 0$, $\sigma_1 = \sigma_{str}$.

Analytically the structural strength is determined by the values of «$\varphi$» and «$c$»:

$$\sigma_{str} = 2c \cdot tg\left(45 + \frac{\varphi}{2}\right). \tag{2}$$

Experimentally the value of $\sigma_{str}$ can be obtained from the soil testing on uniaxial compression—as the ultimate pressure on the soil sample.

The soil strength criteria due to Coulomb-Mohr is defined as following:

$$\frac{\sigma_1 - \sigma_3}{\sigma_1 + \sigma_3 + 2c \cdot ctg\varphi} = \sin\varphi, \tag{3}$$

where $\sigma_1$ and $\sigma_3$—principal stresses, $\sigma_1 > \sigma_2 \geq \sigma_3$, $\sigma$ and $c$—the effective values of angle of internal friction and cohesion.

Equation (3) is often called the condition of the soil strength in a sample or in a point. It specifies that the maximum compressive stresses $\sigma_1$ operating on a closed elementary volume of soil (sample) generate the horizontal stresses of thrust $\sigma_3 = \sigma_2$ on the side boundaries of the elementary volume. The limit proportion between $\sigma_1$ and $\sigma_3$ depends on $\varphi$ and $c$ in accordance with expression (3).

Equation (3) can be written taking into account (2) as follows:

$$\frac{\sigma_3}{\sigma_1 - \sigma_{str}} = tg^2(45 - \varphi/2). \tag{4}$$

The Coulomb-Mohr criterion (4) characterizes also the initial state of soil in the groundmass with horizontal earth surface at depth $Z_i$, when the major vertical stress $\sigma_1 = \gamma Z_i$ (the pressure from the weight of above laying mass) exceeds the structural strength of the soil at a given depth and horizontal principal stresses are equal:

$$\sigma_2 = \sigma_3 = m \cdot (\gamma \cdot Z_i - \sigma_{str}), \tag{5}$$

where $m = tg^2(45 - \varphi/2)$.

When the pressure on the soil exceeds its structural strength, the resistance of soil to external impacts and it's deformational behavior depend not so much from the initial soil properties (strength, viscosity, creep peculiarities etc.), but mostly on the correlation of principal stresses in the groundmass.

Thus, the limit state of a soil mass on horizon $Z_a$ in a central part of a landslide cirque (of radius R) is described as:

$$\sigma_{1a} - \sigma_{str} = \frac{\pi}{2}\sigma_{1p}\frac{1 + \frac{1}{R}}{1 - \frac{1}{R}}, \tag{6}$$

And for the 2D case (Fig. 2) (for extensive landslides cirques, $R \to \infty$):

$$\sigma_{1a} - \sigma_{str} = \frac{\pi}{2}\sigma_{1p} \tag{7}$$

The development of landsliding processes, such as deep block-type movements, dies out once a flat landslide terrace is formed, which represents the end of a landslide cycle. Near the axis of a landslide cirque, the height of a scarp wall reaches critical value $H_{cr}$. At this moment there are temporarily no deformations on a landslide slope. The landslide body (2) is motionless, but the native mass (1) is in a limit-state (see Fig. 2).

So, on slopes with development of extrusive landslides are usually presented a terrace composed of previously

**Fig. 2** The scheme for assessment of a soil state at depth $Z_a$: **1**—considered soil native massif (active zone); **2**—landslide mass, adjoining to massif (passive zone)
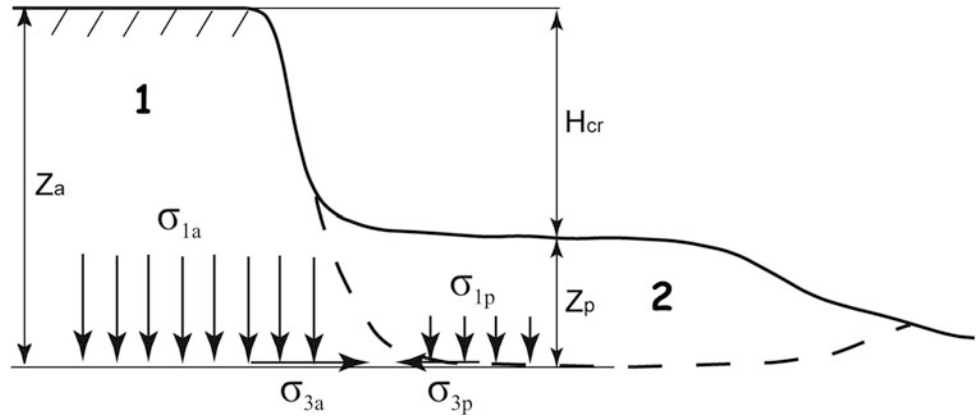


displaced blocks and younger blocks, adjoining the scar wall. Thus, from the slope geomorphology we can receive the value of critical height of a scarp wall $H_{cr}$ (Fig. 3).

The transition from this temporary quasi-equilibrium to a catastrophic activation of a landslide process (with formation of new sliding block and destructive deformations involving entire landslide cirque) may occur as a gradual change in a strain-stress state of a landslide-prone mass, or as a sudden catastrophic event triggered by an external factor.

Therefore, considering landslide-prone slope mass with landslide deformation on i-th horizon, implementing the Mohr-Coulomb theory (for localized zone in a ground mass), the equation for limit-state of a native ground mass (Fig. 3) was developed as:

$$Z_a - \frac{\sigma_{str}}{\gamma} = \frac{\pi}{2} Z_{p,cr} \left(\frac{1 + \frac{1}{R}}{1 - \frac{1}{R}}\right), \text{ or} \tag{8}$$

$$Z_a - \frac{\sigma_{str}}{\gamma} = \frac{\pi}{2} (Z_a - H_{cr}) \left(\frac{1 + \frac{1}{R}}{1 - \frac{1}{R}}\right) \tag{9}$$

$\gamma$—average unit weight of soils above the i-th horizon in a landslide-prone undisturbed mass (Fig. 3); $Z_a$—the depth of the i-th horizon in the undisturbed mass, $\sigma_{1a} = \gamma Z_a$; $\sigma_{str}$—the soil structural strength of the i-th horizon of the undisturbed mass; $\sigma_{str} = 2c \cdot tg\left(45 + \frac{\varphi}{2}\right)$; $H_{cr}$—critical height of the landslide terrace; $Z_{p,cr}$—critical depth to the i-th horizon of potential deformation with soil gravity loading considered as $\sigma_{1p} = \gamma Z_{p,cr}$; $H_f$ and $Z_{p,f}$—height of the scar wall and thickness of the latest landslide block; R—radius of a landslide cirque/m.

For the 2D case, assuming long, i.e. semi-infinite, slope with a curvature of slip plane (ledge line, Fig. 3) approaching zero, the equation for limit-state would be:

$$Z_a - \frac{\sigma_{str}}{\gamma} = \frac{\pi}{2} (Z_a - H_{cr}). \tag{10}$$

Therefore for calculation of $Z_a$ it is required to determine:

- the established position of the landslide terrace;
- the value of $H_{cr}$ (as the difference in elevations of the plateau and the level of the landslide terrace);
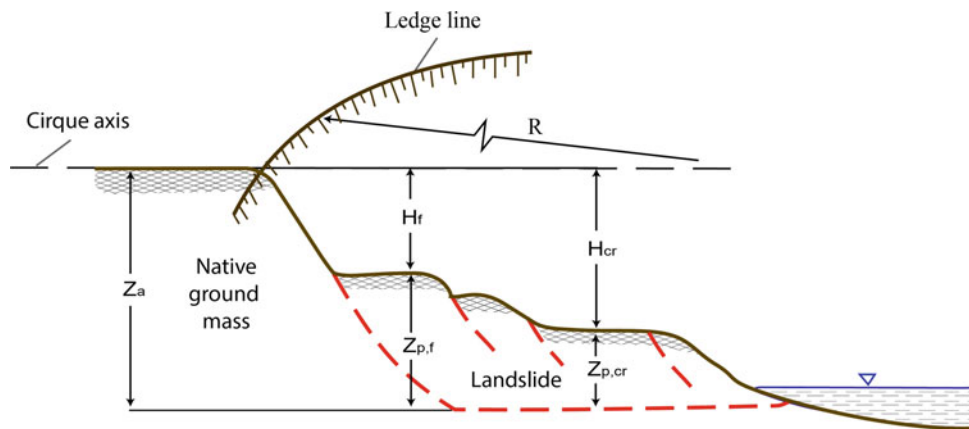


**Fig. 3** The scheme for assessment of the stress-strain state of the soil at depth $Z_a$. $Z_a$—the depth to the slip surface; $H_{cr}$—critical height of the landslide terrace; $Z_{p,cr}$—critical depth of landslide masses, correlating with native ground mass; $H_f$ and $Z_{p,f}$—height of the scar wall and thickness of the latest landslide block; R—radius of a landslide cirque/m

**Fig. 4** Depth to the sliding surface vs. thickness of the landslide body for documented landslide cases, where limit-state was reached prior to catastrophic failure with the development of deep-seated block landslides of compression–extrusion type (Postoev 2013). Refer to Eq. 9 for definitions
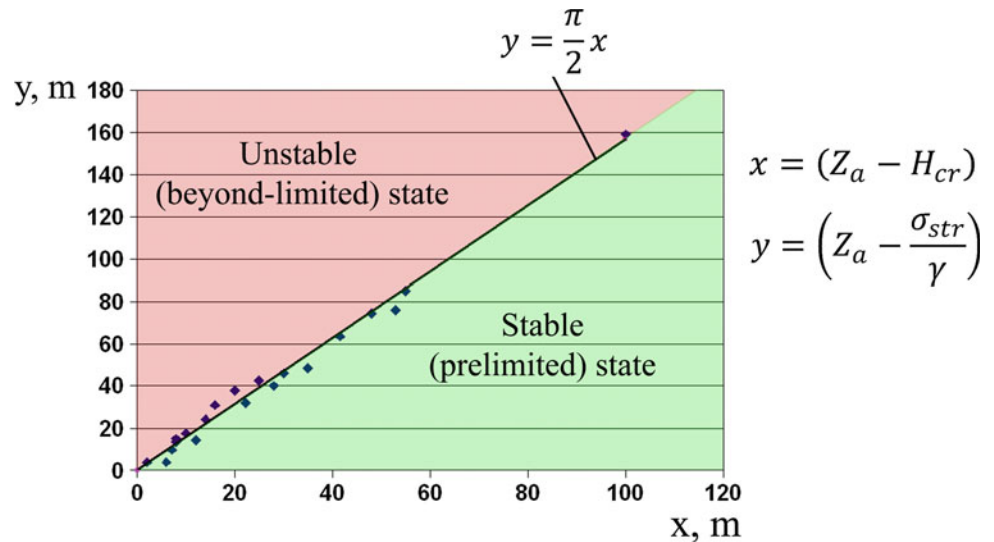
- the value of soil structural strength $\sigma_{str}$ (as ultimate rock strength in uniaxial compression test $R_c$, or the soil strength parameters $\varphi$ and $c$);
- the average value of unit weight for the mass above the considered depth $Z_a$ (i.e. for sandy-clay soils it is possible to take $\gamma = 20$ kN/m$^3$).

The results of the theoretical calculations were calibrated against a large number of real events where limit-state of landslide-prone soil masses and subsequent developments of massive landslide blocks were documented (Kazeev and Postoev 2017) (Fig. 4). It's essential that empirical points, which lay on the line, represent documented landslide cases, where limit-state was reached, with deformation of different kinds of soils (from weak silty loams in Novocheboksarsk, Russia to durable Sarmatian limy clays (with $\sigma_{str} = 1000$ kPa) in Balchik, Bulgaria).

The coefficient of stability, or safety factor of the cliff ($K_{st}$) may be used to characterize how close is the slope (native ground mass) to reaching the critical state (prior the formation of a new landslide block):

$$K_{st} = \frac{Z_{p,f}}{Z_{p,cr}}, \qquad (11)$$

where $Z_{p,f}$—thickness of the landslide mass in place of the youngest block; $Z_{p,cr}$—critical (minimal) thickness of the landslide terrace (see Fig. 3).

## 4 About Methods of Slip Surface Identification

There are various methods for identification of a slip surface on landslide slopes. For example, a method is known of determining of sliding surfaces in a landslide mass through identification of weak zones and layers while drilling boreholes (Komarnitskii 1966). Also, different geophysical methods (seismic, electrical) are applied to identify the slip surface, by identifying horizons with anomalous values of geophysical parameters (Goryainov et al. 1987). However, all these methods have significant disadvantages: they require drilling boreholes, laboratory soil testing, significant time costs, and often simply not applicable (in homogeneous clay mass).

Slope stability calculations are also widespread for assessment of possible landslide sizes by calculation of Safety factor ($K_{st}$) (Grebnev 2008). The disadvantage of this method is that another mechanism of landslide formation is considered—shear-shifting scheme, when a prepared slip surface exists in a mass (for example, defined by tilted lithological strata in the direction of the slope, or weak layers).

The sliding surface can also be determined in the process of instrumental monitoring in boreholes (e.g., inclinometer observations), but this method requires some time (often significant) for fixing landslide displacements.

## 5 New Method of Calculating of a Slip Surface Depth

The developed method allows to calculate and identify the depth of a slip surface, based on common data of geological survey on landslide areas.

The aim of present invention (Postoev and Kazeev 2011) is to eliminate disadvantages of above-mentioned methods of slip surface identification, to improve the accuracy of determining of a slip surface depth in a landslide mass at the stage of absence of landslide displacements along slip surfaces.

The method is carried out as follows. The landslide body is composed of blocks on the site with the existing landslide cirque (with ledge radius R) (see Fig. 3). These landslide blocks were separated from the native ground mass situated upslope and displaced along the slip surfaces at different times. These blocks are usually destroyed to various degrees. The height of the above-landslide slope should be measured in central part of the cirque ($H_{cr}$), as the excess of the scar wall ledge (cirque ledge) over the middle part of the landslide terrace. The radius (R) of the landslide cirque ledge bending in the plan should be also defined. The depth of the slip surface, expressed from Eq. (9), is calculated as follows:

$$Z_a = \frac{2c_d \cdot tg(45 + \varphi_d/2)(1 - \frac{1}{R}) - \frac{\pi}{2} \cdot \gamma_{f,d} \cdot H_{cr} \cdot (1 + \frac{1}{R})}{\gamma_d(1 - \frac{1}{R}) - \frac{\pi}{2} \cdot \gamma_{f,d} \cdot (1 + \frac{1}{R})},$$

(12)

where $Z_a$—slip surface depth (relatively to cirque's ledge)/m; $c_d$ and $\varphi_d$—accordingly cohesion (kN/m$^2$) and angle of internal friction (in degrees) of soil of potentially deformable horizon; R—radius of a landslide cirque/m; $\gamma_d$ and $\gamma_{f,d}$—accordingly average unit weights of soils, overlaying potentially deformable horizon in native part of soil mass and on landslide terrace.

## 6 The Example of Calculation of a Slip Surface Depth

In 2006 a catastrophic activization of the landslide process took place in a compression-extrusion landslide cirque on the banks of Moscow river (Moscow, Khoroshevo district), with formation of a new landslide block and displacement of landslide masses over 350 m along the shore (Fig. 5). Landslide hazard appeared for residential homes and the Life-Giving Trinity Church (architectural monument of 16th century). Engineering-geological surveys and monitoring were carried out on the site of landslide deformations, including instrumental monitoring of deep deformations (inclinometric monitoring), which established the sliding surface at depth of $Z_a = 31$ m.

The needed data for calculation of a slip surface depth were obtain in result of engineering-geological surveys and field observations: for $J_3ox$ clays: $c_d = 47.2$ kN/m$^2$; $\varphi_d = 22°$; R = 180 m; $H_{cr} = 16$ m; $\gamma_d = 20$ kN/m$^3$; $\gamma_{f,d} = 20$ kN/m$^3$.

Setting these values into the formula (12) for determination of $Z_a$, we get: $Z_a = 31.3$ m, i.e. we receive almost full coincidence of results of calculation of a slip surface depth ($Z_a$) and actual inclinometric measurements in boreholes.

## 7 Conclusions

Thus, the proposed elaborated method allows calculating the slip surface depth using common engineering geological data (site relief, geological cross-section and mechanical soil properties).

The information about the location of a slip surface is extremely important for carrying out stability calculations and designing the protective measures to ensure the safety of engineering structures on landslide areas.
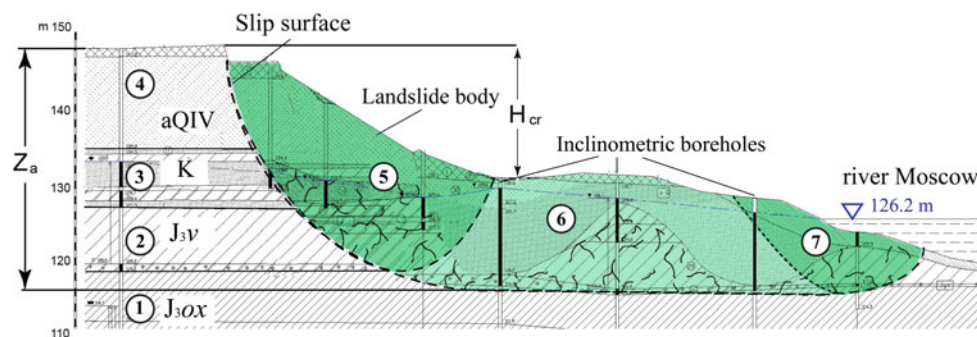


**Fig. 5** Cross-section of the landslide slope thru central part of the cirque in Khoroshevo, Moscow. **1**, **2**—Jurassic Oxford and Tithonian clays; **3** and **4**—cover deposits of loam and sand; **5**—new landslide block with downwards and rotational movement; **6**—landslide terrace (composed by previously displaced blocks) with lateral displacement; **7**—landslide toe (with mostly upward and lateral displacement)

## References

Bromhead, E., Ibsen, M.: An overview of landslide problems in the British Isles, with reference to geology, geography and conservation. In: Sassa, K., Fukuoka, H., Wang, F., Wang, G. (eds.) Progress in Landslide Science, p. 379. Springer, Berlin, Heidelberg (2007)

Cruden, D.M., Varnes, D.J.: Landslide types and processes. In: Turner, A.K., Schuster, R.L. (eds.) Landslides investigation and mitigation: transportation research Board, US National Research Council, Special Report 247, pp. 36–75. Washington, D.C. (1996)

Demin, A.M.: Regularities of manifestations of deformations of slopes in open pits, p. 144. Nauka, Moscow (in Russian) (1981)

Fisenko, G.L.: Stability of pit sides and blades, p. 378. Nedra, Moscow (in Russian) (1965)

Goryainov, N.N., Bogolubov, A.N., Varlamov, N.M. et al.: Methods of geophysical investigations and its possibilities in engineering geological surveys on landslide sites. In: Investigation of landslides by geophysical methods, pp. 13–23. M.: Nedra (in Russian) (1987)

Grebnev, Yu.S.: Engineering protection from hazardous geological processes. In: Guide for calculation and design of anti-landslide protection measures, p. 247. M., Geos (in Russian) (2008)

Kazeev, A., Postoev, G.: Landslide investigations in Russia and the former USSR. Nat. Hazards **88**(1), 81–101 (2017)

Komarnitskii, N.I.: The influence of weak zones and sliding surfaces in rocks on slope stability, p. 144. M.: Nauka (in Russian) (1966)

Petrov, N.F.: Landslide system. Simple landslides (aspects of classification), p. 164. Shtiintsa, Kishinev (in Russian) (1987)

Postoev, G.P.: Main characteristics and features of landslides. Geoecology **2**, 140–148 (in Russian) (2010)

Postoev, G.P., Kazeev, A.I.: Method of determining depth in a landslide radical array of potentially deformed horizon. The patent for invention RF No: 2412305, 20 Feb 2011, Bull. No: 5 (2011)

Postoev, G.P.: Limit state and deformation of soils in the mass (landslides, karst holes, settlings of ground foundations). Nestor-Istoriya, p. 100, Moscow-Saint-Petersburg (in Russian) (2013)

# Comparing Unmanned Aerial Vehicle (UAV), Terrestrial LiDAR, and Brunton Compass Methods for Discontinuity Data Collection

Rachael Delaney, Abdul Shakoor, and Chester F. Watts

## Abstract

Traditionally, discontinuity measurements have been collected manually using a Brunton compass. Ground-based light detection and ranging (LiDAR) scanning has, in recent years, been included as a more efficient method of structural data collection. Emerging technology in the realm of unmanned aerial vehicles (UAVs) focuses on the use of aerial photogrammetry in order to collect data from regions that would be otherwise difficult or impossible to access, and has the added benefit of eliminating "shadow zones" (gaps in data) that are typically a limitation of terrestrial LiDAR methodology. This study compares discontinuity data acquisition via an unmanned aerial vehicle (UAV) to these established methods in order to determine if UAV technology can be used reliably to collect structural data. Two field sites in Virginia were scanned for this study—a cut slope in Deerfield along highway 629, and a shale pit in Cove Mountain. Approximately 300 Brunton compass measurements of orthogonal joint sets and bedding planes were taken at each site in order to provide a "control group" for orientation data. In addition, ground-based LiDAR scans and UAV photogrammetric data were collected at each location. Scans from the LiDAR unit and the UAV were converted into 3D point clouds for statistical comparison with manually collected data. Stereonets of each data set were also prepared for further comparison. Preliminary results indicate that discontinuity data collection from UAV closely matches the data collected using LiDAR or Brunton compass.

## 1 Introduction

### 1.1 Background Information

Remote sensing has undergone vast improvements in technology in recent years, and as a result is gaining popularity for use in field site investigations and data gathering. Light detection and ranging (LiDAR) is a laser scanning technology which measures distance to a target based on the travel time of reflected light (Bemis et al. 2014). Terrestrial LiDAR can be used to map discontinuities for slope stability analysis but is limited by "shadow zones" where gaps in data are produced by a small scan angle or slope features blocking the outcrop, and by physical requirements for placing the surveying equipment relative to the slope face (Fisher et al. 2014).

The method of remote sensing of interest in this study is photogrammetry, specifically the use of unmanned aerial vehicles (UAVs). Photogrammetry works on the basis that 3D point locations can be determined by making measurements of features through analysis of overlapping photographs (McCarthy 2014). Current software algorithms such as VisualSFM and Pix4Dmapper Pro can automatically process collections of overlapping photographs to rapidly extract the 3D coordinates of millions of surface points to create a cloud model (Bemis et al. 2014). Structure from motion (SFM) is a photogrammetric and computer vision technique in which camera positions and orientation are solved automatically, in comparison to traditional photogrammetry, which requires previous knowledge of these parameters (Vasuki et al. 2014). The limitations of ground based surveys can potentially be avoided by using UAV instead of physical measurements or ground based survey equipment. Unmanned aerial vehicles have the benefit of

R. Delaney (✉) · A. Shakoor
Department of Geology, Kent State University, Kent, OH 44240, USA
e-mail: rdelane2@kent.edu

A. Shakoor
e-mail: ashakoor@kent.edu

C. F. Watts
Department of Geology, Radford University, 801 E Main St, Radford, VA 24141, USA

easily accessing portions of an outcrop that may be otherwise physically impossible. UAVs are now a widely available technology, can have programmed flight patterns, and can be outfitted with a camera to record photogrammetric data. When using photogrammetry data, an object of known dimensions must be present near the subject of interest because the data point cloud has no built in absolute scale. Each point in the cloud must be represented in at least three photographs. The more pictures taken with considerable overlap, the better the resulting 3D composite. One hundred to two hundred photos is generally a good range for the sizes of the target slope faces in this study (Falkingham 2013).

Once the 3D cloud models created from LiDAR and UAV data are completed, they can be used to identify discontinuities present in the rock face of interest. Detection of discontinuities such as joints, bedding, and faults can be done manually or through programmed algorithms (Vasuki et al. 2014). These discontinuities can then be used to evaluate possible modes of failure for that region of the slope. In order to use UAV-based photogrammetry for collecting discontinuity data needed for evaluating stability of slopes, there is a need to compare the UAV derived data with the ground based LiDAR data and manual measurements of discontinuities using Brunton compass in order to check for accuracy, precision, and competency of data. The following study has been designed to fulfill this need.

## 1.2  Geologic Setting

Two sites in the state of Virginia were selected for the study. Both sites lie within the Valley and Ridge physiographic province. The first site is a cut slope in Deerfield along highway 629, in Augusta County, which experienced a mass failure in 2009 (Fig. 1). This event involved roughly 10,000 cubic yards of rock material, which forced road closure for a period of three months (Neimann 2013). Deerfield lies on an apparently northeast plunging anticline with the bedrock consisting of generally siltstones and shales of Devonian age, specifically the Brallier (Db) Formation. This formation is approximately 2400 ft. in thickness, and is comprised of micaceous sub-fissile shales, siltstones, and sandstones, with dimpled bedding surfaces. Bedding is several feet thick (roughly 0.5 m) in the upper section, and gradually becomes thinner downward (Kozak 1970). The slope is formed by shales and minor sandstones of the Brallier Formation, which are folded around the axes of a paired anticline-syncline. The Deerfield study site has recently been observed as displaying chevron folding (Bruckno 2016). The intense folding of these strata has resulted in jointing of the rock that promotes release of blocks downslope (Neimann 2013).

The second site consists of an abandoned shale pit at the base of Cove Mountain, which is its namesake. This site is geologically and structurally similar to the nearby Big Walker Mountain (Byron 1965). The primary lithological unit present at this site is shale of lower Devonian and Silurian formations which are surrounded by the Brallier Formation and the Juniata, Reedsville, Trenton, and Eggleston Formations (USGS 2003). The primary regional rock types are sandstone, limestone, and shale.

## 2  Methodology

### 2.1  Site Selection

Field sites were selected based on certain criteria; both sites needed to be within driving distance of Radford University in order to transport equipment, and to both display obvious and regular orthogonal joint sets for the purpose of easy measurement and identification during data modeling. Figure 1 displays the topography of both sites, and links both sites to their regional position in Virginia. Note that Radford University is located near Christiansburg.

Site one (Deerfield) was selected primarily due to the presence of very clean, accessible, and regularly repeating orthogonal joint sets. Despite the presence of fallen rock blocks in the lower middle portion of the site, prominent beds and repeating joint sets were easily followed along the rock slope face. This site was also selected for ease of access due to ownership of the entire cut slope by the Virginia Department of Transportation (VDOT).

Site two (Cove Mountain) was selected for its short distance from Radford University, ease of access due to abandonment and positioning away from any major roadways, and ease of joint measurement. This field site is spatially smaller than site one, but displays equally robust and regular orthogonal joint sets. Figure 2 provides overviews of both field sites. Both sites show the presence of well-developed and easily delineated orthogonal jointing on the rock slope face.

### 2.2  Field Investigations

In order to easily distinguish orthogonal joint sets, both in the field and in resulting scans, joints were visually separated by apparent dip direction and joint faces of similar orientation were assigned a number. For example, all bedding was designated as "1", first joint set as "2", next joint set as "3", etc. Assigned numbers were drawn on the corresponding bedding or joint face with chalk. The Brunton compass was placed on each drawn number, and the number was crossed out with chalk following orientation measurement.
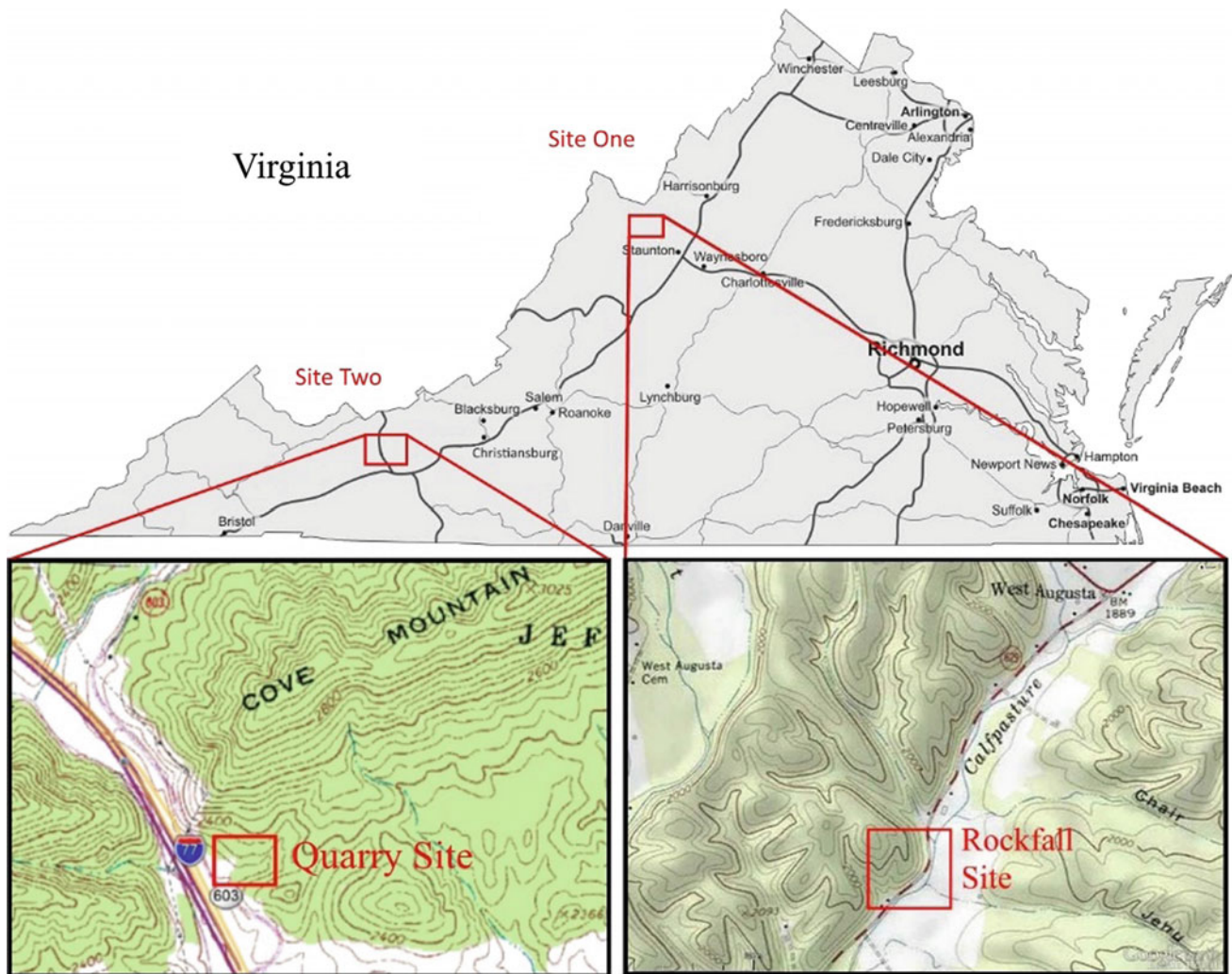
**Fig. 1** General locations of the two study sites in Virginia, with inset maps of corresponding topography. Site one is referred to as "Deerfield" (lat/long: 38° 15′ 32.77″ N/79° 19′ 2.74″ W), and site two is referred to as "Cove Mountain" (lat/long: 36° 59′ 25.75″ N/81° 4′ 29.66″ W) (composite from d-maps.com and Watts 2015)

### 2.2.1 Discontinuity Measurements Using a Brunton Compass

Following the numbering of bedding and major joint sets, orientation measurements were manually obtained with a Brunton compass. Orientation data was measured in terms of dip and bearing, to be later converted into dip and dip direction. Measurements were recorded by hand according to general slope face region (e.g. left, left middle, right middle, and right), assigned number, and discontinuity type. This allowed for data to be easily distinguished during processing and analysis. Between 300 and 400 measurements were recorded at the Deerfield site, and roughly 250 were recorded at the Cove Mountain field site. The difference in sample size is a result of the smaller overall available slope face at the Cove Mountain site.

Some compass data was recorded using the iPhone app GeoID (Apple Inc. 2017). For every data recording session, the GeoID app was tested for accuracy by comparing several measurements to a "control" measurement of the same rock face using a Brunton compass.

### 2.2.2 Discontinuity Measurements Using LiDAR

Terrestrial LiDAR imagery was obtained at both field site locations. Previously established methods by Fisher et al. (2014), were used. The Deerfield site was too large to be encompassed in one scanning location, so several scans were taken from opposite ends of the cut slope. Pole markers were placed in order to have a reference during later data set merging, or registration. Registration of the scans relative to each other allowed the data to be combined, viewed and

**Fig. 2** Top image: Deerfield site, facing the cut slope from the left portion; general bedding orientation dips 20° towards 280°, view bearing is roughly 350°. Bottom image: Cove Mountain site facing the pit slope; general bedding dips 10° towards 300°, view bearing is roughly 30°. Photos taken by author, 2016

interpreted in a single coordinate system (Buckley et al. 2008). The Cove Mountain site was small enough in scale to be scanned in a single shot. However, placement of the instrumentation tripod resulted in data being lost to shadow zones in certain less relevant portions of the slope face.

### 2.2.3 Discontinuity Measurements Using UAV Photogrammetry

Two models of UAV were used in this project. The first is the DJI Phantom 3 Pro, which was selected for the Deerfield site scans. This model is lightweight, includes a 3-axis gimbal for camera stabilization, is equipped with a 1/2.3″ complementary metal-dioxide semiconductor (CMOS) sensor (effective pixels: 12.4 M [total pixels: 12.76 M]), has a lens field of view of 94° 20 mm (35 mm format equivalent) f/2.8 focus at ∞, and has a one battery maximum flight time of approx. 23 min (DJI Official 2017). The second model, the 3D Robotics Solo, was flown at Cove Mountain (site two). Specifications include a Hero 4 camera, a 3-axis gimbal, and a maximum flight time of roughly 16 min (Anderson 2015). Each UAV model was flown to collect photogrammetric data at their respective field site.

## 2.3 Discontinuity Data Analysis

Data analysis consisted of generating point clouds (3D models of xyz data points) from UAV imagery and creating patches (images illustrating the definition of a surface) for determining orientation of discontinuities and comparing the results with those obtained from LiDAR and manually obtained data (Fisher et al. 2014). LiDAR data was processed using Cyclone and UAV imagery was processed using Pix4DMapper software (Watts et al. 2015). Matching points between images were used to calculate the spatial relationship between them, which indirectly derives the positions of the camera during data collection. The eventual result of this calculation is a color 3D model of matching points and their camera positions, and is known as the point cloud (McCarthy 2014). These point clouds were then exported into Split FX software (Split Engineering 2010) which was then used to extract discontinuity data from detected joint and bedding surfaces. Split FX software will automatically determine dip, dip direction, and patch surface

data for each scan (Fisher et al. 2014). However, robust meshes failed to automatically generate for any point cloud in this study. Sparse or low density meshes can result in smoothing of slope face features, which oversimplifies the generated surface and creates inaccuracies in plane representation (Lato et al. 2009). Discontinuity patches were instead drawn onto the point clouds by hand for all data sets. Figure 3 demonstrates the difference in resolution between the LiDAR and UAV data sets. While the same general slope face features are present, there is a marked "fuzziness" in the UAV point cloud. This can lead to difficulty in mesh and patch creation.

Discontinuities extracted from UAV imaging and LiDAR were plotted as poles on a stereonet to determine the principal joint sets using Orient 3.6.3. LiDAR data sets appeared to have all dip directions "rotated" either 90 or 180° relative to the positioning of data from Brunton compass and UAV, so the LiDAR orientation data was further processed to remove this apparent rotation by adding either 90 or 180° to all dip directions.



**Fig. 3** Comparison of resulting 3D point clouds from Deerfield (site one), viewed from above facing the slope. For both cases, bedding patches are those perpendicular to a top down view—all other patches represent joint faces. Top: LiDAR point cloud with patches; bedding planes display increased sampling. Bottom: UAV point cloud with patches in similar locations as the LiDAR cloud. (composite of images from Split-FX, 2017)
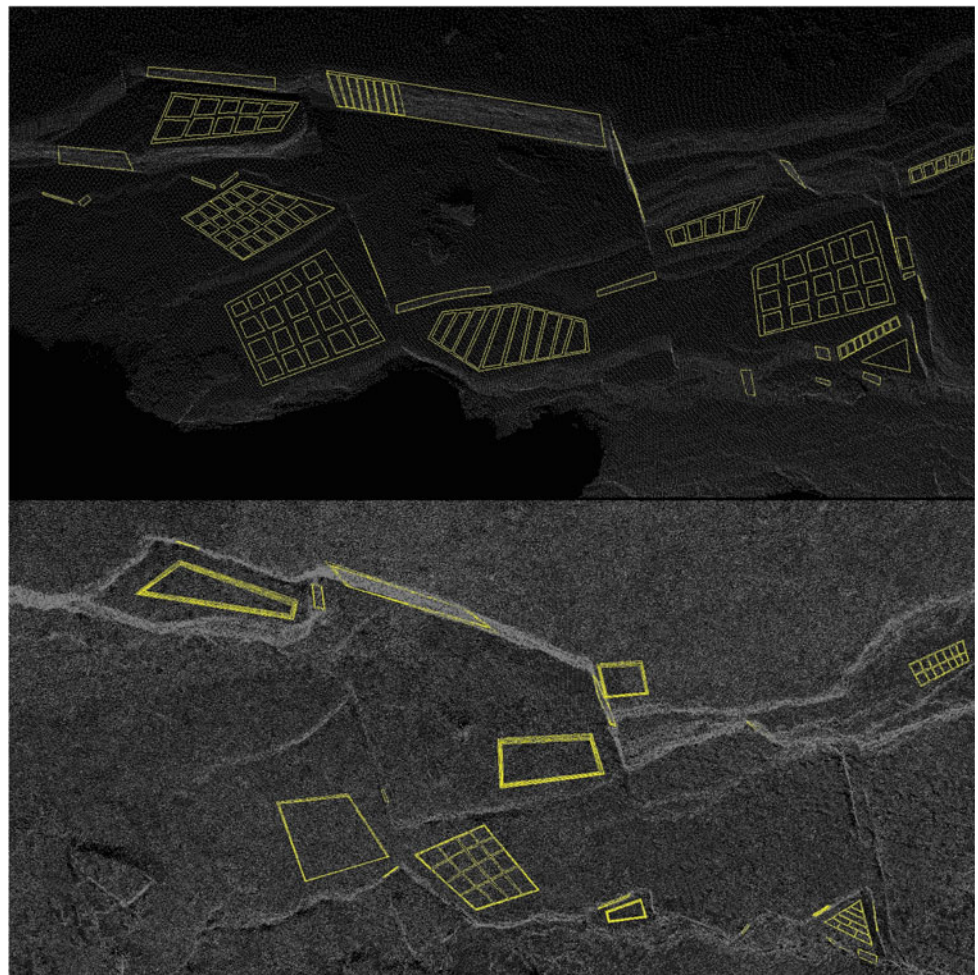
## 3    Results of Data Analysis

### 3.1    Discontinuity Data

#### 3.1.1    Deerfield Site

Between 300 and 400 discontinuity measurements were taken for each collection method. The greatest concentration of data points appears to occur around a dip direction of 280–290° and a dip angle of 20°, and likely represent bedding. Most other measurements (likely jointing) dip at an angle near 90°, with a spread to around 60°. Orthogonal joint set concentrations are more difficult to discern. Figure 4 displays a visual comparison of the three data sets.

#### 3.1.2    Cove Mountain Site

Roughly 250 discontinuity measurements were taken for each data set for this site. For these data, the most obvious concentration of points is generally oriented at a dip direction of 300–310° and a dip angle of about 10°, which likely

represents bedding. Steeper measurements likely represent jointing. Again, orthogonal joint set concentrations are more difficult to separate. Figure 5 shows the visual comparison of the three data sets.

## 4    Comparison of Discontinuity Data Collection Methods

Graphically, the data sets for all three data collection methods appears very similar for both field sites. It is important to note that the most prominent concentration of points across all data sets results from bedding plane measurements. Bedding planes had previously failed to be adequately represented in generated stereonets, so additional patches were drawn into mitigate undersampling. It is encouraging that bedding planes were so consistently represented in each data collection method, but interpretation of orthogonal joint set concentrations is not so obvious.
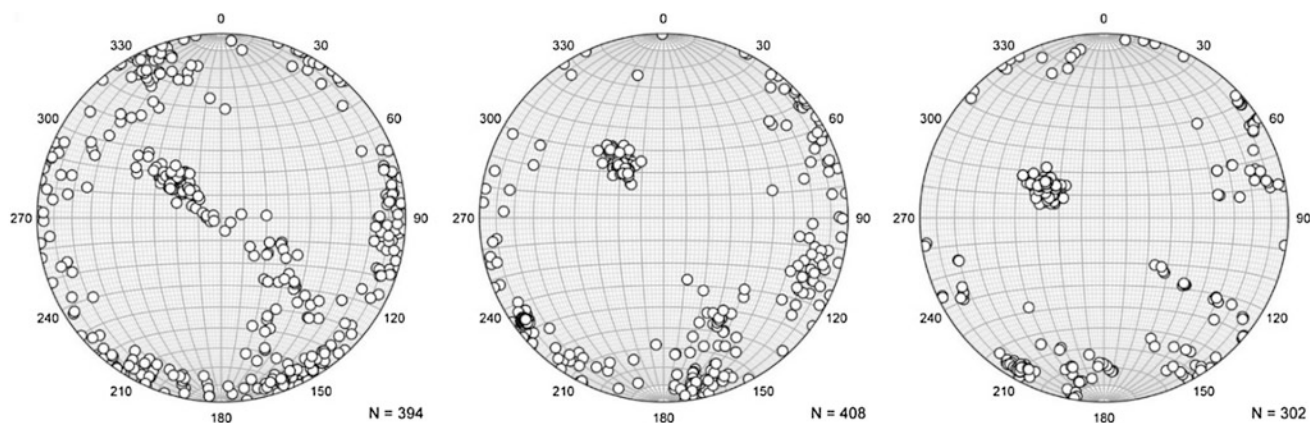


**Fig. 4** Stereonets of discontinuity data for each collection method: (left) data set from Brunton compass measurements; (middle) data set from LiDAR scan measurements; (right) data set from UAV scan measurements
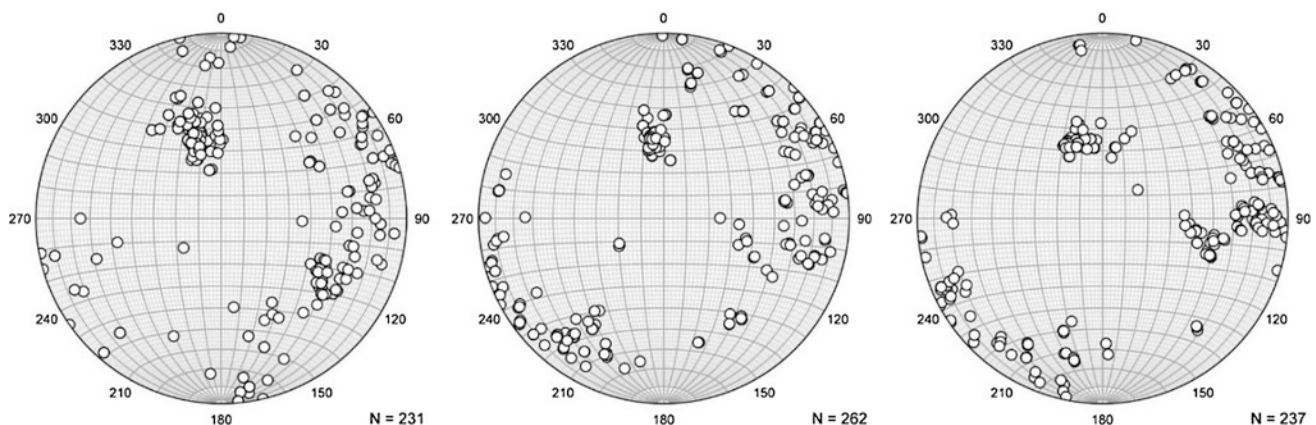


**Fig. 5** Generated stereonets from each collection method data set at the Cove Mountain site. Left: data set for Brunton compass measurements. Middle: data set for LiDAR scan measurements. Right: data set for UAV scan measurements

Arguably, orthogonal joint sets are the main focus of this study, so tighter data point concentrations would be desirable. However, qualitative analysis of graphical results shows that the general spread of data points across all three methods follows the same pattern for each site. Further statistical analysis of each resulting stereonet would shed light on this issue.

It must be kept in mind that additional data manipulation was necessary for the LiDAR data from each field site. A possible reason for this discrepancy is improper georeferencing of the data sets during processing in Cyclone. As this program is proprietary to the survey equipment and has a steep learning curve, LiDAR data sets were processed by technicians at Radford University. It may be necessary to re-process these data sets to ensure accuracy.

## 5 Conclusions

Overall, results for each field site suggest that data collected via an unmanned aerial vehicle is as reliable as data collected via terrestrial LiDAR or Brunton compass. Method selection for a field site should be dependent on ease of access to the target slope face and desired resolution of resulting data sets. Brunton compass measurements will always be the most reliable method of data collection, but this is not always practical or feasible. Unmanned aerial vehicle results are true enough to the orientations of physically collected data to allow for confident use as an alternative when conditions do not allow for traditional "boots on the ground" data gathering methods, or to augment traditionally gathered data sets.

## References

Anderson, C.: Site Scan Drone. Electronic document, available at https://3dr.com/solo-drone/specs/ (2015)

Apple Inc.: GeoID on the Apple Store. Electronic document, available at https://itunes.apple.com/us/app/geoid/id437190196?mt=8 (2017)

Bemis, S., Micklethwaite, S., Turner, D., James, M., Akciz, S., Thiele, S., Bangash, H.: Ground-based and UAV-based photogrammetry: a multi-scale, high-resolution mapping tool for structural geology and paleoseismology. J. Struct. Geol. **69**, 163–178 (2014)

Bruckno, B.: Personal Communication. Virginia Department of Transportation (2016)

Buckley, S.J., Howell, J.A., Enge, H.D., Kurz, T.H.: Terrestrial laser scanning in geology: data acquisition, processing and accuracy considerations. J. Geol. Soc. London **165**, 625–638 (2008)

Byron, C.: Geology of Big Walker Mountain Tunnel on Interstate Route 77, Wythe and Bland Counties, VA. In: 1965 GSA Southeastern Section Meeting, pp. 83–90 (1965)

DJI Official: Phantom 3 Professional—Specs, FAQ, Tutorials, Downloads and DJI GO—DJI. Electronic document, available at http://www.dji.com/phantom-3-pro/info#specs (2017)

Falkingham, P.: Generating a Photogrammetric Model Using VisualSFM and Post-Processing With Meshlab. Electronic document, available at http://academia.edu (2013)

Fisher, J., Shakoor, A., Watts, C.: Comparing discontinuity orientation data collected by terrestrial LiDAR and transit compass methods. Eng. Geol. **181**, 78–92 (2014)

Kozak, S.: Geology of the Elliott Knob, Deerfield, Craigsville, and Augusta Springs Quadrangles, Virginia: Report of Investigations 21, pp. 1–34. Virginia Division of Mineral Resources, Charlottesville, Virginia (1970)

Lato, M., Diederichs, M.S., Hutchinson, D.J., Harrap, R.: Optimization of LiDAR scanning and processing for automated structural evaluation of discontinuities in rockmasses. Int J Rock Mech. Min. Sci. **46**, 194–199 (2009)

McCarthy, J.: Multi-image photogrammetry as a practical tool for cultural heritage survey and community engagement. J. Archaeol. Sci. **43**, 175–185 (2014)

Neimann, W.: Use of digital photogrammetry to monitor change at selected rock slopes. In: Virginia Center for Transportation Innovation & Research: Marshall Proposal 2011-237, p. 14 (2013)

Split Engineering: Split-FX Software. Electronic document available at http://www.spliteng.com/products/split-fx-software/ (2010)

USGS: Digital Representation of the 1993 Geologic Map of Virginia, CD ROM (ISO-9660). This is a digital version of "Geologic Map of Virginia" published in 1993. Available from: https://www.dmme.virginia.gov/commerce/ (2003)

Vasuki, Y., Holden, E., Kovesi, P., Micklethwaite, S.: Semi-automatic mapping of geological structures using UAV-based photogrammetric data: an image analysis approach. Comput. Geosci. **69**, 22–32 (2014)

Watts, C.: Personal Communication. Radford University (2015)

Watts, C., Huber, R., Karki, N.: Rock slope stability analyses using structure-from-motion software and unmanned aerial vehicles. In: GSA 2015 Presentation (2015)

# Comparison of Multi-temporal Elevation Models of a Debris-Flow Channel

Klaus-Peter Keilig, Andreas Dietrich, and Michael Krautblatter

## Abstract

Debris flows are among the most hazardous landslides. Additionally, their relevance increases as a consequence of global climate change, a phenomenon, which has already been observed by other authors. In June 2015 two debris flows occurred due to a radar-inferred rainfall intensity of about 90 mm in 45 min near Oberstdorf (Bavaria, Germany) in the Northern Alps. The debris flows lead to damage costs of several million euros and more than 300 people were evacuated. To monitor geomorphic changes and a potential channel refill after the event, high resolution (5 cm grid size) digital elevation models (DEMs) were derived from terrestrial laser scanning (TLS) in May, July and August 2017 in the Roßbichelgraben, one of these channels. Therefore, the 800 m long channel was observed with 72–78 laser scan positions on each date and DEMs of difference (DoDs) with spatially variable uncertainty were calculated. Simultaneously, DEMs were derived by photogrammetric surveys using an unmanned aerial vehicle (UAV). Photos taken by the UAV were photogrammetrically reconstructed into point clouds using the structure from motion—multi-view stereo workflow (SfM-MVS). The results show a good correlation of detectable areas with geomorphic changes between both methods. However, the accuracy of the SfM-MVS derived DEMs remains uncertain in steep parts of the channel. Nevertheless, the current contribution demonstrated that SFM-MVS offers great potential for topographic surveying and is a promising tool to quantify geomorphic changes in the near future.

## 1 Introduction

Debris flows are rapid mass movements of a continuously deforming mixture of predominantly coarse loose material, water and wood in steep and channelized torrents (Varnes 1978). They occur in alpine regions with mobilisable debris and are triggered by intense rainfall events (e.g. Zimmermann et al. 1997). These rainfall events have increased in frequency and intensity over the last 100 years, especially on the northern slopes of the Alps (Scherrer et al. 2016). Climate models indicate that this trend is expected to persist (e.g. Frei et al. 2006; Rajczak et al. 2013), which leads to an increased occurrence probability of debris flows in the future. Recent studies already observed an enhancement in debris-flow activity over the last decades (e.g. Stoffel and Beniston 2006; Pelfini and Santilli 2008; Pavlova et al. 2014; Dietrich and Krautblatter 2017). Debris flows are already among the most hazardous events in alpine environments. They caused almost 1 billion € in physical losses in Austria between 1972 and 2004 (Oberndorfer et al. 2007) and worldwide nearly 80,000 fatalities between 1950 and 2011 (Dowling and Santi 2014).

The initial volume of a debris flow can grow massively by entrainment of material in the channel, which makes volume estimations difficult (Hungr et al. 2005). However, in order to create hazard maps, calibrate movement models or efficiently dimension mitigation measures, it is important to know the possible magnitude of a debris flow (Jakob 2005). Volume estimations are usually derived by empirical correlation between magnitude and characteristics of the watershed and the torrent (e.g. Rickenmann and Koschni 2010), geometrical approximations of debris-flow cones (e.g. Rickenmann and Scheidl 2013) or geomorphological

K.-P. Keilig (✉) · A. Dietrich · M. Krautblatter
Technical University of Munich, Arcisstr. 21, 80333 Munich, Germany
e-mail: kp.keilig@tum.de

mapping of the torrent (e.g. Gertsch 2009). However, these methods are often limited to the study sites they were developed in or are subjective in their application. Therefore, recent studies increasingly focused on the determination of debris-flow volumes by topographic surveying. Most authors determine the volume by a multi-temporal comparison of airborne laserscans, terrestrial laserscans or a combination of both methods (e.g. Bremer and Sass 2012; Blasone et al. 2014; Theule et al. 2015). With increasing progress in computer infrastructure the photogrammetric method "structure from motion—multi-view stereo" (SfM-MVS) is being used for topographic surveying more and more (e.g. Cook 2016). Only few authors used SfM-MVS in debris-flow environments, though. Blasone et al. (2015) derived topographic information by photogrammetric reconstruction of hand held photos, while Sotier et al. (2013) and Adams et al. (2016) surveyed debris-flow channels with an UAV. This research compares digital elevation models (DEMs) derived by TLS and SfM-MVS in a debris-flow channel for the first time.

## 2 Study Site

The investigated debris-flow torrent is located in a ski and hiking resort east of Oberstdorf in the federal state of Bavaria in southern Germany (Fig. 1). A hiking trail and a ski slope cross the torrent. In the upper parts of the cannel the bedrock consists of the Late Triassic Hauptdolomit-Formation with low and varying contents of iron and organic matter, respectively (Zacher 1990; Scholz 2016). The dolomite shows a very widely spaced bedding but it was jointed during the alpine orogenesis and most joints were filled with calcite in the process (Scholz 2016). Weathering of the jointed rock mass with a thickness of up to 1000 m lead to the creation of large dolomite taluses in the Quaternary (Scholz 2016).

In the lower parts of the torrent the bedrock consists of an alternating flysch sequence of cretaceous sandstones and marly claystones, the so-called Rehbreingraben-Formation (Zacher 1990; Scholz 2016). These sediments were deposited as a result of turbidites in a deep sea environment in the Aptian and Albian (123.5–100.5 Ma) (Zacher 1990; Scholz 2016).

The channel is located at heights between 1410 and 1220 m amsl and has an average slope angle of 19° among a channel length of 800 m. The mean annual precipitation amounts to 1700 mm with a maximum of rainstorms in the summer months. The area of its watershed can be specified as 0.53 km$^2$ (German Meteorological Office).

On 14 July 2015 a rainstorm with a radar-inferred intensity of 90 mm in 45 min triggered a debris flow. Erosion depth of over 6 m were observed during the event which had a magnitude of about 10,100 $\pm$ 950 m$^3$.

## 3 Methods

### 3.1 TLS Data

**Data acquisition**. The channel was surveyed using a Riegl VZ-400 laser scanner (near infrared wavelength, measurement range 1.5–600 m, accuracy 5 mm, precision 3 mm, measurement rate 122,000 pts/s, beam divergence 0.3 mrad) on a length of 800 m. The mapped area was chosen for being the part of the channel with the most detectable geomorphic changes with regard to the debris-flow event of 2015. Three surveys were carried out on 11 May (Fig. 2a), 22 July (Fig. 2b) and 30 August 2017 (Fig. 2c). To minimize occluded areas in the point clouds the channel was surveyed with 72 scan positions in May and 78 scan positions in July and August, respectively (Fig. 2). At few selected scan positions, the point clouds were derived with an increment of 0.04°, while most were derived with an increment of 0.06° (Fig. 2).

**Data processing**. Data processing of the points clouds was executed with RiSCAN Pro (v. 2.5.1) by Riegl LMS GmbH. After a coarse error removal all point clouds of a survey date were coarsely registered with a point-to-point method. Due to the lack of ground control points (GCPs), the TLS point clouds were firstly registered on a pre-event ALS point cloud from 2007 in order to spatially reference the point clouds correctly. This step was performed in three defined areas where no geomorphic change could be observed during the debris flow (Fig. 3). These point clouds were accurately registered by a multi station adjustment (Riegl 2016). This method uses planar patches of the point clouds for the fine-registration (Riegl 2016). The consecutive point clouds were registered on the merged point cloud of the previous survey, following the approach by Schürch et al. (2011).

Each merged point cloud was filtered with an echo filter to remove first and other targets which were not considered to be ground points. The point cloud was then filtered to a point spacing of 5 cm. We removed the vegetation using both a software filter (Fig. 4c) and manual removal (Fig. 4 d). The point clouds were interpolated into DEMs with a grid resolution of 5 cm using a natural neighbor interpolation. Data lacks in the point clouds caused by macro-scale roughness or removal of vegetation were automatically filled during the interpolation process.

### 3.2 UAV Data

**Data acquisition**. The channel was mapped with a DJI Phantom 4 Pro+ simultaneously with the TLS surveys (Fig. 5). Due to the limitations of flight time the upper 550 m of the channel were mapped with the UAV. In this part of the channel all major components of the debris-flow event (i.e. high erosion depth in the upslope parts and main

**Fig. 1** Location map of the Roßbichelgraben with its watershed, geologic setting and extend of mapped areas. Hillshade provided by Bavarian Land Surveying Office; geological information after Zacher (1990)
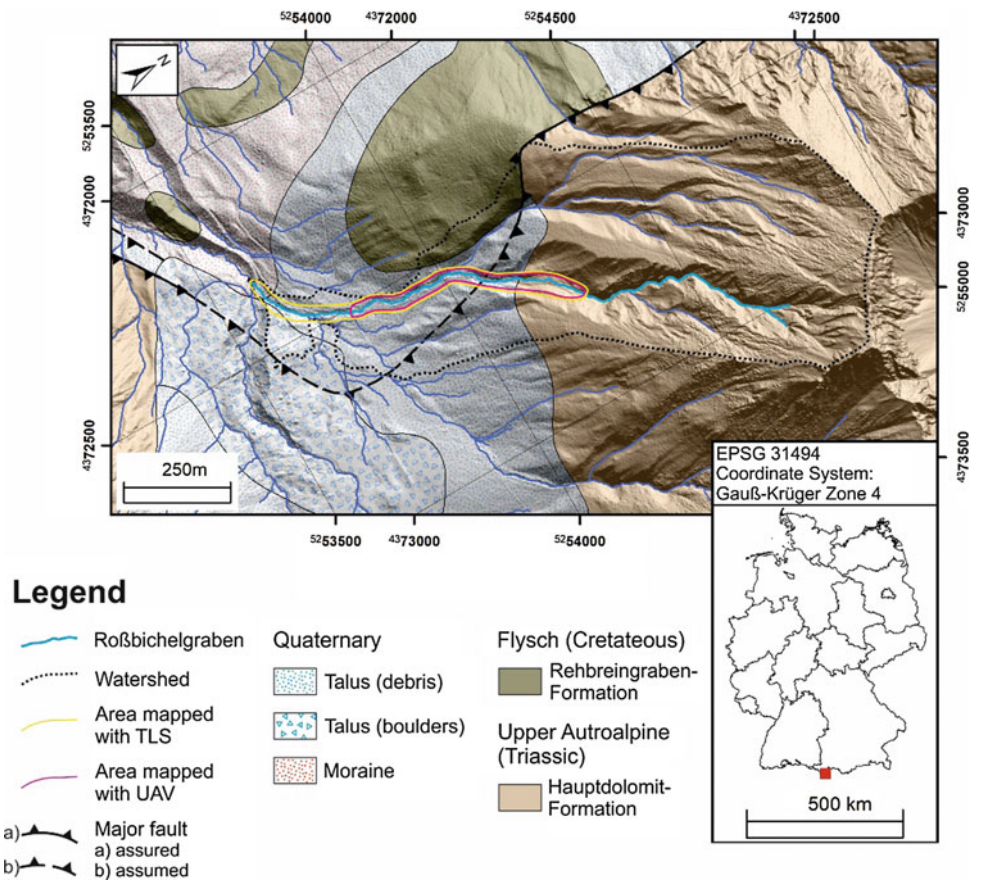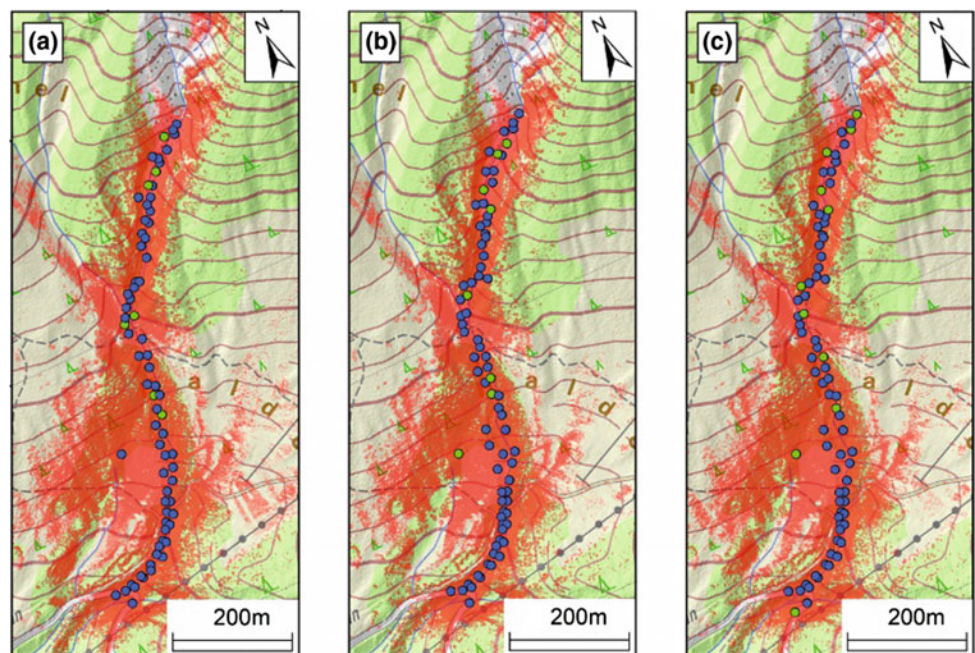


**Fig. 2** Location of scan positions for the topographic surveying of the Roßbichelgraben with TLS. Blue: scans with increment 0.06°; green: scans with 0.04°; red: extension of the raw point clouds. Topographic map provided by Bavarian Land Surveying Office



deposition in the downslope parts) were included. During the flight the camera of the UAV took a photo in a time interval of two seconds. The shutter speed, aperture and ISO values were changed to maximize photo quality during the flight. The photos were spatially referenced by the UAV-internal GNSS systems.

**Fig. 3** Areas without geomorphic change in the study area used for registration of the point clouds. **a** Rock face in the topmost part of the channel; **b** shed and its near range in the middle part of the channel; **c**, **d** drainage and street in the lowermost part of the channel

Each part of the channel was mapped with different camera orientations. The camera was directed perpendicularly to the stream bed and the banks on either side of the channel, respectively.

**Data processing**. The photos of the UAV were processed with PhotoScan Pro (v. 1.3.2) by Agisoft LLC. The software provides a complete workflow of SfM-MVS in order to create a dense point cloud from the photo dataset. However, it is a "black box" and the operation mode of the single algorithms remains mainly unknown.

Firstly, the photos were aligned and their intrinsic and extrinsic camera parameters were optimized based on the spatial information provided by the UAV-GNSS. Photos with obviously wrong projection points were deleted and the remaining points were filtered with the implemented gradual selection tool. With this tool all points that are represented on less than 3 photos were deleted.

Secondly, we identified possible ground control points (GCPs) in the photo dataset and identified their coordinates in the corresponding TLS point cloud. Potential GCPs were edges or cracks of large boulders and logs located inside the channel. The GCPs were identified in the photos in PhotoScan as markers and their coordinates defined. 19–21 GCPs were used to optimize the spatial reference of the three point clouds. Photo alignment and optimization were repeated with the GCPs solely.

Thirdly, we generated a dense point cloud with medium quality settings in order to keep the computation time reasonable. A higher dense cloud quality results in less smoothing of small-scale roughness, but largely increases

**Fig. 4** Vegetation filtering of a point cloud. **a** Photo of a tree in the study area; **b** raw point cloud; **c** automatically filtered point cloud; **d** manually filtered point cloud
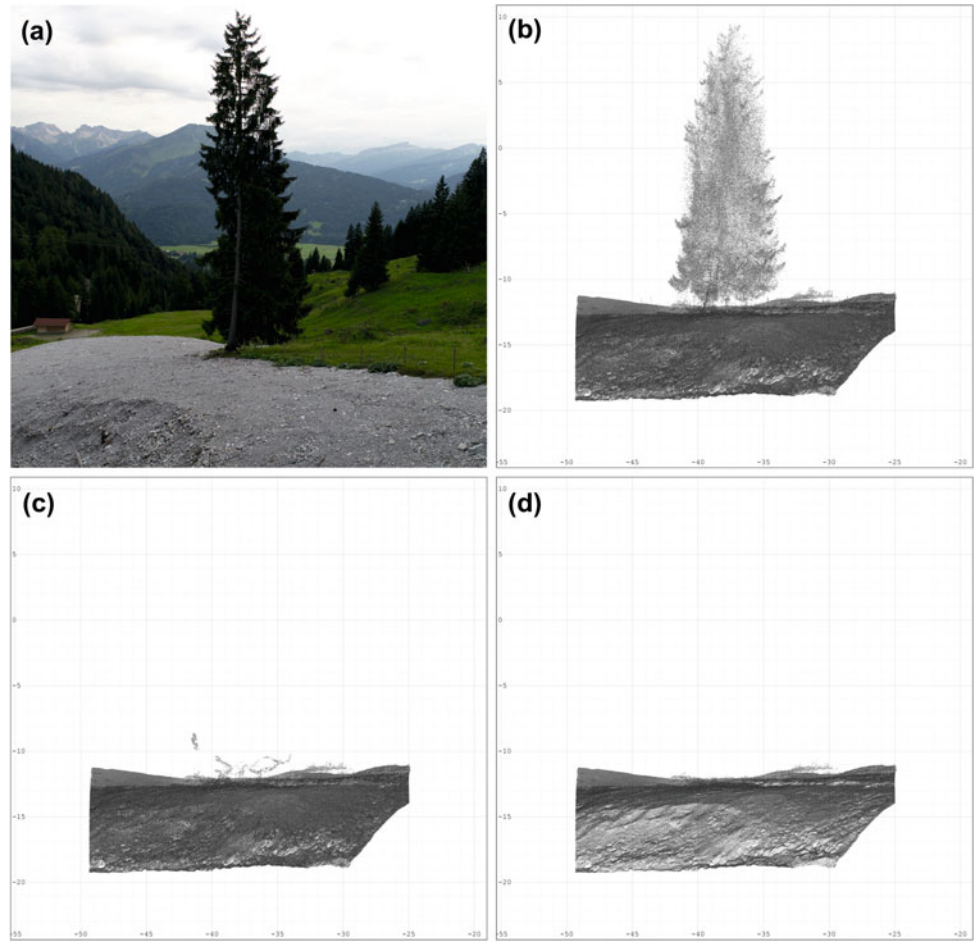


**Fig. 5** DJI Phantom 4 Pro + mapping the channel

**Table 1** Two input fuzzy inference system used to derive elevation uncertainty

| Rule | Input | | Output |
|------|-------|--------------|----------------------|
| | Slope | Point density | Elevation uncertainty |
| 1 | Low | Low | High |
| 2 | Low | Medium | Medium |
| 3 | Low | High | Low |
| 4 | Medium | Low | Extreme |
| 5 | Medium | Medium | Medium |
| 6 | Medium | High | Low |
| 7 | High | Low | Extreme |
| 8 | High | Medium | High |
| 9 | High | High | Medium |

the computation time and leads to more noise in the resulting point cloud (Cook 2016).

The resulting point cloud was imported to RiSCAN Pro and identically processed as the TLS point clouds (octree and vegetation filter, DEM interpolation, see Sect. "Introduction" in Chap. 3).

### 3.3 Geomorphic Change Detection

Calculation of geomorphic changes was performed with the ArcGIS plugin GCD (v. 6.1.14) developed by Wheaton et al. (2010). We used a method based on fuzzy logic, that provides a spatially variable DEM uncertainty based on point density and slope angle. Among others, these parameters are indicators for uncertainty in topographic surveys (e.g. Wheaton et al. 2010; Schürch et al. 2011; Blasone et al. 2014). Therefore, it is possible to distinguish geomorphic changes from noise. Table 1 summarizes the rule system used in this study.

### 4 Results

Comparison of TLS- and SfM-MVS-derived DEMs of the same date show a very good consensus in more shallow parts of the channel, while there are significant deviations in elevation values in areas with steep channel banks. However, it is possible to identify the areas indicating geomorphic changes between two surveys with both approaches (Fig. 6).

### 5 Discussion

While it is possible to identify real geomorphic changes with SfM-MVS-derived DEMs, the accuracy of the DEMs remains unsatisfactory in steep parts of the channel. This may be due to the heterogeneous distribution of GCPs among the torrent. Most GCPs are located in the channel bed and little are located on the steep banks, which is caused by the lack of potential GCPs in these parts. The DEMs could certainly be optimized by implementation of more GCPs and a more regular distribution. During this work we discovered that edges of large blocks are unfeasible GCPs, but cracks or other features with a high contrast to their surroundings are better suited to be picked as GCPs.

The best photo quality was achieved by keeping the shutter speed of the camera constant and only changing aperture and ISO to get equally exposed photos. This is also reflected in the quality of the DEM, which shows the lowest deviations to the corresponding TLS-DEM. More effort in filtering of photos could further improve the DEM quality

**Fig. 6** Comparison of identifiable geomorphic changes between May and July 2017 in SfM-MVS- (left) and TLS-derived (right) DoDs
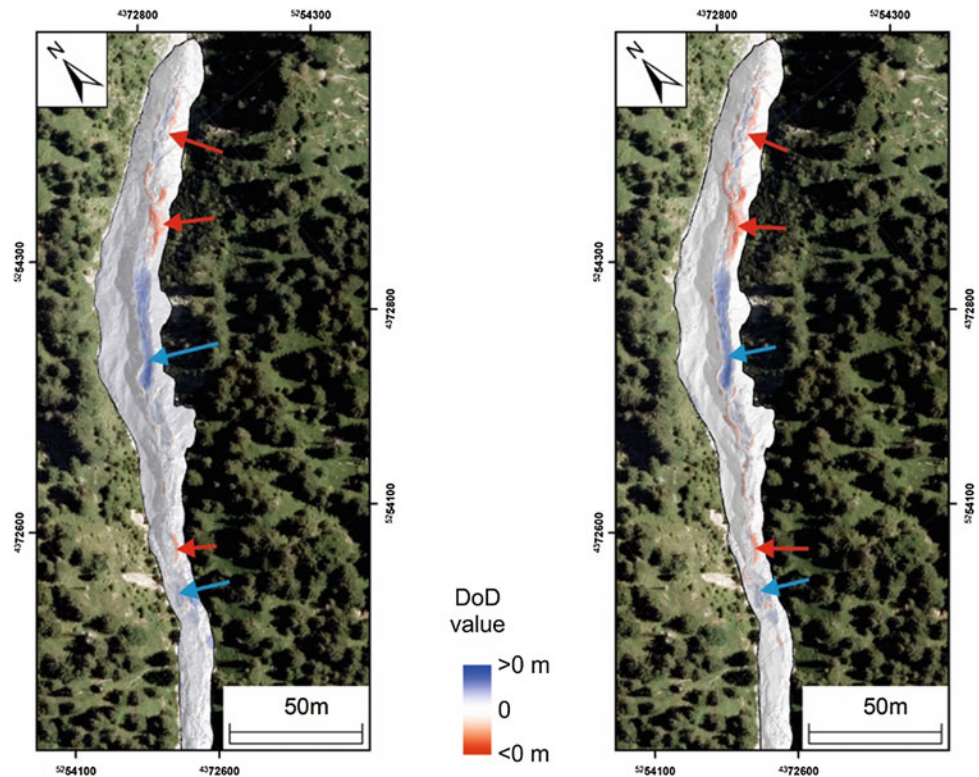
and might provide SfM-MVS as a valuable alternative to TLS surveys in debris-flow channels.

## 6 Conclusions

SfM-MVS provides the opportunity to carry out topographic surveys of torrents in a more efficient way than with TLS in terms of time and costs. In principal, it is possible to identify real geomorphic changes with SfM-MVS-derived DEMs, but the accuracy of the DEMs remains unsatisfactorily in steep parts of the channel. By further improvement of the photogrammetric workflow, especially in GCP identification and photo filtering, significant enhancements in DEM quality can be expected. This will develop SfM-MVS to a genuine alternative to topographic surveys by TLS in the near future, especially for quantifying geomorphic changes in mountain torrents.

## References

Adams, M.S., Fromm, R., Lechner, V.: High-resolution debris flow volume mapping with unmanned aerial systems (UAS) and photogrammetric techniques. Int. Arch. Photogramm. Remote Sens. Spatial Inf. Sci. XLI-B1, 749–755 (2016)

Blasone, G., Cavalli, M., Cazorzi, F.: Debris-flow monitoring and geomorphic change detection combining laser scanning and fast photogrammetric surveys in the Moscardo catchment (Eastern Italian Alps). In: Lollino, G., Arattano, M., Rinaldi, M., Giustolisi, O., Marechal, J.-C., Grant, G.E. (eds.) Engineering Geology for Society and Territory, vol. 3, pp. 51–54. Springer, Cham (2015)

Blasone, G., Cavalli, M., Marchi, L., Cazorzi, F.: Monitoring sediment source areas in a debris-flow catchment using terrestrial laser scanning. CATENA **123**, 23–36 (2014)

Bremer, M., Sass, O.: Combining airborne and terrestrial laser scanning for quantifying erosion and deposition by a debris flow event. Geomorphology **138**, 49–60 (2012)

Cook, K.L.: An evaluation of the effectiveness of low-cost UAVs and structure from motion for geomorphic change detection. Geomorphology **278**, 195–208 (2016)

Dietrich, A., Krautblatter, M.: Evidence for enhanced debris-flow activity in the Northern Calcareous Alps since the 1980s (Plansee, Austria). Geomorphology **287**, 144–158 (2017)

Dowling, C.A., Santi, P.M.: Debris flows and their toll on human life. Nat. Hazards **71**(1), 203–227 (2014)

Frei, C., Schöll, R., Fukutome, S., Schmidli, J., Vidale, P.L.: Future change of precipitation extremes in Europe. J. Geophys. Res. **111** (6), D06105 (2006)

Gertsch, E.: Geschiebelieferung alpiner Wildbachsysteme bei Grossereignissen—Ereignisanalysen und Entwicklung eines Abschätzverfahrens. Geographical Institute, University of Bern, Bern, Ph.D.-Thesis (2009)

Hungr, O., McDougall, S., Bovis, M.: Entrainment of material by debris flows. In: Jakob, M., Hungr, O. (eds.) Debris-flow Hazards and Related Phenomena, pp. 135–158. Springer, Berlin (2005)

Jakob, M.: Debris-flow hazard analysis. In: Jakob, M., Hungr, O. (eds.) Debris-flow Hazards and Related Phenomena, pp. 135–158. Springer, Berlin (2005)

Oberndorfer, S., Fuchs, S., Rickenmann, D., Andrecs, P.: Vulnerabilitätsanalyse und monetäre Schadensbewertung von Wildbachereignissen in Österreich. BFW-Berichte **139**, 1–55 (2007)

Pavlova, I., Jomelli, V., Brunstein, D., Grancher, D., Martin, E., Déqué, M.: Debris flow activity related to recent climate conditions in the French Alps: a regional investigation. Geomorphology **219**, 248–259 (2014)

Pelfini, M., Santilli, M.: Frequency of debris flows and their relation with precipitation: a case study in the Central Alps, Italy. Geomorphology **101**(4), 721–730 (2008)

Rajczak, J., Pall, P., Schär, C.: Projections of extreme precipitation events in regional climate simulations for Europe and the Alpine Region. J. Geophys. Res. Atmos. **118**(9), 3610–3626 (2013)

Rickenmann, D., Koschni, A.: Sediment loads due to fluvial transport and debris flows during the 2005 flood events in Switzerland. Hydrol. Process. **24**(8), 993–1007 (2010)

Rickenmann, D., Scheidl, C.: Debris-flow runout and deposition on the fan. In: Schneuwly-Bollschweiler, M., Stoffel, M., Rudolf-Miklau, F. (eds.) Dating torrential processes on fans and cones, pp. 75–93. Springer, Dordrecht (2013)

Riegl: RiSCAN PRO—User Manual for version 2.4.0. Riegl LMS GmBH, Horn (2016)

Scherrer, S.C., Fischer, E.M., Posselt, R., Liniger, M.A., Croci-Maspoli, M., Knutti, R.: Emerging trends in heavy precipitation and hot temperature extremes in Switzerland. J. Geophys. Res. Atmos. **121**(6), 2626–2637 (2016)

Scholz, H.: Bau und Werden der Allgäuer Landschaft, 3rd edn. Schweizerbart, Stuttgart (2016)

Schürch, P., Densmore, A.L., Rosser, N.J., Lim, M., McArdell, B.W.: Detection of surface change in complex topography using terrestrial laser scanning. Earth Surf. Process. Landforms **36**(14), 1847–1859 (2011)

Sotier, B., Graf, A., Kammerlander, J.: Einsatz von UAV im alpinen Gelände. Erfahrungsbericht und Anwendungsbeispiel aus der Naturgefahrenpraxis. Österr. Z. Verm. Geoinf, **101** (2 + 3), 110–118 (2013)

Stoffel, M., Beniston, M.: On the incidence of debris flows from the early little ice age to a future greenhouse climate: a case study from the Swiss Alps. Geophys. Res. Lett. **33**(16), L16404 (2006)

Theule, J.I., Libault, F., Laigle, D., Loye, A., Jaboyedoff, M.: Channel scour and fill by debris flows and bedload transport. Geomorphology **243**, 92–105 (2015)

Varnes, C.J.: Slope movement types and processes. In: Krizek, R.J., Schuster, R.L. (eds.) Landslides: Analysis and Control—Special Report 176, pp. 11–33. Transportation Research Board, National Research Council, Washington D. C. (1978)

Wheaton, J.M., Brasington, J., Darby, S.E., Sear, D.A.: Accounting for uncertainty in DEMs from repeat topographic surveys: improved sediment budgets. Earth Surf. Process. Landforms **35**(2), 136–156 (2010)

Zacher, W.: Geologische Karte der Republik Österreich 1: 50,000, Blatt 113 Mittelberg, 1st edn. Geologische Bundesanstalt, Vienna (1990)

Zimmermann, M., Mani, P., Romang, H.: Magnitude-frequency aspects of alpine debris flows. Eclogae Geol. Helv. **90**(3), 415–420 (1997)

# Three-Dimensional UAV-Based Photogrammetric Structural Models for Rock Slope Engineering

Qian Liu, D. Scott Kieffer, and Maja Bitenc

## Abstract

This research describes a methodology for acquiring, visualizing, and reconstructing three-dimensional representations of blocky rock masses based on the coordinates of dense surface points. In general, the surface points can be obtained with a variety of sensors and sensor platforms. The workflow described herein considers photogrammetric data sets acquired with Unmanned Aerial Vehicles (UAVs). In the overall, the steps for constructing high resolution 3D geological structural models are: (1) a photogrammetric survey of the investigation area is performed to obtain a true-color georeferenced 3D point cloud; (2) structural geologic measurements are extracted directly from the point cloud or associated digital terrain model (DTM); (3) the 3D rock structure is represented as a discrete fracture network (DFN); (4) identification, computing and visualization of blocks; and (5) on the basis of Block Theory, kinematically removable blocks are identified directly on the point cloud/DTM with embedded DFN and classified according to their criticality.

## 1 Introduction

In rock engineering, reconstructing the realistic 3D geometry of blocky rock masses at the project scale is often predicated on extrapolation of a 3D fracture network from location-dependent field measurements. If the set-based orientations are tightly clustered and fracture planes are highly persistent, traditional sampling approaches (e.g.

scanlines and window mapping) can provide unbiased fracture data, with which the representative rock structure can be inferred using statistical estimators. However, if the rock structure is irregular and characterized by highly dispersive set-based orientations and non-persistent planes, a scanline or window mapping survey is required for each homogeneous domain in order to characterize the spatial variation of rock structure. In alpine terrain, however, access to key rock outcrops is often not possible or fraught with the risk of personal injury.

With the recent advent of Unmanned Aerial Vehicle (UAV) photogrammetric platforms, which enables remote acquisition of surface from different viewing points, site access challenges are greatly solved. Traditional analog hand measurements can be replaced by digital measurements made directly from the photogrammetric data. In this paper the applicability of UAV photogrammetry for developing rock mass fracture network models is investigated and applied in the context of rock slope engineering.

## 2 Considerations for Obtaining a 3D Point Cloud

Sources of point cloud data commonly include laser scan and photogrammetric surveys, which may be undertaken using traditional aerial, terrestrial, or UAV platforms. Traditional Airborne Laser Scanning (ALS) has a high precision in height on flat areas and covers large surfaces. However, the precision decreases with steepening the slope due to extension of laser footprint size and consecutive increase of range error. Consequently, ALS surface models are generally inadequate for capturing rock mass structural details in steep mountainous terrain. On the other hand, Terrestrial Laser Scanning (TLS) effectively improves the angle of incidence as the sensor is setup in the field at a more optimum position. The main limitation of TLS is related to maximum range measurements and access to required instrument setup positions. The maximum effective range

Q. Liu (✉) · D. S. Kieffer · M. Bitenc
Graz University of Technology, Rechbauerstrasse 12,
8010 Graz, Austria
e-mail: qian.liu@tugraz.at

measurement depends on the surface reflectivity, which is a function of the rock mass color (Ullrich et al. 2001), and decreases if the outcrop surface is wet (Lichti and Harvey 2002). In steep mountainous terrain, TLS is often performed from a series of instrument positions along the toe of the slope. This can result in highly oblique lines-of-sight with respect to the cliff top, which can lead to significant orientation bias, as shown in Fig. 1a (Liu and Kaufmann 2015). In the derived 3D laser point cloud model of the outcrop (Fig. 1b) the bedding planes of the limestone, which are sub-parallel to the line of sight, cannot be accurately identified due to orientation bias.

Low-cost UAV platforms can offer significant advantages over ALS and TLS, in that sensor position and orientation can be continually optimized in the air. UAV surveys can be pre-programmed to operate in a fully autonomous mode, or can be carried out manually. The flight plan is designed based on the required resolution for a final 3D model and the overlap between photos. Beside the flight mission, specially designed targets, clearly visible in the photos, are laid on the ground within the acquisition area. The position of targets' center, the so called ground control point (GCP), is independently surveyed. GCP coordinates are needed to georeference the UAV point cloud and to quantify the data quality. A large number of omnidirectional overlapping images covering the survey area are acquired. Considering the ability to obtain consistent data of a larger difficult to assess surface, at very close ranges, resulting in extremely high resolution, and with optimal sensor orientation versus rock slope, UAV platform is considered as the best choice for obtaining high resolution rock mass data in alpine terrain.

In post processing, first Structure from Motion (SfM) image processing algorithm (e.g. Hartley and Zisserman 2004) is used to calculate image orientation and position. Secondly, Multi View Stereo (MVS) algorithm is run to estimate X, Y and Z coordinates for each pixel of the
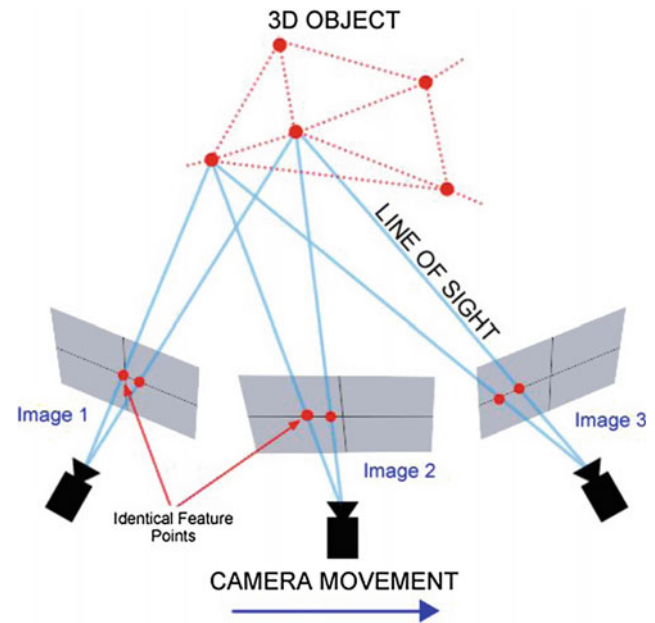


**Fig. 2** 3D reconstruction from multiple images, wherein point coordinates are calculated by the intersection of the two or more projection rays (Mason 2017)

original image (Fig. 2). Result is a 3D dense point cloud. The absolute positional accuracy of the final 3D data depends on the georeferencing method and can be in the range of 2–5 cm, if using GCPs measured with GNSS. The survey error is systematic and thus has little impact on the relative quality of the rock mass model.

## 3 Case Study Workflow

The specific case involves a potentially unstable rock outcrop along a state road in Styria, Austria. The main steps in developing UAV-based 3D rock mass models are:

(1) data acquisition;
(2) point cloud and DTM generation;
(3) embedding a DFN in 3D topography; and
(4) identification and analysis of removable blocks

## 3.1 Data Acquisition

The UAV survey was performed with the Aibotix X6 V2 UAV quadrocopter, and images were acquired with an Olympus E-PL5 camera fitted with a 12 mm objective. The survey control was provided by 4 GCPs (Fig. 3a), whose centers can be accurately marked on the acquired images, and were measured in the field with a Leica GS15 GNSS-rover applying the Real Time Kinematic (RTK) correction of the Austrian Positioning Service (APOS).

The overall flight was performed autonomously, with subsequent manually triggered photographs capturing details of precarious rock blocks that were identified during the autonomous flight. Figure 3b shows the position and orientation of the 296 acquired photographs.

## 3.2 Point Cloud and DTM Generation

For the reconstruction of the 3D scene from 2D images, the SfM-MVS algorithm as implemented in the software *Agisoft PhotoScan Professional* (v 1.3.2) was used. PhotoScan greatly facilitates the complex algorithms necessary for processing a large number of digital images. The 3D point cloud calculated from the 296 is shown in Fig. 4. The textured point cloud appears almost photo-realistic, since each point contains RGB value as well as 3D coordinates. This greatly facilitates the 3D geometrical reconstruction of a blocky rock mass; small details of the rock mass discontinuity surfaces are discernable. Besides, also discontinuity traces, as well as the locations of discontinuity intersections and terminations can be extracted.



**Fig. 3** UAV photogrammetry: **a** A GCP target; **b** position and orientation of UAV images, optimized to cover the area of interest
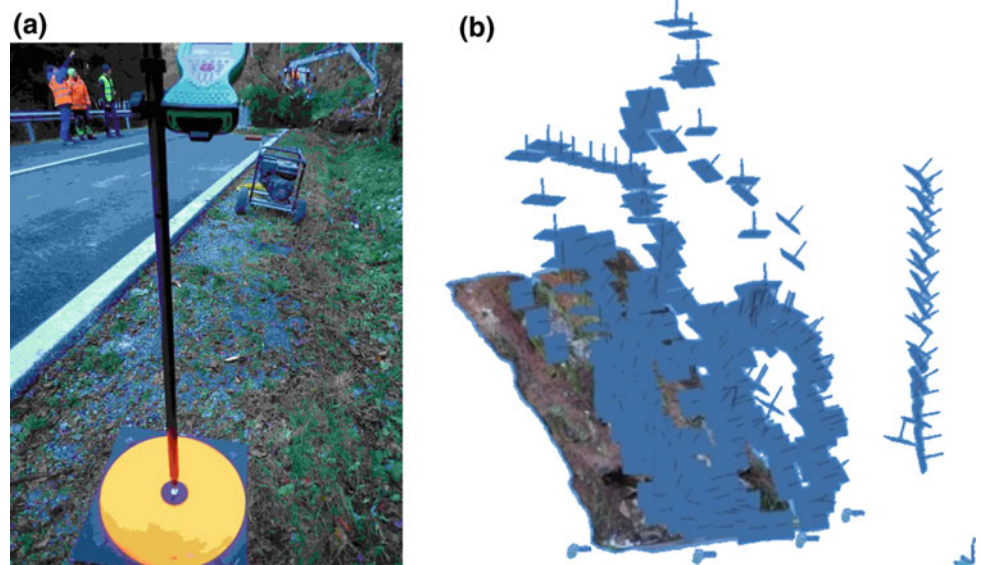


**Fig. 4** True color 3D point cloud of outcrop along road shoulder, in which the following discontinuity properties are discernable: **a** downhill-dipping schistosity; **b** two conjugate joint sets along with the uphill dipping joint set
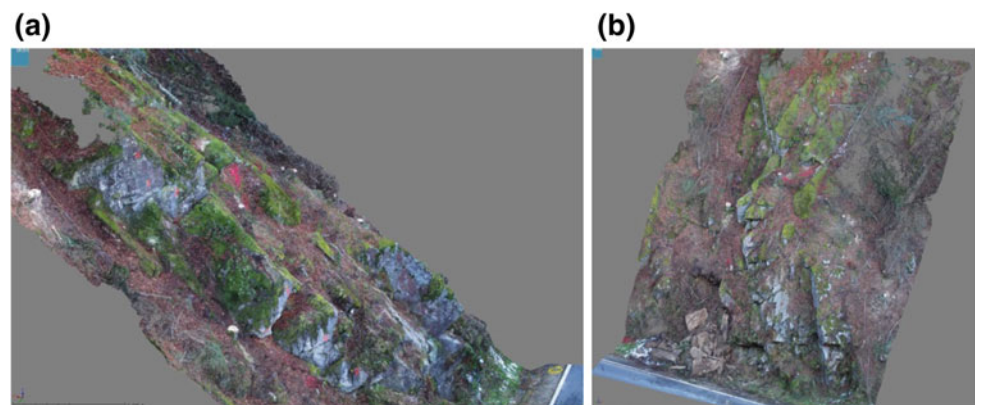
## 3.3 Embedding a DFN in 3D Topography

The conventional statistical estimators for discontinuity spacing and trace length are based on discontinuity traces mapped on a planar outcrop (e.g. Priest 1993). In the UAV data model, the discontinuities are directly embedded in irregular 3D topography. Having a detailed 3D surface model, a realistic fracture network can be developed. Discontinuity orientations were extracted manually, by selecting data points falling on a discontinuity surface. A rectangular plane is then fitted to the selected points, and its attitude, surface area, and 3D corner coordinates are recorded. Although semi-automated and automated discontinuity measuring algorithms could be applied, the location-specific searching and manual fitting of discontinuities is necessary to perform stability analysis of relevant individual blocks. Figure 5a shows the fitted schistosity planes (in red) within the true-color dense point cloud, and Fig. 5b depicts the entire in situ discrete fracture network.

## 3.4 Identification and Analysis of Blocks

A detailed DFN as shown in Fig. 5b facilities identification of blocks that are formed by the intersections of discontinuity and the free slope face. After identifying the bounding planes of a real block, a polyhedron is calculated using the bounding plane vertices. Intersection of three bounding planes defines a vertex, for which the information of location and orientation is necessary. The volume of a block is the calculated and visualized in 3D space. As an example, the block in Fig. 6a is a joint-block bounded by repeated discontinuities: two S planes (red), two J1 planes (green) and two J3 planes (yellow). Figure 6b shows the detailed block shape and its volume computed using the algorithm in Liu and Kaufmann (2015), and Fig. 6c shows the individual block embedded in the topography. Further analyses based on Block Theory (Goodman and Shi 1985) shows that this is a removable block, and that the critical failure mode
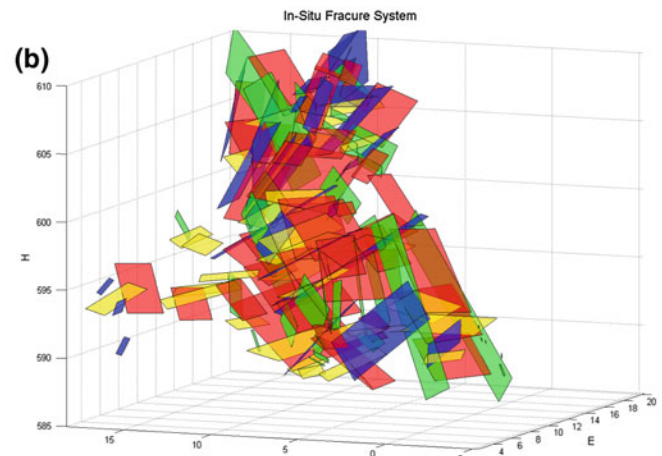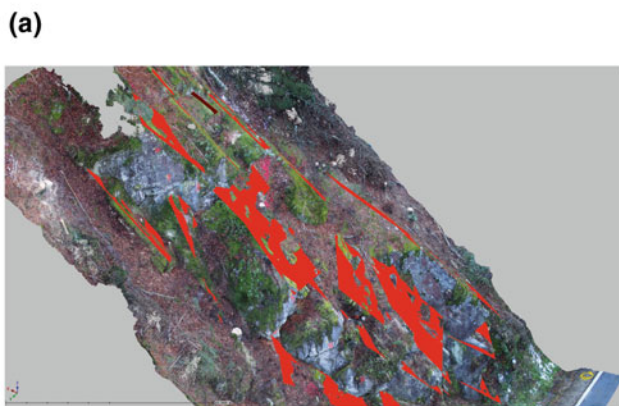


**Fig. 5** In-situ fracture system model: **a** fitting the schistosity set as red planes; **b** mapped 3D discrete fracture network: schistosity set is red (S), two conjugate joint sets are green (J1) and blue (J2), and yellow joint set (J3)



**Fig. 6** Reconstruction of blocky rock mass: **a** block identification; **b** computing and assessment; **c** the block model in the real terrain
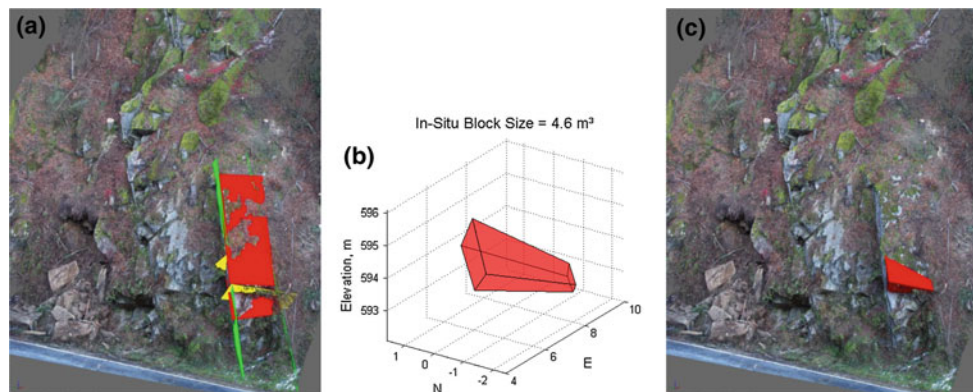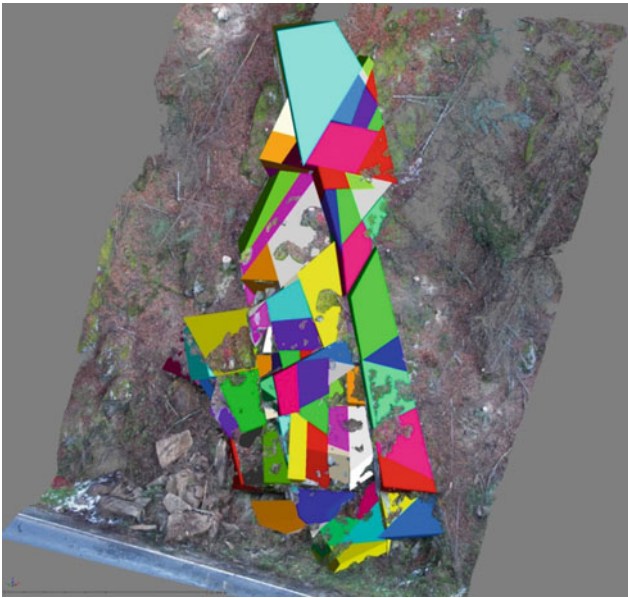
**Fig. 7** The block system derived from the UAV dense point cloud

involves planar sliding along the schistosity. Stability analyses indicate the block mobilizes at 36° of friction, and is therefore classified as a *potential key block*.

Extending this approach across the domain of interest, a total of 80 rock blocks have been identified as intersecting the slope surface (Fig. 7). For each of these blocks, we determined: (1) 3D removability conditions (i.e. *non-removable* vs. *removable*); and (2) criticality of the subset of removable blocks (i.e. classification as *stable blocks*, *potential key blocks*, or *key blocks*).

## 4 Conclusions

Remotely acquired UAV data can provide unbiased and colored 3D point clouds that are of great utility in geomechanical analysis and design. Point coordinates are sufficiently accurate for characterizing the actual location-dependent rock mass discontinuity properties. Such information greatly facilitates rock mass modeling, in particular for determining the spatial relationships between fractures and outcrop surface forming isolated blocks. The resulting block system provides the essential framework necessary for assessing rock mass behavioral tendencies and the stability condition of individual blocks.

## References

Goodman, E.R., Shi, G.H.: Block Theory and Its Application to Rock Engineering. Prentice-Hall, USA (1985)

Hartley, R., Zisserman, A.: Multiple View Geometry in Computer Vision. Cambridge University Press, Cambridge (2004)

Lichti, D.D., Harvey, B.R.: The effects of reflecting surface material properties on time-of-flight laser scanner measurements. In: Proceedings Symposium on Geospatial Theory, Processing and Applications, Ottawa (2002)

Liu, Q., Kaufmann, V.: Integrated assessment of cliff rockfall hazards by means of rock structure modelling applied to TLS data: new development. In: EUROCK 2015 & 64th ÖGG Geomechanics Colloquium, Salzburg (2015)

Mason, A.: Making 3D models with photogrammetry. https://thehaskinssociety.wildapricot.org/photogrammetry/ (2017)

Priest, S.D.: Discontinuity Analysis for Rock Engineering. Chapman & Hall, UK (1993)

Ullrich, A., Reichart, R., Schwarz, R., Riegl, J.: Time-of-flight-based 3-D imaging sensor with true-color channel for automated texturing. In: Optical 3-D Measurement Techniques V, Conference Proceedings, October 1–4 2001, Vienna, pp. 2–9 (2001)

# The Use of UAS in 3D Geotechnical Slope Stability Analysis

V. S. Müller, I. Coutinho, M. K. Flach, T. L. Fornasa, M. S. Espíndola, and J. A. Flores

## Abstract

The relief of an area controls factors such as drainage conditioning, thalweg and interfluve determination, watershed delimitation, and microclimate. In turn, all of these components control the rock alteration process, and origin and formation of soils. For this reason, it is necessary to observe geomorphological features of geotechnical areas of study. One of the emerging technologies in planialtimetric surveys makes use of Unmanned Aerial Systems (UAS), which provide high-resolution aerophotogrammetric surveys. This paper aims to evaluate the efficiency of UAS and obtain geomorphologic data to be used in slope stability analysis. Focusing on low cost solutions able to provide high-quality products data form the automatic flight of an Almost Ready to Fly quadcopter was evaluated and post-processed with the aim of generating a digital surface model and an orthophoto. The 3-dimensional slope stability analysis was performed using SoilVision's SVSlope software, with geotechnical features obtained from physic and mechanic laboratory tests and topographic data from high-resolution digital surface model generated from UAS flight data. It was observed that UAS were effective for the slope stability analysis, since besides providing high-resolution topography, it proved to be a low-cost tool for periodic data acquisition, used to monitor slope failure and validate predicted slope deformations.

## Keywords

UAS photogrammetry • 3D geotechnical analysis

V. S. Müller (✉) · I. Coutinho · M. K. Flach · T. L. Fornasa · M. S. Espíndola · J. A. Flores
Federal University of Santa Catarina, Santa Catarina, Brazil
e-mail: vitor@mullergeo.com

## 1 Introduction

The versatility of Unmanned Aerial Systems (UAS) enables the application of such equipment in many diverse areas. As stated by Honkavaara et al. (2014), gains in quality and time sometimes facilitate tasks that otherwise would be considered unfeasible.

According to Naumann (2013) and Bitelli et al. (2004), who studied the use of UAS in comparison with Terrestrial Laser Scanners, the precision and accuracy of the surface models generated with UAS photogrammetry allow using unmanned aerial vehicles for the monitoring of areas. For Miřijovský and Langhammer (2015), who also compare UAS and LiDAR, aerial images demonstrated it high spatial accuracy and precision. The authors reinforce that, for natural hazards management, as well a range of practical application in geosciences research, the ability to rapidly acquire high-quality spatial information is vital.

The evolution of UAS-embedded technology motivates research on the subject, for instance the literature review by Colomina and Molina (2014).

The evaluation of slope stability using 3D analysis has emerged as an option with great potential for the identification of sites susceptible to mass movements.

The input data for this type of model must be precise and accurate so that the achieved result is as reliable as possible. The use of UAS allows obtaining surface models with Ground Sample Distance (GSD) on the order of centimeters, with improvement in efficiencies of half the time that would normally be spent in a Terrestrial Laser Scanner survey, according to Naumann (2013).

This paper presents a case study using digital surface models obtained in the state of Santa Catarina, Brazil. The state of Santa Catarina is known to be frequently affected by natural hazards involving landslides. The mature and heterogeneous soils found in that region, when not effectively managed tend to, slide down the slopes and hit homes, schools, hospitals and roads.

## 2  Method

The studies carried out to support this paper included a survey with UAS in several areas in the state of Santa Catarina, Brazil, using a UAS DJI Phantom 4 platform with its standard configuration. In order to compare functionalities and the quality of the final product, several applications were used to plan the flight lines. The longitudinal and lateral overlap of the images was 80%, flight height was 100 meters and the camera was set at the nadiral pointing angle.

In order to generate the digital surface models, the processing of the obtained images was done in the Agisoft Photoscan software, with the default workflow.

The digital surface models were used as input data in the Soil Vision SVSlope software.

The Geotechnical parameters used to analyze slope stability in this study were provided by laboratorial direct shear tests.

On Fig. 1 it is possible to check the flowchart of the method. After site definition, soil sample has been collected and aerophotogrametric flights has been done. While laboratorial tests were performed, pictures were processed using Agisoft Photoscan to generate 3D model. The laboratorial results and the 3D model were used in SoilVision's solution to analyses 2D and 3D slope stability.

### 2.1  Study Area

To define the role process, a site placed in Brusque, northwest of Santa Catarina state, Brazil (Fig. 2), is adopted as default.

Geologically, it is a sandy silt residual soil of sericite-biotite phyllite of Brusque Metamorphic Complex.

## 2.2  Pix4D Capture

Pix4D is perhaps the best-known mobile application for flight line planning of aerophotogrammetric surveys with quadcopters. The operation is quite user friendly as seen in the screen captured image (Fig. 3) and allows some customization of the image acquisition process by the user. In terms of usability, a comparison between the Android app and IOs did not indicate significant differences (pix4d.com 2017).

## 2.3  Skydrones

Skydrones is a Brazilian mobile application, with similar functionalities to those of Pix4D. The version available for IOs allows the imaging of polygons in a variety of formats, not just rectangles (as in the Android version). Future updates will have interesting features such as spiral missions (for the imaging of towers), circular and vertical missions (for the imaging of outcrops, for example) (skydrones.com. br 2017).

## 2.4  DJI Ground Station Pro

The DJI Ground Station PRO (DJI GS PRO) application (Fig. 4), available for IOs, was developed by the UAS manufacturer used in this study and, as expected, showed the best compatibility level. The use of this application is the least friendly among the three, but allows more customization of the flight parameters.
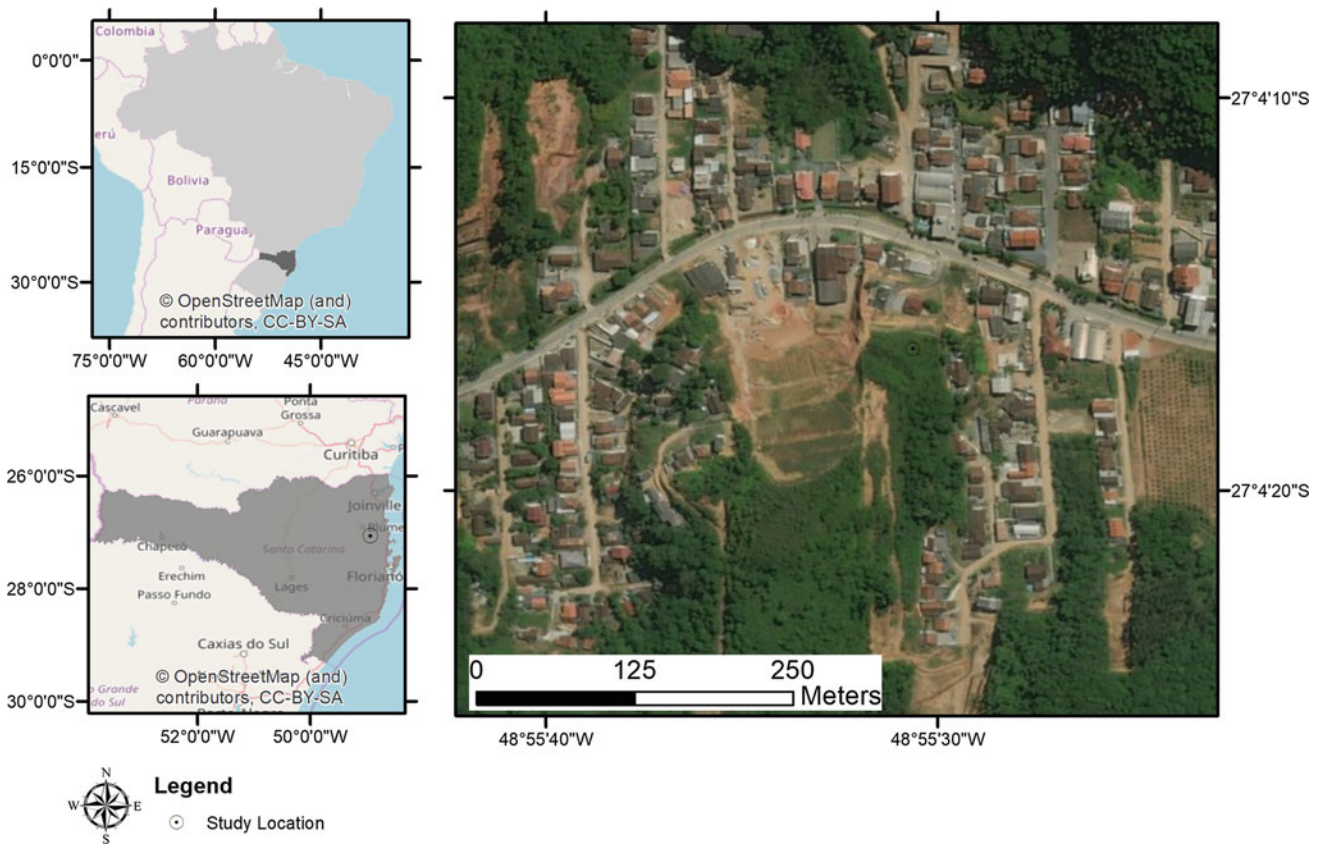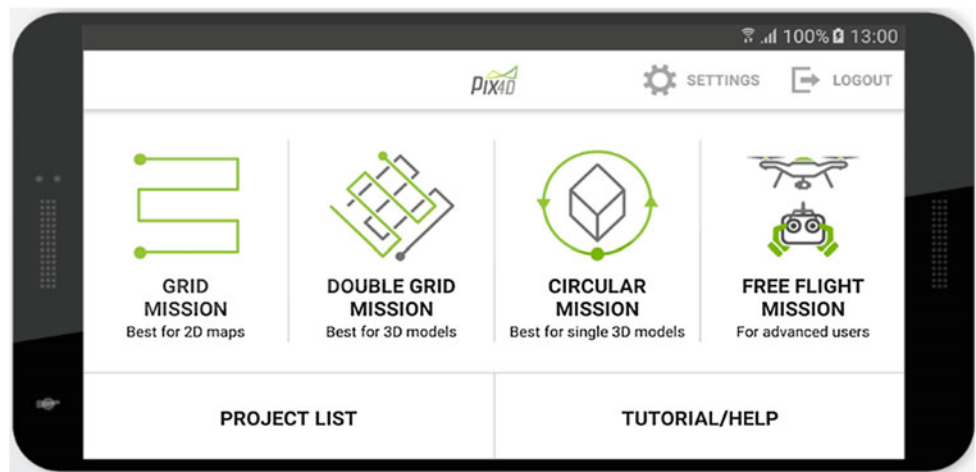
**Fig. 1** Flowchart of the method
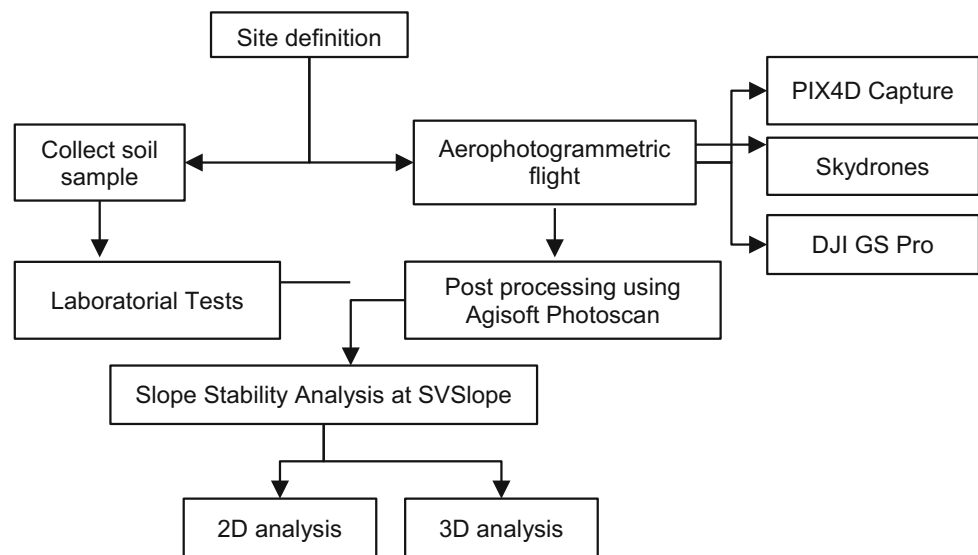
**Fig. 2** Location Map



**Fig. 3** Pix4D home screen. *Source* https://play.google.com/store/apps/details?id=com.pix4d.pix4dmapper

## 2.5 Agisoft Photoscan

A non-commercial license was kindly granted by Agisoft for research purposes involving the processing of images obtained with an UAS for 3D slope stability modeling.

This image processing software is used to obtain digital surface models. It is user friendly thanks to a workflow that
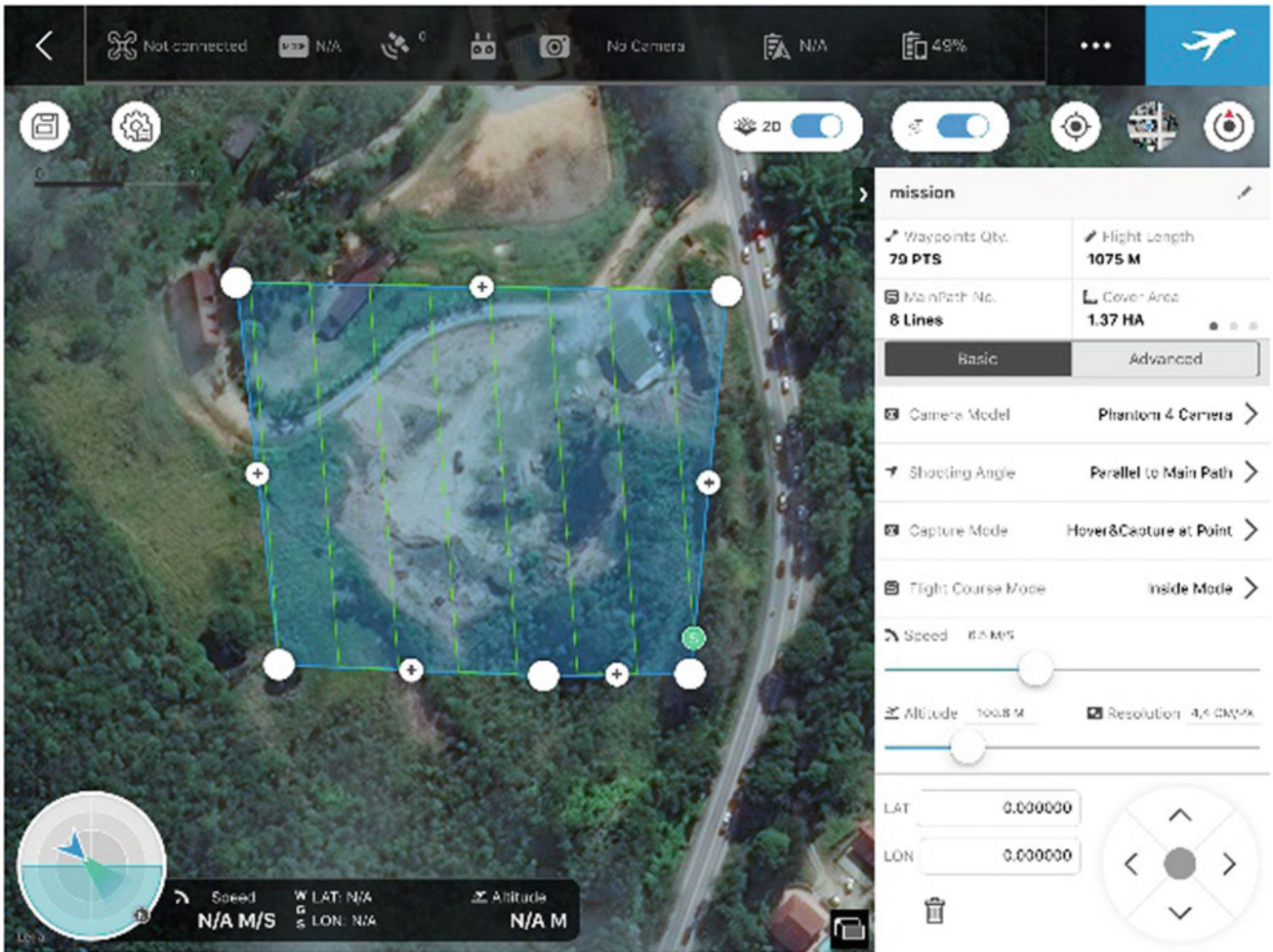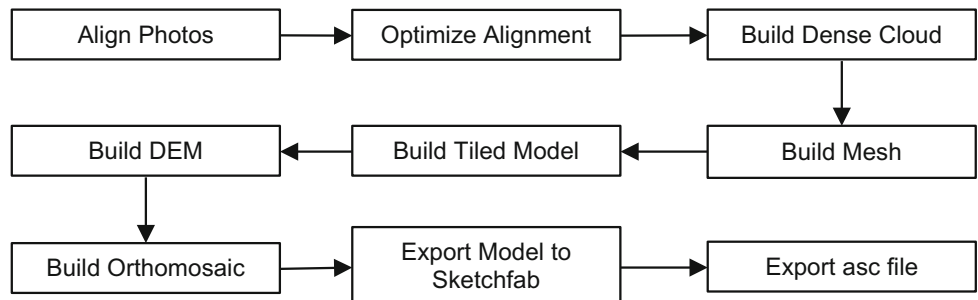
**Fig. 4** DJI GS Pro User Interface



**Fig. 5** Flowchart of the aerophotogrametric default post processing

can be used to generate the models (Fig. 5). Each processing step of the workflow can be configured according to the parameters desired by the user, which allows achieving a final product of greater quality.

## 2.6 SVSlope

The.asc file exported by the Photoscan software was then input into SVSlope using the Geometry > Import menu

**Fig. 6** SVSlope user interface



option. This way, the digital surface models work as input data into the SVSlope software.

The SVSlope software was developed by Soil Vision Ltd and features functionalities for hydraulic flow modeling, 2D/3D slope stability analysis (Fig. 6), finite element stress deformation modeling, finite element groundwater seepage modeling, finite element freeze modeling, finite element contaminant transport modeling, finite element pore-air flow modeling as well as a CAD tool for the assembly of the models to be processed. The CAD and SVSlope modules were used in the present study, and all the necessary training tutorials for the use of the platform are available in the Soilvision University module.

The soil thickness used to finalize the models was determined through outcrops observations in the field.

## 3 Results and Discussion

This section presents the results of the study and some further considerations.

### 3.1 Laboratory Tests

Direct shear tests from samples collected in study area provided cohesion, friction angle and allowed to define natural, dry and saturated density (Table 1).

### 3.2 Application Usage and Flight Planning

Mobile applications used for flight line planning, image overlay and camera angle showed similar usability. The user interfaces in Pix4D Capture and Skydrones are quite simple and intuitive, while those of DJI GS PRO are more detailed and takes more practice and time to master them.

The application of the quadcopter manufacturer (DJI GS PRO) did not present problems related to instability and/or incompatibility during its use, while Pix4D Capture and Skydrones had issues to be solved, such as lack of response to the takeoff command, sporadically.

**Table 1** Results of direct shear test

| C (kN/m$^2$) | $\varphi$ (°) | $\gamma_d$ (kN/m$^3$) | $\gamma_{nat}$ (kN/m$^3$) | $\gamma_{sat}$ (kN/m$^3$) |
|---|---|---|---|---|
| 28.60 | 14.70 | 12.57 | 15.38 | 17.84 |

**Fig. 7** Digital Surface Model

## 3.3   3D Processing

The 3D image processing for obtaining the surface models was quickly performed (2 to 3 h per model) by Agisoft Photoscan. The digital surface models (Figs. 7 and 8) had a ground sampling distance (GSD) of 3 to 10 cm/pixel.

**Model Visualization**

The models processed for this paper are available at sketchfab.com/vitorsm, where they can be viewed dynamically. The sketchfab platform in a fully functional option for this purpose since it can be opened from a web browser or mobile application.

## 3.4   2D & 3D Stability Analysis

The generated digital models, imported to SVSlope, had their safety factors analyzed in 2D and 3D forms (Figs. 9 and 10), by Bishop Simplified, Janbu Simplified, Spencer, Morgenstern-Price and GLE methods.

UAS photogrammetric data reduces imprecision issues from traditional topographic surveys, where human errors may interfere with the quality of the final product, because of the lower resolution.

The locations where the safety factor was below the minimum required (1.5, in 2D analyzes) are being monitored, with periodic aerophotogrammetric surveys for

**Fig. 8** Digital Surface Model allowing the visualization of a lake

**Fig. 9** 3D Slope Stability
Analysis
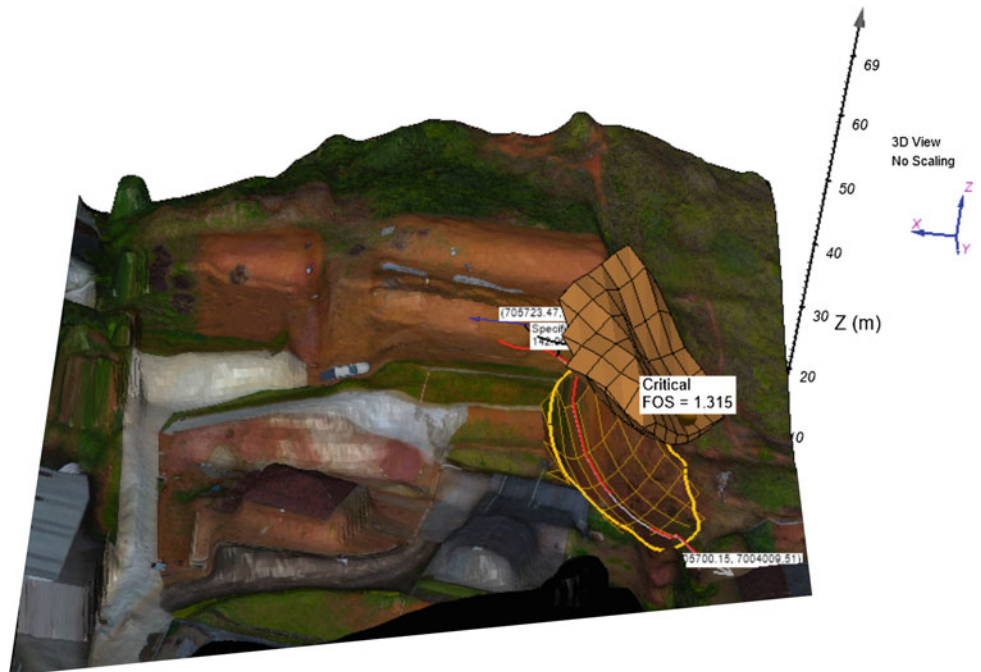
**Fig. 10** 2D Slope Stability Analysis
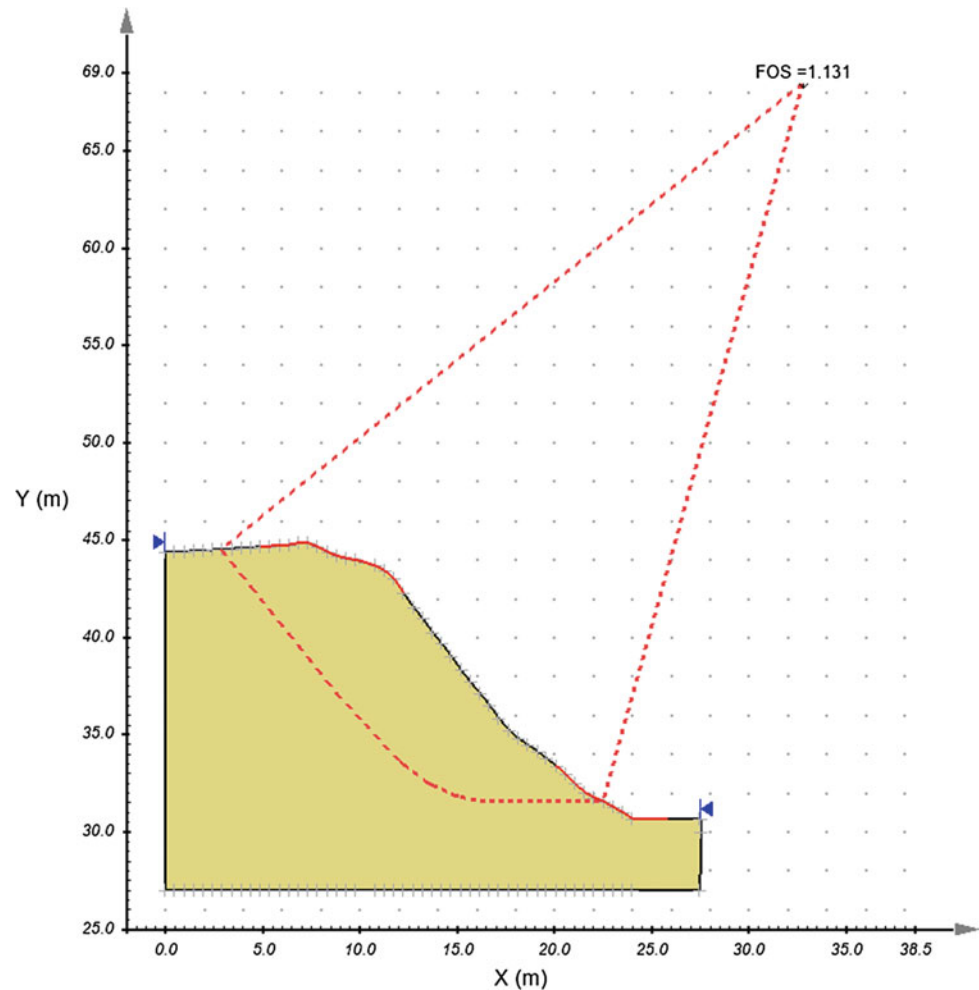


comparison and monitoring of possible mass movements. The data generated by this observation will serve as a potential warning, and/or for future studies.

## 4 Conclusion

The data analysis allowed concluding that, in line with Miřijovský and Langhammer (2015), the use of UAS represent a possibility of using technology for the safety of the population.

The high quality of the data shows that the models generated using UAS are comparable to those based on traditional topography, however much less time-consuming.

The processing in Agisoft Photoscan was considered easy to do; hence, previous specific training was not necessary.

The 3D stability analysis performed in SVSlope was user friendly and posed no greater difficulties to those who are accustomed to using any other slope stability analysis tools. The Soil Vision tutorial module is very instructive, supplemented by the webinars offered by the company.

The low equipment and operational cost for obtaining high quality data favors periodic aerophotogrammetric surveys, thus allowing future comparisons between models and monitoring active landslides.

## References

Bitelli, G., Dubbini, M., Zanutta, A.: Terrestrial laser scanning and digital photogrammetry techniques to monitor landslide bodies. Int. Arch. Photogrammetry Remote Sens. Spat. Inf. Sci. **35** (2004)

Colomina, I., Molina, P.: Unmanned aerial systems for photogrammetry and remote sensing: a review. ISPRS J. Photogrammetry Remote Sens. **92**, 79–97 (2014)

Honkavaara, E., et al.: Autonomous hyperspectral UAS photogrammetry for environmental monitoring applications. Int. Arch. Photogrammetry Remote Sens. Spat. Inf. Sci. **40**(1), 155 (2014)

Miřijovský, J., Langhammer, J.: Multitemporal monitoring of the morphodynamics of a Mid-Mountain stream using UAS photogrammetry. Remote Sens. **7**(7), 8586–8609 (2015)

Naumann, M., et al.: Accuracy comparison of Digital Surface Models created by Unmanned Aerial Systems Imagery and Terrestrial Laser Scanner ISPRS. Int. Arch. Photogrammetry Remote Sens. Spat. Inf. Sci. (2013)

PIX4D: Pix4D. Disponível em: <pix4d.com>. Acesso em: 21 out. 2017 (2017)

SKYDRONES: Skydrones. Disponível em: <skydrones.com.br>. Acesso em: 21 out. 2017 (2017)

# 2D Horizontal Landslide Displacement Estimation by Multi-temporal Image Correlation Techniques

P. Fernandez, J. Garrido, and J. Delgado

## Abstract

Geomatic techniques based on digital images have become a very useful tool for landslide monitoring, quantifying landslide movements over a long period of time. One of these techniques is based on digital image correlation. Digital image correlation estimates 2D displacements by means of statistical techniques, automatically matching identical points in the two digital images. It may be applied using remote sensing or aerial images. Digital image correlation has been applied to multi-temporal aerial photographs at the Cerro Gordo landslide (Granada, Spain) which is badly affecting an urbanized area. This landslide consists of a main deep slide and several minor shallow slides, located around the head scarp or affecting some parts of the main landslide body. Slides involve existing landfills used for urban works as well as in situ materials (colluvial deposits and weathered schists). The period under study (2002–2010) has been divided into four subperiods of approximately two years each. Results provide horizontal displacement in the landslide area and surroundings which allow to assess the landslide movement evolution at different stages according to triggering factors and structural measures that were carried out to stabilize the affected area. Over the period of 2002–2004, displacement rates varied from 2 to 6 cm, meanwhile for the periods of 2004–2006 and 2006–2008 displacements continued with 4–6 cm rates. Then, the period of 2008–2010 generally shows a higher activity with more areas showing 6 cm displacement rates. Surface observations of these periods go along with both location and direction of displacements as shown by the results of digital image correlation techniques. Image correlation results have provided very useful information to understand the complex movements of the landslide as well as the effectiveness of the structural measures implemented.

## 1 Introduction

In the last 20 years geomatic techniques have moved on far ahead of us. For this reason they are a very useful tool to identify, monitor and quantify a wide range of typologies of terrain movements such as landslides.

Landslides studies are quite complex because they are processes that need in situ monitoring with specific instrumental that sometimes is not available over the more active landslide period or it is too expensive to be installed and maintained over a long period of time. And most importantly, all these in situ measurements provide discrete punctual information.

However, change detection geomatic techniques based on digital image analysis may provide spatial information of the image complete area and may also cover long time periods using different images from the first image acquisition date to the last image acquisition date. These characteristics make change detection based on digital image correlation an essential technique for the study of landslides (Debella-Gilo and Kaab 2012; Fernandez and Withworth 2016).

Digital image correlation may be applied using remote sensing or aerial images to estimate 2D displacements by means of automatically matching identical points in two digital images using statistical techniques.

P. Fernandez (✉) · J. Garrido
Dpt. Ingeniería Civil, Universidad de Granada, Campus de Fuentenueva s/n, 18071 Granada, Spain
e-mail: pazferol@ugr.es

J. Delgado
Dpt. Ciencias de la Tierra y Medio Ambiente. Universidad de Alicante, Universidad de Alicante, Ap. Correos 99, 03080 Alicante, Spain

Digital image correlation techniques have been used in our research using corregistration and image correlation (COSI-Corr) software developed by the California Institute of Technology (Caltech) (http://www.caltech.edu), being applied to multi-temporal aerial photographs of an urbanized area badly affected at the Cerro Gordo landslide (Granada, Spain).

## 2  Location and Geological Setting

Cármenes del Mar is a residential area at Cerro Gordo, located on the coast of Granada province (SE Spain). There are eight different residential sections: Calaiza, Casas Especiales, Atarazanas, Pueblo, Los Altos, Balcón, Mirador and Terrazas (Fig. 1). The former four were damaged by different landslides.

Earthworks in the area under review began over the fall of 1998, and housing construction started in the summer of 1999. Works were completed in the Calaiza housing section by the spring of 2001, followed by Pueblo and Atarazanas sections in the summer and fall of 2002, respectively; over the course of 2004 Los Altos and Casas Especiales sections were completed.

The Alpujarride complex of the Betic Cordillera, formed by grey fine-grained schists (Permo-Triassic) and marbles (Triassic) outcrops in the area, with the former in the lower part of the slope and the latter in the upper part of it. However, most of the residential sections were built on colluvial deposits and landfills, while the southern part of the housing sections were built on a debris deposit of marble boulders in a clayey-silty matrix (Gamma Geotécnica 2007).

The residential sections were built on an old deep seated landslide (Mateos et al. 2017) but several minor shallow landslides, have probably damaged many of the houses due to cuts and landfills (Gamma Geotécnica 2007, 2011). Slides involve landfills as well as in situ materials such as colluvial deposits and weathered schists.

## 3  Landslide Activity and Damage

Most of the houses of the Calaiza and Casas Especiales sections and some of Atarazanas and Pueblo sections have been damaged by ground movements, as well as most of the roadways among them. Cracks in the roadways and in the



**Fig. 1** Location of the residential sections of Cármenes del Mar
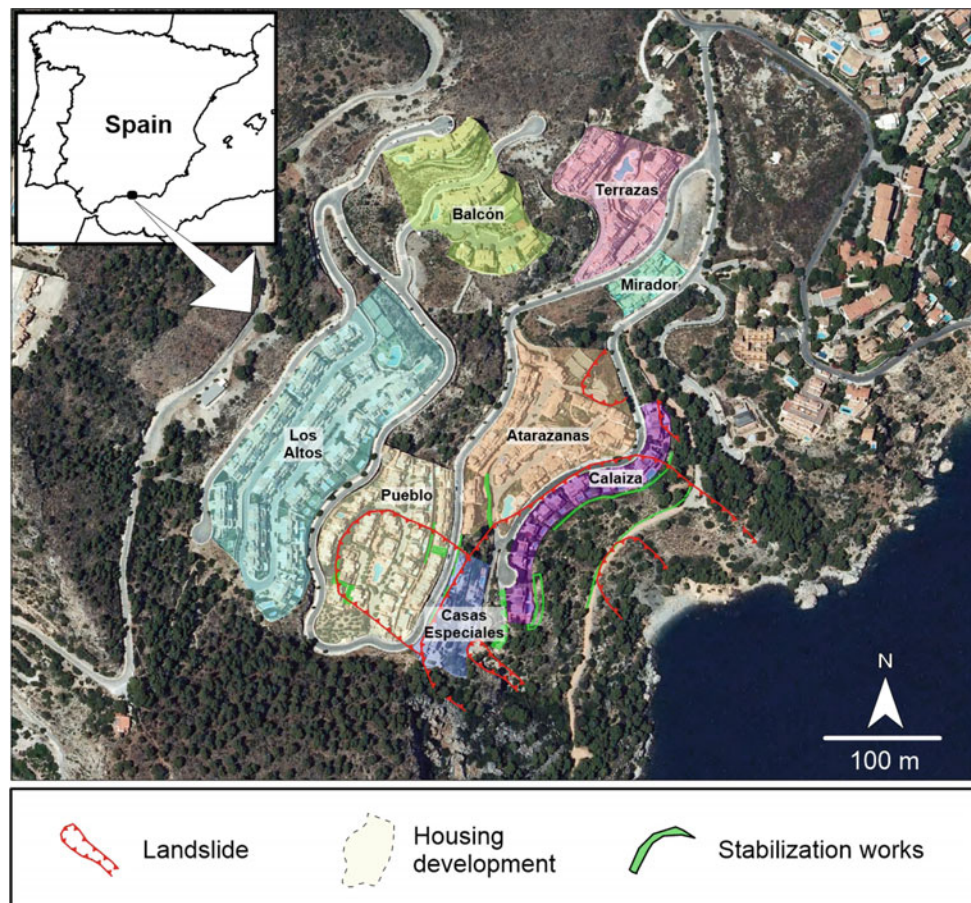
damaged houses have allowed us to determine the landslide area (Fig. 1).

Damages appeared during the fall of 2002 in the Pueblo section followed lately by the Calaiza, Casas Especiales and Atarazanas sections. Since 2004 cracks and displacements substantialy increased mainly in the Pueblo, Calaiza and Casas Especiales sections. Some houses in those areas partially collapsed during the course of 2006 and 2010.

Some countermeasures were constructed to stabilize several areas such as retaining walls, barriers of micropiles, wells or anchors, to minimize the effect of movements (Fig. 1).

## 4 Data and Methods

The aim of our research is to obtain 2D horizontal displacement rates for landslide monitoring and kinematic understanding using image correlation techniques combined with multi-temporal aerial photographic imagery. To do so, COSI-Corr corregistration and image correlation software developed by the California Institute of Technology has been used to process a set of aerial photographs that covers the recent landslide activity since housing construction began.

COSI-Corr allows the corregistration and correlation of aerial and satellite images to provide horizontal ground displacements measurements in multi-temporal analysis by means of sub-pixel correlation in the frequency domain. Software fundamentals and technical development specifications are described in Leprince et al. (2007) and Ayoub et al. (2009). It has been successfully applied with aerial images to determine landslide horizontal displacement every two years (Fernandez and Withworth 2016).

COSI-Corr is a tool suite which provides image correlation as well as orthorectification and resampling as a previous step. Simplified flux chart is shown in Fig. 2 (Fernandez and Withworth 2016). After the complete processing chain using COSI-Corr, three images were obtained: (1) North to South (N–S) horizontal displacement component; (2) East to West (E–W) horizontal displacement component and (3) Signal-to-noise ratio image.

We selected five dates with approximately an interval of two years to cover the movements over the period under study: 2002, 2004, 2006, 2008 and 2010. Images were taken using official photogrametric flights from the ICA (Cartographic Andalusian Institute) and the National Plan of Aerial Orthophotograph (PNOA) from the IGN (National Geographic Institute).

The areas damaged and their displacement rate in the different periods have been delineated according to Gamma Geotécnica (2007, 2011), a damage survey in the area and some in situ inspections.
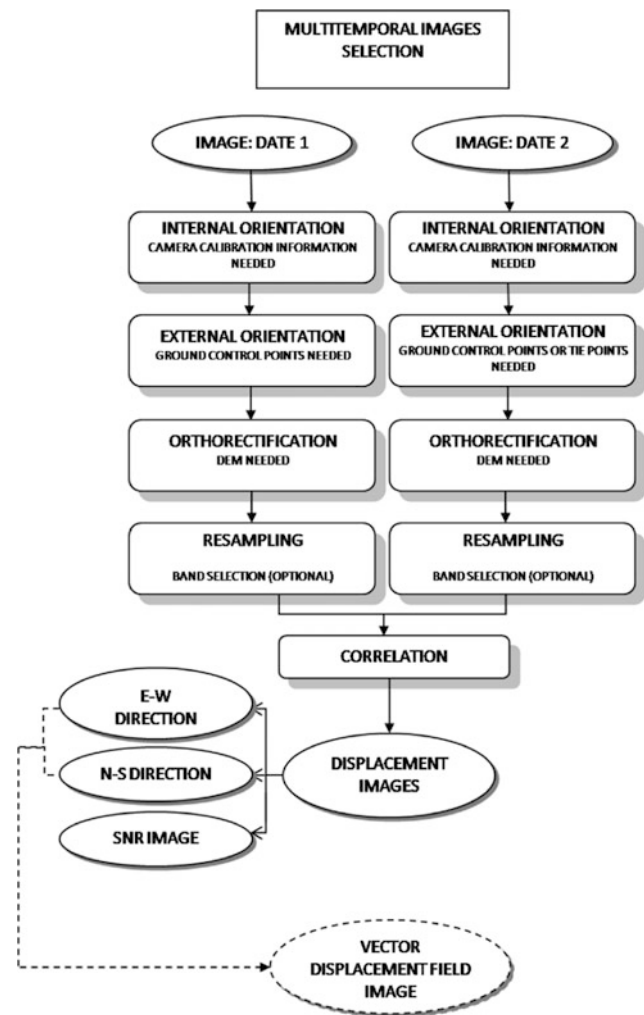


**Fig. 2** Simplified flux chart (Fernandez and Withworth 2016)

## 5 Results

Once COSI-Corr image correlation computation displacements have been calculated from E–W (East–West) and N–S (North–South) horizontal displacement components images corresponding to each period of two years (Figs. 3 and 4).

The 2002–2004 period shows the first lapse of movement for the period under study. Total displacement rates go from 2 to 6 cm. General slope behaviour denotes an incipient but generalized landslide movement in the whole area, including urbanized and vegetated areas (Fig. 3).

The 2004–2006 period shows that the displacement continues with a slow general mass movement that is clearly noticed in the vegetated area of the south flank and the area close to Calaiza beach, while there are some movements in the southern part of the Pueblo section (4 cm displacement), south of Casas Especiales section (4–6 cm) and also between

**Fig. 3** Horizontal displacements over DEM in 2002–2004 and 2004–2006. Pink areas show the housing sectors. Displacements are cumulative over the two year period
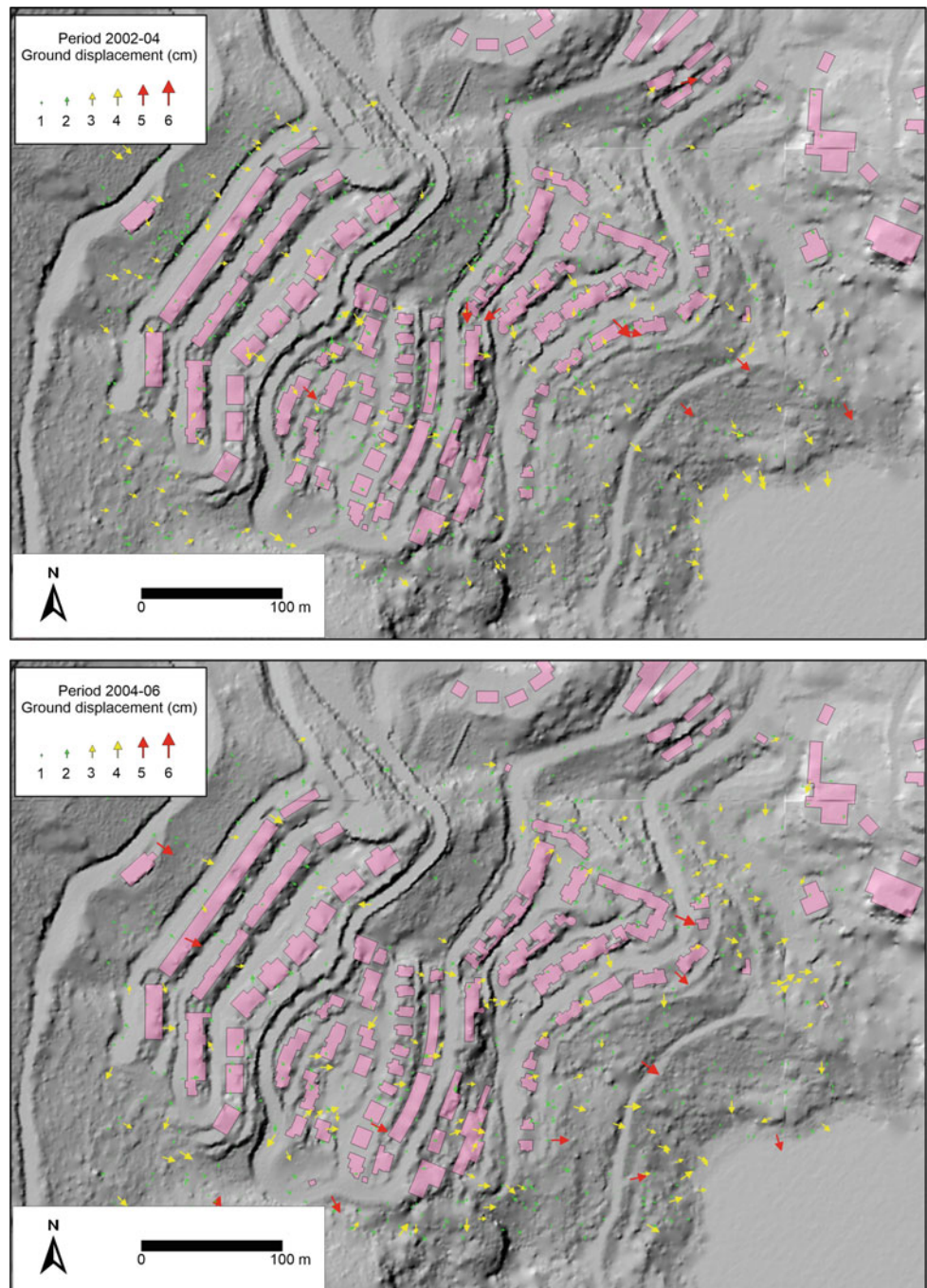


the Casas Especiales and Atarazanas sections (4 cm) and north of the Calaiza section (4–6 cm) (Fig. 3).

The 2006–2008 period shows displacement mainly in the Atarazanas section (4 cm), Casas Especiales (2–4 cm) and also a generalized displacement in the Pueblo section (4 cm).

Casas Especiales No. 3 was so damaged that it was demolished in 2007, so no displacements are shown on the location. Landslide vegetated flanks in the southern and northern part continue to move at rates ranging from 2 to 4 cm as well as the lower part of the landslide in Calaiza beach (Fig. 4).

**Fig. 4** Horizontal displacements over DEM in 2006–2008 and 2008–2010. Pink areas show the housing sectors. Displacements are cumulative over the two year period
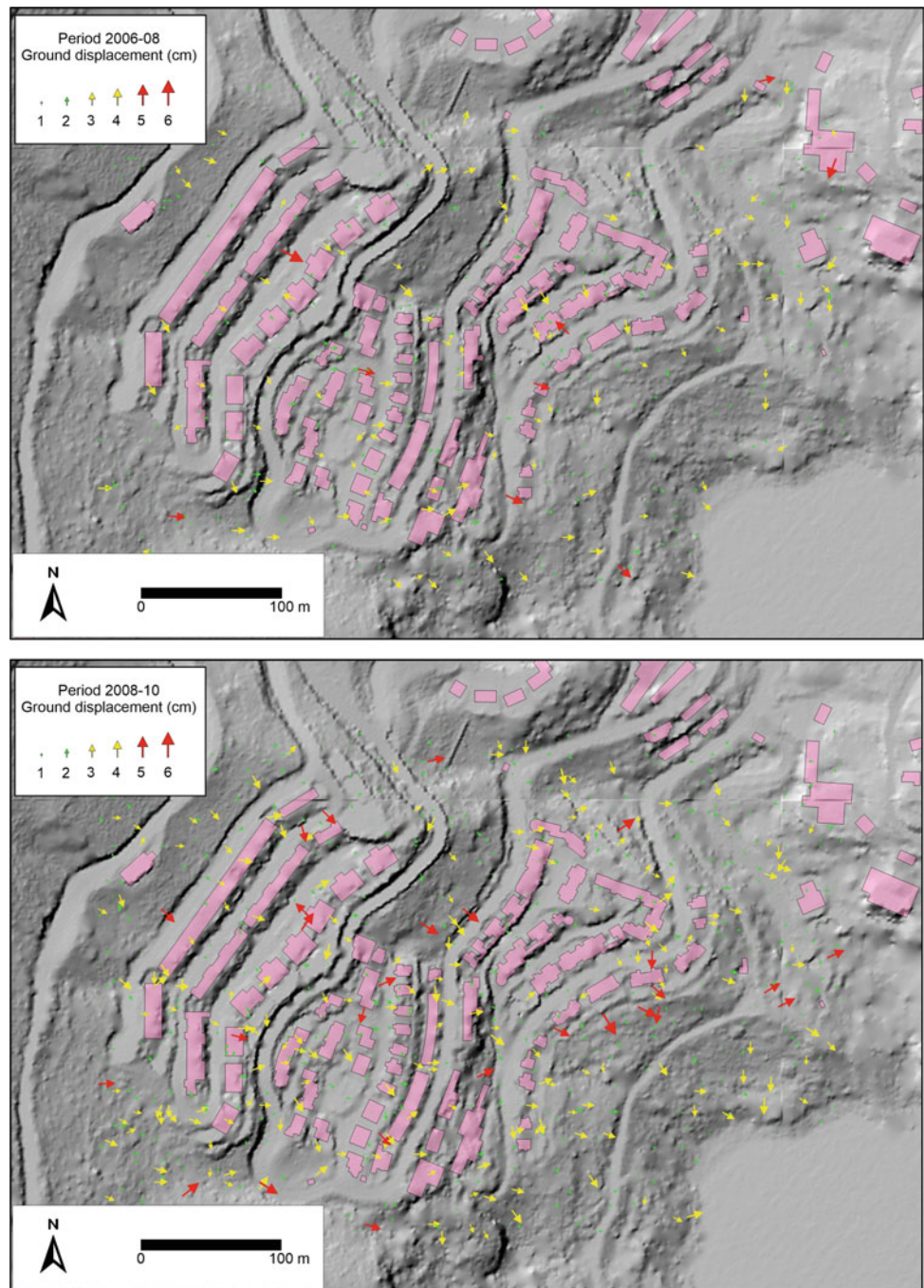


In the 2008–2010 period shows equally distributed movement rates in the area, with more areas showing 6 cm displacement rates: north and central Calaiza section, north of where Pueblo and Atarazanas sections meet, south west and north flank, and very often 4 cm rates in the whole area (Fig. 4).

Results prove the aforementioned historical surface damage observations as shown in the different areas under review.
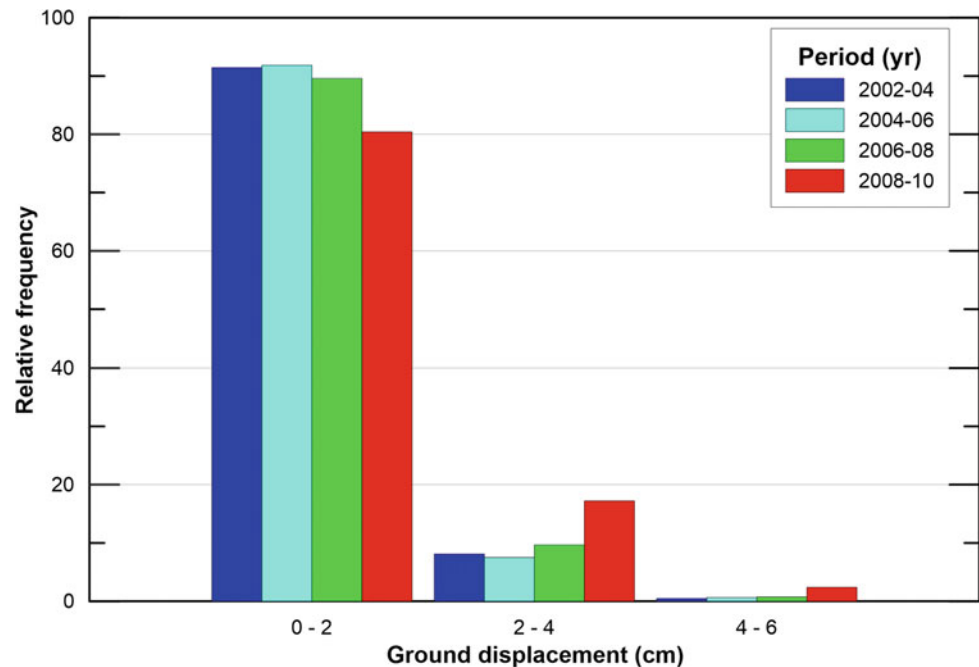
The average displacement rates increased from the 2002–2004 period to the 2008–2010 period, after the movement started (Fig. 5).

## 6    Conclusions

COSI-Corr techniques have proved to be a useful tool to estimate horizontal displacements, not only in geographical favourable conditions as Fernandez and Whitworth (2016) conclude, but also in very difficult coverage environments that make difficult a direct visualization and validation of the movements in aerial photographs. The wide availability of aerial images in the area provide with a velocity estimation over a sustained period of time which contributes to understand the kinematic mechanism of the landslide under study.

Velocity rates have been estimated for different periods covering 2002–2004, 2004–2006, 2006–2008 and 2008–2010, comprising a period of eight year deformation and providing information about the location of the mobilized areas for each period as well as movement rates of each one.

## References

Ayoub, F., Leprince, S., Avouac, J.P.: Co-registration and correlation of aerial photographs for ground deformation measurements. ISPRS J. Photogram. Remote Sens. **64**, 551–560 (2009)

Debella-Gilo, M., Kääb, A.: Measurement of surface displacement and deformation of mass movements using least squares matching of repeat high resolution satellite and aerial images. Remote Sens. **4**, 43–67 (2012)

Fernandez, P., Whitworth, M.: A new technique for the detection of large scale landslides in glacio-lacustrine deposits using image correlation based upon aerial imagery: a case study from the French Alps. Int. J. Appl. Earth Obs. Geoinf. **52**, 1–11 (2016). https://doi.org/10.1016/j.jag.2016.05.002

Gamma Geotécnica: Proyecto de estabilización de laderas en la Urbanización Cármenes del Mar, Cerro Gordo, Almuñécar (Granada), Technical report, 112pp, Unpublished (2007)

Gamma Geotécnica: Informe complementario del proyecto de estabilizacion de laderas en la urbanización Cármenes del Mar (Cerro Gordo, Almuñécar), Technical report, 34pp, Unpublished (2011)

Leprince, S., Barbot, S., Ayoub, F., Avouac, J.-P.: Automatic and precise orthorectification, coregistration, and subpixel correlation of satellite images, application to ground deformation measurements. IEEE Trans. Geosci. Remote Sens. **45**(6, Part 1), 1529–1558 (2007)

Mateos, R.M., Azañón, J.M., Roldán, F.J., et al.: The combined use of PSInSAR and UAV photogrammetry techniques for the analysis of the kinematics of a coastal landslide affecting an urban area (SE Spain). Landslides **14**, 743–754 (2017). https://doi.org/10.1007/s10346-016-0723-5

# Near Real Time Monitoring Systems and Periodic Surveys Using a Multi Sensors UAV: The Case of Ponzano Landslide

Paolo Allasia, Marco Baldo, Daniele Giordan, Danilo Godone, Aleksandra Wrzesniak, and Giorgio Lollino

## Abstract

Following the heavy snowfalls in the central and southern Italy at the end of winter 2017, the reactivation of many landslides in the Apennines area was observed. Some of them had already been subject to several seismic events, with main shocks on 08/24/2016 (M6.0) and 10/26/2016 (M5.9). This paper shows preliminary results concerning the Ponzano landslide activity (Civitella del Tronto—Italy), located in the central Italy at about 40 km from the 2016 main earthquakes areas. This landslide reactivated in the last days of February 2017 with displacements of more than 8 meters in the first few days, probably due to the fast snowmelt (about 1.2 m snowpack, accumulated in the middle of January). In accordance with the Department of Civil Protection, different monitoring systems have been foreseen in order to describe the behavior of the landslide and to monitor the oldest part of the village. To reach these goals, a near-real time monitoring approach was implemented by means of a robotized total station. Additionally, a series of UAV aerial surveys for a multi-temporal site analysis were accomplished. The first approach allowed to perform a continuous displacement monitoring (frequency of measurements 0.5 h ÷ 2 h) and to detect landslide movements due to spring rainfalls. The second one allowed us to perform a rapid mapping of the area immediately after the main reactivation, and its evolution after a few months. Thanks to a modular fixed wing multisensor UAV recently developed in our institute, it was possible to perform a survey using optical and multispectral sensors. In this work, we present the results obtained by both systems, and we describe how they can be used in the emergency scenarios and in subsequent landslide management phases.

## 1 Introduction

The period of 2016–2017 in Italy, from meteorological point of view, was characterized by weather anomalies (NOAA website 2017). The average precipitations (snow and rainfall) was low, however short and extremely intensive events occurred in several regions. In particular, a significant snow accumulation was registered in the Apennines (central and southern Italy). In this work, we present a landslide in Ponzano, a small village located in municipality of Civitella del Tronto (Abruzzo region, Italy). The landslide reactivation was caused by a series of factors, such as elevated snow-melt (snow mainly accumulated in January 2017) and subsequent intensive rainfalls (Meteomont website 2017). Furthermore, during 2016 the area approximately 30 km far from the landslide was subject to an extended sequence of seismic shocks (Fig. 1). The main earthquake caused 299 deaths in 3 regions: Abruzzo, Lazio, Marche and Umbria (DPC website 2016). Due to this critical situation, the Civil Protection Department (DPC) mobilized competency centers that specialized in studying and monitoring landslides, in order to characterize the landslide and to execute monitoring activities. These activities consisted of surveys of the area and an installation of an automatic topographic monitoring system. The aims of this monitoring system were (1) to support the evacuation of people from the habitations at risk; (2) to evaluate the level of landslide activity; (3) to evaluate the potential retrogressive actions that could affect the ancient village of Ponzano.

P. Allasia (✉) · M. Baldo · D. Giordan · D. Godone
A. Wrzesniak · G. Lollino
Research Institute for Hydrogeological Prevention
and Protection of CNR, Rome, Italy
e-mail: paolo.allasia@irpi.cnr.it

**Fig. 1** Earthquake location map (left) and major magnitude map (right)
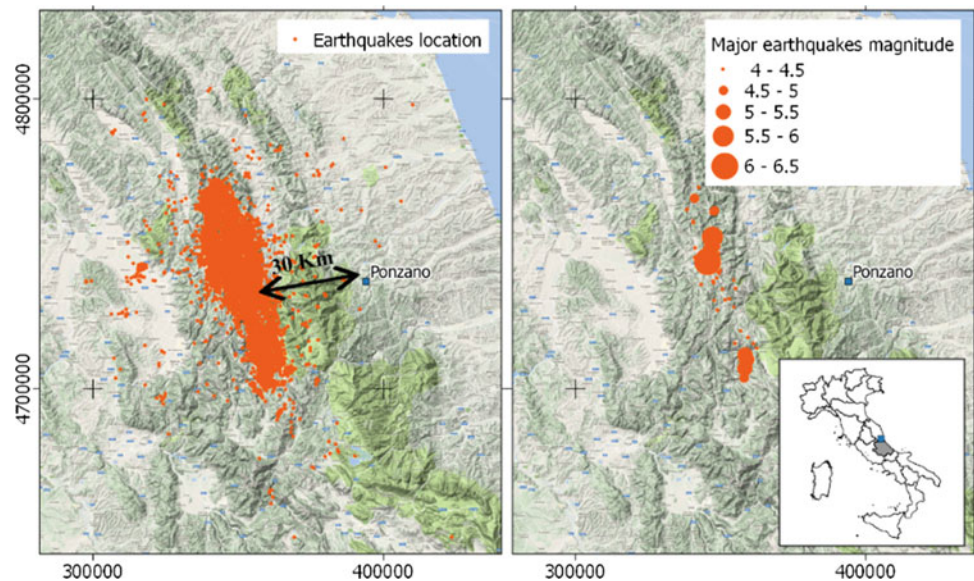
## 2 Landslide Description

On 12 February 2017, a known unstable area in Ponzano reactivated. It involved an area of about 60 ha and resulted in damages to 33 edifices, to the provincial road SP8 and to most of utility services (gas pipeline, electricity line etc.). During the critical phase, the displacement registered in the first two days was approximately 8 m, causing the collapses and translations of many houses and the evacuation of about 100 persons. Previous studies indicated the presence of quiescent landslide, situated in larger dangerous area. The landslide behavior was defined as complex with two principal movement types: (1) the first one characterized by earthflow with a 50 ha area and probable depth of about 15–20 m; (2) the second one classified as rotational slide, located in the upper part of the slope near SP8 road. The main issues subsequent to the critical phase were related to a possible retrogressive phenomena and extension of active area (Fig. 2). In particular, two urbanized lateral areas were identified, as well the NE sector in the old part of Ponzano. This ancient part is located on the border of the landslide and it is supported by reinforced concrete retaining wall, which was affected by recent landslide reactivation (Fig. 2).

During the first few days after the main reactivation, the GPS survey (performed by municipality of Civitella del Tronto) showed a landslide displacement of approximately 8 m, which caused partial or total collapse and rigid translation and rotation of several buildings. Analysis of spaceborne data (dataset from Radarsat-1, Sentinel-1 and TerrasarX satellite) obtained by the Department of Earth Science of University of Florence showed a moderate acceleration of landslide area in the period between 15

January and the end of January, before the reactivation of the landslide (DPC IR 2017). The preliminary analyses showed that the maximum displacement between 15 January and 20 February was approximately 10 m along satellite line-of-sight. This data appears congruent with first survey performed by the municipality and with subsequent surveys. The satellite data did not show significant movements in the period 2013–2017 in the area of ancient part of Ponzano.

## 3 Survey and Monitoring Activity

On 23 February, upon request of the DPC, the Geohazard Monitoring Group (GMG) of Italian National Research Council (CNR IRPI) installed a system for topographic monitoring in order to describe the landslide kinematics and to evaluate potential retrogressive landslide activities especially regarding the center of Ponzano. Additionally, the GMG performed several surveys using unmanned aerial vehicle (UAV). These surveys permitted: (1) to define the landslide area, (2) to provide an updated cartographic support (3) to aid the intensive monitoring activities. Thanks to these surveys, the evolution of the landslide was evaluated immediately after the reactivation and after about 5 months (23 February, 20 June) (Fig. 4).

## 4 RPAS Photogrammetric and Multispectral Surveys

On 23 February, a firefighters corps performed the first RPAS (Remotely Piloted Aircraft System) survey to produce an orthophoto mosaic of the area using a Sensefly© EBEE fixed
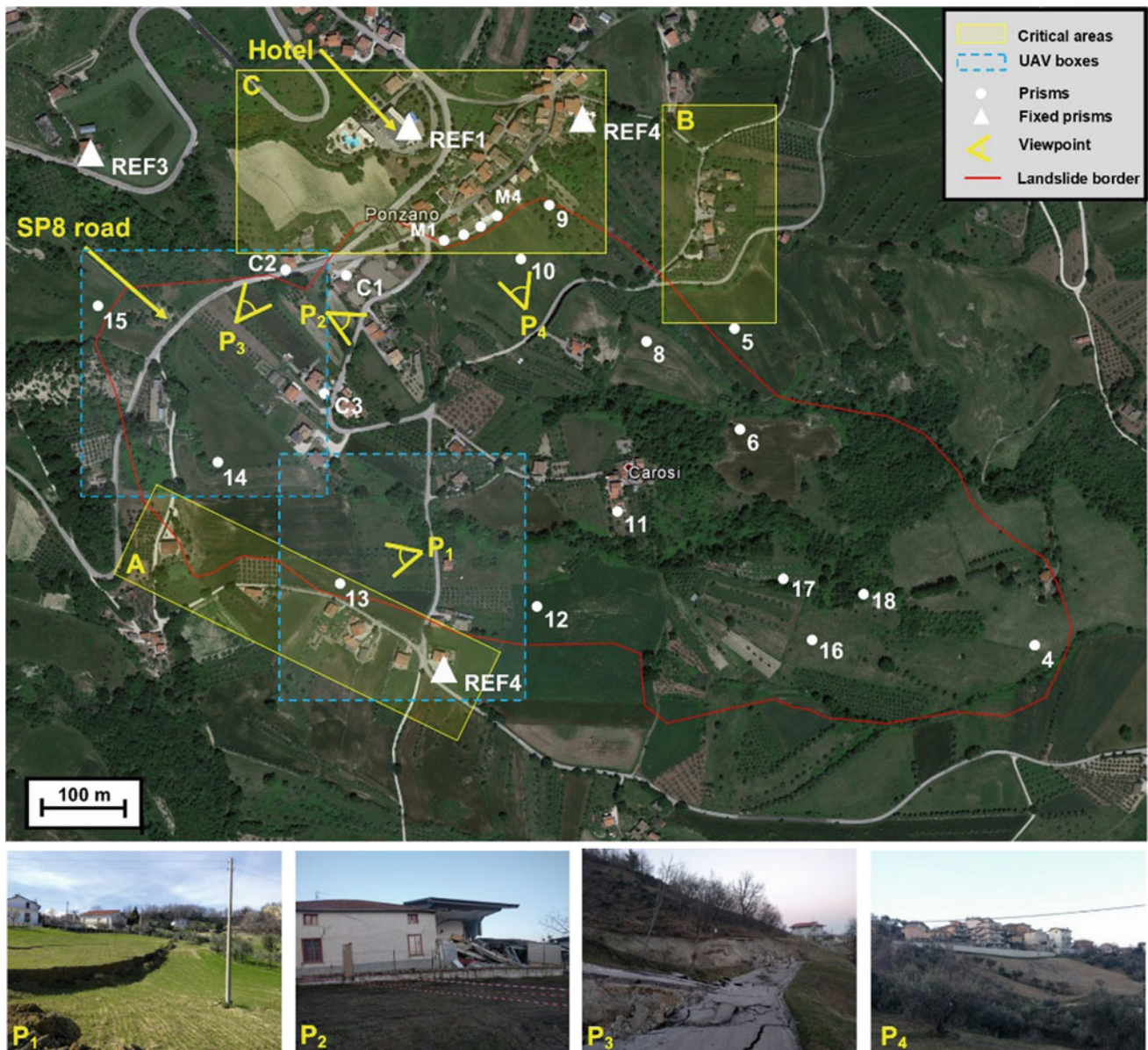
**Fig. 2** Ponzano landslide. The border is a result of first evaluation immediately after the reactivation. The boxes (A, B and C) show potential critical areas close to the main landslide body

wing drone. On the same day, CNR IRPI conducted a GNSS-RTK land survey on 40 cm × 40 cm Ground Control Points (GCPs) to obtain high quality data position for the orthophoto geocoding (Figs. 4 and 5). Those points were used to produce a detailed orthophoto and to evaluate the reliability of DSM/DTM generated from the aerial triangulation process (Giordan 2015). Subsequently, on 20 June a second RPAS aerial survey was performed using the self-constructed fixed wing UAV (belonging to GMG). A second DSM/DTM and orthophoto mosaic dataset were produced to evaluate potential changes in landslide area (Table 1). The goals of these activities were: (i) the qualitative analysis of morphological variations (ii) the evaluation of the repeatability of

measurements carried out using UAVs (iii) testing of multispectral sensors in a real landslide scenario.

Thanks to the modularity of our fixed wing UAV, in few minutes we could replace RGB camera with a 5-band multispectral camera (Micasense RedEdge) and additionally perform an experimental test (Fig. 3). Different indices and RGB composites were generated to detect anomalies in water content and vegetation cover. In particular, we exploited sensor features by computing NDRE (Normalized Difference Red Edge) index and CIR (Color Infrared) composites (Thenkabail and Lyon 2016) to identify the swamp areas in the sector with the largest displacement (Fig. 5).

**Fig. 3** CNR IRPI fixed wing drone with onboard mounted sensors: (i) action camera, (ii) multispectral camera, (iii) RGB mirrorless camera



**Fig. 4** Comparison of a small part of UAVs aerial surveys performed in February and June. The geographic location is shown in Fig. 2. The horizontal lines are reference lines to aid a multitemporal comparison
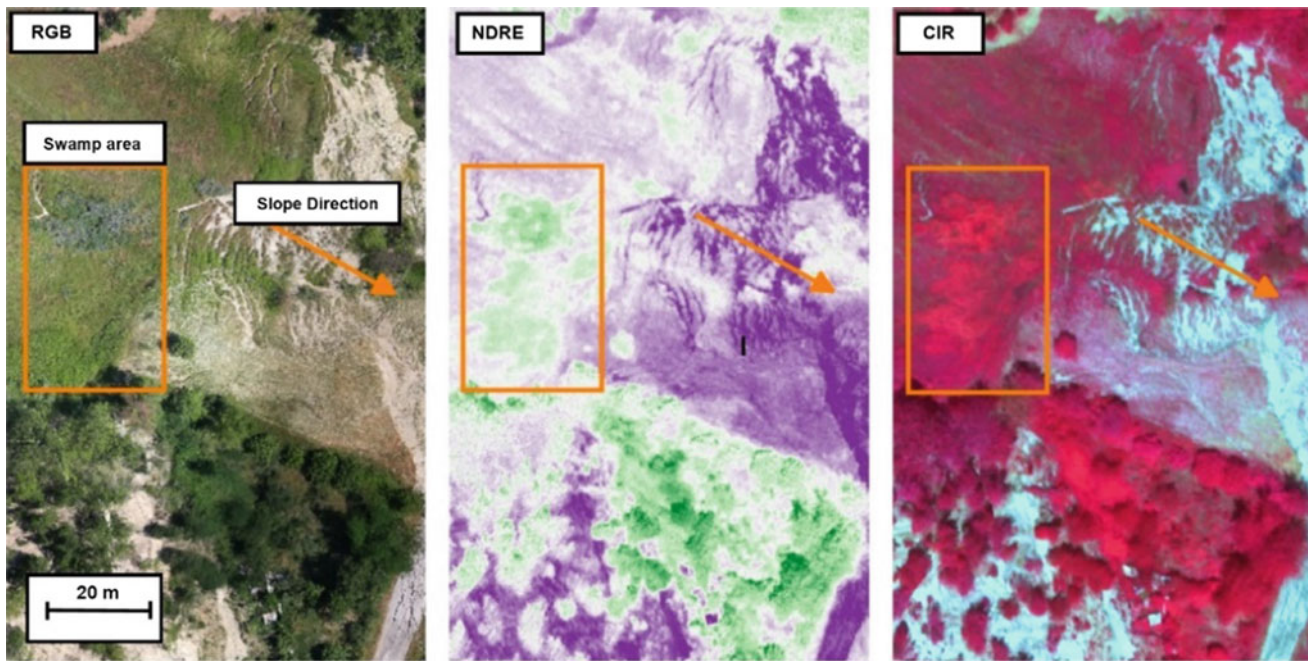
**Fig. 5** Preliminary result of multispectral survey performed in June. In the box, a swamp area extracted from multispectral data (field observations confirmed this result). Images from the left: RGB, NDRE index and CIR composite

**Table 1** Summary of UAV surveys and quality of results obtained by Pix4DMapper PRO software

|  | Sensefly EBEE | CNR IRPI UAV (RGB) | CNR IRPI UAV (Multispectral) |
|---|---|---|---|
| Camera type | Canon Powershot G9X-20 Mpx | Canon EOS M1 18 Mpx | Micasense RedEdge (5 bands)—3.6 Mpx/band |
| Flight height (AGL) | 150 ÷ 170 m | 100 m | 100 m |
| Flight mode | Constant absolute height | Follow terrain | Follow terrain |
| Total shoots | 629 | 1401 | 3121 (for each band) |
| Number of strips | 36 | 42 | 42 |
| Covered area (km$^2$) | 2 | 4.2 | 4.2 |
| Theoretical GSD (cm/px) | 5 | 3 | 13 |
| GCP mean rms (cm) | 5 | 4 | 3 |

## 5 Near Real Time Topographic Monitoring System

The large landslide extension and the complex morphology of the area created numerous issues related to the optimal installation site that would control the entire phenomenon. Such a site was identified in front of the slope, where RTS Leica TM30 was installed. The monitoring network was designed in order to have a representative number of points in the landslide body, in the neighboring areas and in inhabited sector of Ponzano ancient town. The distance between the RTS and the points varied from 900 to 2100 m. On the installation date, the network was composed of 26 points (Fig. 6):

– 4 fixed (REF$_i$) in stable area, but continuously monitored;
– 4 (M$_i$) on the retaining wall on the SE border of Ponzano;
– 3 (C$_i$) on the main building affected by movements (C1, C3), and outside of the landslide area (C2);
– 11 (n$_i$) within landslide area and 3 outside (5, 7, 15).

The REF1 prism was installed on the Hotel Ermocolle (Fig. 2), where elementary schools have been temporary
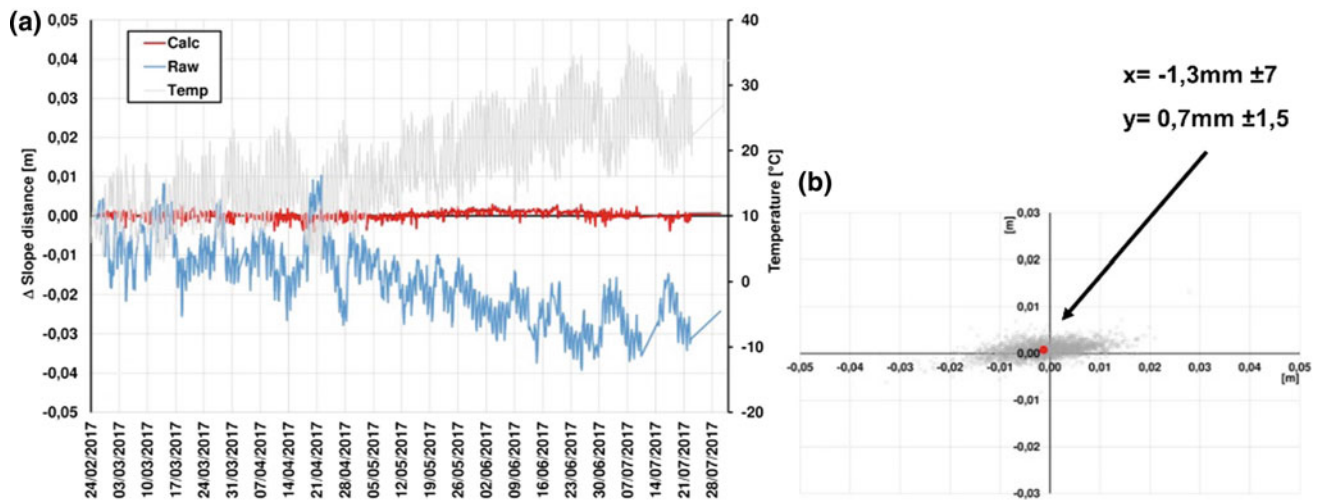
**Fig. 6** **a** Time series of prism M5: raw data (blue), calculated data with simultaneous fixed points measurements approach (red), temperature measured by weather station (grey). **b** Planimetric positions calculated for timespan February–July for the M5 Prism. The red dot indicates the average position

moved after the earthquakes. An automatic weather station was placed close to the RTS.

A robust network of fixed points (REFi), measured together with the ones within landslide area, was implemented to overcome the difficulties due to high operative distance (900–2100 m) and small-expected displacements in the inhabited area. Fixed points measurements were used to reduce the effect of temperature, humidity and refractive index (Fig. 6).

From the monitoring point of view, the installed system is a near-real-time remotely controlled system (Allasia et al. 2013). This system was activated on 23 February and it operated until the end of August 2017. The frequency of measurements were modulated from 30 to 4 h according to the evolution of the landslide. During this period, no major issues were observed, apart from some visibility problems of two prisms due to the growth of vegetation. The analysis of monitoring data permitted to evaluate the landslide kinematics and its behavior in the lateral sectors and in proximity of the Ponzano village. As shown in Figs. 7 and 8 no significant movements were observed on the retaining wall or on the hotel (REF1). The area in close proximity of the wall was characterized by limited displacement (maximum 5 cm, prism 9), but no evident retrogression toward the wall was observed. Concerning C1, C2 and C3 (located on the buildings), the only noticeable movements were measured by the prism C3, placed in the most active and damaged

area. The largest displacements were registered by the prism 14, for a total of 65 cm during the period February-July, in the direction of the maximum local slope. Prism 7 also registered significant displacement, for a total of 25 cm in 5 months, in a direction that is slightly oriented to the line of impluvium of the slope.

## 6 Discussion and Conclusion

The Ponzano landslide was monitored using an approach, which described its evolution from spatial (extensive) and temporal (intensive) point of view. The first one was carried out using two RPAS surveys, which allowed to analyse macro variations over 5 months timespan. The second one was performed through automatic topographic monitoring, in order to follow in near-real time the evolution of landslide body and surrounding area. The preliminary comparison of two UAV surveys did not show significant variations in the landslide area, however some localized displacement appeared in the main scarp. Additionally, during the second flight, a multispectral system was used, confirming the presence of water on the landslide crown. This preliminary result appears to be interesting especially considering very dry year in Ponzano area. The second type of used monitoring (topographic and in near-real time) allowed to monitor the evolution of the phenomenon with a high measurement
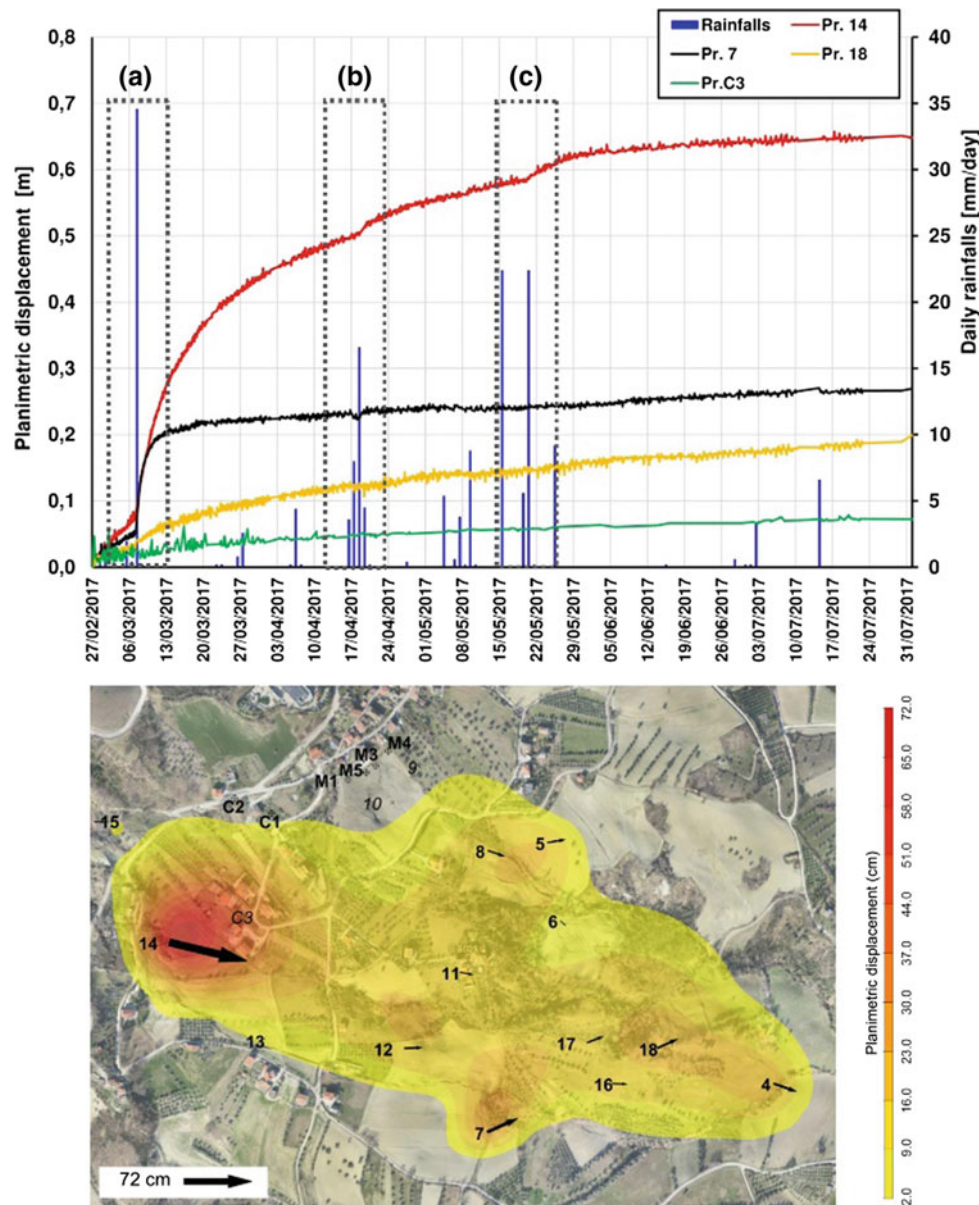
**Fig. 7** Results for timespan February–July 2017. On the top, time vs. planimetric displacement and rainfalls (a, b and c correspond to the main rainfall events). On the bottom, planimetric deformation map with two-dimensional arrows showing the real direction of the movement

frequency. This system was crucial to protect the ancient town and to understand the response of the landslide to meteorological events. The Ponzano landslide after the reactivation in February 2017 probably found a new temporary equilibrium state. During 6 months of monitoring activities, no widespread movements were observed but only some concentrated areas of activity (Fig. 8). An interesting observation was the progressive reduction (approximately 70%) of the displacement rate following the rainfalls. This

paper confirms the usefulness of multi-instrumental systems in the field of landslide monitoring. UAV systems can be useful to update aerial view and to support intensive monitoring systems design and data interpretation. The intensive systems (such as RTS) allow for detailed and timely description (even in near real time) but often do not allow for complete overview of the landslide activities. The use of both systems can provide a more effective and complete approach for landslide monitoring.
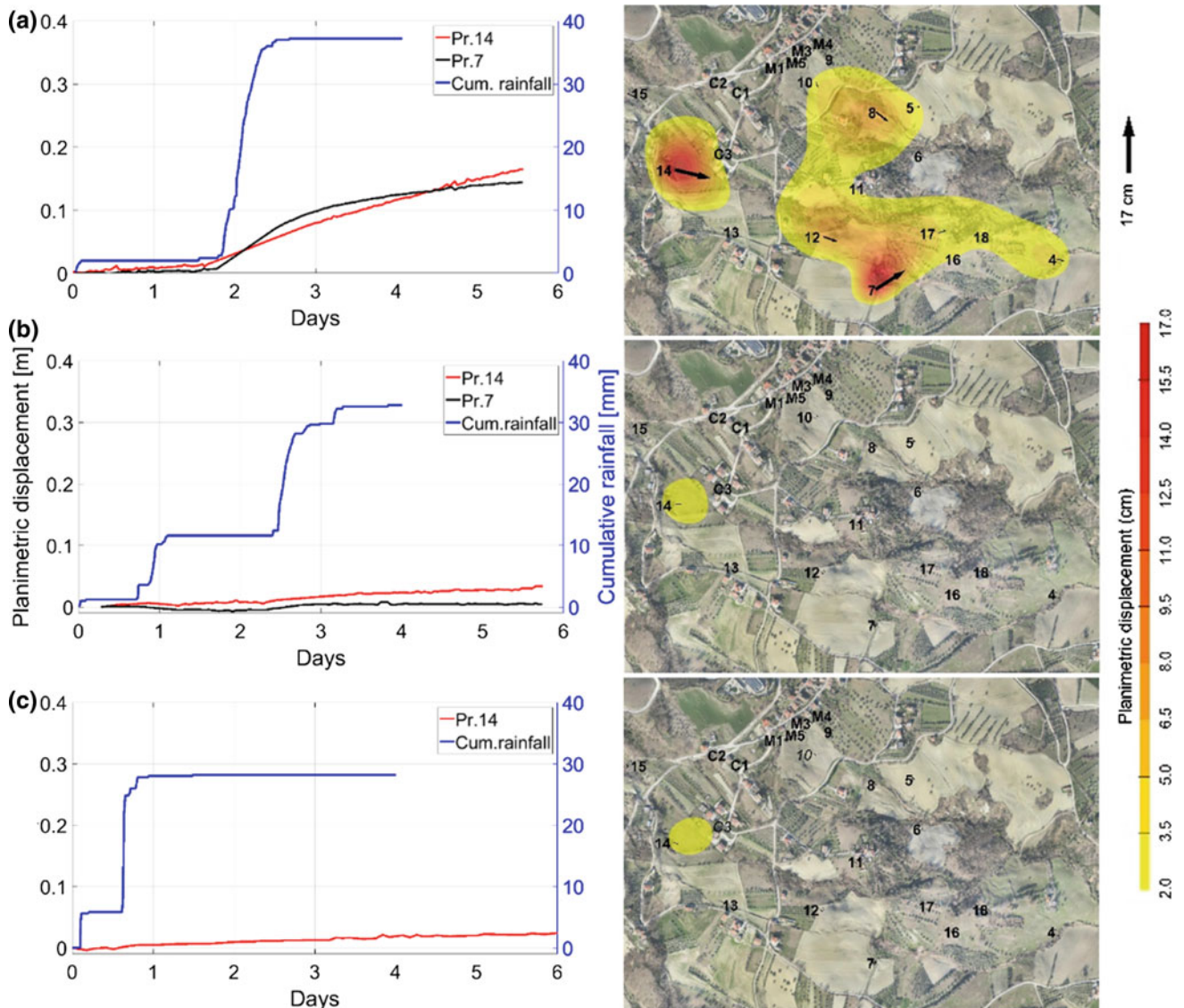
**Fig. 8** The relationship rainfall event-planimetric displacement (on the left) and corresponding deformation maps with movement arrows (on the right). See Fig. 7 for the of a, b and c period

# References

Allasia, P., Manconi, A., Giordan, D., Baldo, M., Lollino, G.: Advice: A new approach for near-real-time monitoring of surface displacements in landslide hazard scenarios. Sensors **13**, 8285–8302 (2013)

Civil Protection Department (DPC). "Internal Report" (June 2017)

Civil Protection Department (DPC). "Terremoto Centro Italia". http://www.protezionecivile.gov.it/jcms/it/terremoto_centro_italia_2016.wp, (10 October 2017)

Giordan, D., Manconi, A., Facello, A., Baldo, M., dell'Anese, F., Allasia, P., Dutto, F.: Brief communication: the use of an unmanned aerial vehicle in a rockfall emergency scenario. Nat. Hazards Earth Syst. Sci. **15**, 163–169 (2015). https://doi.org/10.5194/nhess-15-163-2015

Meteomont. "Servizio nazionale di previsione neve e valanghe". http://www.meteomont.gov.it/infoMeteo/caricaPaginaStorici.do, (10 October 2017)

NOAA National Centers for Environmental Information, State of the Climate: Global Climate Report for Annual 2016 (2017). Published online January 2017, retrieved on November 3, 2017 from https://www.ncdc.noaa.gov/sotc/global/201613

Thenkabail, P.S., Lyon, J.G. (eds.): Hyperspectral remote sensing of vegetation. CRC Press (2016)

# The Scope of Photogrammetry and TLS in the Context of Geomechanical Discontinuity Analysis

Matthias Brugger, Bettina Sellmeier, Florian Menschik, Heiko Käsling, and Kurosch Thuro

## Abstract

Discontinuity analyses along rock slopes become more and more important due to increasing safety requirements, especially for steep slopes like in quarries. The focus of this work is to determine quantitative discontinuity parameters such as orientation, persistence, and spacing, in relation to the slope orientation. In applied projects, the question for an optimized workflow in terms of discontinuity evaluation often arises. An integral approach of discontinuity set extraction can be provided by the combination of the following methods: 1. a quantitative manual recording of discontinuities (scanline sampling), 2. a semi-automatic technique (stereo-photogrammetry with the software ShapeMetriX$^{3D}$), and 3. an evaluation applying an automatized algorithm to the point cloud data obtained by terrestrial laser scanning (TLS). These methods are applied at several quarries located in Variscan granitoids in the southwestern part of the Bavarian Forest (Germany). This contribution aims to discuss the possibilities and limitations of each method for discontinuity set evaluation in the context of applied failure analysis. Knowing geological structure will help us to determine the geomechanical behavior of the rock mass comprehensively, objectively, and reproducibly in further research, as well as to save resources and time.

## Keywords

Discontinuity analysis • Scanline • Stereo-photogrammetry • TLS • Variscan granitoids • Geomechanics

## 1 Introduction

Engineering geologists have to recognize and analyze discontinuities of rock masses to characterize their geomechanical properties. By definition, discontinuities are significant, mechanically-relevant, nearly-planar fractures of negligible tensile strength within a rock mass, caused by any tectonic or geological process (Priest 1993; ISRM 1978). Discontinuities can be categorized as bedding planes, cleavage, faults, or joints (Priest 1993). Joints frequently occur in systematic, sub-parallel fracture sets, providing an indication of tectonic stresses in the regional context, since they are usually associated with major fault systems (Attewell and Farmer 1976; Priest 1993). In assessing the safety of steep slopes, especially in artificial outcrops like quarries, the possibility of rock slope failure due to adverse intersections of discontinuities and planar sliding plays an important role (Attewell and Farmer 1976). In order to describe the geomechanical behavior of the rock mass, important discontinuity properties such as frequency, average orientation, and average spacing must be quantified (Priest 1993; Slob et al. 2005).

The methods applied and evaluated in the current research are as follows:

1. scanline sampling,
2. photogrammetry (ShapeMetriX$^{3D}$) and
3. terrestrial laser scanning (TLS).

Thus, the orientation of discontinuities will be measured (1) manually, (2) semi-automatically, and (3) applying an automatized algorithm, respectively. For the last two decades, several scientists have focused on quantitative rock mass characterization by various approaches. Some conduct research in the field of photogrammetry (e.g. Gaich et al. 2006; Gaich and Pötsch 2011), while others apply TLS (e.g. Slob et al. 2005; Jaboyedoff et al. 2012; Abellán et al. 2014; Becker et al. 2014; Riquelme et al. 2014, 2015; Dewez et al. 2016).

M. Brugger (✉) · B. Sellmeier · H. Käsling · K. Thuro
Technical University of Munich, Arcisstr. 21, 80333 Munich, Germany
e-mail: m.brugger@tum.de

F. Menschik
Laboratory Dr. Ettl & Dr. Schuh, Imhofstr. 3, 80805 Munich, Germany

We are going to apply these three methods in selected quarries located in the Bavarian Forest, a Variscan base complex in northeast Bavaria (Germany). Due to tectonic uplift and erosion, the granitoids of several magmatic intrusions are exposed to the surface and have been successfully quarried for many decades, due to their characteristic orthogonal joint system. Furthermore, we are going to compare our results with structural investigations in the Bavarian Forest made by Zeitlhöfler (2007) and Zeitlhöfler et al. (2015). They provided a tectonic lineament analysis based on digital elevation models confining to lineament lengths of more than 1500 m. Zeitlhöfler et al. (2015) verified these results by mapped faults on geological maps and thousands of manual discontinuity measurements in situ.

## 2 Geological and Tectonic Setting of the Study Area

The Bavarian Forest is the southwestern part of the Bohemian Massif and belongs to the Moldanubian sector within the Variscan basement complex of Central Europe (Rohrmüller et al. 1996). The Moldanubicum is generally characterized by highly metamorphic rocks (mainly gneiss) and a number of late to post-Variscan granitoid intrusions (Fig. 1) (Rohrmüller et al. 1996). The so-called "exterior Bavarian Forest", the region of the project site, is limited by the Austrian border in the SE and by important tectonic lineaments in the SW, W and NE.

Three main discontinuity sets characterize the structural geology of the exterior Bavarian Forest (Zeitlhöfler et al. 2015). These sets are briefly characterized in the following:

- The Bavarian Pfahl shear zone in the NE of the study area and the Danube fault in the SW are distinctive, large-scale NW–SE striking fault systems (Fig. 1). Their main activity was in the Permian and early Mesozoic (Rohrmüller et al. 1996). These systems influence discontinuities in the whole region (Lehrberger 2013; Zeitlhöfler 2007; Zeitlhöfler et al. 2015).
- The second important fault system strikes N–S to NNW–SSE. According to Lehrberger et al. (2003) and Unger (1996), it extends from Thuringia to the northern fringe of the Alps. The Keilberg fault system, for example, traces the western edge of the exterior Bavarian Forest (Fig. 1), and there are additional associated faults between the fault systems mentioned above. These roughly N–S striking faults are clearly observable by studying digital elevation models and also in situ (Lehrberger et al. 2003; Zeitlhöfler 2007; Zeitlhöfler et al. 2015). However, the spatial distribution of these faults is not uniform from NW to SE because, following this

direction, the degree of sub-parallel tectonic rock mass degradation increases (Lehrberger et al. 2003).
- The third fault system, which strikes NE–SW, occurs subordinate to the other ones (Zeitlhöfler et al. 2015). It extends from beyond the Czech borderline to the Alpine Foreland, according to Lehrberger et al. (2003).

In granitoid intrusions a further discontinuity set typically occurs, which is usually oriented sub-parallel to the surface of the rock slope. These joints are mainly caused by stress relaxation, according to erosion (Zeitlhöfler et al. 2015). Hence, these discontinuity sets are oriented perpendicular to each other and cause an orthogonal joint system (Lehrberger et al. 2003) that is characteristic for granitoid intrusions in general. Other discontinuities with different orientations, which can be also found, are less important.

## 3 Methodology

### 3.1 Scanline Sampling

Scanline sampling is one of the commonly applied approaches for discontinuity characterization since it is easy-to-use and cost-efficient (Priest 1993). Priest (1993) recommended an approach for scanline measurements but there is no standardized procedure because the operating geologist must adapt the method to local conditions. It is important to choose a section of the rock face which an experienced geologist considers to be representative for the whole quarry, as well as accessible and safe to work with regard to rock fall, ongoing quarrying, etc. (Priest 1993; Slob et al. 2005; Becker et al. 2014). To increase the explanatory power of the data, it is recommended to perform discontinuity recording along two perpendicular scanlines (Priest and Hudson 1976). The orientation sampling bias, i.e. an under-representation of discontinuities striking approximately parallel to the rock face, is corrected with a weighting with regard to the scanline orientation (Priest 1993; Becker et al. 2014). For each discontinuity trace which intersects the scanline-measuring tape, the following parameters are recorded: consecutive number, intersection distance, orientation, semi-trace lengths, type of termination, roughness, curvature and the type of discontinuity, as well as other observations of interest (Priest 1993; ISRM 1978). Priest (1993) recommended that, for statistical analysis, at least 150 to 350 discontinuities should be measured using a geological compass.

The results of this method yield considerably less structural information and a lower significance than more comprehensive methods like extracting discontinuities from a point cloud (i.e. TLS) (Dewez et al. 2016). Finally,
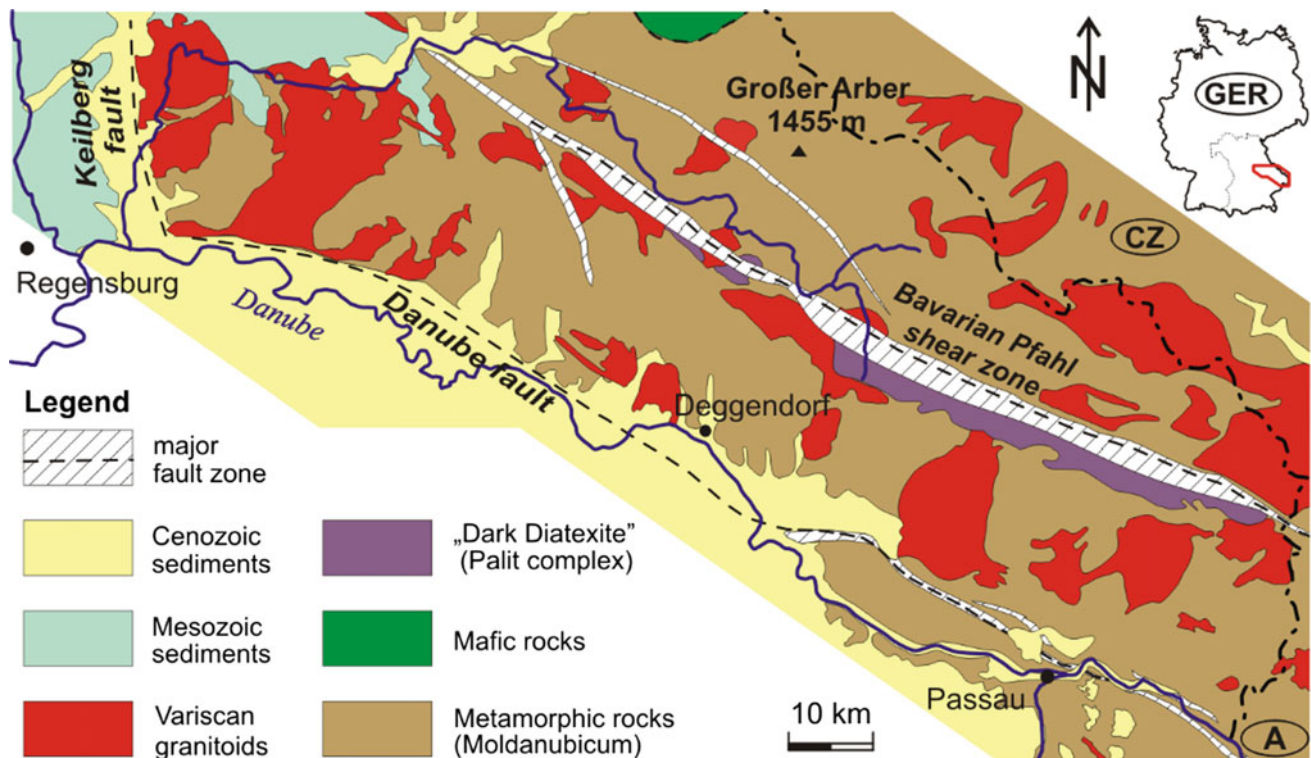
**Fig. 1** Schematic geologic map of the Bavarian Forest with its granitoid intrusions (modified after Lehrberger 2013)

all recorded structures can be clustered and weighted (by a software like Dips by Rocscience) and plotted in stereographic projections.

Overall, scanline sampling is an easy-to-apply method, requiring a time-consuming field work, which depends on the observation and experience of the operating geologist and is subject to human bias (Priest 1993; Slob et al. 2005).

### 3.2 Photogrammetry

There are two photogrammetric methods used for remote sensing, one classical stereo-photogrammetry and the modern 'structure from motion—multi-view stereo' method (SfM-MVS). For ongoing research, we focus on detailed studies on selected quarry berms applying a stereo-photogrammetry technique and a semi-automatic commercial software package of 3G Software & Measurement GmbH, which is called ShapeMetriX$^{3D}$.

The input data (digital image pairs of the same rock face detail) are taken freehand from two different positions using a Nikon D90 camera with calibrated objective lenses. The distance between the two photo spots should be about one-fifth to one-eighth of the distance to the rock wall (3G Software & Measurement GmbH 2010). In order to get a three-dimensional stereoscopic image, a scale reference and the orientation of the image is required (Gaich et al. 2006).

To establish a local coordinate system of the stereoscopic model, it is sufficient to record the orientation of at least one reference discontinuity at an accessible and significant location using a geological compass. Overall, the required equipment is more cost-efficient, more flexible, and easier to handle compared to TLS instruments (Lemmens 2011).

A useful plugin called SMX ModelMerger is able to fuse adjacent and overlapping 3D images (3G Software & Measurement GmbH 2013). An evident advantage is that all single 3D images can get their scaling and orientation from one stereoscopic image pair that, for instance, enables a survey of inaccessible upslope parts of the rock face. That minimizes working time at the base of steep rock faces and increases operational safety immensely (Gaich et al. 2006; Gaich and Pötsch 2011). Furthermore, the rock face is captured in a comprehensive and objective way (Gaich et al. 2006). However, the system limitation is the processing power of the computer: the more 3D images are loaded for merging and editing, the longer the process takes.

Despite a fast data acquisition in the quarry, the data processing in ShapeMetriX$^{3D}$ is time-consuming and still requires manual outlining of discontinuities, depending on operator's experience (Slob et al. 2005). Shadow effects on the rock face due to vegetation, as well as artificial and natural occlusion, complicates and impedes the discontinuity analysis. This is especially true in case of rock ledges (Lemmens 2011). Occurring optical distortion in the 3D

photorealistic model is subject to technical setup, i.e. it primarily depends on the perspective of the photographer. Discontinuities, which either strike parallel to sub-parallel to the photographer's line of sight or which are oriented horizontally to sub-horizontally could cause a considerable optical distortion (3G Software & Measurement GmbH 2010).

In order to determine the geometry of rock mass discontinuities, a few previous processing steps are necessary (Gaich et al. 2006; 3G Software & Measurement GmbH 2010). First, all visible discontinuities have to be extracted, either manually or semi-automatically, by tracing each discontinuity, and all of them can be clustered into structure sets (3G Software & Measurement GmbH 2010). The applied algorithm requires the specification of the minimum and maximum amount of structure sets (1–10) and other geometrical and statistical parameters. Finally, one can get (1) the orientation of the structure sets, including stereographic projection and statistics, and (2) the true spacing of discontinuities within each structure set (measured perpendicular to the surface), including statistics. Furthermore, the scanline tool can be applied, providing a comparison to manually recorded scanline data containing a smaller number of discontinuities (3G Software & Measurement GmbH 2010; Gaich et al. 2006; Gaich and Pötsch 2011).

### 3.3 Evaluation of Point Cloud Data (Terrestrial Laser Scanning)

Methods that use laser scanning technology for reproducing the three-dimensional surface rapidly, accurately, and contact-free have been successfully applied for the last 10 to 20 years (Lemmens 2011). To scan the topography of quarries, a ground-based light detection and ranging scanner (LiDAR), eponymous for terrestrial laser scanning (TLS), is placed on a tripod (Lemmens 2011). In the ongoing research, we use the scanning device Riegl VZ-400, which provides a field of view of 100° in vertical and 360° in horizontal direction. The laser scanner measures the time of flight of the laser pulse from the device to an object and back (Lemmens 2011). The scanning time depends on the requested scan resolution, i.e. the angular step width. The outcome is a three-dimensional point cloud with a high point density, which provides a huge amount of data, but there are also aspects affecting accuracy (Lemmens 2011). Generally, each TLS device uses a laser beam with a natural divergence. The footprint diameter of the emitted laser beam, for example, increases with distance, which consequently causes a decrease in resolution (Lemmens 2011; Slob et al. 2005). In comparison to scanline sampling and photogrammetric methods, the equipment of TLS is heavier, bulkier and more expensive (Lemmens 2011; Gaich et al. 2006).

Based on a single scan from one scan position, there are generally several shaded areas (occlusion) due to obstacles such as vegetation, the surface topography, and the angle of incidence (Slob et al. 2005; Jaboyedoff et al. 2012; Abellán et al. 2014). Furthermore, atmospheric and meteorological conditions (such as rainfall, snow, fog, high humidity, as well as air temperature and air pressure) together with whirled-up dust cause noise or even a lack of data in the point cloud (Charlton et al. 2009; Jaboyedoff et al. 2012). The reflectivity of the rock surface can also be impaired by direct solar irradiation and cause noise (Abellán et al. 2014; Charlton et al. 2009). Multiple overlapping scans from different scan positions, depending on the quarry layout and scan conditions, are required in order to prevent concealed or patchy areas (Kemeny and Turner 2008). They are merged into one by a software like RiSCAN PRO.

After registration, geo-referencing and fusion, the point cloud has to be processed for discontinuity analysis by filtering undesirable data (e.g. construction machines, wires, vegetation, scree, etc.) (Riegl LMS GmbH 2016; Slob et al. 2005; Kemeny and Turner 2008; Abellán et al. 2014). Automatic filtering (e.g. in case of vegetation, if it is not too dense) needs to be adjusted manually, which is time-consuming (Kemeny and Turner 2008; Jaboyedoff et al. 2012; Abellán et al. 2014).

Kemeny and Turner (2008) provide an overview of mainly commercial software, which are primarily based on the same approach for discontinuity set extraction: automatic delimitation of fractures from the interpolated surface mesh (triangulation) by their definition as planes. The normal vectors are calculated and neighboring ones with similar orientations are grouped, where several parameters can be adjusted, e.g. the minimum of neighboring triangles and the deviation of orientations (Kemeny and Turner 2008; Abellán et al. 2014). The average orientations of obtained fractures can be weighted by their area and plotted in a stereographic projection in order to determine discontinuity sets statistically (Kemeny and Turner 2008).

The open source software DSE (discontinuity set extractor) by Riquelme et al. (2014) offers a similar technique, but uses a kernel density estimation to determine discontinuity sets and to extract single discontinuities automatically using a density-based clustering algorithm. Riquelme et al. (2014) extended the algorithm with the functionality of calculating the spacing of non-persistent discontinuities of one set by assuming that they are infinite planes.

CloudCompare is an example of an open source evaluation software for 3D point clouds. The structural geology plugin "FACETS" contains an algorithm for discontinuity analysis (Dewez et al. 2016). While this tool can be useful, fractures, which are oriented roughly parallel to the rock surface, are frequently over-represented (Dewez et al. 2016).

According to Slob et al. (2005), TLS data acquisition is more cost- and time-efficient, less hazardous (contact-free), more objective, reproducible, and more accurate compared to the other methods described above, which contributes to the field of discontinuity evaluation. Surveying quarries in an integral way is a significant advantage of TLS data evaluation because an increasing amount of discontinuities can be recorded taking a larger scan area into account; whereas scanline sampling and stereo-photogrammetry are limited to a certain part of the quarry (Slob et al. 2005; Riquelme et al. 2015). In addition, calculated fracture orientations (dip and dip direction) offer the possibility to average various orientation values of a curved and rough discontinuity (Slob et al. 2005). Consequently, this enables us to apply statistical analyses using clustering techniques and to obtain precise discontinuity sets with associated geometric properties (Slob et al. 2005; Jaboyedoff et al. 2012). This is based on the assumption that all fractures of the rock face are derived from pre-existing internal rock mass fractures which can be defined as geological discontinuities (Chap. 1) (Slob et al. 2005). However, artificial fractures within the intact rock mass (e.g. resulting from blasting damage) and those affected by weathering, contradict the discontinuity definition (Slob et al. 2005). Nevertheless, unless they are not removed manually, these detected fractures are used in the statistical assessment and thus influence the outcome of the discontinuity analysis. In this case, the objectivity of the method turns into a disadvantage because the scanner is only able to capture the rock face topography but not its texture (Lemmens 2011) and cannot perform proper, i.e. subjective, interpretation in terms of geomechanical implications (Riquelme et al. 2015).

## 4 Conclusion and Further Objectives

Quantitative discontinuity analyses contribute significantly to geomechanical rock mass characterization, as demonstrated by several case studies, applying advanced methods besides traditional scanline sampling: stereo-photogrammetry (ShapeMetriX³ᴰ) (e.g. Gaich et al. 2006) and evaluation of point cloud data obtained by TLS (e.g. Dewez et al. 2016). However, each method has its possibilities and limitations, as outlined in this contribution. Thus, traditional field measurements cannot be completely replaced, especially with regard to specific issues, e.g. whether certain discontinuity sets are geomechanically effective or not.

We will apply these methods at active quarries in Variscan granitoids in the Bavarian Forest in order to provide objective and reproducible data about their present discontinuity system in an integral way. The focus of our research will be to determine the geomechanical behavior of the rock mass and to address the following (methodical) research questions:

1. How can we optimize the methodical approach for discontinuity analysis in a certain quarry in the Bavarian Forest, with regards to objectivity and reproducibility, as well as time-efficiency in terms of acquisition, processing and evaluation of data? How can we transfer the optimized methodical approach to other quarries in a similar geological setting?
2. How can we quantify the deviation between manual and (semi-)automatic methods for discontinuity analysis?
3. How can we evaluate our results of the quantitative discontinuity analysis in comparison to the more qualitative ones of the Bavarian Forest [e.g. published by Zeitlhöfler (2007) and Zeitlhöfler et al. (2015)]?

## References

3G Software & Measurement GmbH: ShapeMetriX³ᴰ—3D imaging for measuring and assessing rock and terrain surfaces—User Manual for Version 3.5, 168 p., 3G Software & Measurement GmbH, Graz (2010)

3G Software & Measurement GmbH: ShapeMetriX³ᴰ—SMX ModelMerger—Benutzerhandbuch für Version 3.2, 69 p., 3G Software & Measurement GmbH, Graz (2013)

Abellán, A., Oppikofer, T., Jaboyedoff, M., Rosser, N.J., Lim, M., Lato, M.J.: Terrestrial laser scanning of rock slope instabilities. Earth Surf. Process. Landforms **39**(1), 80–97 (2014)

Attewell, P.B., Farmer, I.W.: Principles of Engineering Geology, 1046 p. Chapman & Hall, London (1976)

Becker, S., Nguyen, H.T., Nollet, S., Fernandez-Steeger, T.M., Laux, D., Hilgers, C.: Methods to analyse fracture orientation patterns in a Lower Carboniferous carbonate reservoir analogue in the Voreifel Germany. German J. Geosci. **165**(3), 319–330 (2014)

Charlton, M.E., Coveney, S.J., McCarthy, T.: Issues in laser scanning. In: Heritage, G.L., Large, A.R. (eds.) Laser Scanning for the Environmental Sciences, pp. 35–48. Wiley-Blackwell, Chichester (2009)

Dewez, T.B.J., Girardeau-Montaut, D., Allanic, C., Rohmer, J.: FACETS: A CloudCompare plugin to extract geological planes from unstructured 3D point clouds. In: 23rd ISPRS Congress, Commission V, vol. XLI-B5, pp. 799–804. ISPRS, Prague (2016)

Gaich, A., Pötsch, M.: Böschungsbewertung mit 3D-Bildern. Berg-Huettenmann. Monatsh. **156**(2), 47–52 (2011)

Gaich, A., Pötsch, M., Schubert, W.: Acquisition and assessment of geometric rock mass features by true 3D images. In: 41st U.S. Symposium on Rock Mechanics: 50 Years of Rock Mechanics—Landmarks and Future Challenges, pp. 1–10. American Rock Mechanics Association, Golden (2006)

ISRM: Suggested methods for the quantitative description of discontinuities in rock masses. Int. J. Rock Mech. Min. Sci. Geomech. Abstr. **15**, 319–368 (1978)

Jaboyedoff, M., Oppikofer, T., Abellán, A., Derron, M.-H., Loye, A., Metzger, R., Pedrazzini, A.: Use of LIDAR in landslide investigations: a review. Nat. Hazards **61**(1), 5–28 (2012)

Kemeny J., Turner, K.: Ground based LIDAR. rock slope mapping and assessment. In: Technical Report of the Central Federal Lands

Highway Division, US Department of Transportation, 114 p. FHWA, Lakewood (2008)

Lehrberger, G.: Granit—das Höchste und das Tiefste. Zur Geologie und Mineralogie der Granite des Bayerischen Waldes. In: Helm, W. (ed.) Granit, 2nd edn., pp. 19–48. Granitzentrum Hauzenberg, Hauzenberg (2013)

Lehrberger, G., Saurle, A., Hartmann, U.: Anwendung des SAR-DGM bei der tektonischen Interpretation des Moldanubikums am Westrand der Böhmischen Masse. Geologica Bavarica 107, 269–280 (2003)

Lemmens, M.: Terrestrial laser scanning. In: Lemmens, M. (ed.) Geo-information. Geotechnologies and the Environment, vol. 5, pp. 101–121. Springer, Dordrecht (2011)

Priest, S.D.: Discontinuity Analysis for Rock Engineering. 1st edn., 395 p. Chapman & Hall, London (1993)

Priest, S.D., Hudson, J.A.: Discontinuity spacings in rock. Int. J. Rock Mech. Min. Sci. Geomech. Abstr. 13, 135–148 (1976)

Riegl L.M.S GmbH (ed.): RiSCAN PRO—User Manual for version 2.4.0, 463 p., Riegl LMS GmbH, Horn (2016)

Riquelme, A.J., Abellán, A., Tomás, R.: Discontinuity spacing analysis in rock masses using 3D point clouds. Eng. Geol. 195, 185–195 (2015)

Riquelme, A.J., Abellán, A., Tomás, R., Jaboyedoff, M.: A new approach for semi-automatic rock mass joints recognition from 3D point clouds. Comput. Geosci. 68, 38–52 (2014)

Rohrmüller, J., Mielke, H., Gebauer, D.: Tektonik des Grundgebirges. In: Erläuterungen zur Geologischen Karte von Bayern 1:500 000 (Geological Survey of Bavaria). 4th edn., pp. 252–265. Geological Survey of Bavaria, Munich (1996)

Slob, S., van Knapen, B., Hack, R., Turner, K., Kemeny, J.: Method for automated discontinuity analysis of rock slopes with three-dimensional laser scanning. In: Transportation Research Record: Journal of the Transportation Research Board, vol. 1913, pp. 187–194. National Academy of Sciences, Washington, D.C. (2005)

Unger, G.: Tektonik des Molassebeckens. In: Erläuterungen zur Geologischen Karte von Bayern 1:500 000 (Geological Survey of Bavaria). 4th edn., pp. 265–266. Geological Survey of Bavaria, Munich (1996)

Zeitlhöfler, M.: Brittle Petrofabrics in the Central Bavarian Forest (SE Germany). Tectonic Evolution, Geomorphological Effects, and Hydrogeologic Implications. 249 p. Ph.D.-thesis, LMU Munich (2007)

Zeitlhöfler, M., Wagner, B., Spörlein, T.: Strukturgeologie und Grundwasserführung im ostbayerischen Grundgebirge. Geologica Bavarica 112, 1–64 (2015)

# UAV-Based Discontinuity Analyses and Rock Fall Source Mapping in Alpine Terrain (Pletzachkogel/Tyrol/Austria)

Georg H. Erharter, D. Scott Kieffer, and Christoph Prager

## Abstract

Three major Holocene rock avalanches have sculpted the morphology of Mount Pletzachkogel (Tyrol, Austria), and rock fall processes continue to show recent activity. Coalescing sets of discontinuities and block moulds exposed in the steep and rugged limestone cliffs exemplify the broad spectrum of rotational and translational block failure modes to which the mountain is prone. As personnel safety concerns strongly limit the ability to access the 200 m high rock cliffs to make traditional structural field measurements, Unmanned Aerial Vehicle (UAV) photogrammetric surveys were performed with a compact portable multicopter. The UAV survey provided a georeferenced point cloud and Digital Terrain Model of sufficient resolution and accuracy to permit efficient extraction of structural geologic measurements by using different open source software packages. This research focuses on comparing discontinuity measurements extracted from the point cloud using manual, semi-automated, and automated techniques, to field measurements made with a geologic compass. The overall workflow of digital image processing and related structural measurement extraction is described, together with data validation procedures. The workflow described herein provides an efficient means for obtaining comprehensive and accurate data sets that mitigate personnel access constraints, are fully auditable and archivable. With increased applications of UAVs for geologic mapping and documentation, such procedures are sure to see rapidly increasing deployment, particularly in alpine terrain.

## 1 Introduction

Assessment of rock fall hazards in steep mountainous terrain having high relief is often encumbered by personnel access constraints and safety concerns. Photogrammetry based on Unmanned Aerial Vehicle (UAV) data collection platforms greatly enhance observational access to restricted terrain, while also providing 3D georeferenced point clouds of sufficient resolution and accuracy to permit reliable digital structural geologic measurements. The primary aim of this study is to evaluate the efficacy of deploying small, portable UAVs in the context of rock fall source area analyses. This evaluation is based on comparing point cloud derived digital discontinuity orientation measurements to structural measurements made in the field with a geologic compass. Methods for extracting the structural measurements from the point cloud included manual/interactive techniques as well as semi-automated and automated discontinuity detection algorithms.

## 2 Site Conditions

Pletzachkogel is located in Tyrol, Austria and has a peak elevation of 1549 m a.s.l. (Fig. 1). The mountain is located at the southern margin of the Northern Calcareous Alps, which consist primarily of Mesozoic sedimentary rocks, featuring polyphase and heteroaxial folding and faulting (Ampferer 1908; Schmid et al. 2004). As depicted in Fig. 1, three major Holocene landslides have sculpted the morphology of Pletzachkogel (Patzelt 2012). The investigated rock fall source area is composed of reddish-grey massive to obscurely bedded, rigid breccia (lower Jurassic).
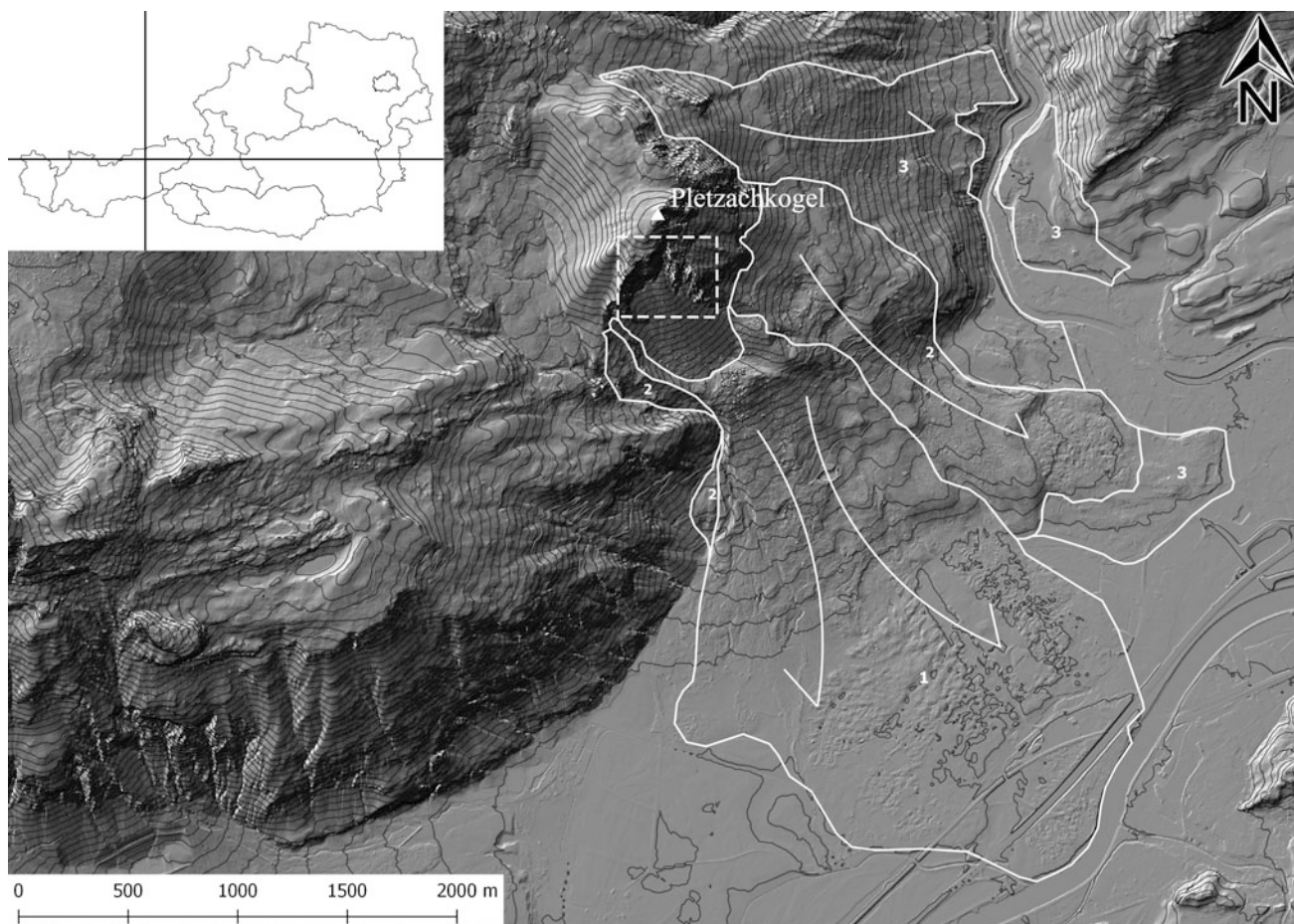
G. H. Erharter (✉) · D. S. Kieffer
Graz University of Technology, Graz, Austria
e-mail: erharter@alumni.tugraz.at

D. S. Kieffer
e-mail: kieffer@tugraz.at

C. Prager
ILF Consulting Austria GmbH & alpS GmbH, Rum, Austria
e-mail: christoph.prager@ilf.com

**Fig. 1** Hillshade DEM from 1 m Airborne laser scan (contour interval 20 m) showing the topography of Pletzachkogel and landslide deposits detached thereof (marked with white lines, 1—last-(120–240 AD), 2— middle Holocene and 3—late Pleistocene—landslide (Patzelt 2012). Dashed rectangle at Pletzachkogel SE-face indicates UAV-surveyed scarp area

The fractured rock mass is characterised by different sets of discontinuities (brittle joints, some folded bedding planes) with rough, stepped and wavy surfaces on mm-, cm- and m-scales, respectively.

Topographically, Pletzachkogel is dominated by a near vertical and southeast facing cliff having a maximum relief of >200 m. On its southeast side Pletzachkogel is bordered by a series of prominent vertical rock towers that are up to 200 m high and are referred to as the "rock buttress" (Fig. 2). The cliff and rock buttress represent the head scarps of major landslides that occurred at around 120–240 AD (Patzelt 2012). Subsequent to these landscaping events, rock falls have represented an ongoing geologic process. The most recent significant rock falls occurred in 2011 and 2015, with debris volumes exceeding 1000 m$^3$ (Fig. 2). The rock fall source areas are located above a 300 m high talus fan, featuring dangerous site access exposed to potential rock fall hazards.

## 3 Methodology

### 3.1 UAV Photogrammetric Survey and Image Processing

Aerial photographs were acquired with the DJI Mavic Pro ("Mavic") quadrocopter. The Mavic is well suited to alpine environments by virtue of its compactness, flight duration and photographic capabilities. Technical specifications of the Mavic are summarized in Table 1. With a standard GPS accuracy of >5 m, the Mavic's on-board GPS system is not sufficiently accurate for direct georeferencing of the photogrammetric point cloud, requiring indirect georeferencing with precisely surveyed ground control points (GCPs). The used GCPs are specially fabricated optical targets, whose center coordinate can be identified and precisely selected directly on overlapping aerial photographs.

**Fig. 2** The southeastern cliff face of the Pletzachkogel (left) and the rock buttress (right). The source areas and deposits of the 2011 and 2015 rock falls are indicated by freshly exposed rocks in the buttress area. Note major joints shaping the rock mass

**Table 1** DJI Mavic Pro key technical specifications (DJI 2017)

| | | |
|---|---|---|
| UAV | Weight [g] | 734 |
| | Size (folded) [mm] | 83 × 83 × 198 |
| | Max. flight time [min] | 27 |
| Camera | Sensor type | CMOS |
| | Sensor format | 1/2.3 |
| | Sensor dimensions [pixels] | 4000 × 3000 |
| | Sensor dimensions [mm] | 6.2 × 4.6 |
| | Image resolution [Mpixels] | 12.35 |
| | Focal length [mm] | 28 |
| | ISO | 100–1600 |

In consideration of model size and computational effort, the UAV survey area was spatially divided into three "chunks". Chunk 1 and 2 include the buttress towers, and Chunk 3 comprises the SE-facing main cliff (see Fig. 2). Six GCPs were established for each chunk. Due to a multitude of topographic obstructions and flight hazards, UAV photograph acquisition was performed in a manual flight mode rather than autonomously (pre-programmed flight plan). In total, 853, 779, and 1931 overlapping photographs were acquired for Chunks 1, 2, and 3, respectively.

The raw photographs were manually sorted (e.g. blurry, heavily over- or underexposed, or redundant images were removed from the data set) and georeferenced point clouds were then generated applying the software *Agisoft PhotoScan Professional* (Agisoft 2017).

## 3.2 Digital Mapping and Kinematic Analysis

Two plugins for the open source 3D point cloud processing software *CloudCompare* (CC) (version 2.9. beta) were used to extract plane orientations (CloudCompare 2017): *Facets* and *Compass*.

*Facets* is a CC plugin for fully automatic structural data extraction (Dewez et al. 2016), which divides the point cloud into clusters of adjacent points and employs a least square plane fitting algorithm. Following user defined criteria of co-planarity, the clusters are reassembled in a three-step process: (1) elementary facets corresponding to small fragments of planes are computed; (2) elementary planes are then re-clustered into encompassing planes; and (3) parallel planes are merged into plane families. The end result is a number of polygons that are color coded according to their spatial orientation (azimuth/dip). The data can be exported as.csv or.shp files, or analyzed directly in CC (Dewez et al. 2016). The user defined input parameters selected for the *Facets* analysis are summarized in Table 2.

*Compass* is an additional CC plugin for extracting and exporting manual or semi-automated structural measurements from point clouds using a plane-, trace- and lineation-measurement tool (Thiele et al. 2017). Using a least square algorithm, *Compass* fits a plane to a group of sampled points. Selection of points is facilitated by an adjustable sampling-circle around the cursor. The *plane-tool* is applicable to exposed surfaces, while the *trace-tool* can extract orientation based on the geometry of a discontinuity edge intersecting an irregular outcrop surface. The start and end points of a discontinuity trace are specified, and the tool finds the linking "structural trace" using a "least cost path" algorithm. A planar surface is then fitted to each trace with a least square algorithm to obtain an "estimate of the structure orientation". The *lineation-tool* simply measures the trend and plunge of a straight line between two points.

On the basis of UAV derived structural measurements (orientations of discontinuities), simple kinematic analyses were performed to obtain an initial estimate of block failure mode tendencies. The main focus of the kinematic analyses included the Pletzachkogel southeastern cliff face and neighboring rock buttress area. The kinematic conditions for planar sliding, wedge sliding and toppling were manually evaluated (e.g. Wyllie et al. 2004) and the stereonets generated with the programs *Dips* (Rocscience Inc. 2018) and *Stereonet* (Allmendinger et al. 2012; Cardozo and Allmendinger 2013).

## 4 Results

For Chunk 1 a dense point cloud (DPC) consisting of 41,805,462 points was generated with a ground resolution of 3.04 cm/pix and a reprojection error of 1.11 pix. The DPC for Chunk 2 consists of 49,762,919 points with a ground resolution of 2.3 cm/pix and a reprojection error of 1.23 pix. For Chunk 3, the DPC consists of 42,481,210 points with a ground resolution of 3.42 cm/pix and a reprojection error of 1.68 pix. In the areas of primary interest (i.e. bedrock outcrops), the image overlap is greater than nine. A portion of the DPC covering the southeastern cliff face is shown in Fig. 3a.

With the CC plugin *Compass*, 1394 structural measurements were extracted, and with the plugin *Facets*, 5238 planes were extracted. As shown in Fig. 3, there are two main orientation clusters. For the *Compass* measurements, the cluster centers have a dip direction/dip of 127/68(JS1) and 183/88(JS2), and for the *Facets* measurements, the corresponding center orientations are nearly identical at 124/69(JS1) and 180/86(JS2). The joint set orientations determined on the basis of point cloud- and manual field measurements are summarized in Table 3.

As indicated therein, the point cloud derived measurements underrepresent a third discontinuity set having an orientation of approximately 280/60(JS3). The underrepresentation of this joint set is related to the characteristically small surface areas of joint faces exposed in the outcrops.

Discontinuity set orientations measured for the rock buttress are similar, but scattering of the results is more significant than for the southeastern cliff face. The underrepresented third joint set, having an orientation of 270/70, was also detected in the point cloud for the rock buttress.

## 5 Interpretation

In the simple kinematic analyses, the entire populations of structural measurements derived from the DPCs were utilized as input and separated into the measurements from the southeastern cliff face and from the rock buttress

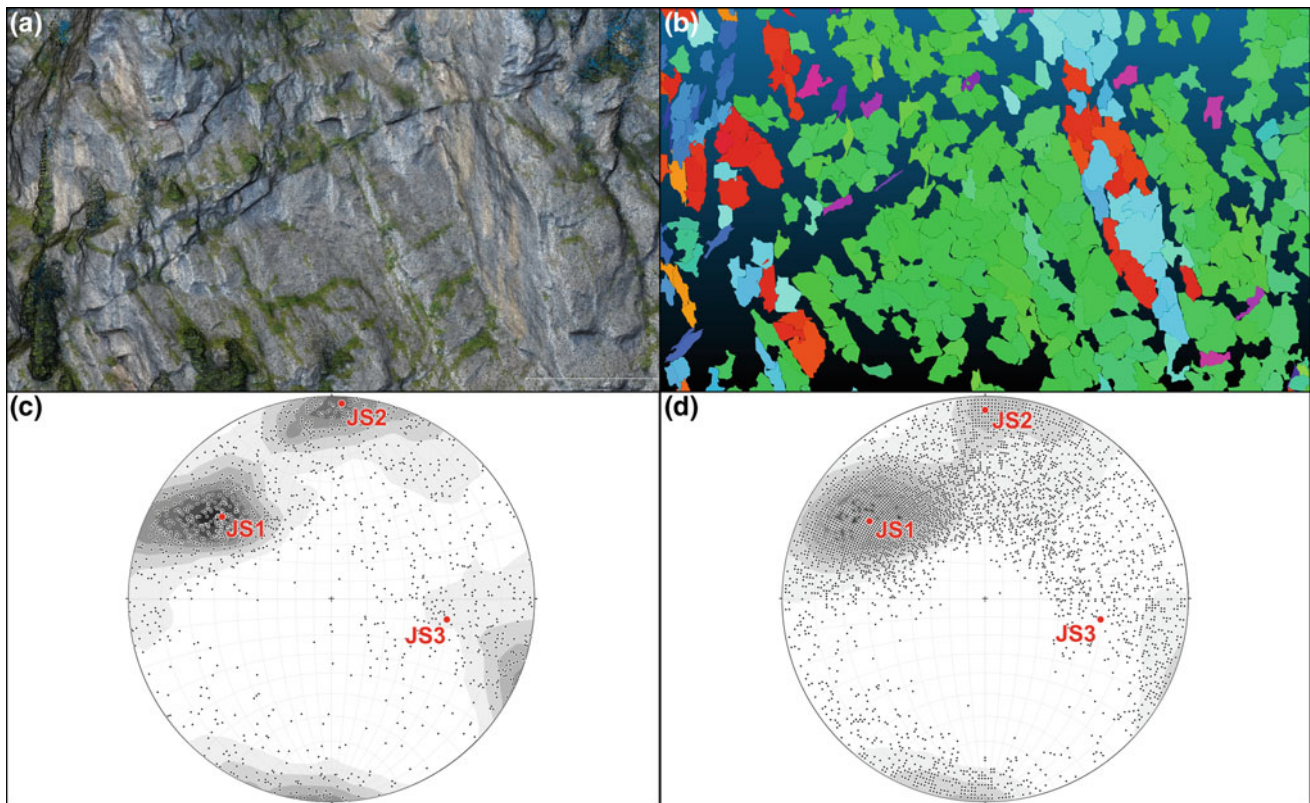| **Table 2** Input parameters for the facets "fast marching approach." | | |
|---|---|---|
| | Octree level | 10 |
| | Use retro projection error for propagation | Yes |
| | Max distance @99% | 0.213 |
| | Min points per facet | 3500 |
| | Max edge length | 0.7 |

**Fig. 3** **a** Portion of dense point cloud covering the southeastern cliff face; **b** automatically extracted planes with *Facets*; **c** equal angle, lower hemisphere, stereographic projection of the 1394 poles from *Compass*; and **d** stereographic projection of the 5238 poles from *Facets*

**Table 3** Average joint set orientations (dip direction/dip) obtained from photogrammetric point clouds (SE-facing main cliff and rock buttress), and from manual field measurements in the investigated area

|             | Southeastern cliff face | Rock buttress | Field measurements |
|-------------|--------------------------|---------------|--------------------|
| Joint set 1 | 129/64                   | 116/75        | 103/65             |
| Joint set 2 | 181/88                   | 202/87        | 190/80             |
| Joint set 3 | 280/60                   | 270/70        | 270/35             |

(see Sect. 3). The southeastern cliff face orientation was taken at 140/70, and kinematic analyses for the rock buttress area explicitly considered the near-vertical columnar geometry of the rock towers by introducing a composite convex free-space formed by the intersection of slope orientations: 110/75, 200/75, and 290/75. The analysis results for the southeastern cliff are shown in Fig. 4. A mean joint friction angle of 35° was estimated, in view of discontinuity properties observed in the field and literature data (e.g. Barton 1976). The analyses indicate that planar sliding is kinematically permissible along Joint Set 1, as is wedge sliding along the intersection lines Joint Sets 1 and 2. Concerning the representative mean slope orientation (SE-facing), there are comparatively few structural elements that are susceptible to toppling failure. However, in a more detailed view

also some other oriented slope faces, may be prone to planar and/or toppling failure modes (e.g. S- to SSW-facing areas, see Fig. 4a).

Analysis results for the rock buttress area are summarized in Fig. 5. As shown, planar and toppling failure are kinematically permissible along every side of the rock towers, excluding the not free northern side. Due to the increased scattering of joint orientations at the rock buttress, the analyzed joint intersections produce a wide range of intersection lines meeting the kinematic requirements for wedge failure, notably along intersection lines plunging toward the south. The increased data scattering is possibly related to the near-vertical columnar structure of the rock towers, providing an opportune geometry for long-term relaxation of the rock mass in the absence of lateral stresses.
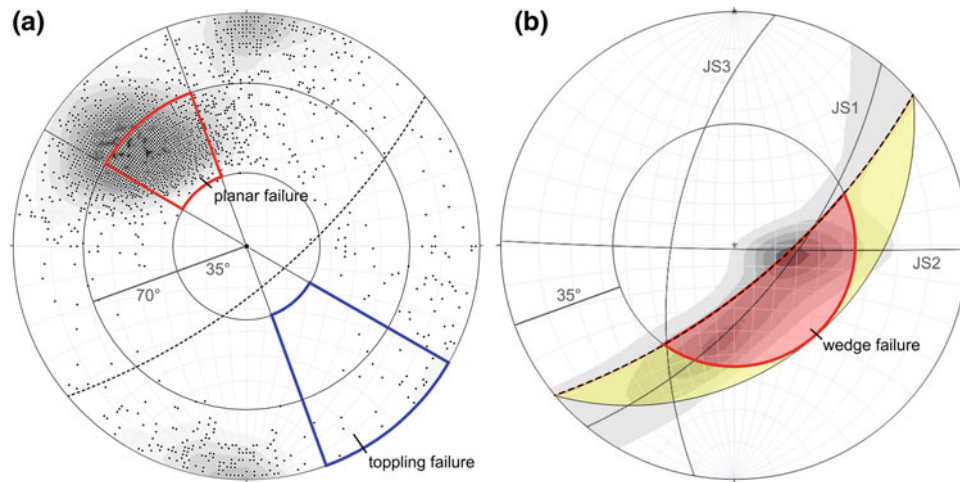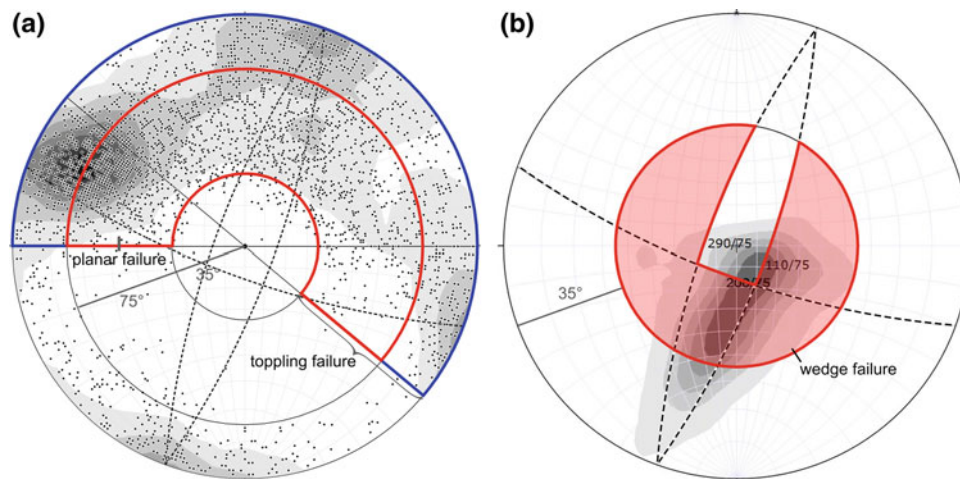
**Fig. 4** Kinematic analysis of southeastern cliff (equal angle, lower hemisphere stereographic projection of discontinuity poles): **a** structural elements susceptible to planar and toppling failure (inner circle: friction angle = 35°; intermediate circle: slope angle = 70°); and **b** density contour plot of 2,413,850 joint intersection lines, with red shaded domain indicating structural elements susceptible to wedge failure (inner circle: friction angle = 35°). Free slope surface is indicated as dashed great circle and mean joint orientations as grey great circles (JS1-3)



**Fig. 5** Kinematic analysis of rock buttress area (equal angle, lower hemisphere stereographic projection of discontinuity poles): **a** structural elements susceptible to planar and toppling failure (inner circle: friction angle = 35°; intermediate circle: slope angle = 75°); and **b** density contour plot of 4,618,676 joint intersection lines, with red shaded domain indicating structural elements susceptible to wedge failure (inner circle: friction angle = 35°). Free slope surfaces are indicated as dashed great circles

## 6 Conclusions

Compact portable drone platforms for UAV photogrammetry provide an unprecedented ability to capture high resolution 3D georeferenced structural geologic data. Considering the great efficiency with which data can be acquired, UAV–based survey methods are sure to see rapidly increasing deployment, particularly in alpine terrain where site access limitations and personnel safety concerns are significant.

The UAV workflow presented herein has been applied for rock fall source area analysis, and greatly facilitates identification of rock blocks that meet kinematic requirements for a variety of block detachment modes. A key step in the workflow involves extraction of discontinuity orientations from the 3D point cloud. For developing large data sets, efficiency becomes increasingly important, and automated or semi-automated point cloud orientation extraction tools are necessary. The plugins *Facets* and *Compass* developed for the open source software CloudCompare permit automated and semi-automated measurements, respectively, and

coincide well with data obtained from manual field measurements. As a result, three different oriented main joint sets were identified, and analyzed concerning potential block failure modes. The data sets obtained are sufficient for performing accurate structural geological analyses of inaccessible areas, and thus can substantially support ground-based geologic field surveys.

## References

Agisoft: Agisoft PhotoScan, http://www.agisoft.com/. Accessed 8 Oct 2017 (2017)

Allmendinger, R.C., Cardozo, N., Fisher, D.M.: Structural Geology Algorithms: Vectors and Tensors, 1. publ. Cambridge Univ. Press, Cambridge (2012)

Ampferer, O.: Studien über die Tektonik des Sonnwendgebirges, p. 58. Jahrbuch d. k. k. geol, Reichsanstalt (1908)

Barton, N.: The shear strength of rock and rock joints. Int. J. Rock Mech. Min. Sci. Geomech. Abstr. **13**, 255–279 (1976). https://doi.org/10.1016/0148-9062(76)90003-6

Cardozo, N., Allmendinger, R.W.: Spherical projections with OSXStereonet. Comput. Geosci. **51**, 193–205 (2013). https://doi.org/10.1016/j.cageo.2012.07.021

CloudCompare: CloudCompare, http://www.cloudcompare.org/. Accessed 8 Oct 2017 (2017)

Dewez, T.B., Girardeau-Montaut, D., Allanic, C., Rohmer, J.: Facets: a CloudCompare plugin to extract geological planes from unstructured 3D point clouds. Int. Arch. Photogramm. Remote Sens. Spatial Inf. Sci. **XLI-B5**, 799–804. https://doi.org/10.5194/isprsarchives-xli-b5-799-2016 (2016)

DJI: MAVIC SPECS, http://www.dji.com/mavic/info#specs. Accessed 8 Oct 2017 (2017)

Patzelt, G.: Die Bergstürze vom Pletzachkogel, Kramsach, Tirol. Jahrbuch der Geologischen Bundesanstalt: 25–38 (2012)

Rocscience Inc.: Dips, Toronto, https://www.rocscience.com/rocscience/products/dips (2018)

Schmid, S.M., Fuegenschuh, B., Kissling, E., Schuster, R.: Tectonic map and overall architecture of the Alpine orogen. Eclogae Geol. Helv. **97**, 93–117 (2004). https://doi.org/10.1007/s00015-004-1113-x

Thiele, S.T., Grose, L., Samsu, A., Micklethwaite, S., Vollgger, S.A., Cruden, A.R.: Rapid, semi-automatic fracture and contact mapping for point clouds, images and geophysical data. Solid Earth Discuss., 1–19. https://doi.org/10.5194/se-2017-83 (2017)

Wyllie, D.C., Mah, C.W., Hoek, E.: Rock slope engineering: civil and mining, 4th edn. Spon Press, London, New York (2004)

# Author Index